Stockholm University

The Beauty in Broken Symmetries

b-jet identification and searches for Supersymmetry, Dark Matter and multi-Higgs boson production with the ATLAS experiment

Laura Pereira Sánchez

Doctoral Thesis in Physics at Stockholm University, Sweden 2023

The Beauty in Broken Symmetries

b-jet identification and searches for Supersymmetry, Dark Matter and multi-Higgs boson production with the ATLAS experiment

Laura Pereira Sánchez

Academic dissertation for the Degree of Doctor of Philosophy in Physics at Stockholm University to be publicly defended on Friday 5 May 2023 at 13.00 in sal FR4, AlbaNova universitetscentrum, Roslagstullsbacken 21 and online via Zoom, public link is available at the department website.

Abstract

The Large Hadron Collider is the largest and most powerful accelerator in the world. Proton bunches are accelerated to 6.5 TeV inside the LHC ring in opposite directions and are then collided at four different points around the ring with an energy of 13 TeV. The ATLAS detector is a general purpose particle physics detector built around one of the collision points and is used to study the products of the high energy proton-proton collisions. The identification of jets containing *b*-hadrons (*b*-jets) is an important part of many physics analyses, including those presented in this thesis. The calibration of the *b*-jet identification algorithms is performed with data. The first paper of this thesis describes the method to calibrate the probability of a light jet to be mistakenly identified as a *b*-jet. The second paper presents a search for new phenomena in events with top quark pairs and large missing transverse energy. No evidence for physics beyond the Standard Model is found and the analysis is instead used to exclude various extensions of the Standard Model. The third paper describes the search for Higgs boson pair production in a final state with two photons and two *b*-jets and the fourth paper a novel Effective Field Theory interpretation of this search. Finally, a search for models with beyond the Standard Model Higgs bosons, *X* and S*,* in a final state with two photons and two *b*-jets is presented. The signal targeted by this search is the resonant production of an *X* boson that decays to an *S* and the Standard Model Higgs boson *H*. This search is under development and the results have not yet been published. All papers included in this thesis use data recorded by the ATLAS detector between 2015 and 2018, during the Run 2 of the Large Hadron Collider.

Keywords: *ATLAS, b-tagging, HH, mistag rate, BSM.*

Stockholm 2023
http://urn.kb.se/resolve?urn=urn:nbn:se:su:diva-215570

ISBN 978-91-8014-250-2
ISBN 978-91-8014-251-9

Department of Physics

Stockholm University, 106 91 Stockholm

Errata

- Page 3. The graviton has spin **2**.
- Page 10. The Higgs potential has a maximum at $\phi = 0$ and is "bound from **above**".
- Page 13. The coupling constant α_S for QCD **decreases with energy**.
- Page 26. The $x - y$ plane, also referred to as the **transverse** plane.
- Page 81. BSM diagrams in Figure **7.5**.

THE BEAUTY IN BROKEN SYMMETRIES

Laura Pereira Sánchez

Stockholm University

The Beauty in Broken Symmetries

b-jet identification and searches for Supersymmetry, Dark Matter and multi-Higgs boson production with the ATLAS experiment

Laura Pereira Sánchez

ISBN print 978-91-8014-250-2
ISBN PDF 978-91-8014-251-9

Cover illustration by Aishwarya Khoche

Printed in Sweden by Universitetsservice US-AB, Stockholm 2023

A mi familia que
siempre me ha apoyado

Abstract

The Large Hadron Collider is the largest and most powerful accelerator in the world. Proton bunches are accelerated to 6.5 TeV inside the LHC ring in opposite directions and are then collided at four different points around the ring with an energy of 13 TeV. The ATLAS detector is a general purpose particle physics detector built around one of the collision points and is used to study the products of the high energy proton-proton collisions. The identification of jets containing b-hadrons (b-jets) is an important part of many physics analyses, including those presented in this thesis. The calibration of the b-jet identification algorithms is performed with data. The first paper of this thesis describes the method to calibrate the probability of a light-flavour jet to be mistakenly identified as a b-jet. The second paper presents a search for new phenomena in events with top quark pairs and large missing transverse energy. No evidence for physics beyond the Standard Model is found and the analysis is instead used to exclude various extensions of the Standard Model. The third paper describes the search for Higgs boson pair production in a final state with two photons and two b-jets and the fourth paper a novel Effective Field Theory interpretation of this search. Finally, a search for models with beyond the Standard Model Higgs bosons, X and S, in a final state with two photons and two b-jets is presented. The signal targeted by this search is the resonant production of an X boson that decays to an S and the Standard Model Higgs boson H. This search is under development and the results have not yet been published. All papers included in this thesis use data recorded by the ATLAS detector between 2015 and 2018, during the Run 2 of the Large Hadron Collider.

Acknowledgments

Esta tesis es el resultado de cinco años de duro trabajo. No ha sido un camino fácil pero estoy feliz de haber escogido este sendero que tantas cosas buenas me ha traído. Quiero agradecer a mis padres que siempre me han apoyado. Me han dado confianza en mi misma y enseñado a volar. Sin vosotros no sería la persona que soy hoy ni habría llegado hasta aquí. Quiero agradecer también a mi hermano Yago, mi compañero de juegos. Tú me mantienes con los pies en la tierra y me recuerdas lo que es verdaderamente importante. A mis amigas, Clara y Nerea, gracias por seguir estando en mi vida a lo largo de los años y a pesar de la distáncia. Sois un tesoro. No pueden faltar palabras de agradecimiento para mi amor, Ajinkya. There are no words to describe how important you are to me and how much you have helped me during these five years. Thank you for taking care of me and making sure I don't skip a meal while writing this thesis, for always listening when I want to discuss my work and even giving me insightful suggestions about neural networks. More importantly, you have been my rock during the many hard times and have always found a way to make me laugh. This thesis is also yours.

I would like to express the deepest appreciation to my supervisor Sara Strandberg. She believed in me and gave me the tools to become the independent researcher I am today. Thank you for always being supportive on all of my projects, having the patience to explain the concepts I did not understand and providing detailed feedback on my scientific texts. I want to believe that your insightful comments have made me not only a better physicist but also a better writer. I would also like to thank my deputy supervisor, Olof Lundberg. It has been a pleasure working with you, from the long discussions about neural networks to your insightful comments on this thesis. This thesis would not have been possible without Sara and Olle's help and support.

The work presented in this thesis would also have not been possible without the work of the many physicists and engineers that have designed, built, and now run the Large Hadron Collider and the ATLAS experiment. I have so much to acknowledge to my colleagues at CERN for. Paper I is the result of several years of collaboration with the awesome people in the *b*-tagging group, a special thanks goes Andy Chisholm, Angela Burger, Laura Barranco, Bingxuan Liu and Dominik Duda. For my contribution in Paper II I want to thank the SUSY group, but in particular my supervisor Sara Strandberg, Christophe Clement, Patrawan Pasuwan and Stefio Yosse. Paper III is the result of the great work of many people in the amazing HDBS group, thank you for being so welcoming and organising the best social activities. For Paper IV, I want to give a special thanks to Christina Dimitriadi who started this work from scratch with me. Finally, Chapter 8 would have not been possible without the awesome SH analysis team and the support of the HH conveners. A special thanks goes to my co-analysis contact Elisabeth Petit, I learn so much from you.

To the members of the elementary particle physics group at Stockholm University, thank you for the fruitful discussions, fikas and fun times.

To Aishwarya, thank you for this beautiful cover. You have been able to illustrate the content of this thesis better than I could have ever dreamed of.

I also want to thank my bestie Vipin for feeding me more chai than I could ever return and my friends Ana, Vivek, Johanna, Kunal, Prim, Connor, Neeraj and Sree. You are my family here in Stockholm and a big reason why I am still sane despite a world pandemic and the Swedish winters. Thank you for always being there.

List of Papers

Paper I: ATLAS Collaboration. *Calibration of the light-flavour jet mistagging efficiency of the b-tagging algorithms with Z+jets events using 139 fb*$^{-1}$ *of ATLAS proton-proton collision data at* $\sqrt{s}$ *=13 TeV*, accepted for publication in the European Physical Journal C (EPJC), arXiv:2301.06319, 2023.

Paper II: ATLAS Collaboration. *Search for new phenomena with top quark pairs in final states with one lepton, jets, and missing transverse momentum in pp collisions at* $\sqrt{s} = 13$ *TeV with the ATLAS detector*, JHEP 04:174, 2021.

Paper III: ATLAS Collaboration. *Search for Higgs boson pair production in the two bottom quarks plus two photons final state in pp collisions at* $\sqrt{s} = 13$ *TeV with the ATLAS detector*, Phys. Rev. D, 106(5):052001, 2022.

Paper IV: ATLAS Collaboration. *HEFT interpretations of Higgs boson pair searches in* $b\bar{b}\gamma\gamma$ *and* $b\bar{b}\tau\tau$ *final states and of their combination in ATLAS*, ATL-PHYS-PUB-2022-019, 2022.

Preface

Symmetries play a crucial role in our Universe. The Standard Model of particle physics, a quantum field theory that describes the most fundamental forces and particles in the Universe, is built on symmetries. Emmy Noether was the first to realise the fundamental relation between the presence of a differentiable symmetry in a Lagrangian, and the conservation of a quantity. Her theorem describes the conservation of electric charge as the result of the symmetries of the electromagnetic Lagrangian, which make it invariant under gauge transformations.

If symmetries are the foundation of the Universe, it is the spontaneous breaking of a symmetry that makes it what we know today. It was only after a phase transition in the early Universe, referred to as spontaneous breaking of the electroweak symmetry, that most particles acquired mass and the Higgs boson was generated.

The Standard Model is a powerful theory that has been widely challenged by many precision tests and searches and which holds to an extremely impressive accuracy. But even with all its success the theory has some limitations.

Broken symmetries are also fundamental in theories for new physics beyond the Standard Model that try to describe some shortcomings of the Standard Model by predicting new particles. This is the case for supersymmetry, where a breaking of the supersymmetry at a high energy scale postulates heavy new particles that have yet to be observed. Furthermore, deviations in the electroweak symmetry breaking from that predicted by the phase transition in the Standard Model, could for example explain the matter-antimatter asymmetry in the Universe or predict additional Higgs bosons that could play a role in Cosmology.

Thesis Outline

This thesis describes different analyses of data from proton-proton collisions at a centre-of-mass energy of 13 TeV recorded by the ATLAS detector during the Run 2 of the Large Hadron Collider.

During the almost five years of my PhD, I have contributed to several searches for beyond the Standard Model physics, all of which contain *beauty* (or b-) quarks from the decay of Higgs bosons or top quarks. In particular I have contributed to a search for the supersymmetric partner of the top quark and two searches for beyond the Standard Model Higgs bosons. The nature of these beyond the Standard Model particles is strongly influenced by the *breaking* of the supersymmetry or electroweak *symmetry*, respectively. Therefore the title, *The Beauty in Broken Symmetries*, nicely encompasses the work that is presented in this thesis.

Chapter 1 gives an introduction to the theoretical concepts necessary to understand the thesis. The Standard Model of particle physics and its limitations are presented and some theories for new physics beyond the Standard Model are introduced. Chapter 2 describes the ATLAS detector and the Large Hadron Collider. Chapter 3 describes the analysis tools used in the data analyses presented in this thesis. Chapter 4 introduces the particle identification and object reconstruction techniques, which make it possible to identify the hits observed in the detectors as the particles or physics objects introduced in Chapter 1. Special focus is put on the reconstruction and identification of b-jets. Chapter 5 describes the mistag rate calibration, a correction to the rate at which light-flavour jets are misidentified as b-jets. This work is published in Paper I. Chapter 6 describes a search for supersymmetry and Dark Matter, published in Paper II. The search focuses on signatures with a pair of top quarks and missing transverse energy, compatible with the production of supersymmetric top-quark partners, in a final state with one charged lepton. Chapters 7 and 8 present searches for multiple Higgs bosons in a final state with two photons and two b-jets. Chapter 7 describes a search for non-resonant HH production, published in Paper III, and its interpretation in the Effective Field Theory framework, published in Paper IV. Chapter 8 presents a search for resonant multi-Higgs boson production that has not yet been published.

Author's Contribution

ATLAS is a complex experiment which is run by a collaboration of several thousand scientists and engineers. The collaboration takes joint responsibility for building, operating and upgrading the detector as well as analysing the data. Hence it is not possible for a single person to work on all the necessary steps that go into a scientific publication. I, the author of this thesis, have carried out the work described below.

Paper I [1]: I have been responsible for calibrating the light-flavour jet mistag rate of the b-tagging algorithms. These calibrations are used by all ATLAS publications based on the full Run 2 dataset that rely on b-tagging algorithms. I produced the samples, fits and results. Furthermore, I evaluated most systematic uncertainties except for the extrapolation and impact parameter uncertainties. I was also one of three editors of the paper.

Paper II [2]: I have contributed to the search for supersymmetry and Dark Matter in the final state with two jets, missing energy and one charged lepton. My work focused on defining the $t\bar{t}Z$ control region and calculating the systematic uncertainties that affect the $t\bar{t}Z$ background. I was also responsible for setting up the first version of the fitting framework used in part of the parameter space.

Paper III [3] and Paper IV [4]: My main contribution to the general search for $HH \to b\bar{b}\gamma\gamma$, described in Paper III, was setting up the signal re-weighting required to perform the κ_λ scans and improving the analysis framework. The Effective Field Theory interpretation of the $HH \to b\bar{b}\gamma\gamma$ search, described in Paper IV, was carried out by me in its entirety. I was also one of two editors of this publication. It is the first time that the Effective Field Theory framework has been used within the ATLAS collaboration to constrain beyond the Standard Model contributions to HH production. Moreover, I have been responsible for developing the strategy and delivering recommendations for all HH Effective Field Theory studies in ATLAS.

Chapter 8: I am one of two coordinators of the search for resonant multi-Higgs boson production in the $b\bar{b}\gamma\gamma$ final state. I am therefore responsible for over-seeing the full organisation of the analysis. Furthermore, I have developed the full analysis strategy based on a parametrised Neural Network, from designing and training the Neural Network to defining the signal and control regions and performing the statistical analysis.

Sammanfattning på Svenska

Large Hadron Collider är en partikelaccelerator belägen vid det europeiska kärnforskningscentret CERN utanför Genève. Det är den största och mest kraftfulla partikelaccelerator som någonsin konstruerats. I Large Hadron Collider kolliderar protoner med en masscentrumsenergi på 13 TeV, vid fyra olika detektorer som placerats runt acceleratorn. En av de detektorerna är ATLAS, som används för att studera produkterna från de högenergetiska protonkollisionerna. I denna avhandling presenteras ett antal studier som alla behandlar data insamlad med ATLAS under åren 2015-2018.

Att korrekt kunna identifiera hadronskurar, s.k. jets, som innehåller b-hadroner är en viktig del av många analyser av ATLAS-data, inklusive de som presenteras i denna avhandling. För att kalibrera de algoritmer som används för att identifiera dessa b-jets används data från kollisioner. Kapitel fem i denna avhandling beskriver en metod för att beräkna sannolikheten för att en jet som inte innehåller b-hadroner felaktigt identifieras som en b-jet, och presenterar resultaten av dessa beräkningar.

I kapitel sex presenteras en sökning efter ny fysik i kollisioner där det skapats par av toppkvarkar tillsammans med en stor mängd så kallad saknad transversell rörelsemängd (ett tecken på att det skapats partiklar som är osynliga för detektorn). Eftersom ny fysik bortom partikelfysikens standardmodell inte kan påvisas används analysen istället för att utesluta delar av det tillåtna parameterrummet för utvidgningar av Standardmodellen.

Kapitel sju innehåller en analys där parproduktion av Higgsbosoner studeras i den specifika sönderfallskanal där den ena Higgsbosonen sönderfaller till två b-kvarkar och den andra sönderfaller till två fotoner. Avhandlingen presenterar en tolkning av en sökning efter sådana händelser, här inom ramen för en effektiv fältteori. Resultatet är nya gränser för de tillåtna tvärsnitten för olika s.k. benchmark-modeller - detta är första gången som ATLAS-kollaborationen sätter sådana gränser.

Kapitel åtta beskriver en sökning efter fysikmodeller som innehåller flera Higgsbosoner utöver Standardmodellens enda. Denna sökning är specifikt inriktad på ett sluttillstånd med två fotoner och två b-jets. Signalen utgörs av en resonant produktion av en ny X-boson som sönderfaller till en S-boson och standardmodellens Higgsbosoner. I sökningen tränas ett s.k. parametriserat neuralt nätverk för att skilja bakgrundshändelser från signalhändelser. Detta är en fortsatt pågående analys och resultaten har ännu inte publicerats när denna avhandling går till tryck.

List of Abbreviations

2HDM Two-Higgs-Doublet Model

BDT Boosted Decision Tree

BSM Beyond the Standard Model

CERN European Organisation for Nuclear Research

CL Confidence Level

CR Control Region

DM Dark Matter

EFT Effective Field Theory

EM Electromagnetism/Electromagnetic

EW Electro-Weak

EWSB Electro-Weak Symmetry Breaking

FSR Final-State Radiation

HEFT Higgs Effective Field Theory

HLT High-Level Trigger

ID Inner Detector

IP Impact Parameter

ISR Initial-State Radiation

JER Jet Energy Resolution

JES Jet Energy Scale

L1 Level 1

LAr Liquid Argon

LHC Large Hadron Collider

LO Leading Order

LSP Lightest Supersymmetric Particle

MC Monte Carlo

ME Matrix Element

MS Muon Spectrometer

MSSM Minimal Supersymmetric Standard Model

NF Normalisation Factor

NLO Next-to-Leading Order

NN Neural Network

NP Nuisance Parameter

OP Operating Point

PDF Parton Distribution Function

PNN Parametrised Neural Network

PV Primary Vertex

QCD Quantum Chromodynamics

QED Quantum Electrodynamics

QFT Quantum Field Theory

SCT Semi-Conductor Tracker

SF Scale Factor

SM Standard Model

SMEFT Standard Model Effective Field Theory

SPS Super Proton Synchrotron

SR Signal Region

SSB Spontaneous Symmetry Breaking

SUSY Supersymmetry

SV Secondary Vertex

TF Transfer Factor

TRT Transition Radiation Tracker

UV Ultraviolet

VBF Vector Boson Fusion

ggF Gluon-Gluon Fusion

pflow Particle Flow

vev Vacuum Expectation Value

Contents

Part I

Comprehensive Summary

Chapter 1

Theoretical Overview

1.1. General Overview of the Standard Model of Particle Physics

The Standard Model (SM) of particle physics is a relativistic quantum field theory that describes most fundamental forces in the Universe and the way in which they make the matter particles and force carriers in the model interact. It was developed during the 20$^{\text{th}}$ century based on the concepts of symmetry and unification of the different fundamental forces of nature. This theory describes how the field carriers or quantas (*bosons*) of the electromagnetic, weak and strong forces interact with the matter particles ($fermions$) and each other. Gravity is the only known fundamental force that is not included in the SM.

Figure 1.1 summarises the fundamental particles that, together with their antimatter counterparts[1], make up the SM. Bosons have integer spin and follow Bose-Einstein statistics. The spin 1 bosons are field carriers of the different fundamental forces: 8 gluons for the strong nuclear force, the photon (γ) for the electromagnetic force, the $W^{+/-}$ and Z bosons for the weak force and, outside the SM, a theorised force carrier for the gravitational force; the graviton. The only scalar (spin 0) particle included in this theory is the Higgs boson, which is described in detail in Section 1.2.4. Fermions are half-integer spin particles that follow Fermi-Dirac statistics and hence Pauli's exclusion principle. All fundamental fermions have spin $= \frac{1}{2}$ and can be divided in two types: quarks and leptons. Quarks couple to the strong force and therefore cannot exist as free particles in nature but must instead combine to form hadrons (i.e.

[1] Antimatter particles have the same properties as their matter counterparts but opposite charge.

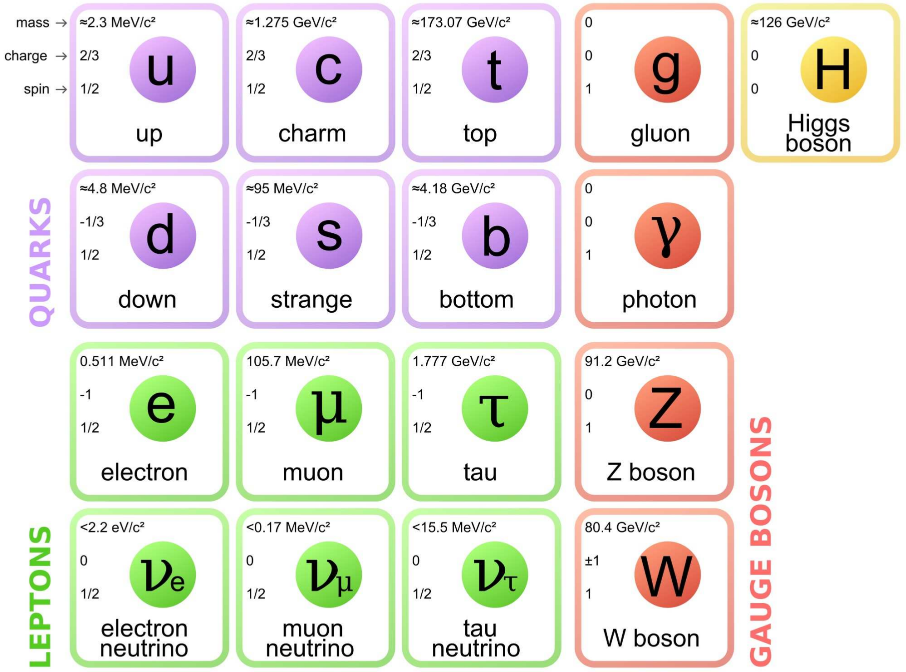

Figure 1.1.: Classification of particles in the Standard Model of particle physics [5].

protons and neutrons). On the contrary, leptons do not interact via the strong force and can therefore exist in isolation. Both quarks and leptons are divided in three generations that differ only by their masses. The first family contains the lightest particles that form every-day matter; up quarks, down quarks and electrons.

1.2. Building the Standard Model

The SM is a gauge quantum field theory (QFT) that contains the internal symmetries of the unitary group SU(3) $\times$ SU(2) $\times$ U(1) and describes the fundamental forces in nature with the exception of gravity. The Lagrangian follows a global Poincaré symmetry and hence its terms must be both gauge and Lorentz invariant. This means that translational and rotational symmetries, as well as the inertial reference frame invariance defined by special relativity must be fulfilled. The SM was developed over several years in many steps. This section presents the chronology of the pieces that had to be put together to build the theory we have today. More information on this topic can be found in [6], [7] and [8].

1.2.1. From Maxwell's Equations to QED

Quantum electrodynamics (QED) is the relativistic QFT that describes the interactions of the electromagnetic force at quantum level. These interactions can be described at the classical level through Maxwell's equations.

Even though a deep explanation of Maxwell's equations is beyond the scope of this thesis, it is important to notice that the first successful attempt to unify two interactions was achieved by Maxwell in 1865, when he proved that electricity and magnetism can be unified into a single theory involving a vector field interacting with charged particles. Maxwell's formulation was also the first field theory to introduce a gauge symmetry, even though the importance of it was unnoticed at the time. It was not until 1954 that gauge symmetry was generalised mathematically by Mills and Yang [9] in an attempt to describe strong nuclear forces. It later found an application in QFT and the unification of the weak and electromagnetic interactions.

Gauge Invariance in QED

The simplest example of global gauge invariance can be given for electromagnetism (EM). It can be proven that the Dirac Lagrangian (Equation 1.1), which describes the free fermionic fields $\Psi(x)$, is invariant under global U(1) transformations given by Equation 1.2, where Q is the electric charge and θ is a scalar constant.

$$\mathscr{L}_{\text{Dirac}} = \bar{\Psi(x)}(i\not{\partial} - m)\Psi(x) \tag{1.1}$$

$$\Psi(x) \rightarrow e^{iQ\theta}\Psi(x) \tag{1.2}$$

Noether's theorem [10] states that for every differentiable symmetry which leaves the Lagrangian of a physical system invariant, exists a corresponding conserved current. In the case of EM, global gauge invariance results in electric charge conservation.

EM is also invariant under local gauge transformations, where θ is no longer a constant but depends on the position $\theta(x)$. At first glance, if we try to apply local gauge invariance to Equation 1.1, we observe that the Lagrangian is not invariant under local transformations because the partial derivative of $\Psi(x)$ yields extra factors when $\theta(x)$ depends on the position. This can be solved by introducing a gauge vector field $A_\mu(x)$ (already used by Maxwell in his equations) and defining a new covariant derivative given by Equation 1.3, where e is a dimensionless numerical constant and $A_\mu(x)$ transforms as shown by Equation 1.4.

$$\partial_\mu \rightarrow D_\mu \equiv \partial_\mu - ieQA_\mu(x) \tag{1.3}$$

$$A_\mu(x) \rightarrow A_\mu(x) - \frac{1}{e}\partial_\mu\theta(x) \tag{1.4}$$

The addition of $A_\mu(x)$ (the photon field) and the new covariant derivative results in a transformation of the Dirac Lagrangian (Equation 1.1) to the QED Lagrangian given by

$$\mathscr{L}_{\text{QED}} = \bar{\Psi}(x)(i\not{D} - m)\Psi(x) - \frac{1}{4}F_{\mu\nu}F^{\mu\nu} =$$
$$\bar{\Psi}(x)(i\not{\partial} - m)\Psi(x) + e\bar{\Psi}(x)\gamma^{\mu}Q\Psi(x)A_{\mu}(x) - \frac{1}{4}F_{\mu\nu}F^{\mu\nu}. \tag{1.5}$$

The first term of the Lagrangian (Dirac term) describes the kinematics of free fermions. The second term, obtained from imposing local gauge invariance, describes the photon-fermion interactions. Furthermore, due to the addition of the vector field $A_{\mu}(x)$ in the interaction, a kinetic term for $A_{\mu}(x)$ needs to be added, this is given by the third term, where $F_{\mu\nu} \equiv \partial_{\mu}A_{\nu} - \partial_{\nu}A_{\mu}$. The kinematic term for $A_{\mu}(x)$ is invariant under U(1) local gauge transformations. A mass term for this vector, given by $m^2 A_{\mu}A^{\mu}(x)$, would however not fulfil the invariance. This imposes the photon to be massless.

1.2.2. Weak Interactions

The weak interaction was first described by Enrico Fermi in 1933 to explain beta decay as a direct interaction of four fermions [11]. Fermi's theory of the weak interaction can now be considered an Effective Field Theory (EFT) of the current theory for the weak interaction, where beta decay is mediated by a virtual W^- boson rather than a direct point-like interaction. This means that Fermi's theory is able to describe weak interactions at low energy, but the use of a more complex theory is needed to describe higher energy interactions. An important difference between EM and the weak interaction is that, unlike the photon, the $W^{+/-}$ bosons need to be massive. If $W^{+/-}$ bosons were massless they would be directly produced in nuclear decays mediated by the weak interaction, a process that has not been observed.

Weak interactions can partially be described as a Yang-Mills theory with an SU(2) symmetry of the so-called weak isospin. This symmetry is inspired by the strong isospin described in Section 1.2.5. It can be proven that the Dirac Lagrangian (Equation 1.1) is invariant under global isospin transformations similar to Equation 1.2 but with vectors instead of the scalar Q. The existence of weak neutral currents which are compatible with EM currents, required the development of a more complicated model which included both weak and electromagnetic interactions.

1.2.3. Weinberg-Salam Model

The theory of electromagnetic and weak interactions was developed by Glashow [12], Salam and Weinberg [13, 14] in the 1960s. It describes the two interactions as different low energy manifestations of a single electroweak (EW) interaction. At high energies, the EW interaction is described by a $SU(2)_L$ group of weak isospin, where the subscript indicates that the weak interaction only couples to left-handed fermions, and a $U(1)_Y$ group of weak hypercharge (Y). This symmetry is invariant under global gauge transformations but unlike QED, it runs into some problems when imposing local gauge invariance:

- Massive gauge bosons are forbidden by local gauge invariance. This was also the case for the photon field A_μ in QED but, as described in Section 1.2.2, the $W^{+/-}$ bosons mediating the weak interaction were already known to be massive.
- Due to left- and right-handed particles behaving differently under weak isospin rotations, a mass term for fermions which would be invariant in QED is not invariant in the EW theory.
- The EW theory is not renormalizable, meaning that it suffers from divergencies (infinities) that forbid calculations. The divergencies appear e.g. in the calculations of some production cross sections (σ) that are proportional to the energy squared, such as $\sigma(WW \rightarrow ZZ)$.

1.2.4. Electroweak Spontaneous Symmetry Breaking

The problems described can be solved by introducing a new field with a potential that keeps the Lagrangian invariant under local $SU(2)_L \times U(1)$ transformations but makes the vacuum not invariant. This method is known as spontaneous symmetry breaking (SSB).

The idea to explore SSB stems from condensed matter physics, where it had already been successfully used to explain superconductivity as the formation of a charged Bose-Einstein condensate that breaks the global U(1) symmetry. The superconductivity theory of 1957, named BCS after its authors [15], has many similarities with the EW symmetry breaking (EWSB) described by R. Brout, F. Englert [16] and P. Higgs [17] in 1964, which is referred to as the Higgs or BEH mechanism.

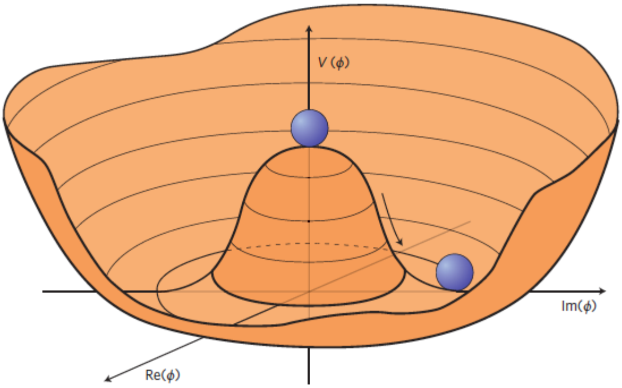

Figure 1.2.: Illustration of the Higgs potential with $\mu^2 < 0$. [18]

A good way to visualise SSB is to imagine a pencil standing on its tip. At this position it is in a rotationally invariant state with respect to the z-axis along which the pencil stands, however it is also in a very unstable position. When the pencil drops to one side, it goes to a stable ground state, but the symmetry is spontaneously broken. Such a system can be described by the "Mexican-hat" shaped potential shown in Figure 1.2, where the potential is rotationally invariant, i.e. has a local maximum at $\phi = 0$ and a ring-shaped minimum at $\phi \neq 0$. The state at $\phi = 0$ is unstable, and the system will spontaneously transition to the ground state and thereby acquire a non-vanishing vacuum expectation value (vev) since the field ϕ is non-zero at the minimum.

The BEH or Higgs mechanism introduces a scalar field ϕ in the form of a complex doublet of the weak isospin SU(2) symmetry described by Equation 1.6. This field needs to have a potential $V(\phi)$ given by Equation 1.7 that will break the symmetry spontaneously.

$$\phi = \begin{pmatrix} \phi^+ \\ \phi^0 \end{pmatrix} = \frac{1}{\sqrt{2}} \begin{pmatrix} \phi_1 + i\phi_2 \\ \phi_3 + i\phi_4 \end{pmatrix} \tag{1.6}$$

$$V(\phi) = \mu^2(\phi^\dagger\phi) + \lambda(\phi^\dagger\phi)^2 \tag{1.7}$$

For the potential to have the shape shown in Figure 1.2 and SSB to occur, μ^2 must be negative and λ must be positive. If μ^2 would be positive, the potential would have a minimum at $\phi = 0$ and the symmetry would be conserved. On the other hand, if both μ^2 and λ were negative, the potential would have a maximum at $\phi = 0$ and be "bound from below", resulting in all symmetries being broken. The Lagrangian of the new scalar field is therefore given by Equation 1.8, where D_μ is the covariant derivative associated to $\mathrm{SU(2)_L} \times \mathrm{U(1)_Y}$.

$$\mathscr{L} = (D^\mu \phi)^\dagger (D_\mu \phi) - V(\phi) \tag{1.8}$$

If we focus on one of the components of the scalar doublet ϕ, for example the second, we can see that there is an infinite number of vacuum states that satisfy

$$v = \sqrt{\phi_3^2 + \phi_4^2} = \sqrt{\frac{-\mu^2}{\lambda}} \tag{1.9}$$

By convention the vacuum state corresponding to $\phi_3 = v$ and $\phi_4 = 0$ is chosen.The vacuum ϕ_0 of the full doublet is chosen as $\phi_1 = \phi_2 = \phi_4$ and $\phi_3 = v$.

Spontaneous Symmetry Breaking of a Global Gauge Symmetry: the Goldstone Theorem

It is instructive to focus on the second component of ϕ to describe the breaking of a global symmetry in a more comprehensive way. Dropping the covariant derivative terms not needed for the global gauge invariance, the Lagrangian of the scalar field ϕ can be written in terms of $\phi_3 = v$ and $\phi_4 = 0$ as

$$\mathscr{L}(\phi_3, \phi_4) = \frac{1}{2}(\partial\phi_3)^2 + \frac{1}{2}(\partial\phi_4)^2 + \frac{1}{2}\mu^2(\phi_3^2 + \phi_4^2) - \frac{1}{4}\lambda(\phi_3^2 + \phi_4^2). \tag{1.10}$$

The first two terms describe the kinematics of the field components, the third is a mass term and the fourth a self-interaction term.

To study perturbations around the minimum, shifted fields $\eta = \phi_3 - v$ and $\xi = \phi_4$ are introduced, leading to the new field definition

$$\phi_0 = \frac{1}{\sqrt{2}}(\eta + v + i\xi) \tag{1.11}$$

Equation 1.11 can be used to re-write the Lagrangian given by Equation 1.10 in terms of the shifted fields:

$$\mathscr{L}(\eta,\xi) = \frac{1}{2}(\partial\eta)^2 - (\lambda v^2)\eta^2 + \frac{1}{2}(\partial\xi)^2 + 0\cdot\xi^2 + \text{higher order terms} \quad (1.12)$$

From Equation 1.12 two particles can be identified, a massless ξ and a massive η with mass $m_\eta = \sqrt{2\lambda v^2} = \sqrt{-2\mu^2} > 0$.

The Goldstone theorem is key in the EWSB. It states that massless scalars (also called Goldstone bosons) occur whenever a continuous symmetry is not present in the ground state. If a Lagrangian with a degenerate ground state is invariant under global gauge transformations, and hence the symmetry has been spontaneously broken acquiring a vev, then for every generator of the symmetry not leaving the vev of the field invariant, a massless boson exists. For the simplified case described above a Goldstone boson ξ and a massive scalar η are produced due to the SSB.

For the case of a $\mathrm{SU(2)_L} \times \mathrm{U(1)_Y}$ symmetry, where the full ϕ doublet should be used, there are four original generators, three for the weak isospin (τ_1,τ_2,τ_3) and one for Y. Apparently all four generators are broken by the SSB, however it can be proven that the combination $\tau_3 - Y = Q$ remains invariant. Thus electric charge (Q) remains a conserved quantity and the SSB results in only three massless Goldstone bosons.

Spontaneous Symmetry Breaking of a Local Gauge Symmetry: Higgs Mechanism

If a similar process described for global gauge invariance is applied to a local gauge, using covariant derivatives and introducing gauge fields, new terms containing $(\partial^\mu\xi)$ will appear in $\mathscr{L}(\eta,\xi)$. These terms can be re-written by choosing the so-called unitary gauge, which corresponds to defining the phase $\alpha(x)$ from the local gauge transformations as $\alpha = -\xi/v$ to remove all terms involving the ξ field. Choosing this gauge also transforms the scalar field ϕ_0

$$\phi_0 \to e^{-i\xi/v}\phi_0 = e^{-i\xi/v}\frac{1}{\sqrt{2}}(v+\eta+i\xi) = \frac{1}{\sqrt{2}}(v+h) \quad (1.13)$$

where a real scalar field h has been introduced. The scalar doublet ϕ then becomes:

$$\phi = \frac{1}{\sqrt{2}}\begin{pmatrix} 0 \\ v+h \end{pmatrix} \tag{1.14}$$

It has already been stated that global EW SSB results in three Goldstone bosons due to the fact that only electric charge is conserved in the symmetry breaking. Furthermore, in local EW SSB, four gauge fields (W_1, W_2, W_3, B) are generated, which will mix to produce the three massive weak bosons $W^{+/-}$, Z and the massless QED gauge boson γ. The remaining degree of freedom is used to give mass to the Higgs field h.

SSB has allowed us to maintain local gauge invariance in the EW Lagrangian, at the expense of adding the Higgs field and spontaneously breaking its potential. This does not only solve the massive weak boson problem but also the renormalisability of the EW Lagrangian by making it local gauge invariant. Furthermore fermions can acquire mass by interacting with the Higgs field, resulting in a fermion-mass term:

$$\mathscr{L}_{\text{fermion-mass}} = -\lambda_f[\bar{\Psi}_L\phi\Psi_R + \bar{\Psi}_R\bar{\phi}\Psi_L] \tag{1.15}$$

The Weinberg-Salam model with EWSB results in the $\mathrm{SU(2)_L \times U(1)_Y}$ part of the SM symmetry and fully describes EM and weak interactions.

1.2.5. The Strong Interaction

The strong interaction is responsible for the stability of the atomic nucleus and is described by Quantum Chromodynamics (QCD). The first steps towards this theory came from the observed similarities between neutrons and protons. In 1932, Heisenberg [19] introduced the concept of (strong) isospin to explain symmetries between the two particles which have very similar masses. Isospin allows to rotate the neutron into a proton by treating both particles as different states of the same object: the nucleon.

In 1961, Murray Gell-Mann [20] and Yuval Ne'eman [21] independently generalised the (strong) isospin symmetry with an octet or SU(3) symmetry. Colour was first introduced by Greenberg [22] in 1964 to account for the apparent violation of the Pauli exclusion principle for certain hadrons. He suggested the existence of an extra degree of freedom which differentiated quarks. He postulated the existence of three colours and that free particles need to be colour singlets. In 1973, the concept of colour as a symmetry, analogous to QED, was developed by Murray Gell-Mann and Harald Fritzsch [23]. In QCD, global gauge invariance of the SU(3) symmetry implies the conservation of colour and local gauge invariance implies the existence of eight massless gauge bosons, the gluons. The QCD Lagrangian is given by

$$\mathscr{L}_{\mathrm{QCD}} = \bar{\Psi}_i(x)(i\not{D}_{\mu,ij} - m\delta_{ij})\Psi_j(x) - \frac{1}{4}G^a_{\mu\nu}G^{\mu\nu}_a, \tag{1.16}$$

where $\Psi_i(x)$ is the quark field, D_μ the covariant derivative and $G^a_{\mu\nu}$ the gluon field strength tensor, analogous to $F_{\mu\nu}$ in QED.

In 1973, David J. Gross, Frank Wilczek [24] and David Politzer [25] discovered asymptotic freedom while evaluating effects of vacuum polarisation in QCD. Vacuum polarisation exists for both QED and QCD, however, the fact that gluons themselves carry colour charge in contrast to the photon which is electrically neutral has very important consequences for quark-gluon interactions. Gross, Wilczek and Politzer independently found that virtual gluons tend to stick to quarks generating a charge that grows with the distance. Contrary to QED, the strength of the coupling constant α_s for QCD is inversely proportional to energy, resulting in an asymptotic freedom behaviour at high energy (small distances), where the coupling becomes negligible and quarks and gluons can move like free particles. On the other hand, at low energies (large distances), the coupling becomes very large and perturbative treatment is no longer valid. It is at these distances that the process of hadronisation takes place. Hadronisation is the process of formation of colour-less hadrons out of quarks and gluons which, due to the colour confinement characteristic of QCD, cannot exist as isolated particles. A consequence of hadronisation is the formation of jets, objects that will be extensively studied in this thesis.

1.2.6. The Standard Model: Piecing it all Together

The combination of the EW $\mathrm{SU(2)_L \times U(1)_Y}$ and QCD SU(3) Lagrangians form the full Lagrangian of the SM of particle physics. The final confirmation of the validity of the Standard Model arrived in 2012 when the

ATLAS and CMS experiments announced independent observations of a particle with a mass of 125 GeV compatible with the Higgs boson [26], [27], the last missing piece of the model. This discovery earned François Englert and Peter Higgs the Nobel Prize in Physics in 2013 for their theoretical prediction.

Some models suggest that analogous to the EM and weak interactions being described by the same interaction at higher energies, the strong interaction could also be unified with the other fundamental forces, resulting in a grand unified theory [28]. Maybe with time one could even include gravity and therefore complete the very ambitious goal to formulate a "theory of everything".

1.3. Shortcomings of the Standard Model

The Standard Model is a powerful theory that has been widely challenged by many precision tests and searches and which holds to an extremely impressive accuracy. But even with all its success the theory has some limitations.

Perhaps the most obvious shortcoming is that gravity is not included in the SM. For this reason, the SM is only valid up to the so-called Planck scale $\sim 10^{19}$ GeV, where gravity is expected to become as strong as the other forces. Some extensions of the SM include the graviton, the gauge boson postulated to mediate gravity, but such a particle has not been observed experimentally.

The SM describes neutrinos as neutral, massless particles which only interact weakly. They were predicted by Pauli to appear in beta decays which are governed by the weak interaction, and therefore only left-handed neutrinos are predicted. There is however a strong observational evidence for neutrino oscillations from several experiments including SNO and Super-Kamiokande [29] [30]. Neutrino oscillations are quantum mechanical phenomena which occur when a neutrino originally created with a specific lepton flavour e.g ν_μ is later measured to have a different flavour e.g. ν_τ. For this process to occur, neutrinos must have mass since the transition probabilities depend on the squared mass differences between the neutrino mass eigenstates.

The current Standard Model of Cosmology assumes that our Universe originated from a hot, compressed state also known as "Big Bang". Experimental evidence suggest that the Universe is composed of about 68%

dark energy, 27% Dark Matter (DM) and 5% ordinary matter. The SM of particle physics only describes the 5% of ordinary matter. DM was first suggested in 1933 by Fritz Zwicky to explain a discrepancy in the velocity dispersion of some galaxy clusters [31]. He suggested that there must be some mass in the systems which emits no EM radiation and is therefore invisible to us, hence the name DM. At the Large Hadron Collider (LHC) several analyses search for DM particles, one such search is presented in Chapter 6.

The SM predicts matter and antimatter to be produced in equal amounts, and that matter and antimatter particles annihilate each other if they interact. Therefore one would expect the Universe to be composed of the same amount of matter and antimatter. However most of our Universe is made of matter so one must wonder, where did all the antimatter go? An asymmetry in charge and parity, known as CP violation, is one of the necessary conditions for a matter-antimatter asymmetry to arise, but it is only present in the SM in very small amounts and hence cannot explain the asymmetry observed in the Universe.

A problem of a different kind is the so-called naturalness problem. In the SM, the mass of the Higgs boson is not stable under radiative corrections since it is not protected by a symmetry. Therefore particles coupling to the Higgs boson induce large loop corrections, making the Higgs mass quadratically dependent on the energy cut-off of the theory. For the theory to be completely natural, a beyond the SM (BSM) extension with new physics around or below the TeV scale would be needed. A more comprehensive description of the naturalness problem and possible solutions can be found in [32].

1.4. Extensions Beyond the Standard Model

There are many theories that try to solve some of the shortcomings described above while maintaining the carefully tested predictions by the SM. BSM theories can be divided in two groups, models which are ultraviolet (UV) complete, i.e. valid up to an arbitrarily high energy scale, and EFTs, which are valid only up to a specific energy scale or cutoff (Λ).

Perhaps the most famous UV-complete extension of the SM is Supersymmetry (SUSY) [33], for which there were great experimental expectations during the first run of the LHC. No observations of SUSY particles have been claimed so far, however SUSY is still being tested because there are many regions of the parameter space where realisations of this theory could be hiding. There are other extensions of the SM, which will not be explained in detail in this thesis, like composite Higgs models [34] or Two-Higgs-Doublet models (2HDM) [35] which also reproduce the already tested physics of the SM, but predict some new phenomena that are being searched for experimentally.

EFTs are low-energy approximations of more complex UV-complete theories. They are characterised by including only the strictly necessary degrees of freedom, while additional substructure and higher degrees of freedom needed to describe processes at higher energies are ignored. An example of an EFT was already introduced in Section 1.2.2. Fermi's theory was able to describe the weak interaction at low energies, but the full electroweak theory is needed to describe the interactions with the $W^{\pm}$ and Z bosons at the energies that we reach today at the LHC. In a similar sense, the SM can also be considered an EFT of a more complete theory which should ideally explain the shortcomings described in Section 1.3. EFTs therefore present an alternative way to approach BSM physics and complement theories like SUSY.

1.4.1. Supersymmetry

SUSY is one of the most tested BSM theories at the LHC. It solves the naturalness problem by adding an extra symmetry that protects the Higgs mass. SUSY introduces a fermion-boson symmetry, where each SM boson has a fermionic BSM partner and vice versa. This symmetry thus results in at least twice as many particles. The new bosonic particles are named by the prefix "s" and the fermionic partners by the suffix "ino". The supersymmetric partner of the top quark is hence a boson, called stop. The minimal supersymmetric extension of the Standard Model (MSSM) [36] requires, other than the already described particles, two Higgs-doublets instead of one.

The new fermion-boson symmetry, can also make the coupling constants of the different forces unify, i.e. become of the same strength, at a certain energy scale. In the MSSM one can naturally get the unification of all three couplings at an energy of 2×10^{16} GeV. In contrast, for the SM case the gauge coupling strengths become comparable but do not fully coincide at an energy of $\sim 10^{14}$ GeV.

The biggest drawback of a theory like SUSY is that it predicts many new particles that in principle should have masses similar to the SM particles but which have never been detected. To account for this, there must be a breaking of the fermion-boson symmetry, similar to what occurs in the SM for the Higgs mechanism. The fermion-boson symmetry would break at a scale higher than the EW, resulting in much higher masses for the supersymmetric particles compared to the SM counterparts. It should be noticed that to keep SUSY natural, the energy of the SUSY breaking and hence the masses of the new particles cannot be much higher than the TeV scale.

Last but not least, the most relevant characteristic of SUSY for the scope of this thesis is R-parity conservation. Baryon and lepton number conservation is a characteristic of the SM that has been throughly tested experimentally to high precision. In the MSSM however, these quantities are no longer conserved, so R-parity needs to be introduced in order not to conflict with experimental data. Due to this characteristic, SUSY particles cannot decay uniquely to SM particles or vice-versa. The lightest supersymmetric particle (LSP), which should be neutral, cannot decay to other SUSY particles since it is the lightest and R-parity conservation forbids its decay to SM particles. This makes it stable and a great candidate for DM. Chapter 6 presents a search for supersymmetry and DM in a final state with jets, one charged lepton and missing transverse energy.

1.4.2. Effective Field Theories

Assuming that the SM is only valid up to a scale Λ, a valid theory above Λ needs to fulfull the following requirements:

- Its gauge group should contain the $\mathrm{SU}(3)_\mathrm{C} \times \mathrm{SU}(2)_\mathrm{L} \times \mathrm{U}(1)_\mathrm{Y}$ symmetry of the SM.
- All the SM degrees of freedom should be incorporated as fundamental or composite fields.
- At low energies, it should reduce to the SM.

In most BSM theories, the reduction to the SM at low energies proceeds via decoupling of heavy particles with mass of order Λ or larger. This was the case of the weak bosons and Fermi's theory. Hence an extension of the SM, which is characterised by having dimension 4 operators, leads to the appearance of higher-dimension operators in the SM Lagrangian that are suppressed by powers of Λ. An EFT extension to the SM can be described by

$$\mathscr{L}_{\mathrm{SM}} = \mathscr{L}_{\mathrm{SM}}^{(4)} + \frac{1}{\Lambda}\sum_k C_k^{(5)} Q_k^{(5)} + \frac{1}{\Lambda^2}\sum_k C_k^{(6)} Q_k^{(6)} + \mathscr{O}(\frac{1}{\Lambda^3}) + ... \quad (1.17)$$

where $Q^{(i)}$ are the dimension i operators and $C^{(i)}$ are the corresponding Wilson coefficients which can be determined by integrating out the heavy fields. It should be noted that from all possible dimension 5 operators, only one fulfils the SM gauge symmetry constraints, namely $Q_{\nu\nu}$ which generates neutrino masses and mixings solving one of the described shortcomings of the SM. For this reason, further EFT extensions to the SM consider mostly dimension 6 operators [37], which are expected to dominate over operators of even higher dimensions.

1.4.3. Effects of BSM Physics on the Higgs Potential

As already described in Section 1.2.4, the SM predicts the existence of the so-called Higgs field ϕ with a potential $V(\phi)$. In the early Universe $V(\phi)$ had a minimum at $\phi = 0$ and all particles were massless, but a few picoseconds after the Big Bang the Universe underwent a phase transition to a new ground state where $\phi \neq 0$. Due to this phase transition, also known as SSB, a massive scalar boson known as the Higgs boson (H) was generated and most particles acquired mass.

Beyond the mass-generation mechanism, the shape of the Higgs potential has implications in cosmology where it determines the stability of our Universe [38]. According to current constraints on the top quark and Higgs boson masses, we could live in a metastable Universe if the minimum reached after SSB is not the true minimum. In the SM, the SSB occurs in a smooth way with a second-order transition, however a strong first-order transition could also have occurred. A first-order transition could explain the matter-antimatter asymmetry in the Universe. Several BSM models predict such a transition and the existence of an extended Higgs sector which could include the cosmological inflaton as an additional scalar to the Higgs boson. Furthermore, the Higgs boson could be a portal to a dark sector under the reasonable assumption that DM, like visible matter, obtains its mass by interacting with the Higgs field [39]. These different scenarios would have an effect on the shape of the Higgs potential.

In the SM, the Higgs potential, after the transformation given in Equation 1.14, is defined as

$$V(h) = \frac{1}{2}m_H^2 h^2 + \lambda_3 \nu h^3 + O(h^4). \tag{1.18}$$

The first term is determined by the Higgs mass $(m_H) \sim 125$ GeV, a value which was only found experimentally when the Higgs boson was observed. The second term is given by the triple Higgs self-interaction (λ_3), which has never been measured experimentally. Measuring this coupling is crucial to understand whether the shape of the potential is compatible with the SM predictions or if BSM physics is needed to explain the measured shape.

Given the current sensitivity to λ_3, and lack of sensitivity to higher order self-interactions, variations of the shape of the Higgs potential from the SM prediction are still compatible with experimental constraints as shown in Figure 1.3. The red line indicates the predicted shape of the potential by the SM. The blue line shows an alternative potential which is compatible with the current experimental knowledge obtained from the measured m_H and the current constraints on λ_3. Deviations in the SM prediction could arise from the existence of new particles not predicted in the SM.

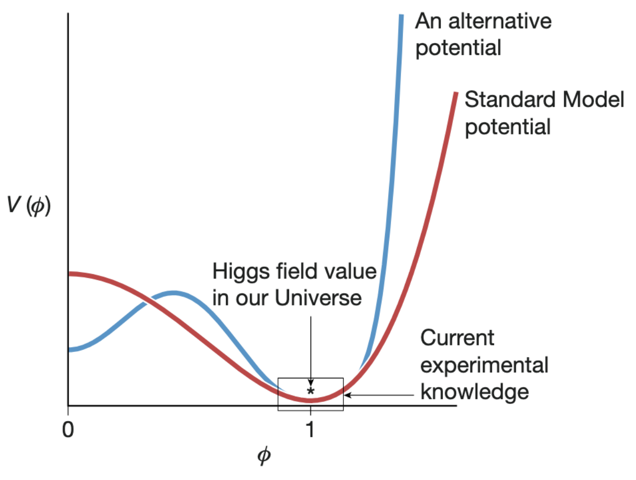

Figure 1.3.: Shape of the Higgs field potential $V(\phi)$ in the SM (red) and alternative possible shape also allowed by current experimental constraints (blue) [38].

Because of the unknown mass of the hypothetical new particles complementary search strategies need to be pursued. If the BSM particles are heavy and cannot be produced at the LHC energies, EFT frameworks can be used to search for them. Light BSM particles that could be produced at the LHC energies can instead be targeted by dedicated searches. Both approaches are studied in this thesis. Chapter 7 presents the EFT interpretation of a search for non-resonant Higgs pair production. Chapter 8 presents a search for resonant multi-Higgs boson production. Both searches are performed in a final state with two jets and two photons.

Chapter 2

Experimental Overview

2.1. The Large Hadron Collider

The LHC is a circular accelerator where proton bunches are collided at unprecedentedly high energies. It is located at the European Organisation for Nuclear Research (CERN) in Geneva, Switzerland. The tunnel housing the LHC has a circumference of 27 km and was previously used to collide electron and positron bunches at the Large Electron-Positron Collider from 1989 to 2000.

Protons are generated from hydrogen gas by ionisation: An electric field is applied to strip the electrons from the hydrogen atoms yielding protons. A set of accelerators (shown in Figure 2.1) is used to accelerate the protons until they are injected into the LHC where they are brought to collide. Protons are first accelerated to 50 MeV using the Linac 2 linear accelerator. Then the proton beam is injected into the ring of the Proton Synchrotron Booster that accelerates the protons to 1.4 GeV. The proton beam is accelerated further to 25 GeV by the Proton Synchrotron before it is injected into the Super Proton Synchrotron (SPS), where it is accelerated to 450 GeV in a last step before being transferred to the LHC ring.

The LHC is composed of two different beam pipes where proton bunches circulate until they are ready to be collided. Protons from the SPS are injected in the two beam pipes of the LHC in opposite directions and a set of radio-frequency cavities and magnets are used to accelerate and focus the proton bunches. Once the required energy per beam is reached, the proton bunches are collided in four interaction points housing different detectors. The proton-proton (pp) collisions recorded by the ATLAS detector during the Run 2 of the LHC, which are analysed in this thesis,

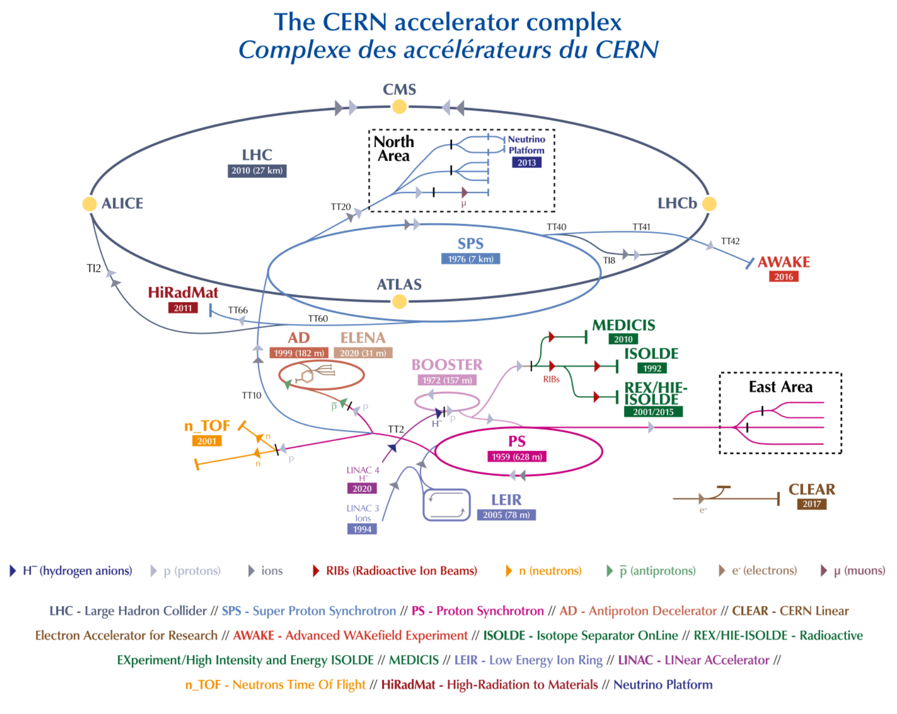

Figure 2.1.: The CERN accelerator complex [40].

have a centre-of-mass energy $\sqrt{s} = 13$ TeV. The LHC can also be used to collide heavy ions (e.g. Pb-Pb) or to collide protons with heavy ions (e.g. p-Pb). The collision energy for heavy-ion collisions can vary but is often set to 5.02 TeV.

Four different experiments are located at the LHC interaction points; ATLAS, CMS, LHCb and ALICE. The first two are general-purpose detectors. They were designed mainly to discover or rule out the existence of the Higgs boson but also pursue a wide program of measurements of SM observables and searches for BSM physics. LHCb is a smaller asymmetrical detector specialised in flavour physics and ALICE is a heavy ion detector that studies the heavy-ion collisions, for instance the formation of quark-gluon plasma.

2.1.1. Luminosity

An accurate measurement of the amount of pp collisions in the LHC is crucial to draw clear conclusions from the experimental results. The predicted number of events of a certain physics process, i.e. $pp \to X$, can be obtained as

$$N_{\text{events}}(pp \to X) = \int_{t_0}^{t_1} \mathscr{L}(t)dt \times \sigma(pp \to X) = \mathscr{L}_{\text{int}} \times \sigma(pp \to X), \tag{2.1}$$

where the production cross section $\sigma(pp \to X)$ is related to the likelihood of producing X in the pp collision and the instantaneous luminosity $\mathscr{L}$ is related to the rate of pp collisions. The instantaneous luminosity can be integrated over time to give the integrated luminosity $\mathscr{L}_{\text{int}}$, which is related to the total number of pp collisions in a certain interval. The integrated luminosity is measured in *inverse barn* (b^{-1}), where $1\text{b} = 10^{-28}\text{m}^2$.

The searches presented in this thesis are performed using data collected during the Run 2 of the LHC by the ATLAS detector. Figure 2.2 shows the integrated luminosity delivered by the LHC (green), recorded by the ATLAS detector (yellow) and certified to be good quality data (blue) during stable beams for pp collisions at $\sqrt{s} = 13$ TeV between 2015–2018. The total integrated luminosity that is valid for physics is 139 fb^{-1}. The integrated luminosity differs between years. The LHC achieved its highest peak luminosity for Run 2 $\mathscr{L} = 21.0 \times 10^{33}\ \text{cm}^{-2}\text{s}^{-1}$ in 2018.

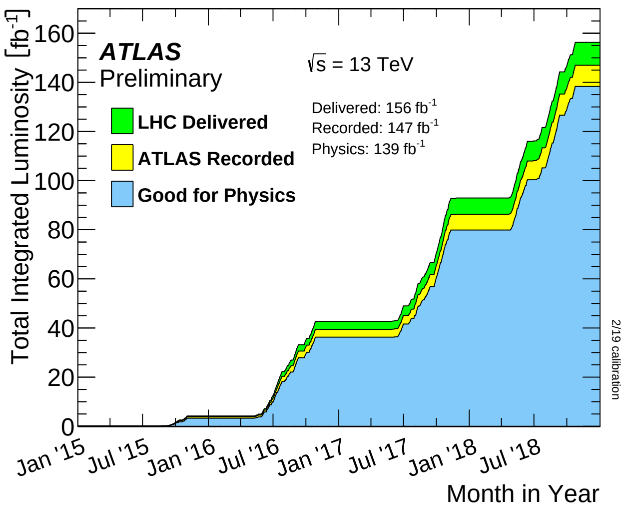

Figure 2.2.: Overall integrated luminosity delivered by the LHC (green), recorded by the ATLAS detector (yellow) and certified to be good quality data (blue) during stable beams for *pp* collisions at $\sqrt{s} = 13$ TeV during the Run 2 of the LHC [42].

The analysis presented in Chapter 8 of this thesis uses the most recent luminosity calibration, for which the integrated luminosity of the Run 2 dataset is 140 fb^{-1} and the uncertainty is significantly reduced [41].

2.1.2. Pileup

At the LHC, the number of interactions per bunch crossing μ is usually larger than 1 and the main high energy collision or hard scattering that is interesting for physics needs to be separated from the additional softer un-interesting interactions, referred to as *pileup*. This is due to the fact that multiple protons are collided in each bunch crossing. The average number of interactions per bunch crossing $\langle\mu\rangle$ recorded by ATLAS during the individual years that make up the Run2 weighted by the integrated luminosity is shown in Figure 2.3.

The instantaneous luminosity is given by the sum of the luminosity per bunch crossing $\mathscr{L}_b$ over all colliding bunches n_b

$$\mathscr{L} = \sum_{b=1}^{n_b} \mathscr{L}_b = n_b \frac{\langle\mu\rangle f_r}{\sigma_{\text{inel}}}, \tag{2.2}$$

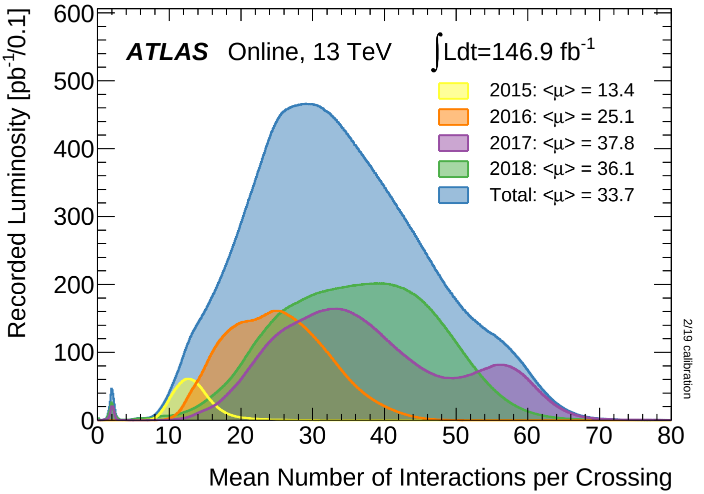

Figure 2.3.: Average number of interactions per bunch crossing weighted by the integrated luminosity for the individual years in the Run 2 of the LHC as well as for the entire period [42].

where f_r the revolution frequency of the bunches, and σ_{inel} is the cross section of the inelastic pp collision.

2.2. The ATLAS Experiment

ATLAS stands for A Toroidal LHC ApparatuS, and is a massive detector shown in Figure 2.4 located 100 meters underground. It is a cylindrical-shaped experiment with a diameter of 25 meters, a length of 44 meters and a mass of 7000 tons.

The ATLAS collaboration comprises over 5000 members and almost 3000 scientific authors from around the world that work together to build, upgrade and operate the detector and analyse its data.

The proton beams travel along the axis of the cylinder and collide in the middle of the detector. The experiment is built up of several subdetector systems around the collision point to detect the different particles produced in the collisions. The different detecting technologies used in each subdetector allow to reconstruct the charge, momentum, energy and

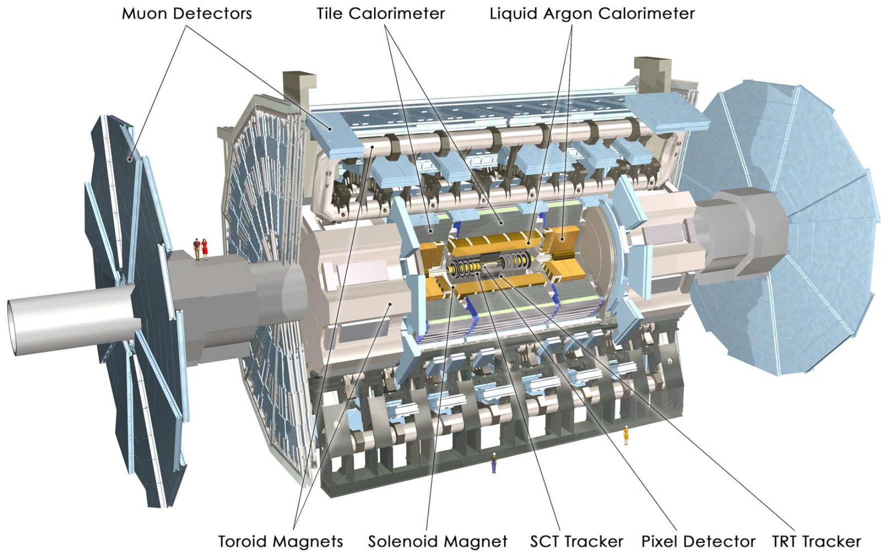

Figure 2.4.: The ATLAS detector and its components [43]

mass of the produced particles. This information is used to make precise measurements of SM processes or search for characteristic signatures predicted by BSM models.

Two coordinate systems are used in ATLAS, cartesian and polar. Figure 2.5 shows the layout of these coordinate systems in the ATLAS detector. Due to the cylindrical shape of the detector, the polar coordinates are more commonly used.

The origin is chosen as the pp collision point or interaction point located in the centre of the detector. In cartesian coordinates, the z-axis is defined along the beam pipe with positive values towards the side A of the detector, the y-axis points upwards and the x-axis is oriented horizontally towards the centre of the LHC ring. The polar coordinate system shares the same origin and z axis. The radial distance r and the azimuthal angle ϕ are defined in the $x-y$ plane, also referred to as the longitudinal plane, with ϕ ranging from 0 to 2π. The polar angle θ ranges between 0 and π with 0 along the z-axis. As will be seen in the different analyses described in this thesis, pseudorapidity $\eta = -\ln(\tan\frac{\theta}{2})$ is often used instead of θ. Positive values in η correspond to the positive direction along the z-axis, while $\eta = 0$ (or $\theta = 90°$) corresponds to the transverse plane. Objects with small η values are referred to as *central*,

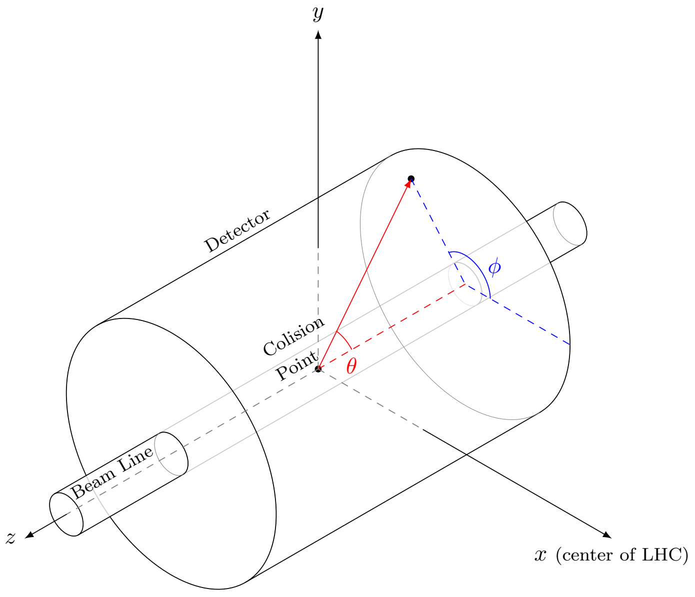

Figure 2.5.: ATLAS coordinate system [44]

while objects with large $|\eta|$ values are referred to as $forward$. Forward particles with $|\eta| > 2.5$ ($\theta < 9°$ from the z-axis) go undetected because detectors cannot be located inside the beam pipe. The four-momentum of a particle inside the detector is described in the coordinates $p =$(p_{T}, η, ϕ, m), where $p_{\mathrm{T}}= p \sin\theta$ is the transverse momentum and m the mass of the particle. The distance between two systems of particles in the detector can be defined as $\Delta R = \sqrt{\Delta\phi^2 + \Delta\eta^2}$.

The three main subdetectors in ATLAS are the inner tracking detector, the calorimeters and the muon spectrometer. The characteristics of each of the subdetectors will be described in this section.

2.2.1. The Inner Detector

The Inner Detector (ID) [45, 46] is a tracking device that makes up the innermost subdetector system located closest to the beam pipe. The ID is surrounded by a solenoid magnet with a magnetic field of 2 T which deflects the charged particles. The curvature of the tracks can be used to determine both charge and momentum of the particles. Furthermore primary and secondary vertices, which will be described in Section 4.1 can be reconstructed in the ID.

The ID geometry, which consists of several barrel layers around the collision point and end-cap disks at larger values of z, allows to detect particles with $|\eta| \leq 2.5$. Different technologies need to be used in the ID depending on the radial distance r to the beam line in order to optimise the detector performance and obtain a detector design that can sustain the high radiation produced in the collisions. For this reason the ID is made up of several subdetectors: The Pixel detector, the Semi-conductor tracker (SCT) and the Transition radiation tracker (TRT).

Pixel Detector

The innermost ID subdetector is based on pixelated silicon technology providing high granularity. It is composed of almost 100 million pixels or read-out channels located in four barrel layers and three end-cap disks. The pixel detector extends from $r = 33.25$ mm up to $r = 122.5$ mm and its proximity to the interaction point makes it crucial for a precise reconstruction of the impact parameters of tracks from long-lived particles such as b-hadrons. As shown in Figure 2.6, the closest layer to the beam line is called the IBL or Insertable B-Layer [47]. This layer was added during the first long shut-down of the LHC. It was installed in the small space between the existing pixel detector and the beam pipe in order to improve the tracking by reducing the distance between the interaction point and the first detector layer for the Run 2. The pixels in the IBL have a size of 50 μm $\times$ 250 μm and an intrinsic resolution of about 8 μm $\times$ 40 μm, while the other detector layers have a size of 50 μm $\times$ 400 μm and an intrinsic resolution of about 10 μm $\times$ 115 μm. When a charged particle passes through the pixel material it produces electron-hole pairs. The electrons then drift in an externally applied electric field towards the read-out system. A hit occurs if the resulting current passes a predefined threshold. Each track has an average of 4 hits in the pixel detector.

Semi-Conductor Tracker

The SCT is a silicon micro-strip tracker with 6 million read-out channels located in the the intermediate region of the ID. It spans a radial distance of about 20 cm, starting from $r = 299$ mm. Composed of silicon strips

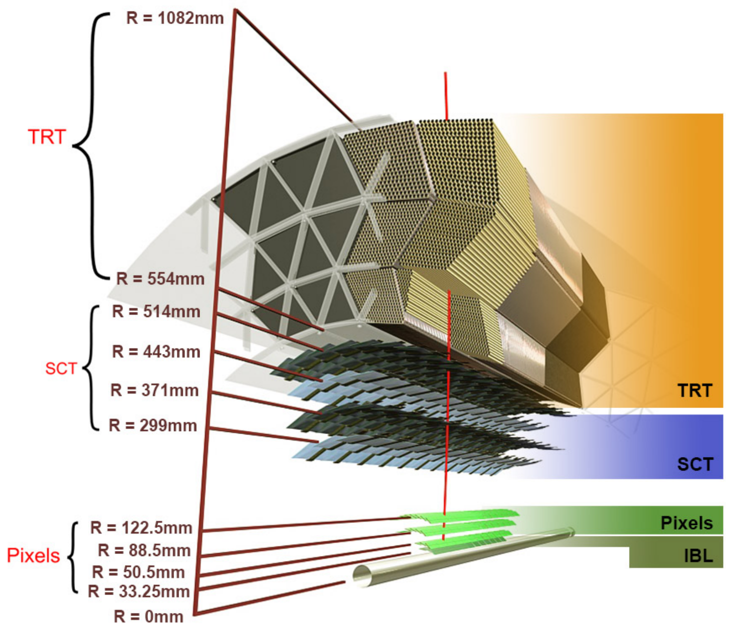

Figure 2.6.: Detailed layout of the ATLAS inner detector [48].

modules instead of pixels, the SCT has a similar function to the pixel detector but with coarser granularity. It consists of four rectangular barrel layers in the central region and nine trapezoidal disks on each end-cap. The silicon micro-strip modules have a mean strip pitch of 80 μm, while for the end-cap modules the strip pitch varies between 56.9 μm and 94.9 μm. Each module features two layers of sensors that are glued back to back with a small stereo angle of 50 mrad to allow a 2D hit reconstruction in the module plane. The modules provide an intrinsic resolution of 17 $\times$ 580 μm^2. Each track has an average of 8 hits in the SCT.

Transition Radiation Tracker

The TRT is the largest and outermost subdetector of the ID. The barrel covers a radial distance of around 50 cm, starting from $r = 554$ mm. In this volume 50,000 gas-filled straw tubes are installed, each with a gold plated tungsten wire in the middle of the tube. When a charged particle crosses the tube, the gas is ionised and the electrons drift towards the wire, where the signal is read out. The straw tubes have a diameter of 4mm and provide an intrinsic resolution of 130 μm via drift time measurements. Each track has an average of 36 hits in the TRT, allowing for a precise track reconstruction and momentum measurement.

Furthermore, the TRT allows to differentiate between electrons and pions or other massive hadrons. Relativistic particles produce transition radiation when crossing the foils and polymer fibers located between the wires. The amplitude of this radiation is inversely proportional to the mass of the particle resulting in stronger emission of light from electrons in comparison to hadrons.

2.2.2. The Calorimeters

Calorimeters are designed to stop and absorb most particles generated in a collision and measure their energy. Particles interact with the calorimeter material producing particle showers and depositing all their energy within the detector. ATLAS uses sampling calorimeters where layers of absorber material to induce the particle showers are alternated with active media to provide a detectable signal.

The calorimeter system is located outside the solenoid magnet which surrounds the ID. It consists of several specialised calorimeters with two different technologies. The layout of the calorimeter system is shown in Figure 2.7. Liquid Argon (LAr) is used as the active medium in the electromagnetic barrel and end-cap calorimeters but also in the hadronic end-cap calorimeter and the Forward Calorimeter due to the high radiation environment in those regions. The rest of the hadronic calorimeters, referred to as the Tile calorimeter, are located further away from the beam pipe and consist of the Tile barrel and the Tile extended barrel. The Tile calorimeter uses scintillating plastic tiles as active material.

The EM Calorimeter

The LAr EM calorimeter [50] is used to measure the energy of electrons and photons by exploiting the fact that they produce an EM shower. Positrons, electrons or photons with energies of above a few MeV undergo mainly two dominant types of interactions with matter:

- Pair production, corresponding to a photon interacting with a nucleus producing an electron positron pair.
- Bremsstrahlung, corresponding to electrons or positrons emitting a photon.

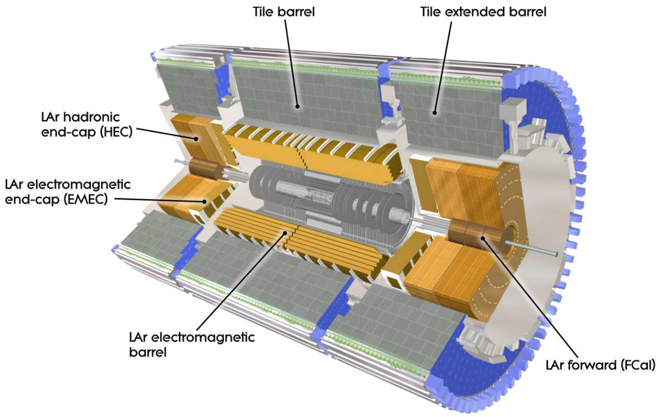

Figure 2.7.: Detailed layout of the ATLAS calorimeter system [49].

The alternation of these two processes produce particle showers which end when the photon's energy falls below the pair production energy threshold and other processes start to dominate.

In ATLAS, lead or stainless steel and liquid argon are interspaced to build the EM calorimeters. The lead has a short radiation length which initiates a particle shower. The secondary electrons produced in the shower ionise the narrow gaps of liquid argon inducing a signal via the released electrons. This allows to absorb the EM shower and measure the energy of the original particle which induced the shower.

The Hadronic Calorimeter

Hadronic showers are drastically different from EM showers. They are longer and start later, hence the hadronic calorimeter is located further away from the collision point, after the EM calorimeter. They are also much more complicated than EM showers since a certain fraction of the energy is fundamentally undetectable and the EM showers are also produced within the hadronic showers.

Hadrons, which are sensitive to the strong force, interact with the nuclei in the calorimeter material (nuclear interactions) producing pions and other hadrons. This is the start of a hadronic shower. Different types of interactions and energy depositions can occur inside the shower:

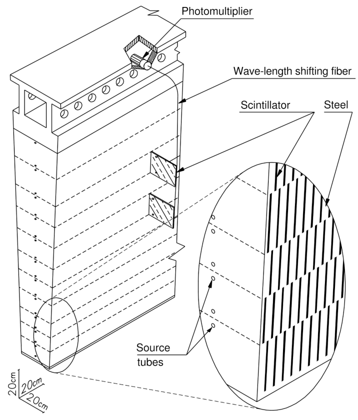

Figure 2.8.: Composition of the ATLAS Tile calorimeter [52].

- Nuclear interactions: These include ionising particles (e.g. protons or pions) and neutrons.
- EM interactions: Approximately 1/3 of the pions produced in hadronic showers are neutral π^0 which quickly decay to a pair of photons generating EM showers.
- Invisible component: Some energy of the hadronic showers is fundamentally undetectable. For example, muons created as decay products of pions or kaons, which deposit a very small part of their energy in the calorimeter, and long lived or stable neutral particles like κ_L^0 or neutrinos.

The hadronic Tile calorimeter [51], shown in Figure 2.8, uses steel plates as absorber and plastic scintillating tiles as the active material. The light from these tiles is transmitted by fibers to photo multiplier tubes, which produce electronic signals.

2.2.3. The Muon Spectrometer

As mentioned in the previous section, muons escape the calorimeters without depositing much of their energy so a specific system needs to be used to detect and measure these particles. The muon spectrometer (MS) [53] is composed of three large superconducting magnet systems, high resolution tracking chambers and a fast triggering system.

Eight toroidal superconducting coils are used to bend a muon's path and a total of 4000 individual muon chambers are used to measure its curvature and hence calculate the muon's direction and momentum. The muon chambers are constructed using four different technologies depending on the location and the purpose of the system. The Thin Gap and Resistive Plate Chambers are part of the trigger system and they are used, respectively, in the forward regions of the detector (high $|\eta|$) where there is no bending from the magnets, and the central region. The Monitored Drift Tubes (Cathode Strip Chambers) are used to measure the muon momentum with high precision, by measuring the track trajectory with a spatial resolution of 80 μm (60 μm), in the central (forward) regions.

2.2.4. Triggering and Data Acquisition

Proton bunches collide at the centre of the ATLAS detector 40 million times per second. Out of the 40 million events per second only a few are interesting enough to be used in physics analyses. To handle the challenges posed by such large amounts of data, ATLAS makes use of a trigger system in order to find and save only those events that might be interesting for further analysis.

The trigger system is composed of two consecutive stages. First the level one (L1) trigger reduces the number of events per second from 40 million to 75 thousand. L1 is a real time hardware trigger, which means that certain detector components are designed to flag events that leave certain signatures in the detector. The second step is the high level trigger (HLT) which further reduces the number of events to approximately a thousand events per second. HLT is a software trigger composed of a large farm of CPUs which are used to perform a detailed analysis of the events selected by the L1 trigger. This is done by looking at the event as a whole or using data in smaller isolated regions of the detector. It is in this step that objects are reconstructed by using all the detector information and events with reconstructed electrons, muons or jets are saved.

A thorough work has to be done at both levels of the trigger system to optimise the thresholds of the hardware trigger and the algorithms of the software trigger to ensure that interesting events are not discarded.

Chapter 3

Analysis Tools

3.1. Simulation of *pp* Collisions

Computer programs based on Monte Carlo (MC) methods are widely used in particle physics. These simulations are used together with data in order to test the different physics models as will be described in Chapters 5-8. In this section, the the introduction to QCD that was given in Chapter 1 is completed with a detailed description of the simulation of *pp* collisions.

Due to the complexity of QCD, several steps are needed to define *pp* collisions [54]. The main collision event, also referred to as the hard scattering, is illustrated in Figure 3.1. It occurs when two partons from the protons collide, interacting at very short distances. The remnants of the original protons are no longer colour singlet states and will therefore interact with each other, presumably softly, generating an underlying distribution of soft partons known as the underlying event. Prior to the hard scattering, partons can emit radiation resulting in initial state radiation (ISR). After the hard scattering, the resulting particles are emitted in different directions. All resulting particles carrying colour charge can emit quarks or gluons in so-called final state radiation (FSR).

The full simulation of the *pp* collisions can be divided in two blocks: The high energy hard scattering collision which can be described by perturbative QCD, and the parton shower and hadronisation process which occurs at lower energies and hence needs to be described by a phenomenological model.

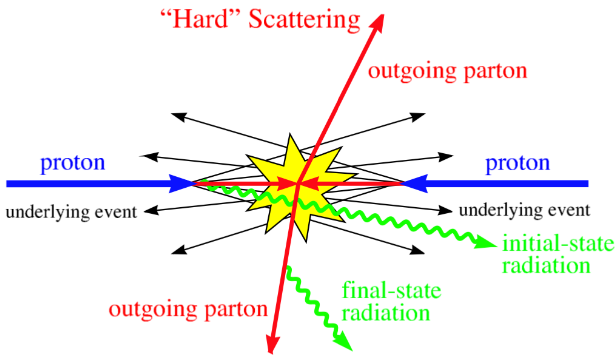

Figure 3.1.: Pictorial representation of a hard scattering event [55]

3.1.1. Hard Scattering

The total cross section from the hard scattering can be factorised into two parts: The Parton Distribution Function (PDF) and the Matrix Element (ME) calculation. The PDF encodes the information about the distribution of partons within the proton and is therefore needed to describe the initial conditions of the process. The ME or hard scattering cross section is computed analytically from the Feynman diagrams of the hard scattering using QFT. This calculation is performed up to a fixed order in perturbation theory e.g Leading Order (LO) or Next-to-Leading Order (NLO), and hence results in infinites and divergencies. If the ME was calculated at infinite precision the divergences originating from loops would exactly cancel against those from real emission. The renormalisation procedure removes these divergencies by absorbing them into definitions of physical quantities that depend on the renormalisation scale. The PDF and the ME depend on the so-called factorisation scale which separates the soft processes described e.g. by PDFs from the hard processes described by perturbative QCD calculations.

3.1.2. Parton Shower and Hadronisation

All partons generated in the hard scattering, or as a result of ISR or FSR, behave as free particles at short distances but undergo an increase in their coupling strength at larger distances (lower energies). During the transition from the high energies of the hard scattering to lower energies, the colour charged partons radiate additional quarks and gluons resulting in parton showers. The radiation process continues until the partons reach an energy scale Q $\sim$ 1 GeV and the resulting partons recombine to form stable colourless hadrons. This stage is referred to as hadronisation.

The parton shower is approximately simulated by the successive emission of quarks and gluons from initial or final state partons. Parton showers are included in the MC simulations to account for the rest of higher order contributions not included in the ME calculation. Hadronisation models are used to describe the evolution of the collision for $Q^2 < 1$ GeV. The most used hadronisation models are the string fragmentation [56] and the cluster hadronisation [57] models.

3.1.3. Monte Carlo Generators

The MC generators can be divided in two groups, those that can describe the full simulation chain (*muti-purpose* generators) and those that cannot (ME generators). Examples of multi-purpose MC generators are Pythia [58], Herwig [59] and Sherpa [60]. The ME generators, such as MadGraph [61] and Powheg [62] only describe the hard scattering up to the ME and hence need to be interfaced with for example Pythia or Herwig to simulate the additional parton shower and hadronisation model.

Some generators may describe a specific process better than others and hence MC simulations are compared to data to find which generator best describes the process. An uncertainty, referred to as a modelling uncertainty, is derived by comparing the prediction from different MC generators and parton shower models in order to account for possible mismodellings by the generators.

3.1.4. Detector Simulation

The MC generators simulate the particles present in the event at the so-called *truth level*. In order to compare these simulations to the data recorded by the ATLAS experiment, the detector response to the truth particles needs to be simulated. The detector simulation models the interaction of the particles with the detector. The detector simulation software GEANT4 [63] is used to obtain a detailed simulation of the ATLAS detector (*full simulation*). Alternatively, a less refined simulation that requires less CPU time can be obtained with the Atlfast-II or AF2 simulation software [64] (*fast simulation*). The output of the detector simulation resembles the raw data that is read out from the ATLAS detector. The last step is to reconstruct the simulated data with the same software as used for the real data. The combination of the MC generator with the detector simulation and data reconstruction results in simulated events at the so-called *reconstruction level*.

3.2. Statistical Analysis

In particle physics the discovery or exclusion of a new physics model is performed using hypothesis testing. The null or background-only hypothesis (H_0) describes the known physics processes (SM). The alternative hypothesis, known as the signal-plus-background hypothesis (H_1) includes the new phenomena (BSM). The level of compatibility of the observed data with each of the two hypotheses is used to make a statement about the validity of the SM or the new physics model. The two hypotheses can be commonly described by introducing a signal strength modifier (μ), which acts as a multiplicative factor for the signal cross section. The signal-plus background hypothesis corresponds to $\mu = 1$ and the background hypothesis corresponds to $\mu = 0$.

3.2.1. Signal and Control Regions

In order to detect a specific signal a set of selection criteria, referred to as a signal region (SR), is defined with the aim to retain the highest possible number of signal events with as few background events as possible. The background events originate from SM processes that result in similar signatures in the detector and therefore pass the selections of the SR. Different methods can be used to define the SR, some analyses take advantage of machine learning techniques to best separate signal from background while others use the so-called "cut & count" approach. The latter involves applying cuts to a set of variables for which the shape differs between signal and background. Examples of both approaches are presented in this thesis: A "cut & count" selection is used in Chapters 5 and 6 while machine learning techniques are used to separate signal and background in Chapters 7 and 8.

Although the SRs are defined to select signal events, some amount of background events is expected to pass the selections. The background events are either estimated purely from MC simulations or from MC simulations that are further corrected using data. The correction is performed by defining a control region (CR), a set of selection criteria similar to the SR but altered to ensure orthogonality to the SR and high purity of a certain type of background events. In the CR, a correction factor (normalisation factor, NF) for the corresponding background is derived by scaling the number of simulated events of that background so that the total number of simulated events matches the number of data events in the CR. Several CRs, defined to correct different backgrounds, may be defined and a global fit is performed to simultaneously obtain all corresponding NFs and apply them to the SR.

3.2.2. Likelihood Function

The probability that the observed data originates from the tested hypothesis is calculated using the likelihood function L. Considering the minimum division in which the observed data is classified, i.e. one single histogram bin for each region, the expected number of events in the bin i can be written as

$$E_i = \mu s_i + b_i \tag{3.1}$$

where s_i and b_i correspond to the expected number of signal and background events respectively in the i-th bin. This expectation has to be compared to the observation of n_i events in data. Assuming that the data follows a Poisson distribution, the likelihood for the observed data to be produced by hypothesis H_μ is

$$L_i(\mu) = \frac{(\mu s_i + b_i)^{n_i}}{n_i!} e^{-(\mu s_i + b_i)} \tag{3.2}$$

The prediction of the model however, is affected by systematic and statistical uncertainties. The effect of these uncertainties on the predictions can be modelled through nuisance parameters (NPs) θ. A variation in a NP produces a change in the expected number of events, $s_i(\theta)$ and $b_i(\theta)$, therefore the maximisation of the likelihood leads to adjustments of the NPs in order to improve the agreement of the expectation with the observed data. A NP is characterised by a probability density function

$\rho(\theta)$, encoding the information about its best estimate and width, which is related to the size of the uncertainty. Gaussian functions are used for the different systematic uncertainties, whereas Gamma functions are used for the statistical uncertainties and log-normal functions for the normalisation uncertainties.

The final likelihood function can be written as

$$L(\mu, \theta) = \prod_{i=1}^{N} \frac{(\mu s_i + b_i)^{n_i}}{n_i!} e^{-(\mu s_i + b_i)} \prod_{k=1}^{M} \rho(\theta_k) \tag{3.3}$$

where the index i runs over the N measurement bins and the index k runs over the M NPs. The likelihood function can be globally maximised, which includes fitting both the signal strength and the NPs to obtain the so-called maximum likelihood estimator or best fit value.

3.2.3. Profile Likelihood Ratio

As demonstrated by the Neyman-Pearson lemma, the optimal discriminator when testing an hypotheses H_μ (which can be either H_0 or H_1) is given by the profile likelihood ratio $\lambda(\mu)$, which is defined as

$$\lambda(\mu) = \frac{L(\mu, \hat{\hat{\theta}}(\mu))}{L(\hat{\mu}, \hat{\theta})} \tag{3.4}$$

where the numerator contains the conditional maximum likelihood $L(\mu, \hat{\hat{\theta}}(\mu))$ i.e. the best fit value for a given μ, and the denominator contains the unconditional maximum likelihood $L(\hat{\mu}, \hat{\theta})$ i.e. the overall best fit value. The profile likelihood ranges from $0 < \lambda < 1$. Values of $\lambda \sim 1$ imply good agreement between the data and the hypothesis H_μ.

3.2.4. Hypothesis Testing

In ATLAS, the compatibility of the observed data with a given hypothesis is quantified using the test statistic q_μ, defined from the profile likelihood ratio as

$$q_\mu = -2 \ln \lambda(\mu) \tag{3.5}$$

The probability that the observed data originates from the considered hypothesis, also known as p-value (p_μ), is computed as

$$p_\mu = \int_{q_{\mu,\mathrm{obs}}}^{\infty} f(q_\mu|\mu) dq_\mu \tag{3.6}$$

where a low enough p_μ indicates that the tested hypothesis is false. The conventions used in the field to make this statement are defined in the next sections.

Testing for Discovery

The first step in hypothesis testing is to calculate the compatibility of the H_0 hypothesis to data. The p_0 gives the probability that the background-only hypothesis generates a number of events at least as large as the observed number. In this sense a high p_0 value indicates that the observed number of events is compatible with the background expectation, making any discovery unlikely. On the other hand, a p_0 very close to 0 would reject the H_0 hypothesis and therefore indicate evidence for or even discovery of new physics.

The p_0 can be converted into the corresponding significance Z, defined as the number of standard deviations (σ) that correspond to an upper-tail probability p_0 for a Gaussian-distributed variable. The significance Z is defined as

$$\mathrm{Z} = \Phi^{-1}(1 - p_0) \tag{3.7}$$

where Φ^{-1} is the inverse Gaussian Cumulative Distribution Function. For large enough datasets where the so-called asymptotic approximation is valid $\mathrm{Z} = \sqrt{q_0}$ [65].

The conventions used in particle physics to reject the H_0 hypothesis as a function of the p-value and significance are summarised in Table 3.1.

A significance $\mathrm{Z} \geq 3\sigma$ is required to claim evidence for new physics while a significance of $\mathrm{Z} \geq 5\sigma$ is required to claim discovery of new physics.

Table 3.1.: Conventions for discovery tests as a function of the signfificance Z and p-value

Conclusion	Z	$1 - p_0$ (%)	p_0
Not signficant	2σ	95%	0.05
Evidence for new physics	3σ	99.7%	0.003
Discovery of new physics	5σ	99.9997%	$3 \cdot 10^{-7}$

If Z $< 3\sigma$ the deviation from the H_0 hypothesis is considered to not be significant and the H_1 hypothesis is tested.

Testing for Exclusion

If H_0 cannot be rejected because no significant evidence of signal is found, the H_μ hypothesis is tested to set upper limits to μ. The p_μ gives the probability that the signal plus background hypothesis with a signal strength $= \mu$ generates a number of events at least as large as the observed number. By convention, a probability $p_\mu \leq 5\%$, equivalent to a Z $\geq 2\sigma$, is considered low enough as to exclude the existence of new physics with a given μ. If $\mu = 1$ is excluded then the new physics model can be considered to be falsified.

The p_μ value extracted from the observed data can lead to unphysical exclusions due to statistical fluctuations when a downward fluctuation in the observed number events occurs. In order to avoid exclusions of μ values that the search is a priori not sensitive to, the CLs method [66] is used. The CLs value is defined as a ratio of probabilities

$$\text{CLs} = \frac{p_\mu}{1 - p_0} \tag{3.8}$$

where p_μ and p_0 quantify the compatibilities between the data and the $H\mu$ or H_0 hypotheses respectively. For searches at the LHC, the CLs value is used instead of p_μ to set upper limits. This convention is also referred to as 95% confidence level (CL). If CLs < 0.05, the signal-plus-background hypothesis with a signal strength μ is excluded at 95% CL.

3.2.5. Blinding and Asimov Dataset

All searches for new physics performed by the ATLAS experiment are *blinded* in their development stage. This means that no data is used in the SR until the analysis strategy has been fixed and the dominant uncertainties have been evaluated. In a blinded analysis real data is used in the CRs and pseudo-data is used in the SRs. This allows to correct the MC-based background prediction with data from the CRs and evaluate the expected performance in the SR without being biased to possible statistical fluctuations from the data in the SR.

The so-called *Asimov dataset*, a pseudo-dataset where the number of events is equal to the background expectation value, is used to evaluate the *expected* significance and upper limits to a given signal. For some tests, e.g. the signal injection tests that will be described in Chapter 8, the predicted signal can also be included in the Asimov dataset.

Once the analysis strategy is fixed and the analysis is unblinded, the H_0 and H_1 hypothesis are tested using real data in the SR. These are referred to as the *observed* results. Both expected and observed results give relevant information about the analysis and are therefore presented in all ATLAS searches.

Chapter 4

Particle Identification and Object Reconstruction

In order to study the pp collisions produced at the centre of the detector, several physics objects need to be reconstructed. Hits in the tracking detector, energy deposits in the calorimeters and hits in the MS are used to reconstruct the particles produced in the collision. These reconstructed physics objects are later employed in the physics analyses. This chapter describes how the different objects, used in Chapters 5-8 are section.

4.1. Tracks and Vertices

Charged particles with pseudorapidities of $|\eta| < 2.5$ produce hits in the ID as they traverse the active measuring elements. These hits or clusters of signals in the silicon pixel, micro-strip sensors and TRT are used to identify trajectories of charged particles usually referred to as tracks. Track reconstruction requires several steps: Cluster information is used in an iterative combinatorial track-finding algorithm to reconstruct all possible track candidates. These tracks are later processed at an ambiguity-solving stage to remove overlaps and only the track candidates that pass the quality criteria are retained. A Neural Network (NN), trained to identify merged clusters, is used to aid the ambiguity solver [67] and minimise the loss of efficiency. Finally, a high resolution fit is performed with all available information. The tracks which pass through the ambiguity-solving without modification are added to the final track collection [68].

Two or more tracks can be used to reconstruct their origin or interaction point known as a vertex. The precision of the reconstructed vertex position improves with increasing track multiplicity. The primary vertex

(PV), corresponding to the position of the hard scattering pp collision, is chosen as the candidate that maximises the p_{T}^2 of the sum of associated tracks [69]. Secondary vertices (SV), coming e.g. from decays of particles with long lifetimes, can also be reconstructed.

4.2. Electrons and Photons

Electrons and photons deposit their energy entirely or mostly in the EM calorimeter in the form of EM showers. The shower, which was described in Section 2.2.2, is reconstructed from groups of calorimeter cells referred to as topological clusters. The calorimeter cells must have an absolute energy at least 4 standard deviations above the average noise to be part of the topological cluster. Superclusters, formed by a seed topological cluster with associated satellite topological clusters, are reconstructed independently for photons and electrons [70]. An object might be reconstructed both as a photon and an electron supercluster. These cases are marked explicitly as ambiguous, allowing the final classification of these objects to be determined based upon the specific requirements of each analysis.

Electrons are charged particles and can therefore be distinguished from photons by the tracks they form in the ID. Electron reconstruction requires the match of a supercluster to at least one track in the ID. If no tracks can be associated to the electromagnetic shower, the object can be reconstructed as a photon. About 20% of the photons at low η and up to about 65% at $|\eta| = 2.3$ pair-produce an $e^+ e^-$ pair within the volume of the ID resulting in two tracks with close trajectory. These photons are referred to as converted and the vertex reconstructed from the decay tracks is referred to as a conversion vertex. Converted photons are reconstructed by matching a supercluster to at least one conversion vertex. Un-converted photons are reconstructed from superclusters that do not match to neither a track nor a conversion vertex. Converted photons may be misidentified as electrons if one of the components of the $e^+ e^-$ pair is not recognised.

The energy of the reconstructed electrons and photons is calibrated following the procedure described in [71]. Different selection criteria that differ on the purity of the selected electron and photon objects, are provided to satisfy the varied requirements from physics analyses. In electron identification, four operating points are defined to cover various possible electron selection efficiencies and their corresponding background rejection efficiencies, these operating points are referred to as Tight, Medium, Loose and VeryLoose, where all electrons passing the Tight criteria also satisfy the other criteria [72]. In photon identification only two levels of identification are considered, Tight and Loose. This is described in detail in [73].

4.3. Muons

Muons are characterised by escaping the calorimeters and leave hits in the MS. Therefore their reconstruction is based on tracks reconstructed in the MS but complemented with information from the ID, and the calorimeters. Three different types of reconstructed muons are considered. Standalone muons are reconstructed linking tracks in the MS to the interaction point taking into account the energy loss in the calorimeters. Combined muons are reconstructed using their full track by matching the standalone muon tracks to the tracks in the ID. Muons with low p_{T} which do not have enough momentum to reach the muon system are reconstructed using calorimeter information and tracks in the ID and are referred to as calorimeter-tagged muons. Four muon identification selections, Tight, Medium, Loose, and High-p_{T}, are provided [74] to be used depending on the specific requirements of different physics analyses.

4.4. Jets

As introduced in Section 3.1, the partons produced in the hard scattering and their radiated partons interact to form different hadrons. The hadrons interact with the detector material, as described in Section 2.2.2, producing hadronic showers in the calorimeters. Since the full process leading to hadronisation begins with an outgoing parton of the hard scattering with a relatively high momentum, the hadrons tend to be produced in the same direction as the outgoing parton resulting in groups of collimated particles (jets).

The ATLAS experiment uses the so-called anti-k_t algorithm [75] to reconstruct jets. This is a successive recombination algorithm which iteratively merges pairs of objects according to a pre-defined distance between them and their p_{T}. Jets can be reconstructed using information from the calorimeter, tracks in the ID or both. The so-called *topo* jets are reconstructed using information from the topological clusters [71]. The particle flow (*pflow*) [76] jets, which are an improved version of the topo jets, use both topological clusters and track information as input to the jet reconstruction algorithm. These methods can reconstruct jets with $p_{\mathrm{T}}>$ 20 GeV. Lower p_{T} jets can also be reconstructed using track information only, these are referred as *track* jets. In this thesis, jets are reconstructed using the anti-k_t algorithm with the distance parameter set to 0.4. The search in Chapter 6 uses topo jets while the more modern pflow jets are used in all other chapters.

Jet reconstruction algorithms are required to perform well when confronted with possible QCD divergencies. The jet algorithm should therefore be able to reconstruct the same jet with the presence or absence of soft radiated particles. This is known as infrared safety. It should also be insensitive to replacing one particle with two collinear particles. This is known as collinear safety. Furthermore, the jet algorithm is expected to be independent of the input type and reconstruct the same final state from simulated partons, simulated particles or energy deposited in the calorimeters.

The ATLAS experiment has what is called non-compensating calorimeters, which means that the response to hadrons is lower than the response to particles interacting electromagnetically and this is corrected through the so-called jet energy scale (JES) calibration. Furthermore, energy from the underlying event and pileup can sometimes be included in the jet reconstruction. To account for these and other effects, the reconstructed jets need to be corrected through different calibration procedures [77].

4.5. B-tagging

Top quarks and Higgs bosons as well as many hypothetical BSM particles often decay to b-quarks which hadronise to form b-hadrons. A jet containing a b-hadron is referred to as a b-jet, a jet containing a c-hadron but no b-hadron is referred to as a c-jet, while a jet containing neither a b-hadron nor a c-hadron is referred to as a light-flavour jet.

The identification of b-jets, referred as b-tagging, is an important tool used in the ATLAS physics program. The b-tagging algorithms exploit the characteristic features of b-hadrons: long lifetime, high decay multiplicity and high mass. Due to the long lifetime of b-hadrons, b-jets are characterised by being spatially matched to a SV which is displaced from the PV. The SV is the point where the the b-hadron decays. The transverse (d_0) track impact parameter (IP) is defined as the distance of closest approach from the track trajectory to the PV in the transverse plane. The longitudinal track IP (z_0) is defined as the distance in the z-direction between the PV and the track trajectory at the point of closest approach in the $x - y$ plane. The presence of the SV results in a high IP of the tracks originating from the b-hadron decay, as illustrated in Figure 4.1.

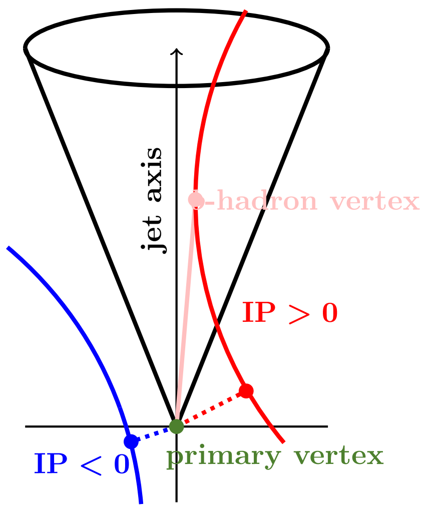

Figure 4.1.: Graphical illustration of the signed IP of tracks in the jet.

The decay point of the b-hadron must lie along its flight path, hence the IP components are signed to discriminate between tracks produced in a b-hadron decay and those that are reconstructed with a large IP but actually originate from the PV. Tracks are assigned a positive IP if the angle between the jet direction and the line joining the PV and the point of closest approach to the track is less than $\pi/2$ and negative otherways [78]. Tracks from decays of long lived particles have large positive IP making the signed IP a suitable discriminating variable for b-tagging. The decay length significance, defined as the distance between the PV and the SV vertex divided by the uncertainty, is also a good discriminant between b-jets and light-flavour jets. This variable is signed with respect to the jet direction in the same way as the track IP is. Vertices are assigned a positive decay length if the angle between the jet direction and the line joining the PV to the SV is less than $\pi/2$ and negative otherwise.

Different low level taggers have been developed to focus on specific flavour-tagging sensitive features [79]. The large IP of tracks originating from the b-hadron decay are exploited by the `IP2D` and the `IP3D` algorithms [80]. The track IP correlations are exploited by the track-based recurrent NN (`RNNIP`) [81]. The `SV` algorithm [82] attempts to reconstruct the SV from the b-hadron decay and the `JetFitter` algorithm [83] focuses on the topological decay structure of weak decays of b-hadrons. These low level taggers are later used as input to more complex high level taggers which result in significantly improved b-jet identification performance.

The analyses described in this thesis use either the `MV2` [80] or the `DL1r` [84] high level taggers. Both algorithms are trained on a hybrid sample of simulated jets where b-jets are considered signal and c- and light-flavour jets are considered background. Furthermore, they use the information from the low level algorithms `IP2D, IP3D, SV1` and `JetFitter` together with the jet variables p_{T} and η as input to the algorithms. The `MV2` tagger is a Boosted Decision Tree (BDT) algorithm which is trained using the ROOT Toolkit for Multivariate Data Analysis (TMVA) [85]. Specifically the widely used `MV2c10` algorithm contains 10% of c-jets in the background sample. The `DL1r` tagger is an artificial deep NN trained using $Keras$ with the $THEANO$ [86] backend. Its topology consists of a mixture of fully-connected hidden layers and maxout layers. Additionally to the already described input, `DL1r` uses the `RNNIP` algorithm as input to the NN, as well as a set of variables to discriminate against c-jets. The background sample used to train this algorithm contains a fraction f_c =1.8% of c-jets. The `DL1r` tagger has a multidimensional output corresponding to the probabilities for a jet to be a b-jet, c-jet or light-flavour jet. The final b-tagging discriminant is given as

$$\text{DL1r discriminant} = \ln \frac{p_b}{f_c \cdot p_c + (1 - f_c) \cdot p_{\text{light}}} \tag{4.1}$$

The performance of the b-tagging algorithms is estimated by the b-tagging efficiency (ϵ^b), c-tagging efficiency (ϵ^c) and light-jet tagging efficiency or mistag rate (ϵ^{light}). The different tagging efficiencies depend on the jet kinematics and are defined as

$$\epsilon^f = \frac{\#\ \text{tagged}\ f\text{-jets}}{\#\ f\text{-jets}}, \tag{4.2}$$

where $f = b$, c, light. A high ϵ^b is essential to correctly identify b-jets, but low ϵ^c and ϵ^{light} are required to avoid large c- and light-jet contamination. Jets are considered b-tagged if the output score of the high level algorithm is above a certain threshold. This threshold is referred to as a operating point (OP). The OPs are chosen such that each of them result in a desired b-tagging efficiency. The tightest is the 60% OP which tags only 60% of the b-jets but in turn has very low mistag rate. The loosest OP corresponds to a b-tagging efficiency of 85% and intermediate OPs of 70% and 77% b-tagging efficiency are also defined. The intervals between the OP boundaries are referred to as pseudo-continuous OPs.

The b-tagging algorithms are trained using simulated events which may not predict data perfectly. A calibration is performed to correct possible mismodellings of the algorithms. The calibration of the mistag rate is described in detail in Chapter 5. The b-tagging and c-tagging efficiencies are calibrated using data samples of b-jets and c-jets from top quark decays [87, 88].

4.6. Missing Transverse Energy

Some particles escape the detector volume without being detected, this is the case for e.g. neutrinos and hypothetical DM particles. To infer the presence of these invisible particles, energy and momentum conservation can be exploited. The longitudinal momentum of the partons before the collision is not known and the outgoing particles close to the beam axis cannot be detected, making the reconstruction of the missing longitudinal momentum impossible. On the other hand, the transverse component of the particles momentum before the collision is zero. It is therefore possible to calculate the negative vectorial sum of the transverse momenta of all reconstructed particles and detector energy deposits in a given event, referred to as missing transverse momentum vector (${p_{\mathrm{T}}}^{\mathrm{miss}}$). The magnitude of ${p_{\mathrm{T}}}^{\mathrm{miss}}$, referred to as missing transverse momentum ($E_{\mathrm{T}}^{\mathrm{miss}}$), is a measure of the sum of the p_{T} of all undetected particles created in the collision [89].

Chapter 5

Mistag Rate Calibration

This chapter describes the calibration of the light-flavour jet mistagging efficiency of the b-tagging algorithms with Z+jets events using 139 fb^{-1} of ATLAS pp collision data at $\sqrt{s} = 13$ TeV [1]. The calibration is performed on different jet collections and algorithms but only the results for pflow jets and the `DL1r` algorithm are shown here.

5.1. Introduction

The most common source of light-flavour jet mistags is the finite resolution of the ID that can cause tracks that originate from the PV to get reconstructed with large IPs or form fake SVs. The mistags of light-flavour jets can also be caused by the presence of tracks from particles with long lifetimes (e.g. K^0_S or Λ^0) and material interactions (hadronic interactions and photon conversions).

To properly evaluate and correct the performance of b-tagging algorithms MC simulations which describe known physics processes are used together with the data recorded by ATLAS. The flavour-tagging efficiency in data (ϵ^f_{data}) is compared to the efficiency in simulation (ϵ^f_{MC}) and scale factors (SF), defined as

$$\text{SF}^f = \frac{\epsilon^f_{\text{data}}}{\epsilon^f_{\text{MC}}} \tag{5.1}$$

are extracted and used to calibrate the b-tagging algorithms. The SFs are measured for each jet flavour and b-tagging OP.

The DL1r algorithm rejects 97.52% (99.96%) of the light-flavour jets at the 85% (60%) OP. Since the fraction of mistagged light-flavour jets is so low, $\epsilon^{\text{light}}_{\text{data}}$ cannot be measured directly with enough precision. Two alternative methods can nevertheless be used to calibrate the ϵ^{light}: The negative-tag method and the adjusted MC method [78]. The former measures $\epsilon^{\text{light}}_{\text{data}}$ using a modified version of the DL1r algorithm that has a higher fraction of mistagged light-flavour jets. This method is thoroughly described in Section 5.3. The latter estimates $\epsilon^{\text{light}}_{\text{data}}$ using MC simulations that have been modified to reproduce data. Accurate measurements of track performance are made for both data and MC and this information is used to modify the MC simulation. The SF^{light} is then obtained using the modified MC as a proxy for data, eliminating the problem of limited statistics.

5.2. Samples and Event Selection

The ϵ^{light} calibration is performed using a sample of Z bosons produced in association with jets (Z+jets). Events with two central same-flavour opposite-sign leptons ($l = e$ or μ) compatible with the decay of a Z boson, i.e. with a di-lepton invariant mass (m_{ll}) of 81.0 GeV $< m_{ll} <$ 101.0 GeV, and $p_{\text{T}}(Z) > 50$ GeV are selected. Electron (muon) candidates must have $|\eta| < 2.47$ (2.5) and the leading (sub-leading) lepton is required to have $p_{\text{T}} > 28$ (18) GeV. Furthermore, all events must have at least one jet with $p_{\text{T}} > 20$ GeV and $|\eta| < 2.5$.

MC samples of Z+jets events are simulated with two different generators. Nominal samples are generated using Sherpa [60]. Alternative samples, used to estimate systematic uncertainties and MC efficiencies, use the MadGraph [61] event generator interfaced with Pythia8 [58] for the parton shower. Other processes that pass the event selection are also simulated. The ZZ and ZW production are generated with Sherpa. Dileptonic top-quark pair production $t\bar{t}$ samples are generated using the Powheg Box v2 [90] generator interfaced with Pythia8 for the parton shower.

Comparisons between data and the simulation for the most relevant kinematic variables are shown in Figure 5.1. The normalisation of the simulated Z+jets events is adjusted to make the number of events in the MC simulation match the data to better appreciate any discrepancies in the shape of the distributions. The discrepancies in the leading jet p_{T} and SV mass (m_{SV}) distributions are mitigated with a binned fit to data which will be described in detail in the next section. The m_{SV} is defined as the invariant mass of the set of tracks selected by the SV algorithm. Negative m_{SV} values indicate that no SV is found in the jet.

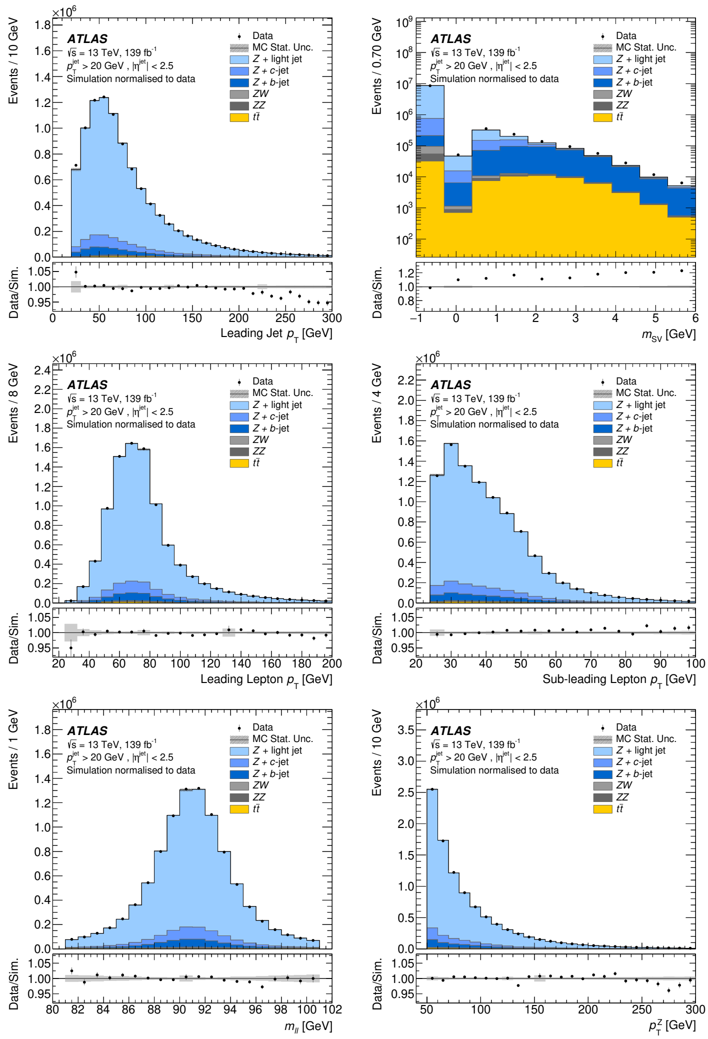

Figure 5.1.: Comparisons between data and simulation for the most relevant kinematic variables after event selection [1]. The shaded area corresponds to the statistical uncertainties of the MC simulations.

5.3. Negative-Tag Method

The negative-tag method calibrates the ϵ^{light} in data using a modified version of the `DL1r` algorithm called `DL1rFlip`. Tracks matched to light-flavour jets typically have nearly symmetric signed IP and signed decay length distributions. On the other hand, tracks matched to b- and c-jets tend to have distributions with positive tails. This is illustrated in Figure 5.2 which shows the d_0 and z_0 components of the IPs of tracks matched to jets. The `DL1rFlip` algorithm uses the same training and OP-threshold as the `DL1r` but it inverts the sign of the IP of tracks, and decay length of vertices achieving a lower ϵ^b to ϵ^{light} ratio than the `DL1r` without significantly modifying ϵ^{light}. This is shown in Figure 5.3, where the distributions of the `DL1r` and `DL1rFlip` discriminant are compared for b-jets and light-flavour jets respectively. The distributions are similar for light-flavour jets but significantly differ for b-jets. The `DL1rFlip` algorithm can therefore be used to calibrate ϵ^{light} in data. A jet that satisfies the normal output discriminant criteria of a flipped algorithm is considered to be negatively tagged. The distributions for the `DL1r` and `DL1rFlip` discriminants are shown in Figure 5.4. These comparisons show that the fraction of light-flavour jets is much higher for high `DL1rFlip` values than for high `DL1r` values. At the 85% (60%) OP, 25% (1%) of the jets selected by the `DL1r` algorithm are light-flavour jets, while at the same OP, 38% (6%) of the jets selected by the `DL1rFlip` algorithm are light-flavour jets.

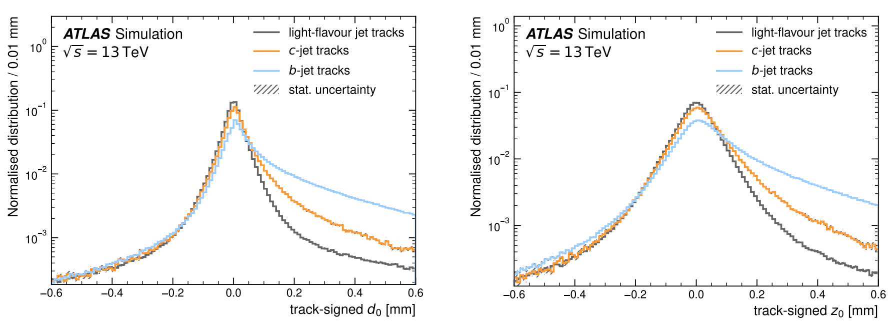

(a) d_0 (b) z_0

Figure 5.2.: Normalised signed IP distributions for tracks associated to light-flavour, c- and b-jets in multijet events generated with the Pythia8 event generator [1].

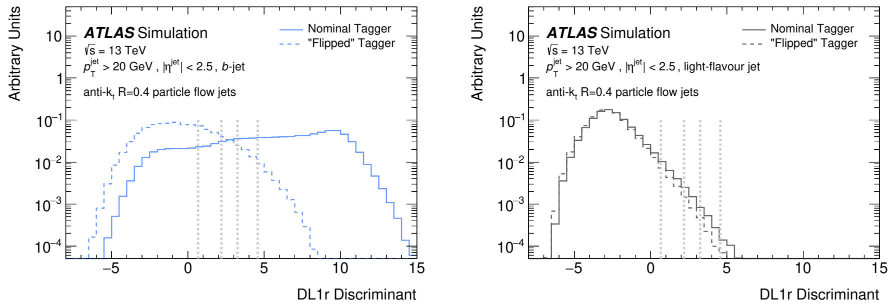

(a) b-jets (b) light-flavour jets

Figure 5.3.: Comparison of the `DL1r` and `DL1rFlip` discriminant for different jet flavours. The dashed vertical lines indicate the boundaries of the pseudo-continuous OP intervals [1].

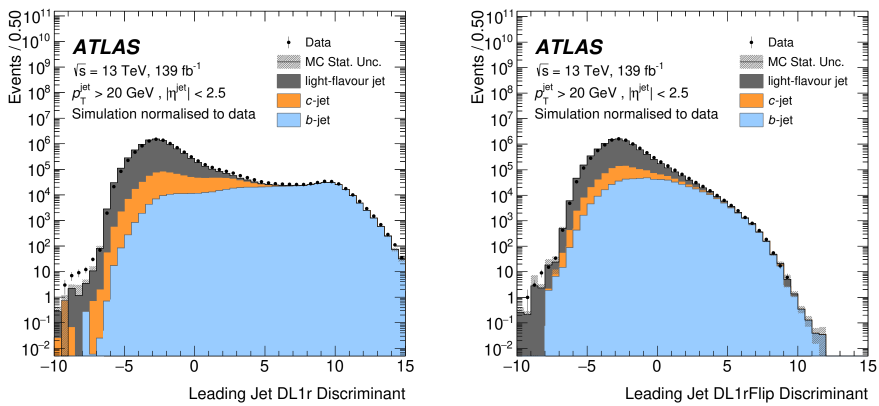

(a) `DL1r` (b) `DL1rFlip`

Figure 5.4.: Comparisons between data and simulation for the discriminant distributions of the b-taggers [1]. Statistical uncertainties of the yields are shown.

In order to account for the p_T dependence of ϵ^{light}, the calibration is performed independently in intervals of the leading jet p_T distribution. The SF^{light} and SF^{b} are then measured in data through a simultaneous binned fit to the m_{SV} distribution in pseudo-continuous intervals of the `DL1rFlip` discriminant. Exploiting m_{SV} to measure SF^{b}, in addition to SF^{light}, considerably reduces the uncertainties arising from the heavy flavour contamination with respect to the previous published calibration [78]. Unfortunately the fit does not have enough discriminating power to calibrate all three flavours and the SF^c needs to be estimated separately and given as inputs to the fit. Figure 5.5 shows the `DL1rFlip` discriminant and the m_{SV} template for the 77-70% pseudo-continuous OP in the $50 <$ jet $p_{\text{T}} < 100$. GeV interval.

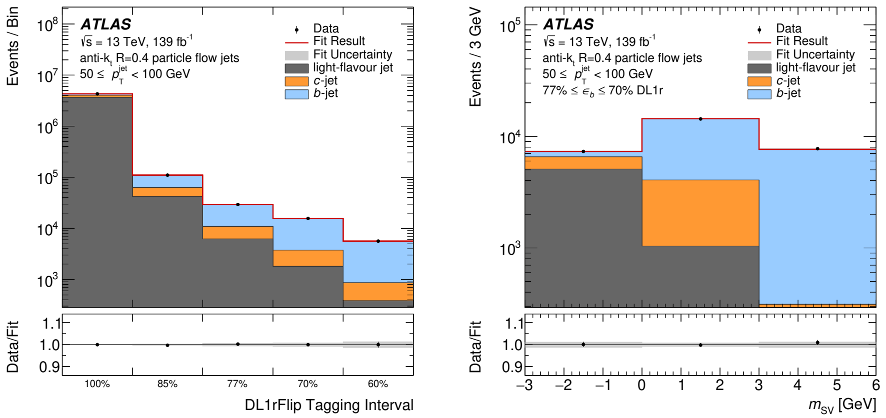

(a) `DL1rFlip` (b) m_{SV}

Figure 5.5.: Distributions of the fit templates for the 77-70% OP [1].

For a given interval of jet p_{T}, the expected number of jets for a given pseudo-continuous OP interval i is given by

$$N_i(m_{\text{SV}}) = N_{i,\text{MC}} \times C \times \left[\sum_{f=\text{light},c,b} F^f \times \text{SF}_i^f \times \epsilon_{i,\text{MC}}^f \times P_i^f(m_{\text{SV}}) \right],$$

where $N_{i,\text{MC}}$ is flavour inclusive event yield in the i^{th} `DL1rFlip` interval predicted by MC; C is a common NF; F^f are the jet flavour fractions; $P_i^f(m_{\text{SV}})$ is the m_{SV} probability density function for jet flavour f in the i^{th} `DL1rFlip` interval. $N_{i,\text{MC}}$ and $\epsilon_{\text{MC}}^{f,i}$ are fixed to the predictions from MC and SF_i^c is set to 1.0 ± 0.3. The C, F^f, SF_i^b and $\text{SF}_i^{\text{light}}$ are free parameters that are allowed to float in the fit. The constraints $F^{\text{light}} = 1 - F^b - F^c$ and $\sum_{i=1}^{5} \epsilon_{i,\text{MC}} \times SF_i = 1$, where the contributions to the first bin are allowed to vary such that unitarity is preserved, are also applied. The parameters of interest, i.e. the SF^{light} are obtained for the `DL1rFlip` algorithm. The calibration of the `DL1rFlip` algorithm is then applied to the `DL1r`. An extrapolation uncertainty is added to account for the differences between these algorithms.

Sherpa Z+jets events are used to build the m_{SV} and `DL1rFlip` discriminant templates because this MC sample better models the data. However, $\epsilon^{f}_{i,\mathrm{MC}}$ is extracted from MadGraph Z+jets events interfaced with Pythia8 for the parton showering. The SFs that are provided by the calibration should therefore be considered as corrections to $\epsilon^{\mathrm{light}}$ in samples produced with MadGraph+Pythia8 parton shower. To correct MC samples produced with other event generators and parton shower models, additional MC-to-MC corrections needs to be applied.

5.4. Uncertainty Estimation

Several sources of uncertainty are considered in this calibration. The aim of this section is to give a brief introduction to the different uncertainties that are included in the results.

The 'Flip' extrapolation uncertainty accounts for the differences between calibrating the `DL1rFlip` and `DL1r` algorithms. The adjusted MC method, described at the beginning of this chapter, is used to extract p_{T}-dependent SFs for both algorithms. The ratio between the different SFs is taken as the extrapolation uncertainty. The largest value among all jet p_{T} intervals is used for the final uncertainty estimate.

The MC modelling uncertainty accounts for differences between MC generators in the modelling of parton showers, hadronisation and the matrix element calculation. Fits using Z+jets events simulated with Sherpa or MadGraph+Pythia8 are performed and the absolute difference between the two SFs is used as an uncertainty.

The c-jet SF uncertainty accounts for the effect of the 30% uncertainty in SF^{c}. This uncertainty is estimated from the ϵ^{c} calibration of the `DL1rFlip` on $t\bar{t}$ events with one lepton [91]. The effect on the SF$^{\mathrm{light}}$ measurement is evaluated by shifting the SF^{c} to 1.3 and 0.7 and taking the SF^{c} uncertainty to be the mean impact on SF$^{\mathrm{light}}$ from the two variations.

The impact parameter (d_0, z_0) uncertainty accounts for modelling uncertainties in the tracking parameters. A correction factor is estimated from $t\bar{t}$ and applied to templates similar to those in Figure 5.5. The impact of extracting SF$^{\mathrm{light}}$ from the fits to the corrected templates is used as an uncertainty.

The impact of the statistical uncertainties of the data and MC templates on SF^{light} are also taken into account. These are implemented following the Beeston-Barlow method [92]. Cross-check studies are also performed using a 'toy' approach. More information can be found in [1].

5.5. Results

This section summarises the light-flavour jet scale factors for `DL1r` obtained with the negative tag method applied to the Z+jets sample. The 85%, 77% and 70% OPs are successfully calibrated. However, even when using the negative tag method, there are not enough b-tagged light-flavour jets to calibrate the 60% OP. Due to this limitation, and given that the SFs for the 77% and 70% OPs do not show significant deviations from unity, the SF for the 60% OP is set to 1. The extrapolation uncertainty, which is expected to be dominant, is derived specifically for the 60% OP and found to the slightly larger than for the 70% OP. The other uncertainties, which are expected to be sub-leading and suffer from large uncertainties when evaluated for the 60% OP, are assumed to be identical to the 70% OP.

The results for the light-flavour jet calibration of the `DL1r` algorithm using pflow jets in Run 2 data in terms of the SFs for the different jet p_T intervals and OPs, are shown in Figure 5.6. Furthermore, Figure 5.7 and Tables 5.1-5.4 show the impact of the different uncertainties for each jet p_T interval and OP. The total uncertainties range from 11% to 23% and do not have a strong dependence on the jet p_T.

Table 5.1.: SF^{light} uncertainties for the 85% efficiency `DL1r` OP as a function of the jet p_T [1].

Relative uncertainties [%], 85% SF^{light} single-cut OP				
p_T bin [GeV]	$20 < p_T < 50$	$50 < p_T < 100$	$100 < p_T < 150$	$150 < p_T < 300$
c-jet SF	6.1	5.9	6.2	5.3
'Flip' extrapolation	9.7	9.7	9.7	9.7
MC modelling	0.38	2.4	4.4	1
Impact parameter (d_0, z_0)	1	1.3	1	1.2
Total systematic uncertainty	11	12	12	11
Data statistical	0.52	0.56	1.1	1.4
MC statistical	0.88	0.84	0.72	0.4
Total statistical uncertainty	1.1	1	1.4	1.6
Total uncertainty	12	12	12	11

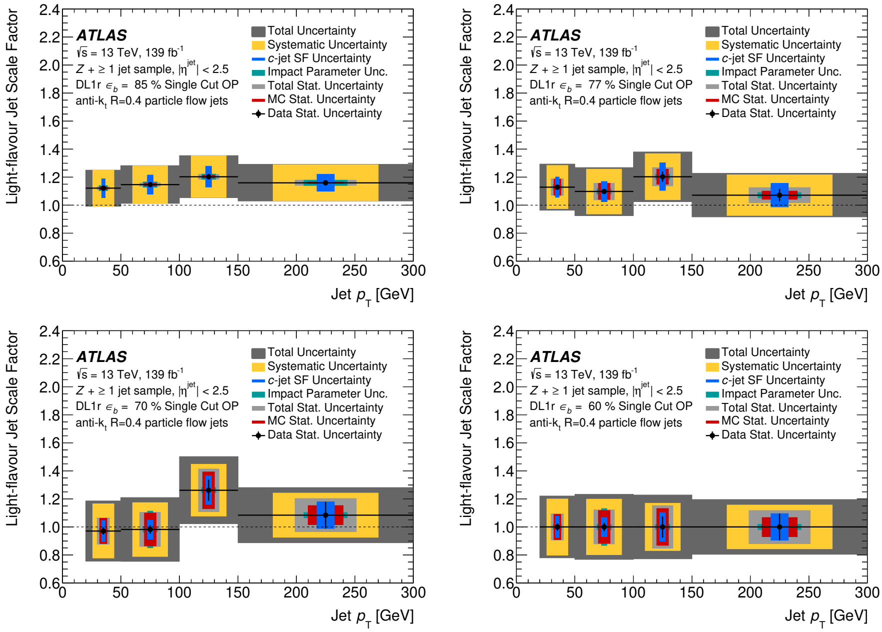

Figure 5.6.: SFs to calibrate ϵ^{light} for the `DL1r` algorithm for the different OPs [1].

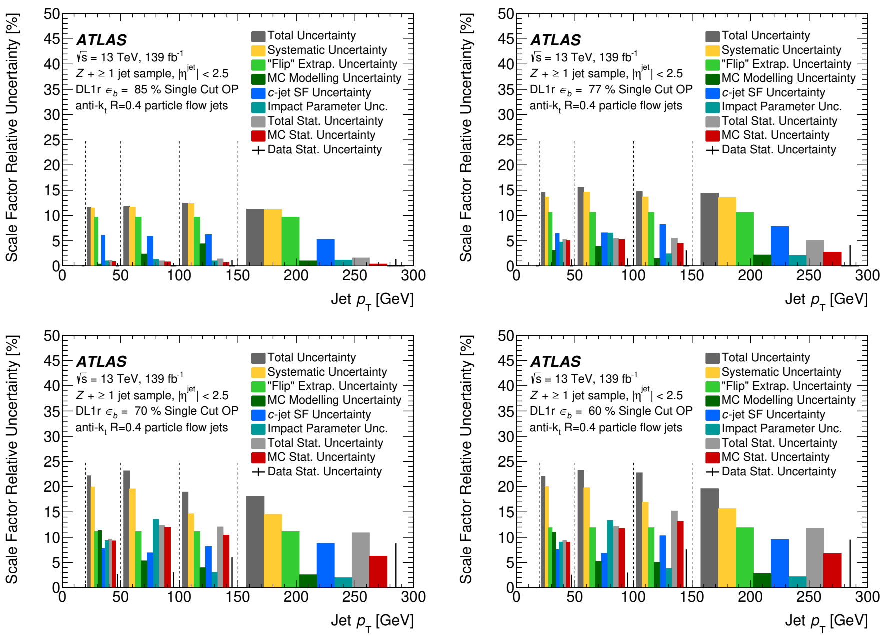

Figure 5.7.: Uncertainties on the `DL1r` SF^{light} for the different OPs [1].

Table 5.2.: SF^{light} uncertainties for the 77% efficiency DL1r OP as a function of the jet p_T [1].

Relative uncertainties [%], 77% SF^{light} single-cut OP				
p_T bin [GeV]	$20 < p_T < 50$	$50 < p_T < 100$	$100 < p_T < 150$	$150 < p_T < 300$
c-jet SF	6.4	6.6	8.2	7.8
'Flip' extrapolation	11	11	11	11
MC modelling	3.1	3.9	1.4	2.2
Impact parameter (d_0, z_0)	4.8	6.5	2.4	2.1
Total systematic uncertainty	14	15	14	14
Data statistical	1.3	1.5	3.1	4.1
MC statistical	5.1	5.2	4.5	2.7
Total statistical uncertainty	5.2	5.4	5.5	5.1
Total uncertainty	15	16	15	14

Table 5.3.: SF^{light} uncertainties for the 70% efficiency DL1r OP as a function of the jet p_T [1].

Relative uncertainties [%], 70% SF^{light} single-cut OP				
p_T bin [GeV]	$20 < p_T < 50$	$50 < p_T < 100$	$100 < p_T < 150$	$150 < p_T < 300$
c-jet SF	7.8	6.9	8.2	8.8
'Flip' extrapolation	11	11	11	11
MC modelling	11	5.3	4	2.6
Impact parameter (d_0, z_0)	9.3	14	3	2
Total systematic uncertainty	20	20	15	15
Data statistical	2.6	3	6	8.8
MC statistical	9.3	12	10	6.3
Total statistical uncertainty	9.7	12	12	11
Total uncertainty	22	23	19	18

Table 5.4.: SF^{light} uncertainties for the 60% efficiency DL1r OP as a function of the jet p_T [1].

Relative uncertainties [%], 60% SF^{light} single-cut OP				
p_T bin [GeV]	$20 < p_T < 50$	$50 < p_T < 100$	$100 < p_T < 150$	$150 < p_T < 300$
c-jet SF	7.6	6.8	10	9.5
'Flip' extrapolation	12	12	12	12
MC modelling	11	5.2	5	2.8
Impact parameter (d_0, z_0)	9.1	13	3.8	2.2
Total systematic uncertainty	20	20	17	16
Data statistical	2.6	3	7.6	9.5
MC statistical	9	12	13	6.8
Total statistical uncertainty	9.4	12	15	12
Total uncertainty	22	23	23	20

The obtained SFs have central values close to one, which indicates that only a small correction is needed to properly model the tagging of light-flavour jets in data with the DL1r algorithm. Furthermore, since most SFs have values slightly larger than one, we can conclude that the DL1r algorithm slightly under-predicts the amount of light-flavour jets in data in comparison to simulation. The calibration is currently limited by the extrapolation uncertainty for all OPs, however a relatively large MC statistical uncertainty is also observed for the tighter OPs, where less events with a light-flavour jet are selected.

The calibration presented in this Chapter has been used by all ATLAS publications that use data recorded between 2015–2018, including those presented in Chapters 6–8. The light-flavour jet scale factors are applied to correct the performance of the b-tagging algorithms and their uncertainties are included as systematic uncertainties in the analyses. The calibration of the light-flavour jet mistag rate is crucial for analyses that select b-jets using a loose OP. For these analyses, which are characterised by having a large fraction of light-flavour jets, a large uncertainty on $\mathrm{SF}^{\mathrm{light}}$ could hide the targeted signal. For analyses that require tighter b-tag OPs, and hence have a very low fraction of light-flavour jets in the SR, a precise mistag rate calibration is less crucial.

Chapter 6

Search for New Phenomena in Events with Top Quark Pairs

This chapter presents parts of the ATLAS publication [2] on the search for new phenomena with top quark pairs in final states with one charged lepton, jets and missing transverse momentum.

6.1. Introduction

As discussed in Chapter 1. SUSY can provide solutions to many of the shortcomings of the SM by introducing supersymmetric partners to the SM particles. In this chapter an analysis which targets the most minimal unconstrained supersymmetric model, known as the MSSM, is presented. In this model the superpartners of the left- and right-handed top quarks ($\tilde{t}_L$,$\tilde{t}_R$) mix to form two mass eigenstates $\tilde{t}_1$ and $\tilde{t}_2$, where $\tilde{t}_1$ is the lighter of the two. In a similar way, the charged (neutral) SUSY partners of the Higgs and electroweak gauge bosons mix and their linear superposition forms the chargino $\tilde{\chi}^{\pm}_{1,2}$ (neutralino $\tilde{\chi}^0_{1,2,3,4}$) mass eigenstates. In R-parity conserving SUSY models (like the MSSM), the LSP, usually the neutralino ($\tilde{\chi}^0_1$), is a DM candidate.

Many SUSY models predict that $\tilde{t}_1$ should be among the lightest SUSY particles [93] and could therefore be one of the first to be discovered at the LHC. The analysis presented in this chapter includes a search for direct $\tilde{t}_1$ pair production where each $\tilde{t}_1$ decays to $t+\tilde{\chi}^0_1$, resulting in a final state similar to $t\bar{t}$ production but with larger $E_{\mathrm{T}}^{\mathrm{miss}}$ because of the neutralino pair. A similar final state can be produced by models where a single spin-0 mediator (ϕ or a) is produced together with a pair of top quarks and decays to a pair of light DM particles ($\tilde{\chi}$). The Feynman diagrams for both models, which are referred to as signals, are shown in Figure 6.1. Top quarks are massive and decay quickly to a $W^{\pm}$ boson and a b-quark. $W^{\pm}$ can decay either leptonically ($W^{\pm} \rightarrow l^{\pm}\nu$) or hadronically ($W^{\pm} \rightarrow q\bar{q}'$). The search presented in this chapter focuses on the specific case when one top quark decays hadronically and the other leptonically resulting in a final state with one charged lepton (μ or e), jets and $E_{\mathrm{T}}^{\mathrm{miss}}$.

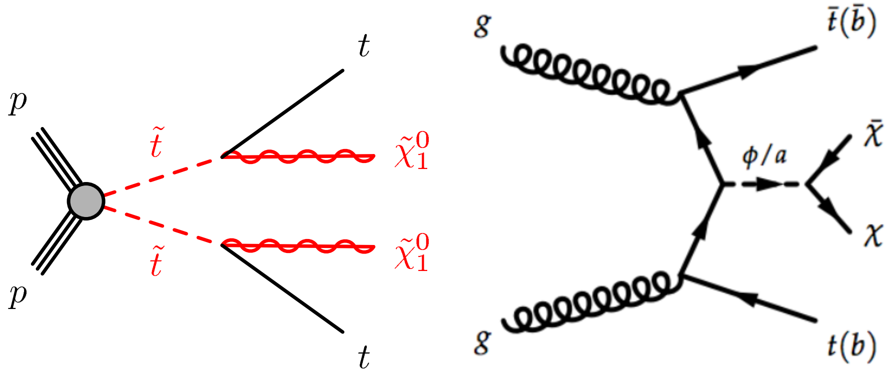

(a) stop (b) DM

Figure 6.1.: Representive Feynman diagrams illustrating the considered signals for the $t\bar{t}$+$E_{\mathrm{T}}^{\mathrm{miss}}$ search: stop production where the stop decays into a top quark and the lightest neutralino and DM s-channel production via a spin-0 mediator. [2]

Due to the fact that SUSY is a broken symmetry, the masses of the supersymmetric particles are unknown. This analysis assumes that the $\tilde{t}_1$ is relatively light and decays directly to the LSP $\tilde{\chi}_1^0$, however, different decay modes are possible depending on the masses of $\tilde{t_1}$ and $\tilde{\chi_1^0}$, as shown in Figure 6.2, and specific search strategies need to be defined for each case. For the specific case where the mass difference (Δm) between the stop and the neutralino ($m_{\tilde{t}_1}$-$m_{\tilde{\chi}_1^0}$) is larger than the top mass (m_t), which is the focus of this chapter, the stop undergoes a 2-body decay $\tilde{t}_1 \rightarrow t\tilde{\chi}_1^0$ as shown in Figure 6.1.

6.2. Signal Regions

In order to detect detect the 2-body stop decay and DM, a set of SRs are defined using a "cut & count" approach. An iterative optimisation

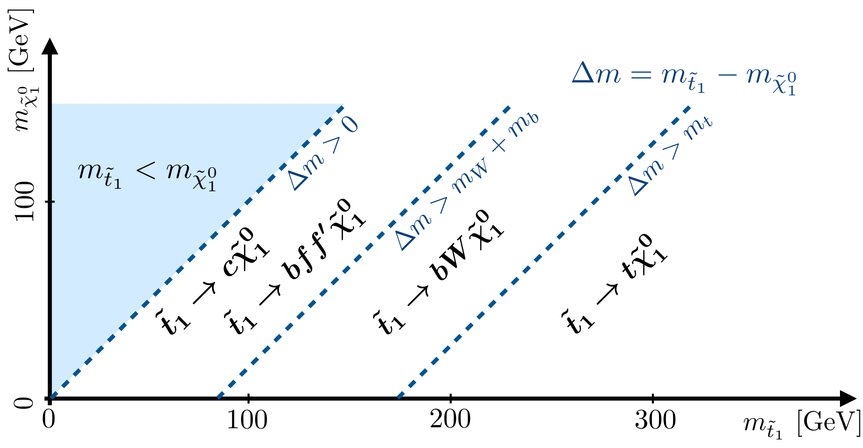

Figure 6.2.: Illustration of the dominant stop decay modes in the plane spanned by the masses of the stop ($\tilde{t}_1$) and the lightest neutralino ($\tilde{\chi}_1^0$), where the latter is assumed to be the lightest supersymmetric particle. Stop decays into supersymmetric particles other than the lightest supersymmetric particle are not considered [94].

algorithm [95], that selects the distributions and cuts that yield the best discovery significance, is used to define a total of 3 SRs. The SRs are characterised by requiring events to pass the so-called hard lepton preselection defined in Table 6.1 (which is also applied prior to optimisation) and the set of cuts selected by the iterative algorithm which are defined in Table 6.2. Details on the SR selection are described in [2]. Two SRs are defined for the 2-body stop decay signal targeting medium (tN_med) and high (tN_high) stop masses. A single SR is defined for the DM signal. Both targeted signals are characterised by large $E_{\mathrm{T}}^{\mathrm{miss}}$ from the LSP or the DM particles and therefore a trigger requiring large $E_{\mathrm{T}}^{\mathrm{miss}}$ at the HLT [96], is used to select events in the SR. The b-jets are reconstructed with the `MV2c10` algorithm at the 77% OP.

The expected background composition in the three SRs is shown in Figure 6.3. CRs are defined for the largest backgrounds in each SR in order to ensure the best possible background prediction. The MC predictions of these large backgrounds are corrected using the NFs that are extracted in the CRs. The smaller backgrounds are estimated purely from MC. The largest background contamination in all SRs comes from top quark pairs

Table 6.1.: Preselection criteria used for the hard lepton signals described in this chapter.

Selection	hard-lepton
Trigger	$E_{\mathrm{T}}^{\mathrm{miss}}$ triggers only
Data quality	jet cleaning, primary vertex
Second-lepton veto	no additional baseline leptons
Number of leptons, tightness	= 1 'loose' lepton
Lepton p_{T}[GeV]	> 25
Number of jets	≥ 4 (25 GeV)
Number of b-jets	≥ 1
$E_{\mathrm{T}}^{\mathrm{miss}}$ [GeV]	> 230
m_{T}[GeV]	> 30
$\lvert\Delta\phi(j_{1,2}, \bar{p}_{\mathrm{T}}^{\mathrm{miss}})\rvert$	> 0.4
$m_{\mathrm{T2}^{\tau}}$	> 80

Table 6.2.: Summary of the selection criteria defining the DM, tN_med and tN_high SRs.

Selection	DM	tN_med	tN_high
Preselection	hard-lepton		
Njet, $N_{b\text{-jet}}$	$\geq (4, 2)$	$\geq (4, 1)$	
jet p_T [GeV]	$> (80, 60, 30, 25)$	$> (100, 90, 70, 50)$	$> (120, 50, 50, 25)$
b-jet p_{T} [GeV]	-		>80
$E_{\mathrm{T}}^{\mathrm{miss}}$ [GeV]	> 230	> 230	> 520
$E_{\mathrm{T},\perp}^{\mathrm{miss}}$ [GeV]	-	> 400	-
$H_{\mathrm{T,sig}}^{\mathrm{miss}}$	> 15	> 16	> 25
m_T [GeV]	> 180	> 220	> 380
topness	> 8	> 9	> 8
$m_{\mathrm{top}}^{\mathrm{reclustered}}$ [GeV]		> 150	
$\Delta R(b, l)$	-	< 2.8	< 2.6
$\Delta\phi(\mathrm{jet}_i, \bar{p}_{\mathrm{T}}^{\mathrm{miss}}),\ i \in [1, 4]$	>0.9	-	-
$\Delta\phi(l, \bar{p}_{\mathrm{T}}^{\mathrm{miss}})$	>1.1	-	-

produced in association with Z bosons ($t\bar{t}Z$). The CR for this background is described in the next section. CRs are also defined for the top quark pair production ($t\bar{t}$) background, which is a large background in all SRs. The tN_med and tN_high SRs also have a relatively large contamination from W+jets and single top-quark production, therefore specific CRs for those backgrounds are also defined for those SRs.

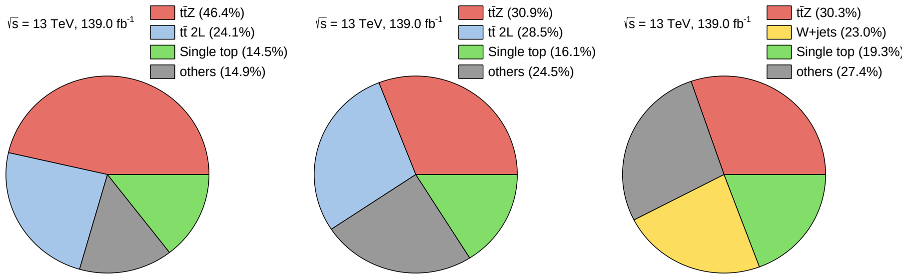

(a) DM (b) tN_med (c) tN_high

Figure 6.3.: Relative background composition for the different SRs.

6.3. Control Region for the $t\bar{t}Z$ Background

The main background in the tN_med, tN_high and DM SRs is $t\bar{t}Z$ production with the Z boson decaying to two neutrinos. The process, shown in Figure 6.4, has very similar characteristics to the targeted signals. The $E_{\mathrm{T}}^{\mathrm{miss}}$ associated with the neutrinos from the Z decay cannot be distinguished from the $E_{\mathrm{T}}^{\mathrm{miss}}$ associated with the $\tilde{\chi}_1^0$ ($\tilde{\chi}$) production in the SUSY stop (DM) signal, making $t\bar{t}Z(\rightarrow \nu\nu)$ an irreducible background.

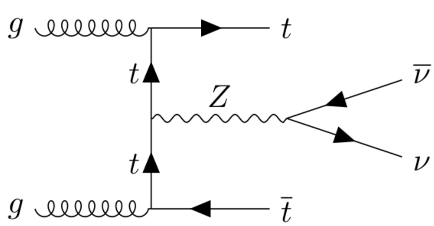

Figure 6.4.: Feynman diagram for $t\bar{t}Z(\rightarrow \nu\nu)$ production.

Due to the large contamination of $t\bar{t}Z(\rightarrow \nu\nu)$ events in the SR, a CR needs to be defined. But because it is an irreducible background and because CRs must be orthogonal to SRs (no events should pass both selections) it is impossible to define a CR which has a sufficient $t\bar{t}Z(\rightarrow \nu\nu)$ purity. Instead, the similarities in event kinematics between $t\bar{t}Z(\rightarrow \nu\nu)$ and $t\bar{t}Z(\rightarrow ll)$ (where $l = e$ or μ) production are exploited. A CR for $t\bar{t}Z(\rightarrow ll)$, which is referred to as the TZCR, requiring three charged leptons is therefore used to obtain the $t\bar{t}Z$ NF. The branching fraction for $t\bar{t}Z(\rightarrow ll)$ is comparatively low and requires a looser CR selection, but provides a high purity sample.

Contrary to $t\bar{t}Z(\rightarrow \nu\nu)$ events, which can be selected by the $E_{\mathrm{T}}^{\mathrm{miss}}$ trigger, $t\bar{t}Z(\rightarrow ll)$ events need to be selected with another trigger. In the TZCR, events are selected using a logical OR of a single electron[97] or muon trigger [98] and are required to have exactly 3 signal leptons, ≥ 4 signal jets, and ≥ 1 or ≥ 2 b-jets depending on the SR selection requirements. The lepton p_{T} is required to be 25 GeV for one of the leptons (imposed by the trigger) and 15 GeV for the rest. For events with electrons, at least one is required to pass the 'Tight' identification criterion. The two leptons with an invariant mass closest to the mass of the Z boson, i.e. $81 < m_{ll} < 101$ GeV, are selected as the $Z(\rightarrow ll)$ leptons, and the other lepton as originating from the top decay.

To mimic the $E_{\mathrm{T}}^{\mathrm{miss}}$ of the $t\bar{t}Z(\rightarrow \nu\nu)$ events, the leptons from the Z decay are treated as invisible and a modified missing transverse energy ($\tilde{E}_{\mathrm{T}}^{\mathrm{miss}}$) is calculated by adding the $p_{\mathrm{T}}^{(ll)}$ from $Z(\rightarrow ll)$ to the original $E_{\mathrm{T}}^{\mathrm{miss}}$. A cut on $\tilde{E}_{\mathrm{T}}^{\mathrm{miss}}> 230$ GeV is applied to define all three CRs. This cut is the same as that in the corresponding SR except for the tN_high-TZCR that uses a looser cut in order to reduce the statistical uncertainties in the CR. The SR jet p_{T} selection criteria are also used to construct the corresponding TZCR. Furthermore, a 80 GeV p_{T} requirement is also applied to the leading b-jet in the DM TZCR. The main selection criteria for the TZCR (except trigger and lepton identification requirements) are summarised Table 6.3.

Table 6.3.: Selection criteria used to define the TZCR for the DM, tN_med, and tN_high SRs.

TZCR	DM	tN_med	tN_high
Number of b-jets	$\geq$2	$\geq$1	
Jet p_{T} [GeV]	>(80,60,30,25)	>(100,90,70,50)	>(120,50,50,25)
Leading b-jet p_{T} [GeV]	>80	> 0	
m_{ll} [GeV]		>81, < 101	
$\tilde{E}_{\mathrm{T}}^{\mathrm{miss}}$ [GeV]		>230	
Lepton p_{T} [GeV]		>(25,15,15)	

The purity of $t\bar{t}Z$ events in the TZCR varies. The TZCR for the tN regions, characterised by ≥ 1 b-jets, have a $t\bar{t}Z$ purity around 60% with large multiboson contamination around 20%. The TZCR for the DM region on the other hand, characterised by ≥ 2 b-jets, has a $t\bar{t}Z$ purity above 75% with a small multiboson contamination around 7%. Table 6.4 shows the yields in each of the TZCRs. The background composition can be found in Figure 6.5.

Table 6.4.: Background composition in the TZCR for DM, tN_med, and tN_high SRs.

TZCR	DM	tN_med	tN_high
$t\bar{t}$Z	49.88 ± 0.56	41.99 ± 0.56	83.94 ± 0.75
Diboson	5.43 ± 0.17	13.72 ± 0.24	34.49 ± 0.40
tWZ	5.18 ± 0.32	5.52 ± 0.34	10.43 ± 0.49
$t+X$	4.10 ± 0.16	3.58 ± 0.15	6.90 ± 0.21
Z+jets	1.05 ± 0.21	1.77 ± 0.23	4.73 ± 0.48
$t\bar{t}$	1.15 ± 0.29	2.33 ± 0.63	5.39 ± 0.94
$t\bar{t}$+W	0.51 ± 0.06	0.45 ± 0.06	0.89 ± 0.08
Single top	0.01 ± 0.01	0.03 ± 0.02	0.29 ± 0.18
W+jets	0.00 ± 0.00	0.00 ± 0.00	0.00 ± 0.00
Total SM	67.32 ± 0.78	69.39 ± 0.98	147.05 ± 1.47
Data	75	65	135
NF	1.11	1.07	0.92

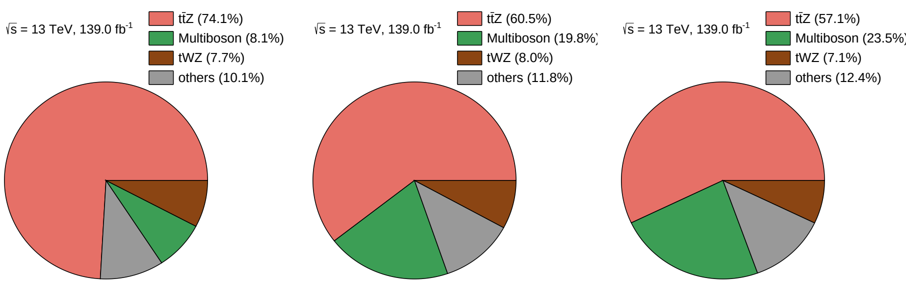

(a) DM (b) tN_med (c) tN_high

Figure 6.5.: Relative background composition for the different TZCRs.

The possibility to define a multiboson CR from the TZCR by requiring zero b-jets was also studied. The purity of multiboson events in such region is around 80% independently of the jet p_{T} requirements. This CR would be used to correct the MC prediction of the multiboson background in the TZCRs. Some studies were performed for tN_high, since it has the largest multiboson contribution in both the SR and the TZCR, but no benefit was observed from the use of a multiboson CR and the option was discarded.

The post-fit distributions and data-to-simulation comparisons of the $\tilde{E}_{\mathrm{T}}^{\mathrm{miss}}$ distributions for the DM and tN_high TZCR are shown in Figure 6.6. For the DM tZCR plot, the requirement on $\tilde{E}_{\mathrm{T}}^{\mathrm{miss}}$ is removed and the arrow indicates the final selection on that variable. Good agreement is observed between data and prediction, within uncertainties.

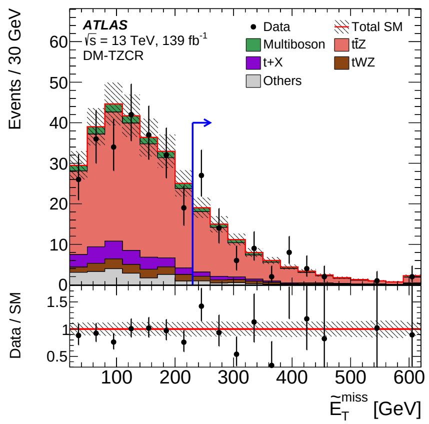

(a) DM TZCR

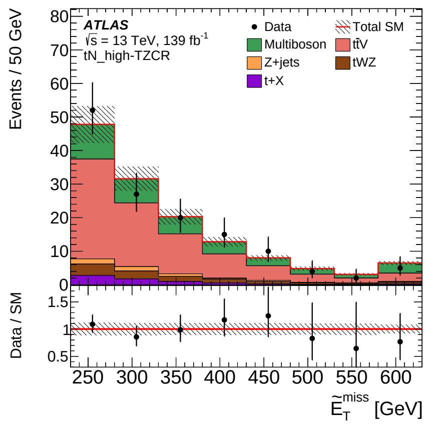

(b) tN_high TZCR

Figure 6.6.: Data-to-simulation comparison of the $\tilde{E}_{\mathrm{T}}^{\mathrm{miss}}$ distributions [2]. The hashed band includes statistical and systematic uncertainties. The lower panel shows the ratio of data events to expected events. The distributions shown are post-fit, i.e. each background is scaled by a NF obtained from a background-only likelihood fit to the CRs. For (a) the requirement on $\tilde{E}_{\mathrm{T}}^{\mathrm{miss}}$ is removed and the arrow indicates the final selection on that variable.

6.4. Systematic Uncertainties

Several sources of systematic uncertainties affecting the signal and background estimates are considered. These uncertainties can arise from the theoretical modelling of the relevant processes or be of experimental origin. They can affect the background estimates in the SR via the theoretical cross section calculations, via the fraction of MC simulated background events entering the SR or via the extrapolation between the CR and SR (the so-called transfer factor). Table 6.5 summarises the dominant systematic uncertainties of the total predicted background yield in the SR, obtained from the background only fits.

Experimental uncertainties arise from imperfect modelling of the detec-

Table 6.5.: Summary of the dominant systematic uncertainties in % of the total predicted background, obtained from the background-only fits.

SR Uncertainty (%)	tN_med	tN_high	DM
$t\bar{t}$ normalisation	4.4	2.7	2.1
$t\bar{t}Z$ normalisation	9.0	6.8	8.0
W+jets normalisation	3.0	4.8	-
single-top normalisation	2.8	3.4	-
$t\bar{t}$ modelling	3.0	9.1	6.1
$t\bar{t}Z$ modelling	7.7	7.1	3.3
W+jets modelling	2.3	3.8	-
single-top modelling	0.5	0.8	4.2
JER	10.9	5.1	8.3
$E_{\mathrm{T}}^{\mathrm{miss}}$ experimental	0.7	0.4	1.9
b-tagging experimental	1.7	3.6	4.2
JES	6.0	2.5	2.5
Leptons experimental	1.0	1.6	1.2
Pile-up	1.1	1.2	1.4
Theory	0.9	1.3	1.1
Monte Carlo statistics	4.1	6.6	3.2
Total	19.0	17.2	23.1

tor response and object reconstruction. One example is the b-tagging experimental uncertainties such as the uncertainty on the light-flavour jet mistag rate introduced in Chapter 5. Other experimental uncertainties include lepton and $E_{\mathrm{T}}^{\mathrm{miss}}$ reconstruction, JES, jet energy resolution (JER) and pile-up.

Theoretical uncertainties are related to the ability of the MC simulations to describe the data, both in terms of event properties (i.e. shapes and kinematic distributions) and the overall normalisation. Different uncertainties are considered depending on whether the backgrounds have a defined CR or not. For backgrounds that are estimated directly from MC simulation using a theoretical cross section, e.g. W+jets and single-top for the DM SR, a *theory* uncertainty from the cross-section calculation and other MC-related characteristics, such as parton distributions, normalisation and factorisation scales, is considered. For the backgrounds estimated using a CR, e.g. $t\bar{t}Z$ and $t\bar{t}$, *modelling* uncertainties which affect the transfer factors and *normalisation* uncertainties arising from limited statistical precision in the CRs are considered. The sources of modelling uncertainties vary depending on the process, but generally include the choice of MC generator, the amount of ISR and FSR and the choice of renormalisation and factorisation scales. Due to the focus of this thesis on the $t\bar{t}Z$ background and the definition of its CR, the estimation of the $t\bar{t}Z$ modelling uncertainties' impact on the transfer factor is described in detail.

$t\bar{t}Z$ Uncertainties

Modelling uncertainties on the $t\bar{t}Z$ background only enter in the SR through the transfer factor $\mathrm{TF} = \mathrm{yield}_{\mathrm{SR}}/\mathrm{yield}_{\mathrm{CR}}$, therefore the uncertainties (σ_{TF}) are estimated as

$$\sigma_{TF} = \frac{\mathrm{TF}_{\mathrm{Nom}} - \mathrm{TF}_{\mathrm{Alt}}}{\mathrm{TF}_{\mathrm{Nom}}} \tag{6.1}$$

where Nom refers to the default $t\bar{t}Z$ simulation used for the analysis (aMC@NLO matrix element generator and Pythia8 parton shower), and Alt refers to alternative MC simulations (either a different choice of matrix element generator or parton shower model, or different choices of parameters within aMC@NLO).

For $t\bar{t}Z$, the considered modelling uncertainties are the renormalisation and factorisation scales, and the amount of ISR and FSR. To calculate the modelling uncertainty, the following variations are used as alternative to the nominal MC:

- Renormalisation scale (μ_{R}) and factorisation scale (μ_{F}) variations [2]: The nominal renormalisation and/or the factorisation scales are scaled with $\times 2$ and $\times 0.5$. The obtained transfer-factor uncertainties for different combinations are shown in Table 6.6.
- Radiation uncertainty: Alternative samples with more (Var3Up) or less (Var3Down) ISR and FSR than the nominal sample are used to obtain the $\mathrm{TF}_{\mathrm{Alt}}$. Table 6.7 shows the estimated transfer-factor radiation uncertainty.

The largest of the obtained $t\bar{t}Z$ renormalisation and factorisation and radiation uncertainties for each SR are selected and used as NPs in the fits. Table 6.8 shows the pre-fit $t\bar{t}Z$ modelling uncertainties used as input to the fits. These NPs are pulled and constrained during the fits resulting in lower post-fit uncertainties, which were already summarised for the background-only fits in Table 6.5. $t\bar{t}Z$ modelling uncertainties on the transfer factor from the TZCR to the other regions used in the fit are also estimated.

Table 6.6.: Impact of using alternative renormalisation and factorisation scales on the transfer factor from the TZCR to the SR. Only the largest variation, which is obtained when multiplying both μ_F and μ_R with 0.5, is chosen as renormalisation and factorisation scale uncertainty. For $\mu_F \times 0.5$, no events pass the CR selection and the TF cannot be estimated.

σ_{TF} (%)	$(\mu_F \& \mu_R) \times 2$	$(\mu_F \& \mu_R) \times 0.5$	$\mu_F \times 2$	$\mu_R \times 2$	$\mu_R \times 0.5$	$\mu_F \times 0.5$
DM	1.2	**-2.4**	0.2	1.1	-1.7	-
tN_med	1.7	**-3.4**	0.8	1.1	-1.9	-
tN_high	1.8	**-2.4**	-0.7	1.0	1.7	-

Table 6.7.: Impact of using alternative high (Var3Up) and low (Var3Down) ISR and FSR scenarios on the transfer factor from the TZCR to the SR. Only the largest variation for each SR is chosen as the radiation uncertainty.

σ_{TF}(%)	Var3Up	Var3Down
DM	**13.9**	-9.6
tN_med	**-18.9**	-15.2
tN_high	13.2	**-16.7**

Table 6.8.: $t\bar{t}Z$ modelling uncertainties on the transfer factor used as input to the fits. Two NPs are introduced, one for the renormalisation and factorisation scales (R&F) and one for the amount of ISR and FSR.

Modelling $t\bar{t}Z$ uncertainty (%)	R&F	radiation
DM	-2.4	14
tN_med	-3.4	-19
tN_high	-2.4	-16.7

6.5. Results

For each SR, a background-only likelihood fit is performed to determine the SM background yield in the SR. The number of observed events and the predicted number of SM background events for each SR are shown in Table 6.9, together with the resulting NFs for each background. Furthermore, the p_0 values (capped at 0.5), which assess the compatibility of the observed events with the background-only hypothesis are shown for all SRs.

A good agreement is observed between data and the SM background estimate in all SRs. The largest excess is observed for the tN_high, where $p_0 = 0.01$. As it was described in Section 3.2.4, a $p_0 \leq 0.003$ ($Z \geq 3\sigma$) is needed to claim evidence of new physics. The small excess in the tN_high SR is therefore compatible with the SM hypothesis. Since no evidence of new physics is found, this result extends previous upper limits on stop pair production models and spin-0 mediator models. The exclusion tests are however not part of this thesis. Detailed results can be found in [2].

Table 6.9.: Number of observed events and the predicted number of SM background events, background NFs and p_0-values obtained from the fit for each SR.

	tN_med	tN_high	DM
Observed	21	17	56
Total SM	21 ± 4	9.5 ± 1.6	56 ± 8
$t\bar{t}$	7.2 ± 1.2	2.0 ± 1.0	14 ± 4
$t\bar{t}Z$	8.3 ± 2.5	3.5 ± 1.0	29 ± 6
single-top	$0.4^{+0.6}_{-0.4}$	$0.27^{+0.34}_{-0.27}$	7 ± 4
W+jets	2.5 ± 2.3	2.3 ± 1.0	2.56 ± 0.24
Multiboson	1.49 ± 0.21	1.06 ± 0.16	1.31 ± 0.18
Other	0.78 ± 0.06	0.320 ± 0.024	2.15 ± 0.16
$t\bar{t}$ NF	$0.98^{+0.14}_{-0.12}$	0.90 ± 0.12	$1.12^{+0.15}_{-0.13}$
$t\bar{t}Z$ NF	$0.95^{+0.22}_{-0.20}$	0.92 ± 0.17	$1.18^{+0.20}_{-0.18}$
single-top NF	$0.11^{+0.26}_{-0.11}$	$0.22^{+0.26}_{-0.22}$	-
W+jets NF	$0.96^{+0.25}_{-0.23}$	0.86 ± 0.17	-
p_0	0.49	0.01	0.50

Chapter 7

EFT Interpretation of the Non-Resonant HH Production Search

This chapter summarises the EFT interpretation of the search for Higgs boson pair production in the $b\bar{b}\gamma\gamma$ final state [4]. The search strategy and event selection, published in [3], are briefly summarised in Section 7.2. The $H \to \gamma\gamma$ decay, one of the channels used for the original Higgs boson discovery [26, 27], has a very low branching fraction but benefits from the very clean discrimination between signal and background provided by the sharp $m_{\gamma\gamma}$ peak. The $H \to b\bar{b}$ decay has the largest branching fraction but is harder to discriminate from other backgrounds with jets. The $HH \to b\bar{b}\gamma\gamma$ decay combines both characteristics, resulting in a clean final state with a branching fraction of 0.26%. Despite its relatively low branching fraction, the $b\bar{b}\gamma\gamma$ is among the most sensitive final states that can be used to try to measure HH production.

7.1. Introduction

The λ_3 coupling, introduced in Section 1.4.3, can be accessed by observing Higgs pair production (HH). The leading production mode, gluon-gluon fusion (ggF), is described in the SM by the Feynman diagrams shown in Figure 7.1. Destructive interference between the two diagrams results in a very small production cross section $\sigma_{HH}^{\text{ggF}} = 31.05$ fb at $\sqrt{s} = 13$ TeV, making it an extremely challenging measurement. In fact, this process has not yet been observed by any experiment.

Measuring λ_3 and comparing to the SM prediction λ_3^{SM} is one of the highest priority physics goals for ATLAS in the coming decade. Searches in

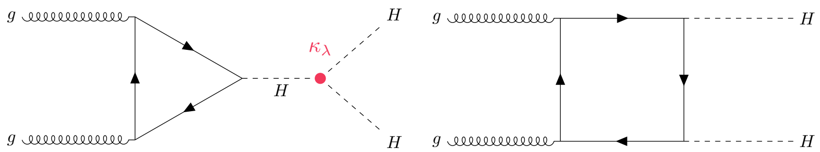

Figure 7.1.: Feynman diagrams for HH production through ggF in the SM [3]. The vertex sensitive to the triple Higgs self-interaction λ_3 is indicated by the κ_λ coupling modifier.

multiple Higgs decay channels are performed by the ATLAS collaboration in order to try to measure the production cross section and deviations from the SM prediction of the Higgs self-coupling ($\kappa_\lambda = \lambda_3/\lambda_3^{\mathrm{SM}}$). By construction, $\kappa_\lambda = 1$ in the SM. Since λ_3 influences the shape of the Higgs potential, as it was shown in Equation 1.18, measuring deviations from $\kappa_\lambda = 1$ would indicate that the true shape of the Higgs potential is different from that predicted by the SM. As discussed in Section 1.4.3, the shape of the Higgs potential has implications in the early Universe electroweak phase transition which could for example explain matter-antimatter asymmetry.

7.2. Search for Non-Resonant $HH \to b\bar{b}\gamma\gamma$ Production

A summary of the search for Higgs boson pairs in a final state with two b-jets and two photons, described in [3], is provided in this section. This search has been optimised to try to measure σ_{HH}^{ggF} and κ_λ.

Events are required to satisfy the preselection given in Table 7.1. The shape of the m_{HH} distribution in HH production is determined by the interference between the two HH production diagrams shown in Figure 7.1. And since κ_λ only affects one of the two diagrams, this distribution is therefore sensitive to variations of κ_λ. The m_{HH} distribution is experimentally accessed through the modified invariant mass of the $b\bar{b}\gamma\gamma$ system, $m^*_{bb\gamma\gamma} = m_{bb\gamma\gamma} - (m_{\gamma\gamma} - 250\ \mathrm{GeV})$, which can be used to define two orthogonal regions that target SM or BSM HH production. The high (low) mass regions are defined by the events that pass the $m^*_{bb\gamma\gamma} \geq (\leq)\ 350$ GeV selection. Independent BDTs are then trained to discriminate the main backgrounds ttH, ggF H, ZH and $\gamma\gamma$+jets from the SM or $\kappa_\lambda = 10$ signal, respectively, for the high mass (HM) and low mass (LM) regions. The BDT score in each region is then used, together with the $m^*_{bb\gamma\gamma}$ selection, to define a total of 4 categories as shown in Table 7.2.

Table 7.1.: The preselection of the $HH \to b\bar{b}\gamma\gamma$ search.

Preselection	
Number of 'Tight' and isolated photons	≥ 2
$m_{\gamma\gamma}$ [GeV]	$\in [105, 160]$
Number of leptons	$== 0$
Number of central jets	$\in [2, 5]$
Number of b-tagged jets @ 70% WP	≥ 1
Number of b-tagged jets @ 77% WP	$== 2$

Table 7.2.: The selection criteria for the four $HH \to b\bar{b}\gamma\gamma$ categories.

Category	Selection Criteria
HM Tight	$m^*_{bb\gamma\gamma} \geq 350$ GeV, HM BDT score $\in [0.967, 1]$
HM Loose	$m^*_{bb\gamma\gamma} \geq 350$ GeV, HM BDT score $\in [0.857, 0.967]$
LM Tight	$m^*_{bb\gamma\gamma} \leq 350$ GeV, LM BDT score $\in [0.966, 1]$
LM Loose	$m^*_{bb\gamma\gamma} \leq 350$ GeV, LM BDT score $\in [0.881, 0.966]$

An unbinned likelihood fit to the $m_{\gamma\gamma}$ distribution is performed to measure the HH production cross section. The non-resonant background is parametrised as an exponential function for which the shape and normalisation are obtained from a fit to data in a region excluding the signal peak at $m_{\gamma\gamma} \in [120, 130]$ GeV.

This search is optimised to target ggF HH production. However, since the sub-leading HH production mode, vector boson fusion (VBF), is also sensitive to λ_3, both ggF and VBF HH production are considered as signal. The Feynman diagrams for VBF HH production are shown in Figure 7.2.

This search sets an observed (expected) upper limit to $\sigma^{\text{ggF+VBF}}_{HH}$ of 4.2 (5.7) times the SM prediction at 95% CL. In terms of hypothesis testing, this result can be understood from the exclusion test described in Section 3.2.4: the observed (expected) signal strength modifier $\mu^{\text{ggF+VBF}} = 4.2$ (5.7) is excluded at Z = 2σ, using the CL method, with real (Asimov) data. The sensitivity to SM HH production is currently very low and hence no discovery test, i.e. p_0 measurements, are

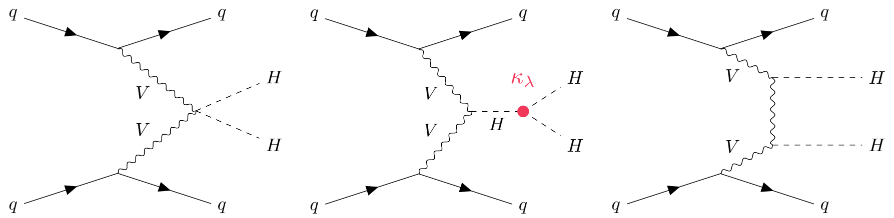

Figure 7.2.: Feynman diagrams for VBF HH production [3]. The vertex sensitive to the triple Higgs self-interaction λ_3 is indicated by the κ_λ coupling modifier.

performed.

The Higgs self-coupling λ_3 is studied through the so-called kappa framework, where all parameters and couplings are set to their SM values except for κ_λ. The observed (expected) limits of the triple-Higgs coupling modifier κ_λ are shown in Figure 7.3. The theory prediction curve is shown in red. As already discussed, variations of κ_λ affect the interference pattern between the two ggF HH production Feynman diagrams shown in Figure 7.1. The interference is maximal, and hence the predicted cross section is minimal, for $\kappa_\lambda \sim 2$. The solid (dashed) black line indicates the observed (expected) upper limit on $\sigma_{HH}^{\text{ggF+VBF}} = \mu^{\text{ggF+VBF}} \times \sigma_{HH}^{\text{ggF+VBF SM}}$ at 95% CL for different κ_λ values. The observed (expected) limits on κ_λ are given by the intersection between the theory prediction and the observed (expected) limit lines. Values outside the -1.5 (-2.4) $< \kappa_\lambda <$ 6.7 (7.7) range are excluded at 95% CL by this search. This range includes the SM prediction ($\kappa_\lambda = 1$) but still allows relatively large deviations with λ_3 up to ~ 7 times larger than the value predicted by the SM.

7.3. HH in the EFT Framework

EFT frameworks, which were introduced in Section 1.4.2, allow the parametrisation of effects of BSM physics at high energies in terms of effective couplings. Contrary to the kappa framework, BSM physics may play a role in multiple interaction vertices in EFT frameworks. These frameworks can therefore be used to make a more general measurement of λ_3 than the kappa framework, which was used in the previous section. Dimension 6 EFT operators introduce new BSM HH production modes.

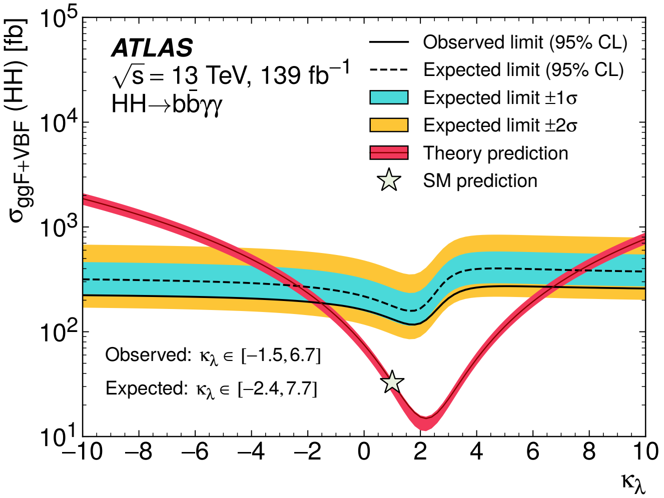

Figure 7.3.: Observed and expected limits at 95% CL on the cross section of non-resonant Higgs boson pair production as a function of the Higgs boson self-coupling modifier κ_λ [3]. The theory prediction curve represents the scenario where all parameters and couplings are set to their SM values except for κ_λ and includes the uncertainty on the cross section. The star marks the cross section ate the κ_λ value predicted by the SM.

Two different EFT formalisms may be used when studying HH production: The SM EFT (SMEFT) [99] and Higgs EFT (HEFT) [100, 101]. In SMEFT, also known as linear EFT, the EFT extension is performed through mass dimensions $(1/\Lambda)$ and the Higgs field is an SU(2) doublet (like in the SM). The HEFT or non-linear EFT is used in this thesis. In this formalism the EFT extension is performed through loops using the so-called chiral Lagrangian [102] and the Higgs field is an (BSM like) EW singlet.

The Feynman diagrams for dimension 6 HEFT operators that play a role in SM (BSM) HH production are shown in Figure 7.4 (7.5), where the role of the Wilson coefficient c_{hhh} is identical to that of κ_λ in the kappa framework. In the SM, the Wilson coefficients $c_{hhh} = c_{tth} = 1$ while $c_{tthh} = c_{ggh} = c_{gghh} = 0$. Since the latter set of Wilson coefficients are only present in the BSM diagrams in Figure 7.4, the above-mentioned choices of Wilson coefficients reduce the set of Feynman diagrams to those of th eSM, making HEFT a natural extension of the kappa framework. The SMEFT formalism is characterised by having strong correlations between different processes (i.e. $c_{ggh} \propto c_{gghh}$ and $c_{tth} \propto c_{tthh}$) and is therefore often used for combinations [103]. In HEFT, these Wilson coefficients are independent and anomalous Higgs couplings are expected to be the dominant new physics effects in the electroweak sector. The c_{gghh} and c_{tthh} Wilson coefficients can therefore only be measured in HH production, making HEFT an especially suitable formalism for a simplified HH interpretation. High energy BSM scenarios [104], which are uniquely sensitive to HH production, can be studied with the HEFT benchmarks defined in Table 7.3 [105]. These benchmarks are obtained using cluster analysis [106] to group Wilson coefficient values which result in similar m_{HH} distributions due to the interference between the relative contributions of the five Feynman diagrams. The m_{HH} distributions for the seven different benchmarks and SM HH production case are shown in Figure 7.6.

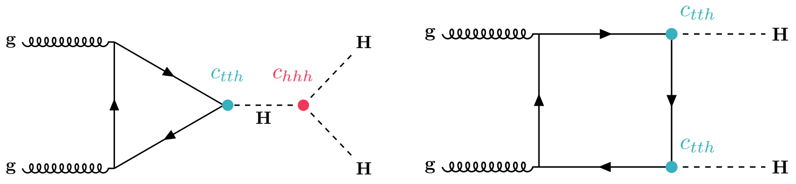

Figure 7.4.: Feynman diagrams for SM HH production through gluon gluon fusion in HEFT [4]. The triple Higgs self-interaction λ_3 is governed by the c_{hhh} Wilson coefficient.

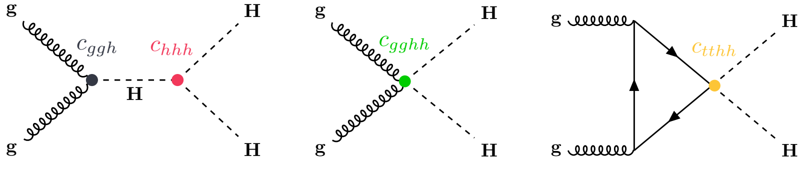

Figure 7.5.: Feynman diagrams for BSM HH production through gluon gluon fusion in HEFT [4]. The triple Higgs self-interaction λ_3 is governed by the c_{hhh} Wilson coefficient.

Table 7.3.: Wilson coefficient values in the SM and the seven BSM benchmark scenarios defined in [105].

Benchmark	c_{hhh}	c_{tth}	c_{tthh}	c_{ggh}	c_{gghh}
SM	1	1	0	0	0
BM 1	3.94	0.94	$-1/3$	0.5	$1/3$
BM 2	6.84	0.61	$1/3$	0.0	$-1/3$
BM 3	2.21	1.05	$-1/3$	0.5	0.5
BM 4	2.79	0.61	$1/3$	-0.5	$1/6$
BM 5	3.95	1.17	$-1/3$	$1/6$	-0.5
BM 6	5.68	0.83	$1/3$	-0.5	$1/3$
BM 7	-0.10	0.94	1	$1/6$	$-1/6$

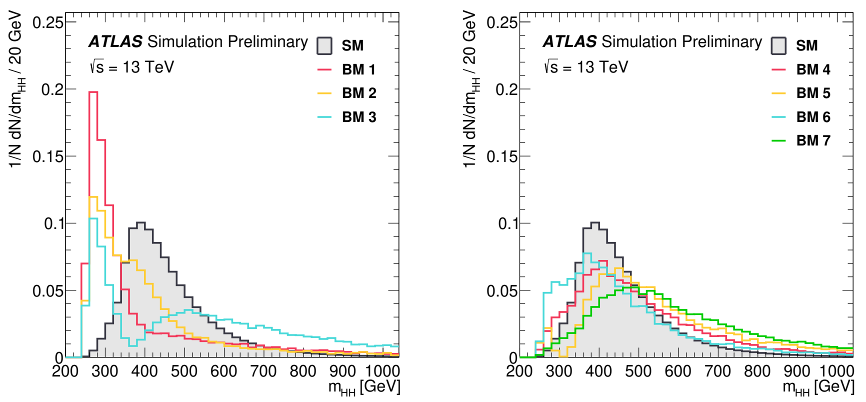

Figure 7.6.: Distribution of the truth level m_{HH} in the SM and the seven BSM HH benchmarks described in Table 7.3 [4].

7.4. Signal Reweighting

The correlation between the Wilson coefficients and m_{HH} cannot only be used to extract information about possible BSM contributions to HH production, but also can be exploited to reweigh a MC-generated HH signal to other points in the EFT parameter space. The σ_{HH} via ggF can be parametrised at NLO for any set of Wilson coefficients as:

$$
\begin{aligned}
\frac{\partial \sigma_{HH}}{\partial m_{HH}} &= \mathrm{Poly}(\mathbf{A}, c_{hhh}, c_{tth}, c_{tthh}, c_{ggh}, c_{gghh} | m_{HH}) \\
&= A_1 c_{tth}^4 + A_2 c_{tthh}^2 + (A_3 c_{tth}^2 + A_4 c_{ggh}^2) \cdot c_{hhh}^2 \\
&+ A_5 c_{gghh}^2 + (A_6 c_{tthh} + A_7 c_{tth} c_{hhh}) \cdot c_{hhh}^2 \\
&+ (A_8 c_{tth} c_{hhh} + A_9 c_{ggh} c_{hhh}) \cdot c_{tthh} + A_{10} c_{tthh} c_{gghh} \\
&+ (A_{11} c_{ggh} c_{hhh} + A_{12} c_{gghh}) \cdot c_{tth}^2 \\
&+ (A_{13} c_{hhh} c_{ggh} + A_{14} c_{gghh}) \cdot c_{tth} c_{hhh} \\
&+ A_{15} c_{ggh} c_{gghh} c_{hhh} + A_{16} c_{tth}^3 c_{ggh} + A_{17} c_{tth} c_{tthh} c_{ggh} \\
&+ A_{18} c_{tth} c_{ggh}^2 c_{hhh} + A_{19} c_{tth} c_{ggh} c_{gghh} + A_{20} c_{tth}^2 c_{ggh}^2 \\
&+ A_{21} c_{tthh} c_{ggh}^2 + A_{22} c_{ggh}^3 c_{hhh} + A_{23} c_{ggh}^2 c_{gghh},
\end{aligned} \tag{7.1}
$$

The A_i coefficients, where $i \in [1-23]$, are parameters which depend on the kinematics of the sample. The unbinned $\mathbf{A}$ and differential $(\mathbf{A}|m_{HH})$ coefficients published in [107] can be used to reweigh the simulated SM HH sample using an event-dependent weight defined as

$$
w(m_{HH}) = \frac{\partial \sigma_{HH} / \partial m_{HH}}{\partial \sigma_{HH}^{\mathrm{SM}} / \partial m_{HH}} = \frac{\mathrm{Poly}(\mathbf{A}|m_{HH})}{\mathrm{Poly}^{\mathrm{SM}}(\mathbf{A}|m_{HH})} \tag{7.2}
$$

This weight changes both the m_{HH} shape and overall normalisation with respect to the simulated SM HH sample. Normalised weights $w^{\mathrm{norm}}(m_{HH})$ are defined in Equation 7.3. The factor $\mathrm{Poly}^{\mathrm{SM}}(A)/\mathrm{Poly}(A)$, which is based on the inclusive A_i coefficients, derived from the full m_{HH} range, is used to cancel the cross section contribution from $w(m_{HH})$ to the normalisation. The reweighting is explained in more detail in [108].

$$
w^{\mathrm{norm}}(m_{HH}) = w(m_{HH}) \cdot \frac{\sigma_{HH}^{\mathrm{SM}}}{\sigma_{HH}} = \frac{\mathrm{Poly}(\mathbf{A}|m_{HH})}{\mathrm{Poly}^{\mathrm{SM}}(\mathbf{A}|m_{HH})} \cdot \frac{\mathrm{Poly}^{\mathrm{SM}}(\mathbf{A})}{\mathrm{Poly}(\mathbf{A})} \tag{7.3}
$$

The SM HH events are simulated at NLO precision considering finite top-quark mass effects using the Powheg Box v2 generator [109, 62, 110, 111, 90] and the PDF4LHC15 PDF [112]. The parton shower and hadronisation is simulated using Pythia8.244 [113] with the NNPDF2.3lo [114] PDF and the A14 tune [115]. In order to interpret the results from [3] in the HEFT framework, the HH SM sample is reweighted to the seven benchmarks following Equation 7.3. The reweighting changes the signal selection efficiency, which is shown for each benchmark scenario and the SM in Table 7.4. The selection efficiency for each SR as a function of the c_{gghh} and c_{tthh} Wilson coefficients is also shown in Figure 7.7.

Table 7.4.: Selection efficiency in each SR for the SM HH and the seven benchmarks.

Acceptance × Efficiency [%]	HM Loose	LM Loose	HM Tight	LM Tight	Total
SM	3.2	0.6	7.7	0.4	11.9
BM 1	1.3	2.9	3.8	1.5	9.5
BM 2	1.8	2.2	4.5	1.2	9.7
BM 3	2.2	1.3	8.3	0.6	12.4
BM 4	2.9	0.7	8.6	0.4	12.6
BM 5	3.1	0.3	9.8	0.1	13.3
BM 6	2.6	1.2	7.0	0.7	11.5
BM 7	3.1	0.3	10.8	0.2	14.4

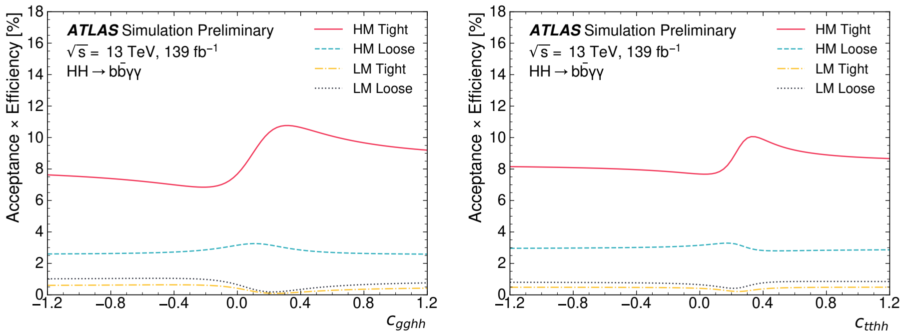

(a) c_{gghh} (b) c_{tthh}

Figure 7.7.: Selection efficiency in each SR as a function of the Wilson coefficients. Only one Wilson coefficient is varied and the others are set to their SM values. [4].

7.5. Systematic Uncertainties

The systematic uncertainties described in [3] for the $HH \rightarrow b\bar{b}\gamma\gamma$ search are also applied in the EFT interpretation. Furthermore, additional uncertainties that may arise from the reweighting procedure are also considered. The reweighting uncertainty is evaluated at truth level by comparing MC-generated BSM samples to SM samples reweighted to the same BSM benchmarks. The BDT selection cannot be applied at truth-level and it is therefore not applied when calculating the HEFT reweighting uncertainty. The effect of the reweighting on the BDT scores has been studied at reconstruction level in the available $\kappa_\lambda = 10$ sample and found to be negligible. The uncertainties on the selection efficiency from the reweighting are summarised in Table 7.5. In the case of c_{tthh} and c_{gghh} scans, the uncertainties are evaluated for the Wilson coefficient values −0.5, 0.5 and 1.0. The largest uncertainty is then used as the overall uncertainty for the full scan.

Region	LM	HM
BM 1	4.9%	0.4%
BM 2	2.4%	4.2%
BM 3	6.1%	4.7%
BM 4	5.3%	1.4%
BM 5	10.8%	2.5%
BM 6	2.8%	1.3%
BM 7	0.3%	2.3%
c_{tthh}	8.7%	1.6%
c_{gghh}	9.8%	6.2%

Table 7.5.: Uncertainties on the selection efficiency from the HEFT reweighting procedure. The uncertainty is estimated individually for each of the HEFT benchmarks, as well as for the SM sample with the c_{gghh} and c_{tthh} Wilson coefficients individually varied to −0.5, 0.5, and 1. In the latter two cases, the maximum of the three variations is used as the uncertainty.

The effect of the reweighting on the theory uncertainties that affect the MC simulations i.e. the choice of the strong coupling constant value, α_S, the renormsalisation and factorisation scales and the PDF set and the parton shower model is also considered. In this case, the uncertainty is evaluated for each signal hypothesis but only the envelope between the SM and BSM hypothesis is used as an uncertainty in order to not reduce the uncertainties with respect to the original publication [3]. The uncertainties on the α_S, the renormalisation and factorisation scales and the PDF set are found to be below 5%. The parton shower uncertainty is found to range from 2–15%. These uncertainties are evaluated at reconstruction level and are therefore estimated for each of the 4 SRs independently.

7.6. Results

This section presents the first interpretations of HH production in the EFT framework ever performed by ATLAS, namely the interpretation of the $HH \rightarrow b\bar{b}\gamma\gamma$ search [3] in the HEFT framework is performed. Upper limits on σ_{HH}^{ggF} are presented for the SM and seven BSM benchmark models. Constraints on the c_{gghh} and c_{tthh} Wilson coefficients, which are uniquely sensitive to HH production and hence have never measured before, are also set, assuming that all other Wilson coefficients have their SM values. The VBF HH production, which depends on c_{hhh}, is treated as background and varied as a function of c_{hhh}.

The observed (expected) upper limits on σ_{HH}^{ggF} for the SM and the seven BSM benchmarks at 95% CL are shown in Table 7.8 and Figure 7.9. For SM the upper limit is $\sigma_{HH}^{\text{ggF}} < 127.7$ (171.6) fb, which corresponds to $\mu^{\text{ggF}} < 4.11$ (5.53), since the SM prediction for $\sigma_{HH}^{\text{ggF}} = 31.05$ fb. It is not surprising that the upper limit obtained for ggF is lower than that obtained for ggF+VBF, which was shown in Section 7.2, given that this search is optimised to maximise the sensitivity to ggF HH production. As expected, the upper limits differ between the different benchmarks. The upper limits are higher for benchmarks 1, 2 and 6, which are characterised by having a peak at low m_{HH}, and lower for benchmarks 3, 4, 5, and 7 that are characterised by having longer tails at high m_{HH} values. In particular, the relatively low upper limit for benchmark 3 can be explained by the long upper m_{HH} tail clearly visible in Figure 7.9, despite the peak at low m_{HH}. The search presented in this chapter is therefore most sensitive to BSM scenarios generating events with larger m_{HH} values. The same trend is observed for the interpretation of the search for HH production in the $b\bar{b}\tau\tau$ that is also presented in [3]. A complementary search that targets BSM scenarios with softer m_{HH} spectra would therefore need to be developed.

The upper limits on σ_{HH}^{ggF} as a function of the c_{gghh} and c_{tthh} Wilson coefficients are shown in Figure 7.10. The theory prediction curve is shown in red. Variations of the Wilson coefficient values away from the SM prediction (= 0) produce the additional Feynman diagrams shown in Figure 7.5 and the interference pattern between the diagrams affects the σ_{HH}^{ggF} prediction. The interference is maximum, and hence the predicted cross section minimum, for $c_{ggh} \sim 0.15$ and $c_{ggh} \sim 0.35$. The solid (dashed) black line indicates the observed (expected) upper limit at 95% CL on $\sigma_{HH}^{\text{ggF}} = \mu^{\text{ggF}} \cdot \sigma_{HH}^{\text{ggF SM}}$ for different c_{gghh} and c_{tthh} values.

Figure 7.8.: Upper limits at 95% CL on σ_{HH}^{ggF} for the SM and the seven BSM benchmarks.

	Upper limits at 95% CL on the ggF HH cross-section [fb]					
Benchmark	Obs.	-2σ	-1σ	Exp.	$+1\sigma$	$+2\sigma$
SM	127.7	92.1	123.6	171.6	253.7	380.4
BM 1	189.3	157.3	211.2	293.0	429.2	632.5
BM 2	183.2	143.7	192.9	267.7	393.5	584.4
BM 3	109.8	87.6	117.6	163.2	242.2	366.4
BM 4	111.2	83.6	112.2	155.8	230.7	347.2
BM 5	97.8	73.9	99.2	137.7	204.2	308.3
BM 6	134.4	101.4	136.1	188.9	279.2	418.5
BM 7	88.9	67.8	91.0	126.3	187.4	283.1

The allowed intervals for the respective Wilson coefficient allowed by the search are given by the intersection between the theory prediction and the limit lines. The observed (expected) intervals at 95% CL are -0.4 (-0.5) $< c_{gghh} <$ 0.5 (0.7) and -0.3 (-0.4) $< c_{tthh} <$ 0.8 (0.9). These Wilson coefficients are much more constrained than the c_{hhh}. However, the results still allow for deviations from the SM prediction, and hence the existence of the additional Feynman diagrams.

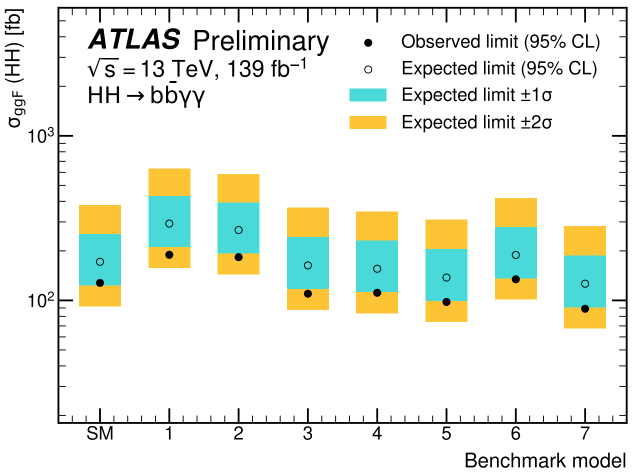

Figure 7.9.: Upper limits at 95% CL on σ_{HH}^{ggF} for the SM and the seven BSM benchmarks. The filled (open) black marker indicates the observed (expected) upper limit and the blue (yellow) bands indicate the expected $+1\sigma$ $(+2\sigma)$ uncertainties [4].

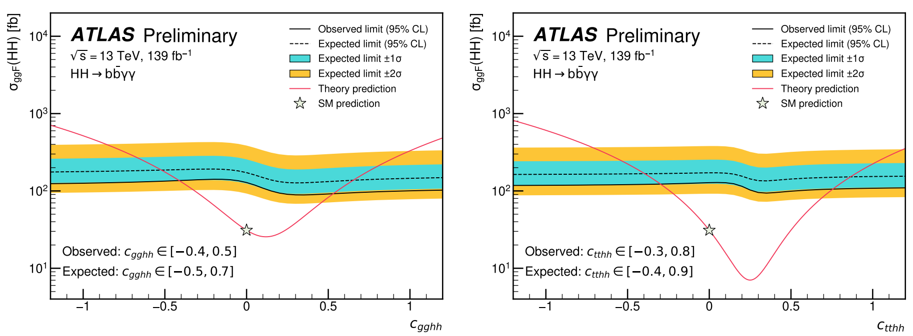

(a) c_{gghh} (b) c_{tthh}

Figure 7.10.: Upper limits on the σ_{HH}^{ggF} as a function of the Wilson coefficients at 95% CL. The theory prediction curve is shown in red. The solid (dashed) black line indicates the observed (expected) upper limit and the blue (yellow) bands the $+1\sigma$ $(+2\sigma)$ uncertainties [4].

Chapter 8

Search for Resonant Multi-Higgs Boson Production

Many BSM extensions of the SM predict the existence of an extended Higgs sector. This chapter presents a novel search for models with a SM Higgs boson H and two additional BSM Higgs bosons X and S in the $b\bar{b}\gamma\gamma$ final state. The analysis is under development and the results have not yet been published.

8.1. Introduction

The signal targeted by this search, the resonant production of an X boson that decays to an S and an H boson, is described by the Feynman diagram shown in Figure 8.1. Since the masses of the postulated BSM Higgs bosons are unknown, signals with a wide variety of X and S masses are considered. However, only models fulfilling $m_X > m_S + m_H$, with $m_H = 125$ GeV, and with $H \to \gamma\gamma$ and $S \to b\bar{b}$ decays are targeted.

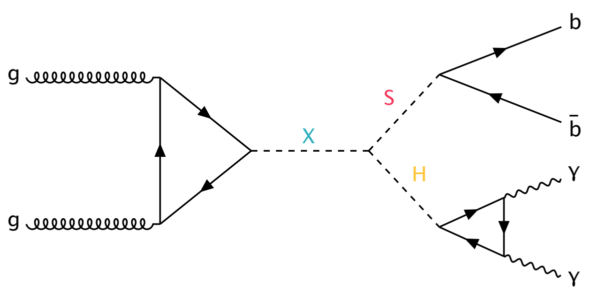

Figure 8.1.: Feynman diagram for resonant multi-Higgs produciton.

The targeted process may exist in, for example, the Next-to-Minimal 2HDM [116], the Complex 2HDM [117], the Next-to-MSSM [118] or the Two-Real-scalar extension of the SM [119]. Given the large variety of cross sections and branching ratios predicted by the different models, a model-agnostic search is performed. The same cross section is assumed for all mass points and the branching ratio for the $S \to b\bar{b}$ decay is assumed to be the same as the branching ratio for $H \to b\bar{b}$.

8.2. Samples and Preselection

A summary of the simulated signal and background samples used in this analysis is shown in Table 8.1. The backgrounds can be divided in two groups: the so-called resonant backgrounds that are characterised by having a $H \to \gamma\gamma$ decay and the non-resonant backgrounds that contain photons that are not produced by the decay of a Higgs boson. The resonant backgrounds include H and HH events produced through VBF or ggF (ggF and VBF H and HH), the production of a H boson in association with a W boson (WH), a Z boson (ZH), top quark pairs (ttH), b-quark pairs (bbH), a top quark and a W boson (tWH) or a top quark, a b-quark and a radiated jet ($tHjb$). The non-resonant backgrounds are composed of events with top quark pairs produced in association with two photons ($tt\gamma\gamma$) and events with photon pairs produced in association with jets ($\gamma\gamma$+jets). A wide range of signals with $m_X \in [170 \text{ GeV}, 1 \text{ TeV}]$ and $m_S \in [30 \text{ GeV}, 500 \text{ GeV}]$ are targeted by this search. The full list of simulated $X \to SH \to b\bar{b}\gamma\gamma$ signals is summarised in Table 8.2.

Due to the large similarities with the $HH \to b\bar{b}\gamma\gamma$ search [3], presented in Chapter 7, the same trigger and preselection criteria are used in this analysis. Events with two photons, two b-jets and $m_{\gamma\gamma} \in [105, 160]$ GeV are selected. The full preselection is shown in Table 7.1. After the preselection, more than 95% of the background events originate from the production of two photons in association with jets, the so-called $\gamma\gamma$+jets background.

Table 8.1.: Summary of simulated signal and background samples used in the analysis.

Process	Generator	PDF set	Showering	Tune
		Signals		
$X \to SH$	PYTHIA8	NNPDF2.3	PYTHIA8	A14
		Single Higgs backgrounds		
ggF H	NNLOPS	PDFLHC	PYTHIA8	AZNLO
VBF H	POWHEG	PDFLHC	PYTHIA8	AZNLO
WH	POWHEG	PDFLHC	PYTHIA8	AZNLO
ZH	POWHEG	PDFLHC	PYTHIA8	AZNLO
ttH	POWHEG	NNPDF3.0	PYTHIA8	A14
bbH	POWHEG	NNPDF3.0	PYTHIA8	A14
$tHbj$	MGMCatNLO	NNPDF3.0	PYTHIA8	A14
tWH	MGMCatNLO	NNPDF3.0	PYTHIA8	A14
		HH backgrounds		
ggF HH	POWHEG	PDFLHC	PYTHIA8	A14
VBF HH	MGMCatNLO	NNPDF3.0	PYTHIA8	A14
		Non-resonant backgrounds		
$\gamma\gamma$+jets	Sherpa 2.2.4	NNPDF3.0	Sherpa 2.2.4.	-
$tt\gamma\gamma$	MGMCatNLO	NNPDF2.3	PYTHIA8	A14

Table 8.2.: Summary of the mass point grid of generated samples for the $X \rightarrow SH \rightarrow b\bar{b}\gamma\gamma$ signal.

m_X(GeV)	m_S(GeV)	m_X(GeV)	m_S(GeV)	m_X(GeV)	m_S(GeV)
170	30	245	90	600	110
180	50	250	100	600	170
185	30	250	110	600	200
190	50	300	30	600	300
200	70	300	70	600	400
205	30	300	110	750	70
205	50	300	170	750	110
210	70	400	30	750	170
220	90	400	70	750	200
225	30	400	110	750	300
225	50	400	170	750	400
225	70	400	200	750	500
230	90	500	30	1000	70
230	100	500	70	1000	110
240	100	500	110	1000	170
240	110	500	170	1000	200
245	30	500	200	1000	300
245	50	600	70	1000	400
245	70	600	110	1000	500

8.3. Event Selection

The $H \to \gamma\gamma$ decay is exploited to separate the signals from the large non-resonant background that arises from $\gamma\gamma$+jets events. After the preselection is applied, the $m_{\gamma\gamma}$ distribution is used to further classify events into a SR and a CR. Events with 120 GeV $< m_{\gamma\gamma} <$ 130 GeV, are selected by the SR while events that do not pass this requirement are included in the side-band CR. Table 8.3 shows the predicted number of events in each region for all backgrounds and a sub-set of the simulated signals. The single bin CR is used to extract a NF for the large non-resonant $\gamma\gamma$+jets background from data which is then used to correct the normalisation predicted by MC in the SR.

Table 8.3.: Predicted number of signal and background events after preselection in the $m_{\gamma\gamma}$ side-band (CR) and $m_{\gamma\gamma}$ peak (SR) regions. Signal cross sections of 1 fb are used.

	Preselection	CR	SR
ggF H	5.452 ± 0.065	0.109 ± 0.009	5.344 ± 0.065
VBF H	0.685 ± 0.012	0.014 ± 0.002	0.671 ± 0.012
WH	0.207 ± 0.004	0.005 ± 0.001	0.202 ± 0.004
ZH	3.689 ± 0.013	0.073 ± 0.002	3.615 ± 0.013
ttH	8.309 ± 0.014	0.205 ± 0.002	8.104 ± 0.014
bbH	0.62 ± 0.023	0.017 ± 0.004	0.603 ± 0.023
$tHjb$	0.969 ± 0.029	0.022 ± 0.004	0.947 ± 0.029
tWH	0.131 ± 0.005	0.003 ± 0.001	0.128 ± 0.005
ggF+VBF HH	1.691 ± 0.004	0.027 ± 0.001	1.664 ± 0.004
$tt\gamma\gamma$	28.672 ± 0.109	22.924 ± 0.097	5.748 ± 0.049
$\gamma\gamma$+jets	1417.57 ± 4.595	1133.58 ± 4.109	283.992 ± 2.056
Total SM	1467.995 ± 4.597	1156.978 ± 4.11	311.019 ± 2.058
Data	-	1479	-
$\text{NF}_{\gamma\gamma+\text{jets}}$	-	1.278	-
$m_{X,S} = (190, 50)$	1.232 ± 0.043	0.06 ± 0.009	1.173 ± 0.042
$m_{X,S} = (250, 110)$	9.938 ± 0.121	0.468 ± 0.026	9.47 ± 0.118
$m_{X,S} = (300, 110)$	11.309 ± 0.13	0.5 ± 0.027	10.809 ± 0.127
$m_{X,S} = (600, 170)$	23.604 ± 0.188	0.735 ± 0.033	22.869 ± 0.185
$m_{X,S} = (750, 300)$	28.118 ± 0.206	0.841 ± 0.036	27.277 ± 0.203
$m_{X,S} = (1000, 300)$	30.834 ± 0.215	0.857 ± 0.036	29.977 ± 0.212

Because of the many different X and S masses targeted by this analysis, a Parametrised Neural Network (PNN) [120], which is described in detail in Section 8.4, is used to further discriminate the different signals from the backgrounds. This network takes m_X and m_S as input parameters and is capable of differentiating between signal and background across a wide (m_X, m_S) plane. The binned PNN(m_X, m_S) distribution is used in the final likelihood fit to extract $\mu(m_X, m_S)$. The binned PNN(m_X, m_S) distributions that target the $(m_X, m_S) =$ (230,90), (600, 170), (750, 300) and (1000, 500) GeV signals are shown for the SR in Figures 8.2 and 8.3. When the PNN parameters match the true (m_X, m_S) values used to generate the signal, the PNN distribution for the signal peaks towards 1. If the PNN parameters are very different from the true (m_X, m_S) values of the generated signal, the PNN distribution for the signal peaks towards 0.

Most analyses that target signals with a $H \to \gamma\gamma$ decay, like the search described in Chapter 7, perform an unbinned likelihood fit to the $m_{\gamma\gamma}$ distribution to exploit the excellent $m_{\gamma\gamma}$ resolution. In comparison, this novel approach allows to simultaneously profit from the clean $m_{\gamma\gamma}$ peak, by cutting on $m_{\gamma\gamma}$, and the flexibility of the PNN to target a wide range of X and S masses by fitting the PNN(m_X, m_S) distribution in the SR.

8.4. Parametrised Neural Network

In this search, a PNN is used to discriminate the signal from backgrounds across the (m_X, m_S) plane. As opposed to standard NNs that are only trained with a set of training variables ($\mathbf{x}$) that are used to separate signal from background, PNNs also include a set of parameters (θ) in the training. A single PNN, which has learned the relation between $\mathbf{x}$ and θ, can act as N different NNs, where each has been trained to target one of N different signals with a specific θ value. The parametrisation not only saves computing resources (N NNs can potentially be replaced by a single PNN), but also allows for interpolation to signals corresponding to values of θ not included in the train set. The variety of signals targeted by this search and the coarse sampling of the (m_X, m_S) plane by the simulated signal samples, especially in the $m_X > 250$ GeV region, makes PNNs particularly suitable. The PNN allows to test the SM hypothesis for any $\theta = (m_X, m_S)$ pair. However, a simulated signal sample or an interpolated PNN signal template is required in order to test the BSM hypothesis.

The signal kinematics are highly dependent on the values of m_X and m_S, and therefore the reconstructed invariant masses of the corresponding

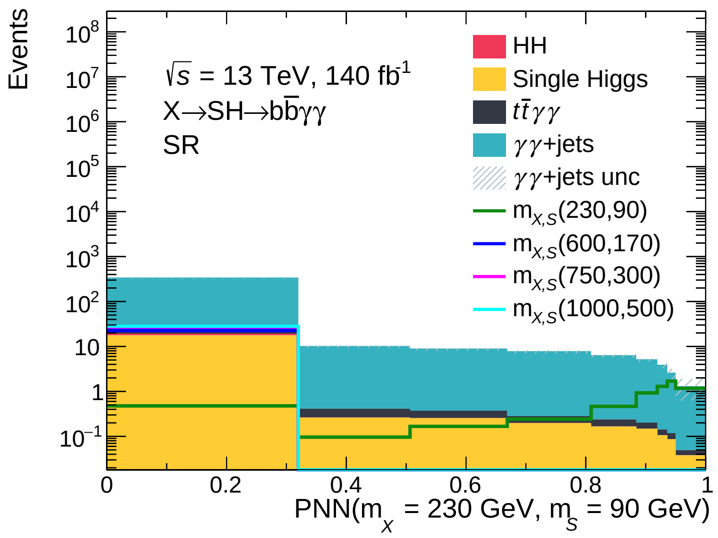

(a) PNN(m_X = 230 GeV, m_S = 90 GeV)

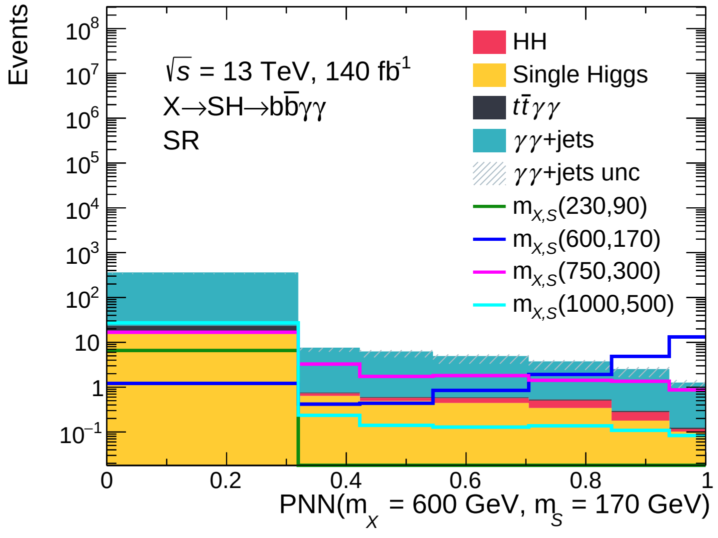

(b) PNN(m_X = 600 GeV, m_S = 170 GeV)

Figure 8.2.: The binned PNN(m_X, m_S) distributions in the SR. The signals with (m_X, m_S) near the PNN parameters peak towards 1, while background and non-targeted signals peak towards 0. A cross section of 1 fb is used for all signals.

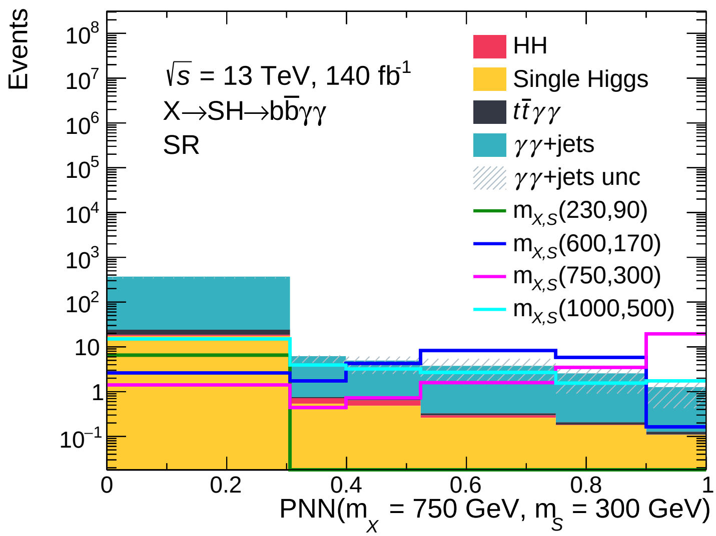

(a) PNN(m_X = 750 GeV, m_S = 300 GeV)

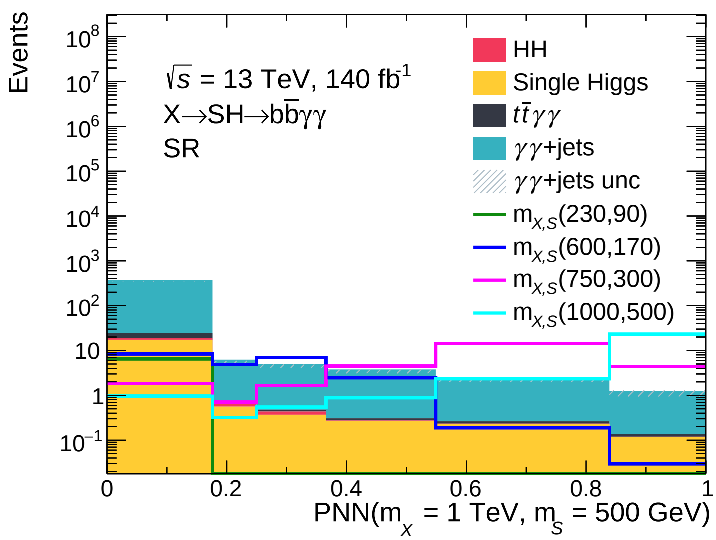

(b) PNN(m_X = 1 TeV, m_S = 500 GeV)

Figure 8.3.: The binned PNN(m_X, m_S) distributions in the SR. The signals with (m_X, m_S) near the PNN parameters peak towards 1, while background and non-targeted signals peak towards 0. A cross section of 1 fb is used for all signals.

final state particles, $m_{bb\gamma\gamma}$ and m_{bb}, become very powerful discriminating variables. A modified version of $m_{bb\gamma\gamma}$, called $m^*_{bb\gamma\gamma}$, is defined as

$$m^*_{bb\gamma\gamma} = m_{bb\gamma\gamma} - (m_{\gamma\gamma} - 125\,\text{GeV})\,. \tag{8.1}$$

The subtracted term improves the resolution of the $m_{bb\gamma\gamma}$ peak by reducing the impact of the finite resolution of the $m_{\gamma\gamma}$ measurement. It also minimises the correlation between the $m^*_{bb\gamma\gamma}$ and $m_{\gamma\gamma}$ variables.

Events that pass the preselection are used to train a PNN with training variables $\mathbf{x} = m^*_{bb\gamma\gamma}, m_{bb}$ and parameters $\theta = m_X, m_S$. The $m_{\gamma\gamma}$ distribution is not included in the training because it is used to assign events to the SR and CR. The CR does not only allow to correct the $\gamma\gamma$+jets normalisation using data but also to validate the shape of the full PNN distribution in MC simulations by comparing it to the shape in data. These comparisons will be shown in Section 8.5. The distributions for the training variables used in the PNN training are shown in Figure 8.4. Including additional training variables to $\mathbf{x}$ has been tested, but the PNN learns best with the most simple configuration. Additional variables seem to act as noise confusing the network rather than helping it. The reduced set of variables is enough to discriminate the signals from the non-resonant $\gamma\gamma$+jets background as well as the resonant ttH, ggF H and ZH backgrounds. The signal events are assigned their corresponding m_X, m_S values, e.g. the $(m_X, m_S) = (250, 100)$ GeV signal is assigned $\theta = (250, 100)$, while background events are randomly assigned θ values from the pool of signals. This procedure results in the same signal-to-background ratio for each (m_X, m_S) signal and ensures that the kinematic properties of all the signal points are learned by the network.

8.4.1. Hyperparameter Optimisation

Events are divided in three sets: train, evaluation and test. The train set is used for training the PNN, the evaluation set is used for evaluating its performance and the test set is used to perform the statistical analysis after the final PNN has been selected. A 3 fold Cross Validation (CV) is applied to recover all of the events for the statistical analysis without biasing the results. Based on their event numbers, events are divided in 3 folds $Y \in 1, 2, 3$, all containing approximately the same number of

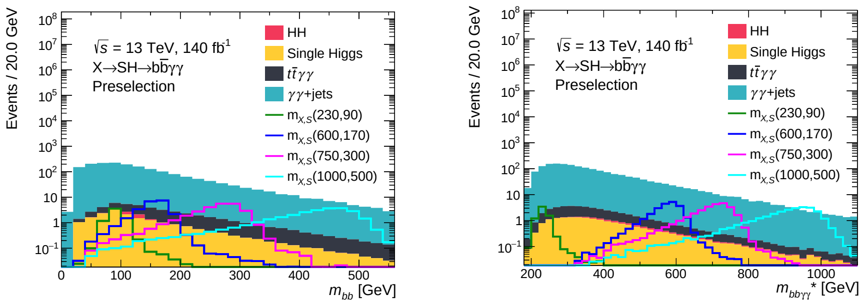

(a) m_{bb} (b) $m^*_{bb\gamma\gamma}$

Figure 8.4.: Training variables for the PNN. Only a subset of signals is shown. A cross section of 1 fb is used for all signals.

Table 8.4.: Definition of train, evaluation and test sets for each of the PNNs trained using cross-validation.

	CV1	CV 2	CV 3
Train set	Fold 1	Fold 2	Fold 3
Evaluation set	Fold 2	Fold 3	Fold 1
Test set	Fold 3	Fold 1	Fold 2

events. Fold Y contains events with EventNumber % 3 $= Y - 1$. Three different PNNs are trained using CV as shown in Table 8.4.

In order to maximise the performance of the network multiple hyperparameters need to be optimised. The PNN parameters are optimised in the CV fold 1. Different hyperparameter configurations, shown in Table 8.5 are tested using `Keras Tuner` [121]. This algorithm selects the hyperparameters that maximise the Area-Under-Curve (AUC) of the evaluation set from a total of 40 rounds using Bayesian Optimisation. The remaining hyperparameters are optimised taking into account the specific characteristics of the dataset.

One of the biggest challenges when training the network is the large imbalance in the number of signal and background events of the dataset. The largest contribution to the preselected sample comes from the $\gamma\gamma$+jets background, as shown in Table 8.3. With such an imbalanced dataset, the PNN tends to classify all events as background. It also struggles to differentiate between the different signals. The imbalance is reduced when considering only the raw number of events without applying event

Table 8.5.: List and ranges of the PNN hyperparameters that are optimised by `Keras Tuner`.

Parameter	Range	Sampling Mode
Number of hidden layers	[1-6]	1
Dropout rate (per-layer)	[0, 0.2]	0.05
Learning rate	[0.0001 - 0.1]	Log

weights from the cross section, the MC generator, the reconstruction efficiency corrections, etc, and hence unweighted event yields are used in the training. The effect of the event weights on the training variable distributions has been found to be negligible. The PNN is trained using class weights defined as

$$\text{weight(class } i) = \frac{\text{total \# events}}{2 \cdot \text{\# class } i \text{ events}} \tag{8.2}$$

for i = signal or background. This weight ensures that the same importance is given to both signal and background classes. Furthermore, an initial bias given by

$$\text{initial bias} = \log\left(\frac{\text{\# signal events}}{\text{\# background events}}\right) \tag{8.3}$$

is applied to the last layer of the PNN. The bias avoids the network's initial tendency to classify everything as background due to the class imbalance. Finally, the batch size is optimised such that all signal processes have approximately 200 events per batch in order to avoid large statistical fluctuations in the signal-to-background ratio between batches. The performance of the PNN improves considerably with this configuration.

8.4.2. Training

A PNN(m_X, m_S) is trained to discriminate all signals from the main backgrounds using $m^*_{bb\gamma\gamma}$, m_{bb} as training variables. The final PNN architecture is shown in Figure 8.5. The input layer consists of 4 nodes (2 training variables and 2 parameters) and the output layer consists of 1 node with a sigmoid activation function (typical of a binary classifier). The network also has 4 hidden layers, each with a standard training layer (dense) with a rectified linear (relu) activation function and a dropout layer (dropout). The number of nodes for each hidden layer, determined by the hyperparameter optimisation, is also specified. The remaining hyperparameters, such as the specific dropout rate of each hidden layer, class weights and batch size is shown in Table 8.6. Each CV fold is trained for 2000 epochs resulting in an AUC for both training and evaluation test set of 0.97 for CV fold 2, shown in Figure 8.6, and 0.98 for CV folds 1 and 3.

Table 8.6.: Hyperparameters of the PNN.

Number of hidden layers	4
Layer 1 dropout rate	0.05
Layer 2 droport rate	0.1
Layer 3 dropout rate	0.2
Layer 4 dropout rate	0.1
Learning rate	0.009137
Optimizer	Adam
Loss function	Binary Loss
Initial bias	0.118
Signal class weight	0.945
Background class weight	1.062
Batch size	212613
Number of batches	2
Number of epochs	2000

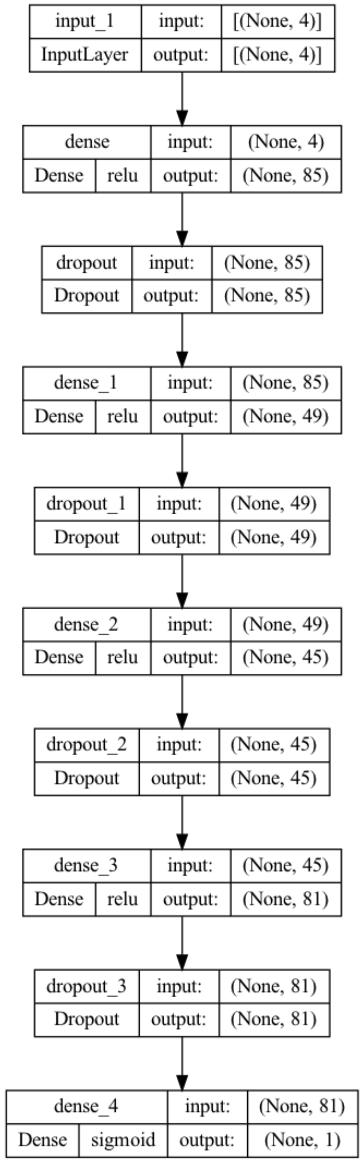

Figure 8.5.: Architecture of the PNN. The input layer consists of 4 nodes (2 training variables and 2 parameters) and the output layer consists of 1 node with a sigmoid activation function. The network also has 4 hidden layers, each with a rectified linear activation function (relu) and a dropout layer. The number of nodes for each hidden layer is also specified.

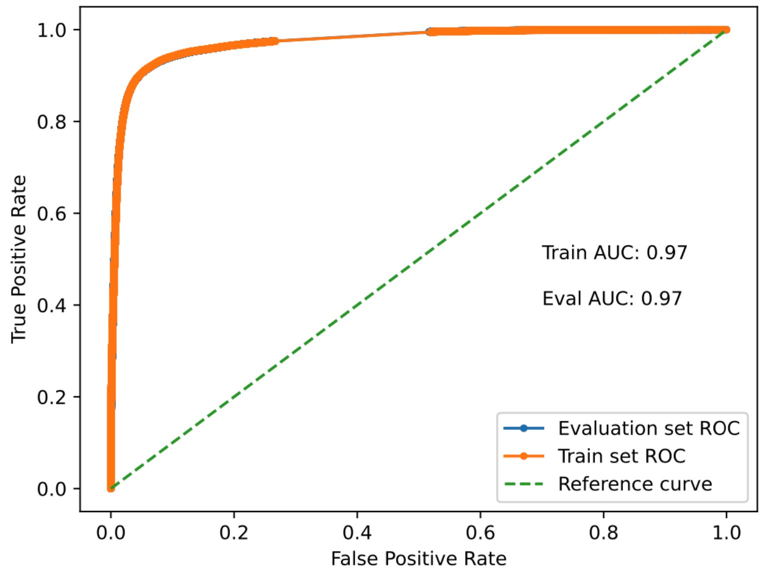

Figure 8.6.: ROC curve for the PNN. This plot corresponds to CV 2. The AUC for both train and evaluation sets increases to 0.98 for CV 1, used in the hyperparameter optimisation, and CV 3.

8.4.3. Performance

The AUC shown in Figure 8.6 is independent of the (m_X,m_S) parameters and therefore it is not a good estimator of the discriminating power between signals. In order to assess whether the PNN is better at discriminating some signals than others, the AUC is evaluated for different (m_X,m_S) parameters. Figure 8.7 shows the AUC(m_X,m_S) for the evaluation set. The worst separation between signal and background is obtained for the $m_X, m_S = (170, 30)$ GeV signal where the AUC=0.76 while better separation is obtained for the $m_X = 1$ TeV signals where AUC $\geq$ 0.99.

In order to assess whether the poorer performance observed for signals with low (m_X, m_S) is caused by the generalisation of the PNN, three NNs are trained to target individual signal points. In Table 8.7, the performance of the PNN is compared to the performance of the three NNs trained to target (m_X, m_S) = (170,30), (250, 100) and (750, 110) GeV, respectively. At high mass both networks have similar performance while

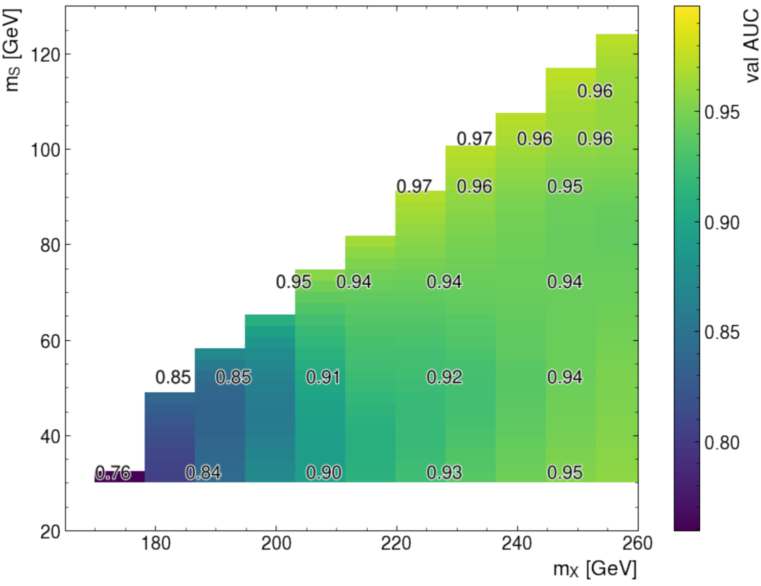

(a) $m_X \leq 250$

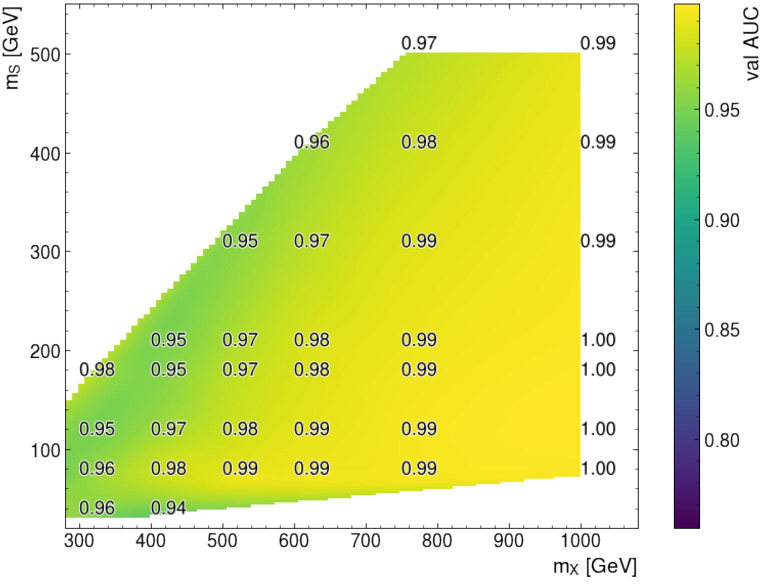

(b) $m_X > 250$ GeV

Figure 8.7.: The AUC(m_X,m_S) for the evaluation set. No event weights are used in the calculation of the AUC.

Table 8.7.: Comparison of the AUC(m_X,m_S) for the PNN and three different non-parametrised NNs optimised for each of the three signals listed.

AUC	PNN		NN	
(m_X,m_S)	validation-set	train-set	validation-set	train-set
(170,30)	0.76	0.74	0.83	0.82
(250, 100)	0.96	0.96	0.95	0.95
(750, 110)	0.99	0.99	0.99	0.99

the PNN shows a better performance for $(m_X, m_S) = (250, 100)$ GeV-due to being able to learn from more mass points. At low mass the performance of the NN is better than the PNN, however both have considerably lower performance than the high mass counterparts indicating that this signal point is harder to discriminate from background independently of the parametrisation. The NN shows a maximum of 9% improvement in performance with respect to the PNN for the $(m_X, m_S) = (170, 30)$ GeV signal. A more complex NN architecture is preferred for the NNs that target low mass signals with respect to those that target high mass signals. In order to help the PNN to learn signals with low (m_X, m_S), sub-class weights could be used. These weights would result in a higher (penalty) reward to the network when (mis-)classifying events with low (m_X, m_S) parameter values. However, this study suggests that the potential improvement in performance from using sub-class weights would be minimal, given that a NN that can focus fully on separating the $(m_X, m_S) = (170, 30)$ GeV signal from background results in a relatively low AUC.

8.4.4. Discriminant

The PNN distribution is used as a final discriminant in the SR. Given the large parameter space targeted by this search, and the computing resources required to perform the likelihood fit using toy MC experiments, the binning is optimised such that the asymptotic approximation is valid and toys do not need to be used. The binning is optimised for each (m_X, m_S) point using the `TransfoJ` algorithm from TRexFitter [122]. This algorithm ensures that there is a falling background distribution with at least 1 background event in the most signal-like bin i.e. the bin with PNN(m_X, m_S) values closest to 1. Starting from a distribution with N bins, an iterative procedure over $i = 0, 1, ..., k-1$ is used to merge bin $N-(i+1)$ with bin $N-i$ until the number of background events in the merged bin exceeds i+1. This iterative procedure is stopped for bin $N-k$ if the signal-to-background ratio in this new bin is smaller than that of the full un-binned distribution. A single background-like bin is used for the remaining distribution i.e. the bin with PNN(m_X, m_S) values closest to 0.

8.5. Comparisons between Data and Simulation

Figure 8.8 shows the data-to-simulation comparison in the CR for $m_{\gamma\gamma}$, m_{bb}, $m^*_{bb\gamma\gamma}$ and a subset of PNN(m_X, m_S) distributions. The $\gamma\gamma$+jets uncertainty, represented by the hashed area, includes the statistical uncertainty that arises from the limited number of MC events and the modelling uncertainty that arises from the comparison between Sherpa and MadGraph simulated events. The shape of all distributions is fairly well predicted by the simulation within uncertainties. The normalisation of the $\gamma\gamma$+jets background predicted by simulation has been corrected with a NF evaluated in the CR.

8.6. Interpolation

Signals have been simulated for the specific (m_X, m_S) points summarised in Table 8.2. However, we would like to study the H_0 and H_1 hypothesis for the full $m_X \in [170\text{ GeV}, 1\text{ TeV}]$ and $m_S \in [30\text{ GeV}, 500\text{ GeV}]$ phase space. This is done by interpolating the PNN shape for signal and background between the simulated points.

The parametrisation of the PNN(m_X, m_S) allows to test any m_X, m_S hypothesis. The background interpolation can be obtained directly from the PNN by specifying any set of m_X, m_S values. This characteristic allows to test the SM hypothesis for any m_X, m_S value. This approach is used for the large phase space shown in Figure 8.9. The (m_X, m_S) space is sampled with a granularity $\leq$ 10 (25) GeV for m_X < (>) 250 GeV. Simulated samples have been produced for the signals marked in red. The parameter space between the simulated points, marked in blue, is interpolated.

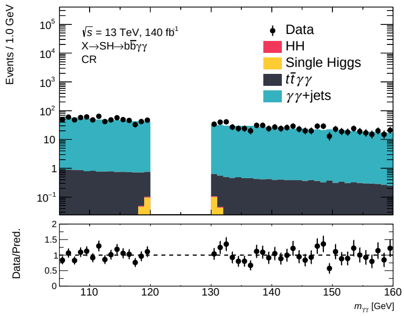

(a) $m_{\gamma\gamma}$

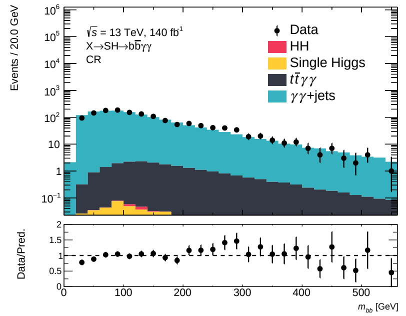

(b) m_{bb}

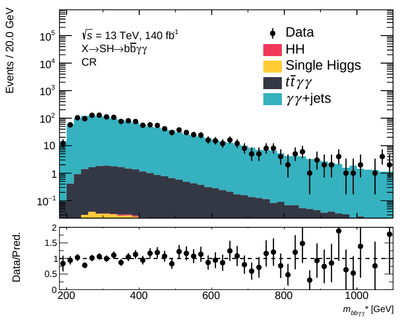

(c) $m^*_{bb\gamma\gamma}$

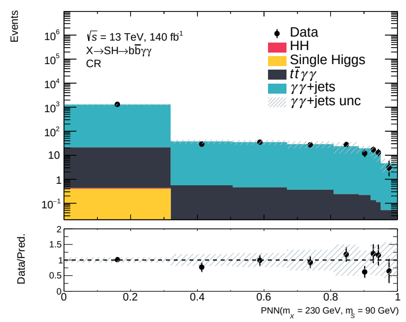

(d) PNN(230 GeV, 90 GeV)

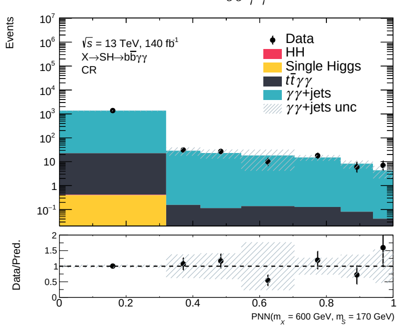

(e) PNN(600 GeV, 170 GeV)

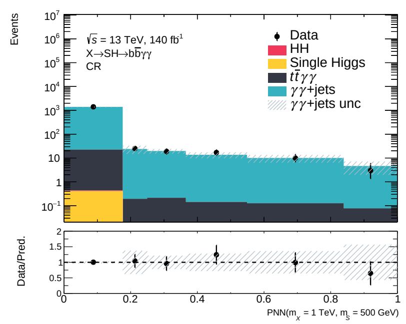

(f) PNN(1 TeV, 500 GeV)

Figure 8.8.: Data-to-simulation comparisons of different discriminating distributions in the CR. The $NF_{\gamma\gamma+\text{jets}}$ is applied to correct the normalisation of the $\gamma\gamma$+jets background. The $\gamma\gamma$+jets uncertainty includes the statistical and modelling uncertainties.

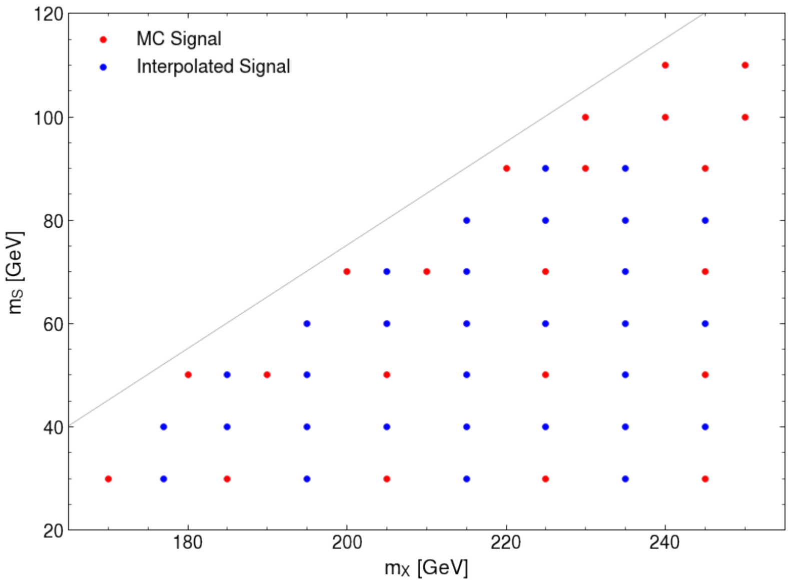

(a) $m_X \leq 250$

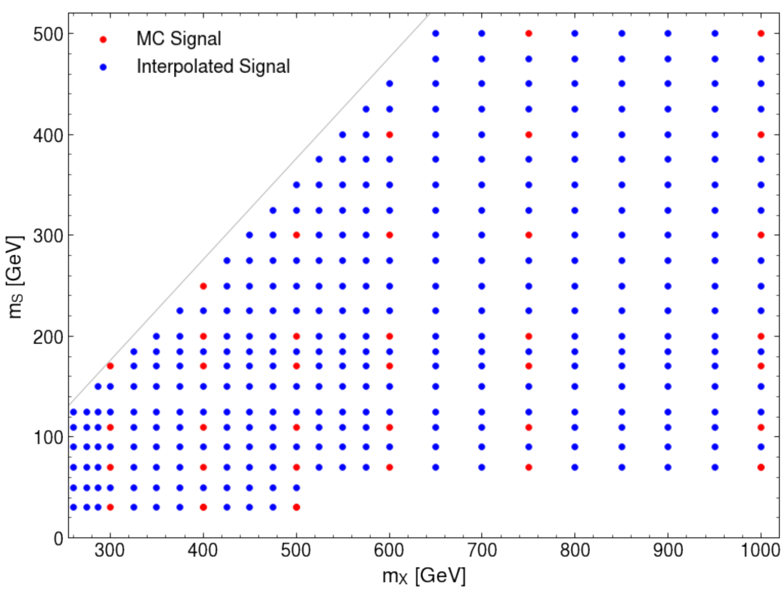

(b) $m_X > 250$ GeV

Figure 8.9.: Targeted $X \to SH$ signals. Simulations are available for the signals marked in red. No signals have been produced for the points marked in blue i.e. results in those points will be based on interpolating the PNN shapes.

8.6.1. Signal Injections

In order to assess the appropriate granularity of the (m_X, m_S) points to be tested, signal injections are performed. If the $(m_X,\ m_S)$ points are too sparse, there is a risk to miss a signal present in the data, while if the mass points are too densely spaced the probability of observing a statistical fluctuation, referred to as the look-else-where effect, becomes unnecessarily large.

A signal is injected with a cross section times branching ratio of approximately twice that of the expected limit and the sensitivity of nearby points to the injected signal is evaluated. For $m_X < (\geq)$ 300 GeV, a window of 25 (50) GeV in the (m_X, m_S) plane around the injected signal is studied. The expected significance obtained from fitting the PNN(m_X, m_S) distribution with the same (m_X, m_S) values as the injected signal have an expected significance of $\sim\ 4\sigma$. It is considered that if the expected significance for at least one other (m_X, m_S) point is $\geq\ 3\sigma$, the granularity is fine enough to ensure that no signal is missed. Figure 8.10 shows two examples of injected signals. In the top plot, the tested granularity is found to be ideal, while for the bottom plot the tested granularity is finer than what is required. For $m_X > 600$ GeV, injection studies show that a granularity of 50 GeV (rather than the tested 25 GeV granularity) is enough not to miss any signal according to the significance criteria (Z $\geq\ 3\sigma$).

8.6.2. Binning for Interpolated PNN Distributions

The PNN distribution is binned using the iterative algorithm described in Section 8.4.4. This optimisation is based on the predicted number of background events and the signal-to-background ratio. The signal is only available for a reduced sub-set of (m_X, m_S) points and therefore, an alternative criterion to the signal-to-background ratio needs to be used for the interpolated (m_X, m_S) points. Figure 8.11 shows two parameters of the binning optimisation, the total number of bins N and the upper-edge of the first bin i.e. the most background-like. Both of these parameters are fixed by the algorithm using the signal-to-background ratio. A correlation between the targeted (m_X, m_S) value and the number of bins is observed, and the first bin edge is found to be $\lesssim 0.55$.

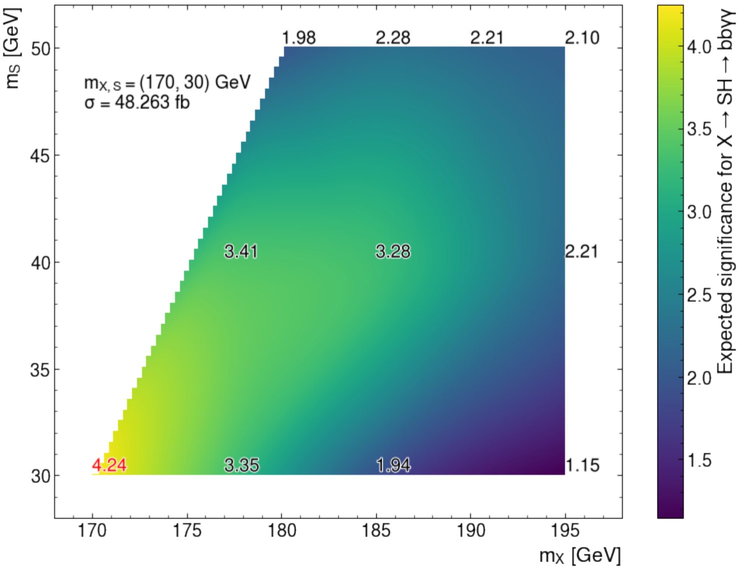

(a) Signal with $m_X, m_S = (170, 30)$ GeV

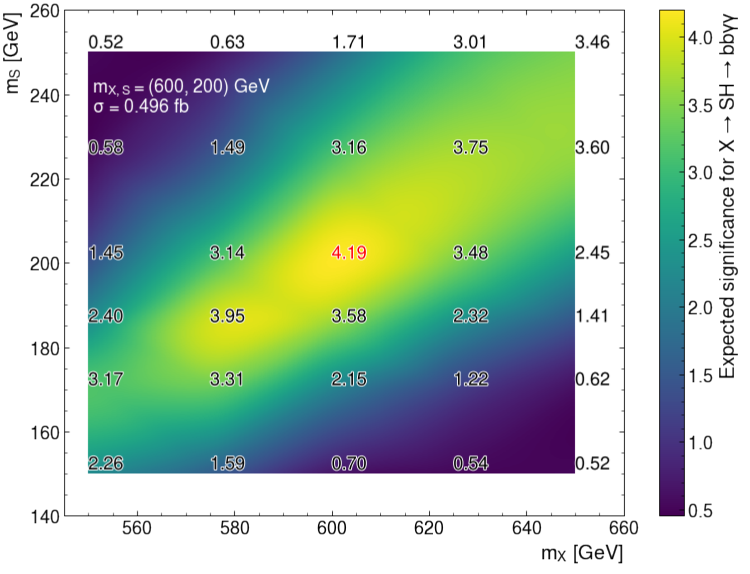

(b) Signal with $m_X, m_S = (600, 200)$ GeV

Figure 8.10.: Expected significance from different injected signals. The significance obtained from the PNN(m_X, m_S) distribution with the same (m_X, mS) values as the injected signal is shown in red.

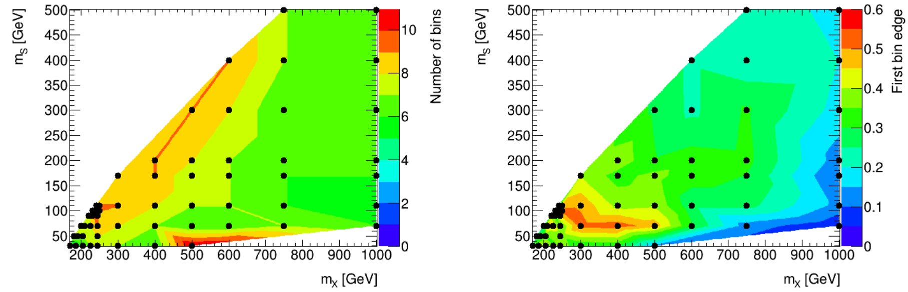

(a) Number of bins (b) First bin edge

Figure 8.11.: Parameters from the binning optimisation algorithm of the PNN(m_X, m_S) distributions for (m_X, m_S) points with available simulated signal samples.

The alternative version of the binning algorithm, which is used to bin the interpolated (m_X, m_S) points (blue), is defined as follows. As before, at least $i+1$ background events are required for bin $N-i$, however, the stopping criterion is based on the correlations extracted from Figure 8.11. In particular, $N = 6$ for signals with $m_X - m_S > 450$ GeV, $N = 7$ for signals with 310 GeV $< m_X - m_S <$ 450 GeV or $m_X <$ 250 GeV, and $N = 8$ for signals with 250 GeV $< m_X - m_S <$ 310 GeV. Additionally, if the N criteria does not guarantee that the upper-edge of the first bin is ≤ 0.55, additional bins are added, each with one additional background event, until this condition is guaranteed. The binning suggested by this algorithm for the red points is very similar to that obtained using the original optimisation. Most PNN distributions obtain the same number of bins with both algorithms, however in some cases the suggested number of bins differ by ± 1. The impact on the cross section upper limits from changing between the two different binnings has been studied for the points with available simulated signal samples and found to be negligible ($< 1\%$).

8.6.3. Signal Interpolation

In addition to interpolating the PNN score distribution, to predict its shape for any X and S, the efficiency of the signal to enter the SR, also needs to be interpolated. The distributions of the training variables, m_{bb} and $m^*_{bb\gamma\gamma}$, from a simulated signal point can be interpolated to a different (m_X, m_S) point using Lorentz transformations. The interpolated m_{bb} and $m^*_{bb\gamma\gamma}$ distributions can then be used to obtain the shape of the PNN (m_X, m_S) distribution for the interpolated signal. Once the shape is available, a 2D graph is used to interpolate the selection efficiency. This method is beyond the scope of this thesis and therefore not documented in detail.

The difference between the expected upper limits on the signal cross section times branching ratio obtained when using interpolated or MC-generated PNN score distributions is used to study the validity of the interpolated signal histograms. In the $m_X \geq 400$ GeV $m_S \geq 70$ GeV region, shown in Figure 8.12, the relative difference is below 10% and the interpolated signals are considered valid to use. This study only considers uncertainties of statistical origin and will be repeated once all systematic uncertainties are available to decide the exact signal interpolation range. A systematic uncertainty on the selection efficiency and shape of the interpolated signal needs to be considered.

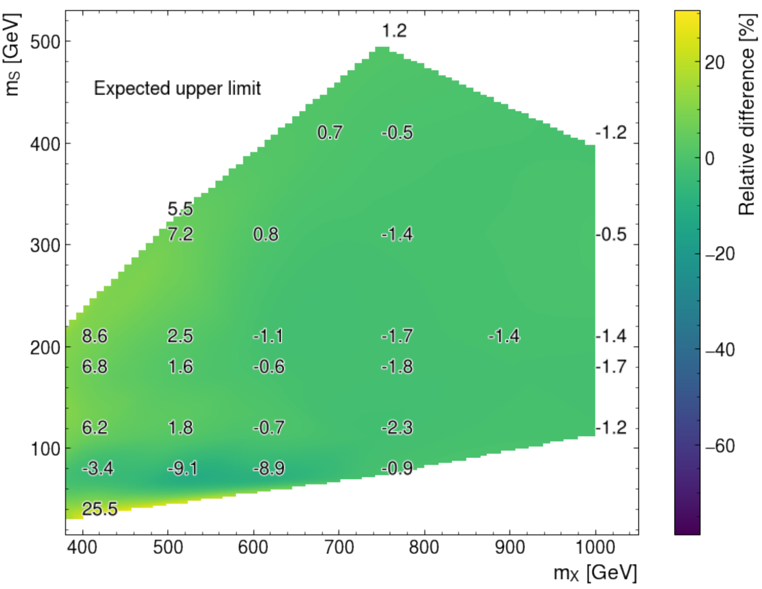

Figure 8.12.: Difference between the expected limits obtained when using MC or interpolated PNN score distributions. The area with a relative difference < 10% is shown.

8.7. Systematic Uncertainties

Systematic uncertainties originate from both experimental and theoretical sources. They may affect the selection efficiency and the shape of the SR discriminant predicted by simulation. The effect of these uncertainties on the predictions in the fit is modelled through NPs.

Systematic uncertainties affect both signal and background predictions. However, the theoretical and experimental uncertainties on the shape and normalisation of the predicted signal are not yet available at the time of writing this thesis and therefore not included in the fits. These uncertainties are expected to be small.

The theoretical systematic uncertainties may arise from the choice of renormalisation and factorisation scales, the PDF set and the choice of strong coupling constant value. The effect of these uncertainties on the production cross section is considered for all processes, additionally, for the $\gamma\gamma$+jets, ttH and ZH backgrounds, the effect of these uncertainties on the shape of the SR discriminant is also considered. These uncertainties are implemented in the likelihood fit as individual NPs. The uncertainty from the choice of the parton shower model is also estimated for the HH, ttH and ZH backgrounds by comparing samples simulated with the Pythia8 or Herwig7 parton shower and hadronisation model. For the $\gamma\gamma$+jets background, a modelling uncertainty that varies both the generator and parton shower models is estimated by comparing events produced with Sherpa, which simulates both the matrix element and the parton shower, and events produced with the MadGraph event generator interfaced with Pythia8 for the parton shower. The effect of these variations in both the shape of the PNN distribution and the selection efficiency in the SR is considered as individual NPs. Furthermore, an additional NP is applied to the signal and the single Higgs and HH backgrounds to model the uncertainty on the branching ratio of the Higgs decaying to photons. The uncertainty on the branching ratio of the Higgs decay to b-quarks is applied to the HH background with another NP. The theory uncertainty that affects the prediction of the $\gamma\gamma$+jets events through the extrapolation between the CR and SR, referred to as theory TF uncertainty, is also considered as an additional NP. This uncertainty is calculated in an analogous way to the $t\bar{t}Z$ uncertainties described in Chapter 6.

The experimental systematic uncertainties arise from imperfect modelling of the detector response and object reconstruction. The impact of the experimental uncertainties on the shape and normalisation of the ttH, ZH, ggF H, HH, $tHjb$ and $\gamma\gamma$+jets backgrounds is considered, while the effect of these variations on the minor VBF H, bbH, tWH and $tt\gamma\gamma$ backgrounds is neglected. The following experimental uncertainties are included in the statistical analysis as NPs:

- Luminosity (1 NP)
- Pileup modelling (3 NP)
- Diphoton trigger efficiency (1 NP)
- Photon identification efficiency (1 NP)
- Photon isolation efficiency (1 NP)
- Photon energy scale (1 NP)
- Photon energy resolution (1 NP)
- Jet energy scale (17 NP)
- Jet energy resolution (11 NP)
- Jet vertex tagger efficiency (1 NP)
- Flavour-tagging efficiencies (10 NP)

The uncertainties that have a highest impact on the fits vary depending on the targeted signal, however, the leading uncertainty generally arises from the modelling of the $\gamma\gamma$+jets MC, followed by uncertainties of statistical origin and other theoretical uncertainties on the prediction of $\gamma\gamma$+jets events, such as the theory TF uncertainty or the renormalisation and factorisation scales uncertainty. The experimental uncertainty with a largest impact arises from the flavour-tagging efficiencies.

The impact of the different NPs on the signal strength modifier μ for the signal point with m_X =230 GeV and m_S = 90 GeV is shown in Figure 8.13. In this case, the $\gamma\gamma$+jets modelling uncertainty has an impact of 30%, the second leading uncertainty arises from the $\gamma\gamma$+jets TF and has a prefit (postfit) impact of 15% (10%). Both of these uncertainties are constrained by the fit to the CR. The remaining NPs have an impact below 10%. This is the case for the statistical uncertainty on the background prediction in the last two bins of the PNN distribution and the uncertainty on the c-jet and light-flavour jet mistag efficiencies.

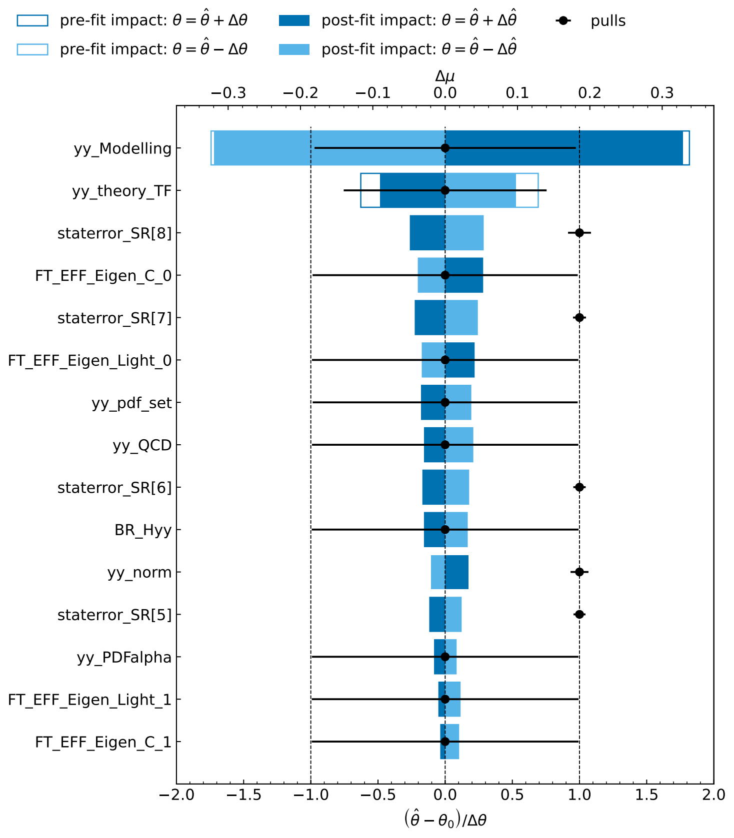

Figure 8.13.: The leading 15 NPs ranked by their impact on the parameter of interest, in this case signal_norm, are shown for the PNN(m_X = 230 GeV, m_S = 90 GeV) fit. The Asimov dataset with $\mu = 1$ is used.

8.8. Results

This section presents the results from the search for $X \to SH \to b\bar{b}\gamma\gamma$. At the time of writing this thesis, the search is still under development and therefore, results are only shown for a subset of the (m_X, m_S) signal points. Expected limits are shown for all (m_X, m_S) points with a MC generated signal sample. Unblinded results are shown for two (m_X, m_S) points where all major systematic uncertainties are available.

8.8.1. Expected Limits

The results presented in this section are obtained using an Asimov dataset, where the data is predicted from simulation after a background-only fit to the CR. The expected upper limits on the signal cross section times branching ratio are shown for all points with MC simulated signals on Figures 8.14 ($m_X \leq 250$ GeV) and 8.15 ($m_X \geq 300$ GeV). The systematic uncertainties of experimental origin and signal uncertainties are not yet available for all the targeted (m_X, m_S) points. The results are therefore obtained without considering these uncertainties. Cross sections between 0.14 fb and 24.50 fb are expected to be excluded depending on (m_X, m_S). The signals with higher (m_X, m_S) are characterised by having a larger selection efficiency, as was already observed in Table 8.3, and therefore smaller cross sections are excluded for these signals.

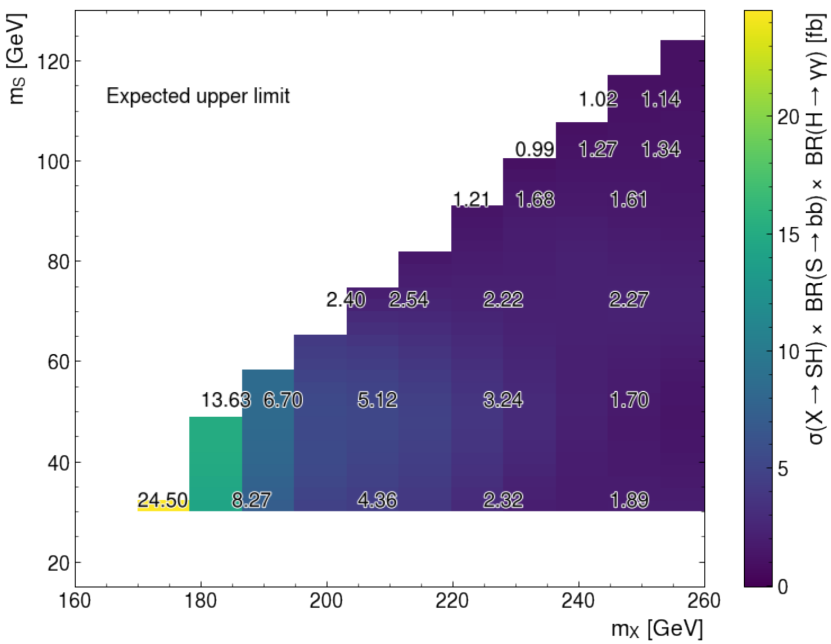

Figure 8.14.: Expected limits on the signal cross section times branching ratio for the different (m_X, m_S) signals with $m_X \leq 250$ GeV. These limits include only statistical and systematic uncertainties of theoretical origin.

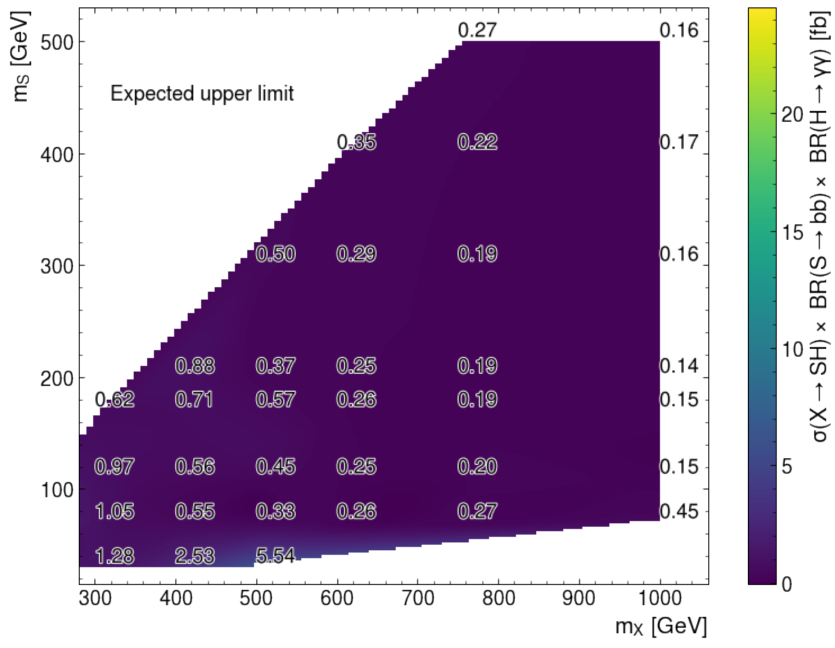

Figure 8.15.: Expected limits on the signal cross section times branching ratio for the different (m_X, m_S) signals with $m_X \geq 300$. These limits include only statistical and systematic uncertainties of theoretical origin.

8.8.2. Unblinded Results

In this section, the results for the $(m_X, m_S) = (600, 170)$ GeV and $(1000, 500)$ GeV signals are presented. These masses are selected because all systematic uncertainties on the background prediction are available for these points. A minor background, the production of a Z boson decaying to b-quark pairs produced in association with two photons, $Z(bb)\gamma\gamma$, is currently being generated and therefore not yet included in these preliminary results.

The PNN(m_X=600 GeV, m_S = 170 GeV) and PNN(m_X = 1 TeV, m_S = 500 GeV) distributions in the SR, with unblinded data, are shown in Figure 8.16. A good agreement is observed between data and the expected SM background for both distributions. In order to assess the compatibility between the H_0 hypothesis and the observed data, a profile likelihood ratio fit is performed to the PNN distribution in the SR and the single bin CR, where the hypothesis testing is based on the asymptotic

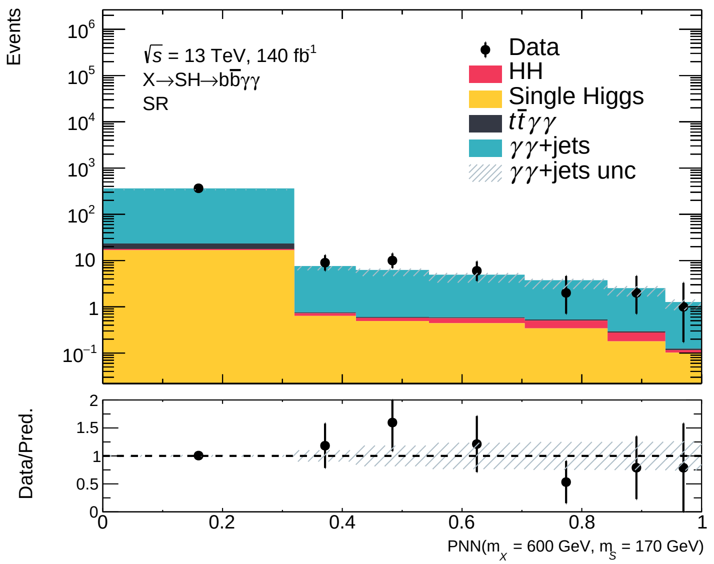

(a) PNN(m_X = 600 GeV, m_S = 170 GeV)

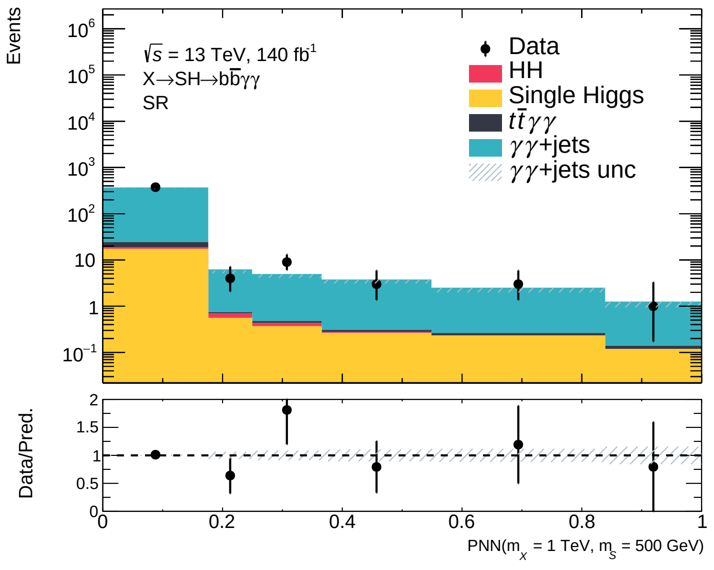

(b) PNN(m_X = 1 TeV, m_S = 500 GeV)

Figure 8.16.: The observed and expected PNN(m_X, m_S) distributions in the SR. The $\mathrm{NF}_{\gamma\gamma+\text{jets}}$ is applied to the expected distributions to correct the normalisation of the $\gamma\gamma$+jets background. The $\gamma\gamma$+jets uncertainty includes the prefit statistical and modelling uncertainties.

approximation (i.e. $Z = \sqrt{q_0}$). The observed p_0-value is greater than 0.5 in both fits meaning that no evidence for BSM physics is found. Upper limits on the production cross section times branching ratio for the $(m_X, m_S) = (600, 170)$ GeV and $(1000, 500)$ GeV signals are therefore set. For $(m_X, m_S) = (600, 170)$ GeV and $(m_X, m_S) = (1000, 500)$ GeV the observed (expected) upper limits at 95% CL are $\sigma \times$BR < 0.217 (0.264) fb and $\sigma \times$BR < 0.146 (0.157) fb respectively. These expected limits are compatible with those shown in Figure 8.15, indicating that the impact of the experimental uncertainties is small.

The two NPs that have the largest impact on μ in the $(m_X, m_S) = (600, 170)$ GeV fit are associated with the modelling of the $\gamma\gamma$+jets background (leading) and the statistical uncertainty in the most-signal like PNN bin (sub-leading). The same NPs, but with inverted order, have the largest impact on μ in the $(m_X, m_S) = (1000, 500)$ GeV fit. Figure 8.17 shows how much the NPs are pulled by the fits. As expected, the $\mathrm{NF}_{\gamma\gamma+\mathrm{jets}}$ NP, referred to as yy_norm, is pulled to 1.28 to correct the $\gamma\gamma$+jets normalisation, and the signal strength μ, referred to as signal_norm, is pulled to 0. The NP related to the $\gamma\gamma$+jets modelling uncertainty, referred to as yy_Modelling, is slightly pulled and constrained by the fit, specially for the (m_X, m_S)=(600, 170) GeV fit where this is the largest uncertainty. The NP for the theory TF uncertainty on the $\gamma\gamma$+jets background estimation, referred to as yy_theory_TF is also slightly constrained and pulled in both fits. This NPs has the third largest impact on μ in the $(m_X, m_S) = (600, 170)$ GeV fit and the fifth largest impact on μ in the $(m_X, m_S) = (1000, 500)$ GeV fit.

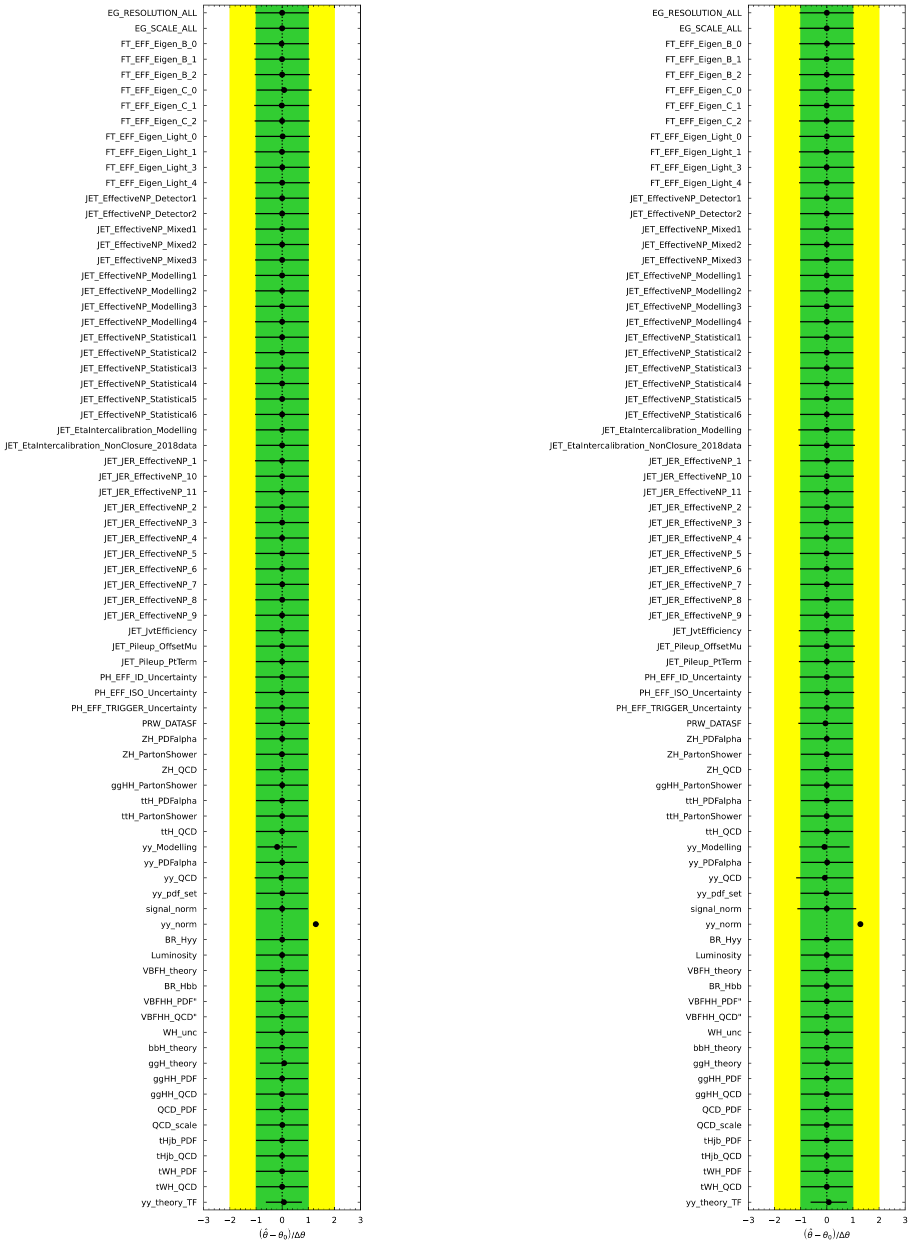

(a) PNN(600 GeV, 170 GeV) (b) PNN(1 TeV, 500 GeV)

Figure 8.17.: The pull of the fit parameters for the PNN(m_X, m_S) fits. The signal_norm is the POI and yy_norm is the $\gamma\gamma$+jets NF, determined from the fit to data in the CR.

Chapter 9

Summary and Conclusions

The Standard Model is a powerful theory that has been widely challenged by many precision tests and searches and which holds to an extremely impressive accuracy. But even with all its success the theory has some limitations. There are many theories that try to solve some of the shortcomings of the Standard Model while maintaining its carefully tested predictions. In this thesis, data from proton-proton collisions recorded by the ATLAS detector during the Run 2 of the Large Hadron Collider is used to test different Beyond Standard Model theories.

The reconstruction of physics objects from the signals in the detector is the pillar on which all physics analyses rest. Particles that decay to b-hadrons, such as the Higgs boson, the top quark or the postulated S boson described in Chapter 8, can be identified using b-tagging algorithms. These algorithms are trained using MC simulations and therefore need to be calibrated in data. Independent calibrations are performed for different jet flavours to correct possible mismodellings of the algorithms. Chapter 5 (Paper I) presents the jet p_{T} dependent Scale Factors that are used to correct the light-flavour jet tagging efficiency of the b-tagging algorithms. These Scale Factors and their corresponding uncertainties are applied to all searches presented in this thesis.

Supersymmetric and Dark Matter particles are perhaps the beyond Standard Model particles most commonly searched for at the Large Hadron Collider. Chapter 6 (Paper II) presents a search for the supersymmetric partner of the top quark and Dark Matter in a final state with one charged lepton, jets and missing transverse momentum. The production of a top quark pair in association with a Z boson, where the Z boson decays to neutrinos, is an irreducible background in this search. The missing transverse momentum from the neutrinos cannot be differentiated from that of the lightest supersymmetric particle or Dark

Matter, making it impossible to differentiate this background from signal. The $t\bar{t}Z$ Control Region, which I have defined, exploits the Z decay to charged leptons to correct the prediction of the irreducible $t\bar{t}Z$ background in data. This search finds no evidence of beyond the Standard Model physics and extends the previous upper limits on the possible masses of these beyond the Standard Model particles. These particles may still exist but have much higher masses and can therefore not be observed at the current energies of the Large Hadron Collider.

The spontaneous symmetry breaking of the Higgs potential is the foundation of the mass-generation mechanism in the Standard Model. A few pico-seconds after the Big Bang the Universe underwent a phase transition that generated a massive scalar boson, known as the Higgs boson, and most particles acquired mass. Depending on how this phase transition occurred and the exact shape of the Higgs potential, some of the shortcomings of the Standard Model may be solved.

The shape of the Higgs potential can be constrained through the Higgs boson properties. At first order it depends on the already measured Higgs boson mass and at second order it depends on the unmeasured triple Higgs self-coupling. The production of Higgs boson pairs in a final state with two photons and two b-jets is one of the best channels to measure the Higgs self-coupling, however, this process is rare and hence very difficult to observe. The current experimental constraints on the Higgs self-coupling, presented in Chapter 7 (Paper III), are relatively loose and therefore still allow for physics beyond the Standard Model.

Through small deviations in the effective couplings, Effective Field Theories can be used to infer the presence of beyond the Standard Model particles much heavier than what can be produced at the energies of the Large Hadron Collider. Chapter 7 (Paper IV) presents the first constraints on the parameters that are relevant to HH production in ATLAS using the Effective Field Theory framework. The experimental data is compatible with the Standard Model hypothesis but the results still allow for beyond the Standard Model interactions. A natural extension of this work is to include HH results into the more general Effective Field Theory combination of single Higgs and electroweak boson measurements [103]. This combination exploits the correlations between parameters of the Standard Model Effective Field Theory framework.

Many beyond the Standard Model theories predict the existence of an extended Higgs sector. The additional Higgs bosons in such theories could affect the shape of the Higgs potential and the electroweak phase transition in the early Universe. Chapter 8 presents a search for models with a Standard Model Higgs boson H and two additional beyond the Standard Model Higgs bosons X and S in the final state with two photons and two b-jets. This search is complementary to that presented in Chapter 7 because it targets beyond the Standard Model particles that are light enough to be produced at the Large Hadron Collider. The analysis strategy is based on a parametrised Neural Network that is sensitive to a wide range of X and S masses.

Bibliography

[1] The ATLAS Collaboration. Calibration of the light-flavour jet mistagging efficiency of the b-tagging algorithms with Z+jets events using 139 fb^{-1} of ATLAS proton-proton collision data at $\sqrt{s} = 13$ TeV. 2023. https://arxiv.org/abs/2301.06319.

[2] The ATLAS Collaboration. Search for new phenomena with top quark pairs in final states with one lepton, jets, and missing transverse momentum in pp collisions at $\sqrt{s} = 13$ TeV with the ATLAS detector. *JHEP*, 04:174, 2021.

[3] The ATLAS Collaboration. Search for Higgs boson pair production in the two bottom quarks plus two photons final state in pp collisions at $\sqrt{s} = 13$ TeV with the ATLAS detector. *Phys. Rev. D*, 106(5):052001, 2022.

[4] The ATLAS Collaboration. HEFT interpretations of Higgs boson pair searches in $b\bar{b}\gamma\gamma$ and $b\bar{b}\tau\tau$ final states and of their combination in ATLAS. ATL-PHYS-PUB-2022-019, Geneva, 2022.

[5] Wikipedia Contributors. Standard model - wikipedia, 2019. https://en.wikipedia.org/wiki/Standard_Model.

[6] D.H. Perkins. *Introduction to high energy physics.* ISBN 978-0-521-62196-0, Cambridge University Press, 1982.

[7] I.S. Hughes. *Elementary particles.* ISBN 978-0-521-260923, Cambridge University Press, 1985.

[8] F. Halzen and Alan D. Martin. *Quarks and leptons: An introductory course in modern particle physics.* ISBN 978-0-471-88741-6, John Wiley and sons, 1984.

[9] C. N. Yang and R. L. Mills. Conservation of isotopic spin and isotopic gauge invariance. *Phys. Rev.*, 96:191–195, Oct 1954.

[10] E. Noether. Invariante Variationsprobleme. *Nachr. d. König. Gesellsch. d. Wiss. zu Göttingen, Math-phys. Klasse, Seite 235-157*, 1918.

[11] Enrico Fermi. Tentativo di una teoria dell'emissione dei raggi beta. *Ric. Sci.*, 4:491–495, 1933.

[12] S. L. Glashow. Partial Symmetries of Weak Interactions. *Nucl. Phys.*, 22:579–588, 1961.

[13] Jeffrey Goldstone, Abdus Salam, and Steven Weinberg. Broken symmetries. *Phys. Rev.*, 127:965–970, Aug 1962.

[14] Steven Weinberg. A model of leptons. *Phys. Rev. Lett.*, 19:1264–1266, Nov 1967.

[15] J. Bardeen, L. N. Cooper, and J. R. Schrieffer. Theory of superconductivity. *Phys. Rev.*, 108:1175–1204, Dec 1957.

[16] F. Englert and R. Brout. Broken symmetry and the mass of gauge vector mesons. *Phys. Rev. Lett.*, 13:321–323, Aug 1964.

[17] Peter W. Higgs. Broken symmetries and the masses of gauge bosons. *Phys. Rev. Lett.*, 13:508–509, Oct 1964.

[18] John Ellis. Higgs Physics. (KCL-PH-TH-2013-49. KCL-PH-TH-2013-49. LCTS-2013-36. CERN-PH-TH-2013-315):117–168. 52 p, Dec 2013. 52 pages, 45 figures, Lectures presented at the ESHEP 2013 School of High-Energy Physics, to appear as part of the proceedings in a CERN Yellow Report.

[19] W. Heisenberg. Über den bau der atomkerne. i. *Zeitschrift für Physik*, 77(1):1–11, 1932.

[20] Murray Gell-Mann. The Eightfold Way: A Theory of strong interaction symmetry. https://doi.org/10.2172/4008239, 1961.

[21] Yuval Ne'eman. Derivation of strong interactions from a gauge invariance. *Nucl. Phys.*, 26:222–229, 1961.

[22] O. W. Greenberg. Spin and Unitary Spin Independence in a Paraquark Model of Baryons and Mesons. *Phys. Rev. Lett.*, 13:598–602, 1964.

[23] H. Fritzsch, Murray Gell-Mann, and H. Leutwyler. Advantages of the Color Octet Gluon Picture. *Phys. Lett. B*, 47:365–368, 1973.

[24] David J. Gross and Frank Wilczek. Ultraviolet Behavior of Non-abelian Gauge Theories. *Phys. Rev. Lett.*, 30:1343–1346, 1973.

[25] H. David Politzer. Reliable Perturbative Results for Strong Interactions? *Phys. Rev. Lett.*, 30:1346–1349, 1973.

[26] The ATLAS Collaboration. Observation of a new particle in the search for the Standard Model Higgs boson with the ATLAS detector at the LHC. *Phys. Lett. B*, 716:1–29, 2012.

[27] The CMS Collaboration. Observation of a New Boson at a Mass of 125 GeV with the CMS Experiment at the LHC. *Phys. Lett. B*, 716:30–61, 2012.

[28] H. Georgi and S. L. Glashow. Unity of All Elementary Particle Forces. *Phys. Rev. Lett.*, 32:438–441, 1974.

[29] Q.R. Ahmad et al. Measurement of the rate of $\nu_e + d \to p + p + e^-$ interactions produced by ^8B solar neutrinos at the Sudbury Neutrino Observatory. *Phys. Rev. Lett.*, 87:071301, 2001.

[30] Y. Fukuda et al. Evidence for oscillation of atmospheric neutrinos. *Phys. Rev. Lett.*, 81:1562–1567, 1998.

[31] F. Zwicky. Die Rotverschiebung von extragalaktischen Nebeln. *Helv. Phys. Acta*, 6:110–127, 1933.

[32] Andrea Wulzer. Behind the Standard Model. In *2015 European School of High-Energy Physics*, 2019. https://arxiv.org/abs/1901.01017.

[33] Pierre Fayet and S. Ferrara. Supersymmetry. *Phys. Rept.*, 32:249–334, 1977.

[34] David B. Kaplan, Howard Georgi, and Savas Dimopoulos. Composite Higgs Scalars. *Phys. Lett. B*, 136:187–190, 1984.

[35] John F. Gunion, Howard E. Haber, Gordon L. Kane, and Sally Dawson. *The Higgs Hunter's Guide*, volume 80. 2000.

[36] Andrew G. Cohen, D. B. Kaplan, and A. E. Nelson. The More minimal supersymmetric standard model. *Phys. Lett. B*, 388:588–598, 1996.

[37] B. Grzadkowski, M. Iskrzynski, M. Misiak, and J. Rosiek. Dimension-Six Terms in the Standard Model Lagrangian. *JHEP*, 10:085, 2010.

[38] Gavin P. Salam, Lian-Tao Wang, and Giulia Zanderighi. The higgs boson turns ten. *Nature*, 607(7917):41–47, Jul 2022.

[39] Giorgio Arcadi, Abdelhak Djouadi, and Marumi Kado. The Higgs-portal for dark matter: effective field theories versus concrete realizations. *Eur. Phys. J. C*, 81(7):653, 2021.

[40] Ewa Lopienska. The CERN accelerator complex, layout in 2022. Complexe des accelerateurs du CERN en janvier. 2022. https://cds.cern.ch/record/2800984.

[41] The ATLAS Collaboration. Luminosity determination in pp collisions at $\sqrt{s} = 13$ TeV using the ATLAS detector at the LHC. 12 2022. https://arxiv.org/abs/2212.09379.

[42] The ATLAS Collaboration. ATLAS Luminosity Results in Run 2. `https://twiki.cern.ch/twiki/bin/view/AtlasPublic/LuminosityPublicResultsRun2`.

[43] Joao Pequenao. Computer generated image of the whole ATLAS detector. https://cds.cern.ch/record/1095924, Mar 2008.

[44] Juan Castaño. ATLAS Coordinate System. https://tex.stackexchange.com/questions/578433/drawing-a-detectors-cartesian-and-spherical-coordinate-in-one-picture-using-tik.

[45] ATLAS Collaboration. ATLAS Inner Detector: Technical Design Report, Volume 1. Atlas-tdr-4; cern-lhcc-97-016, 1997.

[46] ATLAS Collaboration. ATLAS Inner Detector: Technical Design Report, Volume 2. Atlas-tdr-5, cern-lhcc-97-017, 1997.

[47] ATLAS Collaboration. ATLAS Insertable B-Layer Technical Design Report. Atlas-tdr-19; cern-lhcc-2010-013, 2010.

[48] Karolos Potamianos. The upgraded Pixel detector and the commissioning of the Inner Detector tracking of the ATLAS experiment for Run-2 at the Large Hadron Collider. ATL-PHYS-PROC-2016-104, Geneva, Aug 2016. EPS-HEP 2015 Proceedings.

[49] Marija Marjanovic. ATLAS Tile calorimeter calibration and monitoring systems. *IEEE Trans. Nucl. Sci.*, 66(arXiv:1806.09156. 7):1228–1235. 8 p, Jun 2018. IEEE Real Time 2018 proceedings.

[50] ATLAS Collaboration. ATLAS Liquid Argon Calorimeter: Technical Design Report. Atlas-tdr-2; cern-lhcc-96-041, 1996.

[51] ATLAS Collaboration. ATLAS Tile Calorimeter: Technical Design Report. Atlas-tdr-3; cern-lhcc-96-042, 1996.

[52] The ATLAS collaboration. Performance and calibration of the ATLAS Tile Calorimeter. *PoS*, EPS-HEP2021:748, 2022.

[53] ATLAS Collaboration. ATLAS Muon Spectrometer: Technical Design report. Atlas-tdr-10; cern-lhcc-97-022, CERN, 1997.

[54] S.D. Ellis, J. Huston, K. Hatakeyama, P. Loch, and M. Tonnesmann. Jets in hadron-hadron collisions. *Prog. Part. Nucl. Phys.*, 60:484–551, 2008.

[55] T. Affolder et al. Charged Jet Evolution and the Underlying Event in $p\bar{p}$ Collisions at 1.8 TeV. *Phys. Rev. D*, 65:092002, 2002.

[56] Bo Andersson, G. Gustafson, G. Ingelman, and T. Sjöstrand. Parton fragmentation and string dynamics. *Phys. Rept.*, 97:31–145, 1983.

[57] Jan-Christopher Winter, Frank Krauss, and Gerhard Soff. A modified cluster-hadronization model. *Eur. Phys. J. C*, 36:381–395, 2004.

[58] T. Sjöstrand, S. Mrenna, and P. Skands. A brief introduction to PYTHIA 8.1. *Comput. Phys. Commun.*, 178:852–867, 2008.

[59] Johannes Bellm et al. Herwig 7.1 Release Note. 2017.

[60] T. Gleisberg, S. Höche, F. Krauss, M. Schönherr, S. Schumann, et al. Event generation with SHERPA 1.1. *JHEP*, 02:007, 2009.

[61] J. Alwall, R. Frederix, S. Frixione, V. Hirschi, F. Maltoni, et al. The automated computation of tree-level and next-to-leading order differential cross sections, and their matching to parton shower simulations. *JHEP*, 07:079, 2014.

[62] Keith Hamilton, Paolo Nason, and Giulia Zanderighi. Finite quark-mass effects in the NNLOPS POWHEG+MiNLO Higgs generator. *JHEP*, 05:140, 2015.

[63] GEANT4 Collaboration, S. Agostinelli, et al. GEANT4 – a simulation toolkit. *Nucl. Instrum. Meth. A*, 506:250, 2003.

[64] ATLAS Collaboration. The ATLAS Simulation Infrastructure. *Eur. Phys. J. C*, 70:823, 2010.

[65] Glen Cowan, Kyle Cranmer, Eilam Gross, and Ofer Vitells. Asymptotic formulae for likelihood-based tests of new physics. *Eur. Phys. J. C*, 71:1554, 2011.

[66] A L Read. Modified frequentist analysis of search results (the CL_s method). *CERN-OPEN-2000-205, Workshop on confidence limits, CERN, Geneva, Switzerland*, 17-18 Jan, 2000. Proceedings, 81-101.

[67] The ATLAS Collaboration. A neural network clustering algorithm for the ATLAS silicon pixel detector. *JINST*, 9:P09009, 2014.

[68] The ATLAS Collaboration. Performance of the ATLAS Track Reconstruction Algorithms in Dense Environments in LHC Run 2. *Eur. Phys. J. C*, 77(10):673, 2017.

[69] The ATLAS Collaboration. Reconstruction of primary vertices at the ATLAS experiment in Run 1 proton–proton collisions at the LHC. *Eur. Phys. J. C*, 77(5):332, 2017.

[70] The ATLAS Collaboration. Electron and photon performance measurements with the ATLAS detector using the 2015–2017 LHC proton–proton collision data. *JINST*, 14:P12006, 2019.

[71] The ATLAS Collaboration. Topological cell clustering in the ATLAS calorimeters and its performance in LHC Run 1. *Eur. Phys. J. C*, 77:490, 2017.

[72] The ATLAS Collaboration. Electron reconstruction and identification in the ATLAS experiment using the 2015 and 2016 LHC proton–proton collision data at $\sqrt{s} = 13\,\text{TeV}$. *Eur. Phys. J. C*, 79:639, 2019.

[73] The ATLAS Collaboration. Measurement of the photon identification efficiencies with the ATLAS detector using LHC Run-1 data. *Eur. Phys. J. C*, 76:666, 2016.

[74] The ATLAS Collaboration. Muon reconstruction and identification efficiency in ATLAS using the full Run 2 pp collision data set at $\sqrt{s} = 13$ TeV. *Eur. Phys. J. C*, 81(7):578, 2021.

[75] Matteo Cacciari, Gavin P. Salam, and Gregory Soyez. The anti-k_t jet clustering algorithm. *JHEP*, 04:063, 2008.

[76] The ATLAS Collaboration. Jet reconstruction and performance using particle flow with the ATLAS Detector. *Eur. Phys. J. C*, 77(7):466, 2017.

[77] Georges Aad et al. Jet energy scale and resolution measured in proton–proton collisions at $\sqrt{s} = 13$ TeV with the ATLAS detector. *Eur. Phys. J. C*, 81(8):689, 2021.

[78] The ATLAS Collaboration. Calibration of light-flavour b-jet mistagging rates using ATLAS proton-proton collision data at $\sqrt{s} = 13$ TeV. ATLAS-CONF-2018-006, Geneva, Apr 2018.

[79] The ATLAS Collaboration. Performance of b-Jet Identification in the ATLAS Experiment. *JINST*, 11(04):P04008, 2016.

[80] The ATLAS Collaboration. Optimisation and performance studies of the ATLAS b-tagging algorithms for the 2017-18 LHC run. ATL-PHYS-PUB-2017-013, Geneva, Jul 2017.

[81] The ATLAS Collaboration. Identification of Jets Containing b-Hadrons with Recurrent Neural Networks at the ATLAS Experiment. ATL-PHYS-PUB-2017-003, Geneva, Mar 2017.

[82] The ATLAS Collaboration. Secondary vertex finding for jet flavour identification with the ATLAS detector. ATL-PHYS-PUB-2017-011, Geneva, Jun 2017.

[83] The ATLAS Collaboration. Topological b-hadron decay reconstruction and identification of b-jets with the JetFitter package in the ATLAS experiment at the LHC. ATL-PHYS-PUB-2018-025, Geneva, Oct 2018.

[84] The ATLAS Collaboration. ATLAS flavour-tagging algorithms for the LHC Run 2 pp collision dataset. 11 2022. https://arxiv.org/abs/2211.16345.

[85] A. Hoecker et al. Tmva - toolkit for multivariate data analysis. 2007. https://arxiv.org/abs/physics/0703039.

[86] Rami Al-Rfou et al. Theano: A python framework for fast computation of mathematical expressions. *CoRR*, abs/1605.02688, 2016. https://arxiv.org/abs/1605.02688.

[87] Georges Aad et al. ATLAS b-jet identification performance and efficiency measurement with $t\bar{t}$ events in pp collisions at $\sqrt{s} = 13$ TeV. *Eur. Phys. J. C*, 79(11):970, 2019.

[88] Georges Aad et al. Measurement of the c-jet mistagging efficiency in $t\bar{t}$ events using pp collision data at $\sqrt{s} = 13$ TeV collected with the ATLAS detector. *Eur. Phys. J. C*, 82(1):95, 2022.

[89] The ATLAS Collaboration. Performance of missing transverse momentum reconstruction with the ATLAS detector using proton–proton collisions at $\sqrt{s} = 13$ TeV. *Eur. Phys. J. C*, 78:903, 2018.

[90] Stefano Frixione, Paolo Nason, and Carlo Oleari. Matching NLO QCD computations with parton shower simulations: the POWHEG method. *JHEP*, 11:070, 2007.

[91] The ATLAS Collaboration. Measurement of b-tagging efficiency of c-jets in $t\bar{t}$ events using a likelihood approach with the ATLAS detector. ATLAS-CONF-2018-001, 2018.

[92] Kyle Cranmer, George Lewis, Lorenzo Moneta, Akira Shibata, and Wouter Verkerke. HistFactory: A tool for creating statistical models for use with RooFit and RooStats. CERN-OPEN-2012-016, New York, 2012.

[93] Stephen P. Martin. A Supersymmetry primer. *Adv. Ser. Direct. High Energy Phys.*, 18:1–98, 1998.

[94] The ATLAS Collaboration. Search for top-squark pair production in final states with one lepton, jets, and missing transverse momentum using 36 fb^{-1} of $\sqrt{s} = 13$ TeV pp collision data with the ATLAS detector. *JHEP*, 06:108, 2018.

[95] S. Y. Andrean. Search for stop using the ATLAS detector and performance analysis of the Tile Calorimeter with Muons from W decays. DiVA-191555, 2021. Licentiate Thesis.

[96] The ATLAS Collaboration. Performance of the missing transverse momentum triggers for the ATLAS detector during Run-2 data taking. *JHEP*, 08:080, 2020.

[97] The ATLAS Collaboration. Performance of electron and photon triggers in ATLAS during LHC Run 2. *Eur. Phys. J. C*, 80(1):47, 2020.

[98] The ATLAS Collaboration. ATLAS Muon Trigger performance. *PoS*, LHCP2019:007, 2019.

[99] B. Grzadkowski, M. Iskrzynski, M. Misiak, and J. Rosiek. Dimension-Six Terms in the Standard Model Lagrangian. *JHEP*, 10:085, 2010.

[100] R. Alonso, M. B. Gavela, L. Merlo, S. Rigolin, and J. Yepes. The Effective Chiral Lagrangian for a Light Dynamical "Higgs Particle". *Phys. Lett. B*, 722:330–335, 2013. [Erratum: Phys.Lett.B 726, 926 (2013)].

[101] Gerhard Buchalla, Oscar Catà, and Claudius Krause. Complete Electroweak Chiral Lagrangian with a Light Higgs at NLO. *Nucl. Phys. B*, 880:552–573, 2014. [Erratum: Nucl.Phys.B 913, 475–478 (2016)].

[102] Gerhard Buchalla, Oscar Catá, and Claudius Krause. On the Power Counting in Effective Field Theories. *Phys. Lett. B*, 731:80–86, 2014.

[103] The ATLAS Collaboration. Combined effective field theory interpretation of Higgs boson and weak boson production and decay with ATLAS data and electroweak precision observables. ATL-PHYS-PUB-2022-037, Geneva, 2022.

[104] Timothy Cohen, Nathaniel Craig, Xiaochuan Lu, and Dave Sutherland. Is SMEFT Enough? *JHEP*, 03:237, 2021.

[105] Matteo Capozi and Gudrun Heinrich. Exploring anomalous couplings in Higgs boson pair production through shape analysis. *JHEP*, 03:091, 2020.

[106] Alexandra Carvalho, Florian Goertz, Ken Mimasu, Maxime Gouzevitch, and Anamika Aggarwal. On the reinterpretation of non-resonant searches for Higgs boson pairs. 2017. https://arxiv.org/abs/1710.08261.

[107] G. Buchalla, M. Capozi, A. Celis, G. Heinrich, and L. Scyboz. Higgs boson pair production in non-linear Effective Field Theory with full m_t-dependence at NLO QCD. *JHEP*, 09:057, 2018.

[108] Gröber, Ramona and Alasfar, Lina and Cadamuro, Luca and Dimitriadi, Christina and Ferrari, Arnaud and Heinrich, Gudrun Marlen and Ingebretsen Carlson, Tom and Lang, Jannis and Ordek, Serhat and Pereira Sánchez, Laura and Scyboz, Ludovic and Sjölin, Jörgen. Effective Field Theory descriptions of Higgs boson pair production. LHCHWG-2022-004, Geneva, 2022.

[109] Keith Hamilton, Paolo Nason, Emanuele Re, and Giulia Zanderighi. NNLOPS simulation of Higgs boson production. *JHEP*, 10:222, 2013.

[110] Simone Alioli, Paolo Nason, Carlo Oleari, and Emanuele Re. A general framework for implementing NLO calculations in shower Monte Carlo programs: the POWHEG BOX. *JHEP*, 06:043, 2010.

[111] Paolo Nason. A new method for combining NLO QCD with shower Monte Carlo algorithms. *JHEP*, 11:040, 2004.

[112] Jon Butterworth et al. PDF4LHC recommendations for LHC Run II. *J. Phys. G*, 43:023001, 2016.

[113] T. Sjöstrand, S. Mrenna, and P. Skands. A brief introduction to PYTHIA 8.1. *Comput. Phys. Commun.*, 178:852–867, 2008.

[114] Richard D. Ball et al. Parton distributions with LHC data. *Nucl. Phys. B*, 867:244, 2013.

[115] The ATLAS Collaboration. ATLAS Pythia 8 tunes to 7 TeV data. ATL-PHYS-PUB-2014-021, 2014.

[116] Xiao-Gang He, Tong Li, Xue-Qian Li, Jusak Tandean, and Ho-Chin Tsai. Constraints on scalar dark matter from direct experimental searches. *Phys. Rev. D*, 79:0235212, 2009.

[117] Ilya F. Ginzburg, Maria Krawczyk and Per Osland . Two-Higgs-Doublet Models with CP violation. 2002. https://arxiv.org/abs/hep-ph/0211371.

[118] Ulrich Ellwanger, Cyril Hugonie, and Ana M. Teixeira. The next-to-minimal supersymmetric standard model. *Physics Reports*, 496(1):1–77, 2010.

[119] Tim Stefaniak Tania Robens and Jonas Wittbrodt. Two-real-scalar-singlet extension of the SM: LHC phenomenology and benchmark scenarios. *The European Physical Journal C*, 80(151), 2020.

[120] Pierre Baldi, Kyle Cranmer, Taylor Faucett, Peter Sadowski, and Daniel Whiteson. Parameterized neural networks for high-energy physics. *Eur. Phys. J. C*, 76(5):235, 2016.

[121] Tom O'Malley, Elie Bursztein, James Long, François Chollet, Haifeng Jin, Luca Invernizzi, et al. Kerastuner. `https://github.com/keras-team/keras-tuner`, 2019.

[122] The ATLAS Collaboration. TRexFitter Documentation. `https://trexfitter-docs.web.cern.ch/trexfitter-docs/`.

Part II

Papers

Paper I

EUROPEAN ORGANISATION FOR NUCLEAR RESEARCH (CERN)

Submitted to: EPJC

CERN-EP-2022-211
18th January 2023

Calibration of the light-flavour jet mistagging efficiency of the b-tagging algorithms with Z+jets events using 139 fb^{-1} of ATLAS proton–proton collision data at $\sqrt{s}$ = 13 TeV

The ATLAS Collaboration

The identification of b-jets, referred to as b-tagging, is an important part of many physics analyses in the ATLAS experiment at the Large Hadron Collider and an accurate calibration of its performance is essential for high-quality physics results. This publication describes the calibration of the light-flavour jet mistagging efficiency in a data sample of proton–proton collision events at $\sqrt{s}$ = 13 TeV corresponding to an integrated luminosity of 139 fb^{-1}. The calibration is performed in a sample of Z bosons produced in association with jets. Due to the low mistagging efficiency for light-flavour jets, a method which uses modified versions of the b-tagging algorithms referred to as flip taggers is used in this work. A fit to the jet-flavour-sensitive secondary-vertex mass is performed to extract the scale factor from data, while simultaneously correcting the b-jet efficiency. With this procedure the heavy-flavour uncertainties are considerably lower than in previous calibrations of the mistagging scale factors, where they were dominant. The scale factors obtained in this calibration are consistent with unity within uncertainties.

1 Introduction

Many analyses in ATLAS [1], such as measurements or searches involving top quarks or Higgs bosons, rely on the identification of jets containing b-hadrons (b-jets) with high tagging efficiency and low mistagging efficiency for jets containing c-hadrons (c-jets) or containing neither b- nor c-hadrons (light-flavour jets). The relatively long lifetime and high mass of b-hadrons together with the large track multiplicity of their decay products is exploited by b-tagging algorithms to identify b-jets.

The b-tagging algorithms are trained using Monte Carlo (MC) simulated events and therefore need to be calibrated in order to correct for efficiency differences between data and simulation that may arise from an imperfect description of the data, e.g. in the parton shower and fragmentation modelling or in the detector and response simulation. The efficiency of identifying a b-jet (ε^b) and the mistagging efficiencies (ε^c and $\varepsilon^{\text{light}}$), which are the probabilities that other jets are wrongly identified by the algorithms as b-jets, are measured in data and compared with the predictions of the simulation. These tagging and mistagging efficiencies are defined as

$$\varepsilon^f = \frac{N^f_{\text{pass}}}{N^f_{\text{all}}},$$

where $f \in \{b,\ c,\ \text{light}\}$, N^f_{pass} is the number of jets of flavour f selected by the b-tagging algorithm and N^f_{all} is the number of all jets of flavour f. The flavour-tagging efficiency in data ($\varepsilon^f_{\text{data}}$) is compared with the efficiency in MC simulation ($\varepsilon^f_{\text{MC}}$) and a calibration factor, also called the scale factor (SF), is defined as

$$\text{SF}^f = \frac{\varepsilon^f_{\text{data}}}{\varepsilon^f_{\text{MC}}}. \quad (1)$$

The calibration factors correct the efficiencies and mistagging efficiencies in simulation to the ones in data and are applied to all physics analyses in ATLAS that use b-tagging. The b-jet efficiency (ε^b) is calibrated using the method described in Ref. [2], where the SFs^b are extracted from a sample of events containing top-quark pairs decaying into a final state with two charged leptons and two b-jets. The c-jet mistagging efficiency (ε^c) is calibrated via the method described in Ref. [3], where the SFs^c are extracted from events containing top-quark pairs decaying into a final state with exactly one charged lepton and several jets. The events are reconstructed using a kinematic likelihood technique and include a hadronically decaying W boson, whose decay products are rich in c-jets.

This paper describes the measurement of the light-flavour jet mistagging efficiency ($\varepsilon^{\text{light}}$) of the `DL1r` b-tagger, which is widely used in ATLAS Run 2 physics analyses and is discussed in Section 5. The SFs$^{\text{light}}$ are extracted from particle-flow jets [4] using 139 fb^{-1} of proton–proton (pp) collision data collected by the ATLAS detector during Run 2 of the LHC.

The mistagging efficiency $\varepsilon^{\text{light}}$ is difficult to calibrate because after applying a b-tagging requirement, the obtained sample of jets is strongly dominated by b-jets and the fraction of light-flavour jets passing a selection on the b-tagging score is too low to estimate $\varepsilon^{\text{light}}_{\text{data}}$. In order to extract an unbiased and precise SF$^{\text{light}}$, a sample enriched in mistagged light-flavour jets is required.

In this paper, the Negative Tag method [5, 6], which relies on a modified tagger with a reduced ε^b and ε^c but similar $\varepsilon^{\text{light}}$ is used. The method, described in detail in Section 6, has already been used to calibrate $\varepsilon^{\text{light}}$ by using dijet events in 2015–2016 data [7] from the early part of Run 2.

In this work, jets produced in association with Z bosons (Z+jets) are used instead, allowing the use of unprescaled lepton triggers instead of the prescaled single-jet triggers which were used in the previous calibration. The calibration precision is improved by extracting the $\mathrm{SF}^{\mathrm{light}}$ in a fit that simultaneously corrects ε^b using data. Previously, ε^b was estimated from simulation, resulting in large modelling uncertainties which impacted the precision of the result. An alternative approach [7] to the Negative Tag method exists in which $\varepsilon^{\mathrm{light}}_{\mathrm{data}}$ is estimated from simulation by applying data-driven corrections to the input quantities of the low-level b-tagging algorithms. This method is used to assess the extrapolation uncertainty between the modified and nominal tagger as described in Section 7.

The paper is structured as follows. Section 2 describes the ATLAS detector. Section 3 presents the dataset and simulations used in this calibration. The reconstruction of jets, electrons and muons is summarised in Section 4, while the b-tagging algorithms are described in detail in Section 5. The calibration method is detailed in Section 6. Systematic uncertainties and results are presented, respectively, in Section 7 and Section 8 and conclusions are given in Section 9.

2 ATLAS detector

The ATLAS experiment [1] at the LHC is a multipurpose particle detector with a forward–backward symmetric cylindrical geometry and a near 4π coverage in solid angle.[1] It consists of an inner tracking detector (ID) surrounded by a thin superconducting solenoid providing a 2 T axial magnetic field, electromagnetic and hadron calorimeters, and a muon spectrometer with a toroidal magnet system.

The inner tracking detector, which provides full coverage of a pseudorapidity range $|\eta| < 2.5$, consists of silicon pixel, silicon microstrip, and transition radiation tracking detectors. The high-granularity silicon pixel detector covers the vertex region and typically provides four measurements per track, the first measurement normally being in the insertable B-layer (IBL) installed before Run 2, primarily to enhance the b-tagging performance [8, 9]. Sampling calorimeters, made of lead and liquid Argon (LAr), provide electromagnetic (EM) energy measurements with high granularity in the pseudorapidity region $|\eta| < 3.2$. A steel/scintillator-tile hadron calorimeter covers the central pseudorapidity range ($|\eta| < 1.7$) and a copper/LAr hadron calorimeter covers the range $1.5 < |\eta| < 3.2$. The forward region is instrumented with LAr calorimeters in the range $3.1 < |\eta| < 4.9$, measuring both electromagnetic and hadronic energies in copper/LAr and tungsten/LAr modules. The muon spectrometer surrounds the calorimeters and is based on three large superconducting air-core toroidal magnets with eight coils each. The field integral of the toroids ranges between 2.0 and 6.0 T m across most of the detector. The muon spectrometer includes a system of precision tracking chambers and fast detectors for triggering.

A two-level trigger system is used to select events. The first-level trigger is implemented in hardware and uses a subset of the detector information to accept events at a rate below 100 kHz. This is followed by a software-based trigger that reduces the accepted event rate to 1 kHz on average depending on the data-taking conditions [10].

[1] ATLAS uses a right-handed coordinate system with its origin at the nominal interaction point in the centre of the detector and the z-axis along the beam pipe. The x-axis points from the interaction point to the centre of the LHC ring, and the y-axis points upwards. Cylindrical coordinates (r, ϕ) are used in the transverse plane, ϕ being the azimuthal angle around the z-axis. The pseudorapidity is defined in terms of the polar angle θ as $\eta = -\ln\tan(\theta/2)$. The angular distance is measured in units of $\Delta R \equiv \sqrt{(\Delta\eta)^2 + (\Delta\phi)^2}$.

An extensive software suite [11] is used in data simulation, in the reconstruction and analysis of real and simulated data, in detector operations, and in the trigger and data acquisition systems of the experiment.

3 Data and simulated samples

The presented results are based on data from pp collisions with a centre-of-mass energy of $\sqrt{s} = 13$ TeV and a 25 ns proton bunch crossing interval. The data were collected between 2015 and 2018 with the ATLAS detector, corresponding to an integrated luminosity of 139 fb^{-1} [12, 13]. A set of single-electron [14] and single-muon triggers [15] were used, with transverse momentum (p_{T}) thresholds in the range 20–26 GeV and depending on the lepton flavour and data-taking period. All detector subsystems are required to have been operational during data taking and to fulfil data quality requirements [16].

Expected Standard Model (SM) processes were modelled using MC simulation. A summary of the simulated samples used in this calibration and their basic parameter settings is provided in Table 1. All samples were produced using the ATLAS simulation infrastructure [17] and Geant4 [18]. The effect of additional pp interactions per bunch crossing (pile-up) is accounted for by overlaying the hard-scattering process with minimum-bias events generated with Pythia 8.186 [19] using the NNPDF2.3lo set of parton distribution functions (PDF) [20] and the A3 set of tuned parameters [21]. Different pile-up conditions between data and simulation are taken into account by reweighting the mean number of interactions per bunch crossing in simulation to the number observed in data.

The events used in this study originate mostly from the production of a Z boson in association with jets. This process is simulated with two different generators. Nominal predictions of Z/γ^* production were generated using Sherpa 2.2.1 [22] with the NNPDF3.0nnlo PDF [23]. Diagrams with up to two additional parton emissions were simulated with next-to-leading-order (NLO) precision in QCD, and those with three or four additional parton emissions to leading-order accuracy. Matrix elements were merged with the Sherpa parton shower using the MEPS@NLO formalism [24–27] with a merging scale of 20 GeV and the five-flavour numbering scheme (5FNS). The sample used to evaluate the tagging efficiencies predicted by the MC simulation was produced with the MadGraph 2.2.3 [28] event generator with up to four additional partons at matrix-element level interfaced with Pythia 8.210 to model the parton shower, hadronisation, and underlying event with the NNPDF3.0nlo PDF for the processes where the Z boson decays into muons or electrons, and with MadGraph 2.2.2 interfaced with Pythia 8.186 with the NNPDF2.3lo PDF [20] for Z boson decays into τ-leptons. The predictions of the Z+jets MadGraph program are based on calculations using the 5FNS scheme. Sherpa 2.2.1 and MadGraph Z+jets simulations are normalised to the overall cross-section prediction at NNLO precision in QCD [29].

In addition to Z+jets production, some minor backgrounds contribute to the final event sample used for the calibration. These backgrounds consist mostly of diboson production (ZZ and ZW) and top-quark pair production with subsequent decays into final states with two charged leptons. The ZW production and the ZZ production via quark–antiquark annihilation were simulated with Sherpa 2.2.1 with a MEPS@NLO configuration similar to what was used in the simulation of the Z+jets process described above, while loop-induced ZZ processes initiated by gluon–gluon fusion were generated with Sherpa 2.2.2. Both the ZZ and ZW simulation samples used the NNPDF3.0nnlo PDF set. Top-quark pair production was simulated using the Powheg Box v2 generator at NLO precision in QCD [30] interfaced with Pythia 8.230 to model the parton shower, hadronisation, and underlying event, using the A14 set of tuned parameters [31]. This simulation was used to model top-quark pair production with subsequent decays into final states with two charged leptons and as well into final states with one charged lepton. The latter is used to evaluate

Table 1: A summary of MC generators and their basic parameter settings used to simulate the various physics processes.

Process	Generator	PDF set	Hadronisation/Fragmentation
Z+jets	Sherpa 2.2.1	NNPDF3.0	Sherpa 2.2.1
ZW and $q\bar{q}$-initiated ZZ	Sherpa 2.2.1	NNPDF3.0	Sherpa 2.2.1
ZZ from gluon–gluon fusion	Sherpa 2.2.2	NNPDF3.0	Sherpa 2.2.2
$t\bar{t}$	Powheg Box v2	NNPDF3.0	Pythia 8.230
Z+jets ($Z \rightarrow ee$ and $Z \rightarrow \mu\mu$)	MadGraph 2.2.3	NNPDF3.0	Pythia 8.210
Z+jets ($Z \rightarrow \tau\tau$)	MadGraph 2.2.2	NNPDF2.3	Pythia 8.186

the difference between the SFs obtained from the modified (`DL1rFlip`) and nominal (`DL1r`) b-tagging algorithms.

The decays of b- and c-hadrons were handled by EvtGen 1.6.0 [32] in all simulations, except for those generated using Sherpa, for which the default Sherpa configuration recommended by the Sherpa authors was used.

4 Object and event selection

Tracks of charged particles are reconstructed from energy deposits in the material of the ID [33]. Events are required to contain at least one vertex with two or more associated tracks that must have $p_{\mathrm{T}} > 500$ MeV. Among all vertices, the vertex with the highest p_{T}^2 sum of the associated tracks is taken as the primary vertex [34]. The transverse (d_0) track impact parameter (IP) is defined as the distance of closest approach of the track-trajectory to the primary vertex in the transverse plane. The longitudinal track IP (z_0) is defined as the distance in the z-direction between the primary vertex and the track trajectory at the point of the closest approach in the x–y plane.

Jets containing b- and c-hadrons are characterised by having in-flight decays due to the relatively long lifetime of the heavy-flavour hadrons and give rise to secondary vertices (SV) with associated tracks. To exploit the presence of in-flight decays in the jet direction, the signed IP is defined for each track within a jet. As shown in Figure 1, a track has a positive IP if the angle between the jet direction and the line joining the primary vertex to the point of closest approach to the track is less than $\pi/2$ and negative otherwise. The Single Secondary Vertex Finder (`SSVF`) algorithm [35] is used for the reconstruction of the SV.

Electron candidates are reconstructed from energy clusters in the EM calorimeter matched to an ID track [36]. Candidates must satisfy $p_{\mathrm{T}} > 18$ GeV and $|\eta| < 2.47$, excluding the barrel–endcap transition region of $1.37 < |\eta| < 1.52$, and their associated tracks must fulfil $|d_0|/\sigma_{d_0} < 5$ and $|z_0| \sin\theta < 0.5$ mm, where σ_{d_0} is the uncertainty in d_0. Electrons are identified using a likelihood-based discriminant that combines information about shower shapes in the EM calorimeter, track properties and the quality of the track-to-cluster matching [36]. Electrons must fulfill a 'Tight' identification selection. The gradient isolation criteria are applied to reject non-prompt electrons, using energy deposits in the ID and calorimeter within a cone around the electron. Their efficiency is 90% (99%) for electrons from $Z \rightarrow ee$ decays at

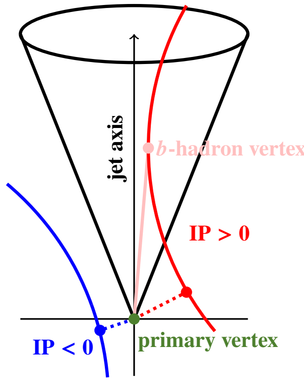

Figure 1: Graphical illustration of the signed IP of tracks in the jet.

p_{T} = 25 (60) GeV. Efficiency scale factors measured in data [36] are used to correct for differences in reconstruction, identification, isolation and trigger selection efficiencies between data and simulation.

Muon candidates are reconstructed by combining tracks in the ID with tracks in the muon spectrometer [37]. Only muons with $|\eta| < 2.5$ and $p_{\mathrm{T}} > 18$ GeV are used. They have to fulfil the 'Tight' identification selection criteria [38] and satisfy $|d_0|/\sigma_{d_0} < 3$ and $|z_0| \sin\theta < 0.5$ mm. The isolation selection reduces the contamination from non-prompt muons by placing an upper bound on the amount of energy measured in the tracking detectors and the calorimeter (combined using the particle-flow algorithm [4]) within a cone of variable size (for $p_{\mathrm{T}}^{\mu} < 50$ GeV) or fixed size (for $p_{\mathrm{T}}^{\mu} > 50$ GeV) around the muon. Efficiency scale factors are used to correct for differences in muon reconstruction, identification, vertex association, isolation and trigger efficiencies between simulation and data [38].

Jets are reconstructed from particle-flow objects combining information from the tracker and calorimeter [4], using the anti-k_t algorithm [39, 40] with a radius parameter of $R = 0.4$. The jet energy is calibrated to the particle scale by using a sequence of corrections, including simulation-based corrections and in situ calibrations [41]. The jet-vertex tagging technique (JVT) [42], which uses a multivariate likelihood approach, is applied to jets with $|\eta| < 2.4$ and $p_{\mathrm{T}} < 60$ GeV to suppress jets from pile-up activity. The 'Tight' selection criterion, corresponding to a JVT score > 0.5, is used. Scale factors are applied to match the JVT MC efficiencies to those in data. All selected jets must have a $p_{\mathrm{T}} > 20$ GeV and $|\eta| < 2.5$.

The b-tagging algorithms use tracks matched to jets as input. This matching uses the angular separation between the track momenta, defined at the point of closest approach to the primary vertex (PV), and the jet axis, $\Delta R(\text{track, jet axis})$. The selection requirement on $\Delta R(\text{track, jet axis})$ varies as a function of the jet p_{T} because the b-hadron decay products are more collimated at larger hadron p_{T} [2].

The jet-flavour labelling in simulation is based on an angular matching of reconstructed jets to generator-level b-hadrons, c-hadrons and τ-leptons with $p_{\mathrm{T}} > 5$ GeV. If a b-hadron is found within a cone of size $\Delta R = 0.3$ around the jet axis, the jet is labelled as a b-jet. If no matching to any b-hadron is possible, the matching procedure is repeated sequentially for c-hadrons and τ-leptons, and the matched jets are called c-jets and τ-jets, respectively. A jet is labelled as a light-flavour jet by default if no matching to any of these particles was successful.

A series of requirements on the angular separation ΔR between muons, electrons and jets are applied to remove overlaps between objects. If an electron candidate shares an ID track with a muon candidate, the electron candidate is rejected. Jets within a cone of $\Delta R = 0.2$ around a lepton are rejected, unless the lepton is a muon and the jet has more than three associated tracks, in which case the muon is rejected. Finally, lepton candidates that are found to be $0.2 < \Delta R < 0.4$ from any remaining jet are discarded.

A jet sample enriched in light-flavour jets is needed for the calibration. A sample constructed using the leading jet in p_{T} in a Z+jets selection is expected to contain a 7%–8% fraction of c-jets and a 4%–6% fraction of b-jets, depending on the jet p_{T}. The mistagging efficiency calibration is performed on the leading jet in a sample of Z+jets candidate events. The distinct signature of a Z boson decaying into either two electrons or two muons allows a clean sample of Z+jets events to be selected. Events are selected for further analysis using single-lepton triggers, where one of the leptons must be matched to an object that triggered the recording of the event. The event must contain exactly two prompt leptons with opposite charges and the same flavour (i.e. either exactly two electrons or exactly two muons). The leading lepton must have $p_{\mathrm{T}} > 28$ GeV and the invariant mass of the dilepton system, $m_{\ell\ell}$, must satisfy $81 < m_{\ell\ell} < 101$ GeV. Only events with a reconstructed Z boson with $p_{\mathrm{T}}^{Z} > 50$ GeV are considered because the overall modelling is better in this range [43]. The event must also contain at least one jet with $p_{\mathrm{T}} > 20$ GeV and $|\eta| < 2.5$.

The event yields obtained after applying all selection requirements are listed in Table 2, while comparisons between the predictions by the simulation and the data are shown in Figure 2 for selected variables. The predictions of the MC simulation are normalised to data for these comparisons. The shapes of the distributions predicted by the simulation are consistent with those observed within statistical uncertainties for most of the considered kinematic range. The discrepancy observed in the SV mass (m_{SV}) distribution is expected because it is affected by a known mismodelling of the jet-flavour fractions [44, 45]; this is mitigated by the fit described in Section 6. The m_{SV} observable is calculated using the `SSVF` algorithm. Negative values of m_{SV} indicate that no SV was found in the jet. The mismodelling in jet p_{T} does not affect the calibration.

Table 2: Expected contributions of processes in the calibration region, compared with the selected data obtained with the full Run 2 dataset. The quoted uncertainties are statistical uncertainties only.

Process	Yield
Z+jets (Sherpa)	$(8.766 \pm 0.015)\cdot 10^6$
$t\bar{t}$	$(7.673 \pm 0.006)\cdot 10^4$
WZ	$(4.188 \pm 0.005)\cdot 10^4$
ZZ	$(2.526 \pm 0.004)\cdot 10^4$
Predictions	$(8.910 \pm 0.015)\cdot 10^6$
Data	$9.560 \cdot 10^6$

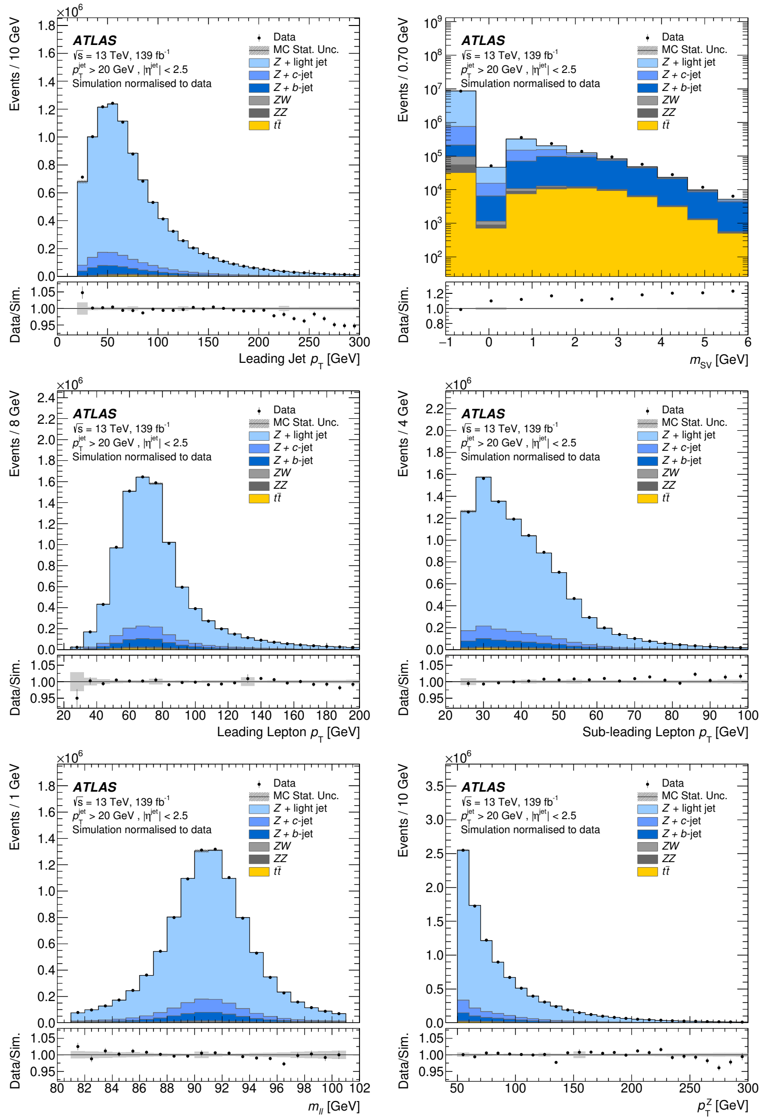

Figure 2: Comparisons between data and simulation for the most relevant kinematic variables after event selection. The MC expectations are normalised to data. The shaded area corresponds to the statistical uncertainties of the MC simulations. The Z+jets events are simulated using SHERPA 2.2.1. Negative values of m_{SV} indicate that no SV was found in the jet.

5 The DL1r b-tagging algorithm

Properties of b-hadrons, such as their relatively high mass, long lifetime and large multiplicity of reconstructed tracks from their decay products, are exploited to distinguish b-jets from c-jets and light-flavour jets. Individual low-level taggers [46, 47] are designed to target the specific properties of b-jets. `IP2D`, `IP3D` and `RNNIP` exploit the individual properties of the tracks from charged particles matched to the jet, especially the track d_0 and z_0. `RNNIP` is based on a recurrent neural network and it explores the correlations between the IPs of different selected tracks in the jet. `SV1` exploits the output of the `SSVF` algorithm and `JetFitter` [48] reconstructs secondary and tertiary vertices, following the expected topology of b-hadron decays. The `DL1r` algorithm is a deep neural network that takes the output of the low-level taggers and jet kinematics as input and builds a single discriminant [49, 50].

ATLAS analyses use selection requirements defining a lower bound on the `DL1r` discriminant to select b-jets with a certain efficiency. Four of these so-called single-cut operating points (OPs) are defined, corresponding to b-jet selection efficiencies of 85%, 77%, 70% and 60%. The OPs are evaluated in a sample of b-jets from simulated $t\bar{t}$ events. These selection requirements divide the `DL1r` score into five intervals to form the pseudo-continuous OPs, where the lower edge of the lowest interval corresponds to 100% `DL1r` b-tagging efficiency, and the upper edge of the highest interval corresponds to 0% efficiency.

The single-cut and pseudo-continuous OPs are calibrated in order to correct for efficiency differences between data and simulation. The calibration SF, defined in Eq. (1), is measured relative to a reference efficiency $\varepsilon^{f}_{\mathrm{MC}}$. The performance of the b-tagging algorithm in simulation is affected by the hadronisation and fragmentation model used in the parton shower simulation [43]. To account for their differences, simulation-to-simulation SFs are applied to those simulated samples that have a fragmentation model different from the default. The calculation of these simulation-to-simulation correction factors is described in Ref. [51]. The top-quark pair production sample produced with Powheg Box v2 + Pythia 8.230 is used to define the reference MC efficiencies in the b- and c-jet calibrations. As no equivalent Z+jets simulation produced with the Powheg Box v2 generator is available, the Z+jets MadGraph + Pythia 8 simulation is used for the definition of the reference efficiency in the calculation of $\mathrm{SF}^{\mathrm{light}}$ for light-flavour jets. Since the Z+jets MadGraph + Pythia 8 simulation uses the same parton shower model and set of tuned parameters as the top-quark pair production simulation, the light-flavour jet results and the b- and c-jet calibrations are obtained relative to similar reference models.

6 The Negative Tag method

The `DL1r` algorithm rejects 97.52% and 99.96% of the light-flavour jets, respectively, at the 85% and 60% OPs, according to simulated $t\bar{t}$ events. Therefore, the fraction of light-flavour jets passing the threshold is too low to estimate $\varepsilon^{\mathrm{light}}$ in data. The Negative Tag method [5, 6] calibrates $\varepsilon^{\mathrm{light}}_{\mathrm{data}}$ using a modified version of the `DL1r` algorithm (called `DL1rFlip`) that achieves lower ε^{b} to $\varepsilon^{\mathrm{light}}$ ratios without changing $\varepsilon^{\mathrm{light}}$ significantly.

Tracks matched to b-jets have relatively large and positively signed IPs due to the long lifetime of the b-hadrons and the presence of displaced decay vertices. In contrast, tracks matched to light-flavour jets typically have IP values consistent with zero within the IP resolution such that a more symmetric[2] IP distribution is expected. The expected IP distributions of the tracks associated with b-jets, c-jets or light-flavour jets are shown in Figure 3. The Negative Tag method assumes that the probability for a light-flavour jet to be mistagged remains almost the same when inverting the IP signs of all tracks and displaced vertices. This is based on the assumption that light-flavour jets are misidentified as b-jets mainly due to resolution effects in the track reconstruction which result in tracks and vertices from tracks with positive IPs inside the jet. Given the symmetric IP distributions, the fractions of tracks and vertices from tracks with positive IPs remain stable after inverting the IP signs of all tracks and vertices. The presence of the positive tail in the IP distribution challenges this assumption and its impact is taken into account by a dedicated uncertainty, which is called the `DL1rFlip`-to-`DL1r` extrapolation uncertainty in the following.

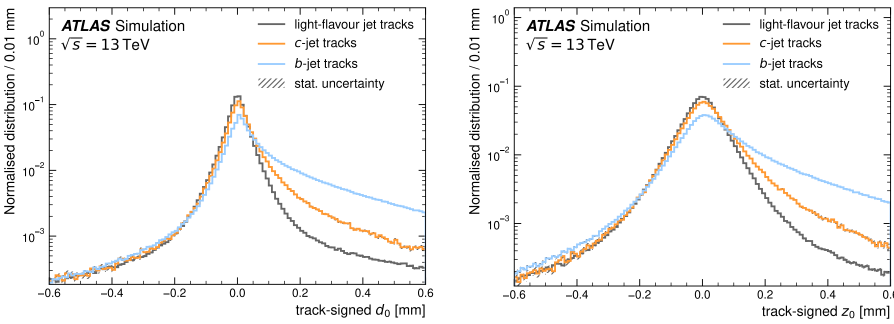

Figure 3: Signed-d_0 (left) and signed-z_0 (right) distributions for tracks matched to b-jets, c-jets and light-flavour jets in simulated $t\bar{t}$ events. The selected tracks are matched to particle-flow jets with $p_T > 20$ GeV and $|\eta| < 2.5$, and pass the jet-vertex tagger selection. The distributions are normalised to unity. Statistical uncertainties are also shown.

The `DL1rFlip` algorithm inverts the signs of the track IPs and the decay length[3], while using the same algorithm training and OP-threshold definitions as the `DL1r` algorithm. The $\varepsilon^{\text{light}}$ values obtained by the two algorithms are approximately the same, while the `DL1rFlip` algorithm selects a smaller fraction of b-jets than the nominal version. The discriminants of the `DL1r` and `DL1rFlip` algorithms are compared between data and simulation in Figure 4. These comparisons show that the heavy-flavour fractions are much lower for high `DL1rFlip` values than for high `DL1r` values. At the 85% (60%) single-cut OP, the `DL1r` algorithm selects a sample of jets in which 25% (1%) are light-flavour jets, while the `DL1rFlip` algorithm selects a sample in which a higher fraction, 38% (6%), are light-flavour jets at the same OP.

The calibration is performed independently in jet p_T intervals in order to account for the p_T dependence of $\varepsilon^{\text{light}}$. A simultaneous binned fit to the m_{SV} distribution in each pseudo-continuous interval of the `DL1rFlip` discriminant is performed in order to simultaneously determine $\varepsilon^{b}_{\text{data}}$ and $\varepsilon^{\text{light}}_{\text{data}}$ in the `DL1rFlip` discriminant intervals. The sensitivity of the fit does not allow the SFs of all three jet flavours to be derived simultaneously. Therefore, $\varepsilon^{c}_{\text{data}}$ is constrained to the MC predictions and SF^{c} is fixed to unity within an uncertainty of 30%, as suggested by studies of the c-jet mistagging efficiency calibration [3].

[2] The tracks matched to light-flavour jets have a slight bias towards positive-sign values due to the presence of some long-lived particles (e.g. K_S or Λ). The contribution from the mismodelling of long-lived particles is expected to be negligible relative to the mismodelling of the d_0 and z_0 resolutions [7].

[3] In this paper, vertices are assigned a negative decay length if they have an angle between the jet direction and the line joining the primary vertex to the secondary vertex of less than $\pi/2$ (see Section 14.2 of Reference [52] for more details).

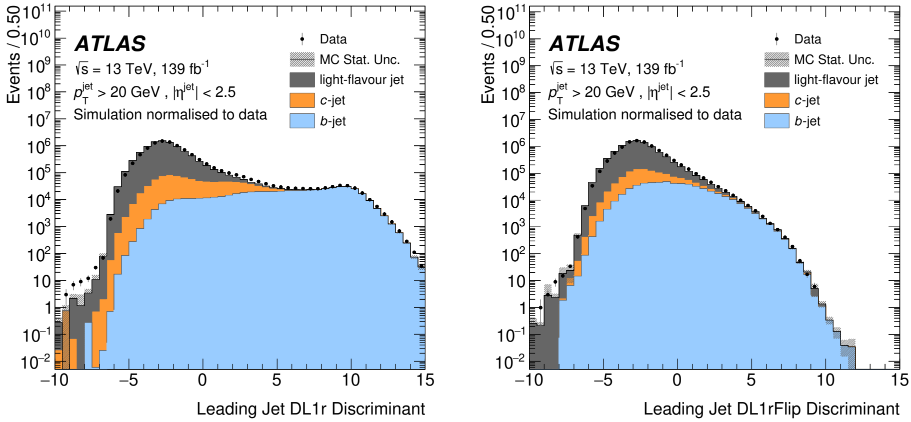

Figure 4: Comparisons between data and simulation for the distributions of the `DL1r` discriminant (left) and `DL1rFlip` discriminant (right). Statistical uncertainties of the yields are shown.

For a given interval of jet p_T, the expected number of jets for a defined discriminant interval i is given by

$$N_i(m_{SV}) = N_{i,MC} \times C \times \left[\sum_{f=\text{light},c,b} F^f \times SF_i^f \times \varepsilon_{i,MC}^f \times P_i^f(m_{SV}) \right],$$

where $N_{i,MC}$ is the predicted flavour-inclusive event yield for each discriminant interval; C is a global normalisation factor and F^f are the jet-flavour fractions; $P_i^f(m_{SV})$ is the probability density function of m_{SV} for jet flavour f in the i-th `DL1rFlip` discriminant interval, taken from simulation. The $P_i^f(m_{SV})$ is defined in such a way to integrate an additional bin ($m_{SV} < 0$ GeV) representing the number of events where no secondary vertex is found. The m_{SV} has been obtained with tracks with nominal sign as input to the `SSVF` algorithm.

The C, F^f and $SF_i^{b,\text{light}}$ parameters are allowed to float in the fit, while $N_{i,MC}$ and $\varepsilon_{i,MC}^f$ are fixed to the predictions from simulated events and SF_i^c is set to 1.0 ± 0.3. The constraints $\sum_{i=1}^{5} \varepsilon_{i,MC}^f \times SF_i^f = 1$, where the contributions to the first bin (corresponding to the 100%–85% OP interval) are allowed to vary such that unitarity is preserved, and $F^{\text{light}} = 1 - F^b - F^c$ are applied, reducing the number of free parameters to 11. Figure 5 shows the post-fit m_{SV} and `DL1rFlip` discriminant distributions for the 50–100 GeV p_T interval. The parameters of interest, i.e. the SF_i^{light}, are obtained from the `DL1rFlip` algorithm. In order to apply this calibration to the `DL1r` algorithm, an extrapolation uncertainty is added to account for the differences between these two tagging algorithms. Details of this `DL1rFlip`-to-`DL1r` extrapolation uncertainty are presented in Section 7.

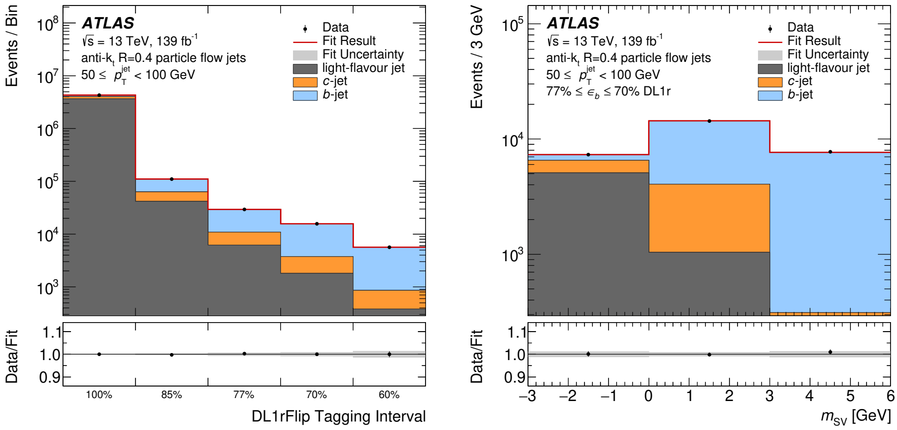

Figure 5: Post-fit distribution of the DL1rFlip discriminant (left) and the m_{SV} distribution in the 77%–70% OP interval (right). Both distributions are shown for the 50–100 GeV p_{T} interval. The shaded area corresponds to the total statistical uncertainty. The binning in m_{SV} allows good separation between the jet flavours and also uses the minimum number of bins necessary to constrain the free parameters of the fit. Choosing the coarsest binning possible allows the statistical uncertainties to be minimised.

7 Systematic uncertainties

The measurement of $\mathrm{SF}^{\mathrm{light}}$ is affected by four types of uncertainties, including those due to experimental effects, the modelling of the Z+jets and background processes, and the limited number of events in data and simulation. For each source of uncertainty, one parameter of the fit model is varied at a time, and the effect of this variation on $\mathrm{SF}^{\mathrm{light}}$ is evaluated. This approach is chosen to prevent the fit from using the data to constrain the impact of individual systematic uncertainties. The probability density functions (PDFs) in m_{SV} are derived from the Sherpa 2.2.1 Z+jets simulation sample. The PDF for each flavour component is separately normalised to unity, so only the shape of the m_{SV} distributions is estimated using the Sherpa 2.2.1 Z+jets simulation. The simulated efficiencies from the MadGraph Z+jets simulation listed in Table 1 are used in the likelihood definition to predict the expected number of events for each flavour category. Given that the flavour fractions and most SFs are extracted from the data, the systematic uncertainty calculation considers mainly effects on the template shapes. An additional uncertainty accounts for differences between $\mathrm{SF}^{\mathrm{light}}$ values from the DL1rFlip and DL1r algorithms to ensure the applicability of this calibration to the DL1r algorithm.

Uncertainties in the modelling of the detector response have a negligible impact on the calibration results. The impact of the jet energy scale uncertainties was estimated by globally shifting the jet energy scale (JES) by 5%, in accord with the most conservative estimate of the JES uncertainty in p_{T} derived in Ref. [41]. This conservative assumption about the magnitude of the jet energy scale uncertainties leads to an estimated impact of less than 1% on the calibration results, owing to the low p_{T} dependence of the scale factors. The impact of d_0 and z_0 IP resolution modelling uncertainties on the m_{SV} templates was estimated by applying data-driven corrections to the simulated d_0 and z_0 in a sample of simulated top-quark pairs with a method similar to the one in Ref. [7]. The impact of these corrections is transfered to the fit templates and is symmetrised around the central value. This approach was chosen in order to mitigate the effect of statistical fluctuations in the available Z+jets samples. Other experimental uncertainties were found to be negligible because they are not correlated with the discriminant used in the fit (m_{SV}).

Simulations of Z+jets via Sherpa 2.2.1 are used as the nominal model to derive the fit templates for b-jets, c-jets and light-flavour jets in the m_{SV} distribution. In order to assess the impact of the resulting choice of parton shower model, shower matching scheme and order of the perturbative QCD calculations on the template shapes, $\mathrm{SFs}^{\mathrm{light}}$ are derived using an alternative model, provided by the Z+jets MadGraph + Pythia 8 simulation. The difference between the obtained $\mathrm{SFs}^{\mathrm{light}}$ is taken as the estimate of the MC modelling uncertainty. The effect of QCD scale uncertainties is estimated by independently doubling or halving the renormalisation and factorisation scales. The impact of choosing a particular PDF set is estimated by propagating its uncertainties. However, the impacts of the QCD scale and PDF set uncertainties are found to be covered by the statistical uncertainties of the MC simulation and these uncertainties are therefore not included.

The effect of the 30% uncertainty in SF^{c}, which was fixed to a value of 1.0 in the fit, is estimated by repeating the fit with SF^{c} set to 1.3 and 0.7 instead. The mean impact of the two variations on $\mathrm{SF}^{\mathrm{light}}$ is taken as the impact of the charm calibration uncertainty on the light-flavour jet calibration.

The $\varepsilon^{\mathrm{light}}$ value is assumed to be the same for `DL1rFlip` and `DL1r` to first order, as described in Section 6. However, mismodelling of the IP resolution, the fake-track rate or the parton shower can have different effects on the tagging performance and $\mathrm{SF}^{\mathrm{light}}$ values of the `DL1r` and `DL1rFlip` algorithms. A `DL1rFlip`-to-`DL1r` extrapolation uncertainty is added to account for residual differences in $\mathrm{SF}^{\mathrm{light}}$ between the two algorithms. $\mathrm{SF}^{\mathrm{light}}$ cannot be measured in data for the `DL1r` algorithm. Therefore, a method similar to the one in Ref. [7] is used to derive $\mathrm{SF}^{\mathrm{light}}$ for `DL1rFlip` and `DL1r` from MC simulation in order to compare the two calibrations. The `DL1rFlip`-to-`DL1r` extrapolation uncertainty consists of two components. One component estimates the impact of the modelling of tracking variables on the `DL1rFlip` and `DL1r` tagging performance, evaluated in a bottom-up approach correcting the simulation, and the second component estimates the impact of the shower and hadronisation model on the tagging performance difference between `DL1rFlip` and `DL1r`. The impact of the modelling of tracking variables is evaluated by applying data-driven corrections to underlying tracking variables affecting the b-tagging performance in a sample of simulated $t\bar{t}$ events generated with Powheg Box v2 + Pythia 8.230. The impact on $\varepsilon^{\mathrm{light}}$ of correcting these observables is evaluated with respect to the uncorrected simulation. Only corrections which have been shown to have a significant impact are considered [7]. These include the IP resolution and fake-track rate modelling [53]. The total impact on the mistagging efficiency is obtained by multiplying the effects of all corrections. The total impact on $\varepsilon^{\mathrm{light}}_{\mathrm{MC}}$ is compared between `DL1r` and `DL1rFlip` and the relative difference is assigned as the first component of the `DL1rFlip`-to-`DL1r` extrapolation uncertainty. A comparison of these simulation-based calibration factors is shown in Figure 6. The impact of the parton shower modelling on the difference between $\mathrm{SF}^{\mathrm{light}}$ in `DL1r` and `DL1rFlip` is estimated by multiplying the $\mathrm{SFs}^{\mathrm{light}}$ for `DL1r` (`DL1rFlip`), derived using the corrected Powheg Box v2 + Pythia 8.230 simulation, by the simulation-to-simulation SFs defined as the ratio of the `DL1r` (`DL1rFlip`) $\varepsilon^{\mathrm{light}}$ for the Sherpa 2.2.1 and the MadGraph + Pythia 8 simulations. The simulation-to-simulation SFs have been derived using the Z+jets samples listed in Table 1. This gives an estimate of the `DL1rFlip`-to-`DL1r` extrapolation uncertainty for an alternative shower model. The difference between this estimate and the estimate obtained using the corrected Powheg Box v2 + Pythia 8.230 simulation is used as the component assessing the impact of the shower and hadronisation model on the tagging performance difference between `DL1rFlip` and `DL1r`. The two components are added in quadrature to obtain the `DL1rFlip`-to-`DL1r` extrapolation uncertainty. The envelope over p_{T} of the `DL1rFlip`-to-`DL1r` extrapolation uncertainty is used for the final uncertainty

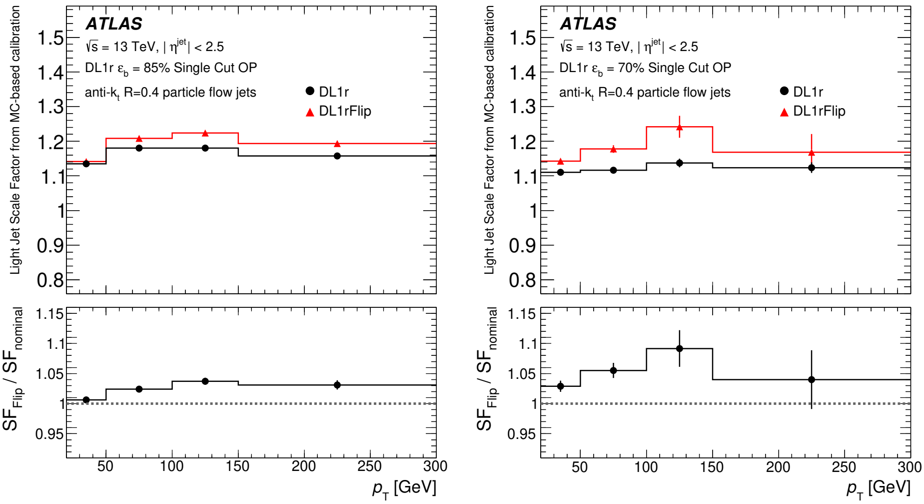

Figure 6: Comparison of the light-flavour jet efficiency scale factor results for the DL1r and DL1rFlip tagger obtained with the MC-based calibration on a Powheg Box v2 + Pythia 8.230 $t\bar{t}$ Monte Carlo simulation, considering the 85% and 70% operating points, as a function of the jet p_T. The error bars correspond to MC statistical uncertainties. The lower panel shows the ratio of DL1rFlip to DL1r tagger MC-based calibration efficiency scale factors. The envelope of this ratio across the considered jet p_T interval is used as an estimate for the impact of the tracking variable mismodelling on the difference between the DL1rFlip and DL1r calibrations, which is a part of the DL1rFlip-to-DL1r extrapolation uncertainty, estimating the impact of applying the calibrations derived for the DL1rFlip algorithm to the DL1r algorithm.

estimate. The shower modelling makes the largest contribution to the DL1rFlip-to-DL1r extrapolation uncertainty and ranges up to 10%. The largest uncertainty contribution in correcting the MC simulation is obtained from the track IP resolution modelling corrections, ranging up to 10% as well. The total DL1rFlip-to-DL1r extrapolation uncertainty is 10%–12% depending on the b-tagging OP and is the dominant systematic uncertainty overall.

Statistical uncertainties of the data and the m_{SV} templates from simulated MC events are taken into account. The statistical uncertainties of the MC-based fit templates are implemented following the light-weight Beeston–Barlow method [54]. As their effect is non-negligible, cross-check studies were performed using a 'toy' approach. The fit template bin entries were fluctuated randomly around the nominal value according to a Gaussian probability distribution with a standard deviation equal to the MC statistical uncertainty in the template bins. SF^{light} was extracted for each of these new fit templates and the standard deviation of the resulting SF^{light} distribution was taken as the statistical uncertainty. The statistical uncertainty estimates via the Beeston–Barlow model and the toy approach were found to be consistent.

8 Results

The calibration SFs^{light} of the DL1r algorithm are presented. The 85%, 77% and 70% OPs were successfully calibrated in data by using the Negative Tag method. However, it is not feasible to calibrate the 60% OP in data because of insufficient statistics and the relatively large contamination by heavy-flavour jets.

Due to these limitations and since the measured SFs for the closest 77%–70% and 70%–60% pseudo-continuous OPs do not show any significant deviation from unity compared to their respective measurement uncertainties, the assumption is made that the same must hold for the 60% OP. The SF for this OP is thus set to 1. Its dominant uncertainty, the DL1rFlip-to-DL1r extrapolation uncertainty, is derived specifically for the 60% OP, and found to be slightly larger than for the 70% OP. The other (sub-leading) uncertainties are assumed to be identical to the 70% OP, since their evaluation suffers from large uncertainties. It should also be noted that extracting very precise SFs^{light} for the 60%–0% pseudo-continuous OP interval is not critical to most physics analyses as only around 0.5 per mille of all light-flavour jets are b-tagged at this OP [49].

The results for the mistagging efficiency calibration of light-flavour jets from the DL1r tagger, using particle-flow jets in Run 2 data, are shown in Figure 7 for the pseudo-continuous OPs of the DL1r algorithm. The calibration of the DL1r single-cut OPs, which is derived from the calibration results of the pseudo-continuous OPs, is shown in Figure 8. Furthermore, Figure 9 shows a breakdown of the uncertainties in the SFs^{light} for each jet p_T interval and single-cut OP.

The measured SFs^{light} are consistent with unity within uncertainties, except for the 85%–77% pseudo-continuous OP and the 85% single-cut OP, where the data prefer SFs^{light} which differ from one by about one standard deviation. Therefore, the results indicate the MC simulation predicts ε^{light} to be similar to that in data.

Mistags of light-flavour jets are mostly caused by the presence of fake tracks and the limited impact parameter resolution [7]. The fake-track rate is underestimated by the MC simulation and the impact parameter resolution is overestimated [7, 53]. An increase in the fake-track rate and a decrease in impact parameter resolution both give rise to larger mistagging efficiencies [7, 55]. Observed SFs slightly larger than unity are therefore expected.

Tables 3–6 feature a detailed breakdown of the uncertainties in the results. Overall, the largest systematic uncertainty is the DL1rFlip-to-DL1r extrapolation uncertainty, with values of 10%–12%, depending on the b-tagging OP. The impact of the charm calibration uncertainty amounts to 5%–10% depending on the jet p_T and the b-tagging OP, and is therefore one of the larger uncertainties. The MC modelling uncertainty is a few percent in most cases, but reaches its maximum of 11% for the 70% single-cut OP in the $20 \leq$ jet $p_T \leq 50$ GeV interval.

The effect of the d_0 and z_0 impact parameter resolution modelling uncertainty is generally of the order of a few percent and therefore mostly subdominant. However, the effect can range up to 14% for low jet p_T and tight OPs. The data statistical uncertainties give subdominant contributions except for high jet p_T and tight OPs, where contributions range from 0.5% to 9.5%. The MC statistical uncertainty is one of the dominant contributions, ranging from 0.4% to 13%, depending on the OP and the jet p_T. The total uncertainty in SF^{light} is between 11% and 32%. In general, higher precision is obtained for the looser OPs and the size of the dominant uncertainties does not depend significantly on the jet p_T.

In the previous calibration with the Negative Tag method using dijet events in 2015–2016 data, the total uncertainty in SF^{light} ranged from 14% to 76% for jets with p_T between 20 and 300 GeV. Dominant

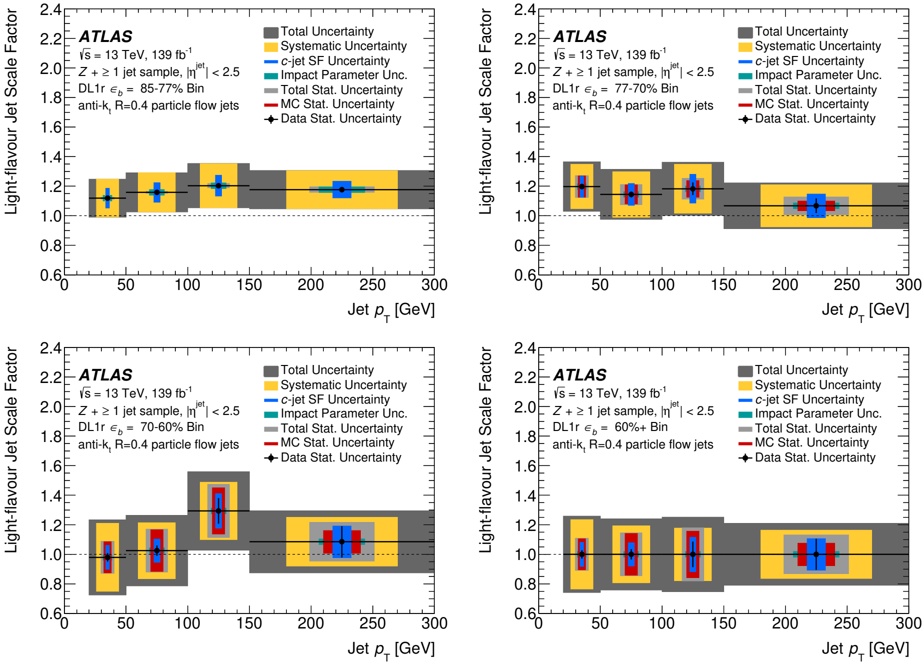

Figure 7: SFs to calibrate the $\varepsilon^{\text{light}}$ of the pseudo-continuous OPs. The SF uncertainty band lengths are arbitrary.

Table 3: Uncertainties for the 85% efficiency OP as a function of the jet p_{T}.

Relative uncertainties [%], 85% SF^{light} single-cut OP				
p_{T} bin [GeV]	$20 < p_{\text{T}} < 50$	$50 < p_{\text{T}} < 100$	$100 < p_{\text{T}} < 150$	$150 < p_{\text{T}} < 300$
c-jet SF	6.1	5.9	6.2	5.3
'Flip' extrapolation	9.7	9.7	9.7	9.7
MC modelling	0.38	2.4	4.4	1
Impact parameter (d_0, z_0)	1	1.3	1	1.2
Total systematic uncertainty	11	12	12	11
Data statistical	0.52	0.56	1.1	1.4
MC statistical	0.88	0.84	0.72	0.4
Total statistical uncertainty	1.1	1	1.4	1.6
Total uncertainty	12	12	12	11

uncertainties arose from the modelling of the track impact parameter resolution and the uncertainty in the fraction of heavy-flavour jets which was estimated using simulation. The reduced uncertainty in the present calibration stems from both improved modelling of the track impact parameters in simulation and the m_{SV} fit, which allows the extraction of SF^{light} while simultaneously correcting ε^{b} and the jet-flavour fractions

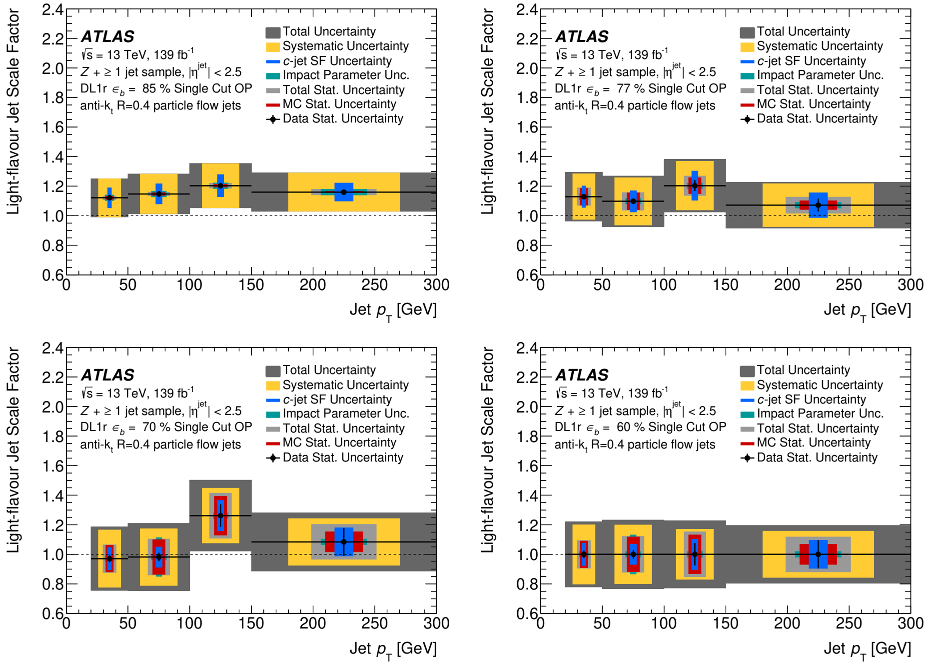

Figure 8: SFs to calibrate the $\varepsilon^{\text{light}}$ of the single-cut OPs. The SF uncertainty band lengths are arbitrary.

Table 4: Uncertainties for the 77% efficiency OP as a function of the jet p_{T}.

	Relative uncertainties [%], 77% SF$^{\text{light}}$ single-cut OP			
p_{T} bin [GeV]	$20 < p_{\text{T}} < 50$	$50 < p_{\text{T}} < 100$	$100 < p_{\text{T}} < 150$	$150 < p_{\text{T}} < 300$
c-jet SF	6.4	6.6	8.2	7.8
'Flip' extrapolation	11	11	11	11
MC modelling	3.1	3.9	1.4	2.2
Impact parameter (d_0, z_0)	4.8	6.5	2.4	2.1
Total systematic uncertainty	14	15	14	14
Data statistical	1.3	1.5	3.1	4.1
MC statistical	5.1	5.2	4.5	2.7
Total statistical uncertainty	5.2	5.4	5.5	5.1
Total uncertainty	15	16	15	14

using data. Previously, ε^b and the heavy-flavour fractions were estimated from simulation, resulting in large modelling uncertainties, which were a limiting factor in the precision of the result.

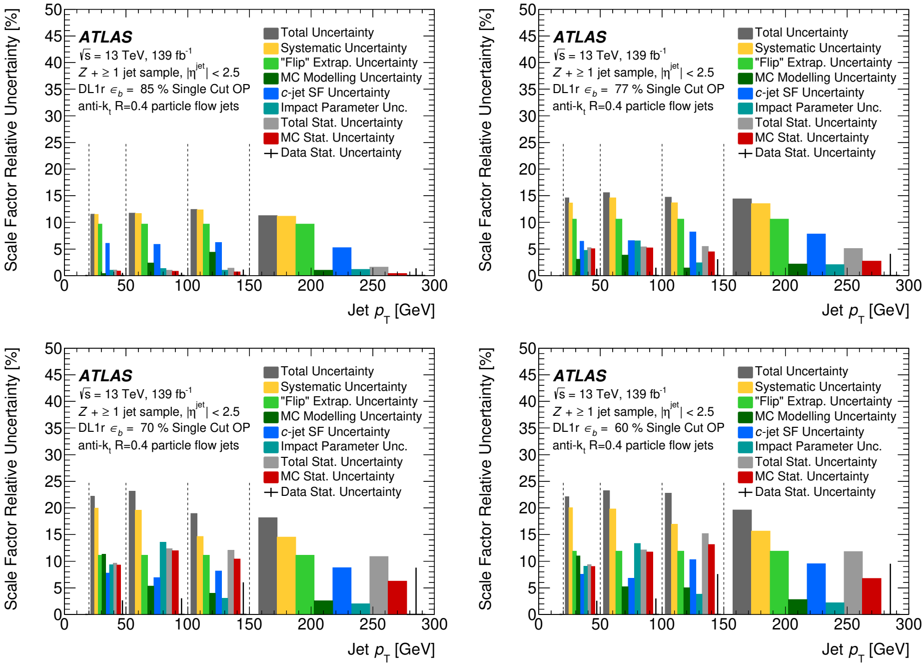

Figure 9: DL1r mistagging efficiency calibration uncertainties. The breakdown of the different uncertainties is shown for the different OPs.

Table 5: Uncertainties for the 70% efficiency OP as a function of the jet p_T.

	Relative uncertainties [%], 70% SF^{light} single-cut OP			
p_T bin [GeV]	$20 < p_T < 50$	$50 < p_T < 100$	$100 < p_T < 150$	$150 < p_T < 300$
c-jet SF	7.8	6.9	8.2	8.8
'Flip' extrapolation	11	11	11	11
MC modelling	11	5.3	4	2.6
Impact parameter (d_0, z_0)	9.3	14	3	2
Total systematic uncertainty	20	20	15	15
Data statistical	2.6	3	6	8.8
MC statistical	9.3	12	10	6.3
Total statistical uncertainty	9.7	12	12	11
Total uncertainty	22	23	19	18

Table 6: Uncertainties for the 60% efficiency OP as a function of the jet p_T.

Relative uncertainties [%], 60% SF^{light} single-cut OP				
p_T bin [GeV]	$20 < p_T < 50$	$50 < p_T < 100$	$100 < p_T < 150$	$150 < p_T < 300$
c-jet SF	7.6	6.8	10	9.5
'Flip' extrapolation	12	12	12	12
MC modelling	11	5.2	5	2.8
Impact parameter (d_0, z_0)	9.1	13	3.8	2.2
Total systematic uncertainty	20	20	17	16
Data statistical	2.6	3	7.6	9.5
MC statistical	9	12	13	6.8
Total statistical uncertainty	9.4	12	15	12
Total uncertainty	22	23	23	20

9 Conclusions

The light-flavour jet mistagging efficiency $\varepsilon^{\text{light}}$ of the DL1r b-tagging algorithm has been measured with a 139 fb^{-1} sample of $\sqrt{s} = 13$ TeV pp collision events recorded during 2015–2018 by the ATLAS detector at the LHC. The measurement is based on an improved method applied to a sample of Z+jets events. The Negative Tag method, based on the application of an alternative b-tagging algorithm, designed to facilitate the measurement of the light-flavour jet mistagging efficiency, is used. Data-to-simulation scale factors for correcting $\varepsilon^{\text{light}}$ in simulation are measured in four different jet transverse momentum intervals, ranging from 20 to 300 GeV, for four separate quantiles of the b-tagging discriminant. The scale factors typically exceed unity by around 10%–20%, with total uncertainties ranging from 11% to 23%, and do not exhibit any strong dependence on jet transverse momentum. These calibration uncertainties are considerably lower than the previous 14% to 76% uncertainties from the Negative Tag method using 2015–2016 data.

References

[1] ATLAS Collaboration, *The ATLAS Experiment at the CERN Large Hadron Collider*, JINST **3** (2008) S08003.

[2] ATLAS Collaboration, *ATLAS b-jet identification performance and efficiency measurement with $t\bar{t}$ events in pp collisions at $\sqrt{s}$ = 13 TeV*, Eur. Phys. J. C **79** (2019) 970, arXiv: 1907.05120 [hep-ex].

[3] ATLAS Collaboration, *Measurement of the c-jet mistagging efficiency in $t\bar{t}$ events using pp collision data at $\sqrt{s}$ = 13 TeV collected with the ATLAS detector*, Eur. Phys. J. C **82** (2021) 95, arXiv: 2109.10627 [hep-ex].

[4] ATLAS Collaboration, *Jet reconstruction and performance using particle flow with the ATLAS Detector*, Eur. Phys. J. C **77** (2017) 466, arXiv: 1703.10485 [hep-ex].

[5] ATLAS Collaboration, *Calibration of the performance of b-tagging for c and light-flavour jets in the 2012 ATLAS data*, ATLAS-CONF-2014-046, 2014, URL: https://cds.cern.ch/record/1741020.

[6] The D0 Collaboration, *Measurement of the t anti-t production cross section in p anti-p collisions at s**(1/2) = 1.96-TeV using secondary vertex b tagging*, Phys. Rev. D **74** (2006) 112004, arXiv: hep-ex/0611002.

[7] ATLAS Collaboration, *Calibration of light-flavour b-jet mistagging rates using ATLAS proton–proton collision data at $\sqrt{s}$ = 13 TeV*, ATLAS-CONF-2018-006, 2018, URL: https://cds.cern.ch/record/2314418.

[8] ATLAS Collaboration, *ATLAS Insertable B-Layer: Technical Design Report*, ATLAS-TDR-19; CERN-LHCC-2010-013, 2010, URL: https://cds.cern.ch/record/1291633, Addendum: ATLAS-TDR-19-ADD-1; CERN-LHCC-2012-009, 2012, URL: https://cds.cern.ch/record/1451888.

[9] B. Abbott et al., *Production and integration of the ATLAS Insertable B-Layer*, JINST **13** (2018) T05008, arXiv: 1803.00844 [physics.ins-det].

[10] ATLAS Collaboration, *Performance of the ATLAS Trigger System in 2015*, Eur. Phys. J. C **77** (2017) 317, arXiv: 1611.09661 [hep-ex].

[11] ATLAS Collaboration, *The ATLAS Collaboration Software and Firmware*, ATL-SOFT-PUB-2021-001, 2021, URL: https://cds.cern.ch/record/2767187.

[12] ATLAS Collaboration, *Luminosity determination in pp collisions at $\sqrt{s}$ = 13 TeV using the ATLAS detector at the LHC*, (2022), arXiv: 2212.09379 [hep-ex].

[13] G. Avoni et al., *The new LUCID-2 detector for luminosity measurement and monitoring in ATLAS*, JINST **13** (2018) P07017.

[14] ATLAS Collaboration, *Performance of electron and photon triggers in ATLAS during LHC Run 2*, Eur. Phys. J. C **80** (2020) 47, arXiv: 1909.00761 [hep-ex].

[15] ATLAS Collaboration, *Performance of the ATLAS muon triggers in Run 2*, JINST **15** (2020) P09015, arXiv: 2004.13447 [hep-ex].

[16] ATLAS Collaboration, *ATLAS data quality operations and performance for 2015–2018 data-taking*, JINST **15** (2020) P04003, arXiv: 1911.04632 [physics.ins-det].

[17] ATLAS Collaboration, *The ATLAS Simulation Infrastructure*, Eur. Phys. J. C **70** (2010) 823, arXiv: 1005.4568 [physics.ins-det].

[18] GEANT4 Collaboration, S. Agostinelli et al., *Geant4 – a simulation toolkit*, Nucl. Instrum. Meth. A **506** (2003) 250.

[19] T. Sjöstrand, S. Mrenna and P. Skands, *A brief introduction to PYTHIA 8.1*, Comput. Phys. Commun. **178** (2008) 852, arXiv: 0710.3820 [hep-ph].

[20] R. D. Ball et al., *Parton distributions with LHC data*, Nucl. Phys. B **867** (2013) 244, arXiv: 1207.1303 [hep-ph].

[21] ATLAS Collaboration, *The Pythia 8 A3 tune description of ATLAS minimum bias and inelastic measurements incorporating the Donnachie–Landshoff diffractive model*, ATL-PHYS-PUB-2016-017, 2016, URL: https://cds.cern.ch/record/2206965.

[22] T. Gleisberg et al., *Event generation with SHERPA 1.1*, JHEP **02** (2009) 007, arXiv: 0811.4622 [hep-ph].

[23] R. D. Ball et al., *Parton distributions for the LHC run II*, JHEP **04** (2015) 040, arXiv: 1410.8849 [hep-ph].

[24] S. Catani, F. Krauss, B. R. Webber and R. Kuhn, *QCD Matrix Elements + Parton Showers*, JHEP **11** (2001) 063, arXiv: hep-ph/0109231.

[25] S. Höche, F. Krauss, M. Schönherr and F. Siegert, *QCD matrix elements + parton showers. The NLO case*, JHEP **04** (2013) 027, arXiv: 1207.5030 [hep-ph].

[26] S. Höche, F. Krauss, S. Schumann and F. Siegert, *QCD matrix elements and truncated showers*, JHEP **05** (2009) 053, arXiv: 0903.1219 [hep-ph].

[27] S. Höche, F. Krauss, M. Schönherr and F. Siegert, *A critical appraisal of NLO+PS matching methods*, JHEP **09** (2012) 049, arXiv: 1111.1220 [hep-ph].

[28] J. Alwall et al., *The automated computation of tree-level and next-to-leading order differential cross sections, and their matching to parton shower simulations*, JHEP **07** (2014) 079, arXiv: 1405.0301 [hep-ph].

[29] C. Anastasiou, L. Dixon, K. Melnikov and F. Petriello, *High-precision QCD at hadron colliders: Electroweak gauge boson rapidity distributions at next-to-next-to leading order*, Phys. Rev. D **69** (2004) 094008, arXiv: hep-ph/0312266.

[30] S. Frixione, P. Nason and C. Oleari, *Matching NLO QCD computations with parton shower simulations: the POWHEG method*, JHEP **11** (2007) 070, arXiv: 0709.2092 [hep-ph].

[31] ATLAS Collaboration, *ATLAS Pythia 8 tunes to 7 TeV data*, ATL-PHYS-PUB-2014-021, 2014, URL: https://cds.cern.ch/record/1966419.

[32] D. J. Lange, *The EvtGen particle decay simulation package*, Nucl. Instrum. Meth. A **462** (2001) 152.

[33] ATLAS Collaboration, *Performance of the ATLAS track reconstruction algorithms in dense environments in LHC Run 2*, Eur. Phys. J. C **77** (2017) 673, arXiv: 1704.07983 [hep-ex].

[34] ATLAS Collaboration, *Vertex Reconstruction Performance of the ATLAS Detector at* $\sqrt{s} = 13$ *TeV*, ATL-PHYS-PUB-2015-026, 2015, URL: https://cds.cern.ch/record/2037717.

[35] ATLAS Collaboration, *Secondary vertex finding for jet flavour identification with the ATLAS detector*, ATL-PHYS-PUB-2017-011, 2017, URL: https://cds.cern.ch/record/2270366.

[36] ATLAS Collaboration, *Electron and photon performance measurements with the ATLAS detector using the 2015–2017 LHC proton–proton collision data*, JINST **14** (2019) P12006, arXiv: 1908.00005 [hep-ex].

[37] ATLAS Collaboration, *Muon reconstruction performance of the ATLAS detector in proton–proton collision data at* $\sqrt{s} = 13$ *TeV*, Eur. Phys. J. C **76** (2016) 292, arXiv: 1603.05598 [hep-ex].

[38] ATLAS Collaboration, *Muon reconstruction and identification efficiency in ATLAS using the full Run 2* pp *collision data set at* $\sqrt{s} = 13$ *TeV*, Eur. Phys. J. C **81** (2021) 578, arXiv: 2012.00578 [hep-ex].

[39] M. Cacciari, G. P. Salam and G. Soyez, *The anti-*k_t *jet clustering algorithm*, JHEP **04** (2008) 063, arXiv: 0802.1189 [hep-ph].

[40] M. Cacciari, G. P. Salam and G. Soyez, *FastJet user manual*, Eur. Phys. J. C **72** (2012) 1896, arXiv: 1111.6097 [hep-ph].

[41] ATLAS Collaboration, *Jet energy scale and resolution measured in proton–proton collisions at* $\sqrt{s} = 13$ *TeV with the ATLAS detector*, Eur. Phys. J. C **81** (2020) 689, arXiv: 2007.02645 [hep-ex].

[42] ATLAS Collaboration, *Performance of pile-up mitigation techniques for jets in* pp *collisions at* $\sqrt{s} = 8$ *TeV using the ATLAS detector*, Eur. Phys. J. C **76** (2016) 581, arXiv: 1510.03823 [hep-ex].

[43] ATLAS Collaboration, *Measurements of b-jet tagging efficiency with the ATLAS detector using* $t\bar{t}$ *events at* $\sqrt{s} = 13$ *TeV*, JHEP **08** (2018) 089, arXiv: 1805.01845 [hep-ex].

[44] ATLAS Collaboration, *Measurements of the production cross-section for a Z boson in association with b-jets in proton–proton collisions at* $\sqrt{s} = 13$ *TeV with the ATLAS detector*, JHEP **07** (2020) 044, arXiv: 2003.11960 [hep-ex].

[45] The CMS Collaboration, *Measurement of differential cross sections for Z bosons produced in association with charm jets in pp collisions at* $\sqrt{s} = 13$ *TeV*, JHEP **04** (2021) 109, arXiv: 2012.04119 [hep-ex].

[46] ATLAS Collaboration, *Optimisation of the ATLAS b-tagging performance for the 2016 LHC Run*, ATL-PHYS-PUB-2016-012, 2016, URL: https://cds.cern.ch/record/2160731.

[47] ATLAS Collaboration, *Identification of Jets Containing b-Hadrons with Recurrent Neural Networks at the ATLAS Experiment*, ATL-PHYS-PUB-2017-003, 2017, URL: https://cds.cern.ch/record/2255226.

[48] ATLAS Collaboration, *Topological b-hadron decay reconstruction and identification of b-jets with the JetFitter package in the ATLAS experiment at the LHC*, ATL-PHYS-PUB-2018-025, 2018, URL: https://cds.cern.ch/record/2645405.

[49] ATLAS Collaboration, *Expected performance of the 2019 ATLAS b-taggers*, 2019, URL: http://atlas.web.cern.ch/Atlas/GROUPS/PHYSICS/PLOTS/FTAG-2019-005/.

[50] ATLAS Collaboration, *Optimisation and performance studies of the ATLAS b-tagging algorithms for the 2017-18 LHC run*, ATL-PHYS-PUB-2017-013, 2017, URL: https://cds.cern.ch/record/2273281.

[51] ATLAS Collaboration, *Monte Carlo to Monte Carlo scale factors for flavour tagging efficiency calibration*, ATL-PHYS-PUB-2020-009, 2020, URL: https://cds.cern.ch/record/2718610.

[52] ATLAS Collaboration, *Performance of b-jet identification in the ATLAS experiment*, JINST **11** (2016) P04008, arXiv: 1512.01094 [hep-ex].

[53] ATLAS Collaboration, *Early Inner Detector Tracking Performance in the 2015 Data at $\sqrt{s}$ = 13 TeV*, ATL-PHYS-PUB-2015-051, 2015, URL: https://cds.cern.ch/record/2110140.

[54] K. Cranmer, G. Lewis, L. Moneta, A. Shibata and W. Verkerke, *HistFactory: A tool for creating statistical models for use with RooFit and RooStats*, CERN-OPEN-2012-016, 2012, URL: https://cds.cern.ch/record/1456844.

[55] The ATLAS Collaboration, *Expected Performance of the ATLAS Experiment - Detector, Trigger and Physics*, (2009), arXiv: 0901.0512 [hep-ex].

Paper II

Published for SISSA by Springer

Received: *December 8, 2020*
Accepted: *March 12, 2021*
Published: *April 19, 2021*

Search for new phenomena with top quark pairs in final states with one lepton, jets, and missing transverse momentum in pp collisions at $\sqrt{s} = 13$ TeV with the ATLAS detector

JHEP04(2021)174

ATLAS EXPERIMENT

The ATLAS collaboration

E-mail: atlas.publications@cern.ch

Abstract: A search for new phenomena with top quark pairs in final states with one isolated electron or muon, multiple jets, and large missing transverse momentum is performed. Signal regions are designed to search for two-, three-, and four-body decays of the directly pair-produced supersymmetric partner of the top quark (stop). Additional signal regions are designed specifically to search for spin-0 mediators that are produced in association with a pair of top quarks and decay into a pair of dark-matter particles. The search is performed using the Large Hadron Collider proton-proton collision dataset at a centre-of-mass energy of $\sqrt{s} = 13$ TeV recorded by the ATLAS detector from 2015 to 2018, corresponding to an integrated luminosity of 139 fb^{-1}. No significant excess above the Standard Model background is observed, and limits at 95% confidence level are set in the stop-neutralino mass plane and as a function of the mediator mass or the dark-matter particle mass. Stops are excluded up to 1200 GeV (710 GeV) in the two-body (three-body) decay scenario. In the four-body scenario stops up to 640 GeV are excluded for a stop-neutralino mass difference of 60 GeV. Scalar and pseudoscalar dark-matter mediators are excluded up to 200 GeV when the coupling strengths of the mediator to Standard Model and dark-matter particles are both equal to one and when the mass of the dark-matter particle is 1 GeV.

Keywords: Hadron-Hadron scattering (experiments), Supersymmetry

ArXiv ePrint: 2012.03799

https://doi.org/10.1007/JHEP04(2021)174

Contents

1 Introduction

This paper presents a search for new phenomena in events with top quark pairs, in a final state with exactly one isolated charged lepton (electron or muon,[1] henceforth referred to as 'lepton') from the decay of an on- or off-shell W boson, jets, and a significant amount of missing transverse momentum ($\vec{p}_{\mathrm{T}}^{\mathrm{miss}}$), the magnitude of which is denoted by $E_{\mathrm{T}}^{\mathrm{miss}}$. This experimental signature may arise in Supersymmetry (SUSY) [1–7] or in models with a spin-0 mediator produced in association with top quarks [8, 9] and subsequently decaying into a pair of dark matter (DM) particles.

SUSY extends the Standard Model (SM) by introducing a supersymmetric partner for each SM particle, the two having identical quantum numbers except for a half-unit difference in spin. Searches for a light supersymmetric partner of the top quark, referred to as the top squark or 'stop', are of particular interest after the discovery of the Higgs boson [10, 11] at the Large Hadron Collider (LHC). Stops may largely cancel out divergent loop corrections to the Higgs boson mass [12–19], and thus, supersymmetry may provide an elegant solution to the hierarchy problem [20–23]. The superpartners of the left- and right-handed top quarks, $\tilde{t}_{\mathrm{L}}$ and $\tilde{t}_{\mathrm{R}}$, mix to form two mass eigenstates, $\tilde{t}_1$ and $\tilde{t}_2$, where $\tilde{t}_1$ is the lighter of the two. Significant mass splitting between the $\tilde{t}_1$ and $\tilde{t}_2$ particles is possible due to the large top quark Yukawa coupling. A generic R-parity-conserving[2] minimal supersymmetric extension of the SM (MSSM) [7, 12, 24–26] predicts pair production of SUSY particles and the existence of a stable lightest supersymmetric particle (LSP). The mass eigenstates from the linear superposition of charged or neutral SUSY partners of the Higgs and electroweak gauge bosons (higgsinos, winos and binos) are called charginos $\tilde{\chi}^{\pm}_{1,2}$ and neutralinos $\tilde{\chi}^0_{1,2,3,4}$. The lightest neutralino ($\tilde{\chi}^0_1$), assumed to be the LSP, may provide a potential dark matter (DM) candidate because it is stable and only interacts weakly with ordinary matter [27, 28]. This paper presents a search for direct pair production of $\tilde{t}_1$ particles, with significant amount of $E_{\mathrm{T}}^{\mathrm{miss}}$, from the two weakly interacting LSPs that escape detection. Scenarios with on- and off-shell production of W bosons and top quarks in the stop decays are considered, leading to two-, three- and four-body decays of the stop.

The search for a spin-0 mediator produced in association with top quarks and subsequently decaying into a pair of DM particles is motivated by SM extensions which respect the principle of minimal flavour violation resulting in the interaction strength between the spin-0 mediator and the SM quarks being proportional to the fermion masses via Yukawa-type couplings.

Dedicated searches for direct $\tilde{t}_1$ pair production were recently reported by the ATLAS [29–32] and CMS [33–40] Collaborations. Previous ATLAS and CMS searches extend the lower limit on $\tilde{t}_1$ masses at 95% confidence level to 1.2 TeV in the two-body decay scenario and up to ∼450 GeV in the three-body decay scenario. Searches for spin-0 mediators produced in association with heavy-flavour quarks and decaying into a pair of DM particles have also been reported by the ATLAS [29, 41] and CMS [42] Collaborations.

[1] Electrons and muons from τ-lepton decays are included.

[2] A multiplicative quantum number, referred to as R-parity, is introduced in SUSY models to conserve baryon and lepton number where R-parity is 1 (−1) for all SM (SUSY) particles.

JHEP04(2021)174

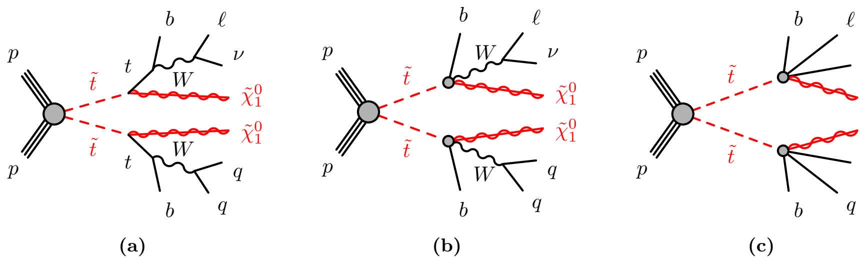

Figure 1. Diagrams illustrating the stop decay modes, which are referred to as (a) $\tilde{t}_1 \to t + \tilde{\chi}_1^0$, (b) $\tilde{t}_1 \to bW\tilde{\chi}_1^0$ and (c) $\tilde{t}_1 \to bff'\tilde{\chi}_1^0$. In these diagrams, the charge-conjugate symbols are omitted for simplicity. All the processes considered involve the production of a squark-antisquark pair.

2 Signal models and search strategy

Two classes of physics models are targeted by this search, the production of $\tilde{t}_1$ pairs in simplified SUSY models [43–45] where the only light sparticles are $\tilde{t}_1$ and $\tilde{\chi}_1^0$, and simplified benchmark models for DM production that assume the existence of a spin-0 mediator particle that can be produced in association with two top quarks [41, 46] and decays into a pair of DM particles $\chi\bar{\chi}$.

The experimental signatures of stop pair production can vary dramatically, depending on the mass-splitting between $\tilde{t}_1$ and $\tilde{\chi}_1^0$. Figure 1 illustrates the two-, three- and four-body stop decays considered in this paper. As flavour-changing neutral current processes are not considered, the dominant among the two-, three- or four-body stop decays is assumed to have a 100% branching ratio in a given $\Delta m_{\tilde{t}_1,\tilde{\chi}_1^0}$ regime. In the regime where $\Delta m_{\tilde{t}_1,\tilde{\chi}_1^0} = m(\tilde{t}_1) - m(\tilde{\chi}_1^0)$ is larger than the top quark mass m_{top}, the two-body decay $\tilde{t}_1 \to t + \tilde{\chi}_1^0$ dominates. At smaller $\Delta m_{\tilde{t}_1,\tilde{\chi}_1^0}$, the three-body decay $\tilde{t}_1 \to bW\tilde{\chi}_1^0$ dominates as long as $\Delta m_{\tilde{t}_1,\tilde{\chi}_1^0}$ is larger than the sum of the b-quark and W boson masses. At the smallest values of $\Delta m_{\tilde{t}_1,\tilde{\chi}_1^0}$ the dominant decay channel is the four-body decay $\tilde{t}_1 \to bff'\tilde{\chi}_1^0$. The stop is always assumed to decay promptly.

The searches for stops presented in this paper use several signal regions dedicated to each of the decay channels $\tilde{t}_1 \to t + \tilde{\chi}_1^0$, $\tilde{t}_1 \to bW\tilde{\chi}_1^0$ and $\tilde{t}_1 \to bff'\tilde{\chi}_1^0$. For instance, specific signal regions target the so-called compressed region where the stop undergoes a $\tilde{t}_1 \to t + \tilde{\chi}_1^0$ decay but where $\Delta m_{\tilde{t}_1,\tilde{\chi}_1^0} \approx m_{\text{top}}$. The selections are optimised for given benchmark model points, and are binned in key variables to retain sensitivity to the widest possible range of $\tilde{t}_1$ and $\tilde{\chi}_1^0$ masses.

The mediator-based DM scenarios consist of simplified models with a DM particle χ that is a SM singlet and a single spin-0 mediator that couples χ to SM fermions. Both the scenarios where the mediator is a scalar, ϕ, or a pseudoscalar, a, are considered, as illustrated in figure 2. These models have four parameters: the mass of the mediator, m_{med}, the DM mass, m_{DM}, the DM-mediator coupling, g_χ, and the coupling of the mediator to the SM fermions, g_{q}. In the models considered, the interaction strength between the mediator and

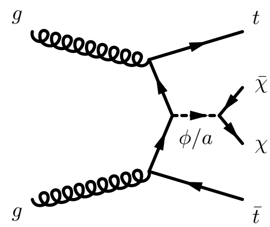

Figure 2. A representative Feynman diagram for spin-0 mediator production. The ϕ/a is the scalar/pseudoscalar mediator, which decays into a pair of dark matter (χ) particles.

SM particles is proportional to the fermion masses via Yukawa-type couplings, and therefore final states involving top quarks dominate over those involving other fermions. Due to the associated production of top quarks with undetected DM particles in the same event, the mediator-based DM model predicts an excess of $t\bar{t}$ $+E_{\mathrm{T}}^{\mathrm{miss}}$ final-state events above the SM expectation. A dedicated signal region common to both the scalar and pseudoscalar models is developed. The signal region is binned in the azimuthal angle $\Delta\phi(\vec{p}_{\mathrm{T}}^{\,\mathrm{miss}}, \ell)$ between the missing transverse momentum and the leading lepton, to retain maximum sensitivity to both the scalar and pseudoscalar models and to a large range of mediator and DM particle masses.

The searches presented are based on eight dedicated analyses that target the various scenarios mentioned above. Each of these analyses corresponds to a set of event selection criteria, referred to as a signal region (SR), and is optimised to achieve three standard deviation expected sensitivity to the targeted benchmark model. Two techniques are employed to define the SRs: 'cut-and-count' and 'shape-fit' methods. The former is based on counting events in a single region of phase space, and is employed in the eight analyses. The latter is used in several SRs to improve the exclusion reach if no excess is observed in the cut-and-count signal regions, and employs SRs split into multiple bins in one or two key discriminating kinematic variables. The shape-fit method exploits the varying signal-to-background ratios in different bins to provide sensitivity to a wider range of new-particle masses than can be achieved by a single cut-and-count SR. Including these background-rich regions in the single-bin discovery SRs would significantly reduce the sensitivity to the targeted signatures.

The main background processes after the signal selections include $t\bar{t}$, $t\bar{t} + Z(\rightarrow \nu\bar{\nu})$, W+jets and the associated production of a single top quark and a W boson (Wt). Backgrounds from these SM processes are estimated by exploiting dedicated control regions (CRs) enriched in these processes. The backgrounds are normalised to data by applying a likelihood fit simultaneously to the SR and associated CRs, making the analysis more robust against potential mis-modelling in simulated events and reducing the uncertainties in the background normalisation. Before looking at the data in the signal regions, the background modelling and the normalisation procedure are tested in a series of validation regions (VRs) by applying the normalisation factors determined by a background-only fit in the CRs. A background-only fit to the CRs and SRs then provides a statistical test that

Signal scenario	Benchmark	Signal Region	Exclusion technique	Section
$\tilde{t}_1 \to t + \tilde{\chi}^0_1$	$m(\tilde{t}_1,\ \tilde{\chi}^0_1) = (800, 400)$ GeV	`tN_med`	shape-fit of $E_{\mathrm{T}}^{\mathrm{miss}}$ and m_{T}	7.1
$\tilde{t}_1 \to t + \tilde{\chi}^0_1$	$m(\tilde{t}_1,\ \tilde{\chi}^0_1) = (950, 1)$ GeV	`tN_high`	–	7.1
$\tilde{t}_1 \to t + \tilde{\chi}^0_1$	$m(\tilde{t}_1,\ \tilde{\chi}^0_1) = (225, 52)$ GeV	`tN_diag_low`	cut-and-count	7.2
$\tilde{t}_1 \to t + \tilde{\chi}^0_1$	$m(\tilde{t}_1,\ \tilde{\chi}^0_1) = (500, 327)$ GeV	`tN_diag_high`	cut-and-count	7.2
$\tilde{t}_1 \to bW\tilde{\chi}^0_1$	$m(\tilde{t}_1,\ \tilde{\chi}^0_1) = (500, 380)$ GeV	`bWN`	shape-fit in RNN score	7.3
$\tilde{t}_1 \to bff'\tilde{\chi}^0_1$	$m(\tilde{t}_1,\ \tilde{\chi}^0_1) = (450, 400)$ GeV	`bffN_btag`	shape-fit in $p_{\mathrm{T}}^{\ell}/E_{\mathrm{T}}^{\mathrm{miss}}$ and $\Delta\phi(\vec{p}_{\mathrm{T}}^{\,b\text{-jet}}, \vec{p}_{\mathrm{T}}^{\,\mathrm{miss}})$	7.4
$\tilde{t}_1 \to bff'\tilde{\chi}^0_1$	$m(\tilde{t}_1,\ \tilde{\chi}^0_1) = (450, 430)$ GeV	`bffN_softb`	shape-fit in $p_{\mathrm{T}}^{\ell}/E_{\mathrm{T}}^{\mathrm{miss}}$	7.4
Spin-0 mediator	$m(\phi/a,\ \chi) = (20, 1)$ GeV	`DM`	shape-fit in $\Delta\phi(\vec{p}_{\mathrm{T}}^{\,\mathrm{miss}}, \ell)$	7.5

Table 1. Signal scenarios, benchmark models and signal regions. For each SR, the table lists the analysis technique used for exclusion limits. The last column points to the section where the signal region is defined. For `tN_high` no exclusion technique is defined. The `tN_med` shape-fit also covers the `tN_high`-like phase space.

quantifies the existence and extent of a potential excess of events in data in the SRs. In the absence of an excess, exclusion limits are set on the associated model parameters by using the theoretical cross-sections. An overview of the signal regions and the benchmark models for optimisation is presented in table 1.

3 ATLAS detector and data collection

The ATLAS detector [47] at the LHC is a multipurpose particle detector with almost 4π coverage in solid angle around the interaction point.[3] It consists of an inner tracking detector (ID) surrounded by a superconducting solenoid providing a 2 T axial magnetic field, electromagnetic and hadronic calorimeters, and a muon spectrometer (MS), which is based on three large air-core toroidal superconducting magnets consisting of eight coils each. The ID provides charged-particle tracking in the range $|\eta| < 2.5$. During the LHC shutdown between Run 1 (2010–2012) and Run 2 (2015–2018), a new innermost layer of silicon pixels was added [48–50], which improves the track impact parameter resolution, vertex position resolution and b-tagging performance [51]. High-granularity electromagnetic and hadronic calorimeters provide energy measurements up to $|\eta| = 4.9$. The electromagnetic calorimeters, as well as the hadronic calorimeters in the endcap and forward regions, are sampling calorimeters with liquid argon as the active medium and lead, copper, or tungsten absorbers. The hadronic calorimeter in the central region of the detector is a sampling calorimeter with scintillator tiles as the active medium and steel absorbers. The MS surrounds the calorimeters and has three layers of precision tracking chambers with coverage up to $|\eta| = 2.7$ and fast detectors for triggering in the region $|\eta| < 2.4$. A two-level trigger

[3] ATLAS uses a right-handed coordinate system with its origin at the nominal interaction point (IP) in the centre of the detector and the z-axis along the beam pipe. The x-axis points from the IP to the centre of the LHC ring, and the y-axis points upwards. Cylindrical coordinates (r, ϕ) are used in the transverse plane, ϕ being the azimuthal angle around the z-axis. The pseudorapidity is defined in terms of the polar angle θ as $\eta = -\ln\tan(\theta/2)$. The transverse momentum, p_{T}, is defined in the x–y plane.

JHEP04(2021)174

Process	ME event generator	ME PDF	PS and hadronisation	UE tune	Cross-section calculation
$t\bar{t}$	Powheg-Box v2 [55]	NNPDF3.0 [56]	Pythia 8 [57]	A14 [58]	NNLO+NNLL [59–64]
Single-top					
t-channel	Powheg-Box v1	NNPDF3.0	Pythia 8	A14	NNLO+NNLL [65]
s- and Wt-channel	Powheg-Box v2	NNPDF3.0	Pythia 8	A14	NNLO+NNLL [66, 67]
V+jets ($V = W/Z$)	Sherpa 2.2.1 [68]	NNPDF3.0	Sherpa	Default	NNLO [69]
Diboson	Sherpa 2.2.1–2.2.2	NNPDF3.0	Sherpa	Default	NLO
Multiboson	Sherpa 2.2.1–2.2.2	NNPDF3.0	Sherpa	Default	NLO
$t\bar{t} + V$	MG5_aMC@NLO 2.3.3 [70]	NNPDF3.0	Pythia 8	A14	NLO [70]
SUSY signal	MadGraph 2.6.2 [70]	NNPDF2.3 [71]	Pythia 8	A14	NNLO+NNLL [72, 73]
DM signal	MadGraph 2.6.2	NNPDF3.0	Pythia 8	A14	NLO [74, 75]

Table 2. Overview of the nominal simulated samples. The cross-sections of top, single-top and SUSY samples were calculated at next-to-next-to-leading order (NNLO) with the resummation of soft gluon emission at next-to-next-to-leading-logarithm (NNLL) accuracy. The V+jets background samples were calculated at NNLO. The cross-sections of other background and DM samples were calculated at next-to-leading order (NLO).

system [52] is used to select events. The first-level trigger is hardware-based, followed by a software-based trigger system.

The results in this paper utilise the full Run 2 data sample collected from 2015 to 2018 at a centre-of-mass energy of $\sqrt{s} = 13\,\text{TeV}$. The average number of simultaneous pp interactions per bunch crossing, referred to as 'pile-up', in the recorded data is approximately 34. After the application of beam, detector and data-quality requirements, the total integrated luminosity is $139\,\text{fb}^{-1}$. The uncertainty in the combined 2015–2018 integrated luminosity is 1.7%. It is derived from the calibration of the luminosity scale using x–y beam-separation scans, following a methodology similar to that detailed in ref. [53], and using the LUCID-2 detector for the baseline luminosity measurements [54].

All events were recorded with triggers that accepted events with $E_{\text{T}}^{\text{miss}}$ above a given threshold. The $E_{\text{T}}^{\text{miss}}$ triggers relied on energy measurements in the calorimeter and on several algorithms based on cells, jets or topological clusters in addition to two methods for correcting for the effects of pile-up. The triggers were fully efficient for events passing an offline-reconstruction requirement of $E_{\text{T}}^{\text{miss}} > 230\,\text{GeV}$.

4 Simulated event samples

Samples of Monte Carlo (MC) simulated events are used for the description of the SM background processes and to model the signals. Details of the simulation samples used, including the matrix element (ME) event generator and parton distribution function (PDF) set, the parton shower (PS) and hadronisation model, the set of tuned parameters (tune) for the underlying event (UE) and the order of the cross-section calculation, are summarised in table 2.

JHEP04(2021)174

The samples produced with MadGraph5_aMC@NLO [70] and Powheg-Box [55, 76–79] used EvtGen v1.6.0 [80] for the modelling of b-hadron decays. The signal samples were all processed with a fast simulation [81], whereas all background samples were processed with the full simulation of the ATLAS detector [81] based on Geant4 [82]. All samples were produced with varying numbers of minimum-bias interactions generated by Pythia 8 with the A3 tune [83] and overlaid on the hard-scattering event to simulate the effect of multiple pp interactions in the same or nearby bunch crossings. The number of interactions per bunch crossing was reweighted to match the distribution in data.

The nominal $t\bar{t}$ sample and single-top sample cross-sections were calculated at NNLO with the resummation of soft gluon emission at NNLL accuracy and were generated with Powheg-Box (at NLO accuracy) interfaced to Pythia 8 for parton showering and hadronisation. Additional $t\bar{t}$ samples were generated with MadGraph5_aMC@NLO (at NLO accuracy)+Pythia 8 and Powheg-Box+Herwig 7 [84, 85] for modelling comparisons and the evaluation of systematic uncertainties [86]. The $t\bar{t}$ and Wt processes have identical $WWbb$ final states and can interfere. Additional $t\bar{t}$, Wt and $WWbb$ samples were generated as multi-leg processes at LO with MadGraph and used to estimate the systematic uncertainty from the interference modelling. The `tN_med` and `tN_high` regions receive significant contributions from both $t\bar{t}$ and Wt in a phase space where the interference is significant. Techniques used to model the interference such as diagram subtraction (DS) and diagram removal (DR) [87] were shown to provide predictions bracketing the data [88], but can lead to large uncertainties. Both schemes are investigated in this paper, but the DR scheme is ultimately used for the nominal Wt sample.

The W+jets and Z+jets samples were generated with Sherpa 2.2.1 [68, 89] with up to two partons at NLO and up to four partons at leading order (LO). Diboson and multiboson [90] events were generated with Sherpa 2.2.1 and 2.2.2. For dibosons, the events include up to one parton at NLO and up to three partons at LO. For triboson processes, up to two extra partons were considered at LO. The Sherpa samples used matrix elements from Comix [91] and OpenLoops [92], which were merged with the Sherpa parton shower [93] using the ME+PS@NLO prescription [94]. The W+jets and Z+jets events were further normalised to the NNLO cross-sections [69].

The $t\bar{t}+V$ samples were generated with MadGraph5_aMC@NLO (at NLO accuracy) interfaced to Pythia 8 for parton showering and hadronisation. The corresponding MC tune and generator comparisons can be found in ref. [95].

The SUSY samples were generated at LO with MadGraph 2.6.2 including up to two extra partons, and interfaced to Pythia 8 for parton showering and hadronisation. For the $\tilde{t}_1 \to t + \tilde{\chi}_1^0$ samples, the stop was decayed in Pythia 8 using only phase-space considerations and not the full ME. Since the decay products in the generated event samples did not preserve spin information, a polarisation reweighting was applied following refs. [96, 97]. A value of $\cos\theta_t = 0.553$ was assumed, corresponding to a $\tilde{t}_1$ composed mainly of $\tilde{t}_{\mathrm{R}}$ (∼70%). For the $\tilde{t}_1 \to bW\tilde{\chi}_1^0$ and $\tilde{t}_1 \to bff'\tilde{\chi}_1^0$ samples the stops were decayed with MadSpin [98], interfaced to Pythia 8 for the parton showering. MadSpin emulates kinematic distributions such as the mass of the $bW^{(*)}$ system to a good approximation without calculating the full ME.

The signal cross-sections for stop pair production were calculated to approximate next-to-next-to-leading order in the strong coupling constant, adding the resummation of soft gluon emission at next-to-next-to-leading-logarithm accuracy (approximate NNLO+NNLL) [73, 99–101]. The nominal cross-section and its uncertainty were derived using the PDF4LHC15_mc PDF set, following the recommendations of ref. [102]. The stop pair production cross-section varies from approximately 200 fb at $m_{\tilde{t}_1} = 600\,\text{GeV}$ to about 2 fb at $m_{\tilde{t}_1} = 1150\,\text{GeV}$.

Signal events for the spin-0 scalar and pseudoscalar mediator models were generated at LO with up to one additional parton with MadGraph 2.6.2 interfaced to Pythia 8 for parton showering and hadronisation. In the DM sample generation the couplings of the mediator to the DM and SM particles (g_χ and g_q) were set to one. When interpreting the experimental results, a single common coupling $g = g_\chi = g_\text{q}$ is always assumed. Coupling values of $g = 1$ as well as $g < 1$ are considered. The kinematics of the mediator decay were found to not depend strongly on the values of the couplings; however, the particle kinematic distributions are sensitive to the scalar or pseudoscalar nature of the mediator and to the mediator and DM particle masses. The cross-sections were computed at NLO [74, 75] and decrease significantly when the mediator is produced off-shell. The production cross-section varies from approximately 26 pb to 130 fb over a scalar mediator mass range of 10 to 200 GeV and from approximately 600 fb to 120 fb over a pseudoscalar mediator mass range of 10 to 200 GeV.

5 Event reconstruction

Events selected in the analysis must satisfy a series of beam, detector and data-quality criteria. The primary vertex, defined as the reconstructed vertex with the highest $\sum_\text{tracks} p_\text{T}^2$, must have at least two associated tracks with $p_\text{T} > 500\,\text{MeV}$.

Depending on the quality and kinematic requirements imposed, reconstructed physics objects are labelled as either *baseline* or *signal*, where the latter is a subset of the former, with tighter selection criteria applied. Baseline objects are used when classifying overlapping selected objects and to compute the missing transverse momentum. Background contributions from $t\bar{t}$ and Wt production where both W bosons decay leptonically, referred to as dileptonic $t\bar{t}$ or Wt events, are suppressed by vetoing events with more than one baseline lepton. Signal objects are used to construct kinematic and discriminating variables necessary for the event selection.

Electrons are identified as energy clusters formed in the electromagnetic calorimeter matched to tracks in the ID. Baseline electrons are required to have $p_\text{T} > 4.5\,\text{GeV}$ and $|\eta| < 2.47$, and to satisfy 'LooseAndBLayer' likelihood identification criteria that follow the methodology described in ref. [103]. Furthermore, their longitudinal impact parameter (z_0), defined as the distance along the beam direction between the primary vertex and the track's point of closest approach to the beam axis, must satisfy $|z_0 \sin\theta| < 0.5$ mm where θ is the polar angle of the track. Signal electrons must satisfy all the baseline requirements and have a transverse impact parameter (d_0) that satisfies $|d_0|/\sigma_{d_0} < 5$, where σ_{d_0} is the uncertainty in d_0. Furthermore, signal electrons are required to be isolated. The isolation is defined as the sum of the transverse energy or momentum reconstructed in a cone of size $\Delta R = \sqrt{(\Delta\eta)^2 + (\Delta\phi)^2}$ around the electron, excluding the energy of the electron itself. The isolation criteria rely on both track- and calorimeter-based information with a fixed requirement on the isolation energy divided by the electron's p_{T}. Electrons that satisfy the signal identification criteria, including the loose isolation, are called loose electrons. In addition, tight electrons must satisfy both a tight electron likelihood identification criterion and a tight isolation criterion.

Muon candidates are reconstructed from combined tracks that are formed from ID and MS tracks, or stand-alone MS tracks. Baseline muons up to $|\eta| = 2.7$ are used, and are required to have $p_{\mathrm{T}} > 4\,\mathrm{GeV}$, a longitudinal impact parameter $|z_0 \sin\theta| < 0.5$ mm, and to satisfy the 'Medium' identification criterion [104]. Signal muons must satisfy all baseline requirements and in addition have a transverse impact parameter satisfying $|d_0|/\sigma_{d_0} < 3$. Tight signal muons must satisfy tight isolation criteria, similar to those used for tight signal electrons, but with a fixed requirement on track-based isolation energy divided by the muon's p_{T}. A category of loose signal muons is also defined, which requires the 'Loose' identification criterion [104] and satisfies a looser isolation criterion.

Dedicated efficiency scale factors are derived from $Z \to \ell\bar{\ell}$ and $J/\psi \to \ell\bar{\ell}$ data samples to correct the simulations for minor mis-modelling of electron and muon identification, impact parameter and isolation selections. The p_{T} threshold of signal leptons is 25 GeV for electrons and muons in all signal regions except for signal regions dedicated to $\tilde{t}_1 \to bff'\tilde{\chi}^0_1$, where electrons with $p_{\mathrm{T}} > 4.5\,\mathrm{GeV}$ and muons with $p_{\mathrm{T}} > 4\,\mathrm{GeV}$ are used.

Jet candidates are built from topological clusters [105, 106] in the calorimeters using the anti-k_t algorithm [107] with a jet radius parameter $R = 0.4$ implemented in the FastJet package [108]. Jets are corrected for contamination from pile-up using the jet area method [109–111] and are then calibrated to account for the detector response [112, 113]. Jets in data are further calibrated according to *in situ* measurements of the jet energy scale [113]. Baseline jets are required to have $p_{\mathrm{T}} > 20\,\mathrm{GeV}$. Signal jets are required to have $|\eta| < 2.5$ and $p_{\mathrm{T}} > 25\,\mathrm{GeV}$ in all signal regions, except in the four-body signal regions, where the p_{T} threshold of signal jets is 20 GeV. Furthermore, signal jets with $p_{\mathrm{T}} < 120\,\mathrm{GeV}$ and $|\eta| < 2.5$ must satisfy track-based criteria designed to reject jets originating from pile-up [111]. Events containing a signal jet that does not satisfy specific jet-quality requirements ('jet cleaning') are rejected to suppress detector noise and non-collision backgrounds [114, 115]. The number of signal jets in an event is denoted N_{jet}. In addition to these jet candidates, the same anti-k_t algorithm is used to define larger radius (large-R) jets to provide discriminating variables for the reconstruction of top quarks, as described in section 6.

Jets identified as containing b-hadrons are referred to as b-tagged jets. Their identification is performed using the MV2c10 b-tagging algorithm, which examines quantities such as the impact parameters of associated tracks and characteristics of reconstructed secondary vertices [116, 117]. The algorithm is used at a working point that provides a 77% b-tagging efficiency in simulated $t\bar{t}$ events, and corresponds to a rejection factor of about 130 for jets originating from gluons and light-flavour quarks (light jets) and about 6 for jets induced by charm quarks. Corrections derived from data control samples are applied to account for differences between data and simulation in the efficiency and mis-tag rate of the b-tagging algorithm. The number of b-tagged jets in an event is denoted $N_{b\text{-jet}}$. Since

MV2c10 is only applicable to baseline jets with $p_{\mathrm{T}} > 20$ GeV, it is not sensitive to low-p_{T} b-hadrons. The presence of low-p_{T} b-hadrons, below 20 GeV, is instead inferred using a soft b-tagging algorithm, which does not rely on the presence of a jet in the calorimeter, but requires the presence of secondary vertices [118]. This technique is used to gain sensitivity to the $\tilde{t}_1 \to bff'\tilde{\chi}_1^0$ signal in the regime with $\Delta m_{\tilde{t}_1,\tilde{\chi}_1^0}$ lower than $\sim$40 GeV. The number of secondary vertices in an event is denoted N_{SV}. Corrections derived from dedicated $t\bar{t}$ and W+jets control regions are applied to the soft b-tagging efficiencies to account for differences between data and simulation.

Jets and associated tracks are also used to identify hadronically decaying τ-leptons using the 'Loose' identification criterion described in refs. [119, 120], which has a 85% (75%) efficiency for reconstructing τ-leptons decaying into one (three) charged pions. The hadronic τ-lepton decay candidates are required to have one or three associated tracks, with total electric charge opposite to that of the signal electron or muon, $p_{\mathrm{T}} > 20$ GeV, and $|\eta| < 2.5$. The τ-lepton candidate p_{T} requirement is applied after a dedicated energy calibration [121, 122].

To avoid labelling the same detector signature as more than one object, an overlap removal procedure is applied. Given a set of baseline objects, the procedure checks for overlap based on either a shared track, ghost-matching [110], or a minimum distance ΔR_y between pairs of objects.[4] First, if a baseline lepton and a baseline jet are separated by $\Delta R_y < 0.2$, then the lepton is retained and the jet is discarded. Second, if a baseline jet and a baseline lepton are separated by $\Delta R_y < 0.4$, then the jet is retained and the lepton is discarded, to minimise the contamination from jets misidentified as leptons. For the remainder of the paper, all baseline and signal objects are those that have survived the overlap removal procedure.

The missing transverse momentum $\vec{p}_{\mathrm{T}}^{\,\mathrm{miss}}$ is reconstructed as the negative vector sum of the transverse momenta of baseline electrons, muons, jets, and a soft term built from high-quality tracks that are associated with the primary vertex but not with the baseline physics objects [123, 124]. Photons and hadronically decaying τ-leptons are not explicitly included but enter either as jets, electrons, or via the soft term.

6 Discriminating variables

The backgrounds contributing to a final state with one isolated lepton, jets and $E_{\mathrm{T}}^{\mathrm{miss}}$ are primarily semileptonic $t\bar{t}$ events with one of the W bosons decaying leptonically, and W+jets events with a leptonic decay of the W boson. Both backgrounds can be efficiently reduced by requiring the transverse mass of the event, m_{T}, to be significantly larger than the W boson mass. The transverse mass is defined as $m_{\mathrm{T}} = \sqrt{2p_{\mathrm{T}}^{\ell} E_{\mathrm{T}}^{\mathrm{miss}}[1 - \cos(\Delta\phi)]}$, where $\Delta\phi$ is the azimuthal angle between the lepton and missing transverse momentum directions and p_{T}^{ℓ} is the transverse momentum of the charged lepton. Other discriminating variables used to distinguish signal from several categories of background events are described below.

[4] Rapidity $y \equiv 1/2 \ln[(E + p_z)/(E - p_z)]$ is used instead of pseudorapidity (η) when computing the distance ΔR_y between objects in the overlap removal procedure.

JHEP04(2021)174

6.1 Dileptonic $t\bar{t}$ reconstruction

The m_{T2} variable [125] is a generalisation of the transverse mass, applied to signatures where two particles are not directly detected. The variable m_{T2}^{τ} [126] is a variant of m_{T2} developed to identify and remove $t\bar{t}$ events where one W boson decays into a hadronically decaying τ-lepton candidate. In this case the 'τ-jet' is used as the visible particle for one top branch and the observed electron or muon for the other top branch. For $t\bar{t}$ events where one W boson decays leptonically and the other into a hadronically decaying τ-lepton, m_{T2}^{τ} has an endpoint at the W boson mass.

Events with dileptonic decays of $t\bar{t}$ pairs, where one lepton is not identified, constitute a significant background. The lost lepton can lead to significant missing transverse momentum and m_{T2} above the W boson mass. The topness variable [127] quantifies how well an event can be reconstructed under a dileptonic top hypothesis and is defined as the logarithm of the minimum of the following quantity $\mathcal{S}$:

$$\mathcal{S}(p_{Wx}, p_{Wy}, p_{Wz}, p_{\nu z}) = \frac{[m_W^2 - (p_\ell + p_\nu)^2]^2}{a_W^4} + \frac{[m_t^2 - (p_{b1} + p_\ell + p_\nu)^2]^2}{a_t^4} + \frac{[m_t^2 - (p_{b2} + p_W)^2]^2}{a_t^4} + \frac{[4m_t^2 - (\Sigma_i p_i)^2]^2}{a_{\mathrm{CM}}^4},$$

when minimised with respect to p_W and p_ν with the constraint $\vec{p}_{\mathrm{T},\nu} + \vec{p}_{\mathrm{T,W}} = \vec{p}_{\mathrm{T}}^{\,\mathrm{miss}}$. The quantity p_W represents the four-momentum vector of the W boson for which the lepton was not reconstructed and is thus completely invisible. The quantities p_ℓ and p_ν are the lepton and neutrino four-momentum vectors from the W boson whose lepton was identified. Finally, p_{b_i} refer to the two b-jets. The sum in the last term runs over the five assumed final-state particles. If the event contains two b-tagged jets, the two permutations are tested in the minimisation. If the event has a single b-tagged jet, then permutations where the second b-jet can be either of the two leading momentum untagged jets are tested during the minimisation. The values of resolution parameters a_W, a_t and a_{CM} are constants taken from ref. [127].

6.2 Reconstruction of hadronic top decays

Signal events contain one hadronic top decay $t \to q\bar{q}'b$, while such decays are absent from the dileptonic $t\bar{t}$ background. Therefore, reconstructing the hadronic top quark decay can provide additional discrimination against dileptonic $t\bar{t}$ events. A recursive reclustering jet algorithm searches for large-radius jets with radius parameter R corresponding to the radius $R(p_{\mathrm{T}}) = 2 \times m_{\mathrm{top}}/p_{\mathrm{T}}$ expected from a hadronic top quark decay $t \to q\bar{q}'b$ [29]. The algorithm is based on the anti-k_t algorithm using signal jets as inputs and with initial radius parameter $R_0 = 3.0$. If a reclustered large-radius jet is significantly narrower than the radius expected from a hadronic top quark decay of that p_{T}, it is discarded. The radius of the remaining reclustered jets is iteratively reduced until the radius approximately matches the radius expected from a hadronic top quark decay. Surviving reclustered jets constitute hadronic top candidates. If more than one hadronic top candidate is found, the candidate whose mass $m_{\mathrm{top}}^{\mathrm{reclustered}}$ is closest to m_{top} is retained.

A second hadronic top quark candidate algorithm is employed that fully reconstructs the direction of both the leptonically and the hadronically decaying top quarks, denoted t_{lep} and t_{had} respectively. This algorithm is applied to events with at least four jets and one b-tagged jet. The m_{top}^{χ} variable is defined as the invariant mass of the triplet of signal jets (one of which must be b-tagged) most compatible with m_{top}, taking into account the jet momentum and energy resolution. The component of the $\vec{p}_{\text{T}}^{\text{ miss}}$ perpendicular to t_{lep} in the $t\bar{t}$ rest frame, $E_{\text{T},\perp}^{\text{miss}}$, is small in semileptonic top quark decays since $\vec{p}_{\text{T}}^{\text{ miss}}$ tends to align with the leptonically decaying top quark.

6.3 Backgrounds with mismeasured missing momentum

In some signal regions, additional suppression against backgrounds with mismeasured missing momentum, arising from mismeasured jets, is required. This additional rejection is provided by $H_{\text{T,sig}}^{\text{miss}} = (|\vec{H}_{\text{T}}^{\text{miss}}| - M)/\sigma_{|\vec{H}_{\text{T}}^{\text{miss}}|}$, where $\vec{H}_{\text{T}}^{\text{miss}}$ is the negative vectorial sum of the momenta of the signal jets and signal lepton [126]. The denominator is computed from the per-event jet energy uncertainties, while the lepton resolution is neglected. The offset parameter M is a characteristic scale of the background processes and is fixed at 100 GeV.

6.4 Variables for compressed $\tilde{t}_1 \to t + \tilde{\chi}_1^0$

To discriminate stop pair production from SM $t\bar{t}$ production, in the phase space dominated by the decay $\tilde{t}_1 \to t+\tilde{\chi}_1^0$ in the compressed regime $\Delta m_{\tilde{t}_1,\tilde{\chi}_1^0} \approx m_{\text{top}}$, events are reconstructed according to both the stop and semileptonic $t\bar{t}$ hypotheses. These techniques are employed in the `tN_diag_low` and `tN_diag_high` SRs.

The reconstruction of the event under the semileptonic $t\bar{t}$ hypothesis starts by searching for the hadronically decaying top quark candidate through the minimisation of the loss function

$$L_t = \frac{(m_W^{\text{cand}} - m_W)^2}{m_W} + \frac{(m_{t_{\text{had}}}^{\text{cand}} - m_{\text{top}})^2}{m_{\text{top}}}$$

with m_W and m_{top} being the experimentally known W boson and top quark masses. The W boson candidate mass m_W^{cand} is either the mass of a single large anti-k_t jet with radius 1.0 or 1.2 or the invariant mass of two anti-k_t jets with radius 0.4. The hadronically decaying top quark candidate t_{had} is either one of the large-R jets or the W boson candidate plus a b-tagged jet. The jet permutation with the minimum loss function is considered as the candidate for the hadronic top. The visible part of the leptonically decaying top quark candidate ($t_{\text{lep}^{\text{vis}}}$) four-momentum vector is determined by adding the four-momentum vectors of the remaining highest-p_{T} b-tagged jet and the signal lepton.

The reconstruction of the event under the stop hypothesis relies on the collinear approximation [128, 129], in which the top quark and the neutralino from the stop decay are collinear. This approximation is valid for compressed $\tilde{t}_1 \to t + \tilde{\chi}_1^0$ models ($\Delta m_{\tilde{t}_1,\tilde{\chi}_1^0} \approx m_{\text{top}}$), where the requirement of a high-p_{T} initial-state radiation (ISR) jet in the event forces the momentum of the $\tilde{t}_1$ to be much larger than the sum of the top and $\tilde{\chi}_1^0$ masses.

With this approximation and a given value of the parameter $\alpha = m_{\tilde{\chi}_1^0}/m_{\tilde{t}_1}$, the four-momentum vector $p^{\mu}(\alpha)$ of the neutrino can be calculated from the missing transverse energy and the measured momenta of the hadronic and visible leptonic top quark candidates under the assumption that the longitudinal neutrino momentum p_z is zero. The resulting $p^\mu(\alpha)$ is then used to compute the leptonically decaying W boson's transverse mass m_{T}^{α} and the difference in m_{T} between the calculation under the hypothesis of a $t\bar{t}$ event and under the signal hypothesis, $\Delta m_{\mathrm{T}}^{\alpha} = m_{\mathrm{T}} - m_{\mathrm{T}}^{\alpha}$.

The `tN_diag_low` SR is optimised to probe the previously unexcluded region around the point with a stop mass of 200 GeV and neutralino mass of 27 GeV [29] which corresponds to $\alpha = 0.135$. Therefore this region uses the variable $\Delta m_{\mathrm{T}}^{\alpha}$ with α fixed to 0.135. For other compressed regions, which are targeted by the `tN_diag_high` SR, α can be determined dynamically by minimising the loss function

$$L_\alpha = \frac{[m(\ell+\nu) - m_W]^2}{m_W} + \frac{[m(t_{\mathrm{lep}^{\mathrm{vis}}} + \nu) - m_{\mathrm{top}}]^2}{m_{\mathrm{top}}}$$

where $m(\ell+\nu)$ is the invariant mass of the lepton and the neutrino, and $m(t_{\mathrm{lep}^{\mathrm{vis}}} + \nu)$ is the invariant mass of the leptonic top candidate and the neutrino. Using the approximation $\alpha = m_{\tilde{\chi}_1^0}/(m_{\tilde{\chi}_1^0} + m_{t_{\mathrm{had}}})$ and the measured value of $m_{t_{\mathrm{had}}}^{\mathrm{cand}}$, the values of $\Delta m_{\mathrm{T}}^{\alpha}$ and the mass of the $\tilde{\chi}_1^0$ at the minimum of the loss function can be determined. These variables are labelled $\Delta m_{\mathrm{T}}^{\mathrm{dyn}}$ and $m_{\tilde{\chi}_1^0}^{\mathrm{dyn}}$ respectively.

Although the neutrino momentum under the collinear approximation is fully known for a given value of α, there is an ambiguity as to how the remaining missing transverse momentum is split between the two neutralinos. To resolve this, the following loss function, which compares the reconstructed leptonic and hadronic $\tilde{t}_1$ masses with a given $\tilde{t}_1$ mass hypothesis, $m_{\tilde{t}_1}$, is defined and used in the `tN_diag_low` SR:

$$L_{\tilde{t}_1} = \frac{\left(m_{\tilde{t}_1}^{\mathrm{had}} - m_{\tilde{t}_1}\right)^2}{m_{\tilde{t}_1}} + \frac{\left(m_{\tilde{t}_1}^{\mathrm{lep}} - m_{\tilde{t}_1}\right)^2}{m_{\tilde{t}_1}}$$

A minimisation of this loss function, again under the assumption that $\alpha = 0.135$, is performed with respect to the angles between each neutralino momentum vector and each of the two top quarks. The mass $m_{\tilde{t}_1}^{\mathrm{lep}}$, which denotes the leptonic $\tilde{t}_1$ mass at the minimum of this loss function, takes lower and more peaked values for compressed $\tilde{t}_1 \to t + \tilde{\chi}_1^0$ models than for the SM top quark backgrounds. Finally, the ratio x_1 of the hadronic top quark momentum to the parent stop momentum is also used to discriminate between the stop signal and the background. Since it is computed as a projection, x_1 can take negative values for background processes, or if the collinear assumption does not hold.

7 Signal regions

A preselection that exploits the basic characteristics of the signals is applied: the presence of a signal lepton, b-tagged jets and missing transverse momentum. The preselection is designed to have very high efficiency for the signal and to remove the most trivial backgrounds. To cover signals with both high-momentum decay products such as in $\tilde{t}_1 \to t + \tilde{\chi}_1^0$ and low-momentum decay products such as in $\tilde{t}_1 \to bff'\tilde{\chi}_1^0$, 'soft-lepton' and 'hard-lepton' preselections are defined and are presented in table 3. All regions require $E_{\mathrm{T}}^{\mathrm{miss}} > 230$ GeV

Selection		hard-lepton	soft-lepton
Trigger		$E_{\mathrm{T}}^{\mathrm{miss}}$ trigger	
Data quality		jet cleaning, primary vertex	
Second-lepton veto		no additional baseline leptons	
Number of leptons, tightness		= 1 'loose' lepton	= 1 'tight' lepton
Lepton p_{T}	[GeV]	> 25	> 4 (4.5) for μ (e)
Number of jets (jet p_{T})		≥ 4 (> 25 GeV)	≥ 1 (> 200 GeV) or ≥ 2 (> 20 GeV)
$E_{\mathrm{T}}^{\mathrm{miss}}$	[GeV]	> 230	
$\Delta\phi(j_{1,2}, \vec{p}_{\mathrm{T}}^{\mathrm{miss}})$	[rad]	> 0.4	
$N_{b\text{-jet}}$		≥ 1	–
m_{T}	[GeV]	> 30	–
m_{T2}^{τ}	[GeV]	> 80	–

Table 3. Preselection criteria used for the hard-lepton signal regions (left) and the soft-lepton signal regions (right).

to ensure that the trigger was fully efficient. To reject multijet events with mismeasured jet momenta, a minimum azimuthal angular distance is required between the missing transverse momentum direction and the two leading jets, $\Delta\phi(j_{1,2}, \vec{p}_{\mathrm{T}}^{\mathrm{miss}}) > 0.4$.

The signal regions are then optimised using simulated event samples to maximise the expected Z significance [130, 131] for the benchmark signals.[5] A set of benchmark signal models, selected to cover the various stop and spin-0 mediator models, is used for optimisation. The optimisation is performed using an iterative algorithm, considering all discriminating variables and accounting for statistical and systematic errors in the evaluation of the discovery significance. An overview of the signal regions and the benchmark models for optimisation is presented in table 1. The SRs are not designed to be orthogonal. The final exclusion limits are obtained by selecting at each point of the model parameter space the SR with the best expected sensitivity.

7.1 $\tilde{t}_1 \to t + \tilde{\chi}_1^0$

Two signal regions, `tN_med` and `tN_high`, are designed for models with $\Delta m_{\tilde{t}_1,\tilde{\chi}_1^0}$ significantly larger than m_{top}, and rely on large missing momentum and energetic jets. Selections on m_{T}, $H_{\mathrm{T,sig}}^{\mathrm{miss}}$, $E_{\mathrm{T},\perp}^{\mathrm{miss}}$ and topness are dictated by the need to suppress the three main backgrounds, namely W+jets, $t\bar{t}$, and $t\bar{t}+V$. The presence of a hadronic top quark candidate with $m_{\mathrm{top}}^{\mathrm{reclustered}} > 150$ GeV is required primarily to ensure orthogonality with the control regions.

[5] Significance Z of observing n events for a prediction of $b \pm \sigma$ is defined as

$$Z = \sqrt{2\left\{n \ln\left[\frac{n(b+\sigma^2)}{b^2+n\sigma^2}\right] - \frac{b^2}{\sigma^2}\ln\left[1+\frac{\sigma^2(n-b)}{b(b+\sigma^2)}\right]\right\}} \quad \text{when } n \geq b \text{, or}$$

$$Z = -\sqrt{2\left\{n \ln\left[\frac{n(b+\sigma^2)}{b^2+n\sigma^2}\right] - \frac{b^2}{\sigma^2}\ln\left[1+\frac{\sigma^2(n-b)}{b(b+\sigma^2)}\right]\right\}} \quad \text{when } n < b.$$

Selection		tN_med	tN_high
Preselection		hard-lepton preselection	
N_{jet}, $N_{b\text{-jet}}$		$\geq (4, 1)$	$\geq (4, 1)$
Jet p_{T}	[GeV]	$>$ (100, 90, 70, 50)	$>$ (120, 50, 50, 25)
$E_{\text{T}}^{\text{miss}}$	[GeV]	> 230	> 520
$E_{\text{T},\perp}^{\text{miss}}$	[GeV]	> 400	–
$H_{\text{T,sig}}^{\text{miss}}$		> 16	> 25
m_{T}	[GeV]	> 220	> 380
Topness		> 9	> 8
$m_{\text{top}}^{\text{reclustered}}$	[GeV]	> 150	
$\Delta R(b, \ell)$		< 2.8	< 2.6
Exclusion technique		Based on shape-fit in $E_{\text{T}}^{\text{miss}}$ and m_{T} in tN_med	
		$E_{\text{T}}^{\text{miss}} \in$ [230, 400], $m_{\text{T}} > 220$	
		$E_{\text{T}}^{\text{miss}} \in$ [400, 500], $m_{\text{T}} > 220$	
Bin boundaries	[GeV]	$E_{\text{T}}^{\text{miss}} \in$ [500, 600], $m_{\text{T}} \in$ [220, 380]	
		$E_{\text{T}}^{\text{miss}} \in$ [500, 600], $m_{\text{T}} > 380$	
		$E_{\text{T}}^{\text{miss}} > 600$, $m_{\text{T}} \in$ [220, 380]	
		$E_{\text{T}}^{\text{miss}} > 600$, $m_{\text{T}} > 380$	

Table 4. Event selections defining the signal regions tN_med and tN_high.

The tN_med and tN_high definitions are given in table 4. A common exclusion region is defined by performing a two-variable shape-fit on the tN_med signal region, if no excess is observed in the single-bin discovery signal regions. The binning is designed to maximise the excluded parameter space in the $m_{\tilde{t}_1}$–$m_{\tilde{\chi}_1^0}$ plane. The two variables chosen for the binning are the two discriminating variables that best distinguish between tN_med and tN_high, namely $E_{\text{T}}^{\text{miss}}$ and m_{T}. The resulting six bins are given in table 4.

7.2 Compressed $\tilde{t}_1 \to t + \tilde{\chi}_1^0$

The kinematics of the decay $\tilde{t}_1 \to t + \tilde{\chi}_1^0$ in the region where $\Delta m_{\tilde{t}_1,\tilde{\chi}_1^0} \approx m_{\text{top}}$ differ significantly from the two signal regions defined above, and the stop signal is kinematically very similar to the dominant $t\bar{t}$ background. This region of parameter space is referred to as the diagonal region. Two dedicated signal regions, tN_diag_low and tN_diag_high, are designed to target scenarios on the diagonal for low-mass and high-mass stops respectively. The sensitivity of the tN_diag_low SR is such that it is expected to be able to exclude scenarios with $\Delta m_{\tilde{t}_1,\tilde{\chi}_1^0} = m_{\text{top}}$ and $m(\tilde{t}_1)$ between 200 and 250 GeV. Both the tN_diag_low and tN_diag_high signal regions rely on the presence of a high-p_{T} ISR jet, which serves to boost the di-stop system. The signal region definitions are shown in table 5 and are used both for exclusion and for discovery.

Selection		tN_diag_low	tN_diag_high
Preselection		hard-lepton preselection without τ-lepton veto	
N_{jet}, $N_{b\text{-jet}}$		$>(4,\ 1)$	
Jet p_{T}	[GeV]	$>(400,\ 40,\ 40,\ 40)$	
m_{T}	[GeV]	>150	>110
$E_{\text{T}}^{\text{miss}}$	[GeV]	–	>400
m_{T2}	[GeV]	–	<360
$\Delta m_{\text{T}}^{\alpha}$	[GeV]	>40	–
$\Delta m_{\text{T}}^{\text{dyn}}$	[GeV]	–	>60
$m_{\tilde{t}_1}^{\text{lep}}$	[GeV]	<600	–
$m_{\tilde{\chi}_1^0}^{\text{dyn}}$	[GeV]	>5	[220, 595]
x_1		–	>-0.2
Exclusion technique		cut-and-count	

Table 5. Event selections defining the signal regions tN_diag_low and tN_diag_high.

7.3 $\tilde{t}_1 \to bW\tilde{\chi}_1^0$

The signal region for the decay $\tilde{t}_1 \to bW\tilde{\chi}_1^0$ is labelled bWN and defined using an optimised two-step machine learning (ML) approach, applied to events preselected according to the hard-lepton preselection criteria and additionally satisfying $m_{\text{T}} > 110$ GeV. The background mostly consists of $t\bar{t}$, which has strong similarities to the signal in this region of phase space. For this reason the ML technique is selected. The jet multiplicity in signal events varies significantly due to the potential presence of ISR jets and fluctuations in the number of low-energy jets reconstructed from the hadronically decaying W boson. To deal with the variable number of signal jets, the first step of the ML procedure is to use a recurrent neural network (RNN) that has the ability to extract information from sequences of variable length [132]. The RNN uses a long short-term memory (LSTM) algorithm [133] and takes the four-momentum vectors of the jets as inputs. The LSTM output becomes the input of the second step, made up of a shallow neutral network (NN) with a single hidden layer and an output corresponding to the signal probability. The RNN and NN are trained simultaneously in one step. The NN uses the following discriminating variables as input: output of the RNN, $E_{\text{T}}^{\text{miss}}$, m_{T}, the azimuthal ϕ angle of $\vec{p}_{\text{T}}^{\text{ miss}}$, the azimuthal angle $\Delta\phi(\vec{p}_{\text{T}}^{\text{ miss}}, \ell)$ between the lepton and $\vec{p}_{\text{T}}^{\text{ miss}}$, the invariant mass $m_{\ell\text{b}}$ of the lepton and the b-tagged jet, the transverse momentum of the b-tagged jet, the lepton four-momentum vector, N_{jet} and $N_{b\text{-jet}}$.

Before training, the hard-lepton preselection and the additional selection $m_{\text{T}} > 110$ GeV are applied. The size of the training sample is a crucial aspect for the performance of any ML method. Generating fully simulated signal samples with adequate sample sizes after the hard-lepton preselection and $m_{\text{T}} > 110$ GeV is computationally expensive. To overcome this difficulty, signal events without detector simulation were used for the training to enhance the number of signal events by two orders of magnitude. Fully simulated SM background

JHEP04(2021)174

Selection		bWN	bWN-TCR	bWN-TVR
Preselection		hard-lepton preselection		
N_{jet}, $N_{b\text{-jet}}$		$\geq (4, 1)$		
Jet p_{T}	[GeV]	$>$ (25, 25, 25, 25)		
m_{T}	[GeV]	> 110	> 150	> 150
$\mathrm{NN}_{\mathrm{bWN}}$		> 0.9	$\in [0.4, 0.6]$	$\in [0.60, 0.65]$
Exclusion technique		shape-fit in $\mathrm{NN}_{\mathrm{bWN}}$		
Bin boundaries		$\{0.65, 0.7, 0.75, 0.8, 0.82, 0.84, 0.86, 0.88, 0.90, 0.92, 1.0\}$ and $m_{\mathrm{T}} > 150$ GeV if $\mathrm{NN}_{\mathrm{bWN}} < 0.8$		

Table 6. Event selections defining the signal region bWN, along with its CR and VR.

events were available in sufficiently large numbers to be used directly for the training. For the signal, the generated events are 'smeared' using a dedicated procedure to emulate the effects of detector simulation and reconstruction. Parameterisations for reconstruction and identification efficiencies are obtained from dedicated ATLAS measurements and applied to jets, leptons and b-tagged jet identification. Particle-level electron, muon and jet four-momentum vectors are smeared according to their respective p_{T}, η and identification working point. The $E_{\mathrm{T}}^{\mathrm{miss}}$ is recomputed from all smeared objects. The kinematic distributions of all input variables after smearing are found to have fair agreement with distributions after full event reconstruction. The output score of the ML classifier, denoted $\mathrm{NN}_{\mathrm{bWN}}$, shows good agreement between smeared samples and fully simulated samples after full event reconstruction. The classifier output also shows a good agreement between simulation and data. The smeared samples are used only for the training, while signal and background predictions are obtained with the samples described in section 4.

The discovery signal region is defined by selecting events with $\mathrm{NN}_{\mathrm{bWN}} > 0.9$. The exclusion limits are obtained by performing a shape-fit using ten bins in $\mathrm{NN}_{\mathrm{bWN}}$, with bin boundaries $\{0.65, 0.7, 0.75, 0.8, 0.82, 0.84, 0.86, 0.88, 0.90, 0.92, 1.0\}$. The $t\bar{t}$ background in the first three bins is reduced by applying an additional selection, namely $m_{\mathrm{T}} > 150$ GeV. The selections that define the bWN signal region are presented in table 6.

7.4 $\tilde{t}_1 \to bff'\tilde{\chi}_1^0$

The four-body decay $\tilde{t}_1 \to bff'\tilde{\chi}_1^0$ occurs when $\Delta m_{\tilde{t}_1,\tilde{\chi}_1^0}$ is smaller than the W boson mass. In this scenario, the decay products have low momenta and often fall below the standard jet and lepton reconstruction p_{T} thresholds. It is therefore necessary to apply a soft-lepton preselection and require the presence of a high-momentum ISR jet, with $p_{\mathrm{T}} > 200$ GeV, to boost the momenta of the final-state particles. A first four-body signal region, labelled as bffN_btag, is optimised by requiring the presence of at least one b-tagged jet. The background in the bffN_btag signal region mostly consists of $t\bar{t}$ events. Because the b-tagged jets are required to have $p_{\mathrm{T}} > 20$ GeV, bffN_btag is not sensitive to $\Delta m_{\tilde{t}_1,\tilde{\chi}_1^0}$ below $\sim$40 GeV. For this reason a second signal region, labelled as bffN_softb, is defined. This

JHEP04(2021)174

Selection		bffN_softb	bffN_btag
Preselection		soft-lepton preselection	
N_{jet}		≥ 1	≥ 2
Jet p_{T}	[GeV]	> 200	
$N_{b\text{-jet}}$		$=0$	≥ 1
b-jet p_{T}	[GeV]	–	< 50
N_{SV}		≥ 1	–
m_{T}	[GeV]	> 90	
$E_{\text{T}}^{\text{miss}}$	[GeV]	> 250	–
$\Delta\phi(\vec{p}_{\text{T}}^{\text{ miss}}, \ell)$	[rad]	< 2.0	–
C_{T2}	[GeV]	–	> 400
$\Delta\phi(p_{\text{T}}^{b\text{-jet}}, \vec{p}_{\text{T}}^{\text{ miss}})$	[rad]	–	< 1.5
$p_{\text{T}}^{\ell}/E_{\text{T}}^{\text{miss}}$		< 0.04	< 0.05
Exclusion technique		shape-fit in $p_{\text{T}}^{\ell}/E_{\text{T}}^{\text{miss}}$	shape-fit in $p_{\text{T}}^{\ell}/E_{\text{T}}^{\text{miss}}$ and $\Delta\phi(p_{\text{T}}^{b\text{-jet}}, \vec{p}_{\text{T}}^{\text{ miss}})$
Bin boundaries in $p_{\text{T}}^{\ell}/E_{\text{T}}^{\text{miss}}$		$\{0, 0.015, 0.025, 0.04, 0.06, 0.08\}$	$\{0, 0.03, 0.06, 0.1\}$
Bin boundaries in $\Delta\phi(p_{\text{T}}^{b\text{-jet}}, \vec{p}_{\text{T}}^{\text{ miss}})$	[rad]		$\{0, 0.8, 1.5\}$

Table 7. Event selections defining the signal regions bffN_softb and bffN_btag.

region does not rely on b-tagged jets but instead requires a soft b-tag identified by the presence of a secondary vertex. The dominant background processes in this region are $t\bar{t}$ and W+jets. The bffN_btag signal region also exploits the correlation between the ISR jet p_{T} and $E_{\text{T}}^{\text{miss}}$ by cutting on the C_{T2} variable defined by $C_{\text{T2}} = \min(E_{\text{T}}^{\text{miss}}, p_{\text{T}}^{\text{ISR}} - 25\,\text{GeV})$. The key variable used at the last stage of the selection is the ratio of the lepton's transverse momentum to the missing transverse momentum, $p_{\text{T}}^{\ell}/E_{\text{T}}^{\text{miss}}$, which has small values for the $\tilde{t}_1 \to bff'\tilde{\chi}_1^0$ signal and large values for the backgrounds. The exact definitions of the four-body signal regions are given in table 7. For exclusion limits, the last selection, namely on $p_{\text{T}}^{\ell}/E_{\text{T}}^{\text{miss}}$, is replaced by a shape-fit. In the bffN_softb, the shape-fit is performed in five bins of the variable $p_{\text{T}}^{\ell}/E_{\text{T}}^{\text{miss}}$ with bin boundaries $\{0, 0.015, 0.025, 0.04, 0.06, 0.08\}$. In the bffN_btag signal region the shape-fit is performed in two variables, namely three bins in $p_{\text{T}}^{\ell}/E_{\text{T}}^{\text{miss}}$ with bin boundaries $\{0, 0.03, 0.06, 0.1\}$ and two bins in $\Delta\phi(p_{\text{T}}^{b\text{-jet}}, \vec{p}_{\text{T}}^{\text{ miss}})$ with bin boundaries $\{0, 0.8, 1.5\}$.

7.5 Dark matter

The dominant background to the search for spin-0 mediator models is the $t\bar{t} + V$ process. The optimisation of this signal region favours a selection with at least two b-tagged jets and a leading b-tagged jet with $p_{\text{T}} > 80\,\text{GeV}$. The distribution of $\Delta\phi(\vec{p}_{\text{T}}^{\text{ miss}}, \ell)$ differentiates the scalar and pseudoscalar models from each other and also from the background. The resulting DM_scalar and DM_pseudoscalar signal region definitions are given in table 8. In addition to the selection criteria optimised for discovery described above, the exclusion sensitivity is maximised by relying on a shape-fit in the region DM_scalar with the binning in $\Delta\phi(\vec{p}_{\text{T}}^{\text{ miss}}, \ell)$ given in table 8.

JHEP04(2021)174

Selection		DM_scalar	DM_pseudoscalar
Preselection		hard-lepton preselection	
N_{jet}, $N_{b\text{-jet}}$		$\geq (4, 2)$	
Jet p_{T}	[GeV]	$> (80, 60, 30, 25)$	
b-tagged jet p_{T}	[GeV]	$> (80, 25)$	
$E_{\text{T}}^{\text{miss}}$	[GeV]	> 230	
$H_{\text{T,sig}}^{\text{miss}}$		> 15	
m_{T}	[GeV]	> 180	
Topness		> 8	
$m_{\text{top}}^{\text{reclustered}}$	[GeV]	> 150	
$\Delta\phi(\text{jet}_i, \vec{p}_{\text{T}}^{\text{miss}})$, $i \in [1, 4]$	[rad]	> 0.9	
$\Delta\phi(\vec{p}_{\text{T}}^{\text{miss}}, \ell)$	[rad]	> 1.1	> 1.5
Exclusion technique		Based on shape-fit in $\Delta\phi(\vec{p}_{\text{T}}^{\text{miss}}, \ell)$	
Bin boundaries in $\Delta\phi(\vec{p}_{\text{T}}^{\text{miss}}, \ell)$		$\{1.1, 1.5, 2.0, 2.5, \pi\}$	

Table 8. Event selections defining the DM signal regions.

8 Backgrounds

Data can be used to constrain the normalisation of the most significant background processes. To this end, control regions (CRs) are defined by minimally modifying the SR selections to suppress the signal while enhancing the fraction of the targeted background process. The CRs are then incorporated into a simultaneous likelihood fit to constrain the background process normalisations in the signal region. The ratio of the number of background events of a given process in the SR to those in a CR is estimated in MC background samples but is allowed to deviate from that ratio within dedicated MC modelling systematic uncertainties. Less significant background processes, such as diboson production and Z+jets, are estimated directly from MC simulation since they typically represent only a few percent of the signal region yields. CRs are defined to normalise $t\bar{t}$ (TCR), W+jets (WCR), single-top (STCR) and $t\bar{t} + Z$ (TZCR). Whether a control region is defined for a given background and signal region depends on the relative contribution of the process to the SR yield.

To validate the background estimates from the CRs, validation regions (VRs) are introduced for $t\bar{t}$ (TVR) and W+jets (WVR). The VRs are disjoint from both the SRs and CRs. The TZCR is designed to be as close as possible to the signal region in order to obtain the most precise estimate of the large $t\bar{t} + Z$ background, and thus does not leave space between the SR and the CR to introduce a VR for this process. Background normalisations, referred to as normalisation factors (NF), determined in the CRs are applied to the VRs and compared with the data. The VRs are not included in the final simultaneous fit, but provide a statistically independent test of the background estimates in background-dominated regions.

Signal Region	Signal Scenario	TCR	WCR	STCR	TZCR	TVR	WVR
tN_med	$\tilde{t}_1 \to t + \tilde{\chi}_1^0$	✓	✓	✓	✓	✓	✓
tN_high	$\tilde{t}_1 \to t + \tilde{\chi}_1^0$	✓	✓	✓	✓	✓	✓
tN_diag_low	$\tilde{t}_1 \to t + \tilde{\chi}_1^0$	✓	–	–	–	✓	–
tN_diag_high	$\tilde{t}_1 \to t + \tilde{\chi}_1^0$	✓	–	–	–	✓	–
bWN	$\tilde{t}_1 \to bW\tilde{\chi}_1^0$	✓	–	–	–	✓	–
bffN_btag	$\tilde{t}_1 \to bff'\tilde{\chi}_1^0$	✓	✓	–	–	✓	✓
bffN_softb	$\tilde{t}_1 \to bff'\tilde{\chi}_1^0$	✓	✓	–	–	✓	✓
DM	spin-0 mediator	✓	–	–	✓	✓	–

Table 9. Summary of the control and validation regions used (✓) for each signal region.

The CRs and VRs are designed to minimise potential contamination from signal processes. The signal contamination is generally well below 10%, but in some TCRs and TVRs, for models close to the previously excluded region of parameter space, it can reach approximately 15%. The signal contributions to the CRs are not included in the background-only fits but are taken into account in the exclusion fits described in section 11. The CRs and VRs used for each SR are summarised in table 9. If a process is not normalised via a control region then it is estimated directly from MC simulation and theoretical cross-sections.

8.1 Control and validation regions for $\tilde{t}_1 \to t + \tilde{\chi}_1^0$ and spin-0 mediator signals

The dominant background process in the tN_med, tN_high and DM signal regions is $t\bar{t} + Z$, and therefore each of these SRs uses a dedicated TZCR. The TZCRs aim at capturing $t\bar{t}+Z$ events where the Z boson decays into two electrons or muons, and thus is kinematically similar to the $t\bar{t} + Z$ background in the signal regions where the Z boson decays into a pair of neutrinos. This CR is built by selecting events with three leptons (electrons or muons), one pair of which must be of opposite charge and same flavour with an invariant mass within 10 GeV of the Z boson mass. The exact definitions of the TZCRs follow the definitions of the tN_med, tN_high and DM SRs in terms of the number of jets, b-tagged jets and jet p_{T} thresholds. A modified missing momentum variable, $\tilde{E}_{\mathrm{T}}^{\mathrm{miss}}$, is defined, where the leptons associated with the Z boson decay are considered invisible. The $\tilde{E}_{\mathrm{T}}^{\mathrm{miss}}$ is the magnitude of the vector with components $\tilde{\vec{p}}_{\mathrm{x,y}}^{\mathrm{miss}}$ derived from the x, y components $\vec{p}_{\mathrm{x,y}}^{\mathrm{miss}}$ of $\vec{p}_{\mathrm{T}}^{\mathrm{miss}}$ introduced in section 5. The components $\tilde{\vec{p}}_{\mathrm{x,y}}^{\mathrm{miss}}$ are obtained as follows: $\tilde{\vec{p}}_{\mathrm{x,y}}^{\mathrm{miss}}=\vec{p}_{\mathrm{x,y}}^{\mathrm{miss}}+\vec{p}_{\mathrm{x,y}}^{\,\ell 2}+\vec{p}_{\mathrm{x,y}}^{\,\ell 3}$, where $\vec{p}_{\mathrm{x,y}}^{\,\ell 2}$ and $\vec{p}_{\mathrm{x,y}}^{\,\ell 3}$ are the x, y components of the momenta of the leptons that make up the Z boson candidate. The TZCRs require $\tilde{E}_{\mathrm{T}}^{\mathrm{miss}} > 230$ GeV. The remaining SR selections are not applied to the TZCRs, in order to retain a large enough event sample.

The W+jets and dileptonic $t\bar{t}$ processes are significant in tN_med and tN_high, and therefore dedicated CRs, WCR and TCR, are employed. The DM signal region also employs a TCR but does not require a WCR due to the smaller size of the W+jets background. These CRs have the same requirements on the number of jets, the number of b-tagged jets and the jet p_{T} thresholds as listed in tables 4 and 8 for their respective signal regions. Table 10 presents the definitions of the TCRs, WCRs and VRs, by showing which selections differ from the tN_med and tN_high SRs definitions. Neither W+jets nor dileptonic $t\bar{t}$ processes yield hadronic top decays, so a veto on the presence of a hadronic reclustered top candidate is used to ensure orthogonality with the signal regions. The number of events in TCR and WCR is increased by relaxing several selections compared with the SR selections. The $H_{\mathrm{T,sig}}^{\mathrm{miss}}$ selection is lowered to 10 for both tN_med and tN_high, and to 13 for DM. In addition, $E_{\mathrm{T},\perp}^{\mathrm{miss}}$ is lowered to 300 GeV for tN_med, while $E_{\mathrm{T}}^{\mathrm{miss}}$ is lowered to 450 GeV for tN_high. In the DM signal region the requirement on $\Delta\phi(\mathrm{jet}_i, \vec{p}_{\mathrm{T}}^{\,\mathrm{miss}})$ is lowered to 0.6.

The topness and m_{T} selections are used to differentiate between WCR and TCR. In the WCR, m_{T} is required to be in the range 30–90 GeV, compatible with the presence of a semileptonic W decay, but incompatible with dileptonic $t\bar{t}$ because of the topness selection. In the TCR, the topness selection of the SR is inverted, thus selecting events compatible with dileptonic $t\bar{t}$, while $m_{\mathrm{T}} > 120$ GeV is required, as larger values are favoured by the presence of two leptonically decaying W bosons. The TCR dedicated to the DM signal region has the same m_{T} selection as its signal region, $m_{\mathrm{T}} > 180$ GeV. The purity of the WCR is further improved by using only positively charged leptons, exploiting the lepton charge asymmetry in W+jets events from pp collisions.

To validate the dileptonic $t\bar{t}$ background normalisation, a TVR dominated by $t\bar{t}$ production is designed. The TVRs for tN_med and tN_high have the same selections as the corresponding TCR, except for the veto on the presence of a hadronic reclustered top quark candidate, which is replaced by a selection requiring the presence of such a hadronic top quark, with a mass $m_{\mathrm{top}}^{\mathrm{reclustered}} > 150$ GeV.

The validation of the W+jets background for tN_high is performed with a WVR with the same selection as tN_high but requiring the presence of a hadronic reclustered top candidate with $m_{\mathrm{top}}^{\mathrm{reclustered}} > 150$ GeV and $H_{\mathrm{T,sig}}^{\mathrm{miss}} > 25$, in order to be closer to the SR. The WVR for tN_med is defined starting from the WCR selections, but replacing several selections with those used in its SR: $E_{\mathrm{T}}^{\mathrm{miss}} > 400$ GeV, $H_{\mathrm{T,sig}}^{\mathrm{miss}} > 16$ and the presence of a hadronic top quark, with a mass $m_{\mathrm{top}}^{\mathrm{reclustered}} > 150$ GeV.

The DM SR contains only a small fraction of W+jets events due to the requirement of two b-tagged jets, and therefore only a TVR is considered. It is constructed from the DM SR definition, but with the topness selection inverted, and to increase the number of events and limit signal contamination, the selection on $\Delta\phi(\mathrm{jet}_i, \vec{p}_{\mathrm{T}}^{\,\mathrm{miss}})$ is relaxed to 0.6.

The tN_med and tN_high definitions permit the construction of a STCR with enough data events for comparison with the DS- and DR-based MC predictions. The STCR is defined with selections close to those of the WCR, but requires a second b-tagged jet, $30 < m_{\mathrm{T}} < 120$ GeV and the distance $\Delta R(b_1, b_2)$ between the two b-tagged jets to be larger than 1.4. To ensure orthogonality with the WCR, events with two b-tagged jets inside the WCR must have $\Delta R(b_1, b_2) < 1.4$. It is found that the DS and DR scheme predictions bracket the observed number of events in the STCR data, with a large discrepancy between the two predictions. The largest discrepancy is observed in the STCR associated with the tN_med SR. The data-to-prediction ratio in the STCR is $0.1^{+0.3}_{-0.1}$ with the DR scheme and 1.5 ± 1.3 with the DS scheme.

JHEP04(2021)174

Selection		`tN_med`	`tN_med`-TCR (-TVR)	`tN_med`-WCR (-WVR)	`tN_med`-STCR
$m_{\text{top}}^{\text{reclustered}}$	[GeV]	> 150	veto (> 150)	veto (> 150)	veto
$H_{\text{T,sig}}^{\text{miss}}$		> 16	> 10	> 10 (> 16)	> 10
$E_{\text{T},\perp}^{\text{miss}}$	[GeV]	> 400	> 300	> 300 (> 400)	350
m_{T}	[GeV]	> 220	> 120	$\in [30, 90]$	$\in [30, 120]$
Topness		> 9	< 9	> 9	> 10
$\Delta R(b, \ell)$		< 2.8	–	–	–
$\Delta R(b_1, b_2)$		–	–	< 1.4	> 1.4
Lepton charge		–	–	> 0	–
$N_{b\text{-jet}}$		≥ 1	≥ 1	≥ 1	≥ 2
Selection		`tN_high`	`tN_high`-TCR (-TVR)	`tN_high`-WCR (-WVR)	`tN_high`-STCR
$m_{\text{top}}^{\text{reclustered}}$	[GeV]	> 150	veto (> 150)	veto (> 150)	veto
$H_{\text{T,sig}}^{\text{miss}}$		> 25	> 10	>10 (> 25)	> 10
$E_{\text{T}}^{\text{miss}}$	[GeV]	> 520	> 450	> 450	> 450
m_{T}	[GeV]	> 380	> 120	$\in [30, 90]$	$\in [30, 120]$
Topness		> 8	< 8	> 8	> 10
$\Delta R(b, \ell)$		< 2.6	–	–	–
$\Delta R(b_1, b_2)$		–	–	< 1.4	> 1.4
Lepton charge		–	–	> 0	–
$N_{b\text{-jet}}$		≥ 1	≥ 1	≥ 1	≥ 2
Selection		`DM`	`DM`-TCR (-TVR)		
$m_{\text{top}}^{\text{reclustered}}$	[GeV]	> 150	veto (> 150)		
$H_{\text{T,sig}}^{\text{miss}}$		> 15	> 13 (> 15)		
Topness		> 8	< 8		
$\Delta\phi(\text{jet}_i, \vec{p}_{\text{T}}^{\text{ miss}})$	[rad]	> 0.9	> 0.6		

Table 10. Event selections defining the CRs and VRs in `tN_med`, `tN_high` and `DM` relative to their respective signal regions. Only variables for which the selection criteria in the CRs or VRs differ from those in the SRs are listed.

The availability of the STCR allows the normalisation of the single-top background to be constrained from data. The fit to the STCR is performed with both the DS and DR MC schemes, and the resulting two predictions for single-top in the STCR and in the SRs are compatible within uncertainties. Therefore, once the STCR is used to constrain the single-top normalisation, the choice of the DS or DR scheme is found to have a negligible impact on the single-top prediction in the SR. In accordance with ref. [88], the DR scheme is used for the default Wt sample.

Figures 3, 4 and 5 compare data and prediction in CRs and VRs for several variables used in the $\tilde{t}_1 \to t + \tilde{\chi}_1^0$ and `DM` SRs. Good agreement is observed between data and prediction, within uncertainties.

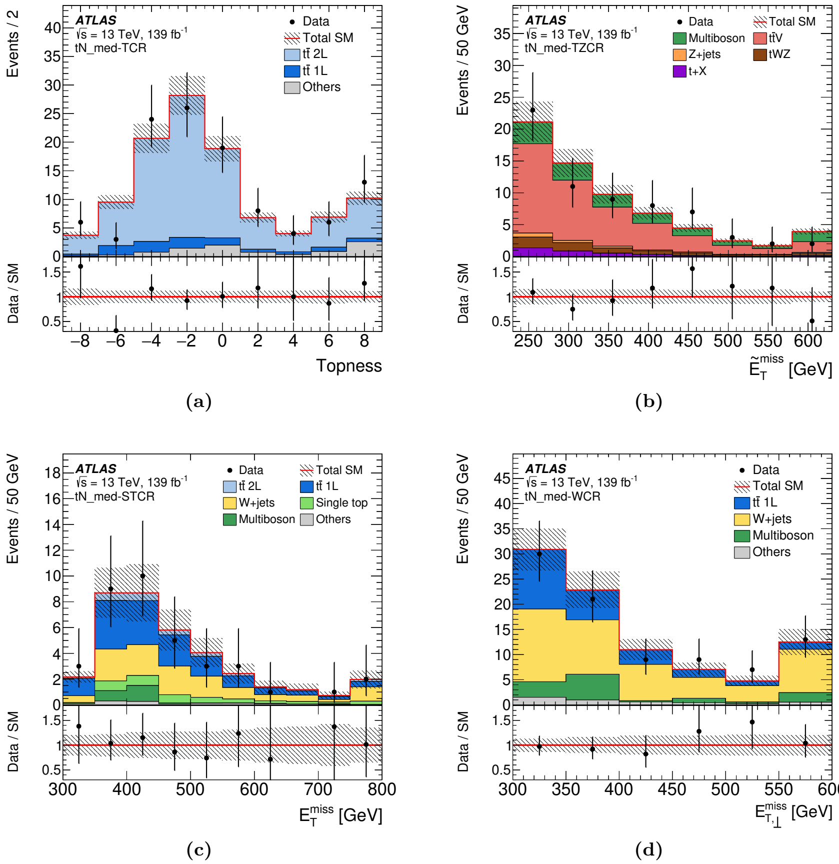

Figure 3. Selected kinematic distributions in `tN_med` CRs: (a) topness in the TCR, (b) $\tilde{E}_{\mathrm{T}}^{\mathrm{miss}}$ in the TZCR, (c) $E_{\mathrm{T}}^{\mathrm{miss}}$ in the STCR, (d) $E_{\mathrm{T},\perp}^{\mathrm{miss}}$ in the WCR. The distributions shown are post-fit, i.e. each background is scaled by a normalisation factor obtained from a background-only likelihood fit to the CRs (see table 14). The hatched area around the total SM prediction and the hatched band in the Data/SM ratio include all statistical and systematic uncertainties. The last (first) bin contains overflows (underflows).

JHEP04(2021)174

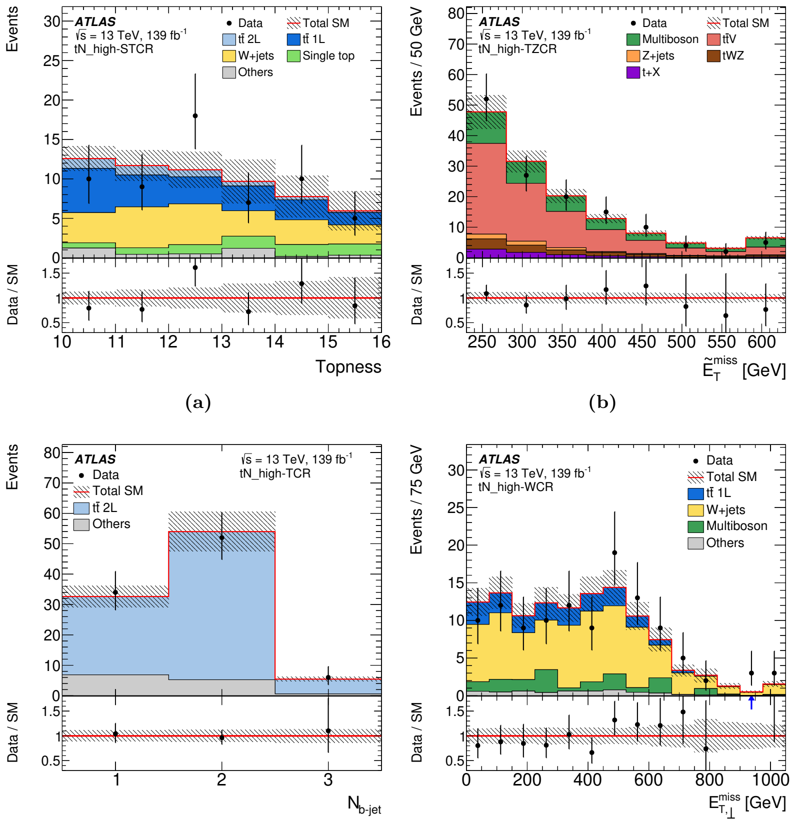

Figure 4. Selected kinematic distributions in `tN_high` CRs: (a) topness in the STCR, (b) $\tilde{E}_{\mathrm{T}}^{\mathrm{miss}}$ in the TZCR, (c) $N_{b\text{-jet}}$ in the TCR, (d) $E_{\mathrm{T},\perp}^{\mathrm{miss}}$ in the WCR. The distributions shown are post-fit, i.e. each background is scaled by a normalisation factor obtained from a background-only likelihood fit to the CRs (see table 14). The hatched area around the total SM prediction and the hatched band in the Data/SM ratio include all statistical and systematic uncertainties. The last (first) bin contains overflows (underflows).

JHEP04(2021)174

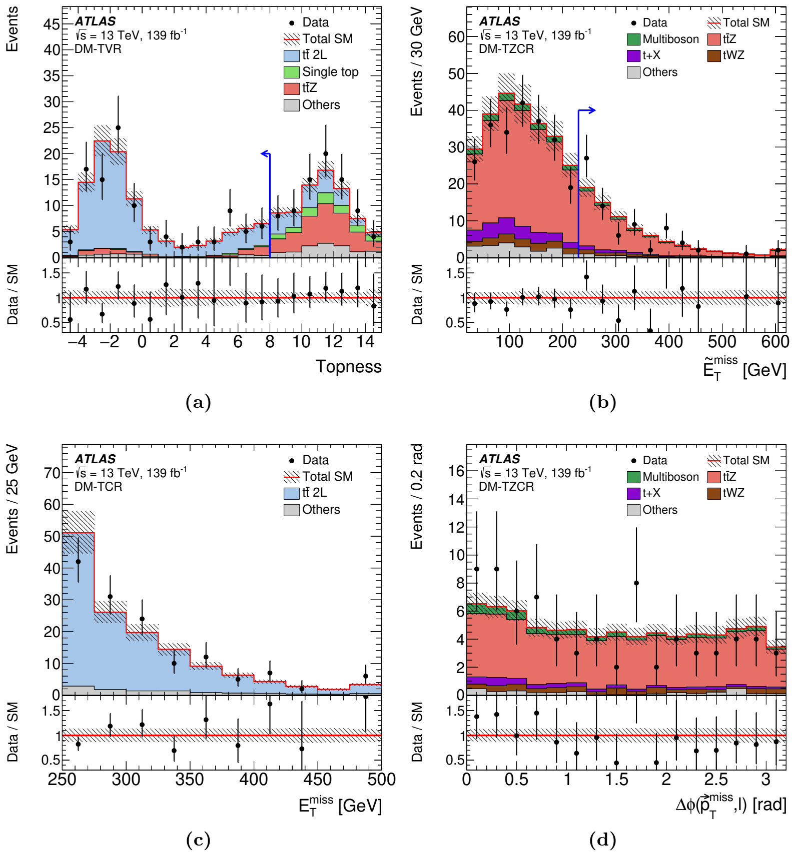

Figure 5. Selected kinematic distributions in DM CRs and VRs: (a) topness in the TVR before applying the topness selection, (b) $\tilde{E}_{\mathrm{T}}^{\mathrm{miss}}$ in the TZCR before applying the $\tilde{E}_{\mathrm{T}}^{\mathrm{miss}}$ selection, (c) $E_{\mathrm{T}}^{\mathrm{miss}}$ in the TCR, (d) $\Delta\phi(\vec{p}_{\mathrm{T}}^{\,\mathrm{miss}}, \ell)$ in the TZCR. For distributions where the requirement on the displayed variable is removed an arrow indicates the final selection on that variable. The distributions shown are post-fit, i.e. each background is scaled by a normalisation factor obtained from a background-only likelihood fit to the CRs (see table 14). The hatched area around the total SM prediction and the hatched band in the Data/SM ratio include all statistical and systematic uncertainties. The last (first) bin contains overflows (underflows).

Selection		tN_diag_low	tN_diag_low-TCR	tN_diag_low-TVR
Leading jet p_T	[GeV]	> 400	[200, 360]	> 400
m_T	[GeV]	> 150	> 110	
Δm_T^{α}	[GeV]	> 40	< 0	
$m_{\tilde{t}_1}^{\mathrm{lep}}$	[GeV]	< 600	–	
Selection		tN_diag_high	tN_diag_high-TCR	tN_diag_high-TVR
Leading jet p_T	[GeV]	> 400	[200, 440]	> 440
E_T^{miss}	[GeV]	> 400	> 350	
m_{T2}	[GeV]	< 360	–	
$\Delta m_T^{\mathrm{dyn}}$	[GeV]	> 60	< 30	
$m_{\tilde{\chi}_1^0}^{\mathrm{dyn}}$	[GeV]	[220, 595]	–	

Table 11. Event selections defining the tN_diag_low and tN_diag_high TCR and TVR relative to their respective signal regions.

8.2 Control and validation regions for compressed $\tilde{t}_1 \to t + \tilde{\chi}_1^0$

The definitions of the control and validation regions for the compressed two-body decays rely on dedicated discriminating variables introduced in section 6.4. The dominant background process in both tN_diag_low and tN_diag_high is $t\bar{t}$ production. Each of these regions has its own dedicated TCR. The TCRs build upon the same N_{jet}, $N_{b\text{-jet}}$, m_T and hard-lepton preselection as the SRs. In both TCRs the selection on the p_T of the leading jet is lower than in the SR, and is chosen to be in the range 200–360 GeV for tN_diag_low and in the range 200–440 GeV for tN_diag_high. In the TCR associated with tN_diag_low, Δm_T^{α} is required to be below zero to avoid signal contamination. In addition, to increase the number of events, the selection on $m_{\tilde{t}_1}^{\mathrm{lep}}$ is removed and the selection on m_T is lowered to 110 GeV. The TCR associated with tN_diag_high requires $\Delta m_T^{\mathrm{dyn}}$ below 30 GeV to ensure orthogonality with the SR and limit signal contamination. To increase the number of events in the TCR associated with tN_diag_high, the E_T^{miss} selection is lowered to 350 GeV and selections on $m_{\tilde{\chi}_1^0}^{\mathrm{dyn}}$ and m_{T2} are removed.

The top background normalisation in the two-body compressed region is validated using one VR for each of the regions tN_diag_low and tN_diag_high. The TVR corresponding to tN_diag_low is identical to the TCR except for the leading jet p_T, required to be above 400 GeV. The TVR associated with tN_diag_high is identical to the TCR, but requires the leading jet p_T to be larger than 440 GeV. Table 11 summarises the definitions of the TCR and TVR for tN_diag_low and tN_diag_high relative to the SR definitions.

Figure 6 compares data and prediction in CRs and VRs for several variables used in the tN_diag_low and tN_diag_high SRs. Good agreement is observed between data and prediction, within uncertainties.

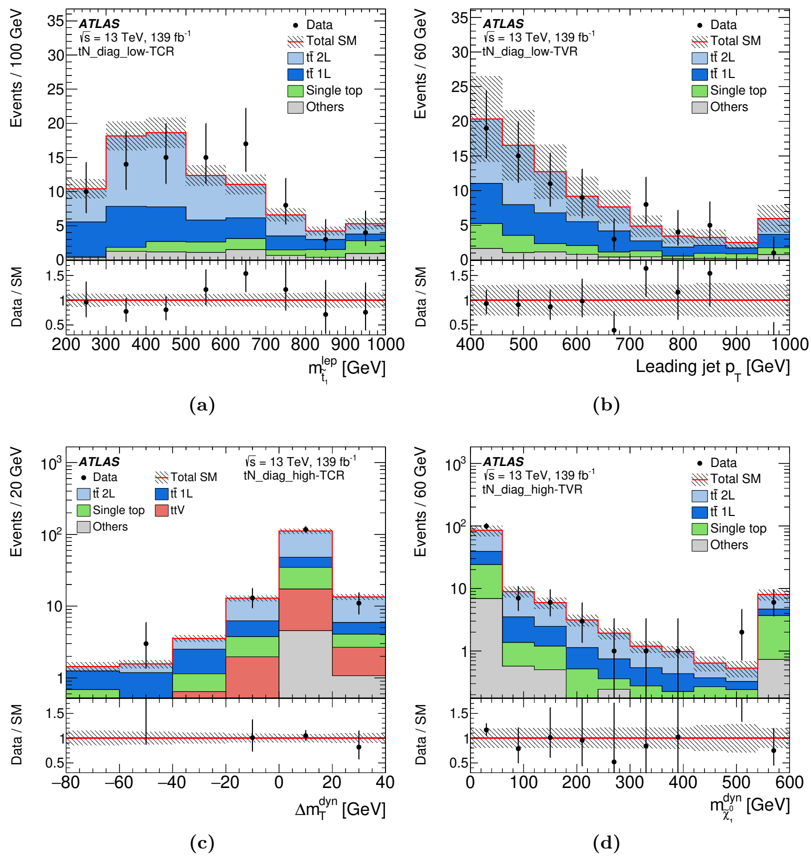

Figure 6. Selected kinematic distributions in `tN_diag_low` and `tN_diag_high` TCRs and TVRs: (a) $m_{\tilde{t}_1}^{\text{lep}}$ in the `tN_diag_low` TCR, (b) leading jet p_{T} in the `tN_diag_low` TVR, (c) $\Delta m_{\text{T}}^{\text{dyn}}$ in the `tN_diag_high` TCR, (d) $m_{\tilde{\chi}_1^0}^{\text{dyn}}$ in the `tN_diag_high` TVR. The distributions shown are post-fit, i.e. each background is scaled by a normalisation factor obtained from a background-only likelihood fit to the CRs (see table 14). The hatched area around the total SM prediction and the hatched band in the Data/SM ratio include all statistical and systematic uncertainties. The last (first) bin contains overflows (underflows).

JHEP04(2021)174

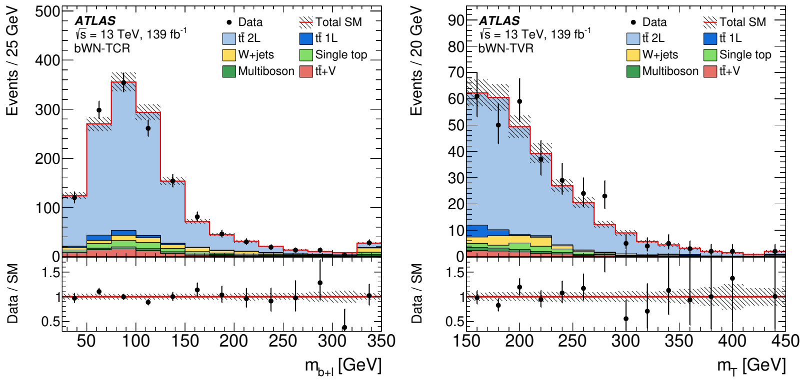

(a) (b)

Figure 7. Selected distributions in the bWN CR and VR: (a) $m_{\mathrm{b}+\ell}$ in the TCR, (b) m_{T} in the TVR. The distributions shown are post-fit, i.e. each background is scaled by a normalisation factor obtained from a background-only likelihood fit to the CRs (see table 14). The hatched area around the total SM prediction and the hatched band in the Data/SM ratio include all statistical and systematic uncertainties. The last (first) bin contains overflows (underflows).

8.3 Control and validation regions for $\tilde{t}_1 \to bW\tilde{\chi}_1^0$

More than 80% of the bWN SR yield consists of dileptonic $t\bar{t}$ events, while other background components range between 2% and 5% of the SR yield. Therefore, the $\tilde{t}_1 \to bW\tilde{\chi}_1^0$ SR requires only a TCR. In addition to the hard-lepton preselection, the bWN SR requires $\mathrm{NN}_{\mathrm{bWN}} > 0.9$ and $m_{\mathrm{T}} > 100$ GeV. To prevent overlap with the signal region, the TCR requires a lower interval of the output score, namely $\mathrm{NN}_{\mathrm{bWN}} \in [0.4, 0.6]$. To preserve the same background composition as the signal region, the selection on m_{T} is tightened to 150 GeV.

The TVR for the $\tilde{t}_1 \to bW\tilde{\chi}_1^0$ signal is designed by selecting $\mathrm{NN}_{\mathrm{bWN}} \in [0.6, 0.65]$, in between the $\mathrm{NN}_{\mathrm{bWN}}$ ranges used for the CR and the SR. In addition, $m_{\mathrm{T}} > 150$ GeV is required to enhance the contribution of semileptonic $t\bar{t}$ events, representative of the background in the SR. The selections that define the TCR and TVR for bWN are summarised in table 6. Figure 7 compares data and prediction in the CR and VR associated with bWN. Good agreement is observed between data and prediction, within uncertainties.

8.4 Control and validation regions for $\tilde{t}_1 \to bff'\tilde{\chi}_1^0$

In the signal region bffN_softb the largest background is W+jets followed by approximately equal amounts of dileptonic and semileptonic $t\bar{t}$. A W+jets control region, WCR, is built upon the same selections as the SR, but to enhance the fraction of W+jets events, $p_{\mathrm{T}}^{\ell}/E_{\mathrm{T}}^{\mathrm{miss}}$ is required to be in the interval [0.16, 0.32] while the lepton charge is required to be positive. A $t\bar{t}$ control region, TCR, is designed to have approximately equal amounts of the two types of $t\bar{t}$ backgrounds. The TCR builds on the same selections as bffN_softb, but it requires

Selection		bffN_softb	bffN_softb-TCR (-TVR)	bffN_softb-WCR (-WVR)
$N_{b\text{-jet}}$		$= 0$	≥ 1	=0
Lepton charge		–	< 0	> 0
$p_{\mathrm{T}}^{\ell}/E_{\mathrm{T}}^{\mathrm{miss}}$		< 0.04	$\in [0.12, 0.25]$ ($\in [0.08, 0.12]$)	$\in [0.16, 0.32]$ ($\in [0.08, 0.16]$)
Selection		bffN_btag	bffN_btag-TCR (-TVR)	bffN_btag-WCR (-WVR)
b-jet p_{T}	[GeV]	< 50	> 100 ($\in [50, 100]$)	–
m_{T}	[GeV]	> 90	> 110	>90
$p_{\mathrm{T}}^{\ell}/E_{\mathrm{T}}^{\mathrm{miss}}$		< 0.05	> 0.05	> 0.05
$\Delta\phi(p_{\mathrm{T}}^{b\text{-jet}}, \vec{p}_{\mathrm{T}}^{\,\mathrm{miss}})$	[rad]	< 1.5	< 1.5	> 2.3 ($\in [1.5, 2.3]$)
Lepton charge		–	–	> 0

Table 12. Event selections defining the CRs and VRs in bffN_softb and bffN_btag relative to their respective signal regions.

the presence of at least one b-tagged jet in order to increase the fraction of $t\bar{t}$ and to ensure orthogonality with the bffN_softb SR. The TCR also requires $p_{\mathrm{T}}^{\ell}/E_{\mathrm{T}}^{\mathrm{miss}}$ to be in the interval [0.12, 0.25] and that the lepton charge be negative for orthogonality with the WCR.

The validation region TVR associated with bffN_softb is defined with the same selections as the TCR, except for the ratio $p_{\mathrm{T}}^{\ell}/E_{\mathrm{T}}^{\mathrm{miss}}$, which is required to be in the interval [0.08, 0.12]. The WVR for bffN_softb has the same selections as the WCR, except $p_{\mathrm{T}}^{\ell}/E_{\mathrm{T}}^{\mathrm{miss}}$ is required to be in the interval [0.08, 0.16]. Table 12 shows the selection differences between the bffN_softb SR and the associated CRs and VRs.

The soft b-tagging efficiency and mis-tag rate depend on the track multiplicity, kinematics of the b-hadrons, and the b-hadron fragmentation. Two highly populated soft b-tagging regions enriched in $t\bar{t}$ and W+jets are defined, where it is found that the track multiplicity differs between data and MC simulations. In each region a weight is defined as a function of the track multiplicity to reweight the MC simulation to the data. After reweighting, good agreement is found between the data and the simulation in a range of secondary vertex variables such as vertex mass, vertex momentum, vertex distance to the primary vertex and vertex track multiplicity. The 'after-to-before-reweighting' ratios of efficiencies and mis-tag rates define scale factors that are derived separately for SHERPA and PYTHIA 8. The largest discrepancy after reweighting is found in the W+jets region and is of the order of 20%. A corresponding 20% systematic uncertainty in the soft b-tagging scale factors is introduced.

In the signal region bffN_btag, the dominant background process is dileptonic $t\bar{t}$, representing almost half of all background events, followed by W+jets. To ensure orthogonality with the SR and limit signal contamination, the TCR control region has the same selections as the SR, but requires the leading b-tagged jet p_{T} to be above 100 GeV, $m_{\mathrm{T}} > 110$ GeV and $p_{\mathrm{T}}^{\ell}/E_{\mathrm{T}}^{\mathrm{miss}} > 0.05$. Compared with the SR, the WCR removes the upper bound on the leading b-tagged jet p_{T}, requires $\Delta\phi(p_{\mathrm{T}}^{b\text{-jet}}, \vec{p}_{\mathrm{T}}^{\,\mathrm{miss}}) > 2.3$, $p_{\mathrm{T}}^{\ell}/E_{\mathrm{T}}^{\mathrm{miss}} > 0.05$ and a positive lepton charge.

The TVR associated with the bffN_btag signal region has the same selections as TCR but the b-tagged jet p_{T} is required to be in the interval [50, 100] GeV, and is thus between

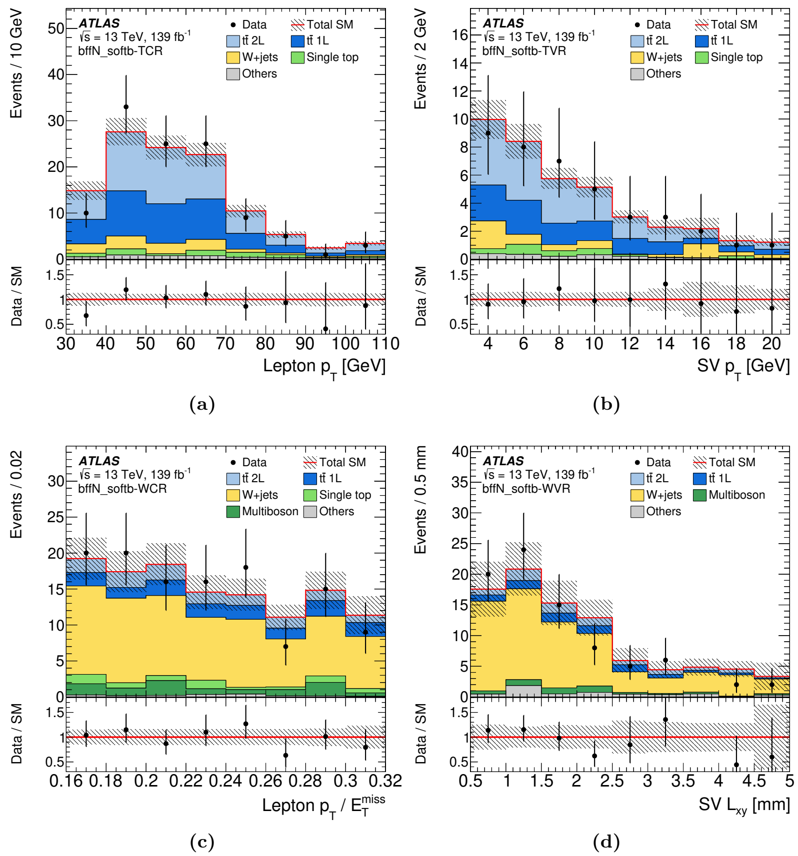

Figure 8. Selected kinematic distributions in `bffN_softb` CRs and VRs: (a) lepton p_{T} in the TCR, (b) transverse component of the total track momentum attached to the secondary vertex, SV p_{T}, in the TVR, (c) $p_{\mathrm{T}}^{\ell}/E_{\mathrm{T}}^{\mathrm{miss}}$ in the WCR, (d) distance from the primary vertex to the secondary vertex in the transverse plane, SV L_{xy}, in the WVR. The distributions shown are post-fit, i.e. each background is scaled by a normalisation factor obtained from a background-only likelihood fit to the CRs (see table 14). The hatched area around the total SM prediction and the hatched band in the Data/SM ratio include all statistical and systematic uncertainties. The last (first) bin contains overflows (underflows).

the signal region and control region. The WVR has the same selections as the WCR except for the angle $\Delta\phi(p_{\mathrm{T}}^{b\text{-jet}}, \vec{p}_{\mathrm{T}}^{\,\mathrm{miss}})$, which is required to be in the intermediate range between the WCR and the SR, namely the interval [1.5, 2.3].

Figures 8 and 9 compare data and predictions in the `bffN_softb` and `bffN_btag` CRs and VRs. Good agreement is observed between data and prediction, within uncertainties.

JHEP04(2021)174

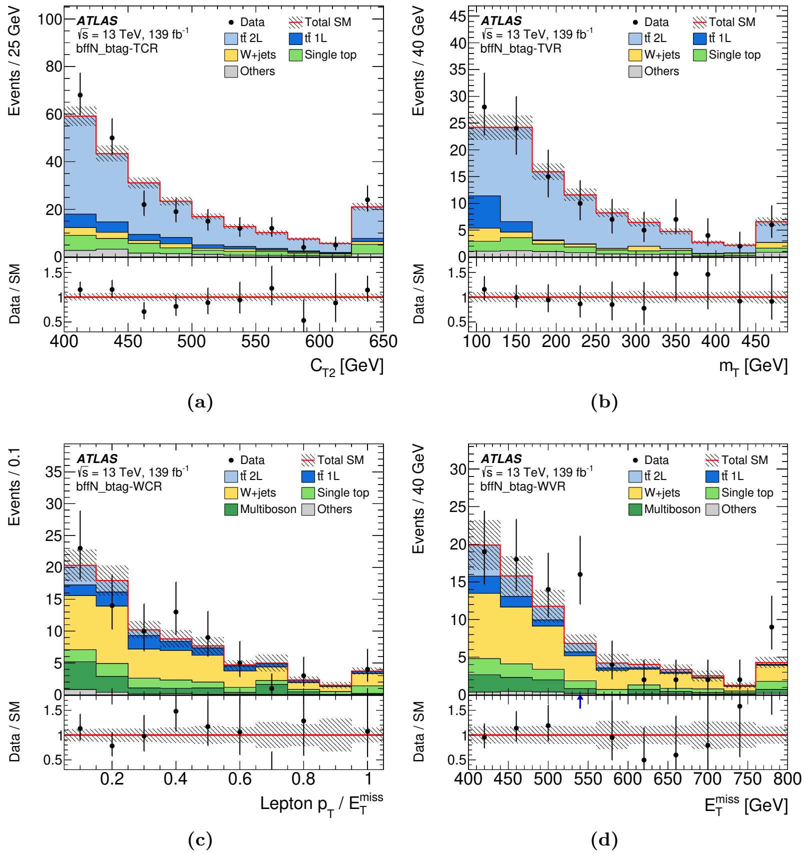

Figure 9. Selected kinematic distributions in `bffN_btag` CRs and VRs: (a) C_{T2} in the TCR, (b) m_{T} in the TVR, (c) $p_{\mathrm{T}}^{\ell}/E_{\mathrm{T}}^{\mathrm{miss}}$ in the WCR, (d) $E_{\mathrm{T}}^{\mathrm{miss}}$ in the WVR. The distributions shown are post-fit, i.e. each background is scaled by a normalisation factor obtained from a background-only likelihood fit to the CRs (see table 14). The hatched area around the total SM prediction and the hatched band in the Data/SM ratio include all statistical and systematic uncertainties. The last (first) bin contains overflows (underflows).

9 Systematic uncertainties

The systematic uncertainties in the background estimates arise from multiple experimental and theoretical sources and can enter the SR background yield either via direct predictions from theoretical cross-sections or from uncertainties in the extrapolation from CRs to SRs. The sources of systematic uncertainties are grouped into categories whose labels are defined in parentheses in the paragraphs below. Their effect on the background predictions in the SRs is summarised in table 13. The systematic uncertainties are included as nuisance parameters constrained by Gaussian probability distributions and profiled in the likelihood fits.

JHEP04(2021)174

Experimental uncertainties arise from imperfect knowledge of the jet energy scale (*JES*), jet energy resolution (*JER*) [113], scale and resolution of the $E_{\mathrm{T}}^{\mathrm{miss}}$ soft term (*E_T^{miss} experimental*) [123], as well as the modelling of the b-tagging or soft b-tagging efficiencies and mis-tag rates [117] (*b-tagging experimental*). Other experimental uncertainties arise from the modelling of the lepton energy scales, energy resolutions, reconstruction and identification efficiencies (*Leptons experimental*). There is also an experimental uncertainty arising from the reweighting of the simulation as a function of the number of interactions per bunch crossing in data and the additional cuts applied to jets to ensure they arise from the hard-scatter primary vertex (*Pile-up*).

Backgrounds such as dibosons and Z+jets, derived directly from a MC prediction and a theoretical cross-section, have theoretical systematic uncertainties (*Theory*) arising from theoretical cross-section calculations, including those related to parton distribution functions and factorisation and normalisation scales. The systematic uncertainty on the integrated luminosity is also included in this category. As shown in table 9, the single-top, $t\bar{t}+Z$ and W+jets backgrounds are also predicted directly from MC simulations for some SRs, in which case the theory uncertainties apply also to those processes.

When the yield from a background such as $t\bar{t}$, single-top, $t\bar{t}+V$ or W+jets is normalised using a CR, modelling uncertainties affect the extrapolation from the control to the signal region, but not the overall normalisation. In each of these cases, the background has a normalisation systematic uncertainty (*Normalisation*) from the fit, arising from the statistical power of the CR for the given background and a modelling uncertainty (*Modelling*) that affects the extrapolation factor from the CR to the SR.

The uncertainties in the modelling of the $t\bar{t}$ background include effects related to the MC event generator, the hadronisation modelling and the amount of initial- and final-state radiation [86]. The MC generator uncertainty is estimated by taking the full difference in event yields between Powheg-Box v2+Pythia 8 and MadGraph5_aMC@NLO v2.6.0 +Pythia 8. Events generated with Powheg-Box v2 are showered and subsequently hadronised with either Pythia 8 or Herwig 7.0 in order to estimate the effect from modelling of the hadronisation. The systematic uncertainty from the amount of initial- and final-state radiation is derived by comparing Powheg-Box results obtained with different shower radiation, NLO radiation and modified factorisation and renormalisation scales.

The single-top Wt process modelling uncertainty is derived from the size of the interference between $t\bar{t}$ and Wt using the $t\bar{t}$, Wt and $WWbb$ samples generated with MadGraph. It is obtained by comparing Wt with the difference between $WWbb$ and $t\bar{t}$. The Wt sample generated with MadGraph is found to be in good agreement with the nominal samples generated with Powheg-Box v2+Pythia 8. For the `tN_med` and `tN_high` SRs where STCR is used, the Wt modelling uncertainty enters via the ratio of the number of Wt events in the signal region to the number in the STCR. Given the potentially large modelling uncertainty in the interference between $t\bar{t}$ and Wt, the modelling uncertainty is also evaluated for the `DM` SR by comparing the predicted single-top yield from Wt with the difference between $WWbb$ and $t\bar{t}$.

The modelling uncertainties considered for $t\bar{t}+Z$ are the renormalisation and factorisation scales, and the amount of initial- and final-state radiation, obtained by

SR Uncertainty [%]	tN_med	tN_high	tN_diag_low	tN_diag_high	bWN	bffN_btag	bffN_softb	DM
$t\bar{t}$ normalisation	4.4	2.7	12.3	15.8	7.8	6.6	3.7	3.0
$t\bar{t}+Z$ normalisation	9.0	6.8	–	–	–	–	–	8.5
W+jets normalisation	3.0	4.8	–	–	–	5.5	11.1	–
Wt normalisation	2.8	3.4	–	–	–	–	–	–
$t\bar{t}$ modelling	3.0	9.1	18.4	29.3	17.6	3.1	3.3	4.1
$t\bar{t}+Z$ modelling	7.7	7.1	–	–	–	–	–	7.4
W+jets modelling	2.3	3.8	–	–	–	4.3	9.7	–
Wt modelling	0.5	0.8	–	–	–	–	–	6.4
JER	10.9	5.1	4.1	5.0	6.1	1.8	7.6	6.5
$E_{\mathrm{T}}^{\mathrm{miss}}$ experimental	0.7	0.4	1.0	0.2	0.9	2.4	3.4	0.1
b-tagging experimental	1.7	3.6	1.3	0.9	1.6	1.9	3.2	3.1
JES	6.0	2.5	4.7	4.1	2.7	6.1	11.7	2.4
Leptons experimental	1.0	1.6	1.3	0.3	0.1	2.3	4.9	0.6
Pile-up	1.1	1.2	1.2	0.3	0.8	1.0	2.1	1.1
Theory	0.9	1.3	1.4	0.5	4.8	3.8	3.7	0.7
MC statistics	4.1	6.6	5.8	3.5	3.1	4.9	17.2	3.2
Total	19	17	24	33	20	12	27	15

Table 13. Summary of the dominant systematic uncertainties as a percentage of the total predicted background yields in the SRs, obtained from the background-only fits described in section 10.

considering the variation of the same parameters used for the $t\bar{t}$ initial- and final-state radiation systematic uncertainties. The W+jets modelling uncertainties include generator modelling, derived by considering an alternative W+jets sample generated with MadGraph as well as modified factorisation, renormalisation, resummation and parton matching scales.

Most of the SRs are binned in one or two variables in order to enhance sensitivity to a wider range of models for exclusion limits. In this situation the normalisation factors to go from the CR to the SR are rederived specifically for each bin of the SR. The modelling systematic uncertainties are also rederived following the scheme above but applied to the normalisation factor from the CR to each specific bin of the SR.

The SUSY signal cross-section uncertainty is taken from an envelope of cross-section predictions using different PDF sets and factorisation and renormalisation scales as described in ref. [134]. The uncertainty in the DM production cross-section is derived from the scale variations and PDF choices. Dedicated uncertainties in the SUSY and DM signal acceptance due to the modelling of additional radiation, factorisation, renormalisation and parton matching scales are considered. The total systematic uncertainty for the SUSY models varies between 9% and 35%, increasing at higher stop mass and at lower values of $\Delta m_{\tilde{t}_1,\tilde{\chi}_1^0}$. For the spin-0 mediator signals the total systematic uncertainty is between 15% and 18%.

JHEP04(2021)174

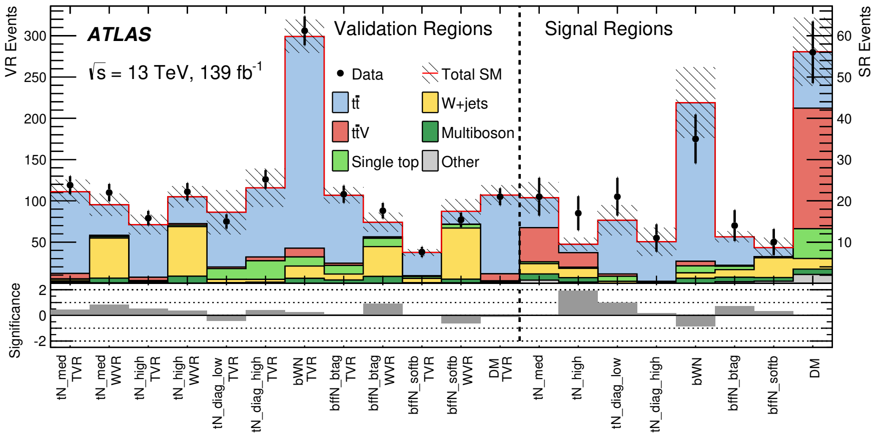

Figure 10. The upper panel shows the comparison between the observed data (n_{obs}) and the predicted SM background (n_{exp}) in all VRs and SRs. The background predictions are obtained using the background-only fit, and the hatched area around the SM prediction includes all uncertainties. The bottom panel shows the Z significance of the observed number of events given the SM expectation.

10 Results

To determine the SM background yields in the SRs, a background-only likelihood fit is performed for each analysis. The fit does not use the signal region data, but only the dedicated CRs to normalise the backgrounds.

The number of observed events and the predicted number of SM background events from the background-only fits in all VRs and SRs are shown in figure 10 together with the Z significance of the observation. The SRs are not mutually exclusive and are therefore not statistically independent. In all SRs, the distributions indicate good agreement between the data and the SM background estimate. The largest excess over the background-only hypothesis is 1.9σ observed in the `tN_high` SR.

The number of observed events together with the predicted number of SM background events in all SRs are summarised in table 14, showing the breakdown of the various backgrounds that contribute to the SRs. The table also lists the results for the fit parameters that control the normalisation of the main backgrounds (normalisation factors, NFs),[6] together with the associated fit uncertainties including the theoretical modelling uncertainties. To quantify the level of agreement of the SM background-only hypothesis with the observations in the SRs, a profile-likelihood-ratio test [135] is performed. The resulting p-values (p_0) are also presented in the table together with the Z significances. For SRs with an observed number of events below the SM prediction, the p_0 values are capped at 0.5. Model-independent upper limits on beyond-the-SM contributions are derived for

[6]The $t\bar{t}$ NFs in the `tN_diag_low`, `bffN_btag`, and `bffN_softb` SRs are applied to semileptonic and dileptonic $t\bar{t}$ events while all other SRs apply the $t\bar{t}$ NFs to the dileptonic component only.

JHEP04(2021)174

	tN_med	tN_high	tN_diag_low	tN_diag_high	bWN	bffN_btag	bffN_softb	DM
Observed	21	17	21	11	35	14	10	56
Total SM	21 ± 4	9.5 ± 1.6	15 ± 4	10.1 ± 3.4	44 ± 9	11.3 ± 1.4	8.7 ± 2.3	56 ± 8
$t\bar{t}$	7.2 ± 1.2	2.0 ± 1.0	13.0 ± 2.8	9.6 ± 2.6	38 ± 9	6.9 ± 1.1	2.2 ± 0.6	14 ± 4
$t\bar{t}V$	8.3 ± 2.5	3.5 ± 1.0	0.55 ± 0.17	0.12 ± 0.04	1.1 ± 1.1	0.21 ± 0.12	0.06 ± 0.04	29 ± 6
Single top	$0.4^{+0.6}_{-0.4}$	$0.27^{+0.34}_{-0.27}$	1.24 ± 0.27	0.26 ± 0.06	1.7 ± 1.7	0.8 ± 0.5	0.22 ± 0.08	7 ± 4
W+jets	2.5 ± 2.3	2.3 ± 1.0	0.41 ± 0.13	0.080 ± 0.020	1.3 ± 0.6	1.9 ± 0.8	4.8 ± 2.1	2.56 ± 0.24
Multiboson	1.49 ± 0.21	1.06 ± 0.16	0.070 ± 0.020	0.020 ± 0.010	1.22 ± 0.30	1.07 ± 0.35	0.89 ± 0.32	1.31 ± 0.18
Other	0.78 ± 0.06	0.320 ± 0.024	–	–	–	0.40 ± 0.13	0.52 ± 0.19	2.15 ± 0.16
$t\bar{t}$ NF	$0.98^{+0.14}_{-0.12}$	0.90 ± 0.12	$0.88^{+0.13}_{-0.12}$	$0.73^{+0.14}_{-0.13}$	1.06 ± 0.10	$0.80^{+0.09}_{-0.08}$	0.68 ± 0.10	$1.12^{+0.15}_{-0.13}$
$t\bar{t}V$ NF	$0.95^{+0.22}_{-0.20}$	0.92 ± 0.17	–	–	–	–	–	$1.18^{+0.20}_{-0.18}$
Single top NF	$0.11^{+0.26}_{-0.11}$	$0.12^{+0.22}_{-0.12}$	–	–	–	–	–	–
W+jets NF	$0.96^{+0.25}_{-0.23}$	0.86 ± 0.17	–	–	–	0.83 ± 0.28	$1.04^{+0.22}_{-0.20}$	-
p_0 (Z)	0.49 (0.03)	0.01 (2.20)	0.17 (0.95)	0.31 (0.50)	0.50 (0.00)	0.20 (0.84)	0.26 (0.64)	0.50 (0.00)
$N^{\text{limit}}_{\text{non-SM}}$ exp.	$12.4^{+5.4}_{-2.6}$	$9.8^{+2.8}_{-1.8}$	$14.1^{+4.8}_{-3.3}$	$9.7^{+3.7}_{-2.1}$	$21.8^{+7.6}_{-7.9}$	$8.6^{+3.6}_{-1.2}$	$8.9^{+3.8}_{-2.0}$	$27.4^{+7.6}_{-5.0}$
$N^{\text{limit}}_{\text{non-SM}}$ obs.	12.9	16.2	17.7	10.9	15.3	11.7	10.5	28.2

Table 14. The number of observed events in the various SRs together with the expected numbers of background events and their uncertainties as predicted by the background-only fits, the normalisation factors for the background predictions obtained in the fit, the probabilities (represented by p_0 and Z values) that the observed numbers of events are compatible with the background-only hypothesis, and the expected ($N^{\text{limit}}_{\text{non-SM}}$ exp.) and observed ($N^{\text{limit}}_{\text{non-SM}}$ obs.) 95% CL upper limits on the number of beyond-SM events.

each SR. A generic signal model is assumed that contributes only to the SR and for which neither experimental nor theoretical systematic uncertainties except for the luminosity uncertainty are considered. All limits are calculated using the CL_s prescription [136]. The NFs are compatible with unity in most cases. One exception is for the single-top NFs in the `tN_med` and `tN_high` SRs. The single-top NFs are significantly below unity when using the DR scheme for the treatment of the interference between the Wt and $t\bar{t}$ processes. When changing to the DS scheme, the NFs become larger than unity but the predicted number of single-top events in the signal regions after the fit does not change significantly. This is explained by the fact that the DS and DR schemes give the same SR to STCR event yield ratio, within uncertainties. The $t\bar{t}$ NFs in `tN_diag_high`, `bffN_btag` and `bffN_softb` are below unity, which could potentially point to some mismodelling in this extreme region of phase-space. But good agreement is seen in the $t\bar{t}$ VRs, giving confidence in the $t\bar{t}$ background estimates.

Figures 11 and 12 show comparisons between the observed data and the SM background prediction with all SR selections applied except the requirement on the plotted variable. The expected distributions from representative signal benchmark models are overlaid.

JHEP04(2021)174

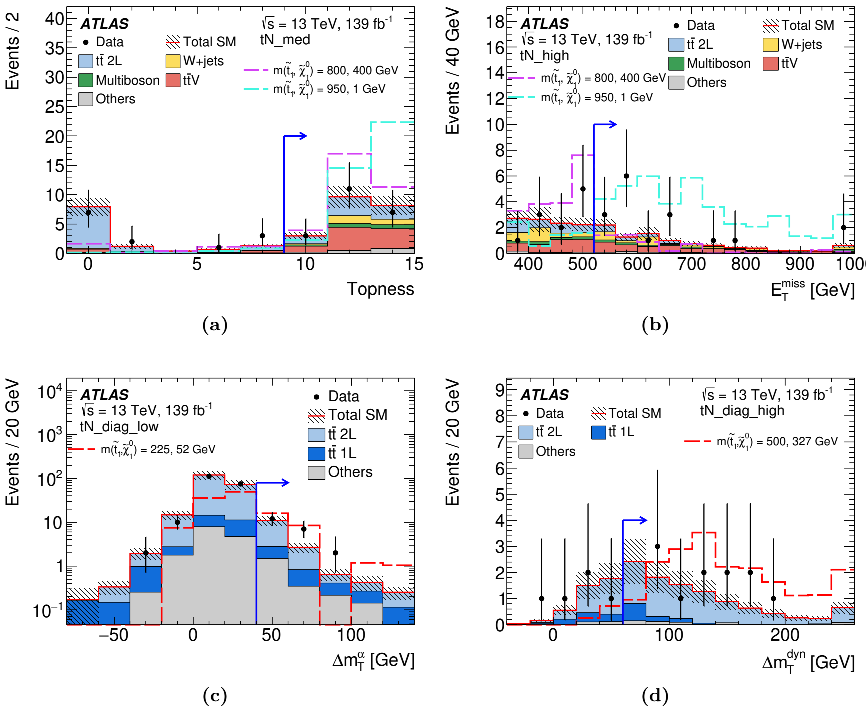

Figure 11. Kinematic distributions in the (a) `tN_med`, (b) `tN_high`, (c) `tN_diag_low` and (d) `tN_diag_high` SRs. The full event selection in the corresponding signal region is applied, except for the requirement (indicated by an arrow) that is imposed on the variable being plotted. The distributions shown are post-fit, i.e. each background is scaled by a normalisation factor obtained from a background-only likelihood fit to the CRs (see table 14). In addition to the background prediction, a signal model is shown on each plot. The hatched area around the total SM prediction includes statistical and experimental uncertainties. The last (first) bin contains overflows (underflows).

11 Interpretations

No significant excess is observed, and exclusion limits based on profile-likelihood fits are set for the stop pair production models and the spin-0 mediator models. Exclusion limits at 95% confidence level (CL) are obtained by selecting the signal region with the lowest expected $\mathrm{CL_s}$ value for each signal model and the exclusion contours are derived by interpolating in the $\mathrm{CL_s}$ value. The signal uncertainties and potential signal contributions to all regions are taken into account, and all uncertainties except those in the theoretical signal cross-section are included in the fit. In all exclusion plots, the $\pm 1\sigma_{\mathrm{exp}}$ uncertainty band indicates how much the expected limit is affected by the systematic and statistical uncertainties included in the fit. The $\pm 1\sigma^{\mathrm{SUSY}}_{\mathrm{theory}}$ uncertainty lines around the observed limit illustrate the change

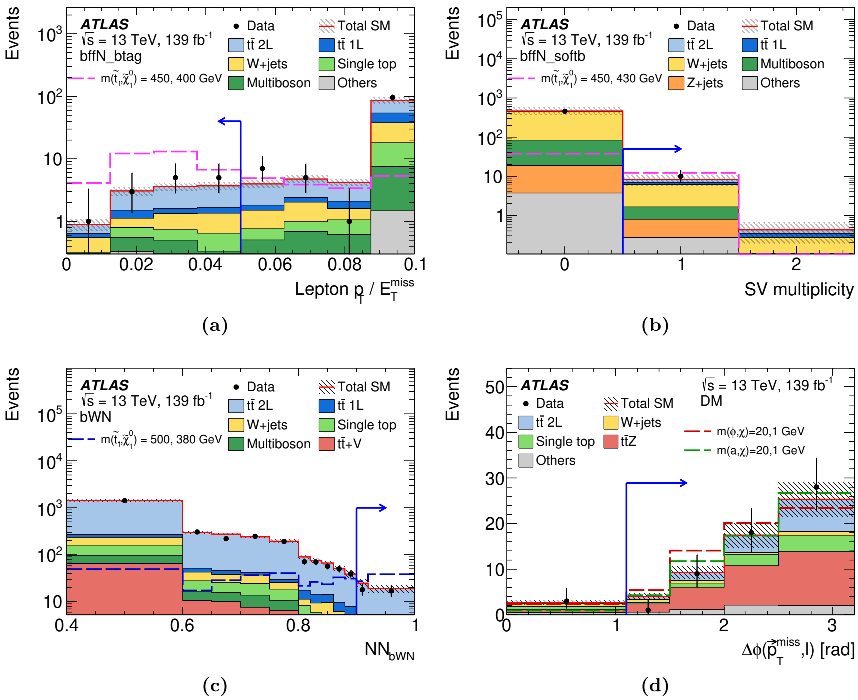

Figure 12. Kinematic distributions in the (a) `bffN_btag`, (b) `bffN_softb`, (c) `bWN` and (d) `DM` SRs. The full event selection in the corresponding signal region is applied, except for the requirement (indicated by an arrow) that is imposed on the variable being plotted. In the `DM` SR, the signal is normalised under the assumption of the coupling strength g=1.0. The distributions shown are post-fit, i.e. each background is scaled by a normalisation factor obtained from a background-only likelihood fit to the CRs (see table 14). In addition to the background prediction, a signal model is shown on each plot. The hatched area around the total SM prediction includes statistical and experimental uncertainties. The last (first) bin contains overflows (underflows).

in the observed limit as the nominal signal cross-section is scaled up and down by the theoretical cross-section uncertainty.

Figures 13 and 14 show the expected and observed exclusion contours as a function of the stop mass, the neutralino mass and the mass difference between the stop and the neutralino, for the $\tilde{t}_1 \to t + \tilde{\chi}_1^0$, $\tilde{t}_1 \to bW\tilde{\chi}_1^0$ and $\tilde{t}_1 \to bff'\tilde{\chi}_1^0$ scenarios. In models with a massless neutralino, stop masses up to 1200 GeV are excluded at 95% CL. In the diagonal region, where the mass difference between the stop and the neutralino coincides with the mass of the top quark, stop masses up to 600 GeV are excluded, which covers the previously unexcluded diagonal region between 210 GeV and 250 GeV in stop mass. In the three-body (four-body) region, stop masses up to 710 GeV (640 GeV) are excluded for a neutralino mass

JHEP04(2021)174

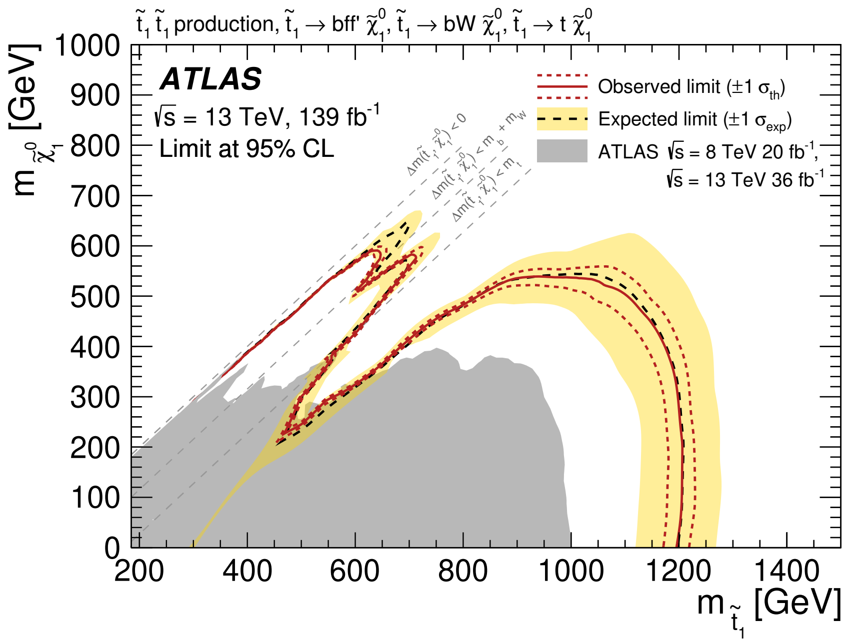

Figure 13. Expected and observed 95% CL excluded regions in the plane of $m_{\tilde{\chi}^0_1}$ and $m_{\tilde{t}_1}$ for direct stop pair production assuming either a $\tilde{t}_1 \to t + \tilde{\chi}^0_1$, $\tilde{t}_1 \to bW\tilde{\chi}^0_1$ or $\tilde{t}_1 \to bff'\tilde{\chi}^0_1$ decay with a branching ratio of 100%. The excluded regions from previous publications [29–31, 137] are shown by the shaded area and include additional topologies. The diagonal dashed lines indicate the kinematical border of the stop decay modes.

of approximately 580 GeV. The small excess observed in `tN_high` does not appear because the exclusion limits are obtained from the shape-fit in the `tN_med` signal region (table 4). The $E_{\mathrm{T},\perp}^{\mathrm{miss}}$ requirement applied in `tN_med` but not in `tN_high` removes most of the excess. The shape-fit is designed to have better expected sensitivity than the single-bin SRs over the whole $\tilde{t}_1 \to t + \tilde{\chi}^0_1$ parameter space.

Figure 15 shows the upper limit on the ratio of the production cross-section for the spin-0 mediator model to the theoretical cross-section. Limits are shown under the hypothesis of a scalar or pseudoscalar mediator for a fixed DM candidate mass. Scalar and pseudoscalar mediator masses up to approximately 200 GeV are excluded at 95% CL, assuming a 1 GeV dark-matter particle mass and a common coupling of $g = 1$ to SM and dark-matter particles. With the common coupling reduced to $g = 0.8$, mediator masses up to approximately 100 GeV are excluded. Models with a mediator mass of 10 GeV and a dark-matter particle mass of 1 GeV are excluded down to a coupling of approximately $g = 0.7$.

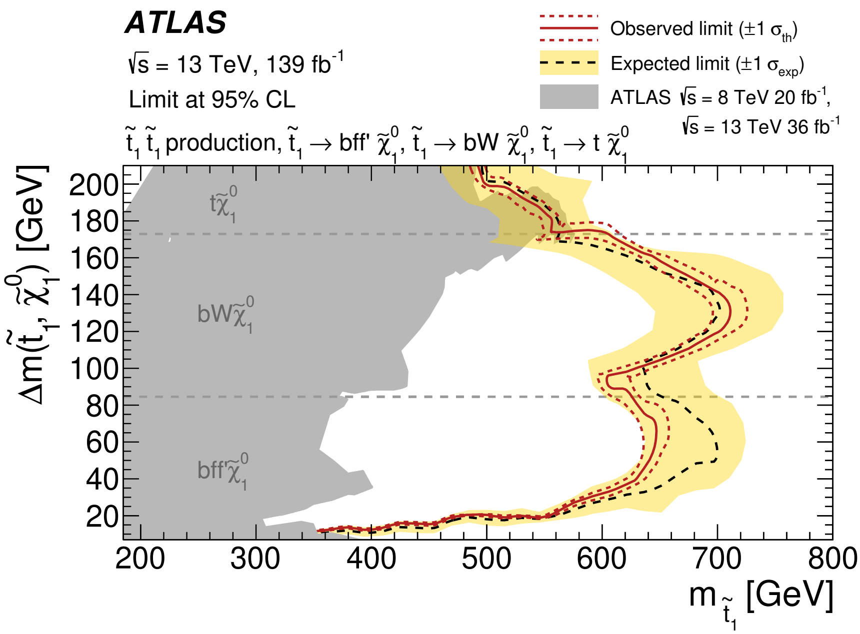

Figure 14. Expected and observed 95% CL excluded regions in the plane of $\Delta(m_{\tilde{t}_1}, m_{\tilde{\chi}^0_1})$ and $m_{\tilde{t}_1}$ for direct stop pair production assuming either a $\tilde{t}_1 \to t + \tilde{\chi}^0_1$, $\tilde{t}_1 \to bW\tilde{\chi}^0_1$ or $\tilde{t}_1 \to bff'\tilde{\chi}^0_1$ decay with a branching ratio of 100%. The excluded regions from previous publications [29–31, 137] are shown by the shaded area and include additional topologies. The horizontal dashed lines indicate the kinematical border of the stop decay modes.

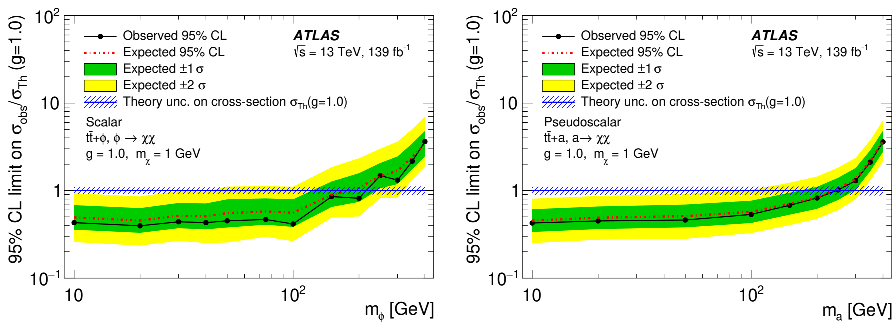

(a) (b)

Figure 15. Upper limit on the ratio of the production cross-section for the spin-0 mediator model to the theoretical cross-section under the hypothesis of (a) a scalar or (b) a pseudoscalar mediator. The limit is shown as a function of the mediator mass for a fixed mass of the DM candidate of 1 GeV. The coupling of the mediator to SM and DM particles is assumed to be $g = 1$.

JHEP04(2021)174

12 Conclusion

This paper presents searches for direct stop pair production covering various regions of SUSY phase space and searches for a spin-0 mediator decaying into pair-produced dark-matter particles. The searches use the final state with one isolated lepton, jets, and $E_{\mathrm{T}}^{\mathrm{miss}}$.

The analysis uses $139\,\mathrm{fb}^{-1}$ of pp collision data collected with the ATLAS detector at the LHC at a centre-of-mass energy of $\sqrt{s} = 13\,\mathrm{TeV}$. The largest excess over the background-only hypothesis is 1.9σ in the `tN_high` signal region. As no significant deviation from the Standard Model expectation is observed, exclusion limits at 95% confidence level are derived for the models considered. Stops are excluded up to 1200 GeV (710 GeV) in the two-body (three-body) decay scenario, extended from about 1000 GeV (400–600 GeV) in previous results. The introduction of ML techniques contributes to the significantly improved sensitivity in the challenging three-body decay scenario. In the four-body scenario, the exclusion of stops is extended from about 400 GeV in earlier results to up to 640 GeV for a stop-neutralino mass difference of 60 GeV. The introduction of the soft b-tagging algorithm contributes to the significantly improved sensitivity at small mass differences between the stop and the lightest neutralino. Scalar and pseudoscalar dark-matter mediators are excluded up to 200 GeV for a common coupling of $g = 1$ to Standard Model and dark-matter particles, from 100 GeV in earlier results. The introduction of a shape-fit in the DM signal region contributes to this improvement.

Acknowledgments

We thank CERN for the very successful operation of the LHC, as well as the support staff from our institutions without whom ATLAS could not be operated efficiently.

We acknowledge the support of ANPCyT, Argentina; YerPhI, Armenia; ARC, Australia; BMWFW and FWF, Austria; ANAS, Azerbaijan; SSTC, Belarus; CNPq and FAPESP, Brazil; NSERC, NRC and CFI, Canada; CERN; ANID, Chile; CAS, MOST and NSFC, China; COLCIENCIAS, Colombia; MSMT CR, MPO CR and VSC CR, Czech Republic; DNRF and DNSRC, Denmark; IN2P3-CNRS and CEA-DRF/IRFU, France; SRNSFG, Georgia; BMBF, HGF and MPG, Germany; GSRT, Greece; RGC and Hong Kong SAR, China; ISF and Benoziyo Center, Israel; INFN, Italy; MEXT and JSPS, Japan; CNRST, Morocco; NWO, Netherlands; RCN, Norway; MNiSW and NCN, Poland; FCT, Portugal; MNE/IFA, Romania; MES of Russia and NRC KI, Russia Federation; JINR; MESTD, Serbia; MSSR, Slovakia; ARRS and MIZŠ, Slovenia; DST/NRF, South Africa; MICINN, Spain; SRC and Wallenberg Foundation, Sweden; SERI, SNSF and Cantons of Bern and Geneva, Switzerland; MOST, Taiwan; TAEK, Turkey; STFC, United Kingdom; DOE and NSF, United States of America. In addition, individual groups and members have received support from BCKDF, CANARIE, Compute Canada and CRC, Canada; ERC, ERDF, Horizon 2020, Marie Skłodowska-Curie Actions and COST, European Union; Investissements d'Avenir Labex, Investissements d'Avenir Idex and ANR, France; DFG and AvH Foundation, Germany; Herakleitos, Thales and Aristeia programmes co-financed by EU-ESF and the Greek NSRF, Greece; BSF-NSF and GIF, Israel; La Caixa Banking Foundation, CERCA

JHEP04(2021)174

Programme Generalitat de Catalunya and PROMETEO and GenT Programmes Generalitat Valenciana, Spain; Göran Gustafssons Stiftelse, Sweden; The Royal Society and Leverhulme Trust, United Kingdom.

The crucial computing support from all WLCG partners is acknowledged gratefully, in particular from CERN, the ATLAS Tier-1 facilities at TRIUMF (Canada), NDGF (Denmark, Norway, Sweden), CC-IN2P3 (France), KIT/GridKA (Germany), INFN-CNAF (Italy), NL-T1 (Netherlands), PIC (Spain), ASGC (Taiwan), RAL (U.K.) and BNL (U.S.A.), the Tier-2 facilities worldwide and large non-WLCG resource providers. Major contributors of computing resources are listed in ref. [138].

References

[1] Y.A. Golfand and E.P. Likhtman, *Extension of the Algebra of Poincaré Group Generators and Violation of p Invariance*, *JETP Lett.* **13** (1971) 323 [INSPIRE].

[2] D.V. Volkov and V.P. Akulov, *Is the Neutrino a Goldstone Particle?*, *Phys. Lett. B* **46** (1973) 109 [INSPIRE].

[3] J. Wess and B. Zumino, *Supergauge Transformations in Four-Dimensions*, *Nucl. Phys. B* **70** (1974) 39 [INSPIRE].

[4] J. Wess and B. Zumino, *Supergauge Invariant Extension of Quantum Electrodynamics*, *Nucl. Phys. B* **78** (1974) 1 [INSPIRE].

[5] S. Ferrara and B. Zumino, *Supergauge invariant Yang-Mills theories*, *Nucl. Phys. B* **79** (1974) 413.

[6] A. Salam and J.A. Strathdee, *Supersymmetry and Nonabelian Gauges*, *Phys. Lett. B* **51** (1974) 353 [INSPIRE].

[7] G.R. Farrar and P. Fayet, *Phenomenology of the Production, Decay, and Detection of New Hadronic States Associated with Supersymmetry*, *Phys. Lett. B* **76** (1978) 575 [INSPIRE].

[8] G. D'Ambrosio, G.F. Giudice, G. Isidori and A. Strumia, *Minimal flavor violation: An Effective field theory approach*, *Nucl. Phys. B* **645** (2002) 155 [hep-ph/0207036] [INSPIRE].

[9] G. Isidori and D.M. Straub, *Minimal Flavour Violation and Beyond*, *Eur. Phys. J. C* **72** (2012) 2103 [arXiv:1202.0464] [INSPIRE].

[10] ATLAS collaboration, *Observation of a new particle in the search for the Standard Model Higgs boson with the ATLAS detector at the LHC*, *Phys. Lett. B* **716** (2012) 1 [arXiv:1207.7214] [INSPIRE].

[11] CMS collaboration, *Observation of a New Boson at a Mass of* 125 *GeV with the CMS Experiment at the LHC*, *Phys. Lett. B* **716** (2012) 30 [arXiv:1207.7235] [INSPIRE].

[12] S. Dimopoulos and H. Georgi, *Softly broken supersymmetry and* SU(5), *Nucl. Phys. B* **193** (1981) 150.

[13] E. Witten, *Dynamical Breaking of Supersymmetry*, *Nucl. Phys. B* **188** (1981) 513 [INSPIRE].

JHEP04(2021)174

[14] M. Dine, W. Fischler and M. Srednicki, *Supersymmetric Technicolor*, *Nucl. Phys. B* **189** (1981) 575 [INSPIRE].

[15] S. Dimopoulos and S. Raby, *Supercolor*, *Nucl. Phys. B* **192** (1981) 353 [INSPIRE].

[16] N. Sakai, *Naturalness in Supersymmetric Guts*, *Z. Phys. C* **11** (1981) 153 [INSPIRE].

[17] R.K. Kaul and P. Majumdar, *Cancellation of Quadratically Divergent Mass Corrections in Globally Supersymmetric Spontaneously Broken Gauge Theories*, *Nucl. Phys. B* **199** (1982) 36 [INSPIRE].

[18] R. Barbieri and G.F. Giudice, *Upper Bounds on Supersymmetric Particle Masses*, *Nucl. Phys. B* **306** (1988) 63 [INSPIRE].

[19] B. de Carlos and J.A. Casas, *One loop analysis of the electroweak breaking in supersymmetric models and the fine tuning problem*, *Phys. Lett. B* **309** (1993) 320 [hep-ph/9303291] [INSPIRE].

[20] S. Weinberg, *Implications of Dynamical Symmetry Breaking*, *Phys. Rev. D* **13** (1976) 974 [INSPIRE].

[21] E. Gildener, *Gauge Symmetry Hierarchies*, *Phys. Rev. D* **14** (1976) 1667 [INSPIRE].

[22] S. Weinberg, *Implications of dynamical symmetry breaking: An addendum*, *Phys. Rev. D* **19** (1979) 1277. [INSPIRE].

[23] L. Susskind, *Dynamics of Spontaneous Symmetry Breaking in the Weinberg-Salam Theory*, *Phys. Rev. D* **20** (1979) 2619 [INSPIRE].

[24] P. Fayet, *Supersymmetry and Weak, Electromagnetic and Strong Interactions*, *Phys. Lett. B* **64** (1976) 159 [INSPIRE].

[25] P. Fayet, *Spontaneously Broken Supersymmetric Theories of Weak, Electromagnetic and Strong Interactions*, *Phys. Lett. B* **69** (1977) 489 [INSPIRE].

[26] P. Fayet, *Relations Between the Masses of the Superpartners of Leptons and Quarks, the Goldstino Couplings and the Neutral Currents*, *Phys. Lett. B* **84** (1979) 416 [INSPIRE].

[27] H. Goldberg, *Constraint on the Photino Mass from Cosmology*, *Phys. Rev. Lett.* **50** (1983) 1419 [*Erratum ibid.* **103** (2009) 099905] [INSPIRE].

[28] J.R. Ellis, J.S. Hagelin, D.V. Nanopoulos, K.A. Olive and M. Srednicki, *Supersymmetric Relics from the Big Bang*, *Nucl. Phys. B* **238** (1984) 453 [INSPIRE].

[29] ATLAS collaboration, *Search for top-squark pair production in final states with one lepton, jets, and missing transverse momentum using* 36 fb^{-1} *of* $\sqrt{s} = 13$ *TeV pp collision data with the ATLAS detector*, *JHEP* **06** (2018) 108 [arXiv:1711.11520] [INSPIRE].

[30] ATLAS collaboration, *Search for a scalar partner of the top quark in the jets plus missing transverse momentum final state at* $\sqrt{s} = 13$ *TeV with the ATLAS detector*, *JHEP* **12** (2017) 085 [arXiv:1709.04183] [INSPIRE].

[31] ATLAS collaboration, *Search for direct top squark pair production in final states with two leptons in* $\sqrt{s} = 13$ *TeV pp collisions with the ATLAS detector*, *Eur. Phys. J. C* **77** (2017) 898 [arXiv:1708.03247] [INSPIRE].

[32] ATLAS collaboration, *ATLAS Run 1 searches for direct pair production of third-generation squarks at the Large Hadron Collider*, *Eur. Phys. J. C* **75** (2015) 510 [*Erratum ibid.* **76** (2016) 153] [arXiv:1506.08616] [INSPIRE].

[33] CMS collaboration, *Searches for physics beyond the standard model with the M_{T2} variable in hadronic final states with and without disappearing tracks in proton-proton collisions at $\sqrt{s} = 13$ TeV*, Eur. Phys. J. C **80** (2020) 3 [arXiv:1909.03460] [INSPIRE].

[34] CMS collaboration, *Search for direct production of supersymmetric partners of the top quark in the all-jets final state in proton-proton collisions at $\sqrt{s} = 13$ TeV*, *JHEP* **10** (2017) 005 [arXiv:1707.03316] [INSPIRE].

[35] CMS collaboration, *Search for top squark pair production in pp collisions at $\sqrt{s} = 13$ TeV using single lepton events*, *JHEP* **10** (2017) 019 [arXiv:1706.04402] [INSPIRE].

[36] CMS collaboration, *Search for top squarks and dark matter particles in opposite-charge dilepton final states at $\sqrt{s} = 13$ TeV*, *Phys. Rev. D* **97** (2018) 032009 [arXiv:1711.00752] [INSPIRE].

[37] CMS collaboration, *Searches for pair production of third-generation squarks in $\sqrt{s} = 13$ TeV pp collisions*, *Eur. Phys. J. C* **77** (2017) 327 [arXiv:1612.03877] [INSPIRE].

[38] CMS collaboration, *A search for new phenomena in pp collisions at $\sqrt{s} = 13$ TeV in final states with missing transverse momentum and at least one jet using the α_T variable*, *Eur. Phys. J. C* **77** (2017) 294 [arXiv:1611.00338] [INSPIRE].

[39] CMS collaboration, *Inclusive search for supersymmetry using razor variables in pp collisions at $\sqrt{s} = 13$ TeV*, *Phys. Rev. D* **95** (2017) 012003 [arXiv:1609.07658] [INSPIRE].

[40] CMS collaboration, *Search for direct top squark pair production in events with one lepton, jets, and missing transverse momentum at* 13 *TeV with the CMS experiment*, *JHEP* **05** (2020) 032 [arXiv:1912.08887] [INSPIRE].

[41] ATLAS collaboration, *Search for dark matter produced in association with bottom or top quarks in $\sqrt{s} = 13$ TeV pp collisions with the ATLAS detector*, *Eur. Phys. J. C* **78** (2018) 18 [arXiv:1710.11412] [INSPIRE].

[42] CMS collaboration, *Search for dark matter produced in association with heavy-flavor quark pairs in proton-proton collisions at $\sqrt{s} = 13$ TeV*, *Eur. Phys. J. C* **77** (2017) 845 [arXiv:1706.02581] [INSPIRE].

[43] J. Alwall, M.-P. Le, M. Lisanti and J.G. Wacker, *Searching for Directly Decaying Gluinos at the Tevatron*, *Phys. Lett. B* **666** (2008) 34 [arXiv:0803.0019] [INSPIRE].

[44] J. Alwall, P. Schuster and N. Toro, *Simplified Models for a First Characterization of New Physics at the LHC*, *Phys. Rev. D* **79** (2009) 075020 [arXiv:0810.3921] [INSPIRE].

[45] LHC New Physics Working Group collaboration, *Simplified Models for LHC New Physics Searches*, *J. Phys. G* **39** (2012) 105005 [arXiv:1105.2838] [INSPIRE].

[46] D. Abercrombie et al., *Dark Matter Benchmark Models for Early LHC Run-2 Searches: Report of the ATLAS/CMS Dark Matter Forum*, *Phys. Dark Univ.* **27** (2020) 100371 [arXiv:1507.00966] [INSPIRE].

[47] ATLAS collaboration, *The ATLAS Experiment at the CERN Large Hadron Collider*, 2008 *JINST* **3** S08003 [INSPIRE].

[48] ATLAS collaboration, *Atlas Insertable B-Layer Technical Design Report*, ATLAS-TDR-19 (2010).

[49] ATLAS collaboration, *ATLAS Insertable B-Layer Technical Design Report Addendum*, ATLAS-TDR-19-ADD-1 (2012).

[50] ATLAS IBL collaboration, *Production and Integration of the ATLAS Insertable B-Layer*, 2018 *JINST* **13** T05008 [arXiv:1803.00844] [INSPIRE].

[51] ATLAS collaboration, *Optimisation of the ATLAS b-tagging performance for the 2016 LHC Run*, ATL-PHYS-PUB-2016-012 (2016).

[52] ATLAS collaboration, *Performance of the ATLAS Trigger System in 2015*, *Eur. Phys. J. C* **77** (2017) 317 [arXiv:1611.09661] [INSPIRE].

[53] ATLAS collaboration, *Luminosity determination in pp collisions at* $\sqrt{s} = 8$ *TeV using the ATLAS detector at the LHC*, *Eur. Phys. J. C* **76** (2016) 653 [arXiv:1608.03953] [INSPIRE].

[54] G. Avoni et al., *The new LUCID-2 detector for luminosity measurement and monitoring in ATLAS*, 2018 *JINST* **13** P07017 [INSPIRE].

[55] S. Alioli, P. Nason, C. Oleari and E. Re, *A general framework for implementing NLO calculations in shower Monte Carlo programs: the POWHEG BOX*, *JHEP* **06** (2010) 043 [arXiv:1002.2581] [INSPIRE].

[56] NNPDF collaboration, *Parton distributions for the LHC Run II*, *JHEP* **04** (2015) 040 [arXiv:1410.8849] [INSPIRE].

[57] T. Sjöstrand, S. Mrenna and P.Z. Skands, *A Brief Introduction to PYTHIA 8.1*, *Comput. Phys. Commun.* **178** (2008) 852 [arXiv:0710.3820] [INSPIRE].

[58] *ATLAS PYTHIA 8 tunes to 7 TeV data*, ATL-PHYS-PUB-2014-021 (2014).

[59] M. Czakon, P. Fiedler and A. Mitov, *Total Top-Quark Pair-Production Cross Section at Hadron Colliders Through* $O(\alpha_S^4)$, *Phys. Rev. Lett.* **110** (2013) 252004 [arXiv:1303.6254] [INSPIRE].

[60] M. Czakon and A. Mitov, *NNLO corrections to top pair production at hadron colliders: the quark-gluon reaction*, *JHEP* **01** (2013) 080 [arXiv:1210.6832] [INSPIRE].

[61] M. Czakon and A. Mitov, *NNLO corrections to top-pair production at hadron colliders: the all-fermionic scattering channels*, *JHEP* **12** (2012) 054 [arXiv:1207.0236] [INSPIRE].

[62] P. Bärnreuther, M. Czakon and A. Mitov, *Percent Level Precision Physics at the Tevatron: First Genuine NNLO QCD Corrections to* $q\bar{q} \to t\bar{t} + X$, *Phys. Rev. Lett.* **109** (2012) 132001 [arXiv:1204.5201] [INSPIRE].

[63] M. Cacciari, M. Czakon, M. Mangano, A. Mitov and P. Nason, *Top-pair production at hadron colliders with next-to-next-to-leading logarithmic soft-gluon resummation*, *Phys. Lett. B* **710** (2012) 612 [arXiv:1111.5869] [INSPIRE].

[64] M. Czakon and A. Mitov, *Top++: A Program for the Calculation of the Top-Pair Cross-Section at Hadron Colliders*, *Comput. Phys. Commun.* **185** (2014) 2930 [arXiv:1112.5675] [INSPIRE].

[65] N. Kidonakis, *Next-to-next-to-leading-order collinear and soft gluon corrections for t-channel single top quark production*, *Phys. Rev. D* **83** (2011) 091503 [arXiv:1103.2792] [INSPIRE].

[66] N. Kidonakis, *Two-loop soft anomalous dimensions for single top quark associated production with a* W^- *or* H^-, *Phys. Rev. D* **82** (2010) 054018 [arXiv:1005.4451] [INSPIRE].

[67] N. Kidonakis, *NNLL resummation for s-channel single top quark production*, *Phys. Rev. D* **81** (2010) 054028 [arXiv:1001.5034] [INSPIRE].

[68] T. Gleisberg et al., *Event generation with SHERPA 1.1*, *JHEP* **02** (2009) 007 [arXiv:0811.4622] [INSPIRE].

[69] S. Catani, L. Cieri, G. Ferrera, D. de Florian and M. Grazzini, *Vector boson production at hadron colliders: a fully exclusive QCD calculation at NNLO*, Phys. Rev. Lett. **103** (2009) 082001 [arXiv:0903.2120] [INSPIRE].

[70] J. Alwall et al., *The automated computation of tree-level and next-to-leading order differential cross sections, and their matching to parton shower simulations*, JHEP **07** (2014) 079 [arXiv:1405.0301] [INSPIRE].

[71] R.D. Ball et al., *Parton distributions with LHC data*, Nucl. Phys. B **867** (2013) 244 [arXiv:1207.1303] [INSPIRE].

[72] M. Beneke, M. Czakon, P. Falgari, A. Mitov and C. Schwinn, *Threshold expansion of the $gg(q\bar{q}) \to \overline{Q}Q + X$ cross section at $O(\alpha_s^4)$*, Phys. Lett. B **690** (2010) 483 [*Erratum ibid.* **778** (2018) 464] [arXiv:0911.5166] [INSPIRE].

[73] W. Beenakker, C. Borschensky, M. Krämer, A. Kulesza and E. Laenen, *NNLL-fast: predictions for coloured supersymmetric particle production at the LHC with threshold and Coulomb resummation*, JHEP **12** (2016) 133 [arXiv:1607.07741] [INSPIRE].

[74] O. Mattelaer and E. Vryonidou, *Dark matter production through loop-induced processes at the LHC: the s-channel mediator case*, Eur. Phys. J. C **75** (2015) 436 [arXiv:1508.00564] [INSPIRE].

[75] M. Backović, M. Krämer, F. Maltoni, A. Martini, K. Mawatari and M. Pellen, *Higher-order QCD predictions for dark matter production at the LHC in simplified models with s-channel mediators*, Eur. Phys. J. C **75** (2015) 482 [arXiv:1508.05327] [INSPIRE].

[76] E. Re, *Single-top Wt-channel production matched with parton showers using the POWHEG method*, Eur. Phys. J. C **71** (2011) 1547 [arXiv:1009.2450] [INSPIRE].

[77] S. Frixione, P. Nason and G. Ridolfi, *A Positive-weight next-to-leading-order Monte Carlo for heavy flavour hadroproduction*, JHEP **09** (2007) 126 [arXiv:0707.3088] [INSPIRE].

[78] R. Frederix, E. Re and P. Torrielli, *Single-top t-channel hadroproduction in the four-flavour scheme with POWHEG and aMC@NLO*, JHEP **09** (2012) 130 [arXiv:1207.5391] [INSPIRE].

[79] S. Alioli, P. Nason, C. Oleari and E. Re, *NLO single-top production matched with shower in POWHEG: s- and t-channel contributions*, JHEP **09** (2009) 111 [*Erratum ibid.* **02** (2010) 011] [arXiv:0907.4076] [INSPIRE].

[80] D.J. Lange, *The EvtGen particle decay simulation package*, Nucl. Instrum. Meth. A **462** (2001) 152 [INSPIRE].

[81] ATLAS collaboration, *The ATLAS Simulation Infrastructure*, Eur. Phys. J. C **70** (2010) 823 [arXiv:1005.4568] [INSPIRE].

[82] GEANT4 collaboration, *GEANT4: a simulation toolkit*, Nucl. Instrum. Meth. A **506** (2003) 250 [INSPIRE].

[83] ATLAS collaboration, *The PYTHIA 8 A3 tune description of ATLAS minimum bias and inelastic measurements incorporating the Donnachie-Landshoff diffractive model*, ATL-PHYS-PUB-2016-017 (2016).

[84] M. Bahr et al., *HERWIG++ Physics and Manual*, Eur. Phys. J. C **58** (2008) 639 [arXiv:0803.0883] [INSPIRE].

[85] J. Bellm et al., *HERWIG 7.0/HERWIG++ 3.0 release note*, Eur. Phys. J. C **76** (2016) 196 [arXiv:1512.01178] [INSPIRE].

JHEP04(2021)174

[86] ATLAS collaboration, *Studies on top-quark Monte Carlo modelling with Sherpa and MG5_aMC@NLO*, ATL-PHYS-PUB-2017-007 (2017).

[87] S. Frixione, E. Laenen, P. Motylinski, B.R. Webber and C.D. White, *Single-top hadroproduction in association with a W boson*, JHEP **07** (2008) 029 [arXiv:0805.3067] [INSPIRE].

[88] ATLAS collaboration, *Probing the quantum interference between singly and doubly resonant top-quark production in pp collisions at* $\sqrt{s} = 13$ *TeV with the ATLAS detector*, Phys. Rev. Lett. **121** (2018) 152002 [arXiv:1806.04667] [INSPIRE].

[89] ATLAS collaboration, *ATLAS simulation of boson plus jets processes in Run 2*, ATL-PHYS-PUB-2017-006 (2017).

[90] ATLAS collaboration, *Multi-Boson Simulation for* 13 *TeV ATLAS Analyses*, ATL-PHYS-PUB-2017-005 (2017).

[91] T. Gleisberg and S. Höche, *Comix, a new matrix element generator*, JHEP **12** (2008) 039 [arXiv:0808.3674] [INSPIRE].

[92] F. Cascioli, P. Maierhofer and S. Pozzorini, *Scattering Amplitudes with Open Loops*, Phys. Rev. Lett. **108** (2012) 111601 [arXiv:1111.5206] [INSPIRE].

[93] S. Schumann and F. Krauss, *A Parton shower algorithm based on Catani-Seymour dipole factorisation*, JHEP **03** (2008) 038 [arXiv:0709.1027] [INSPIRE].

[94] S. Höche, F. Krauss, M. Schönherr and F. Siegert, *QCD matrix elements + parton showers: The NLO case*, JHEP **04** (2013) 027 [arXiv:1207.5030] [INSPIRE].

[95] *Modelling of the* $t\bar{t}H$ *and* $t\bar{t}V$ $(V = W, Z)$ *processes for* $\sqrt{s} = 13$ *TeV ATLAS analyses*, ATL-PHYS-PUB-2016-005 (2016).

[96] I. Low, *Polarized charginos (and top quarks) in scalar top quark decays*, Phys. Rev. D **88** (2013) 095018 [arXiv:1304.0491] [INSPIRE].

[97] M. Perelstein and A. Weiler, *Polarized Tops from Stop Decays at the LHC*, JHEP **03** (2009) 141 [arXiv:0811.1024] [INSPIRE].

[98] P. Artoisenet, R. Frederix, O. Mattelaer and R. Rietkerk, *Automatic spin-entangled decays of heavy resonances in Monte Carlo simulations*, JHEP **03** (2013) 015 [arXiv:1212.3460] [INSPIRE].

[99] W. Beenakker, M. Krämer, T. Plehn, M. Spira and P.M. Zerwas, *Stop production at hadron colliders*, Nucl. Phys. B **515** (1998) 3 [hep-ph/9710451] [INSPIRE].

[100] W. Beenakker, S. Brensing, M. Krämer, A. Kulesza, E. Laenen and I. Niessen, *Supersymmetric top and bottom squark production at hadron colliders*, JHEP **08** (2010) 098 [arXiv:1006.4771] [INSPIRE].

[101] W. Beenakker, C. Borschensky, R. Heger, M. Krämer, A. Kulesza and E. Laenen, *NNLL resummation for stop pair-production at the LHC*, JHEP **05** (2016) 153 [arXiv:1601.02954] [INSPIRE].

[102] J. Butterworth et al., *PDF4LHC recommendations for LHC Run II*, J. Phys. G **43** (2016) 023001 [arXiv:1510.03865] [INSPIRE].

[103] ATLAS collaboration, *Electron reconstruction and identification in the ATLAS experiment using the 2015 and 2016 LHC proton-proton collision data at* $\sqrt{s} = 13$ TeV, Eur. Phys. J. C **79** (2019) 639 [arXiv:1902.04655] [INSPIRE].

JHEP04(2021)174

[104] ATLAS collaboration, *Muon reconstruction performance of the ATLAS detector in proton-proton collision data at $\sqrt{s} = 13$ TeV*, Eur. Phys. J. C **76** (2016) 292 [arXiv:1603.05598] [INSPIRE].

[105] ATLAS collaboration, *Topological cell clustering in the ATLAS calorimeters and its performance in LHC Run 1*, Eur. Phys. J. C **77** (2017) 490 [arXiv:1603.02934] [INSPIRE].

[106] ATLAS collaboration, *Jet energy measurement with the ATLAS detector in proton-proton collisions at $\sqrt{s} = 7$ TeV*, Eur. Phys. J. C **73** (2013) 2304 [arXiv:1112.6426] [INSPIRE].

[107] M. Cacciari, G.P. Salam and G. Soyez, *The anti-k_t jet clustering algorithm*, JHEP **04** (2008) 063 [arXiv:0802.1189] [INSPIRE].

[108] M. Cacciari, G.P. Salam and G. Soyez, *FastJet User Manual*, Eur. Phys. J. C **72** (2012) 1896 [arXiv:1111.6097] [INSPIRE].

[109] M. Cacciari and G.P. Salam, *Pileup subtraction using jet areas*, Phys. Lett. B **659** (2008) 119 [arXiv:0707.1378] [INSPIRE].

[110] M. Cacciari, G.P. Salam and G. Soyez, *The Catchment Area of Jets*, JHEP **04** (2008) 005 [arXiv:0802.1188] [INSPIRE].

[111] ATLAS collaboration, *Performance of pile-up mitigation techniques for jets in pp collisions at $\sqrt{s} = 8$ TeV using the ATLAS detector*, Eur. Phys. J. C **76** (2016) 581 [arXiv:1510.03823] [INSPIRE].

[112] ATLAS collaboration, *Jet energy measurement and its systematic uncertainty in proton-proton collisions at $\sqrt{s} = 7$ TeV with the ATLAS detector*, Eur. Phys. J. C **75** (2015) 17 [arXiv:1406.0076] [INSPIRE].

[113] ATLAS collaboration, *Jet energy scale measurements and their systematic uncertainties in proton-proton collisions at $\sqrt{s} = 13$ TeV with the ATLAS detector*, Phys. Rev. D **96** (2017) 072002 [arXiv:1703.09665] [INSPIRE].

[114] ATLAS collaboration, *Characterisation and mitigation of beam-induced backgrounds observed in the ATLAS detector during the 2011 proton-proton run*, 2013 *JINST* **8** P07004 [arXiv:1303.0223] [INSPIRE].

[115] *Selection of jets produced in 13TeV proton-proton collisions with the ATLAS detector*, ATLAS-CONF-2015-029 (2015).

[116] ATLAS collaboration, *Performance of b-Jet Identification in the ATLAS Experiment*, 2016 *JINST* **11** P04008 [arXiv:1512.01094] [INSPIRE].

[117] ATLAS collaboration, *ATLAS b-jet identification performance and efficiency measurement with $t\bar{t}$ events in pp collisions at $\sqrt{s} = 13$ TeV*, Eur. Phys. J. C **79** (2019) 970 [arXiv:1907.05120] [INSPIRE].

[118] ATLAS collaboration, *Soft b-hadron tagging for compressed SUSY scenarios*, ATLAS-CONF-2019-027 (2019).

[119] ATLAS collaboration, *Measurement of the tau lepton reconstruction and identification performance in the ATLAS experiment using pp collisions at $\sqrt{s} = 13$ TeV*, ATLAS-CONF-2017-029 (2017).

[120] ATLAS collaboration, *Reconstruction of hadronic decay products of tau leptons with the ATLAS experiment*, Eur. Phys. J. C **76** (2016) 295 [arXiv:1512.05955] [INSPIRE].

[121] ATLAS collaboration, *Modelling $Z \to \tau\tau$ processes in ATLAS with τ-embedded $Z \to \mu\mu$ data*, 2015 *JINST* **10** P09018 [arXiv:1506.05623] [INSPIRE].

[122] ATLAS collaboration, *Identification and energy calibration of hadronically decaying tau leptons with the ATLAS experiment in pp collisions at $\sqrt{s} = 8$ TeV*, *Eur. Phys. J. C* **75** (2015) 303 [arXiv:1412.7086] [INSPIRE].

[123] ATLAS collaboration, *Performance of missing transverse momentum reconstruction with the ATLAS detector using proton-proton collisions at $\sqrt{s} = 13$ TeV*, *Eur. Phys. J. C* **78** (2018) 903 [arXiv:1802.08168] [INSPIRE].

[124] ATLAS collaboration, *E_T^{miss} performance in the ATLAS detector using 2015-2016 LHC p-p collisions*, ATLAS-CONF-2018-023 (2018).

[125] C.G. Lester and D.J. Summers, *Measuring masses of semiinvisibly decaying particles pair produced at hadron colliders*, *Phys. Lett. B* **463** (1999) 99 [hep-ph/9906349] [INSPIRE].

[126] ATLAS collaboration, *Search for top squark pair production in final states with one isolated lepton, jets, and missing transverse momentum in $\sqrt{s} = 8$ TeV pp collisions with the ATLAS detector*, *JHEP* **11** (2014) 118 [arXiv:1407.0583] [INSPIRE].

[127] M.L. Graesser and J. Shelton, *Hunting Mixed Top Squark Decays*, *Phys. Rev. Lett.* **111** (2013) 121802 [arXiv:1212.4495] [INSPIRE].

[128] H. An and L.-T. Wang, *Opening up the compressed region of top squark searches at 13 TeV LHC*, *Phys. Rev. Lett.* **115** (2015) 181602 [arXiv:1506.00653] [INSPIRE].

[129] S. Macaluso, M. Park, D. Shih and B. Tweedie, *Revealing Compressed Stops Using High-Momentum Recoils*, *JHEP* **03** (2016) 151 [arXiv:1506.07885] [INSPIRE].

[130] R.D. Cousins, J.T. Linnemann and J. Tucker, *Evaluation of three methods for calculating statistical significance when incorporating a systematic uncertainty into a test of the background-only hypothesis for a Poisson process*, *Nucl. Instrum. Meth. A* **595** (2008) 480 [physics/0702156] [INSPIRE].

[131] T.P. Li and Y.Q. Ma, *Analysis methods for results in gamma-ray astronomy*, *Astrophys. J.* **272** (1983) 317 [INSPIRE].

[132] I. Goodfellow, Y. Bengio and A. Courville, *Deep Learning*, MIT Press (2016) [ISBN: 9780262035613].

[133] S. Hochreiter and J. Schmidhuber, *Long short-term memory*, *Neural Comput.* **9** (1997) 1735.

[134] C. Borschensky et al., *Squark and gluino production cross sections in pp collisions at $\sqrt{s} = 13, 14, 33$ and 100 TeV*, *Eur. Phys. J. C* **74** (2014) 3174 [arXiv:1407.5066] [INSPIRE].

[135] G. Cowan, K. Cranmer, E. Gross and O. Vitells, *Asymptotic formulae for likelihood-based tests of new physics*, *Eur. Phys. J. C* **71** (2011) 1554 [*Erratum ibid.* **73** (2013) 2501] [arXiv:1007.1727] [INSPIRE].

[136] A.L. Read, *Presentation of search results: The CL_s technique*, *J. Phys. G* **28** (2002) 2693 [INSPIRE].

[137] ATLAS collaboration, *Search for dark matter and other new phenomena in events with an energetic jet and large missing transverse momentum using the ATLAS detector*, *JHEP* **01** (2018) 126 [arXiv:1711.03301] [INSPIRE].

[138] ATLAS collaboration, *ATLAS Computing Acknowledgements*, ATL-SOFT-PUB-2020-001 (2020).

The ATLAS collaboration

G. Aad[102], B. Abbott[128], D.C. Abbott[103], A. Abed Abud[36], K. Abeling[53], D.K. Abhayasinghe[94], S.H. Abidi[167], O.S. AbouZeid[40], N.L. Abraham[156], H. Abramowicz[161], H. Abreu[160], Y. Abulaiti[6], B.S. Acharya[67a,67b,n], B. Achkar[53], L. Adam[100], C. Adam Bourdarios[5], L. Adamczyk[84a], L. Adamek[167], J. Adelman[121], M. Adersberger[114], A. Adiguzel[12c,ae], S. Adorni[54], T. Adye[143], A.A. Affolder[145], Y. Afik[160], C. Agapopoulou[65], M.N. Agaras[38], A. Aggarwal[119], C. Agheorghiesei[27c], J.A. Aguilar-Saavedra[139f,139a,ad], A. Ahmad[36], F. Ahmadov[80], W.S. Ahmed[104], X. Ai[18], G. Aielli[74a,74b], S. Akatsuka[86], T.P.A. Åkesson[97], E. Akilli[54], A.V. Akimov[111], K. Al Khoury[65], G.L. Alberghi[23b,23a], J. Albert[176], M.J. Alconada Verzini[161], S. Alderweireldt[36], M. Aleksa[36], I.N. Aleksandrov[80], C. Alexa[27b], T. Alexopoulos[10], A. Alfonsi[120], F. Alfonsi[23b,23a], M. Alhroob[128], B. Ali[141], S. Ali[158], M. Aliev[166], G. Alimonti[69a], C. Allaire[36], B.M.M. Allbrooke[156], B.W. Allen[131], P.P. Allport[21], A. Aloisio[70a,70b], F. Alonso[89], C. Alpigiani[148], E. Alunno Camelia[74a,74b], M. Alvarez Estevez[99], M.G. Alviggi[70a,70b], Y. Amaral Coutinho[81b], A. Ambler[104], L. Ambroz[134], C. Amelung[26], D. Amidei[106], S.P. Amor Dos Santos[139a], S. Amoroso[46], C.S. Amrouche[54], F. An[79], C. Anastopoulos[149], N. Andari[144], T. Andeen[11], J.K. Anders[20], S.Y. Andrean[45a,45b], A. Andreazza[69a,69b], V. Andrei[61a], C.R. Anelli[176], S. Angelidakis[9], A. Angerami[39], A.V. Anisenkov[122b,122a], A. Annovi[72a], C. Antel[54], M.T. Anthony[149], E. Antipov[129], M. Antonelli[51], D.J.A. Antrim[171], F. Anulli[73a], M. Aoki[82], J.A. Aparisi Pozo[174], M.A. Aparo[156], L. Aperio Bella[46], N. Aranzabal[36], V. Araujo Ferraz[81a], R. Araujo Pereira[81b], C. Arcangeletti[51], A.T.H. Arce[49], F.A. Arduh[89], J-F. Arguin[110], S. Argyropoulos[52], J.-H. Arling[46], A.J. Armbruster[36], A. Armstrong[171], O. Arnaez[167], H. Arnold[120], Z.P. Arrubarrena Tame[114], G. Artoni[134], K. Asai[126], S. Asai[163], T. Asawatavonvanich[165], N. Asbah[59], E.M. Asimakopoulou[172], L. Asquith[156], J. Assahsah[35e], K. Assamagan[29], R. Astalos[28a], R.J. Atkin[33a], M. Atkinson[173], N.B. Atlay[19], H. Atmani[65], K. Augsten[141], V.A. Austrup[182], G. Avolio[36], M.K. Ayoub[15a], G. Azuelos[110,am], H. Bachacou[144], K. Bachas[162], M. Backes[134], F. Backman[45a,45b], P. Bagnaia[73a,73b], M. Bahmani[85], H. Bahrasemani[152], A.J. Bailey[174], V.R. Bailey[173], J.T. Baines[143], C. Bakalis[10], O.K. Baker[183], P.J. Bakker[120], E. Bakos[16], D. Bakshi Gupta[8], S. Balaji[157], E.M. Baldin[122b,122a], P. Balek[180], F. Balli[144], W.K. Balunas[134], J. Balz[100], E. Banas[85], M. Bandieramonte[138], A. Bandyopadhyay[24], Sw. Banerjee[181,i], L. Barak[161], W.M. Barbe[38], E.L. Barberio[105], D. Barberis[55b,55a], M. Barbero[102], G. Barbour[95], T. Barillari[115], M-S. Barisits[36], J. Barkeloo[131], T. Barklow[153], R. Barnea[160], B.M. Barnett[143], R.M. Barnett[18], Z. Barnovska-Blenessy[60a], A. Baroncelli[60a], G. Barone[29], A.J. Barr[134], L. Barranco Navarro[45a,45b], F. Barreiro[99], J. Barreiro Guimarães da Costa[15a], U. Barron[161], S. Barsov[137], F. Bartels[61a], R. Bartoldus[153], G. Bartolini[102], A.E. Barton[90], P. Bartos[28a], A. Basalaev[46], A. Basan[100], A. Bassalat[65,aj], M.J. Basso[167], R.L. Bates[57], S. Batlamous[35f], J.R. Batley[32], B. Batool[151], M. Battaglia[145], M. Bauce[73a,73b], F. Bauer[144,*], K.T. Bauer[171], H.S. Bawa[31], J.B. Beacham[49], T. Beau[135], P.H. Beauchemin[170], F. Becherer[52], P. Bechtle[24], H.C. Beck[53], H.P. Beck[20,p], K. Becker[178], C. Becot[46], A. Beddall[12d], A.J. Beddall[12a], V.A. Bednyakov[80], M. Bedognetti[120], C.P. Bee[155], T.A. Beermann[182], M. Begalli[81b], M. Begel[29], A. Behera[155], J.K. Behr[46], F. Beisiegel[24], M. Belfkir[5], A.S. Bell[95], G. Bella[161], L. Bellagamba[23b], A. Bellerive[34], P. Bellos[9], K. Beloborodov[122b,122a], K. Belotskiy[112], N.L. Belyaev[112], D. Benchekroun[35a], N. Benekos[10], Y. Benhammou[161], D.P. Benjamin[6], M. Benoit[54], J.R. Bensinger[26], S. Bentvelsen[120], L. Beresford[134], M. Beretta[51], D. Berge[19], E. Bergeaas Kuutmann[172], N. Berger[5], B. Bergmann[141], L.J. Bergsten[26], J. Beringer[18], S. Berlendis[7], G. Bernardi[135], C. Bernius[153], F.U. Bernlochner[24], T. Berry[94], P. Berta[100], C. Bertella[15a], A. Berthold[48], I.A. Bertram[90], O. Bessidskaia Bylund[182], N. Besson[144], A. Bethani[101], S. Bethke[115], A. Betti[42], A.J. Bevan[93], J. Beyer[115],

JHEP04(2021)174

D.S. Bhattacharya[177], P. Bhattarai[26], V.S. Bhopatkar[6], R. Bi[138], R.M. Bianchi[138], O. Biebel[114], D. Biedermann[19], R. Bielski[36], K. Bierwagen[100], N.V. Biesuz[72a,72b], M. Biglietti[75a], T.R.V. Billoud[110], M. Bindi[53], A. Bingul[12d], C. Bini[73a,73b], S. Biondi[23b,23a], C.J. Birch-sykes[101], M. Birman[180], T. Bisanz[36], J.P. Biswal[3], D. Biswas[181,i], A. Bitadze[101], C. Bittrich[48], K. Bjørke[133], T. Blazek[28a], I. Bloch[46], C. Blocker[26], A. Blue[57], U. Blumenschein[93], G.J. Bobbink[120], V.S. Bobrovnikov[122b,122a], S.S. Bocchetta[97], D. Bogavac[14], A.G. Bogdanchikov[122b,122a], C. Bohm[45a], V. Boisvert[94], P. Bokan[53], T. Bold[84a], A.E. Bolz[61b], M. Bomben[135], M. Bona[93], J.S. Bonilla[131], M. Boonekamp[144], C.D. Booth[94], H.M. Borecka-Bielska[91], L.S. Borgna[95], A. Borisov[123], G. Borissov[90], J. Bortfeldt[36], D. Bortoletto[134], D. Boscherini[23b], M. Bosman[14], J.D. Bossio Sola[104], K. Bouaouda[35a], J. Boudreau[138], E.V. Bouhova-Thacker[90], D. Boumediene[38], S.K. Boutle[57], A. Boveia[127], J. Boyd[36], D. Boye[33c], I.R. Boyko[80], A.J. Bozson[94], J. Bracinik[21], N. Brahimi[60d,60c], G. Brandt[182], O. Brandt[32], F. Braren[46], B. Brau[103], J.E. Brau[131], W.D. Breaden Madden[57], K. Brendlinger[46], L. Brenner[46], R. Brenner[172], S. Bressler[180], B. Brickwedde[100], D.L. Briglin[21], D. Britton[57], D. Britzger[115], I. Brock[24], R. Brock[107], G. Brooijmans[39], W.K. Brooks[146d], E. Brost[29], P.A. Bruckman de Renstrom[85], B. Brüers[46], D. Bruncko[28b], A. Bruni[23b], G. Bruni[23b], L.S. Bruni[120], S. Bruno[74a,74b], M. Bruschi[23b], N. Bruscino[73a,73b], L. Bryngemark[153], T. Buanes[17], Q. Buat[36], P. Buchholz[151], A.G. Buckley[57], I.A. Budagov[80], M.K. Bugge[133], F. Bührer[52], O. Bulekov[112], B.A. Bullard[59], T.J. Burch[121], S. Burdin[91], C.D. Burgard[120], A.M. Burger[129], B. Burghgrave[8], J.T.P. Burr[46], C.D. Burton[11], J.C. Burzynski[103], V. Büscher[100], E. Buschmann[53], P.J. Bussey[57], J.M. Butler[25], C.M. Buttar[57], J.M. Butterworth[95], P. Butti[36], W. Buttinger[36], C.J. Buxo Vazquez[107], A. Buzatu[158], A.R. Buzykaev[122b,122a], G. Cabras[23b,23a], S. Cabrera Urbán[174], D. Caforio[56], H. Cai[138], V.M.M. Cairo[153], O. Cakir[4a], N. Calace[36], P. Calafiura[18], G. Calderini[135], P. Calfayan[66], G. Callea[57], L.P. Caloba[81b], A. Caltabiano[74a,74b], S. Calvente Lopez[99], D. Calvet[38], S. Calvet[38], T.P. Calvet[102], M. Calvetti[72a,72b], R. Camacho Toro[135], S. Camarda[36], D. Camarero Munoz[99], P. Camarri[74a,74b], M.T. Camerlingo[75a,75b], D. Cameron[133], C. Camincher[36], S. Campana[36], M. Campanelli[95], A. Camplani[40], V. Canale[70a,70b], A. Canesse[104], M. Cano Bret[78], J. Cantero[129], T. Cao[161], Y. Cao[173], M.D.M. Capeans Garrido[36], M. Capua[41b,41a], R. Cardarelli[74a], F. Cardillo[149], G. Carducci[41b,41a], I. Carli[142], T. Carli[36], G. Carlino[70a], B.T. Carlson[138], E.M. Carlson[176,168a], L. Carminati[69a,69b], R.M.D. Carney[153], S. Caron[119], E. Carquin[146d], S. Carrá[46], G. Carratta[23b,23a], J.W.S. Carter[167], T.M. Carter[50], M.P. Casado[14,f], A.F. Casha[167], F.L. Castillo[174], L. Castillo Garcia[14], V. Castillo Gimenez[174], N.F. Castro[139a,139e], A. Catinaccio[36], J.R. Catmore[133], A. Cattai[36], V. Cavaliere[29], E. Cavallaro[14], V. Cavasinni[72a,72b], E. Celebi[12b], F. Celli[134], K. Cerny[130], A.S. Cerqueira[81a], A. Cerri[156], L. Cerrito[74a,74b], F. Cerutti[18], A. Cervelli[23b,23a], S.A. Cetin[12b], Z. Chadi[35a], D. Chakraborty[121], J. Chan[181], W.S. Chan[120], W.Y. Chan[91], J.D. Chapman[32], B. Chargeishvili[159b], D.G. Charlton[21], T.P. Charman[93], C.C. Chau[34], S. Che[127], S. Chekanov[6], S.V. Chekulaev[168a], G.A. Chelkov[80,ah], B. Chen[79], C. Chen[60a], C.H. Chen[79], H. Chen[29], J. Chen[60a], J. Chen[39], J. Chen[26], S. Chen[136], S.J. Chen[15c], X. Chen[15b], Y. Chen[60a], Y-H. Chen[46], H.C. Cheng[63a], H.J. Cheng[15a], A. Cheplakov[80], E. Cheremushkina[123], R. Cherkaoui El Moursli[35f], E. Cheu[7], K. Cheung[64], T.J.A. Chevalérias[144], L. Chevalier[144], V. Chiarella[51], G. Chiarelli[72a], G. Chiodini[68a], A.S. Chisholm[21], A. Chitan[27b], I. Chiu[163], Y.H. Chiu[176], M.V. Chizhov[80], K. Choi[11], A.R. Chomont[73a,73b], S. Chouridou[162], Y.S. Chow[120], L.D. Christopher[33e], M.C. Chu[63a], X. Chu[15a,15d], J. Chudoba[140], J.J. Chwastowski[85], L. Chytka[130], D. Cieri[115], K.M. Ciesla[85], D. Cinca[47], V. Cindro[92], I.A. Cioară[27b], A. Ciocio[18], F. Cirotto[70a,70b], Z.H. Citron[180,j], M. Citterio[69a], D.A. Ciubotaru[27b], B.M. Ciungu[167], A. Clark[54], M.R. Clark[39], P.J. Clark[50], S.E. Clawson[101], C. Clement[45a,45b], Y. Coadou[102], M. Cobal[67a,67c], A. Coccaro[55b], J. Cochran[79], R. Coelho Lopes De Sa[103], H. Cohen[161], A.E.C. Coimbra[36], B. Cole[39], A.P. Colijn[120], J. Collot[58],

JHEP04(2021)174

P. Conde Muiño[139a,139h], S.H. Connell[33c], I.A. Connelly[57], S. Constantinescu[27b], F. Conventi[70a,an], A.M. Cooper-Sarkar[134], F. Cormier[175], K.J.R. Cormier[167], L.D. Corpe[95], M. Corradi[73a,73b], E.E. Corrigan[97], F. Corriveau[104,ab], M.J. Costa[174], F. Costanza[5], D. Costanzo[149], G. Cowan[94], J.W. Cowley[32], J. Crane[101], K. Cranmer[125], R.A. Creager[136], S. Crépé-Renaudin[58], F. Crescioli[135], M. Cristinziani[24], V. Croft[170], G. Crosetti[41b,41a], A. Cueto[5], T. Cuhadar Donszelmann[171], H. Cui[15a,15d], A.R. Cukierman[153], W.R. Cunningham[57], S. Czekierda[85], P. Czodrowski[36], M.M. Czurylo[61b], M.J. Da Cunha Sargedas De Sousa[60b], J.V. Da Fonseca Pinto[81b], C. Da Via[101], W. Dabrowski[84a], F. Dachs[36], T. Dado[28a], S. Dahbi[33e], T. Dai[106], C. Dallapiccola[103], M. Dam[40], G. D'amen[29], V. D'Amico[75a,75b], J. Damp[100], J.R. Dandoy[136], M.F. Daneri[30], M. Danninger[152], V. Dao[36], G. Darbo[55b], O. Dartsi[5], A. Dattagupta[131], T. Daubney[46], S. D'Auria[69a,69b], C. David[168b], T. Davidek[142], D.R. Davis[49], I. Dawson[149], K. De[8], R. De Asmundis[70a], M. De Beurs[120], S. De Castro[23b,23a], N. De Groot[119], P. de Jong[120], H. De la Torre[107], A. De Maria[15c], D. De Pedis[73a], A. De Salvo[73a], U. De Sanctis[74a,74b], M. De Santis[74a,74b], A. De Santo[156], J.B. De Vivie De Regie[65], C. Debenedetti[145], D.V. Dedovich[80], A.M. Deiana[42], J. Del Peso[99], Y. Delabat Diaz[46], D. Delgove[65], F. Deliot[144], C.M. Delitzsch[7], M. Della Pietra[70a,70b], D. Della Volpe[54], A. Dell'Acqua[36], L. Dell'Asta[74a,74b], M. Delmastro[5], C. Delporte[65], P.A. Delsart[58], D.A. DeMarco[167], S. Demers[183], M. Demichev[80], G. Demontigny[110], S.P. Denisov[123], L. D'Eramo[121], D. Derendarz[85], J.E. Derkaoui[35e], F. Derue[135], P. Dervan[91], K. Desch[24], K. Dette[167], C. Deutsch[24], M.R. Devesa[30], P.O. Deviveiros[36], F.A. Di Bello[73a,73b], A. Di Ciaccio[74a,74b], L. Di Ciaccio[5], W.K. Di Clemente[136], C. Di Donato[70a,70b], A. Di Girolamo[36], G. Di Gregorio[72a,72b], B. Di Micco[75a,75b], R. Di Nardo[75a,75b], K.F. Di Petrillo[59], R. Di Sipio[167], C. Diaconu[102], F.A. Dias[40], T. Dias Do Vale[139a], M.A. Diaz[146a], F.G. Diaz Capriles[24], J. Dickinson[18], E.B. Diehl[106], J. Dietrich[19], S. Díez Cornell[46], A. Dimitrievska[18], W. Ding[15b], J. Dingfelder[24], S.J. Dittmeier[61b], F. Dittus[36], F. Djama[102], T. Djobava[159b], J.I. Djuvsland[17], M.A.B. Do Vale[147], M. Dobre[27b], D. Dodsworth[26], C. Doglioni[97], J. Dolejsi[142], Z. Dolezal[142], M. Donadelli[81c], B. Dong[60c], J. Donini[38], A. D'onofrio[15c], M. D'Onofrio[91], J. Dopke[143], A. Doria[70a], M.T. Dova[89], A.T. Doyle[57], E. Drechsler[152], E. Dreyer[152], T. Dreyer[53], A.S. Drobac[170], D. Du[60b], T.A. du Pree[120], Y. Duan[60d], F. Dubinin[111], M. Dubovsky[28a], A. Dubreuil[54], E. Duchovni[180], G. Duckeck[114], O.A. Ducu[27b], D. Duda[115], A. Dudarev[36], A.C. Dudder[100], E.M. Duffield[18], M. D'uffizi[101], L. Duflot[65], M. Dührssen[36], C. Dülsen[182], M. Dumancic[180], A.E. Dumitriu[27b], A.K. Duncan[57], M. Dunford[61a], A. Duperrin[102], H. Duran Yildiz[4a], M. Düren[56], A. Durglishvili[159b], D. Duschinger[48], B. Dutta[46], D. Duvnjak[1], G.I. Dyckes[136], M. Dyndal[36], S. Dysch[101], B.S. Dziedzic[85], M.G. Eggleston[49], T. Eifert[8], G. Eigen[17], K. Einsweiler[18], T. Ekelof[172], H. El Jarrari[35f], V. Ellajosyula[172], M. Ellert[172], F. Ellinghaus[182], A.A. Elliot[93], N. Ellis[36], J. Elmsheuser[29], M. Elsing[36], D. Emeliyanov[143], A. Emerman[39], Y. Enari[163], M.B. Epland[49], J. Erdmann[47], A. Ereditato[20], P.A. Erland[85], M. Errenst[36], M. Escalier[65], C. Escobar[174], O. Estrada Pastor[174], E. Etzion[161], H. Evans[66], M.O. Evans[156], A. Ezhilov[137], F. Fabbri[57], L. Fabbri[23b,23a], V. Fabiani[119], G. Facini[178], R.M. Faisca Rodrigues Pereira[139a], R.M. Fakhrutdinov[123], S. Falciano[73a], P.J. Falke[24], S. Falke[36], J. Faltova[142], Y. Fang[15a], Y. Fang[15a], G. Fanourakis[44], M. Fanti[69a,69b], M. Faraj[67a,67c,q], A. Farbin[8], A. Farilla[75a], E.M. Farina[71a,71b], T. Farooque[107], S.M. Farrington[50], P. Farthouat[36], F. Fassi[35f], P. Fassnacht[36], D. Fassouliotis[9], M. Faucci Giannelli[50], W.J. Fawcett[32], L. Fayard[65], O.L. Fedin[137,o], W. Fedorko[175], A. Fehr[20], M. Feickert[173], L. Feligioni[102], A. Fell[149], C. Feng[60b], M. Feng[49], M.J. Fenton[171], A.B. Fenyuk[123], S.W. Ferguson[43], J. Ferrando[46], A. Ferrante[173], A. Ferrari[172], P. Ferrari[120], R. Ferrari[71a], D.E. Ferreira de Lima[61b], A. Ferrer[174], D. Ferrere[54], C. Ferretti[106], F. Fiedler[100], A. Filipčič[92], F. Filthaut[119], K.D. Finelli[25], M.C.N. Fiolhais[139a,139c,a], L. Fiorini[174], F. Fischer[114], J. Fischer[100], W.C. Fisher[107], T. Fitschen[21], I. Fleck[151], P. Fleischmann[106], T. Flick[182], B.M. Flierl[114], L. Flores[136],

JHEP04(2021)174

L.R. Flores Castillo[63a], F.M. Follega[76a,76b], N. Fomin[17], J.H. Foo[167], G.T. Forcolin[76a,76b], B.C. Forland[66], A. Formica[144], F.A. Förster[14], A.C. Forti[101], E. Fortin[102], M.G. Foti[134], D. Fournier[65], H. Fox[90], P. Francavilla[72a,72b], S. Francescato[73a,73b], M. Franchini[23b,23a], S. Franchino[61a], D. Francis[36], L. Franco[5], L. Franconi[20], M. Franklin[59], G. Frattari[73a,73b], A.N. Fray[93], P.M. Freeman[21], B. Freund[110], W.S. Freund[81b], E.M. Freundlich[47], D.C. Frizzell[128], D. Froidevaux[36], J.A. Frost[134], M. Fujimoto[126], C. Fukunaga[164], E. Fullana Torregrosa[174], T. Fusayasu[116], J. Fuster[174], A. Gabrielli[23b,23a], A. Gabrielli[36], S. Gadatsch[54], P. Gadow[115], G. Gagliardi[55b,55a], L.G. Gagnon[110], G.E. Gallardo[134], E.J. Gallas[134], B.J. Gallop[143], G. Galster[40], R. Gamboa Goni[93], K.K. Gan[127], S. Ganguly[180], J. Gao[60a], Y. Gao[50], Y.S. Gao[31,l], F.M. Garay Walls[146a], C. García[174], J.E. García Navarro[174], J.A. García Pascual[15a], C. Garcia-Argos[52], M. Garcia-Sciveres[18], R.W. Gardner[37], N. Garelli[153], S. Gargiulo[52], C.A. Garner[167], V. Garonne[133], S.J. Gasiorowski[148], P. Gaspar[81b], A. Gaudiello[55b,55a], G. Gaudio[71a], I.L. Gavrilenko[111], A. Gavrilyuk[124], C. Gay[175], G. Gaycken[46], E.N. Gazis[10], A.A. Geanta[27b], C.M. Gee[145], C.N.P. Gee[143], J. Geisen[97], M. Geisen[100], C. Gemme[55b], M.H. Genest[58], C. Geng[106], S. Gentile[73a,73b], S. George[94], T. Geralis[44], L.O. Gerlach[53], P. Gessinger-Befurt[100], G. Gessner[47], S. Ghasemi[151], M. Ghasemi Bostanabad[176], M. Ghneimat[151], A. Ghosh[65], A. Ghosh[78], B. Giacobbe[23b], S. Giagu[73a,73b], N. Giangiacomi[23b,23a], P. Giannetti[72a], A. Giannini[70a,70b], G. Giannini[14], S.M. Gibson[94], M. Gignac[145], D.T. Gil[84b], D. Gillberg[34], G. Gilles[182], D.M. Gingrich[3,am], M.P. Giordani[67a,67c], P.F. Giraud[144], G. Giugliarelli[67a,67c], D. Giugni[69a], F. Giuli[74a,74b], S. Gkaitatzis[162], I. Gkialas[9,g], E.L. Gkougkousis[14], P. Gkountoumis[10], L.K. Gladilin[113], C. Glasman[99], J. Glatzer[14], P.C.F. Glaysher[46], A. Glazov[46], G.R. Gledhill[131], I. Gnesi[41b,b], M. Goblirsch-Kolb[26], D. Godin[110], S. Goldfarb[105], T. Golling[54], D. Golubkov[123], A. Gomes[139a,139b], R. Goncalves Gama[53], R. Gonçalo[139a,139c], G. Gonella[131], L. Gonella[21], A. Gongadze[80], F. Gonnella[21], J.L. Gonski[39], S. González de la Hoz[174], S. Gonzalez Fernandez[14], C. Gonzalez Renteria[18], R. Gonzalez Suarez[172], S. Gonzalez-Sevilla[54], G.R. Gonzalvo Rodriguez[174], L. Goossens[36], N.A. Gorasia[21], P.A. Gorbounov[124], H.A. Gordon[29], B. Gorini[36], E. Gorini[68a,68b], A. Gorišek[92], A.T. Goshaw[49], M.I. Gostkin[80], C.A. Gottardo[119], M. Gouighri[35b], A.G. Goussiou[148], N. Govender[33c], C. Goy[5], I. Grabowska-Bold[84a], E.C. Graham[91], J. Gramling[171], E. Gramstad[133], S. Grancagnolo[19], M. Grandi[156], V. Gratchev[137], P.M. Gravila[27f], F.G. Gravili[68a,68b], C. Gray[57], H.M. Gray[18], C. Grefe[24], K. Gregersen[97], I.M. Gregor[46], P. Grenier[153], K. Grevtsov[46], C. Grieco[14], N.A. Grieser[128], A.A. Grillo[145], K. Grimm[31,k], S. Grinstein[14,w], J.-F. Grivaz[65], S. Groh[100], E. Gross[180], J. Grosse-Knetter[53], Z.J. Grout[95], C. Grud[106], A. Grummer[118], J.C. Grundy[134], L. Guan[106], W. Guan[181], C. Gubbels[175], J. Guenther[36], A. Guerguichon[65], J.G.R. Guerrero Rojas[174], F. Guescini[115], D. Guest[171], R. Gugel[100], T. Guillemin[5], S. Guindon[36], U. Gul[57], J. Guo[60c], W. Guo[106], Y. Guo[60a], Z. Guo[102], R. Gupta[46], S. Gurbuz[12c], G. Gustavino[128], M. Guth[52], P. Gutierrez[128], C. Gutschow[95], C. Guyot[144], C. Gwenlan[134], C.B. Gwilliam[91], E.S. Haaland[133], A. Haas[125], C. Haber[18], H.K. Hadavand[8], A. Hadef[60a], M. Haleem[177], J. Haley[129], J.J. Hall[149], G. Halladjian[107], G.D. Hallewell[102], K. Hamano[176], H. Hamdaoui[35f], M. Hamer[24], G.N. Hamity[50], K. Han[60a,v], L. Han[60a], S. Han[18], Y.F. Han[167], K. Hanagaki[82,t], M. Hance[145], D.M. Handl[114], M.D. Hank[37], R. Hankache[135], E. Hansen[97], J.B. Hansen[40], J.D. Hansen[40], M.C. Hansen[24], P.H. Hansen[40], E.C. Hanson[101], K. Hara[169], T. Harenberg[182], S. Harkusha[108], P.F. Harrison[178], N.M. Hartman[153], N.M. Hartmann[114], Y. Hasegawa[150], A. Hasib[50], S. Hassani[144], S. Haug[20], R. Hauser[107], L.B. Havener[39], M. Havranek[141], C.M. Hawkes[21], R.J. Hawkings[36], S. Hayashida[117], D. Hayden[107], C. Hayes[106], R.L. Hayes[175], C.P. Hays[134], J.M. Hays[93], H.S. Hayward[91], S.J. Haywood[143], F. He[60a], M.P. Heath[50], V. Hedberg[97], S. Heer[24], A.L. Heggelund[133], C. Heidegger[52], K.K. Heidegger[52], W.D. Heidorn[79], J. Heilman[34], S. Heim[46], T. Heim[18], B. Heinemann[46,ak], J.G. Heinlein[136], J.J. Heinrich[131], L. Heinrich[36], J. Hejbal[140], L. Helary[61b],

A. Held[125], S. Hellesund[133], C.M. Helling[145], S. Hellman[45a,45b], C. Helsens[36], R.C.W. Henderson[90], Y. Heng[181], L. Henkelmann[32], A.M. Henriques Correia[36], H. Herde[26], Y. Hernández Jiménez[33e], H. Herr[100], M.G. Herrmann[114], T. Herrmann[48], G. Herten[52], R. Hertenberger[114], L. Hervas[36], T.C. Herwig[136], G.G. Hesketh[95], N.P. Hessey[168a], H. Hibi[83], A. Higashida[163], S. Higashino[82], E. Higón-Rodriguez[174], K. Hildebrand[37], J.C. Hill[32], K.K. Hill[29], K.H. Hiller[46], S.J. Hillier[21], M. Hils[48], I. Hinchliffe[18], F. Hinterkeuser[24], M. Hirose[132], S. Hirose[52], D. Hirschbuehl[182], B. Hiti[92], O. Hladik[140], D.R. Hlaluku[33e], J. Hobbs[155], N. Hod[180], M.C. Hodgkinson[149], A. Hoecker[36], D. Hohn[52], D. Hohov[65], T. Holm[24], T.R. Holmes[37], M. Holzbock[114], L.B.A.H. Hommels[32], T.M. Hong[138], J.C. Honig[52], A. Hönle[115], B.H. Hooberman[173], W.H. Hopkins[6], Y. Horii[117], P. Horn[48], L.A. Horyn[37], S. Hou[158], A. Hoummada[35a], J. Howarth[57], J. Hoya[89], M. Hrabovsky[130], J. Hrdinka[77], J. Hrivnac[65], A. Hrynevich[109], T. Hryn'ova[5], P.J. Hsu[64], S.-C. Hsu[148], Q. Hu[29], S. Hu[60c], Y.F. Hu[15a,15d,ao], D.P. Huang[95], Y. Huang[60a], Y. Huang[15a], Z. Hubacek[141], F. Hubaut[102], M. Huebner[24], F. Huegging[24], T.B. Huffman[134], M. Huhtinen[36], R. Hulsken[58], R.F.H. Hunter[34], P. Huo[155], N. Huseynov[80,ac], J. Huston[107], J. Huth[59], R. Hyneman[106], S. Hyrych[28a], G. Iacobucci[54], G. Iakovidis[29], I. Ibragimov[151], L. Iconomidou-Fayard[65], P. Iengo[36], R. Ignazzi[40], O. Igonkina[120,y,*], R. Iguchi[163], T. Iizawa[54], Y. Ikegami[82], M. Ikeno[82], D. Iliadis[162], N. Ilic[119,167,ab], F. Iltzsche[48], H. Imam[35a], G. Introzzi[71a,71b], M. Iodice[75a], K. Iordanidou[168a], V. Ippolito[73a,73b], M.F. Isacson[172], M. Ishino[163], W. Islam[129], C. Issever[19,46], S. Istin[160], F. Ito[169], J.M. Iturbe Ponce[63a], R. Iuppa[76a,76b], A. Ivina[180], H. Iwasaki[82], J.M. Izen[43], V. Izzo[70a], P. Jacka[140], P. Jackson[1], R.M. Jacobs[46], B.P. Jaeger[152], V. Jain[2], G. Jäkel[182], K.B. Jakobi[100], K. Jakobs[52], T. Jakoubek[180], J. Jamieson[57], K.W. Janas[84a], R. Jansky[54], M. Janus[53], P.A. Janus[84a], G. Jarlskog[97], A.E. Jaspan[91], N. Javadov[80,ac], T. Javůrek[36], M. Javurkova[103], F. Jeanneau[144], L. Jeanty[131], J. Jejelava[159a], P. Jenni[52,c], N. Jeong[46], S. Jézéquel[5], H. Ji[181], J. Jia[155], H. Jiang[79], Y. Jiang[60a], Z. Jiang[153], S. Jiggins[52], F.A. Jimenez Morales[38], J. Jimenez Pena[115], S. Jin[15c], A. Jinaru[27b], O. Jinnouchi[165], H. Jivan[33e], P. Johansson[149], K.A. Johns[7], C.A. Johnson[66], R.W.L. Jones[90], S.D. Jones[156], T.J. Jones[91], J. Jongmanns[61a], J. Jovicevic[36], X. Ju[18], J.J. Junggeburth[115], A. Juste Rozas[14,w], A. Kaczmarska[85], M. Kado[73a,73b], H. Kagan[127], M. Kagan[153], A. Kahn[39], C. Kahra[100], T. Kaji[179], E. Kajomovitz[160], C.W. Kalderon[29], A. Kaluza[100], A. Kamenshchikov[123], M. Kaneda[163], N.J. Kang[145], S. Kang[79], Y. Kano[117], J. Kanzaki[82], L.S. Kaplan[181], D. Kar[33e], K. Karava[134], M.J. Kareem[168b], I. Karkanias[162], S.N. Karpov[80], Z.M. Karpova[80], V. Kartvelishvili[90], A.N. Karyukhin[123], A. Kastanas[45a,45b], C. Kato[60d,60c], J. Katzy[46], K. Kawade[150], K. Kawagoe[88], T. Kawaguchi[117], T. Kawamoto[144], G. Kawamura[53], E.F. Kay[176], S. Kazakos[14], V.F. Kazanin[122b,122a], R. Keeler[176], R. Kehoe[42], J.S. Keller[34], E. Kellermann[97], D. Kelsey[156], J.J. Kempster[21], J. Kendrick[21], K.E. Kennedy[39], O. Kepka[140], S. Kersten[182], B.P. Kerševan[92], S. Ketabchi Haghighat[167], M. Khader[173], F. Khalil-Zada[13], M. Khandoga[144], A. Khanov[129], A.G. Kharlamov[122b,122a], T. Kharlamova[122b,122a], E.E. Khoda[175], A. Khodinov[166], T.J. Khoo[54], G. Khoriauli[177], E. Khramov[80], J. Khubua[159b], S. Kido[83], M. Kiehn[54], C.R. Kilby[94], E. Kim[165], Y.K. Kim[37], N. Kimura[95], B.T. King[91,*], A. Kirchhoff[53], D. Kirchmeier[48], J. Kirk[143], A.E. Kiryunin[115], T. Kishimoto[163], D.P. Kisliuk[167], V. Kitali[46], C. Kitsaki[10], O. Kivernyk[24], T. Klapdor-Kleingrothaus[52], M. Klassen[61a], C. Klein[34], M.H. Klein[106], M. Klein[91], U. Klein[91], K. Kleinknecht[100], P. Klimek[121], A. Klimentov[29], T. Klingl[24], T. Klioutchnikova[36], F.F. Klitzner[114], P. Kluit[120], S. Kluth[115], E. Kneringer[77], E.B.F.G. Knoops[102], A. Knue[52], D. Kobayashi[88], T. Kobayashi[163], M. Kobel[48], M. Kocian[153], T. Kodama[163], P. Kodys[142], D.M. Koeck[156], P.T. Koenig[24], T. Koffas[34], N.M. Köhler[36], M. Kolb[144], I. Koletsou[5], T. Komarek[130], T. Kondo[82], K. Köneke[52], A.X.Y. Kong[1], A.C. König[119], T. Kono[126], V. Konstantinides[95], N. Konstantinidis[95], B. Konya[97], R. Kopeliansky[66], S. Koperny[84a], K. Korcyl[85], K. Kordas[162], G. Koren[161], A. Korn[95], I. Korolkov[14], E.V. Korolkova[149],

JHEP04(2021)174

N. Korotkova[113], O. Kortner[115], S. Kortner[115], V.V. Kostyukhin[149,166], A. Kotsokechagia[65], A. Kotwal[49], A. Koulouris[10], A. Kourkoumeli-Charalampidi[71a,71b], C. Kourkoumelis[9], E. Kourlitis[6], V. Kouskoura[29], R. Kowalewski[176], W. Kozanecki[101], A.S. Kozhin[123], V.A. Kramarenko[113], G. Kramberger[92], D. Krasnopevtsev[60a], M.W. Krasny[135], A. Krasznahorkay[36], D. Krauss[115], J.A. Kremer[100], J. Kretzschmar[91], P. Krieger[167], F. Krieter[114], A. Krishnan[61b], K. Krizka[18], K. Kroeninger[47], H. Kroha[115], J. Kroll[140], J. Kroll[136], K.S. Krowpman[107], U. Kruchonak[80], H. Krüger[24], N. Krumnack[79], M.C. Kruse[49], J.A. Krzysiak[85], O. Kuchinskaia[166], S. Kuday[4b], D. Kuechler[46], J.T. Kuechler[46], S. Kuehn[36], A. Kugel[61a], T. Kuhl[46], V. Kukhtin[80], Y. Kulchitsky[108,af], S. Kuleshov[146b], Y.P. Kulinich[173], M. Kuna[58], T. Kunigo[86], A. Kupco[140], T. Kupfer[47], O. Kuprash[52], H. Kurashige[83], L.L. Kurchaninov[168a], Y.A. Kurochkin[108], A. Kurova[112], M.G. Kurth[15a,15d], E.S. Kuwertz[36], M. Kuze[165], A.K. Kvam[148], J. Kvita[130], T. Kwan[104], F. La Ruffa[41b,41a], C. Lacasta[174], F. Lacava[73a,73b], D.P.J. Lack[101], H. Lacker[19], D. Lacour[135], E. Ladygin[80], R. Lafaye[5], B. Laforge[135], T. Lagouri[146b], S. Lai[53], I.K. Lakomiec[84a], J.E. Lambert[128], S. Lammers[66], W. Lampl[7], C. Lampoudis[162], E. Lançon[29], U. Landgraf[52], M.P.J. Landon[93], M.C. Lanfermann[54], V.S. Lang[52], J.C. Lange[53], R.J. Langenberg[103], A.J. Lankford[171], F. Lanni[29], K. Lantzsch[24], A. Lanza[71a], A. Lapertosa[55b,55a], S. Laplace[135], J.F. Laporte[144], T. Lari[69a], F. Lasagni Manghi[23b,23a], M. Lassnig[36], T.S. Lau[63a], A. Laudrain[65], A. Laurier[34], M. Lavorgna[70a,70b], S.D. Lawlor[94], M. Lazzaroni[69a,69b], B. Le[101], E. Le Guirriec[102], A. Lebedev[79], M. LeBlanc[7], T. LeCompte[6], F. Ledroit-Guillon[58], A.C.A. Lee[95], C.A. Lee[29], G.R. Lee[17], L. Lee[59], S.C. Lee[158], S. Lee[79], B. Lefebvre[168a], H.P. Lefebvre[94], M. Lefebvre[176], C. Leggett[18], K. Lehmann[152], N. Lehmann[20], G. Lehmann Miotto[36], W.A. Leight[46], A. Leisos[162,u], M.A.L. Leite[81c], C.E. Leitgeb[114], R. Leitner[142], D. Lellouch[180,*], K.J.C. Leney[42], T. Lenz[24], S. Leone[72a], C. Leonidopoulos[50], A. Leopold[135], C. Leroy[110], R. Les[167], C.G. Lester[32], M. Levchenko[137], J. Levêque[5], D. Levin[106], L.J. Levinson[180], D.J. Lewis[21], B. Li[15b], B. Li[106], C-Q. Li[60a], F. Li[60c], H. Li[60a], H. Li[60b], J. Li[60c], K. Li[148], L. Li[60c], M. Li[15a,15d], Q. Li[15a,15d], Q.Y. Li[60a], S. Li[60d,60c], X. Li[46], Y. Li[46], Z. Li[60b], Z. Li[134], Z. Li[104], Z. Liang[15a], M. Liberatore[46], B. Liberti[74a], A. Liblong[167], K. Lie[63c], S. Lim[29], C.Y. Lin[32], K. Lin[107], R.A. Linck[66], R.E. Lindley[7], J.H. Lindon[21], A. Linss[46], A.L. Lionti[54], E. Lipeles[136], A. Lipniacka[17], T.M. Liss[173,al], A. Lister[175], J.D. Little[8], B. Liu[79], B.X. Liu[6], H.B. Liu[29], J.B. Liu[60a], J.K.K. Liu[37], K. Liu[60d,60c], M. Liu[60a], P. Liu[15a], Y. Liu[46], Y. Liu[15a,15d], Y.L. Liu[106], Y.W. Liu[60a], M. Livan[71a,71b], A. Lleres[58], J. Llorente Merino[152], S.L. Lloyd[93], C.Y. Lo[63b], E.M. Lobodzinska[46], P. Loch[7], S. Loffredo[74a,74b], T. Lohse[19], K. Lohwasser[149], M. Lokajicek[140], J.D. Long[173], R.E. Long[90], L. Longo[36], K.A. Looper[127], I. Lopez Paz[101], A. Lopez Solis[149], J. Lorenz[114], N. Lorenzo Martinez[5], A.M. Lory[114], P.J. Lösel[114], A. Lösle[52], X. Lou[46], X. Lou[15a], A. Lounis[65], J. Love[6], P.A. Love[90], J.J. Lozano Bahilo[174], M. Lu[60a], Y.J. Lu[64], H.J. Lubatti[148], C. Luci[73a,73b], F.L. Lucio Alves[15c], A. Lucotte[58], F. Luehring[66], I. Luise[135], L. Luminari[73a], B. Lund-Jensen[154], M.S. Lutz[161], D. Lynn[29], H. Lyons[91], R. Lysak[140], E. Lytken[97], F. Lyu[15a], V. Lyubushkin[80], T. Lyubushkina[80], H. Ma[29], L.L. Ma[60b], Y. Ma[95], D.M. Mac Donell[176], G. Maccarrone[51], A. Macchiolo[115], C.M. Macdonald[149], J.C. MacDonald[149], J. Machado Miguens[136], D. Madaffari[174], R. Madar[38], W.F. Mader[48], M. Madugoda Ralalage Don[129], N. Madysa[48], J. Maeda[83], T. Maeno[29], M. Maerker[48], V. Magerl[52], N. Magini[79], J. Magro[67a,67c,q], D.J. Mahon[39], C. Maidantchik[81b], T. Maier[114], A. Maio[139a,139b,139d], K. Maj[84a], O. Majersky[28a], S. Majewski[131], Y. Makida[82], N. Makovec[65], B. Malaescu[135], Pa. Malecki[85], V.P. Maleev[137], F. Malek[58], U. Mallik[78], D. Malon[6], C. Malone[32], S. Maltezos[10], S. Malyukov[80], J. Mamuzic[174], G. Mancini[70a,70b], I. Mandić[92], L. Manhaes de Andrade Filho[81a], I.M. Maniatis[162], J. Manjarres Ramos[48], K.H. Mankinen[97], A. Mann[114], A. Manousos[77], B. Mansoulie[144], I. Manthos[162], S. Manzoni[120], A. Marantis[162], G. Marceca[30], L. Marchese[134], G. Marchiori[135], M. Marcisovsky[140], L. Marcoccia[74a,74b], C. Marcon[97], C.A. Marin Tobon[36], M. Marjanovic[128],

Z. Marshall[18], M.U.F. Martensson[172], S. Marti-Garcia[174], C.B. Martin[127], T.A. Martin[178], V.J. Martin[50], B. Martin dit Latour[17], L. Martinelli[75a,75b], M. Martinez[14,w], P. Martinez Agullo[174], V.I. Martinez Outschoorn[103], S. Martin-Haugh[143], V.S. Martoiu[27b], A.C. Martyniuk[95], A. Marzin[36], S.R. Maschek[115], L. Masetti[100], T. Mashimo[163], R. Mashinistov[111], J. Masik[101], A.L. Maslennikov[122b,122a], L. Massa[23b,23a], P. Massarotti[70a,70b], P. Mastrandrea[72a,72b], A. Mastroberardino[41b,41a], T. Masubuchi[163], D. Matakias[29], A. Matic[114], N. Matsuzawa[163], P. Mättig[24], J. Maurer[27b], B. Maček[92], D.A. Maximov[122b,122a], R. Mazini[158], I. Maznas[162], S.M. Mazza[145], J.P. Mc Gowan[104], S.P. Mc Kee[106], T.G. McCarthy[115], W.P. McCormack[18], E.F. McDonald[105], J.A. Mcfayden[36], G. Mchedlidze[159b], M.A. McKay[42], K.D. McLean[176], S.J. McMahon[143], P.C. McNamara[105], C.J. McNicol[178], R.A. McPherson[176,ab], J.E. Mdhluli[33e], Z.A. Meadows[103], S. Meehan[36], T. Megy[38], S. Mehlhase[114], A. Mehta[91], B. Meirose[43], D. Melini[160], B.R. Mellado Garcia[33e], J.D. Mellenthin[53], M. Melo[28a], F. Meloni[46], A. Melzer[24], E.D. Mendes Gouveia[139a,139e], L. Meng[36], X.T. Meng[106], S. Menke[115], E. Meoni[41b,41a], S. Mergelmeyer[19], S.A.M. Merkt[138], C. Merlassino[134], P. Mermod[54], L. Merola[70a,70b], C. Meroni[69a], G. Merz[106], O. Meshkov[113,111], J.K.R. Meshreki[151], J. Metcalfe[6], A.S. Mete[6], C. Meyer[66], J-P. Meyer[144], F. Miano[156], M. Michetti[19], R.P. Middleton[143], L. Mijović[50], G. Mikenberg[180], M. Mikestikova[140], M. Mikuž[92], H. Mildner[149], M. Milesi[105], A. Milic[167], C.D. Milke[42], D.W. Miller[37], A. Milov[180], D.A. Milstead[45a,45b], R.A. Mina[153], A.A. Minaenko[123], I.A. Minashvili[159b], A.I. Mincer[125], B. Mindur[84a], M. Mineev[80], Y. Minegishi[163], L.M. Mir[14], M. Mironova[134], A. Mirto[68a,68b], K.P. Mistry[136], T. Mitani[179], J. Mitrevski[114], V.A. Mitsou[174], M. Mittal[60c], O. Miu[167], A. Miucci[20], P.S. Miyagawa[93], A. Mizukami[82], J.U. Mjörnmark[97], T. Mkrtchyan[61a], M. Mlynarikova[142], T. Moa[45a,45b], S. Mobius[53], K. Mochizuki[110], P. Mogg[114], S. Mohapatra[39], R. Moles-Valls[24], K. Mönig[46], E. Monnier[102], A. Montalbano[152], J. Montejo Berlingen[36], M. Montella[95], F. Monticelli[89], S. Monzani[69a], N. Morange[65], D. Moreno[22a], M. Moreno Llácer[174], C. Moreno Martinez[14], P. Morettini[55b], M. Morgenstern[160], S. Morgenstern[48], D. Mori[152], M. Morii[59], M. Morinaga[179], V. Morisbak[133], A.K. Morley[36], G. Mornacchi[36], A.P. Morris[95], L. Morvaj[155], P. Moschovakos[36], B. Moser[120], M. Mosidze[159b], T. Moskalets[144], H.J. Moss[149], J. Moss[31,m], E.J.W. Moyse[103], S. Muanza[102], J. Mueller[138], R.S.P. Mueller[114], D. Muenstermann[90], G.A. Mullier[97], D.P. Mungo[69a,69b], J.L. Munoz Martinez[14], F.J. Munoz Sanchez[101], P. Murin[28b], W.J. Murray[178,143], A. Murrone[69a,69b], J.M. Muse[128], M. Muškinja[18], C. Mwewa[33a], A.G. Myagkov[123,ah], A.A. Myers[138], J. Myers[131], M. Myska[141], B.P. Nachman[18], O. Nackenhorst[47], A.Nag Nag[48], K. Nagai[134], K. Nagano[82], Y. Nagasaka[62], J.L. Nagle[29], E. Nagy[102], A.M. Nairz[36], Y. Nakahama[117], K. Nakamura[82], T. Nakamura[163], H. Nanjo[132], F. Napolitano[61a], R.F. Naranjo Garcia[46], R. Narayan[42], I. Naryshkin[137], T. Naumann[46], G. Navarro[22a], P.Y. Nechaeva[111], F. Nechansky[46], T.J. Neep[21], A. Negri[71a,71b], M. Negrini[23b], C. Nellist[119], C. Nelson[104], M.E. Nelson[45a,45b], S. Nemecek[140], M. Nessi[36,e], M.S. Neubauer[173], F. Neuhaus[100], M. Neumann[182], R. Newhouse[175], P.R. Newman[21], C.W. Ng[138], Y.S. Ng[19], Y.W.Y. Ng[171], B. Ngair[35f], H.D.N. Nguyen[102], T. Nguyen Manh[110], E. Nibigira[38], R.B. Nickerson[134], R. Nicolaidou[144], D.S. Nielsen[40], J. Nielsen[145], M. Niemeyer[53], N. Nikiforou[11], V. Nikolaenko[123,ah], I. Nikolic-Audit[135], K. Nikolopoulos[21], P. Nilsson[29], H.R. Nindhito[54], Y. Ninomiya[82], A. Nisati[73a], N. Nishu[60c], R. Nisius[115], I. Nitsche[47], T. Nitta[179], T. Nobe[163], D.L. Noel[32], Y. Noguchi[86], I. Nomidis[135], M.A. Nomura[29], M. Nordberg[36], J. Novak[92], T. Novak[92], O. Novgorodova[48], R. Novotny[141], L. Nozka[130], K. Ntekas[171], E. Nurse[95], F.G. Oakham[34,am], H. Oberlack[115], J. Ocariz[135], A. Ochi[83], I. Ochoa[39], J.P. Ochoa-Ricoux[146a], K. O'Connor[26], S. Oda[88], S. Odaka[82], S. Oerdek[53], A. Ogrodnik[84a], A. Oh[101], S.H. Oh[49], C.C. Ohm[154], H. Oide[165], M.L. Ojeda[167], H. Okawa[169], Y. Okazaki[86], M.W. O'Keefe[91], Y. Okumura[163], T. Okuyama[82], A. Olariu[27b], L.F. Oleiro Seabra[139a], S.A. Olivares Pino[146a], D. Oliveira Damazio[29], J.L. Oliver[1], M.J.R. Olsson[171], A. Olszewski[85], J. Olszowska[85], D.C. O'Neil[152], A.P. O'neill[134], A. Onofre[139a,139e], P.U.E. Onyisi[11], H. Oppen[133], R.G. Oreamuno Madriz[121], M.J. Oreglia[37], G.E. Orellana[89], D. Orestano[75a,75b], N. Orlando[14], R.S. Orr[167], V. O'Shea[57], R. Ospanov[60a], G. Otero y Garzon[30], H. Otono[88], P.S. Ott[61a], G.J. Ottino[18], M. Ouchrif[35e], J. Ouellette[29], F. Ould-Saada[133], A. Ouraou[144,*], Q. Ouyang[15a], M. Owen[57], R.E. Owen[21], V.E. Ozcan[12c], N. Ozturk[8], J. Pacalt[130], H.A. Pacey[32], K. Pachal[49], A. Pacheco Pages[14], C. Padilla Aranda[14], S. Pagan Griso[18], G. Palacino[66], S. Palazzo[50], S. Palestini[36], M. Palka[84b], D. Pallin[38], P. Palni[84a], C.E. Pandini[54], J.G. Panduro Vazquez[94], P. Pani[46], G. Panizzo[67a,67c], L. Paolozzi[54], C. Papadatos[110], K. Papageorgiou[9,g], S. Parajuli[42], A. Paramonov[6], C. Paraskevopoulos[10], D. Paredes Hernandez[63b], S.R. Paredes Saenz[134], B. Parida[180], T.H. Park[167], A.J. Parker[31], M.A. Parker[32], F. Parodi[55b,55a], E.W. Parrish[121], J.A. Parsons[39], U. Parzefall[52], L. Pascual Dominguez[135], V.R. Pascuzzi[18], J.M.P. Pasner[145], F. Pasquali[120], E. Pasqualucci[73a], S. Passaggio[55b], F. Pastore[94], P. Pasuwan[45a,45b], S. Pataraia[100], J.R. Pater[101], A. Pathak[181,i], J. Patton[91], T. Pauly[36], J. Pearkes[153], B. Pearson[115], M. Pedersen[133], L. Pedraza Diaz[119], R. Pedro[139a], T. Peiffer[53], S.V. Peleganchuk[122b,122a], O. Penc[140], H. Peng[60a], B.S. Peralva[81a], M.M. Perego[65], A.P. Pereira Peixoto[139a], L. Pereira Sanchez[45a,45b], D.V. Perepelitsa[29], E. Perez Codina[168a], F. Peri[19], L. Perini[69a,69b], H. Pernegger[36], S. Perrella[139a], A. Perrevoort[120], K. Peters[46], R.F.Y. Peters[101], B.A. Petersen[36], T.C. Petersen[40], E. Petit[102], A. Petridis[1], C. Petridou[162], F. Petrucci[75a,75b], M. Pettee[183], N.E. Pettersson[103], K. Petukhova[142], A. Peyaud[144], R. Pezoa[146d], L. Pezzotti[71a,71b], T. Pham[105], F.H. Phillips[107], P.W. Phillips[143], M.W. Phipps[173], G. Piacquadio[155], E. Pianori[18], A. Picazio[103], R.H. Pickles[101], R. Piegaia[30], D. Pietreanu[27b], J.E. Pilcher[37], A.D. Pilkington[101], M. Pinamonti[67a,67c], J.L. Pinfold[3], C. Pitman Donaldson[95], M. Pitt[161], L. Pizzimento[74a,74b], M.-A. Pleier[29], V. Pleskot[142], E. Plotnikova[80], P. Podberezko[122b,122a], R. Poettgen[97], R. Poggi[54], L. Poggioli[135], I. Pogrebnyak[107], D. Pohl[24], I. Pokharel[53], G. Polesello[71a], A. Poley[152], A. Policicchio[73a,73b], R. Polifka[142], A. Polini[23b], C.S. Pollard[46], V. Polychronakos[29], D. Ponomarenko[112], L. Pontecorvo[36], S. Popa[27a], G.A. Popeneciu[27d], L. Portales[5], D.M. Portillo Quintero[58], S. Pospisil[141], K. Potamianos[46], I.N. Potrap[80], C.J. Potter[32], H. Potti[11], T. Poulsen[97], J. Poveda[174], T.D. Powell[149], G. Pownall[46], M.E. Pozo Astigarraga[36], P. Pralavorio[102], S. Prell[79], D. Price[101], M. Primavera[68a], M.L. Proffitt[148], N. Proklova[112], K. Prokofiev[63c], F. Prokoshin[80], S. Protopopescu[29], J. Proudfoot[6], M. Przybycien[84a], D. Pudzha[137], A. Puri[173], P. Puzo[65], D. Pyatiizbyantseva[112], J. Qian[106], Y. Qin[101], A. Quadt[53], M. Queitsch-Maitland[36], A. Qureshi[1], M. Racko[28a], F. Ragusa[69a,69b], G. Rahal[98], J.A. Raine[54], S. Rajagopalan[29], A. Ramirez Morales[93], K. Ran[15a,15d], T. Rashid[65], D.M. Rauch[46], F. Rauscher[114], S. Rave[100], B. Ravina[149], I. Ravinovich[180], J.H. Rawling[101], M. Raymond[36], A.L. Read[133], N.P. Readioff[58], M. Reale[68a,68b], D.M. Rebuzzi[71a,71b], G. Redlinger[29], K. Reeves[43], J. Reichert[136], D. Reikher[161], A. Reiss[100], A. Rej[151], C. Rembser[36], A. Renardi[46], M. Renda[27b], M.B. Rendel[115], S. Resconi[69a], E.D. Resseguie[18], S. Rettie[95], B. Reynolds[127], E. Reynolds[21], O.L. Rezanova[122b,122a], P. Reznicek[142], E. Ricci[76a,76b], R. Richter[115], S. Richter[46], E. Richter-Was[84b], M. Ridel[135], P. Rieck[115], O. Rifki[46], M. Rijssenbeek[155], A. Rimoldi[71a,71b], M. Rimoldi[46], L. Rinaldi[23b], T.T. Rinn[173], G. Ripellino[154], I. Riu[14], P. Rivadeneira[46], J.C. Rivera Vergara[176], F. Rizatdinova[129], E. Rizvi[93], C. Rizzi[36], S.H. Robertson[104,ab], M. Robin[46], D. Robinson[32], C.M. Robles Gajardo[146d], M. Robles Manzano[100], A. Robson[57], A. Rocchi[74a,74b], E. Rocco[100], C. Roda[72a,72b], S. Rodriguez Bosca[174], A.M. Rodríguez Vera[168b], S. Roe[36], J. Roggel[182], O. Røhne[133], R. Röhrig[115], R.A. Rojas[146d], B. Roland[52], C.P.A. Roland[66], J. Roloff[29], A. Romaniouk[112], M. Romano[23b,23a], N. Rompotis[91], M. Ronzani[125], L. Roos[135], S. Rosati[73a], G. Rosin[103], B.J. Rosser[136], E. Rossi[46], E. Rossi[75a,75b], E. Rossi[70a,70b], L.P. Rossi[55b], L. Rossini[69a,69b], R. Rosten[14], M. Rotaru[27b], B. Rottler[52], D. Rousseau[65], G. Rovelli[71a,71b], A. Roy[11], D. Roy[33e], A. Rozanov[102], Y. Rozen[160], X. Ruan[33e], F. Rühr[52],

A. Ruiz-Martinez[174], A. Rummler[36], Z. Rurikova[52], N.A. Rusakovich[80], H.L. Russell[104], L. Rustige[38,47], J.P. Rutherfoord[7], E.M. Rüttinger[149], M. Rybar[39], G. Rybkin[65], E.B. Rye[133], A. Ryzhov[123], J.A. Sabater Iglesias[46], P. Sabatini[53], S. Sacerdoti[65], H.F-W. Sadrozinski[145], R. Sadykov[80], F. Safai Tehrani[73a], B. Safarzadeh Samani[156], M. Safdari[153], P. Saha[121], S. Saha[104], M. Sahinsoy[115], A. Sahu[182], M. Saimpert[36], M. Saito[163], T. Saito[163], H. Sakamoto[163], D. Salamani[54], G. Salamanna[75a,75b], A. Salnikov[153], J. Salt[174], A. Salvador Salas[14], D. Salvatore[41b,41a], F. Salvatore[156], A. Salvucci[63a,63b,63c], A. Salzburger[36], J. Samarati[36], D. Sammel[52], D. Sampsonidis[162], D. Sampsonidou[162], J. Sánchez[174], A. Sanchez Pineda[67a,36,67c], H. Sandaker[133], C.O. Sander[46], I.G. Sanderswood[90], M. Sandhoff[182], C. Sandoval[22a], D.P.C. Sankey[143], M. Sannino[55b,55a], Y. Sano[117], A. Sansoni[51], C. Santoni[38], H. Santos[139a,139b], S.N. Santpur[18], A. Santra[174], A. Sapronov[80], J.G. Saraiva[139a,139d], O. Sasaki[82], K. Sato[169], F. Sauerburger[52], E. Sauvan[5], P. Savard[167,am], R. Sawada[163], C. Sawyer[143], L. Sawyer[96,ag], I. Sayago Galvan[174], C. Sbarra[23b], A. Sbrizzi[67a,67c], T. Scanlon[95], J. Schaarschmidt[148], P. Schacht[115], D. Schaefer[37], L. Schaefer[136], S. Schaepe[36], U. Schäfer[100], A.C. Schaffer[65], D. Schaile[114], R.D. Schamberger[155], E. Schanet[114], N. Scharmberg[101], V.A. Schegelsky[137], D. Scheirich[142], F. Schenck[19], M. Schernau[171], C. Schiavi[55b,55a], L.K. Schildgen[24], Z.M. Schillaci[26], E.J. Schioppa[68a,68b], M. Schioppa[41b,41a], K.E. Schleicher[52], S. Schlenker[36], K.R. Schmidt-Sommerfeld[115], K. Schmieden[36], C. Schmitt[100], S. Schmitt[46], J.C. Schmoeckel[46], L. Schoeffel[144], A. Schoening[61b], P.G. Scholer[52], E. Schopf[134], M. Schott[100], J.F.P. Schouwenberg[119], J. Schovancova[36], S. Schramm[54], F. Schroeder[182], A. Schulte[100], H-C. Schultz-Coulon[61a], M. Schumacher[52], B.A. Schumm[145], Ph. Schune[144], A. Schwartzman[153], T.A. Schwarz[106], Ph. Schwemling[144], R. Schwienhorst[107], A. Sciandra[145], G. Sciolla[26], M. Scodeggio[46], M. Scornajenghi[41b,41a], F. Scuri[72a], F. Scutti[105], L.M. Scyboz[115], C.D. Sebastiani[91], P. Seema[19], S.C. Seidel[118], A. Seiden[145], B.D. Seidlitz[29], T. Seiss[37], C. Seitz[46], J.M. Seixas[81b], G. Sekhniaidze[70a], S.J. Sekula[42], N. Semprini-Cesari[23b,23a], S. Sen[49], C. Serfon[29], L. Serin[65], L. Serkin[67a,67b], M. Sessa[60a], H. Severini[128], S. Sevova[153], F. Sforza[55b,55a], A. Sfyrla[54], E. Shabalina[53], J.D. Shahinian[145], N.W. Shaikh[45a,45b], D. Shaked Renous[180], L.Y. Shan[15a], M. Shapiro[18], A. Sharma[134], A.S. Sharma[1], P.B. Shatalov[124], K. Shaw[156], S.M. Shaw[101], M. Shehade[180], Y. Shen[128], A.D. Sherman[25], P. Sherwood[95], L. Shi[95], S. Shimizu[82], C.O. Shimmin[183], Y. Shimogama[179], M. Shimojima[116], I.P.J. Shipsey[134], S. Shirabe[165], M. Shiyakova[80,z], J. Shlomi[180], A. Shmeleva[111], M.J. Shochet[37], J. Shojaii[105], D.R. Shope[128], S. Shrestha[127], E.M. Shrif[33e], E. Shulga[180], P. Sicho[140], A.M. Sickles[173], E. Sideras Haddad[33e], O. Sidiropoulou[36], A. Sidoti[23b,23a], F. Siegert[48], Dj. Sijacki[16], M.Jr. Silva[181], M.V. Silva Oliveira[36], S.B. Silverstein[45a], S. Simion[65], R. Simoniello[100], C.J. Simpson-allsop[21], S. Simsek[12b], P. Sinervo[167], V. Sinetckii[113], S. Singh[152], M. Sioli[23b,23a], I. Siral[131], S.Yu. Sivoklokov[113], J. Sjölin[45a,45b], A. Skaf[53], E. Skorda[97], P. Skubic[128], M. Slawinska[85], K. Sliwa[170], R. Slovak[142], V. Smakhtin[180], B.H. Smart[143], J. Smiesko[28b], N. Smirnov[112], S.Yu. Smirnov[112], Y. Smirnov[112], L.N. Smirnova[113,r], O. Smirnova[97], H.A. Smith[134], M. Smizanska[90], K. Smolek[141], A. Smykiewicz[85], A.A. Snesarev[111], H.L. Snoek[120], I.M. Snyder[131], S. Snyder[29], R. Sobie[176,ab], A. Soffer[161], A. Søgaard[50], F. Sohns[53], C.A. Solans Sanchez[36], E.Yu. Soldatov[112], U. Soldevila[174], A.A. Solodkov[123], A. Soloshenko[80], O.V. Solovyanov[123], V. Solovyev[137], P. Sommer[149], H. Son[170], W. Song[143], W.Y. Song[168b], A. Sopczak[141], A.L. Sopio[95], F. Sopkova[28b], S. Sottocornola[71a,71b], R. Soualah[67a,67c], A.M. Soukharev[122b,122a], D. South[46], S. Spagnolo[68a,68b], M. Spalla[115], M. Spangenberg[178], F. Spanò[94], D. Sperlich[52], T.M. Spieker[61a], G. Spigo[36], M. Spina[156], D.P. Spiteri[57], M. Spousta[142], A. Stabile[69a,69b], B.L. Stamas[121], R. Stamen[61a], M. Stamenkovic[120], E. Stanecka[85], B. Stanislaus[134], M.M. Stanitzki[46], M. Stankaityte[134], B. Stapf[120], E.A. Starchenko[123], G.H. Stark[145], J. Stark[58], P. Staroba[140], P. Starovoitov[61a], S. Stärz[104], R. Staszewski[85], G. Stavropoulos[44], M. Stegler[46], P. Steinberg[29], A.L. Steinhebel[131], B. Stelzer[152],

JHEP04(2021)174

H.J. Stelzer[138], O. Stelzer-Chilton[168a], H. Stenzel[56], T.J. Stevenson[156], G.A. Stewart[36], M.C. Stockton[36], G. Stoicea[27b], M. Stolarski[139a], S. Stonjek[115], A. Straessner[48], J. Strandberg[154], S. Strandberg[45a,45b], M. Strauss[128], T. Strebler[102], P. Strizenec[28b], R. Ströhmer[177], D.M. Strom[131], R. Stroynowski[42], A. Strubig[50], S.A. Stucci[29], B. Stugu[17], J. Stupak[128], N.A. Styles[46], D. Su[153], W. Su[60c,148], S. Suchek[61a], V.V. Sulin[111], M.J. Sullivan[91], D.M.S. Sultan[54], S. Sultansoy[4c], T. Sumida[86], S. Sun[106], X. Sun[101], K. Suruliz[156], C.J.E. Suster[157], M.R. Sutton[156], S. Suzuki[82], M. Svatos[140], M. Swiatlowski[168a], S.P. Swift[2], T. Swirski[177], A. Sydorenko[100], I. Sykora[28a], M. Sykora[142], T. Sykora[142], D. Ta[100], K. Tackmann[46,x], J. Taenzer[161], A. Taffard[171], R. Tafirout[168a], H. Takai[29], R. Takashima[87], K. Takeda[83], T. Takeshita[150], E.P. Takeva[50], Y. Takubo[82], M. Talby[102], A.A. Talyshev[122b,122a], K.C. Tam[63b], N.M. Tamir[161], J. Tanaka[163], R. Tanaka[65], S. Tapia Araya[173], S. Tapprogge[100], A. Tarek Abouelfadl Mohamed[107], S. Tarem[160], K. Tariq[60b], G. Tarna[27b,d], G.F. Tartarelli[69a], P. Tas[142], M. Tasevsky[140], T. Tashiro[86], E. Tassi[41b,41a], A. Tavares Delgado[139a], Y. Tayalati[35f], A.J. Taylor[50], G.N. Taylor[105], W. Taylor[168b], H. Teagle[91], A.S. Tee[90], R. Teixeira De Lima[153], P. Teixeira-Dias[94], H. Ten Kate[36], J.J. Teoh[120], S. Terada[82], K. Terashi[163], J. Terron[99], S. Terzo[14], M. Testa[51], R.J. Teuscher[167,ab], S.J. Thais[183], N. Themistokleous[50], T. Theveneaux-Pelzer[46], F. Thiele[40], D.W. Thomas[94], J.O. Thomas[42], J.P. Thomas[21], E.A. Thompson[46], P.D. Thompson[21], E. Thomson[136], E.J. Thorpe[93], R.E. Ticse Torres[53], V.O. Tikhomirov[111,ai], Yu.A. Tikhonov[122b,122a], S. Timoshenko[112], P. Tipton[183], S. Tisserant[102], K. Todome[23b,23a], S. Todorova-Nova[142], S. Todt[48], J. Tojo[88], S. Tokár[28a], K. Tokushuku[82], E. Tolley[127], R. Tombs[32], K.G. Tomiwa[33e], M. Tomoto[117], L. Tompkins[153], P. Tornambe[103], E. Torrence[131], H. Torres[48], E. Torró Pastor[148], C. Tosciri[134], J. Toth[102,aa], D.R. Tovey[149], A. Traeet[17], C.J. Treado[125], T. Trefzger[177], F. Tresoldi[156], A. Tricoli[29], I.M. Trigger[168a], S. Trincaz-Duvoid[135], D.A. Trischuk[175], W. Trischuk[167], B. Trocmé[58], A. Trofymov[65], C. Troncon[69a], F. Trovato[156], L. Truong[33c], M. Trzebinski[85], A. Trzupek[85], F. Tsai[46], J.C-L. Tseng[134], P.V. Tsiareshka[108,af], A. Tsirigotis[162,u], V. Tsiskaridze[155], E.G. Tskhadadze[159a], M. Tsopoulou[162], I.I. Tsukerman[124], V. Tsulaia[18], S. Tsuno[82], D. Tsybychev[155], Y. Tu[63b], A. Tudorache[27b], V. Tudorache[27b], T.T. Tulbure[27a], A.N. Tuna[59], S. Turchikhin[80], D. Turgeman[180], I. Turk Cakir[4b,s], R.J. Turner[21], R. Turra[69a], P.M. Tuts[39], S. Tzamarias[162], E. Tzovara[100], K. Uchida[163], F. Ukegawa[169], G. Unal[36], A. Undrus[29], G. Unel[171], F.C. Ungaro[105], Y. Unno[82], K. Uno[163], J. Urban[28b], P. Urquijo[105], G. Usai[8], Z. Uysal[12d], V. Vacek[141], B. Vachon[104], K.O.H. Vadla[133], T. Vafeiadis[36], A. Vaidya[95], C. Valderanis[114], E. Valdes Santurio[45a,45b], M. Valente[54], S. Valentinetti[23b,23a], A. Valero[174], L. Valéry[46], R.A. Vallance[21], A. Vallier[36], J.A. Valls Ferrer[174], T.R. Van Daalen[14], P. Van Gemmeren[6], I. Van Vulpen[120], M. Vanadia[74a,74b], W. Vandelli[36], M. Vandenbroucke[144], E.R. Vandewall[129], A. Vaniachine[166], D. Vannicola[73a,73b], R. Vari[73a], E.W. Varnes[7], C. Varni[55b,55a], T. Varol[158], D. Varouchas[65], K.E. Varvell[157], M.E. Vasile[27b], G.A. Vasquez[176], F. Vazeille[38], D. Vazquez Furelos[14], T. Vazquez Schroeder[36], J. Veatch[53], V. Vecchio[101], M.J. Veen[120], L.M. Veloce[167], F. Veloso[139a,139c], S. Veneziano[73a], A. Ventura[68a,68b], N. Venturi[36], A. Verbytskyi[115], V. Vercesi[71a], M. Verducci[72a,72b], C.M. Vergel Infante[79], C. Vergis[24], W. Verkerke[120], A.T. Vermeulen[120], J.C. Vermeulen[120], C. Vernieri[153], M.C. Vetterli[152,am], N. Viaux Maira[146d], T. Vickey[149], O.E. Vickey Boeriu[149], G.H.A. Viehhauser[134], L. Vigani[61b], M. Villa[23b,23a], M. Villaplana Perez[3], E.M. Villhauer[50], E. Vilucchi[51], M.G. Vincter[34], G.S. Virdee[21], A. Vishwakarma[50], C. Vittori[23b,23a], I. Vivarelli[156], M. Vogel[182], P. Vokac[141], S.E. von Buddenbrock[33e], E. Von Toerne[24], V. Vorobel[142], K. Vorobev[112], M. Vos[174], J.H. Vossebeld[91], M. Vozak[101], N. Vranjes[16], M. Vranjes Milosavljevic[16], V. Vrba[141,*], M. Vreeswijk[120], R. Vuillermet[36], I. Vukotic[37], S. Wada[169], P. Wagner[24], W. Wagner[182], J. Wagner-Kuhr[114], S. Wahdan[182], H. Wahlberg[89], R. Wakasa[169], V.M. Walbrecht[115], J. Walder[90], R. Walker[114], S.D. Walker[94], W. Walkowiak[151], V. Wallangen[45a,45b], A.M. Wang[59], A.Z. Wang[181],

C. Wang[60c], F. Wang[181], H. Wang[18], H. Wang[3], J. Wang[63a], P. Wang[42], Q. Wang[128], R.-J. Wang[100], R. Wang[60a], R. Wang[6], S.M. Wang[158], W.T. Wang[60a], W. Wang[15c], W.X. Wang[60a], Y. Wang[60a], Z. Wang[106], C. Wanotayaroj[46], A. Warburton[104], C.P. Ward[32], D.R. Wardrope[95], N. Warrack[57], A.T. Watson[21], M.F. Watson[21], G. Watts[148], B.M. Waugh[95], A.F. Webb[11], C. Weber[29], M.S. Weber[20], S.A. Weber[34], S.M. Weber[61a], A.R. Weidberg[134], J. Weingarten[47], M. Weirich[100], C. Weiser[52], P.S. Wells[36], T. Wenaus[29], T. Wengler[36], S. Wenig[36], N. Wermes[24], M. Wessels[61a], T.D. Weston[20], K. Whalen[131], N.L. Whallon[148], A.M. Wharton[90], A.S. White[106], A. White[8], M.J. White[1], D. Whiteson[171], B.W. Whitmore[90], W. Wiedenmann[181], C. Wiel[48], M. Wielers[143], N. Wieseotte[100], C. Wiglesworth[40], L.A.M. Wiik-Fuchs[52], H.G. Wilkens[36], L.J. Wilkins[94], H.H. Williams[136], S. Williams[32], S. Willocq[103], P.J. Windischhofer[134], I. Wingerter-Seez[5], E. Winkels[156], F. Winklmeier[131], B.T. Winter[52], M. Wittgen[153], M. Wobisch[96], A. Wolf[100], R. Wölker[134], J. Wollrath[52], M.W. Wolter[85], H. Wolters[139a,139c], V.W.S. Wong[175], N.L. Woods[145], S.D. Worm[46], B.K. Wosiek[85], K.W. Woźniak[85], K. Wraight[57], S.L. Wu[181], X. Wu[54], Y. Wu[60a], J. Wuerzinger[134], T.R. Wyatt[101], B.M. Wynne[50], S. Xella[40], J. Xiang[63c], X. Xiao[106], X. Xie[60a], I. Xiotidis[156], D. Xu[15a], H. Xu[60a], H. Xu[60a], L. Xu[29], T. Xu[144], W. Xu[106], Z. Xu[60b], Z. Xu[153], B. Yabsley[157], S. Yacoob[33a], K. Yajima[132], D.P. Yallup[95], N. Yamaguchi[88], Y. Yamaguchi[165], A. Yamamoto[82], M. Yamatani[163], T. Yamazaki[163], Y. Yamazaki[83], J. Yan[60c], Z. Yan[25], H.J. Yang[60c,60d], H.T. Yang[18], S. Yang[60a], T. Yang[63c], X. Yang[60b,58], Y. Yang[163], Z. Yang[106,60a], W-M. Yao[18], Y.C. Yap[46], Y. Yasu[82], E. Yatsenko[60c,60d], H. Ye[15c], J. Ye[42], S. Ye[29], I. Yeletskikh[80], M.R. Yexley[90], E. Yigitbasi[25], P. Yin[39], K. Yorita[179], K. Yoshihara[79], C.J.S. Young[36], C. Young[153], J. Yu[79], R. Yuan[60b,h], X. Yue[61a], M. Zaazoua[35f], B. Zabinski[85], G. Zacharis[10], E. Zaffaroni[54], J. Zahreddine[135], A.M. Zaitsev[123,ah], T. Zakareishvili[159b], N. Zakharchuk[34], S. Zambito[36], D. Zanzi[36], D.R. Zaripovas[57], S.V. Zeißner[47], C. Zeitnitz[182], G. Zemaityte[134], J.C. Zeng[173], O. Zenin[123], T. Ženiš[28a], D. Zerwas[65], M. Zgubič[134], B. Zhang[15c], D.F. Zhang[15b], G. Zhang[15b], J. Zhang[6], K. Zhang[15a], L. Zhang[15c], L. Zhang[60a], M. Zhang[173], R. Zhang[181], S. Zhang[106], X. Zhang[60c], X. Zhang[60b], Y. Zhang[15a,15d], Z. Zhang[63a], Z. Zhang[65], P. Zhao[49], Z. Zhao[60a], A. Zhemchugov[80], Z. Zheng[106], D. Zhong[173], B. Zhou[106], C. Zhou[181], H. Zhou[7], M.S. Zhou[15a,15d], M. Zhou[155], N. Zhou[60c], Y. Zhou[7], C.G. Zhu[60b], C. Zhu[15a,15d], H.L. Zhu[60a], H. Zhu[15a], J. Zhu[106], Y. Zhu[60a], X. Zhuang[15a], K. Zhukov[111], V. Zhulanov[122b,122a], D. Zieminska[66], N.I. Zimine[80], S. Zimmermann[52,*], Z. Zinonos[115], M. Ziolkowski[151], L. Živković[16], G. Zobernig[181], A. Zoccoli[23b,23a], K. Zoch[53], T.G. Zorbas[149], R. Zou[37], L. Zwalinski[36]

[1] *Department of Physics, University of Adelaide, Adelaide; Australia*
[2] *Physics Department, SUNY Albany, Albany NY; United States of America*
[3] *Department of Physics, University of Alberta, Edmonton AB; Canada*
[4] *[(a)] Department of Physics, Ankara University, Ankara;[(b)] Istanbul Aydin University, Application and Research Center for Advanced Studies, Istanbul;[(c)] Division of Physics, TOBB University of Economics and Technology, Ankara; Turkey*
[5] *LAPP, Université Grenoble Alpes, Université Savoie Mont Blanc, CNRS/IN2P3, Annecy; France*
[6] *High Energy Physics Division, Argonne National Laboratory, Argonne IL; United States of America*
[7] *Department of Physics, University of Arizona, Tucson AZ; United States of America*
[8] *Department of Physics, University of Texas at Arlington, Arlington TX; United States of America*
[9] *Physics Department, National and Kapodistrian University of Athens, Athens; Greece*
[10] *Physics Department, National Technical University of Athens, Zografou; Greece*
[11] *Department of Physics, University of Texas at Austin, Austin TX; United States of America*
[12] *[(a)] Bahcesehir University, Faculty of Engineering and Natural Sciences, Istanbul;[(b)] Istanbul Bilgi University, Faculty of Engineering and Natural Sciences, Istanbul;[(c)] Department of Physics, Bogazici University, Istanbul;[(d)] Department of Physics Engineering, Gaziantep University, Gaziantep; Turkey*
[13] *Institute of Physics, Azerbaijan Academy of Sciences, Baku; Azerbaijan*

[14] *Institut de Física d'Altes Energies (IFAE), Barcelona Institute of Science and Technology, Barcelona; Spain*
[15] [(a)] *Institute of High Energy Physics, Chinese Academy of Sciences, Beijing;*[(b)] *Physics Department, Tsinghua University, Beijing;*[(c)] *Department of Physics, Nanjing University, Nanjing;*[(d)] *University of Chinese Academy of Science (UCAS), Beijing; China*
[16] *Institute of Physics, University of Belgrade, Belgrade; Serbia*
[17] *Department for Physics and Technology, University of Bergen, Bergen; Norway*
[18] *Physics Division, Lawrence Berkeley National Laboratory and University of California, Berkeley CA; United States of America*
[19] *Institut für Physik, Humboldt Universität zu Berlin, Berlin; Germany*
[20] *Albert Einstein Center for Fundamental Physics and Laboratory for High Energy Physics, University of Bern, Bern; Switzerland*
[21] *School of Physics and Astronomy, University of Birmingham, Birmingham; United Kingdom*
[22] [(a)] *Facultad de Ciencias y Centro de Investigaciónes, Universidad Antonio Nariño, Bogotá;*[(b)] *Departamento de Física, Universidad Nacional de Colombia, Bogotá, Colombia; Colombia*
[23] [(a)] *INFN Bologna and Università di Bologna, Dipartimento di Fisica;*[(b)] *INFN Sezione di Bologna; Italy*
[24] *Physikalisches Institut, Universität Bonn, Bonn; Germany*
[25] *Department of Physics, Boston University, Boston MA; United States of America*
[26] *Department of Physics, Brandeis University, Waltham MA; United States of America*
[27] [(a)] *Transilvania University of Brasov, Brasov;*[(b)] *Horia Hulubei National Institute of Physics and Nuclear Engineering, Bucharest;*[(c)] *Department of Physics, Alexandru Ioan Cuza University of Iasi, Iasi;*[(d)] *National Institute for Research and Development of Isotopic and Molecular Technologies, Physics Department, Cluj-Napoca;*[(e)] *University Politehnica Bucharest, Bucharest;*[(f)] *West University in Timisoara, Timisoara; Romania*
[28] [(a)] *Faculty of Mathematics, Physics and Informatics, Comenius University, Bratislava;*[(b)] *Department of Subnuclear Physics, Institute of Experimental Physics of the Slovak Academy of Sciences, Kosice; Slovak Republic*
[29] *Physics Department, Brookhaven National Laboratory, Upton NY; United States of America*
[30] *Departamento de Física, Universidad de Buenos Aires, Buenos Aires; Argentina*
[31] *California State University, CA; United States of America*
[32] *Cavendish Laboratory, University of Cambridge, Cambridge; United Kingdom*
[33] [(a)] *Department of Physics, University of Cape Town, Cape Town;*[(b)] *iThemba Labs, Western Cape;*[(c)] *Department of Mechanical Engineering Science, University of Johannesburg, Johannesburg;*[(d)] *University of South Africa, Department of Physics, Pretoria;*[(e)] *School of Physics, University of the Witwatersrand, Johannesburg; South Africa*
[34] *Department of Physics, Carleton University, Ottawa ON; Canada*
[35] [(a)] *Faculté des Sciences Ain Chock, Réseau Universitaire de Physique des Hautes Energies - Université Hassan II, Casablanca;*[(b)] *Faculté des Sciences, Université Ibn-Tofail, Kénitra;*[(c)] *Faculté des Sciences Semlalia, Université Cadi Ayyad, LPHEA-Marrakech;*[(d)] *Moroccan Foundation for Advanced Science Innovation and Research (MAScIR), Rabat;*[(e)] *LPMR, Faculté des Sciences, Université Mohamed Premier, Oujda;*[(f)] *Faculté des sciences, Université Mohammed V, Rabat; Morocco*
[36] *CERN, Geneva; Switzerland*
[37] *Enrico Fermi Institute, University of Chicago, Chicago IL; United States of America*
[38] *LPC, Université Clermont Auvergne, CNRS/IN2P3, Clermont-Ferrand; France*
[39] *Nevis Laboratory, Columbia University, Irvington NY; United States of America*
[40] *Niels Bohr Institute, University of Copenhagen, Copenhagen; Denmark*
[41] [(a)] *Dipartimento di Fisica, Università della Calabria, Rende;*[(b)] *INFN Gruppo Collegato di Cosenza, Laboratori Nazionali di Frascati; Italy*
[42] *Physics Department, Southern Methodist University, Dallas TX; United States of America*
[43] *Physics Department, University of Texas at Dallas, Richardson TX; United States of America*
[44] *National Centre for Scientific Research "Demokritos", Agia Paraskevi; Greece*
[45] [(a)] *Department of Physics, Stockholm University;*[(b)] *Oskar Klein Centre, Stockholm; Sweden*

JHEP04(2021)174

[46] *Deutsches Elektronen-Synchrotron DESY, Hamburg and Zeuthen; Germany*
[47] *Lehrstuhl für Experimentelle Physik IV, Technische Universität Dortmund, Dortmund; Germany*
[48] *Institut für Kern- und Teilchenphysik, Technische Universität Dresden, Dresden; Germany*
[49] *Department of Physics, Duke University, Durham NC; United States of America*
[50] *SUPA - School of Physics and Astronomy, University of Edinburgh, Edinburgh; United Kingdom*
[51] *INFN e Laboratori Nazionali di Frascati, Frascati; Italy*
[52] *Physikalisches Institut, Albert-Ludwigs-Universität Freiburg, Freiburg; Germany*
[53] *II. Physikalisches Institut, Georg-August-Universität Göttingen, Göttingen; Germany*
[54] *Département de Physique Nucléaire et Corpusculaire, Université de Genève, Genève; Switzerland*
[55] [(a)] *Dipartimento di Fisica, Università di Genova, Genova;* [(b)] *INFN Sezione di Genova; Italy*
[56] *II. Physikalisches Institut, Justus-Liebig-Universität Giessen, Giessen; Germany*
[57] *SUPA - School of Physics and Astronomy, University of Glasgow, Glasgow; United Kingdom*
[58] *LPSC, Université Grenoble Alpes, CNRS/IN2P3, Grenoble INP, Grenoble; France*
[59] *Laboratory for Particle Physics and Cosmology, Harvard University, Cambridge MA; United States of America*
[60] [(a)] *Department of Modern Physics and State Key Laboratory of Particle Detection and Electronics, University of Science and Technology of China, Hefei;* [(b)] *Institute of Frontier and Interdisciplinary Science and Key Laboratory of Particle Physics and Particle Irradiation (MOE), Shandong University, Qingdao;* [(c)] *School of Physics and Astronomy, Shanghai Jiao Tong University, Key Laboratory for Particle Astrophysics and Cosmology (MOE), SKLPPC, Shanghai;* [(d)] *Tsung-Dao Lee Institute, Shanghai; China*
[61] [(a)] *Kirchhoff-Institut für Physik, Ruprecht-Karls-Universität Heidelberg, Heidelberg;* [(b)] *Physikalisches Institut, Ruprecht-Karls-Universität Heidelberg, Heidelberg; Germany*
[62] *Faculty of Applied Information Science, Hiroshima Institute of Technology, Hiroshima; Japan*
[63] [(a)] *Department of Physics, Chinese University of Hong Kong, Shatin, N.T., Hong Kong;* [(b)] *Department of Physics, University of Hong Kong, Hong Kong;* [(c)] *Department of Physics and Institute for Advanced Study, Hong Kong University of Science and Technology, Clear Water Bay, Kowloon, Hong Kong; China*
[64] *Department of Physics, National Tsing Hua University, Hsinchu; Taiwan*
[65] *IJCLab, Université Paris-Saclay, CNRS/IN2P3, 91405, Orsay; France*
[66] *Department of Physics, Indiana University, Bloomington IN; United States of America*
[67] [(a)] *INFN Gruppo Collegato di Udine, Sezione di Trieste, Udine;* [(b)] *ICTP, Trieste;* [(c)] *Dipartimento Politecnico di Ingegneria e Architettura, Università di Udine, Udine; Italy*
[68] [(a)] *INFN Sezione di Lecce;* [(b)] *Dipartimento di Matematica e Fisica, Università del Salento, Lecce; Italy*
[69] [(a)] *INFN Sezione di Milano;* [(b)] *Dipartimento di Fisica, Università di Milano, Milano; Italy*
[70] [(a)] *INFN Sezione di Napoli;* [(b)] *Dipartimento di Fisica, Università di Napoli, Napoli; Italy*
[71] [(a)] *INFN Sezione di Pavia;* [(b)] *Dipartimento di Fisica, Università di Pavia, Pavia; Italy*
[72] [(a)] *INFN Sezione di Pisa;* [(b)] *Dipartimento di Fisica E. Fermi, Università di Pisa, Pisa; Italy*
[73] [(a)] *INFN Sezione di Roma;* [(b)] *Dipartimento di Fisica, Sapienza Università di Roma, Roma; Italy*
[74] [(a)] *INFN Sezione di Roma Tor Vergata;* [(b)] *Dipartimento di Fisica, Università di Roma Tor Vergata, Roma; Italy*
[75] [(a)] *INFN Sezione di Roma Tre;* [(b)] *Dipartimento di Matematica e Fisica, Università Roma Tre, Roma; Italy*
[76] [(a)] *INFN-TIFPA;* [(b)] *Università degli Studi di Trento, Trento; Italy*
[77] *Institut für Astro- und Teilchenphysik, Leopold-Franzens-Universität, Innsbruck; Austria*
[78] *University of Iowa, Iowa City IA; United States of America*
[79] *Department of Physics and Astronomy, Iowa State University, Ames IA; United States of America*
[80] *Joint Institute for Nuclear Research, Dubna; Russia*
[81] [(a)] *Departamento de Engenharia Elétrica, Universidade Federal de Juiz de Fora (UFJF), Juiz de Fora;* [(b)] *Universidade Federal do Rio De Janeiro COPPE/EE/IF, Rio de Janeiro;* [(c)] *Instituto de Física, Universidade de São Paulo, São Paulo; Brazil*
[82] *KEK, High Energy Accelerator Research Organization, Tsukuba; Japan*
[83] *Graduate School of Science, Kobe University, Kobe; Japan*

JHEP04(2021)174

[84] [(a)] AGH University of Science and Technology, Faculty of Physics and Applied Computer Science, Krakow;[(b)] Marian Smoluchowski Institute of Physics, Jagiellonian University, Krakow; Poland
[85] Institute of Nuclear Physics Polish Academy of Sciences, Krakow; Poland
[86] Faculty of Science, Kyoto University, Kyoto; Japan
[87] Kyoto University of Education, Kyoto; Japan
[88] Research Center for Advanced Particle Physics and Department of Physics, Kyushu University, Fukuoka; Japan
[89] Instituto de Física La Plata, Universidad Nacional de La Plata and CONICET, La Plata; Argentina
[90] Physics Department, Lancaster University, Lancaster; United Kingdom
[91] Oliver Lodge Laboratory, University of Liverpool, Liverpool; United Kingdom
[92] Department of Experimental Particle Physics, Jožef Stefan Institute and Department of Physics, University of Ljubljana, Ljubljana; Slovenia
[93] School of Physics and Astronomy, Queen Mary University of London, London; United Kingdom
[94] Department of Physics, Royal Holloway University of London, Egham; United Kingdom
[95] Department of Physics and Astronomy, University College London, London; United Kingdom
[96] Louisiana Tech University, Ruston LA; United States of America
[97] Fysiska institutionen, Lunds universitet, Lund; Sweden
[98] Centre de Calcul de l'Institut National de Physique Nucléaire et de Physique des Particules (IN2P3), Villeurbanne; France
[99] Departamento de Física Teorica C-15 and CIAFF, Universidad Autónoma de Madrid, Madrid; Spain
[100] Institut für Physik, Universität Mainz, Mainz; Germany
[101] School of Physics and Astronomy, University of Manchester, Manchester; United Kingdom
[102] CPPM, Aix-Marseille Université, CNRS/IN2P3, Marseille; France
[103] Department of Physics, University of Massachusetts, Amherst MA; United States of America
[104] Department of Physics, McGill University, Montreal QC; Canada
[105] School of Physics, University of Melbourne, Victoria; Australia
[106] Department of Physics, University of Michigan, Ann Arbor MI; United States of America
[107] Department of Physics and Astronomy, Michigan State University, East Lansing MI; United States of America
[108] B.I. Stepanov Institute of Physics, National Academy of Sciences of Belarus, Minsk; Belarus
[109] Research Institute for Nuclear Problems of Byelorussian State University, Minsk; Belarus
[110] Group of Particle Physics, University of Montreal, Montreal QC; Canada
[111] P.N. Lebedev Physical Institute of the Russian Academy of Sciences, Moscow; Russia
[112] National Research Nuclear University MEPhI, Moscow; Russia
[113] D.V. Skobeltsyn Institute of Nuclear Physics, M.V. Lomonosov Moscow State University, Moscow; Russia
[114] Fakultät für Physik, Ludwig-Maximilians-Universität München, München; Germany
[115] Max-Planck-Institut für Physik (Werner-Heisenberg-Institut), München; Germany
[116] Nagasaki Institute of Applied Science, Nagasaki; Japan
[117] Graduate School of Science and Kobayashi-Maskawa Institute, Nagoya University, Nagoya; Japan
[118] Department of Physics and Astronomy, University of New Mexico, Albuquerque NM; United States of America
[119] Institute for Mathematics, Astrophysics and Particle Physics, Radboud University/Nikhef, Nijmegen; Netherlands
[120] Nikhef National Institute for Subatomic Physics and University of Amsterdam, Amsterdam; Netherlands
[121] Department of Physics, Northern Illinois University, DeKalb IL; United States of America
[122] [(a)] Budker Institute of Nuclear Physics and NSU, SB RAS, Novosibirsk;[(b)] Novosibirsk State University Novosibirsk; Russia
[123] Institute for High Energy Physics of the National Research Centre Kurchatov Institute, Protvino; Russia
[124] Institute for Theoretical and Experimental Physics named by A.I. Alikhanov of National Research Centre "Kurchatov Institute", Moscow; Russia

[125] *Department of Physics, New York University, New York NY; United States of America*
[126] *Ochanomizu University, Otsuka, Bunkyo-ku, Tokyo; Japan*
[127] *Ohio State University, Columbus OH; United States of America*
[128] *Homer L. Dodge Department of Physics and Astronomy, University of Oklahoma, Norman OK; United States of America*
[129] *Department of Physics, Oklahoma State University, Stillwater OK; United States of America*
[130] *Palacký University, RCPTM, Joint Laboratory of Optics, Olomouc; Czech Republic*
[131] *Institute for Fundamental Science, University of Oregon, Eugene, OR; United States of America*
[132] *Graduate School of Science, Osaka University, Osaka; Japan*
[133] *Department of Physics, University of Oslo, Oslo; Norway*
[134] *Department of Physics, Oxford University, Oxford; United Kingdom*
[135] *LPNHE, Sorbonne Université, Université de Paris, CNRS/IN2P3, Paris; France*
[136] *Department of Physics, University of Pennsylvania, Philadelphia PA; United States of America*
[137] *Konstantinov Nuclear Physics Institute of National Research Centre "Kurchatov Institute", PNPI, St. Petersburg; Russia*
[138] *Department of Physics and Astronomy, University of Pittsburgh, Pittsburgh PA; United States of America*
[139] [(a)] *Laboratório de Instrumentação e Física Experimental de Partículas - LIP, Lisboa;* [(b)] *Departamento de Física, Faculdade de Ciências, Universidade de Lisboa, Lisboa;* [(c)] *Departamento de Física, Universidade de Coimbra, Coimbra;* [(d)] *Centro de Física Nuclear da Universidade de Lisboa, Lisboa;* [(e)] *Departamento de Física, Universidade do Minho, Braga;* [(f)] *Departamento de Física Teórica y del Cosmos, Universidad de Granada, Granada (Spain);* [(g)] *Dep Física and CEFITEC of Faculdade de Ciências e Tecnologia, Universidade Nova de Lisboa, Caparica;* [(h)] *Instituto Superior Técnico, Universidade de Lisboa, Lisboa; Portugal*
[140] *Institute of Physics of the Czech Academy of Sciences, Prague; Czech Republic*
[141] *Czech Technical University in Prague, Prague; Czech Republic*
[142] *Charles University, Faculty of Mathematics and Physics, Prague; Czech Republic*
[143] *Particle Physics Department, Rutherford Appleton Laboratory, Didcot; United Kingdom*
[144] *IRFU, CEA, Université Paris-Saclay, Gif-sur-Yvette; France*
[145] *Santa Cruz Institute for Particle Physics, University of California Santa Cruz, Santa Cruz CA; United States of America*
[146] [(a)] *Departamento de Física, Pontificia Universidad Católica de Chile, Santiago;* [(b)] *Universidad Andres Bello, Department of Physics, Santiago;* [(c)] *Instituto de Alta Investigación, Universidad de Tarapacá;* [(d)] *Departamento de Física, Universidad Técnica Federico Santa María, Valparaíso; Chile*
[147] *Universidade Federal de São João del Rei (UFSJ), São João del Rei; Brazil*
[148] *Department of Physics, University of Washington, Seattle WA; United States of America*
[149] *Department of Physics and Astronomy, University of Sheffield, Sheffield; United Kingdom*
[150] *Department of Physics, Shinshu University, Nagano; Japan*
[151] *Department Physik, Universität Siegen, Siegen; Germany*
[152] *Department of Physics, Simon Fraser University, Burnaby BC; Canada*
[153] *SLAC National Accelerator Laboratory, Stanford CA; United States of America*
[154] *Physics Department, Royal Institute of Technology, Stockholm; Sweden*
[155] *Departments of Physics and Astronomy, Stony Brook University, Stony Brook NY; United States of America*
[156] *Department of Physics and Astronomy, University of Sussex, Brighton; United Kingdom*
[157] *School of Physics, University of Sydney, Sydney; Australia*
[158] *Institute of Physics, Academia Sinica, Taipei; Taiwan*
[159] [(a)] *E. Andronikashvili Institute of Physics, Iv. Javakhishvili Tbilisi State University, Tbilisi;* [(b)] *High Energy Physics Institute, Tbilisi State University, Tbilisi; Georgia*
[160] *Department of Physics, Technion, Israel Institute of Technology, Haifa; Israel*
[161] *Raymond and Beverly Sackler School of Physics and Astronomy, Tel Aviv University, Tel Aviv; Israel*
[162] *Department of Physics, Aristotle University of Thessaloniki, Thessaloniki; Greece*

JHEP04(2021)174

[163] International Center for Elementary Particle Physics and Department of Physics, University of Tokyo, Tokyo; Japan
[164] Graduate School of Science and Technology, Tokyo Metropolitan University, Tokyo; Japan
[165] Department of Physics, Tokyo Institute of Technology, Tokyo; Japan
[166] Tomsk State University, Tomsk; Russia
[167] Department of Physics, University of Toronto, Toronto ON; Canada
[168] [(a)] TRIUMF, Vancouver BC;[(b)] Department of Physics and Astronomy, York University, Toronto ON; Canada
[169] Division of Physics and Tomonaga Center for the History of the Universe, Faculty of Pure and Applied Sciences, University of Tsukuba, Tsukuba; Japan
[170] Department of Physics and Astronomy, Tufts University, Medford MA; United States of America
[171] Department of Physics and Astronomy, University of California Irvine, Irvine CA; United States of America
[172] Department of Physics and Astronomy, University of Uppsala, Uppsala; Sweden
[173] Department of Physics, University of Illinois, Urbana IL; United States of America
[174] Instituto de Física Corpuscular (IFIC), Centro Mixto Universidad de Valencia - CSIC, Valencia; Spain
[175] Department of Physics, University of British Columbia, Vancouver BC; Canada
[176] Department of Physics and Astronomy, University of Victoria, Victoria BC; Canada
[177] Fakultät für Physik und Astronomie, Julius-Maximilians-Universität Würzburg, Würzburg; Germany
[178] Department of Physics, University of Warwick, Coventry; United Kingdom
[179] Waseda University, Tokyo; Japan
[180] Department of Particle Physics and Astrophysics, Weizmann Institute of Science, Rehovot; Israel
[181] Department of Physics, University of Wisconsin, Madison WI; United States of America
[182] Fakultät für Mathematik und Naturwissenschaften, Fachgruppe Physik, Bergische Universität Wuppertal, Wuppertal; Germany
[183] Department of Physics, Yale University, New Haven CT; United States of America

[a] Also at Borough of Manhattan Community College, City University of New York, New York NY; United States of America
[b] Also at Centro Studi e Ricerche Enrico Fermi; Italy
[c] Also at CERN, Geneva; Switzerland
[d] Also at CPPM, Aix-Marseille Université, CNRS/IN2P3, Marseille; France
[e] Also at Département de Physique Nucléaire et Corpusculaire, Université de Genève, Genève; Switzerland
[f] Also at Departament de Fisica de la Universitat Autonoma de Barcelona, Barcelona; Spain
[g] Also at Department of Financial and Management Engineering, University of the Aegean, Chios; Greece
[h] Also at Department of Physics and Astronomy, Michigan State University, East Lansing MI; United States of America
[i] Also at Department of Physics and Astronomy, University of Louisville, Louisville, KY; United States of America
[j] Also at Department of Physics, Ben Gurion University of the Negev, Beer Sheva; Israel
[k] Also at Department of Physics, California State University, East Bay; United States of America
[l] Also at Department of Physics, California State University, Fresno; United States of America
[m] Also at Department of Physics, California State University, Sacramento; United States of America
[n] Also at Department of Physics, King's College London, London; United Kingdom
[o] Also at Department of Physics, St. Petersburg State Polytechnical University, St. Petersburg; Russia
[p] Also at Department of Physics, University of Fribourg, Fribourg; Switzerland
[q] Also at Dipartimento di Matematica, Informatica e Fisica, Università di Udine, Udine; Italy
[r] Also at Faculty of Physics, M.V. Lomonosov Moscow State University, Moscow; Russia
[s] Also at Giresun University, Faculty of Engineering, Giresun; Turkey
[t] Also at Graduate School of Science, Osaka University, Osaka; Japan

JHEP04(2021)174

[u] Also at Hellenic Open University, Patras; Greece
[v] Also at IJCLab, Université Paris-Saclay, CNRS/IN2P3, 91405, Orsay; France
[w] Also at Institucio Catalana de Recerca i Estudis Avancats, ICREA, Barcelona; Spain
[x] Also at Institut für Experimentalphysik, Universität Hamburg, Hamburg; Germany
[y] Also at Institute for Mathematics, Astrophysics and Particle Physics, Radboud University/Nikhef, Nijmegen; Netherlands
[z] Also at Institute for Nuclear Research and Nuclear Energy (INRNE) of the Bulgarian Academy of Sciences, Sofia; Bulgaria
[aa] Also at Institute for Particle and Nuclear Physics, Wigner Research Centre for Physics, Budapest; Hungary
[ab] Also at Institute of Particle Physics (IPP); Canada
[ac] Also at Institute of Physics, Azerbaijan Academy of Sciences, Baku; Azerbaijan
[ad] Also at Instituto de Fisica Teorica, IFT-UAM/CSIC, Madrid; Spain
[ae] Also at Istanbul University, Dept. of Physics, Istanbul; Turkey
[af] Also at Joint Institute for Nuclear Research, Dubna; Russia
[ag] Also at Louisiana Tech University, Ruston LA; United States of America
[ah] Also at Moscow Institute of Physics and Technology State University, Dolgoprudny; Russia
[ai] Also at National Research Nuclear University MEPhI, Moscow; Russia
[aj] Also at Physics Department, An-Najah National University, Nablus; Palestine
[ak] Also at Physikalisches Institut, Albert-Ludwigs-Universität Freiburg, Freiburg; Germany
[al] Also at The City College of New York, New York NY; United States of America
[am] Also at TRIUMF, Vancouver BC; Canada
[an] Also at Università di Napoli Parthenope, Napoli; Italy
[ao] Also at University of Chinese Academy of Sciences (UCAS), Beijing; China
[*] Deceased

JHEP04(2021)174

Paper III

Search for Higgs boson pair production in the two bottom quarks plus two photons final state in pp collisions at $\sqrt{s} = 13$ TeV with the ATLAS detector

G. Aad *et al.*[*]
(ATLAS Collaboration)

(Received 23 December 2021; accepted 1 August 2022; published 6 September 2022)

Searches are performed for nonresonant and resonant di-Higgs boson production in the $b\bar{b}\gamma\gamma$ final state. The dataset used corresponds to an integrated luminosity of 139 fb^{-1} of proton–proton collisions at a center-of-mass energy of 13 TeV recorded by the ATLAS detector at the CERN Large Hadron Collider. No excess above the expected background is found and upper limits on the di-Higgs boson production cross sections are set. A 95% confidence-level upper limit of 4.2 times the cross section predicted by the Standard Model is set on $pp \to HH$ nonresonant production, where the expected limit is 5.7 times the Standard Model predicted value. The expected constraints are obtained for a background hypothesis excluding $pp \to HH$ production. The observed (expected) constraints on the Higgs boson trilinear coupling modifier κ_λ are determined to be $[-1.5, 6.7]$ ($[-2.4, 7.7]$) at 95% confidence level, where the expected constraints on κ_λ are obtained excluding $pp \to HH$ production from the background hypothesis. For resonant production of a new hypothetical scalar particle X ($X \to HH \to b\bar{b}\gamma\gamma$), limits on the cross section for $pp \to X \to HH$ are presented in the narrow-width approximation as a function of m_X in the range 251 GeV $\leq m_X \leq$ 1000 GeV. The observed (expected) limits on the cross section for $pp \to X \to HH$ range from 640 fb to 44 fb (391 fb to 46 fb) over the considered mass range.

DOI: 10.1103/PhysRevD.106.052001

I. INTRODUCTION

Since the discovery of the Higgs boson in 2012 [1,2], one of the priorities of the ATLAS and CMS Collaborations has been to better understand the properties of the Brout-Englert-Higgs mechanism [3–8]. The Higgs boson self-coupling provides information about the structure of the Higgs potential. It is possible to directly probe the self-coupling of the Higgs boson by studying Higgs boson pair (HH) production. Furthermore, any deviation of the Higgs boson pair production rate from the Standard Model (SM) prediction would point to new physics beyond the Standard Model (BSM) and may be within the sensitivity reach of the proton–proton (pp) collision data collected at $\sqrt{s} = 13$ TeV during Run 2 of the Large Hadron Collider (LHC) [9].

At leading order (LO), the production of Higgs boson pairs via gluon–gluon fusion (ggF) proceeds through the two diagrams shown in Fig. 1. These diagrams interfere destructively, leading to a small-production cross section [10–12]. For 13 TeV pp collisions and a Higgs boson mass $m_H = 125.09$ GeV [13], the ggF cross section, calculated at next-to-next-to-leading-order (NNLO) accuracy in the finite top-quark mass approximation (FTapprox), is $\sigma_{HH}(\mathrm{ggF}) = 31.02^{+2.2\%}_{-5.0\%}(\mathrm{Scale})^{+4\%}_{-18\%}(m_{\mathrm{top}}) \pm 3.0\%(\alpha_s + \mathrm{PDF})$ fb [14–17], where "Scale" represents the uncertainty due to the finite order of the quantum chromodynamics (QCD) calculation, "m_{top}" the uncertainty related to the top-quark mass scheme [17,18] which is added linearly to the Scale uncertainty, and "α_s + PDF" the effect of uncertainties in the strong coupling constant and parton distribution functions.

The di-Higgs vector-boson fusion (VBF) production cross section, calculated at next-to-next-to-next-to-leading order (N3LO) for $m_H = 125.09$ GeV, is $\sigma_{HH}(\mathrm{VBF}) = 1.72^{+0.03\%}_{-0.04\%}(\mathrm{Scale}) \pm 2.1\%(\alpha_s + \mathrm{PDF})$ fb [14], which is one order of magnitude lower than the cross section of the ggF process. The VBF production mode provides the analysis with additional sensitivity to the Higgs trilinear coupling, as shown in Fig. 2. Both the ggF and VBF production modes of Higgs boson pairs are considered as signal modes in this paper. The other production modes have lower cross sections [19] and are neglected.

Nonresonant enhancements to the Higgs boson pair cross section can originate either from loop corrections involving new particles, such as light, colored scalars [20], or from non-SM couplings between the Higgs boson and other SM particles. The nonresonant production cross section can also be altered by the trilinear self-coupling, λ_{HHH}, being different from the SM prediction, as discussed

[*]Full author list given at the end of the article.

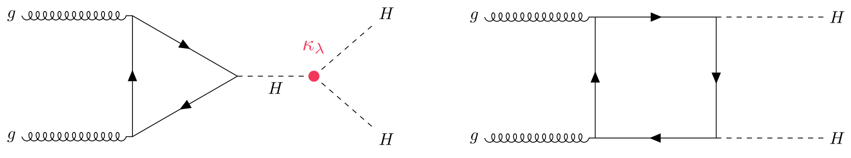

(a) Trilinear coupling (b) Box diagram

FIG. 1. The Feynman diagrams for the dominant gluon–gluon fusion production processes. In the Standard Model, the (a) trilinear coupling process, and (b) the box diagram, and the destructive interference between the two processes, contribute to the total cross section. In the figure, κ_λ represents the Higgs boson trilinear coupling modifier. The quark content in the diagram is dominated by the top-quark contribution due to the large top-quark Yukawa coupling to the Higgs boson.

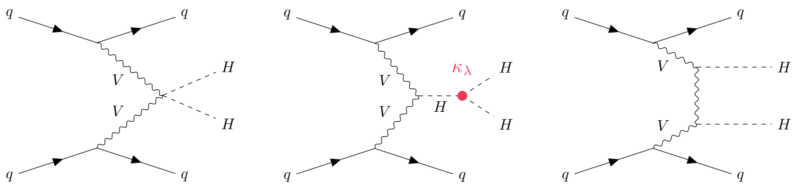

(a) $HHVV$ vertex (b) Trilinear coupling (c) VVH Production mode

FIG. 2. The VBF production of Higgs boson pairs via (a) the $HHVV$ vertex, (b) the trilinear coupling, and (c) the VVH production mode. In the figure, κ_λ denotes the Higgs boson trilinear coupling modifier.

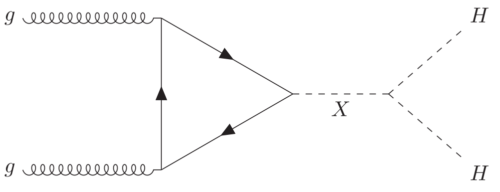

FIG. 3. Gluon–gluon fusion production of a heavy resonance decaying into a Higgs boson pair.

in Refs. [21,22]. Such an effect can be captured by a scale factor κ_λ defined as $\kappa_\lambda = \lambda_{HHH}/\lambda_{HHH}^{\mathrm{SM}}$, where $\lambda_{HHH}^{\mathrm{SM}}$ is the SM value of the parameter.

In addition to the nonresonant enhancements, searching for resonant production of Higgs boson pairs is well motivated. Figure 3 shows a ggF production diagram possible in BSM theories predicting the existence of heavy scalar particles that can decay into a pair of Higgs bosons. Such theories include models with two Higgs doublets [23], such as the minimal supersymmetric extension of the SM [24], twin Higgs models [25], and composite Higgs models [26], adding a second complex scalar doublet to the Higgs sector. Alternatively, the Randall-Sundrum model of warped extra dimensions [27] predicts spin-0 radions that could couple to a Higgs boson pair.

This paper presents a search for di-Higgs production in the $b\bar{b}\gamma\gamma$ final state, including dedicated assessments of nonresonant and resonant contributions. The analysis considers the full Run 2 dataset of 139 fb^{-1} at 13 TeV. For both the nonresonant and resonant HH searches, the analysis employs a multivariate method designed to reject background processes, and the statistical results are obtained from a fit of the diphoton invariant mass, $m_{\gamma\gamma}$. For the nonresonant search, data are divided into different categories based on the four-body invariant mass to target different κ_λ ranges. The resonant search focuses on probing the existence of a narrow-width scalar particle X in the mass range $251 < m_X < 1000$ GeV decaying into a pair of Higgs bosons. The selection criteria depend on the mass of the probed scalar particle. The main background processes are diphoton-plus-jets production and processes where a Higgs boson is produced and decays into a pair of photons. In the context of the resonant search, nonresonant HH production is considered as a background.

Previous results from the ATLAS Collaboration were obtained in this channel with an integrated luminosity of 36 fb^{-1} of data at 13 TeV collected during Run 2, and they were found to be consistent with SM expectations within uncertainties [28]. The search for nonresonant enhancements of Higgs boson pair production set an observed (expected) 95% confidence level (C.L.) upper limit on the HH cross section of 0.73 (0.93) pb, corresponding to 22

(28) times the SM prediction. The Higgs trilinear coupling was constrained to the range $-8.2 < \kappa_\lambda < 13.2$ at 95% C.L. ($-8.3 < \kappa_\lambda < 13.2$ expected). A previous combination of searches for HH pair production performed by the ATLAS Collaboration with up to 36 fb^{-1} of 13 TeV data provided constraints of $-5.0 < \kappa_\lambda < 12.0$ at 95% C.L. [29]. A search for enhancements due to the decay of a narrow-width scalar particle was performed in this channel as well, and results were given as a function of the resonance mass, m_X. The observed (expected) limits were between 1.1 pb and 0.12 pb over the range 260 GeV $< m_X <$ 1000 GeV. A combination of searches by the ATLAS Collaboration with up to 36 fb^{-1} of 13 TeV data for a narrow-width scalar resonance decaying into a HH pair was performed and provided upper limits between 851 fb and 4.6 fb over the range 260 GeV $< m_X <$ 3000 GeV [29]. The CMS Collaboration also set observed (expected) upper limits of 7.7 (5.2) times the SM prediction at 95% C.L. on nonresonant enhancements of Higgs boson pair production in the $b\bar{b}\gamma\gamma$ final state with 137 fb^{-1} of 13 TeV data [30]. In the same final state, the CMS Collaboration set 95% C.L. upper limits on the production cross section of a narrow-width scalar particle between 4.2 pb and 0.23 pb over the range $260 < m_X <$ 900 GeV with 35.9 fb^{-1} of 13 TeV data [31].

II. THE ATLAS DETECTOR

The ATLAS detector [32] at the LHC covers nearly the entire solid angle around the collision point.[1] It consists of an inner tracking detector surrounded by a thin superconducting solenoid, electromagnetic and hadron calorimeters, and a muon spectrometer incorporating three large superconducting air-core toroidal magnets.

The inner-detector system (ID) is immersed in a 2 T axial magnetic field and provides charged-particle tracking in the range $|\eta| < 2.5$. The high-granularity silicon pixel detector covers the vertex region and typically provides four measurements per track, the first hit normally being in the insertable B-layer installed before Run 2 [33,34]. It is followed by the silicon microstrip tracker, which usually provides eight measurements per track. These silicon detectors are complemented by the transition radiation tracker (TRT), which enables radially extended track reconstruction up to $|\eta| = 2.0$. The TRT also provides electron identification information.

[1] ATLAS uses a right-handed coordinate system with its origin at the nominal interaction point (IP) in the center of the detector and the z-axis along the beam pipe. The x-axis points from the IP to the center of the LHC ring, and the y-axis points upwards. Cylindrical coordinates (r, ϕ) are used in the transverse plane, ϕ being the azimuthal angle around the z-axis. The pseudorapidity is defined in terms of the polar angle θ as $\eta = -\ln\tan(\theta/2)$. The rapidity y is defined in terms of the energy, the momentum and the polar angle θ: $y = \frac{1}{2}\ln(\frac{E+p\cdot\cos\theta}{E-p\cdot\cos\theta})$. The angular distance is measured in units of $\Delta R \equiv \sqrt{(\Delta\eta)^2 + (\Delta\phi)^2}$.

The calorimeter system covers the pseudorapidity range $|\eta| < 4.9$. Within the region $|\eta| < 3.2$, electromagnetic calorimetry is provided by barrel and end cap high-granularity lead/liquid-argon (LAr) calorimeters, with an additional thin LAr presampler covering $|\eta| < 1.8$ to correct for energy loss in material upstream of the calorimeters. Hadron calorimetry is provided by the steel/scintillator-tile calorimeter, segmented into three barrel structures within $|\eta| < 1.7$, and two copper/LAr hadron end cap calorimeters. The solid angle coverage is completed with forward copper/LAr and tungsten/LAr calorimeter modules optimized for electromagnetic and hadronic energy measurements respectively.

The muon spectrometer (MS) comprises separate trigger and high-precision tracking chambers measuring the deflection of muons in a magnetic field generated by the superconducting air-core toroidal magnets. The field integral of the toroids ranges between 2.0 Tm and 6.0 Tm across most of the detector. A set of precision chambers covers the region $|\eta| < 2.7$ with three layers of monitored drift tubes, complemented by cathode-strip chambers in the forward region, where the background is highest. The muon trigger system covers the range $|\eta| < 2.4$ with resistive-plate chambers in the barrel and thin-gap chambers in the end cap regions.

Interesting events are selected by the first-level trigger system implemented in custom hardware, followed by selections made by algorithms implemented in software in the high-level trigger [35]. The first-level trigger accepts events from the 40 MHz bunch crossings at a rate below 100 kHz, which the high-level trigger reduces in order to record events at rate of about 1 kHz. An extensive software suite [36] is used in the reconstruction and analysis of real and simulated data, in detector operations, and in the trigger and data acquisition systems of the experiment.

III. DATA AND SIMULATION SAMPLES

This analysis uses pp collision data collected by the ATLAS experiment from 2015 to 2018 with proton beams colliding at a center-of-mass energy of $\sqrt{s} = 13$ TeV. After data quality requirements [37] the full dataset represents an integrated luminosity of 139.0 ± 2.4 fb^{-1} [38,39]. The mean number of inelastic pp interactions per bunch crossing is 34.2 [40].

Monte Carlo (MC) simulations are available for the signal as well as most background processes as detailed in the rest of this section. The reducible backgrounds from final states with jets wrongly identified as photons (γ–jet and dijet backgrounds) are, however, estimated using a data-driven technique detailed in Sec. IV C.

Events from ggF nonresonant HH production were generated at next-to-leading-order accuracy in QCD with finite top-quark mass in both the real and virtual corrections (NLO FT) [11], using the POWHEG BOX v2 [41] generator in the finite top-quark mass approximation [42,43] with the

PDF4LHC 15 parton distribution function (PDF) set [44]. The PYTHIA 8.244 generator was used for parton showering, hadronization and underlying-event simulation. HERWIG 7.1.6 was used as an alternative generator to calculate the theory uncertainty from the parton shower. Samples were generated for coupling modifier values $\kappa_\lambda = 1$ and 10.

For ggF nonresonant HH production, a reweighting method based on the di-Higgs invariant mass m_{HH} is used to provide predictions on the cross section at different κ_λ values, starting from the existing $\kappa_\lambda = 1$ sample. The reweighting method derives the scale factors as a function of κ_λ in bins of m_{HH} by performing a linear combination of samples generated at different κ_λ values [45]. Histograms of the truth m_{HH} distribution are produced for each κ_λ sample and the distributions of the other relevant kinematic variables are obtained applying an event-per-event weight based on the ratio between the binned m_{HH} distribution for the targeted κ_λ by the binned m_{HH} distribution for the SM ($\kappa_\lambda = 1$) sample.

This method was validated by comparing the event yields and the distributions of the relevant Higgs boson kinematic variables, including the $m_{\gamma\gamma}$ variable, of the sample generated with $\kappa_\lambda = 10$ to the sample generated with $\kappa_\lambda = 1$ and reweighted to $\kappa_\lambda = 10$. Good agreement is obtained in all categories. A systematic uncertainty in the range of 3%–4% is associated with the reweighting process, based on the maximum differences of signal yields observed in this validation. For each κ_λ value, the inclusive cross section is normalized according to Ref. [46]. A fit with a second order polynomial to the MC prediction is performed in each analysis category, in order to parametrize the event yields as a function of κ_λ.

For VBF nonresonant HH production, MadGraph5_aMC@NLO 2.6.0 [47] was used to generate events at LO [47,48]. The NNPDF3.0NLO PDF set [49] was used in the matrix element, interfaced to PYTHIA 8.244. The cross section of the VBF HH process is evaluated at N3LO in QCD [50–52], as outlined in Sec. I. Since samples were generated at LO for four values of the coupling modifier, $\kappa_\lambda = 0$, 1, 2 and 10, the N3LO-to-LO cross section ratio at the SM value is calculated and this factor is applied to the VBF HH cross section. These samples are used to derive a parametrization of the signal yields in the signal region as a function of κ_λ by fitting a second-order polynomial to the MC predictions in each analysis category, as described in Sec. IV B 2.

The production of a heavy spin-0 resonance X via ggF and its decay into a pair of Higgs bosons, $pp \to X \to HH$, was simulated using MadGraph5_aMC@NLO 2.6.1 [47] at LO accuracy with the NNPDF2.3LO PDF set. The event generator was interfaced with HERWIG7.1.3 [53,54] to model the parton shower, hadronization, and underlying event. No specific theoretical model for the phenomenology of the new particle is assumed in the process generation. The mass of X was varied between 251 GeV and 1000 GeV in the simulation, while its width was set to 10 MeV. In total 25 m_X mass hypotheses have been generated, corresponding to $m_X = 251$, 260, 270, 280, 290, 300, 312.5, 325, 337.5, 350, 375, 400, 425, 450, 475, 500, 550, 600, 650, 700, 750, 800, 850, 900, 1000 GeV. The interference with nonresonant Higgs boson pair production was neglected.

Production of single Higgs bosons via ggF, VBF, WH, ZH ($qq \to ZH$ and $gg \to ZH$), $t\bar{t}H$, tH (tHq and tHW), and bbH was modeled using the same set of MC samples as described in Ref. [55]. For single Higgs boson production, as well as both nonresonant and resonant di-Higgs production, a Higgs boson mass of 125.09 GeV was assumed [13]. The analysis assumes a branching ratio of 0.227% for the Higgs boson decay into two photons and a branching ratio of 58.2% for the Higgs boson decay into two b-quarks [56,57]. The inclusive cross sections of these processes are normalized to the most precise available theoretical values [56].

The $\gamma\gamma +$ jets process was simulated with the SHERPA 2.2.4 [58] generator. QCD NLO-accurate matrix elements for up to one parton, and LO-accurate matrix elements for up to three partons, were calculated with the Comix [59] and OPENLOOPS [60–62] libraries. These were calculated in the five-flavor scheme including b-quarks in the massless approximation and merged with the SHERPA parton shower [63] using the MEPS@NLO prescription [64,65] with a dynamic merging cut [66] of 10 GeV. Within the parton shower, b-quarks were then treated as being massive. Finally, events from $t\bar{t}\gamma\gamma$ processes were produced with MadGraph5_aMC@NLO in the four-flavor scheme [47]. The simulation samples used in the analysis are listed in Table I.

Different pileup conditions from additional interactions the same and neighboring bunch crossings were simulated by overlaying the hard-scattering event with inelastic pp events generated by PYTHIA8.186 using the NNPDF2.3LO PDF set and the A3 tune [85]. Differences between the simulated and observed distributions of the number of interactions per bunch crossing are corrected for by applying pileup scale factors to simulated events. A full simulation of the ATLAS detector [86] based on GEANT4 [87] was used to reproduce the detector response to single-Higgs-boson processes. The continuum background and signal samples were processed by AtlFastII [88], a fast simulation of the ATLAS detector response which was shown to be able to accurately simulate diphoton events.

IV. OBJECT AND EVENT SELECTIONS

A. Object selection

Photons are reconstructed from topologically connected clusters [89] of energy deposits in the electromagnetic calorimeter in the region $|\eta| < 2.37$. The transition region between the barrel and end cap electromagnetic calorimeters, $1.37 < |\eta| < 1.52$, is excluded. Photon candidates matched to conversion vertices or tracks that are consistent with originating from photon conversions are classified as

TABLE I. Summary of nominal Higgs boson pair signal samples and single-Higgs-boson background samples, split by production mode, and continuum background samples. The generator used in the simulation, the PDF set, and set of tuned parameters (tune) are also provided.

Process	Generator	PDF set	Showering	Tune
Nonresonant ggF HH	POWHEG BOXv2+FT [41,42,43]	PDFLHC [44]	PYTHIA8.2 [67]	A14 [68]
Nonresonant VBF HH	MadGraph5_aMC@NLO [47]	NNPDF3.0NLO [69]	PYTHIA8.2	A14
Resonant ggF HH	MadGraph5_aMC@NLO	NNPDF2.3LO	HERWIG7.1.3 [53,54]	H7.1—Default [70]
ggF H	NNLOPS [71–73] [74,75]	PDFLHC	PYTHIA8.2	AZNLO [76]
VBF H	POWHEG BOXv2 [41,72,77–83]	PDFLHC	PYTHIA8.2	AZNLO
WH	POWHEG BOXv2	PDFLHC	PYTHIA8.2	AZNLO
$qq \to ZH$	POWHEG BOXv2	PDFLHC	PYTHIA8.2	AZNLO
$gg \to ZH$	POWHEG BOXv2	PDFLHC	PYTHIA8.2	AZNLO
$t\bar{t}H$	POWHEG BOXv2 [78–80,83,84]	NNPDF3.0NLO	PYTHIA8.2	A14
bbH	POWHEG BOXv2	NNPDF3.0NLO	PYTHIA8.2	A14
tHq	MadGraph5_aMC@NLO	NNPDF3.0NLO	PYTHIA8.2	A14
tHW	MadGraph5_aMC@NLO	NNPDF3.0NLO	PYTHIA8.2	A14
$\gamma\gamma$ + jets	SHERPA 2.2.4 [58]	NNPDF3.0NNLO	SHERPA 2.2.4	⋯
$t\bar{t}\gamma\gamma$	MadGraph5_aMC@NLO	NNPDF2.3LO	PYTHIA8.2	⋯

converted photons. Those without a matched conversion vertex or track are classified as unconverted photons.

The calibration of the photon energy is based on a multivariate regression algorithm trained with MC samples, where the input variables are corrected with data-driven techniques. The calibrated energy is finally corrected by applying scale factors derived from $Z \to e^+e^-$ events [90]. The photon direction is reconstructed using the longitudinal (i.e., shower-depth) segmentation of the calorimeters and constrained to be compatible with the luminous region of the proton-beam collisions. Additionally, information about the position of the conversion vertex and about the tracks associated with the conversion vertex is considered in the case of converted photons.

Events are required to have at least one reconstructed collision vertex, defined as a vertex associated with at least two tracks with transverse momentum (p_T) larger than 0.5 GeV. The primary vertex is selected from the reconstructed collision vertices using a neural-network algorithm [91] based on the extrapolated photon trajectories and the tracks associated with each candidate vertex.

Photon identification is based on the lateral shower profile of the energy deposits in the first and second electromagnetic calorimeter layers and on the energy leakage fraction in the hadronic calorimeter. It reduces the misidentification of hadronic jets containing large neutral components, primarily π^0 particles, which decay into a pair of highly collimated photons. "Tight" identification criteria, which are tuned for converted and unconverted photons separately, are applied [90].

To further improve the rejection of misidentified photons, two isolation variables are defined to quantify the activity around a photon. Calorimeter-based isolation E_T^{iso} is defined as the sum of the transverse energy of topological clusters within a cone of size $\Delta R = 0.2$ around the photon, correcting for the energy of the photon candidate itself as well as for an average expected pileup contribution. Track-based isolation p_T^{iso} is defined as the scalar sum of the transverse momenta of all tracks with $p_T > 1$ GeV that originate from the primary vertex and are within a cone of $\Delta R = 0.2$ around the photon. Isolated photons must have $E_T^{iso} < 0.065 \cdot E_T$ and $p_T^{iso} < 0.05 \cdot E_T$ (the "loose" working point [90]), where E_T is the transverse energy of the photon. For isolated photons with transverse momenta between 30 GeV and 250 GeV, the identification efficiency for unconverted and converted photons ranges from 84% to 98% [90].

Electrons are reconstructed from energy deposits measured in the electromagnetic calorimeter which are matched to ID tracks [90]. They are required to satisfy $|\eta| < 2.47$, excluding the calorimeter transition region $1.37 < |\eta| < 1.52$, and have a transverse momentum $p_T > 10$ GeV. Electrons are required to satisfy a "medium" identification criterion based on the use of shower shape, track-cluster matching and TRT parameters in a likelihood-based algorithm [90]. Muons are reconstructed from high-quality tracks found in the MS [92]. A matching of these tracks to ID tracks is required in the region $|\eta| < 2.5$. Muons are required to have $|\eta| < 2.7$ and $p_T > 10$ GeV, and to satisfy a "medium" identification criterion [93]. Both the electrons and muons are matched to the primary vertex via requirements on the tracks' longitudinal and transverse impact parameters, $|z_0|$ and $|d_0|$, respectively. These requirements are $|z_0| \sin\theta < 0.5$ mm (where θ is the polar angle of the track) for electrons and muons and $|d_0|/\sigma_{d_0} < 5(3)$ for electrons (muons).

Reconstructed jets are based on particle-flow objects built from noise-suppressed positive-energy topological clusters in the calorimeter and reconstructed tracks [94]. The anti-k_t algorithm [95,96] with a radius parameter of $R = 0.4$ is used. They are required to have rapidity $|y| < 4.4$ and

$p_T > 25$ GeV. To further suppress jets produced in concurrent pp interactions, each jet within the tracking acceptance of $|\eta| < 2.4$, and with $p_T < 60$ GeV, is required to satisfy the "tight" jet-vertex tagger [97] criteria used to identify the jet as originating from the selected primary vertex of the event.

The flavor of jets is determined using a deep-learning neural network, DL1r. The DL1r b-tagging is based on distinctive features of b-hadron decays in terms of the impact parameters of the tracks and the displaced vertices reconstructed in the inner detector [98]. The inputs of the DL1r network also include discriminating variables constructed by a recurrent neural network (RNNIP) [99], which exploits the spatial and kinematic correlations between tracks originating from the same b-hadron. For high-p_T jets, this approach is found to give better performance [100] than a previously used multivariate technique [101]. Operating points are defined by a single selection value on the discriminant output distribution and are chosen to provide a specific b-jet efficiency for an inclusive $t\bar{t}$ MC sample. The b-tagging requirements result in an efficiency of 77% for jets containing b-hadrons (b-tagged jets), and the misidentification rate is 1/130 (1/4.9) for light-flavor (charm) jets [98]. Scale factors are applied to the simulated events to correct for differences in b-tagging efficiency between data and simulation. These scale factors are measured as a function of jet p_T using a likelihood-based method in a sample highly enriched in $t\bar{t}$ events [98]. Only jets with $|\eta| < 2.5$ are considered for flavor-tagging.

The energy of b-tagged jets is corrected for the possible contribution of muons from semileptonic b-hadron decays. In addition, the undetected energy of the neutrinos and out-of-cone effects are corrected for with scale factors derived as a function of the b-jet p_T from a $t\bar{t}$ MC sample. The two corrections together improve the resolution of the invariant mass of the two jets with the highest b-tagging score ($m_{b\bar{b}}$) by about 20%. The procedure closely follows the one used in Ref. [102].

An overlap removal procedure is applied to avoid multiple usage of the same detector signals in the same event. Photons are prioritized in this analysis, requiring the removal of electrons, muons and jets within $\Delta R = 0.4$ of a selected photon. Next, jets within $\Delta R = 0.2$ of electrons are removed. In the last step, electrons and muons within $\Delta R = 0.4$ of any jet are removed.

The missing transverse momentum E_T^{miss} in an event is calculated as the magnitude of the negative vectorial sum of the transverse momenta of all selected and calibrated physics objects that can be matched to the primary vertex. A component called the "soft term" is calculated from the residual tracks that originate from the primary vertex but are not associated with any other object and is added to the E_T^{miss} calculation [103].

B. Event selection

Both the nonresonant and resonant HH searches employ multivariate analysis techniques to select events. Events are selected if they satisfy a common set of preselection requirements; they are then required to fulfill different requirements for the nonresonant search and the resonant search. Both analyses employ a fit of the diphoton invariant mass distribution to extract the HH signal contribution.

1. Common preselection

For both the nonresonant and resonant analyses, events are selected using diphoton triggers requiring two reconstructed photon candidates with minimum transverse energies of 35 GeV for the leading photon and 25 GeV for the subleading photon, where leading (subleading) refers to the photon candidate with the highest (second-highest) transverse energy [104]. The triggers used in 2015 and 2016 required both photons to satisfy a Loose photon identification criterion, while the Medium criterion [90] was adopted in 2017–2018 to cope with the increased pp interaction rate. Once the full diphoton event selection described in this section is applied, the average trigger efficiency for $H \to \gamma\gamma$ events is found to be greater than 99% for the 2015–2016 data-taking period, and greater than 98% for the 2017–2018 data-taking period.

On top of the trigger requirements, events are selected if:

(i) At least two photons satisfy the object selection criteria detailed in Sec. IV A.
(ii) The diphoton invariant mass, built with the two leading photons, satisfies 105 GeV $< m_{\gamma\gamma} <$ 160 GeV.
(iii) The leading (subleading) photon p_T is larger than 35% (25%) of the mass of the diphoton system.
(iv) Exactly two b-tagged jets are present. In order to remain statistically independent of the ATLAS search for $HH \to b\bar{b}b\bar{b}$ [105], any event with more than two b-jets passing the 77% efficient working point is rejected.
(v) No electrons or muons are present.
(vi) Fewer than six central ($|\eta| < 2.5$) jets are present. This helps to reject $t\bar{t}H$ events where the top quarks decay hadronically.

The acceptance times efficiency of the common preselection for the SM ggF HH simulation sample is 14% and it is 8.5% (14%) for a resonant scalar particle with $m_X =$ 300 GeV ($m_X = 500$ GeV). Multivariate techniques are then used to target the nonresonant ggF production mode or the resonant production mode of Higgs boson pairs. For both the nonresonant and resonant analyses, the resulting categories, each based on a boosted decision tree (BDT), must have at least nine continuum background events in the data sideband region. This guarantees that the final selection on the data sideband retains enough events to perform a

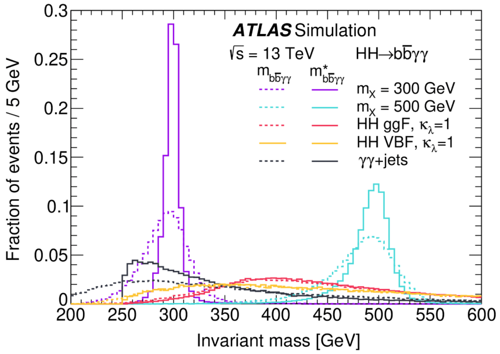

FIG. 4. Reconstructed four-body mass for $m_X = 300$ GeV and $m_X = 500$ GeV resonant signal benchmarks, for the SM HH production processes and for the $\gamma\gamma +$ jets background. Dashed lines represent the distribution of $m_{b\bar{b}\gamma\gamma}$ while solid lines represent the distribution of $m^*_{b\bar{b}\gamma\gamma}$, defined in Sec. IV B 1. Distributions are normalized to unit area.

fit to the distribution of the diphoton invariant mass, $m_{\gamma\gamma}$. The data sideband region is defined as the range $105\ \text{GeV} < m_{\gamma\gamma} < 160\ \text{GeV}$, excluding $120\ \text{GeV} < m_{\gamma\gamma} < 130\ \text{GeV}$.

The invariant mass of the diphoton plus b-tagged jets system, $m^*_{b\bar{b}\gamma\gamma}$, is defined as $m^*_{b\bar{b}\gamma\gamma} = m_{b\bar{b}\gamma\gamma} - m_{b\bar{b}} - m_{\gamma\gamma} + 250$ GeV (where 250 GeV is about twice the Higgs boson mass value and $m_{b\bar{b}}$ is the invariant mass of the two jets with the highest b-tagging score). It is used to implement selection criteria for both the nonresonant and resonant analyses. Figure 4 shows that, compared with $m_{b\bar{b}\gamma\gamma}$, the $m^*_{b\bar{b}\gamma\gamma}$ variable improves the four-object mass resolution, particularly for resonant signal particles decaying into a pair of Higgs bosons, due to detector resolution effects canceling out.

2. Nonresonant selection

Following the preselection, events are divided into two regions using the value of the $m^*_{b\bar{b}\gamma\gamma}$ variable. A high-mass region, with $m^*_{b\bar{b}\gamma\gamma} > 350$ GeV, targets the SM signal ($\kappa_\lambda = 1$), while a low-mass region, with $m^*_{b\bar{b}\gamma\gamma} < 350$ GeV, is used to retain sensitivity for BSM signals ($\kappa_\lambda = 10$). The dependence of $m^*_{b\bar{b}\gamma\gamma}$ on κ_λ can be seen in Fig. 5.

In each mass region, a dedicated BDT is trained using XGBoost [106] to discriminate between a benchmark HH signal and a combination of $\gamma\gamma$, $t\bar{t}H$, ggH, and ZH simulated backgrounds. In the high-mass region, the SM HH sample is used as signal, while in the low-mass region, the $\kappa_\lambda = 10$ sample is used as signal.

The BDT input variables are summarized in Table II. Identical variable sets are used for high-mass and low-mass categories. The BDT combines several input variables that exploit the different kinematic properties of signal and background events, as well as the b-tagging information. Observables based on the kinematic properties of the reconstructed photons, such as the leading and subleading photon's angular information, and the transverse momentum of the diphoton system divided by its invariant mass, are combined with jet-based information. The "single topness" variable (χ_{Wt}) is also used. It is defined as

$$\chi_{Wt} = \min \sqrt{\left(\frac{m_{j_1 j_2} - m_W}{m_W}\right)^2 + \left(\frac{m_{j_1 j_2 j_3} - m_t}{m_t}\right)^2}, \quad (1)$$

where the minimum is taken over all combinations of three jets in the event (with no requirements on b-tagging status), $m_W = 80$ GeV, and $m_t = 173$ GeV. Among the input variables in Table II, $m_{b\bar{b}}$ and H_{T} show the highest discriminating power against the $\gamma\gamma +$ jets continuum background. Particular care was taken to ensure that the BDT event selection does not lead to biases in the $m_{\gamma\gamma}$ background distribution. Variables which have a strong

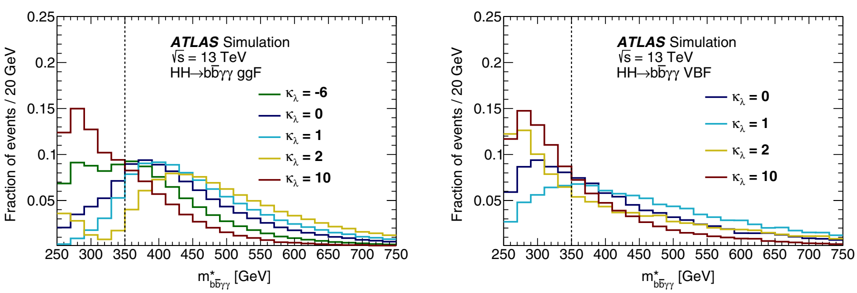

(a) ggF HH production mode

(b) VBF HH production mode

FIG. 5. The $m^*_{b\bar{b}\gamma\gamma}$ distributions after the common preselection for (a) nonresonant ggF HH and (b) VBF HH signals with several κ_λ values. The value of $m^*_{b\bar{b}\gamma\gamma} = 350$ GeV is chosen as the boundary between categories targeting the SM and BSM κ_λ signals.

TABLE II. Variables used in the BDT for the nonresonant analysis. All vectors in the event are rotated so that the leading photon ϕ is equal to zero, while their relative azimuthal angular differences are kept unchanged.

Variable	Definition
Photon-related kinematic variables	
$p_T/m_{\gamma\gamma}$	Transverse momentum of each of the two photons divided by the diphoton invariant mass $m_{\gamma\gamma}$
η and ϕ	Pseudorapidity and azimuthal angle of the leading and subleading photon
Jet-related kinematic variables	
b-tag status	Tightest fixed b-tag working point (60%, 70%, or 77%) that the jet passes
p_T, η and ϕ	Transverse momentum, pseudorapidity and azimuthal angle of the two jets with the highest b-tagging score
$p_T{}^{b\bar{b}}$, $\eta_{b\bar{b}}$ and $\phi_{b\bar{b}}$	Transverse momentum, pseudorapidity and azimuthal angle of the b-tagged jets system
$m_{b\bar{b}}$	Invariant mass of the two jets with the highest b-tagging score
H_T	Scalar sum of the p_T of the jets in the event
Single topness	For the definition, see Eq. (1)
Missing transverse momentum variables	
E_T^{miss} and ϕ^{miss}	Missing transverse momentum and its azimuthal angle

correlation with the diphoton invariant mass are avoided in the training in order to prevent the BDT event selection from biasing the $m_{\gamma\gamma}$ background distribution. To this end, the transverse momentum values of the photons are divided by $m_{\gamma\gamma}$ before being used as BDT input variables. A check for potential biases in the $m_{\gamma\gamma}$ background distribution is described in Sec. V B. The BDT score distributions in the low-mass and high-mass regions are shown in Fig. 6 for events passing the common preselection. In each mass region, two categories based on the BDT score are defined. The boundaries of the categories are chosen by maximizing the combined number-counting significance [107] using signal and background yields in the mass window 120 GeV $< m_{\gamma\gamma} <$ 130 GeV in the chosen categories. The four resulting BDT categories are defined in Table III.

3. Resonant selection

The resonant search uses a multivariate analysis based on a BDT technique. A potential limitation of a BDT-based selection is the low number of background events for higher resonance masses. To overcome this limitation, BDTs are trained jointly for all resonance masses hypotheses and background. The signal events corresponding to the different mass hypotheses are combined. The signal events are reweighted event-by-event to match the $m^*_{b\bar{b}\gamma\gamma}$ distribution of the background events, such that the training is independent of the resonant signal mass hypothesis, but it still retains information of the correlation with the rest of the event variables. The procedure allows to reduce the fluctuations of the BDT performance between nearby mass points. It was checked that the procedure provides similar or better performance than employing separated BDT trainings for each individual signal mass hypothesis.

Using the TMVA toolkit [108], two BDTs are trained to better separate the signal from backgrounds of different nature; the $\gamma\gamma$ and $t\bar{t}\gamma\gamma$ backgrounds (BDT$_{\gamma\gamma}$) and the single-Higgs-boson background (BDT$_{\mathrm{Single}H}$), where the ZH and $t\bar{t}H$ processes produce the dominant resonant backgrounds.

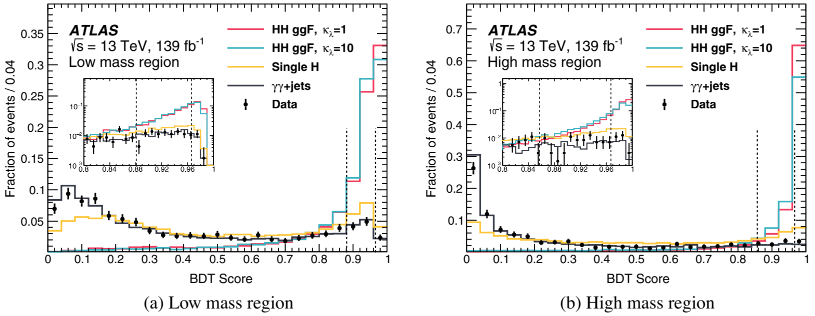

(a) Low mass region (b) High mass region

FIG. 6. The BDT distribution of the di-Higgs ggF signal for two different values of k_λ and the main backgrounds in the (a) low-mass region and (b) high-mass region. Distributions are normalized to unit area. The dashed lines denote the category boundaries. Events with a BDT score below 0.881 in the low-mass region or below 0.857 in the high-mass region are discarded.

TABLE III. Definition of the categories used in the HH nonresonant search. Before entering the BDT-based categories, events are required to satisfy the common preselection.

Category	Selection criteria
High mass BDT tight	$m^*_{b\bar{b}\gamma\gamma} \geq 350$ GeV, BDT score $\in [0.967, 1]$
High mass BDT loose	$m^*_{b\bar{b}\gamma\gamma} \geq 350$ GeV, BDT score $\in [0.857, 0.967]$
Low mass BDT tight	$m^*_{b\bar{b}\gamma\gamma} < 350$ GeV, BDT score $\in [0.966, 1]$
Low mass BDT loose	$m^*_{b\bar{b}\gamma\gamma} < 350$ GeV, BDT score $\in [0.881, 0.966]$

The nonresonant HH process is not included in the training of the BDTs. A complete list of the variables used for the BDT training is given in Table IV. The $E_{\mathrm{T}}^{\mathrm{miss}}$ information is used in the training because it is useful in rejecting the single-Higgs-boson background ($t\bar{t}H$ in particular) and the $t\bar{t}\gamma\gamma$ background.

The combined BDT score of an event is obtained by combining the two BDT scores in quadrature, as shown in Eq. (2),

$$\mathrm{BDT}_{\mathrm{tot}} = \frac{1}{\sqrt{C_1^2 + C_2^2}} \times \sqrt{C_1^2 \left(\frac{\mathrm{BDT}_{\gamma\gamma} + 1}{2}\right)^2 + C_2^2 \left(\frac{\mathrm{BDT}_{\mathrm{Single}H} + 1}{2}\right)^2}. \quad (2)$$

The two coefficients C_1 and C_2 ($C_2 = 1 - C_1$) and $\mathrm{BDT}_{\mathrm{tot}}$ take values in the range [0, 1]. Only events passing a minimum requirement on the value of $\mathrm{BDT}_{\mathrm{tot}}$ are considered in the analysis. To reduce the effect of limited statistics of the Monte Carlo samples in the determination the minimum value required for $\mathrm{BDT}_{\mathrm{tot}}$, and of the C_1 and C_2 coefficients, a two-stage procedure is used. The values of the C_1 and C_2 as well as the BDT cut value are scanned twice in order to maximize the significance. This two-stage optimization procedure first finds the maximum significance that can be achieved for each resonance mass point independently, leading to different coefficient values and $\mathrm{BDT}_{\mathrm{tot}}$ requirement values for the various mass points. A second scan is done to select all coefficients providing a significance within 5% of the maximum value, for each of the resonance mass values. From those possible combinations a common C_1 coefficient is sought (resulting in $C_1 = 0.65$) across all the resonances so that the selection will have common coefficients for all resonance mass points, but different $\mathrm{BDT}_{\mathrm{tot}}$ values. For each of the resonance mass hypotheses, a requirement is set on the $m^*_{b\bar{b}\gamma\gamma}$ value to select events within $\pm 2\sigma$ of the expected mean value for signal events (where σ is the standard deviation parameter of the Crystal Ball function that best fits the $m^*_{b\bar{b}\gamma\gamma}$ distribution). In the case of the 900 GeV and 1000 GeV mass hypotheses, the requirement is relaxed to $\pm 4\sigma$ to increase the number of events used for the signal extraction. The $\mathrm{BDT}_{\mathrm{tot}}$ distributions are shown in Fig. 7 for two signal hypotheses ($m_X = 300$ GeV and 500 GeV).

TABLE IV. Variables used in the BDT for the resonant analysis. For variables depending on b-tagged jets, only jets b-tagged using the 77% working point are considered as described in Sec. IV A.

Variable	Definition
Photon-related kinematic variables	
$p_{\mathrm{T}}^{\gamma\gamma}$, $y^{\gamma\gamma}$	Transverse momentum and rapidity of the diphoton system
$\Delta\phi_{\gamma\gamma}$ and $\Delta R_{\gamma\gamma}$	Azimuthal angle and ΔR between the two photons
Jet-related kinematic variables	
$m_{b\bar{b}}$, $p_{\mathrm{T}}^{b\bar{b}}$ and $y_{b\bar{b}}$	Invariant mass, transverse momentum and rapidity of the b-tagged jets system
$\Delta\phi_{b\bar{b}}$ and $\Delta R_{b\bar{b}}$	Azimuthal angle and ΔR between the two b-tagged jets
N_{jets} and $N_{b\text{-jets}}$	Number of jets and number of b-tagged jets
H_{T}	Scalar sum of the p_{T} of the jets in the event
Diphoton + dijet-related kinematic variables	
$m^*_{b\bar{b}\gamma\gamma}$	Invariant mass of the diphoton plus b-tagged jets system
$\Delta y_{\gamma\gamma,b\bar{b}}$, $\Delta\phi_{\gamma\gamma,b\bar{b}}$ and $\Delta R_{\gamma\gamma,b\bar{b}}$	Distance in rapidity, azimuthal angle and ΔR between the diphoton and the b-tagged jets system
Missing transverse momentum variables	
$E_{\mathrm{T}}^{\mathrm{miss}}$	Missing transverse momentum

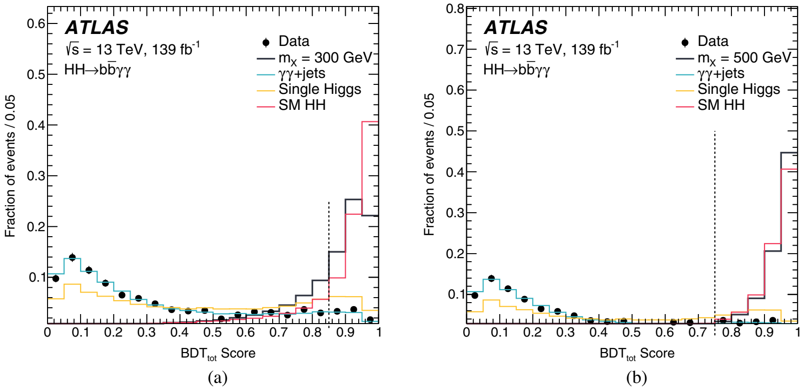

FIG. 7. The $\mathrm{BDT_{tot}}$ score for the benchmark signals ((a) $m_X = 300$ GeV and (b) $m_X = 500$ GeV) and for the main backgrounds. Distributions are normalized to unit area. The dashed lines denote the event selection thresholds. Events with a $\mathrm{BDT_{tot}}$ score below 0.85 for $m_X = 300$ GeV or below 0.75 for $m_X = 500$ GeV are discarded.

C. Comparison of data and predictions

The analysis selection described in Sec. IV B requires two "tight" photons and this region is mainly composed of $\gamma\gamma$, γ–jet, and dijet events, where either one or two jets are misidentified as photons. The fractional contribution of each component can be estimated using a data-driven approach [109] based on the photon identification and isolation distributions from genuine and misidentified photons. After the common preselection, $(85 \pm 3)\%$ of sideband events are genuine diphoton events, with the remaining $(15 \pm 4)\%$ consisting of γ–jet events and a negligible number of dijet events. The uncertainties in the above fractions include both the statistical and systematic uncertainties, where the systematic uncertainty is estimated by using different photon identification criteria. In the BDT-based categories, the proportion of genuine diphoton events increases but the method suffers from a low event count for both the nonresonant and resonant cases.

Figure 8 shows the level of agreement between data and the background prediction for the $m_{\gamma\gamma}$ and $m^*_{b\bar{b}\gamma\gamma}$ distributions, after the common preselection. The continuum background is scaled by the $\gamma\gamma$, γ–jet, and dijet fractions and normalized to the data sideband. The $\gamma\gamma +$ jets continuum background is further divided according to the flavors of the two jets (for example $b\bar{b}$ or other jets). This decomposition is taken directly from the proportions predicted by the SHERPA event generator, as described in Sec. III, and it is shown for illustration. Figures 9 and 10 show the $m_{\gamma\gamma}$ distribution after the nonresonant and resonant BDT categorization and for two benchmark mass points $m_X = 300$ GeV and $m_X = 500$ GeV. The figures illustrate the signal and background composition. The background distributions shown in these figures are not directly used to model the background processes in the analysis workflow explained in Sec. V.

V. SIGNAL AND BACKGROUND PARAMETRIZATION

The signal and backgrounds are extracted by fitting analytic functions to the diphoton invariant mass distribution in the range $105 < m_{\gamma\gamma} < 160$ GeV in both the resonant and nonresonant HH searches.

A. $H \to \gamma\gamma$ parametrization

For the di-Higgs signal and single-Higgs-boson background distributions, the parameterized forms are determined through fits to simulated samples and the expected normalizations are obtained from their theoretical cross sections multiplied by the product of the acceptance times efficiency from the simulation. The diphoton invariant mass distribution shapes are modeled with a double-sided Crystal Ball function [91,110], which is characterized by a Gaussian core and asymmetric power-law tails. This function allows the modeling of event distributions in which non-Gaussian tails can arise from experimental effects, such as photon-energy mismeasurements.

The shape parameters are determined by fitting the diphoton mass distribution in simulation for each category. The width of the fitted function is largely insensitive to the specific signal processes considered in the analysis, with maximum variations of approximately 10%. For the nonresonant search, the parameterized form of $m_{\gamma\gamma}$ is obtained from the simulation of the ggF and VBF HH processes with $\kappa_\lambda = 1$, described in Sec. III. No significant dependence of the functional form on κ_λ was found. For the resonant search, the functional form is obtained from the simulation of the heavy-resonance signals. Table V shows

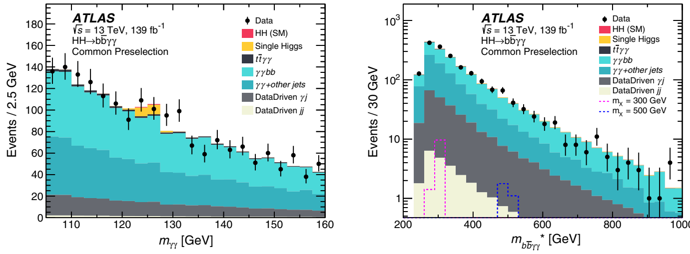

(a) (b)

FIG. 8. Distributions of (a) $m_{\gamma\gamma}$ and (b) $m^*_{b\bar{b}\gamma\gamma}$ for events satisfying the common preselection criteria. The data-derived fractions of nonresonant $\gamma\gamma$, γ–jet or jet–γ, and dijet background are applied and the total background is normalized to the data sideband. The scalar resonance signal is scaled to a total production cross section $\sigma(pp \to X \to HH) = 370$ fb for $m_X = 300$ GeV or $\sigma(pp \to X \to HH) = 67$ fb for $m_X = 500$ GeV, corresponding to the expected exclusion limits presented in Sec. VII C.

the resolution parameter of the double-sided Crystal Ball functional form fit to the $m_{\gamma\gamma}$ distribution for simulated Higgs boson pair events in the nonresonant categories and for two different mass hypotheses for a heavy resonant signal. For both searches, the chosen functional forms are found to model both the single Higgs and di-Higgs boson events well. As no statistically significant bias is observed in injection tests between the input and fitted signals, the same parametrized functions are used for both the single Higgs and di-Higgs boson processes.

B. Background parametrization

The continuum diphoton background is modeled using a functional form chosen by fitting a highly populated MC

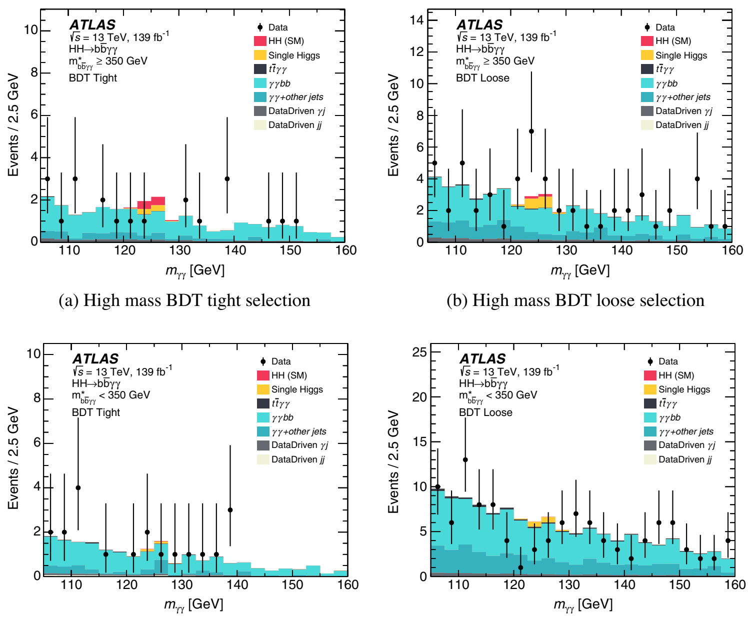

(a) High mass BDT tight selection
(b) High mass BDT loose selection
(c) Low mass BDT tight selection
(d) Low mass BDT loose selection

FIG. 9. Distributions of $m_{\gamma\gamma}$ in all signal categories for the nonresonant HH search: (a) high mass BDT tight, (b) high mass BDT loose, (c) low mass BDT tight, (d) low mass BDT loose. The data-derived fractions of nonresonant $\gamma\gamma$, γ–jet or jet–γ, and dijet background are applied and the total background is normalized to the data sideband.

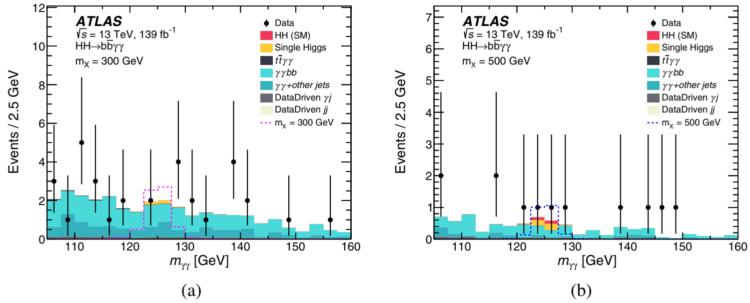

FIG. 10. Distributions of $m_{\gamma\gamma}$ for the selections used for the resonance mass points (a) $m_X = 300$ GeV and (b) $m_X = 500$ GeV for the resonant search. The data-derived fractions of nonresonant $\gamma\gamma$, γ–jet or jet–γ, and dijet background are applied and the total background is normalized to the data sideband. The scalar resonance signal is scaled to a total production cross section $\sigma(pp \to X \to HH) = 370$ fb for $m_X = 300$ GeV or $\sigma(pp \to X \to HH) = 67$ fb for $m_X = 500$ GeV, corresponding to the expected exclusion limits presented in Sec. VII C.

background template. Given the high $\gamma\gamma$ purity quoted in Sec. IV C, the background template is constructed in each category from the $\gamma\gamma$ + jets simulation which is normalized to the data sideband in the mass windows of 105 GeV–120 GeV and 130 GeV–160 GeV in the $m_{\gamma\gamma}$ spectrum.

The potential bias associated with the choice of a specific analytic function to model the continuum background is estimated for each category as prescribed in Refs. [91,111]. It is obtained as the signal event yield extracted from a signal-plus-background fit to the background-only diphoton invariant mass distribution in the range 105 GeV $< m_{\gamma\gamma} <$ 160 GeV. This bias is also called the "spurious signal". The number of fitted signal events is computed for Higgs boson masses in intervals of 1 GeV from 121 GeV to 129 GeV. The bias is taken as the largest number of fitted spurious signal events in this 8 GeV mass window. Of the different analytic functions that are tested, the one with the smallest number of parameters is chosen from the functions with a spurious signal smaller than 20% of the data's statistical uncertainty plus two times the MC statistical uncertainty.

TABLE V. The resolution parameter of the double-sided Crystal Ball functional form and the corresponding statistical uncertainty are obtained from the fit to the $m_{\gamma\gamma}$ distribution for simulated Higgs boson pair events for the nonresonant categories and for two different mass hypotheses for a heavy-resonance signal.

Category	σ_{DSCB} [GeV]
High mass BDT tight	1.33 ± 0.01
High mass BDT loose	1.47 ± 0.02
Low mass BDT tight	1.50 ± 0.06
Low mass BDT loose	1.64 ± 0.03
Resonant $m_X = 300$ GeV	1.78 ± 0.02
Resonant $m_X = 500$ GeV	1.46 ± 0.01

In each category of the nonresonant search and in all the analysis regions defined in the resonant HH search, an exponential function $\exp(a \cdot m_{\gamma\gamma})$ is found to be the best choice since it has the smallest number of degrees of freedom and yields a consistently small bias. Wald tests [112] on data show that the data do not prefer a higher-degree functional form to the exponential form. The bias is found to be at most 40% (60%) of the expected error on the fitted signal yield originating from the data statistics for the nonresonant (resonant) search. The difference in shape between the simulated events and the exponential form measured in the sidebands is found to have a negligible impact on the spurious signal. To study the impact on the spurious signal from the difference in shape between the MC background template and the data sideband, the MC template is reweighted to data using a linear function of $m_{\gamma\gamma}$ derived from the MC-data difference. The spurious signal value evaluated from the reweighted MC template is found to be compatible with the nominal one used as the systematic uncertainty.

VI. SYSTEMATIC UNCERTAINTIES

The sensitivity of the analysis is limited by the statistical precision. The assessment of the systematic uncertainties is described below and their impact on the results is discussed in Sec. VII D. The uncertainty in the integrated luminosity of the full Run 2 dataset is 1.7% [39], obtained using the LUCID-2 detector [38] for the primary luminosity measurements.

The continuum background processes of the analysis are estimated from data and are subject to uncertainties related to the potential bias arising from the chosen background model, as described in Sec. V B. The background functional form bias is assessed as an additional uncertainty in the total number of signal events in each category. For the single

Higgs boson and di-Higgs boson production processes, both of which are estimated using simulation, experimental and theoretical systematic uncertainties are propagated through the full analysis procedure, as described in the following.

The efficiency of the diphoton trigger used to select events is evaluated in simulation and data using a bootstrap method and radiative Z decays [113]. The difference between data and MC is taken as a systematic uncertainty. In the diphoton invariant mass range of $105 < m_{\gamma\gamma} < 160$ GeV, the trigger efficiency uncertainty affects the acceptance by 1% in each category. The uncertainty in the vertex selection efficiency is assessed by comparing the efficiency of finding photon-pointing vertices in $Z \to e^+e^-$ events in data with that in simulation [114]. The resulting uncertainty is found to have a negligible effect on the signal selection efficiency.

The systematic uncertainties from the photon identification and isolation efficiencies are estimated following the prescriptions in Ref. [90]. They are evaluated by varying the correction factors for photon selection efficiencies in simulation by the corresponding uncertainties and affect the diphoton selection efficiency. The experimental uncertainties in the photon-energy scale and resolution are obtained from Ref. [90].

The jet-energy scale and resolution uncertainties [115] affect the $m_{b\bar{b}}$ distribution, while flavor-tagging uncertainties affect the acceptance of the analysis categories. The experimental uncertainties in jet energy scale and resolution are propagated to the $E_{\mathrm{T}}^{\mathrm{miss}}$ calculation. In addition, the uncertainties in the scale and resolution of the $E_{\mathrm{T}}^{\mathrm{miss}}$ soft term are evaluated by using the method described in Ref. [103]. The flavor-tagging uncertainties for b- and c-jets are estimated in $t\bar{t}$ events [98,116], while the misidentification uncertainty of light-flavor jets is determined using dijet events [117]. Additional uncertainties from the b-jet momentum correction accounting for the presence of muons and neutrinos are found to be negligible.

For single Higgs boson and SM HH production, the effects of theoretical scale uncertainties due to missing higher-order corrections on the production rates are estimated by varying the factorization and renormalization scales up and down from their nominal values by a factor of two, recalculating the cross section in each case, and taking the largest deviation from the nominal cross section as the uncertainty. The uncertainties in SM HH ggF production arising from the choice of renormalization scheme and scale of the top-quark mass and their combination with those from factorization and renormalization scale variations are based on Ref. [17]. The uncertainties in the cross sections, including effects of PDF + α_{s} uncertainties, and the uncertainties in the $H \to \gamma\gamma$ and $H \to b\bar{b}$ branching fractions, are taken from Refs. [14,56]. The uncertainty in the value of the Higgs boson mass is considered [13]. An additional 100% uncertainty is assigned to the single-Higgs-boson ggF and VBF production modes and to Higgs boson production in association with a W boson. This is motivated by studies of heavy-flavor production in association with top-quark pairs [118,119] and of W boson production in association with b-jets [120]. No additional heavy-flavor uncertainty is assigned to the single-Higgs-boson $t\bar{t}H$ and ZH production modes, where the dominant heavy-flavor production is already accounted for in the LO process. For all samples, the uncertainty related to the choice of parton showering model is evaluated by comparing the predictions of the nominal MC samples and alternative samples using a different parton showering model. In addition, for the nonresonant HH production processes, a systematic uncertainty is assigned to the κ_λ reweighting, as discussed in Sec. III.

In the resonant search, the systematic uncertainty sources considered are the same as for the nonresonant case, except that uncertainties due to the finite order of the QCD calculations are not assigned to the resonant signal cross section. In this search the SM HH production processes are considered as background.

VII. RESULTS

The statistical framework used to derive the results for both the nonresonant and resonant searches is described in the following.

A. Statistical framework

For both the nonresonant and resonant searches, the results of the analysis are obtained from a maximum-likelihood fit of the $m_{\gamma\gamma}$ distribution in the range $105\ \mathrm{GeV} < m_{\gamma\gamma} < 160\ \mathrm{GeV}$, performed simultaneously over all relevant categories described in Sec. IV B. The likelihood function is defined in Eq. (3),

$$\mathcal{L} = \prod_c \left(\mathrm{Pois}(n_c | N_c(\boldsymbol{\theta})) \cdot \prod_{i=1}^{n_c} f_c(m^i_{\gamma\gamma}, \boldsymbol{\theta}) \cdot G(\boldsymbol{\theta}) \right), \quad (3)$$

where for each event i in a category c, n_c is the observed number of events, N_c is the expected number of events, f_c is the value of the probability density function, $\boldsymbol{\theta}$ are nuisance parameters, and $G(\boldsymbol{\theta})$ are constraint pdfs for the nuisance parameters.

The expected number of events N_c, defined in Eq. (4), is the sum of the expected yields from di-Higgs boson production processes, single Higgs boson production, the nonresonant background, as well as the spurious-signal uncertainty,

$$N_c(\boldsymbol{\theta}) = \mu \cdot N_{HH,\mathrm{c}}(\boldsymbol{\theta}^{\mathrm{yield}}_{HH}) + N^{\mathrm{res}}_{\mathrm{bkg,c}}(\boldsymbol{\theta}^{\mathrm{yield}}_{\mathrm{res}}) + N_{\mathrm{SS,c}} \cdot \boldsymbol{\theta}^{\mathrm{SS,c}} + N^{\mathrm{nonres}}_{\mathrm{bkg,c}}, \quad (4)$$

where μ is the signal strength, $\boldsymbol{\theta}^{\mathrm{SS,c}}$ represent the nuisance parameters associated with the background function bias and $\boldsymbol{\theta}^{\mathrm{yield}}$ represent the nuisance parameters affecting the event yield, as detailed in Sec. VI. Correlation of the nuisance parameters across different signal and background components, as well as categories, is taken into account. In the case of the nonresonant search, $N^{\mathrm{res}}_{\mathrm{bkg,c}} = N_{H,\mathrm{c}}$, while in the case of the resonant analysis $N^{\mathrm{res}}_{\mathrm{bkg,c}} = N_{H,\mathrm{c}} + N_{\mathrm{SM}HH,\mathrm{c}}$.

The probability density function f_c represents the shape information. The sum of the double-sided Crystal Ball functions modeling the HH production processes, single Higgs boson production, and the spurious signal, and of the analytic function modeling the nonresonant background as described in Sec. V B, is shown in Eq. (5),

$$\begin{aligned} f_c(m_{\gamma\gamma},\boldsymbol{\theta}) = [&\mu\cdot N_{HH,\mathrm{c}}(\boldsymbol{\theta}^{\mathrm{yield}}_{HH})\cdot f_{HH,\mathrm{c}}(m_{\gamma\gamma},\boldsymbol{\theta}^{\mathrm{shape}}_{HH}) \\ &+ N^{\mathrm{res}}_{\mathrm{bkg,c}}(\boldsymbol{\theta}^{\mathrm{yield}}_{\mathrm{res}})\cdot f^{\mathrm{res}}_{\mathrm{bkg,c}}(m_{\gamma\gamma},\boldsymbol{\theta}^{\mathrm{shape}}_{\mathrm{res}}) \\ &+ N_{\mathrm{SS,c}}\cdot\boldsymbol{\theta}^{\mathrm{SS,c}}_{HH}\cdot f_{HH,\mathrm{c}}(m_{\gamma\gamma},\boldsymbol{\theta}^{\mathrm{shape}}_{HH}) \\ &+ N^{\mathrm{nonres}}_{\mathrm{bkg,c}}\cdot f^{\mathrm{nonres}}_{\mathrm{bkg,c}}(m_{\gamma\gamma},\boldsymbol{\theta}^{\mathrm{shape}}_{\mathrm{nonres}})]/N_c(\boldsymbol{\theta}^{\mathrm{yield}}_{\mathrm{nonres}}), \end{aligned} \quad (5)$$

where $\boldsymbol{\theta}^{\mathrm{shape}}$ represent nuisance parameters related to the shape variations of the functional forms. When a nuisance parameter is related to shape and yield variations at the same time, the two effects are correlated.

The nominal yields of the resonant background processes are initially set to values from simulation. The likelihood function includes all the nuisance parameters that describe the systematic uncertainties. The signal strength is a free parameter in the fit. The measurement of the parameter of interest is carried out using a statistical test based on the profile likelihood ratio [107], as shown in Eq. (6),

$$\Lambda(\mu) = \frac{\mathcal{L}(\mu,\hat{\hat{\boldsymbol{\theta}}}(\mu))}{\mathcal{L}(\hat{\mu},\hat{\boldsymbol{\theta}})}, \quad (6)$$

where μ and $\boldsymbol{\theta}$ are respectively the parameter of interest and the nuisance parameters. In the numerator, the nuisance parameters are set to their profiled values $\hat{\hat{\boldsymbol{\theta}}}(\mu)$, which maximize the likelihood function for a fixed value of the parameter of interest μ. In the denominator, the parameter of interest and the nuisance parameters are set to the values $\hat{\mu}$ and $\hat{\boldsymbol{\theta}}$, respectively, which jointly maximize the likelihood.

In the absence of signal, exclusion limits are set on Higgs boson pair production in the $b\bar{b}\gamma\gamma$ final state. The limits for both nonresonant and resonant production are calculated

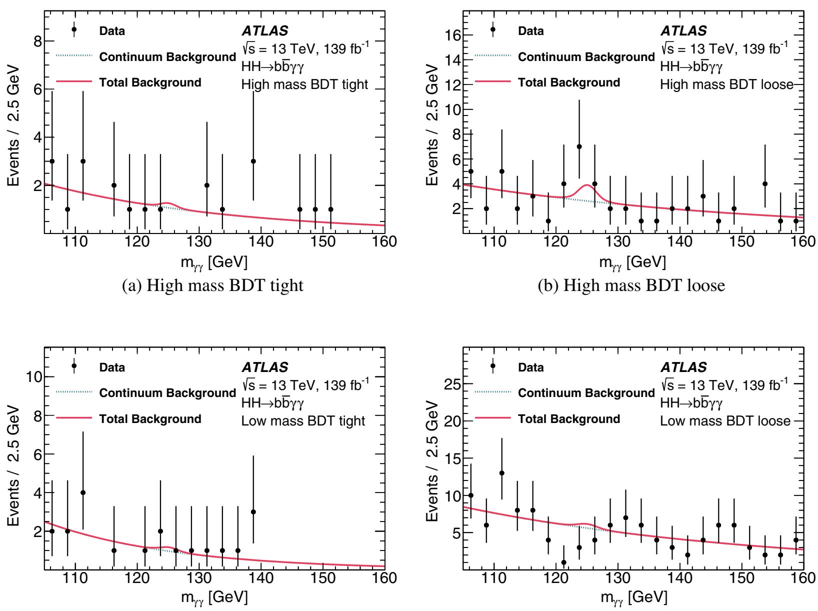

(a) High mass BDT tight

(b) High mass BDT loose

(c) Low mass BDT tight

(d) Low mass BDT loose

FIG. 11. Data are compared with the background-only fit for the four categories of the nonresonant search: (a) high mass BDT tight, (b) high mass BDT loose, (c) low mass BDT tight, and (d) low mass BDT loose. Both the continuum background and the background from single Higgs boson production are considered. The data points in the Figure are the same as shown in Fig. 9.

TABLE VI. The number of data events observed in the 120 GeV $< m_{\gamma\gamma} <$ 130 GeV window, the number of HH signal events expected for $\kappa_\lambda = 1$ and for $\kappa_\lambda = 10$, and events expected for single Higgs boson production (estimated using MC simulation), as well as for continuum background. For the single Higgs boson, "Rest" includes the following production modes: VBF, WH, tHq, and tHW. The values are obtained from a fit of the Asimov dataset [107] generated under the SM signal-plus-background hypothesis, $\kappa_\lambda = 1$. The continuum background component of the Asimov dataset is obtained from the fit of the data sideband. The uncertainties in HH signals and single Higgs boson background include the systematic uncertainties discussed in Sec. VI. The uncertainty in the continuum background is given by the sum in quadrature of the statistical uncertainty from the fit to the data and the spurious-signal uncertainty.

	High mass BDT tight	High mass BDT loose	Low mass BDT tight	Low mass BDT loose
Continuum background	$4.9^{+1.1}_{-1.3}$	$9.5^{+1.5}_{-1.7}$	$3.7^{+0.9}_{-1.1}$	$24.9^{+2.3}_{-2.5}$
Single Higgs boson background	$0.67^{+0.29}_{-0.13}$	$1.6^{+0.6}_{-0.2}$	$0.23^{+0.09}_{-0.03}$	$1.40^{+0.33}_{-0.16}$
ggF + bbH	$0.26^{+0.28}_{-0.16}$	$0.4^{+0.5}_{-0.2}$	$0.07^{+0.08}_{-0.04}$	$0.27^{+0.27}_{-0.16}$
$t\bar{t}H$	$0.19^{+0.03}_{-0.03}$	$0.49^{+0.09}_{-0.07}$	$0.107^{+0.022}_{-0.017}$	$0.75^{+0.13}_{-0.11}$
ZH	$0.142^{+0.035}_{-0.025}$	$0.48^{+0.09}_{-0.07}$	$0.040^{+0.020}_{-0.014}$	$0.27^{+0.06}_{-0.04}$
Rest	$0.074^{+0.032}_{-0.014}$	$0.16^{+0.07}_{-0.03}$	$0.012^{+0.008}_{-0.004}$	$0.111^{+0.030}_{-0.012}$
SM $HH(\kappa_\lambda = 1)$ signal	$0.87^{+0.10}_{-0.18}$	$0.37^{+0.04}_{-0.07}$	$0.049^{+0.006}_{-0.010}$	$0.078^{+0.008}_{-0.015}$
ggF	$0.86^{+0.10}_{-0.18}$	$0.35^{+0.04}_{-0.07}$	$0.046^{+0.006}_{-0.010}$	$0.072^{+0.008}_{-0.015}$
VBF	$(12.6^{+1.3}_{-1.2}) \times 10^{-3}$	$(16.1^{+1.4}_{-1.2}) \times 10^{-3}$	$(3.2^{+0.4}_{-0.4}) \times 10^{-3}$	$(6.9^{+0.5}_{-0.6}) \times 10^{-3}$
Alternative $HH(\kappa_\lambda = 10)$ signal	$6.5^{+1.0}_{-0.8}$	$3.6^{+0.6}_{-0.4}$	$4.5^{+0.7}_{-0.6}$	$8.5^{+1.3}_{-1.0}$
Data	2	17	5	14

using the CL_S method [121], with the profile-likelihood-ratio-based test statistic $\tilde{q}_\mu$, defined in Eq. (7) [107],

$$\tilde{q}_\mu = \begin{cases} -2\ln\frac{\Lambda(\mu,\hat{\hat{\theta}}(\mu))}{\Lambda(0,\hat{\hat{\theta}}(0))} & \hat{\mu} < 0, \\ -2\ln\frac{\Lambda(\mu,\hat{\hat{\theta}}(\mu))}{\Lambda(\hat{\mu},\hat{\theta}(\mu))} & 0 \le \hat{\mu} \le \mu, \\ 0 & \hat{\mu} > \mu. \end{cases} \quad (7)$$

The asymptotic approximation [107] is used for the test-statistic distribution. The inaccuracy of the asymptotic approximation is checked with pseudoexperiment studies for the key results reported in this paper.

B. Nonresonant search results

Figure 11 shows the background fits to the data. No significant excess over the SM background expectations is found, as summarized in Table VI. The statistical analysis sets a 95% C.L. upper limit on the nonresonant HH production cross section at 130 fb, while 180 fb is expected. An observed (expected) upper limit at 95% C.L. on the signal strength of 4.2 (5.7) times the SM prediction is obtained. The expected constraints are obtained for a background hypothesis excluding $pp \to HH$ production. For the upper limits on the cross section, all theoretical uncertainties are included, except those related to the signal cross section itself, while constraints on the signal strength are computed including uncertainties in the predicted signal cross section. A check of the results that quantifies the upper limits by using pseudoexperiments is performed and the increase of the limit value relative to the asymptotic approximation is found to be less than 8% for both the observed and expected upper limits. A check of the expected upper limits using prefit values for the nuisance parameters associated with the systematic uncertainties is

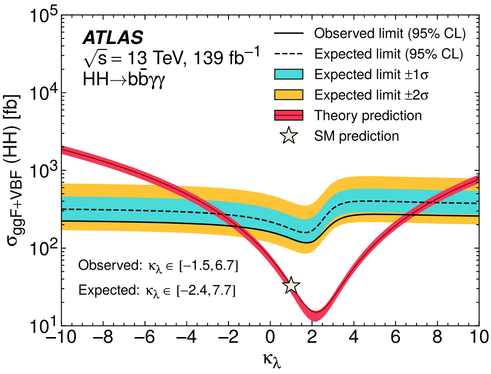

FIG. 12. Observed and expected limits at 95% C.L. on the cross section of nonresonant Higgs boson pair production as a function of the Higgs boson self-coupling modifier $\kappa_\lambda = \lambda_{HHH}/\lambda_{HHH}^{SM}$. The expected constraints on κ_λ are obtained with a background hypothesis excluding $pp \to HH$ production. The $\pm 1\sigma$ and $\pm 2\sigma$ variations about the expected limit due to statistical and systematic uncertainties are also shown. The theory prediction curve represents the scenario where all parameters and couplings are set to their SM values except for κ_λ. The uncertainty band of the theory prediction curve shows the cross section uncertainty.

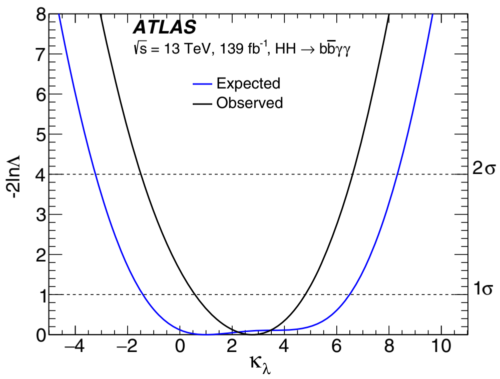

FIG. 13. Values of the negative log-profile-likelihood ratio ($-2\ln\Lambda$) as a function of κ_λ evaluated for the combination of all the categories of the nonresonant search. The coupling of the Higgs boson to fermions and gauge bosons is set to SM values in the profile likelihood calculation. The expected result corresponds to a Asimov dataset [107] generated under the SM signal-plus-background hypothesis, $\kappa_\lambda = 1$. All systematic uncertainties, including the theoretical uncertainties in the di-Higgs boson production cross section, are included. The intersections of the solid curves and the horizontal dashed lines indicate the 1σ and 2σ confidence level intervals.

performed and an increase of 4% relative to the nominal result is found. The difference is dominated by the contribution from the spurious signal.

Upper limits on the HH production cross section are also computed as a function of κ_λ, as shown in Fig. 12. For this purpose, single-Higgs-boson production cross sections and Higgs boson decay branching ratios are assumed to have SM values, and the coupling strength between the Higgs boson and other particles are also set to their SM values [55]. The theory uncertainties related to the signal cross section are not included.

TABLE VII. The number of events observed in the $120 < m_{\gamma\gamma} < 130$ GeV window in data, the number of events expected for scalar resonance signals of masses $m_X = 300$ GeV and $m_X = 500$ GeV assuming a total production cross section $\sigma(pp \to X \to HH)$ equal to the observed exclusion limits of Fig. 15, and events expected for SM HH and single Higgs boson production (estimated using MC simulation), as well as for continuum background. The values are obtained from a fit of the Asimov dataset [107] generated under the signal-plus-background hypothesis. The continuum background component of the Asimov dataset is obtained from the fit of the data sideband. The uncertainties in the resonant signals and the SM HH and single-Higgs-boson backgrounds include the systematic uncertainties discussed in Sec. VI. The uncertainty in the continuum background is given by the sum in quadrature of the statistical uncertainty from the fit to the data and the spurious-signal uncertainty.

	$m_X = 300$ GeV	$m_X = 500$ GeV
Continuum background	$5.5^{+1.3}_{-1.5}$	$1.6^{+0.6}_{-0.9}$
Single Higgs boson background	$0.34^{+0.14}_{-0.07}$	$0.40^{+0.18}_{-0.08}$
SM HH background	$0.021^{+0.005}_{-0.009}$	$0.20^{+0.09}_{-0.09}$
$X \to HH$ signal	$6.1^{+0.9}_{-0.8}$	$6.1^{+0.8}_{-0.6}$
Data	6	4

The expected constraints on κ_λ at 95% C.L., as obtained with a background hypothesis excluding $pp \to HH$ production, are $[-2.4, 7.7]$, whereas the observed constraints are $[-1.5, 6.7]$ at 95% C.L. The inclusion of the VBF HH production mode tightens the constraints by about 5% relative to an alternative fit considering only the ggF production mode.

An alternative statistical analysis consists in determining the best-fit value of the κ_λ coupling modifier. The best-fit value of κ_λ and its uncertainty are obtained by means of a negative log-likelihood scan. The coupling strengths of the Higgs boson to fermions and gauge bosons are set to their SM values. The values of the negative log-likelihood ratio,

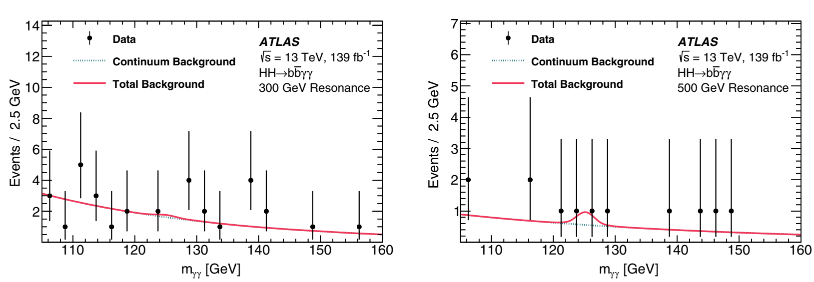

(a) (b)

FIG. 14. Data are compared with the background-only fit for the resonant search for the (a) $m_X = 300$ GeV and (b) $m_X = 500$ GeV mass hypotheses. The continuum background, as well as the background from single Higgs boson production and from SM HH production, is considered. The data points in the Figure are the same as shown in Fig. 10.

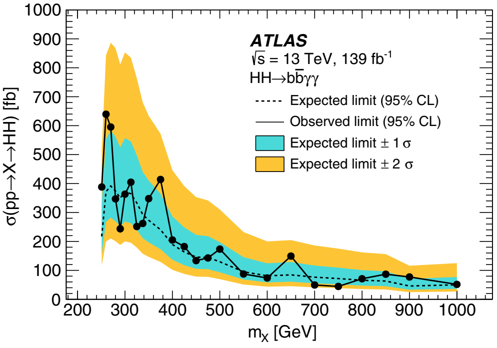

FIG. 15. Observed and expected limits at 95% C.L. on the production cross section of a narrow-width scalar resonance X as a function of the mass m_X of the hypothetical scalar particle. The black solid line represents the observed upper limits. The dashed line represents the expected upper limits. The $\pm 1\sigma$ and $\pm 2\sigma$ variations about the expected limit due to statistical and systematic uncertainties are also shown.

$-2\ln\Lambda(\mu)$, as a function of κ_λ are shown in Fig. 13. The Asimov dataset [107] is generated under the SM signal-plus-background hypothesis, $\kappa_\lambda = 1$. All systematic uncertainties, including those of the theoretical prediction of the HH production cross section, are included. The best-fit value corresponds to $\kappa_\lambda = 2.8^{+2.0}_{-2.2}$ $(^{+3.8}_{-4.3})$ for the 1σ (2σ) confidence interval. The expected value corresponds to $\kappa_\lambda = 1.0^{+5.5}_{-2.4}$ $(^{+7.3}_{-4.2})$ for the 1σ (2σ) confidence interval. The second minimum in the expected likelihood scan curve corresponds to a similar fitted signal yield with respect to the κ_λ point at the first minimum, which is a consequence of a higher cross section, but lower acceptance and worse signal-to-background separation. The m_{HH} distribution has a different shape at each of the two minima, as shown in Fig. 5.

C. Resonant search results

Figure 14 shows the fit to the data of the resonant search for two benchmark values of the mass m_X of a hypothetical scalar particle. No significant excess over the SM background expectations is found, as shown in Table VII. Figure 15 shows the observed and expected upper limits at 95% C.L. on the production cross section of a narrow-width scalar resonance. The observed (expected) upper limits vary between 640–44 fb (391–46 fb) in the range 251 GeV $\leq m_X \leq$ 1000 GeV. A check on the upper limits using pseudoexperiments is performed. For the expected limits, the results based on the pseudo-experiments are found to be up to 10% higher compared with those derived based on the asymptotic approximation. As for the observed limits, the pseudoexperiments yield typically 10% higher results compared with the asymptotic approximation in most of the m_X range explored, and the difference increases to 15% for the $m_X = 700$ GeV signal hypothesis.

D. Impact of systematic uncertainties

The dominant systematic uncertainties are listed in Table VIII for both the nonresonant and resonant searches. The main uncertainties are related to the choice of functional form for the continuum background (spurious signal), to the parton showering model, and to the photon energy resolution.

TABLE VIII. Breakdown of the dominant systematic uncertainties. The impact of the uncertainties corresponds to the relative variation of the expected upper limit on the cross section when reevaluating the profile likelihood ratio after fixing the nuisance parameter in question to its best-fit value, while all remaining nuisance parameters remain free to float. The impact is shown in %. Only systematic uncertainties with an impact of at least 0.2% are shown. Uncertainties of the "Norm + Shape" type affect both the normalization and the parameters of the functional form. The rest of the uncertainties affect only the yields.

		Relative impact of the systematic uncertainties [%]	
Source	Type	Nonresonant analysis HH	Resonant analysis $m_X = 300$ GeV
Experimental			
Photon energy resolution	Norm. + Shape	0.4	0.6
Jet energy scale and resolution	Normalization	<0.2	0.3
Flavor tagging	Normalization	<0.2	0.2
Theoretical			
Factorization and renormalization scale	Normalization	0.3	<0.2
Parton showering model	Norm. + Shape	0.6	2.6
Heavy-flavor content	Normalization	0.3	<0.2
$\mathcal{B}(H \to \gamma\gamma, b\bar{b})$	Normalization	0.2	<0.2
Spurious signal	Normalization	3.0	3.3

VIII. CONCLUSIONS

Searches for nonresonant and resonant Higgs boson pair production are performed in the $b\bar{b}\gamma\gamma$ final state using 139 fb^{-1} of 13 TeV pp collision data collected with the ATLAS detector at the LHC. No significant excess above the Standard Model background expectation is observed. A 95% C.L. upper limit of 130 fb is set on the $pp \to HH$ nonresonant production cross section, where the expected limit is 180 fb. The observed (expected) limit corresponds to 4.2 (5.7) times the cross section predicted by the Standard Model. Constraints on the Higgs boson self-coupling are also derived and limits of $-1.5 < \kappa_\lambda < 6.7$ are obtained, where $-2.4 < \kappa_\lambda < 7.7$ is expected. The expected constraints on the HH nonresonant production cross section and on κ_λ are obtained with a background hypothesis excluding $pp \to HH$ production. For resonant production of a scalar particle $X \to HH \to b\bar{b}\gamma\gamma$, upper limits on the production cross section are obtained for the narrow-width hypothesis as a function of m_X. The observed (expected) upper limits are in the range 640–44 fb (391–46 fb) for $251\,\mathrm{GeV} \leq m_X \leq 1000\,\mathrm{GeV}$. Compared to the previous ATLAS result based on 36 fb^{-1} of 13 TeV pp collisions, the present analysis uses a dataset about four times larger, incorporates a categorization based on $m^*_{b\bar{b}\gamma\gamma}$ and multivariate event selections, and expands the analyzed mass range of the resonance search to lower values. The results improve upon the previous ATLAS limits on the $HH \to b\bar{b}\gamma\gamma$ production cross section by up to a factor of five, and the allowed κ_λ range shrinks by about a factor of two. For the resonant search, the expected limit on the cross section improves by a factor of two to three depending on the m_X value. Of those improvements, a factor of two arises from the increase in integrated luminosity, while the additional improvement can be attributed to the use of multivariate techniques, more precise object reconstruction and calibration and, for the nonresonant search, the categorization based on $m^*_{b\bar{b}\gamma\gamma}$. The present analysis also sets constraints that are tighter than those from a combination of ATLAS searches for HH production in up to 36 fb^{-1} of 13 TeV data.

ACKNOWLEDGMENTS

We thank CERN for the very successful operation of the LHC, as well as the support staff from our institutions without whom ATLAS could not be operated efficiently. We acknowledge the support of ANPCyT, Argentina; YerPhI, Armenia; ARC, Australia; BMWFW and FWF, Austria; ANAS, Azerbaijan; SSTC, Belarus; CNPq and FAPESP, Brazil; NSERC, NRC and CFI, Canada; CERN; ANID, Chile; CAS, MOST and NSFC, China; Minciencias, Colombia; MEYS CR, Czech Republic; DNRF and DNSRC, Denmark; IN2P3-CNRS and CEA-DRF/IRFU, France; SRNSFG, Georgia; BMBF, HGF and MPG, Germany; GSRI, Greece; RGC and Hong Kong SAR, China; ISF and Benoziyo Center, Israel; INFN, Italy; MEXT and JSPS, Japan; CNRST, Morocco; NWO, Netherlands; RCN, Norway; MEiN, Poland; FCT, Portugal; MNE/IFA, Romania; JINR; MES of Russia and NRC KI, Russian Federation; MESTD, Serbia; MSSR, Slovakia; ARRS and MIZŠ, Slovenia; DSI/NRF, South Africa; MICINN, Spain; SRC and Wallenberg Foundation, Sweden; SERI, SNSF and Cantons of Bern and Geneva, Switzerland; MOST, Taiwan; TAEK, Turkey; STFC, United Kingdom; DOE and NSF, USA. In addition, individual groups and members have received support from BCKDF, CANARIE, Compute Canada and CRC, Canada; COST, ERC, ERDF, Horizon 2020 and Marie Skłodowska-Curie Actions, European Union; Investissements d'Avenir Labex, Investissements d'Avenir Idex and ANR, France; DFG and AvH Foundation, Germany; Herakleitos, Thales and Aristeia programmes co-financed by EU-ESF and the Greek NSRF, Greece; BSF-NSF and GIF, Israel; Norwegian Financial Mechanism 2014-2021, Norway; NCN and NAWA, Poland; La Caixa Banking Foundation, CERCA Programme Generalitat de Catalunya and PROMETEO and GenT Programmes Generalitat Valenciana, Spain; Göran Gustafssons Stiftelse, Sweden; The Royal Society and Leverhulme Trust, United Kingdom. The crucial computing support from all WLCG partners is acknowledged gratefully, in particular from CERN, the ATLAS Tier-1 facilities at TRIUMF (Canada), NDGF (Denmark, Norway, Sweden), CC-IN2P3 (France), KIT/GridKA (Germany), INFN-CNAF (Italy), NL-T1 (Netherlands), PIC (Spain), ASGC (Taiwan), RAL (UK) and BNL (USA), the Tier-2 facilities worldwide and large non-WLCG resource providers. Major contributors of computing resources are listed in Ref. [122].

[1] ATLAS Collaboration, Observation of a new particle in the search for the Standard Model Higgs boson with the ATLAS detector at the LHC, Phys. Lett. B **716**, 1 (2012).
[2] CMS Collaboration, Observation of a new boson at a mass of 125 GeV with the CMS experiment at the LHC, Phys. Lett. B **716**, 30 (2012).
[3] F. Englert and R. Brout, Broken Symmetry and the Mass of Gauge Vector Mesons, Phys. Rev. Lett. **13**, 321 (1964).
[4] P. W. Higgs, Broken symmetries, massless particles and gauge fields, Phys. Lett. **12**, 132 (1964).
[5] P. W. Higgs, Broken Symmetries and the Masses of Gauge Bosons, Phys. Rev. Lett. **13**, 508 (1964).

[6] G. S. Guralnik, C. R. Hagen, and T. W. B. Kibble, Global Conservation Laws and Massless Particles, Phys. Rev. Lett. **13**, 585 (1964).
[7] P. W. Higgs, Spontaneous symmetry breakdown without massless bosons, Phys. Rev. **145**, 1156 (1966).
[8] T. W. B. Kibble, Symmetry breaking in non-abelian gauge theories, Phys. Rev. **155**, 1554 (1967).
[9] P. Huang, A. J. Long, and L.-T. Wang, Probing the electroweak phase transition with Higgs factories and gravitational waves, Phys. Rev. D **94**, 075008 (2016).
[10] S. Dawson, S. Dittmaier, and M. Spira, Neutral Higgs-boson pair production at hadron colliders: QCD corrections, Phys. Rev. D **58**, 115012 (1998).
[11] S. Borowka, N. Greiner, G. Heinrich, S. P. Jones, M. Kerner, J. Schlenk, U. Schubert, and T. Zirke, Higgs Boson Pair Production in Gluon Fusion at Next-to-Leading Order with Full Top-Quark Mass Dependence, Phys. Rev. Lett. **117**, 012001 (2016); Erratum, Phys. Rev. Lett. **117**, 079901 (2016).
[12] D. de Florian and J. Mazzitelli, Higgs Boson Pair Production at Next-to-Next-to-Leading Order in QCD, Phys. Rev. Lett. **111**, 201801 (2013).
[13] ATLAS and CMS Collaborations, Combined Measurement of the Higgs Boson Mass in pp Collisions at $\sqrt{s} = 7$ and 8 TeV with the ATLAS and CMS Experiments, Phys. Rev. Lett. **114**, 191803 (2015).
[14] J. Alison, M. Gouzevitch, J. Mazzitelli, and C. Vernieri, Higgs boson potential at colliders: Status and perspectives, Rev. Phys. **5**, 100045 (2020).
[15] D. Y. Shao, C. S. Li, H. T. Li, and J. Wang, Threshold resummation effects in Higgs boson pair production at the LHC, J. High Energy Phys. 07 (2013) 169.
[16] D. de Florian and J. Mazzitelli, Higgs pair production at next-to-next-to-leading logarithmic accuracy at the LHC, J. High Energy Phys. 09 (2015) 053.
[17] J. Baglio, F. Campanario, S. Glaus, M. Mühlleitner, J. Ronca, and M. Spira, $gg \to HH$: Combined uncertainties, Phys. Rev. D **103**, 056002 (2021).
[18] M. Grazzini, G. Heinrich, S. Jones, S. Kallweit, M. Kerner, J. M. Lindert, and J. Mazzitelli, Higgs boson pair production at NNLO with top quark mass effects, J. High Energy Phys. 05 (2018) 059.
[19] R. Frederix, S. Frixione, V. Hirschi, F. Maltoni, O. Mattelaer, P. Torrielli, E. Vryonidou, and M. Zaro, Higgs pair production at the LHC with NLO and parton-shower effects, Phys. Lett. B **732**, 142 (2014).
[20] G. D. Kribs and A. Martin, Enhanced di-Higgs production through light colored scalars, Phys. Rev. D **86**, 095023 (2012).
[21] L. Di Luzio, R. Gröber, and M. Spannowsky, Maxi-sizing the trilinear Higgs self-coupling: How large could it be?, Eur. Phys. J. C **77**, 788 (2017).
[22] G. D. Kribs, A. Maier, H. Rzehak, M. Spannowsky, and P. Waite, Electroweak oblique parameters as a probe of the trilinear Higgs boson self-interaction, Phys. Rev. D **95**, 093004 (2017).
[23] T. D. Lee, A theory of spontaneous T violation, Phys. Rev. D **8**, 1226 (1973).
[24] S. Dimopoulos and H. Georgi, Softly broken supersymmetry and SU(5), Nucl. Phys. **B193**, 150 (1981).
[25] Z. Chacko, Y. Nomura, M. Papucci, and G. Perez, Natural little hierarchy from a partially goldstone twin Higgs, J. High Energy Phys. 01 (2006) 126.
[26] J. Mrazek, A. Pomarol, R. Rattazzi, M. Redi, J. Serra, and A. Wulzer, The other natural two Higgs doublet model, Nucl. Phys. **B853**, 1 (2011).
[27] L. Randall and R. Sundrum, Large Mass Hierarchy from a Small Extra Dimension, Phys. Rev. Lett. **83**, 3370 (1999).
[28] ATLAS Collaboration, Search for Higgs boson pair production in the $\gamma\gamma b\bar{b}$ final state with 13 TeV pp collision data collected by the ATLAS experiment, J. High Energy Phys. 11 (2018) 040.
[29] ATLAS Collaboration, Combination of searches for Higgs boson pairs in pp collisions at $\sqrt{s} = 13$ TeV with the ATLAS detector, Phys. Lett. B **800**, 135103 (2020).
[30] CMS Collaboration, Search for nonresonant Higgs boson pair production in final states with two bottom quarks and two photons in proton–proton collisions at $\sqrt{s} = 13$ TeV, J. High Energy Phys. 03 (2021) 257.
[31] CMS Collaboration, Search for Higgs boson pair production in the $\gamma\gamma b\bar{b}$ final state in pp collisions at $\sqrt{s} = 13$ TeV, Phys. Lett. B **788**, 7 (2019).
[32] ATLAS Collaboration, The ATLAS experiment at the CERN Large Hadron Collider, J. Instrum. **3**, S08003 (2008).
[33] ATLAS Collaboration, ATLAS insertable B-layer: Technical design report, Reports No. ATLAS-TDR-19, No. CERN-LHCC-2010-013, 2010, https://cds.cern.ch/record/1291633; Addendum, Reports No. ATLAS-TDR-19-ADD-1, No. CERN-LHCC-2012-009, 2012, https://cds.cern.ch/record/1451888.
[34] B. Abbott *et al.*, Production and integration of the ATLAS Insertable B-Layer, J. Instrum. **13**, T05008 (2018).
[35] ATLAS Collaboration, Performance of the ATLAS trigger system in 2015, Eur. Phys. J. C **77**, 317 (2017).
[36] ATLAS Collaboration, The ATLAS Collaboration software and firmware, Report No. ATL-SOFT-PUB-2021-001, 2021, https://cds.cern.ch/record/2767187.
[37] ATLAS Collaboration, ATLAS data quality operations and performance for 2015–2018 data-taking, J. Instrum. **15**, P04003 (2020).
[38] G. Avoni *et al.*, The new LUCID-2 detector for luminosity measurement and monitoring in ATLAS, J. Instrum. **13**, P07017 (2018).
[39] ATLAS Collaboration, Luminosity determination in pp collisions at $\sqrt{s} = 13$ TeV using the ATLAS detector at the LHC, Report No. ATLAS-CONF-2019-021, 2019, https://cds.cern.ch/record/2677054.
[40] ATLAS Collaboration, Emulating the impact of additional proton-proton interactions in the ATLAS simulation by pre-sampling sets of inelastic Monte Carlo events, Comput. Softw. Big Sci. **6**, 3 (2022).
[41] P. Nason and C. Oleari, NLO Higgs boson production via vector-boson fusion matched with shower in POWHEG, J. High Energy Phys. 02 (**2010**) 037.
[42] G. Heinrich, S. P. Jones, M. Kerner, G. Luisoni, and E. Vryonidou, NLO predictions for Higgs boson pair production with full top quark mass dependence matched to parton showers, J. High Energy Phys. 08 (2017) 088.
[43] G. Heinrich, S. Jones, M. Kerner, G. Luisoni, and L. Scyboz, Probing the trilinear Higgs boson coupling in di-

Higgs production at NLO QCD including parton shower effects, J. High Energy Phys. 06 (2019) 066.
[44] J. Butterworth et al., PDF4LHC recommendations for LHC Run II, J. Phys. G **43**, 023001 (2016).
[45] ATLAS Collaboration, Validation of signal Monte Carlo event generation in searches for Higgs boson pairs with the ATLAS detector, Report No. ATL-PHYS-PUB-2019-007, 2019, https://cds.cern.ch/record/2665057.
[46] S. Amoroso et al., Les Houches 2019: Physics at TeV Colliders: Standard Model Working Group Report, Proceedings of the 11th Les Houches Workshop on Physics at TeV Colliders: PhysTeV Les Houches, 2020, arXiv:2003.01700.
[47] J. Alwall, S. Frixione, V. Hirschi, F. Maltoni, O. Mattelaer, H.-S. Shao, T. Stelzer, P. Torrielli, and M. Zaro et al., The automated computation of tree-level and next-to-leading order differential cross sections, and their matching to parton shower simulations, J. High Energy Phys. 07 (2014) 079.
[48] F. Bishara, R. Contino, and J. Rojo, Higgs pair production in vector-boson fusion at the LHC and beyond, Eur. Phys. J. C **77**, 481 (2017).
[49] R. D. Ball et al., Parton distributions with LHC data, Nucl. Phys. **B867**, 244 (2013).
[50] L.-S. Ling , R.-Y. Zhang, W.-G. Ma, L. Guo, W.-H. Li, and X.-Z. Li et al., NNLO QCD corrections to Higgs pair production via vector boson fusion at hadron colliders, Phys. Rev. D **89**, 073001 (2014).
[51] F. A. Dreyer and A. Karlberg, Vector-boson fusion Higgs pair production at N3LO, Phys. Rev. D **98**, 114016 (2018).
[52] F. A. Dreyer and A. Karlberg, Fully differential vector-boson fusion Higgs pair production at next-to-next-to-leading order, Phys. Rev. D **99**, 074028 (2019).
[53] M. Bähr et al., HERWIG++ physics and manual, Eur. Phys. J. C **58**, 639 (2008).
[54] J. Bellm et al., HERWIG 7.0/HERWIG++ 3.0 release note, Eur. Phys. J. C **76**, 196 (2016).
[55] ATLAS Collaboration, Combined measurements of Higgs boson production and decay using up to 80 fb^{-1} of proton–proton collision data at $\sqrt{s} = 13$ TeV collected with the ATLAS experiment, Phys. Rev. D **101**, 012002 (2020).
[56] D. de Florian et al., Handbook of LHC Higgs cross sections: 4. Deciphering the nature of the Higgs sector, arXiv:1610.07922.
[57] A. Djouadi, J. Kalinowski, and M. Spira, HDECAY: A program for Higgs boson decays in the standard model and its supersymmetric extension, Comput. Phys. Commun. **108**, 56 (1998).
[58] E. Bothmann et al., Event generation with SHERPA 2.2, SciPost Phys. **7**, 034 (2019).
[59] T. Gleisberg and S. Höche, Comix, a new matrix element generator, J. High Energy Phys. 12 (2008) 039.
[60] F. Buccioni, J.-N. Lang, J. M. Lindert, P. Maierhöfer, S. Pozzorini, H. Zhang, and M. F. Zoller et al., OPENLOOPS2, Eur. Phys. J. C **79**, 866 (2019).
[61] F. Cascioli, P. Maierhöfer, and S. Pozzorini, Scattering Amplitudes with Open Loops, Phys. Rev. Lett. **108**, 111601 (2012).
[62] A. Denner, S. Dittmaier, and L. Hofer, Collier: A fortran-based complex one-loop library in extended regularizations, Comput. Phys. Commun. **212**, 220 (2017).
[63] S. Schumann and F. Krauss, A parton shower algorithm based on Catani–Seymour dipole factorisation, J. High Energy Phys. 03 (2008) 038.
[64] S. Höche, F. Krauss, M. Schönherr, and F. Siegert, A critical appraisal of NLO + PS matching methods, J. High Energy Phys. 09 (2012) 049.
[65] S. Höche, F. Krauss, M. Schönherr, and F. Siegert, QCD matrix elements + parton showers. The NLO case, J. High Energy Phys. 04 (2013) 027.
[66] F. Siegert, A practical guide to event generation for prompt photon production with SHERPA, J. Phys. G **44**, 044007 (2017).
[67] T. Sjöstrand, S. Ask, J. R. Christiansen, R. Corke, N. Desai, P. Ilten, S. Mrenna, S. Prestel, C. O. Rasmussen, and P. Z. Skands, An introduction to PYTHIA8.2, Comput. Phys. Commun. **191**, 159 (2015).
[68] ATLAS Collaboration, ATLAS PYTHIA8 tunes to 7 TeV data, Report No. ATL-PHYS-PUB-2014-021, 2014, https://cds.cern.ch/record/1966419.
[69] R. D. Ball et al., Parton distributions for the LHC run II, J. High Energy Phys. 04 (2015) 040.
[70] S. Gieseke, C. Röhr, and A. Siodmok, Colour reconnections in HERWIG++, Eur. Phys. J. C **72**, 2225 (2012).
[71] K. Hamilton, P. Nason, and G. Zanderighi, MINLO: multi-scale improved NLO, J. High Energy Phys. 10 (2012) 155.
[72] J. M. Campbell, R. Keith Ellis, R. Frederix, P. Nason, C. Oleari, and C. Williams, NLO Higgs boson production plus one and two jets using the POWHEG BOX, MadGraph4 and MCFM, J. High Energy Phys. 07 (2012) 092.
[73] K. Hamilton, P. Nason, C. Oleari, and G. Zanderighi, Merging H/W/Z + 0 and 1 jet at NLO with no merging scale: a path to parton shower + NNLO matching, J. High Energy Phys. 05 (2013) 082.
[74] G. Bozzi, S. Catani, D. de Florian, and M. Grazzini, Transverse-momentum resummation and the spectrum of the Higgs boson at the LHC, Nucl. Phys. **B737**, 73 (2006).
[75] D. de Florian, G. Ferrera, M. Grazzini, and D. Tommasini, Transverse-momentum resummation: Higgs boson production at the Tevatron and the LHC, J. High Energy Phys. 11 (2011) 064.
[76] ATLAS Collaboration, Measurement of the Z/γ^* boson transverse momentum distribution in pp collisions at $\sqrt{s} = 7$ TeV with the ATLAS detector, J. High Energy Phys. 09 (2014) 145.
[77] K. Hamilton, P. Nason, E. Re, and G. Zanderighi, NNLOPS simulation of Higgs boson production, J. High Energy Phys. 10 (2013) 222.
[78] P. Nason, A new method for combining NLO QCD with shower Monte Carlo algorithms, J. High Energy Phys. 11 (2004) 040.
[79] S. Frixione, P. Nason, and C. Oleari, Matching NLO QCD computations with parton shower simulations: the POWHEG method, J. High Energy Phys. 11 (2007) 070.
[80] S. Alioli, P. Nason, C. Oleari, and E. Re, A general framework for implementing NLO calculations in shower Monte Carlo programs: The POWHEG BOX, J. High Energy Phys. 06 (2010) 043.
[81] K. Mimasu, V. Sanz, and C. Williams, Higher order QCD predictions for associated Higgs production with

anomalous couplings to gauge bosons, J. High Energy Phys. 08 (2016) 039.
[82] G. Luisoni, P. Nason, C. Oleari, and F. Tramontano, $HW^{\pm}/\mathrm{HZ}+0$ and 1 jet at NLO with the POWHEG BOX interfaced to GoSam and their merging within MiNLO, J. High Energy Phys. 10 (2013) 083.
[83] H. B. Hartanto, B. Jäger, L. Reina, and D. Wackeroth, Higgs boson production in association with top quarks in the POWHEG BOX, Phys. Rev. D **91**, 094003 (2015).
[84] S. Frixione, G. Ridolfi, and P. Nason, A positive-weight next-to-leading-order Monte Carlo for heavy flavour hadroproduction, J. High Energy Phys. 09 (2007) 126.
[85] ATLAS Collaboration, The PYTHIA8 A3 tune description of ATLAS minimum bias and inelastic measurements incorporating the Donnachie–Landshoff diffractive model, Report No. ATL-PHYS-PUB-2016-017, 2016, https://cds.cern.ch/record/2206965.
[86] ATLAS Collaboration, The ATLAS simulation infrastructure, Eur. Phys. J. C **70**, 823 (2010).
[87] S. Agostinelli *et al.* (GEANT4 Collaboration), GEANT 4—a simulation toolkit, Nucl. Instrum. Methods Phys. Res., Sect. A **506**, 250 (2003).
[88] ATLAS Collaboration, The simulation principle and performance of the ATLAS fast calorimeter simulation FastCaloSim, Report No. ATL-PHYS-PUB-2010-013, 2010, http://cdsweb.cern.ch/record/1300517.
[89] ATLAS Collaboration, Electron and photon reconstruction and performance in ATLAS using a dynamical, topological cell clustering-based approach, Report No. ATL-PHYS-PUB-2017-022, 2017, https://cds.cern.ch/record/2298955.
[90] ATLAS Collaboration, Electron and photon performance measurements with the ATLAS detector using the 2015–2017 LHC proton–proton collision data, J. Instrum. **14**, P12006 (2019).
[91] ATLAS Collaboration, Measurement of Higgs boson production in the diphoton decay channel in pp collisions at center-of-mass energies of 7 and 8 TeV with the ATLAS detector, Phys. Rev. D **90**, 112015 (2014).
[92] ATLAS Collaboration, Muon reconstruction performance of the ATLAS detector in proton–proton collision data at $\sqrt{s}=13$ TeV, Eur. Phys. J. C **76**, 292 (2016).
[93] ATLAS Collaboration, Muon reconstruction and identification efficiency in ATLAS using the full Run $2pp$ collision data set at $\sqrt{s}=13$ TeV, Eur. Phys. J. C **81**, 578 (2021).
[94] ATLAS Collaboration, Jet reconstruction and performance using particle flow with the ATLAS Detector, Eur. Phys. J. C **77**, 466 (2017).
[95] M. Cacciari, G. P. Salam, and G. Soyez, FastJet user manual, Eur. Phys. J. C **72**, 1896 (2012).
[96] M. Cacciari, G. P. Salam, and G. Soyez, The anti-k_t jet clustering algorithm, J. High Energy Phys. 04 (2008) 063.
[97] ATLAS Collaboration, Tagging and suppression of pileup jets with the ATLAS detector, Report No. ATLAS-CONF-2014-018, 2014, https://cds.cern.ch/record/1700870.
[98] ATLAS Collaboration, ATLAS b-jet identification performance and efficiency measurement with $t\bar{t}$, Eur. Phys. J. C **79**, 970 (2019).
[99] ATLAS Collaboration, Identification of jets containing b-hadrons with recurrent neural networks at the ATLAS experiment, Report No. ATL-PHYS-PUB-2017-003, 2017, https://cds.cern.ch/record/2255226.
[100] ATLAS Collaboration, Optimisation and performance studies of the ATLAS b-tagging algorithms for the 2017-18 LHC run, Report No. ATL-PHYS-PUB-2017-013, 2017, https://cds.cern.ch/record/2273281.
[101] ATLAS Collaboration, Performance of b-jet identification in the ATLAS experiment, J. Instrum. **11**, P04008 (2016).
[102] ATLAS Collaboration, Evidence for the $H\to b\bar{b}$ decay with the ATLAS detector, J. High Energy Phys. 12 (2017) 024.
[103] ATLAS Collaboration, Performance of missing transverse momentum reconstruction with the ATLAS detector using proton–proton collisions at $\sqrt{s}=13$ TeV, Eur. Phys. J. C **78**, 903 (2018).
[104] ATLAS Collaboration, Performance of electron and photon triggers in ATLAS during LHC Run 2, Eur. Phys. J. C **80**, 47 (2020).
[105] ATLAS Collaboration, Search for pair production of Higgs bosons in the $b\bar{b}b\bar{b}$ final state using proton–proton collisions at $\sqrt{s}=13$ TeV with the ATLAS detector, J. High Energy Phys. 01 (2019) 030.
[106] T. Chen and C. Guestrin, XGBoost: A scalable tree boosting system, *KDD'16: Proceedings of the 22nd ACM SIGKDD International Conference on Knowledge Discovery and Data Mining* (2016), pp. 785–794, arXiv:1603.02754.
[107] G. Cowan, K. Cranmer, E. Gross, and O. Vitells, Asymptotic formulae for likelihood-based tests of new physics, Eur. Phys. J. C **71**, 1554 (2011); Erratum, Eur. Phys. J. C **73**, 2501 (2013).
[108] A. Hoecker *et al.*, TMVA—Toolkit for multivariate data analysis, arXiv:physics/0703039.
[109] ATLAS Collaboration, Measurement of isolated-photon pair production in pp collisions at $\sqrt{s}=7$ TeV with the ATLAS detector, J. High Energy Phys. 01 (2013) 086.
[110] M. Oreglia, A study of the reactions $\psi'\to\gamma\gamma\psi$, https://www.slac.stanford.edu/cgi-wrap/getdoc/slac-r-236.pdf.
[111] ATLAS Collaboration, Recommendations for the modeling of smooth backgrounds, Report No. ATL-PHYS-PUB-2020-028, 2020, https://cds.cern.ch/record/2743717.
[112] A. Wald, Sequential tests of statistical hypotheses, Ann. Math. Stat. **16**, 117 (1945).
[113] ATLAS Collaboration, Performance of electron and photon triggers in ATLAS during LHC Run 2, Eur. Phys. J. C **80**, 47 (2020).
[114] ATLAS Collaboration, Search for resonances in diphoton events at $\sqrt{s}=13$ TeV with the ATLAS detector, J. High Energy Phys. 09 (2016) 001.
[115] ATLAS Collaboration, Jet energy scale and resolution measured in proton–proton collisions at $\sqrt{s}=13$ TeV with the ATLAS detector, Eur. Phys. J. C **81**, 689 (2020).
[116] ATLAS Collaboration, Measurement of b-tagging efficiency of c-jets in $t\bar{t}$ events using a likelihood approach with the ATLAS detector, Report No. ATLAS-CONF-2018-001, 2018, https://cds.cern.ch/record/2306649.
[117] ATLAS Collaboration, Calibration of light-flavour b-jet mistagging rates using ATLAS proton–proton collision data at $\sqrt{s}=13$ TeV, Report No. ATLAS-CONF-2018-006, 2018, https://cds.cern.ch/record/2314418.

[118] ATLAS Collaboration, Measurements of inclusive and differential fiducial cross-sections of $t\bar{t}$ production with additional heavy-flavour jets in proton–proton collisions at $\sqrt{s} = 13$ TeV with the ATLAS detector, J. High Energy Phys. 04 (2019) 046.
[119] ATLAS Collaboration, Study of heavy-flavor quarks produced in association with top quark pairs at $\sqrt{s} = 7$ TeV using the ATLAS detector, Phys. Rev. D **89**, 072012 (2014).
[120] ATLAS Collaboration, Measurement of the cross-section for W boson production in association with b-jets in pp collisions at $\sqrt{s} = 7$ TeV with the ATLAS detector, J. High Energy Phys. 06 (**2013**) 084.
[121] A. L. Read, Presentation of search results: The CL_S technique, J. Phys. G **28**, 2693 (2002).
[122] ATLAS Collaboration, ATLAS computing acknowledgements, Report No. ATL-SOFT-PUB-2021-003, https://cds.cern.ch/record/2776662.

G. Aad,[99] B. Abbott,[124] D. C. Abbott,[100] A. Abed Abud,[34] K. Abeling,[51] D. K. Abhayasinghe,[91] S. H. Abidi,[27] H. Abramowicz,[157] H. Abreu,[156] Y. Abulaiti,[5] A. C. Abusleme Hoffman,[142a] B. S. Acharya,[64a,64b,b] B. Achkar,[51] L. Adam,[97] C. Adam Bourdarios,[4] L. Adamczyk,[81a] L. Adamek,[162] J. Adelman,[117] A. Adiguzel,[11c,c] S. Adorni,[52] T. Adye,[139] A. A. Affolder,[141] Y. Afik,[156] C. Agapopoulou,[62] M. N. Agaras,[12] J. Agarwala,[68a,68b] A. Aggarwal,[115] C. Agheorghiesei,[25c] J. A. Aguilar-Saavedra,[135f,135a,d] A. Ahmad,[34] F. Ahmadov,[77,e] W. S. Ahmed,[101] X. Ai,[44] G. Aielli,[71a,71b] S. Akatsuka,[83] M. Akbiyik,[97] T. P. A. Åkesson,[94] A. V. Akimov,[108] K. Al Khoury,[37] G. L. Alberghi,[21b] J. Albert,[171] M. J. Alconada Verzini,[86] S. Alderweireldt,[48] M. Aleksa,[34] I. N. Aleksandrov,[77] C. Alexa,[25b] T. Alexopoulos,[9] A. Alfonsi,[116] F. Alfonsi,[21b,21a] M. Alhroob,[124] B. Ali,[137] S. Ali,[154] M. Aliev,[161] G. Alimonti,[66a] C. Allaire,[34] B. M. M. Allbrooke,[152] P. P. Allport,[19] A. Aloisio,[67a,67b] F. Alonso,[86] C. Alpigiani,[144] E. Alunno Camelia,[71a,71b] M. Alvarez Estevez,[96] M. G. Alviggi,[67a,67b] Y. Amaral Coutinho,[78b] A. Ambler,[101] L. Ambroz,[130] C. Amelung,[34] D. Amidei,[103] S. P. Amor Dos Santos,[135a] S. Amoroso,[44] C. S. Amrouche,[52] C. Anastopoulos,[145] N. Andari,[140] T. Andeen,[10] J. K. Anders,[18] S. Y. Andrean,[43a,43b] A. Andreazza,[66a,66b] V. Andrei,[59a] S. Angelidakis,[8] A. Angerami,[37] A. V. Anisenkov,[118b,118a] A. Annovi,[69a] C. Antel,[52] M. T. Anthony,[145] E. Antipov,[125] M. Antonelli,[49] D. J. A. Antrim,[16] F. Anulli,[70a] M. Aoki,[79] J. A. Aparisi Pozo,[169] M. A. Aparo,[152] L. Aperio Bella,[44] N. Aranzabal,[34] V. Araujo Ferraz,[78a] C. Arcangeletti,[49] A. T. H. Arce,[47] E. Arena,[88] J-F. Arguin,[107] S. Argyropoulos,[50] J.-H. Arling,[44] A. J. Armbruster,[34] A. Armstrong,[166] O. Arnaez,[162] H. Arnold,[34] Z. P. Arrubarrena Tame,[111] G. Artoni,[130] H. Asada,[113] K. Asai,[122] S. Asai,[159] N. A. Asbah,[57] E. M. Asimakopoulou,[167] L. Asquith,[152] J. Assahsah,[33d] K. Assamagan,[27] R. Astalos,[26a] R. J. Atkin,[31a] M. Atkinson,[168] N. B. Atlay,[17] H. Atmani,[58b] P. A. Atmasiddha,[103] K. Augsten,[137] S. Auricchio,[67a,67b] V. A. Austrup,[177] G. Avner,[156] G. Avolio,[34] M. K. Ayoub,[13c] G. Azuelos,[107,f] D. Babal,[26a] H. Bachacou,[140] K. Bachas,[158] F. Backman,[43a,43b] A. Badea,[57] P. Bagnaia,[70a,70b] H. Bahrasemani,[148] A. J. Bailey,[169] V. R. Bailey,[168] J. T. Baines,[139] C. Bakalis,[9] O. K. Baker,[178] P. J. Bakker,[116] E. Bakos,[14] D. Bakshi Gupta,[7] S. Balaji,[153] R. Balasubramanian,[116] E. M. Baldin,[118b,118a] P. Balek,[138] E. Ballabene,[66a,66b] F. Balli,[140] W. K. Balunas,[130] J. Balz,[97] E. Banas,[82] M. Bandieramonte,[134] A. Bandyopadhyay,[17] L. Barak,[157] E. L. Barberio,[102] D. Barberis,[53b,53a] M. Barbero,[99] G. Barbour,[92] K. N. Barends,[31a] T. Barillari,[112] M-S. Barisits,[34] J. Barkeloo,[127] T. Barklow,[149] B. M. Barnett,[139] R. M. Barnett,[16] A. Baroncelli,[58a] G. Barone,[27] A. J. Barr,[130] L. Barranco Navarro,[43a,43b] F. Barreiro,[96] J. Barreiro Guimarães da Costa,[13a] U. Barron,[157] S. Barsov,[133] F. Bartels,[59a] R. Bartoldus,[149] G. Bartolini,[99] A. E. Barton,[87] P. Bartos,[26a] A. Basalaev,[44] A. Basan,[97] I. Bashta,[72a,72b] A. Bassalat,[62,g] M. J. Basso,[162] C. R. Basson,[98] R. L. Bates,[55] S. Batlamous,[33e] J. R. Batley,[30] B. Batool,[147] M. Battaglia,[141] M. Bauce,[70a,70b] F. Bauer,[140,a] P. Bauer,[22] H. S. Bawa,[29] A. Bayirli,[11c] J. B. Beacham,[47] T. Beau,[131] P. H. Beauchemin,[165] F. Becherer,[50] P. Bechtle,[22] H. P. Beck,[18,h] K. Becker,[173] C. Becot,[44] A. J. Beddall,[11a] V. A. Bednyakov,[77] C. P. Bee,[151] T. A. Beermann,[177] M. Begalli,[78b] M. Begel,[27] A. Behera,[151] J. K. Behr,[44] C. Beirao Da Cruz E Silva,[34] J. F. Beirer,[51,34] F. Beisiegel,[22] M. Belfkir,[4] G. Bella,[157] L. Bellagamba,[21b] A. Bellerive,[32] P. Bellos,[19] K. Beloborodov,[118b,118a] K. Belotskiy,[109] N. L. Belyaev,[109] D. Benchekroun,[33a] Y. Benhammou,[157] D. P. Benjamin,[27] M. Benoit,[27] J. R. Bensinger,[24] S. Bentvelsen,[116] L. Beresford,[34] M. Beretta,[49] D. Berge,[17] E. Bergeaas Kuutmann,[167] N. Berger,[4] B. Bergmann,[137] L. J. Bergsten,[24] J. Beringer,[16] S. Berlendis,[6] G. Bernardi,[131] C. Bernius,[149] F. U. Bernlochner,[22] T. Berry,[91] P. Berta,[44] A. Berthold,[46] I. A. Bertram,[87] O. Bessidskaia Bylund,[177] S. Bethke,[112] A. Betti,[40] A. J. Bevan,[90] S. Bhatta,[151] D. S. Bhattacharya,[172] P. Bhattarai,[24] V. S. Bhopatkar,[5] R. Bi,[134] R. M. Bianchi,[134] O. Biebel,[111] R. Bielski,[34] N. V. Biesuz,[69a,69b] M. Biglietti,[72a] T. R. V. Billoud,[137] M. Bindi,[51] A. Bingul,[11d] C. Bini,[70a,70b] S. Biondi,[21b,21a] C. J. Birch-sykes,[98] G. A. Bird,[19,139] M. Birman,[175] T. Bisanz,[34] J. P. Biswal,[2] D. Biswas,[176,i] A. Bitadze,[98] C. Bittrich,[46] K. Bjørke,[129] I. Bloch,[44] C. Blocker,[24]

A. Blue,[55] U. Blumenschein,[90] J. Blumenthal,[97] G. J. Bobbink,[116] V. S. Bobrovnikov,[118b,118a] D. Bogavac,[12] A. G. Bogdanchikov,[118b,118a] C. Bohm,[43a] V. Boisvert,[91] P. Bokan,[44] T. Bold,[81a] M. Bomben,[131] M. Bona,[90] M. Boonekamp,[140] C. D. Booth,[91] A. G. Borbély,[55] H. M. Borecka-Bielska,[107] L. S. Borgna,[92] G. Borissov,[87] D. Bortoletto,[130] D. Boscherini,[21b] M. Bosman,[12] J. D. Bossio Sola,[101] K. Bouaouda,[33a] J. Boudreau,[134] E. V. Bouhova-Thacker,[87] D. Boumediene,[36] R. Bouquet,[131] A. Boveia,[123] J. Boyd,[34] D. Boye,[27] I. R. Boyko,[77] A. J. Bozson,[91] J. Bracinik,[19] N. Brahimi,[58d,58c] G. Brandt,[177] O. Brandt,[30] F. Braren,[44] B. Brau,[100] J. E. Brau,[127] W. D. Breaden Madden,[55] K. Brendlinger,[44] R. Brener,[175] L. Brenner,[34] R. Brenner,[167] S. Bressler,[175] B. Brickwedde,[97] D. L. Briglin,[19] D. Britton,[55] D. Britzger,[112] I. Brock,[22] R. Brock,[104] G. Brooijmans,[37] W. K. Brooks,[142d] E. Brost,[27] P. A. Bruckman de Renstrom,[82] B. Brüers,[44] D. Bruncko,[26b] A. Bruni,[21b] G. Bruni,[21b] M. Bruschi,[21b] N. Bruscino,[70a,70b] L. Bryngemark,[149] T. Buanes,[15] Q. Buat,[151] P. Buchholz,[147] A. G. Buckley,[55] I. A. Budagov,[77] M. K. Bugge,[129] O. Bulekov,[109] B. A. Bullard,[57] T. J. Burch,[117] S. Burdin,[88] C. D. Burgard,[44] A. M. Burger,[125] B. Burghgrave,[7] J. T. P. Burr,[44] C. D. Burton,[10] J. C. Burzynski,[100] V. Büscher,[97] P. J. Bussey,[55] J. M. Butler,[23] C. M. Buttar,[55] J. M. Butterworth,[92] W. Buttinger,[139] C. J. Buxo Vazquez,[104] A. R. Buzykaev,[118b,118a] G. Cabras,[21b] S. Cabrera Urbán,[169] D. Caforio,[54] H. Cai,[134] V. M. M. Cairo,[149] O. Cakir,[3a] N. Calace,[34] P. Calafiura,[16] G. Calderini,[131] P. Calfayan,[63] G. Callea,[55] L. P. Caloba,[78b] A. Caltabiano,[71a,71b] S. Calvente Lopez,[96] D. Calvet,[36] S. Calvet,[36] T. P. Calvet,[99] M. Calvetti,[69a,69b] R. Camacho Toro,[131] S. Camarda,[34] D. Camarero Munoz,[96] P. Camarri,[71a,71b] M. T. Camerlingo,[72a,72b] D. Cameron,[129] C. Camincher,[171] M. Campanelli,[92] A. Camplani,[38] V. Canale,[67a,67b] A. Canesse,[101] M. Cano Bret,[75] J. Cantero,[125] Y. Cao,[168] M. Capua,[39b,39a] A. Carbone,[66a,66b] R. Cardarelli,[71a] F. Cardillo,[169] G. Carducci,[39b,39a] T. Carli,[34] G. Carlino,[67a] B. T. Carlson,[134] E. M. Carlson,[171,163a] L. Carminati,[66a,66b] M. Carnesale,[70a,70b] R. M. D. Carney,[149] S. Caron,[115] E. Carquin,[142d] S. Carrá,[44] G. Carratta,[21b,21a] J. W. S. Carter,[162] T. M. Carter,[48] D. Casadei,[31c] M. P. Casado,[12,j] A. F. Casha,[162] E. G. Castiglia,[178] F. L. Castillo,[59a] L. Castillo Garcia,[12] V. Castillo Gimenez,[169] N. F. Castro,[135a,135e] A. Catinaccio,[34] J. R. Catmore,[129] A. Cattai,[34] V. Cavaliere,[27] N. Cavalli,[21b,21a] V. Cavasinni,[69a,69b] E. Celebi,[11b] F. Celli,[130] K. Cerny,[126] A. S. Cerqueira,[78a] A. Cerri,[152] L. Cerrito,[71a,71b] F. Cerutti,[16] A. Cervelli,[21b] S. A. Cetin,[11b] Z. Chadi,[33a] D. Chakraborty,[117] M. Chala,[135f] J. Chan,[176] W. S. Chan,[116] W. Y. Chan,[88] J. D. Chapman,[30] B. Chargeishvili,[155b] D. G. Charlton,[19] T. P. Charman,[90] M. Chatterjee,[18] C. C. Chau,[32] S. Chekanov,[5] S. V. Chekulaev,[163a] G. A. Chelkov,[77,k] A. Chen,[103] B. Chen,[157] C. Chen,[58a] C. H. Chen,[76] H. Chen,[13c] H. Chen,[27] J. Chen,[58a] J. Chen,[37] J. Chen,[24] S. Chen,[132] S. J. Chen,[13c] X. Chen,[58c] X. Chen,[13b] Y. Chen,[58a] Y-H. Chen,[44] C. L. Cheng,[176] H. C. Cheng,[60a] H. J. Cheng,[13a] A. Cheplakov,[77] E. Cheremushkina,[44] R. Cherkaoui El Moursli,[33e] E. Cheu,[6] K. Cheung,[61] L. Chevalier,[140] V. Chiarella,[49] G. Chiarelli,[69a] G. Chiodini,[65a] A. S. Chisholm,[19] A. Chitan,[25b] I. Chiu,[159] Y. H. Chiu,[171] M. V. Chizhov,[77,l] K. Choi,[10] A. R. Chomont,[70a,70b] Y. Chou,[100] E. Y. S. Chow,[116] L. D. Christopher,[31f] M. C. Chu,[60a] X. Chu,[13a,13d] J. Chudoba,[136] J. J. Chwastowski,[82] D. Cieri,[112] K. M. Ciesla,[82] V. Cindro,[89] I. A. Cioară,[25b] A. Ciocio,[16] F. Cirotto,[67a,67b] Z. H. Citron,[175,m] M. Citterio,[66a] D. A. Ciubotaru,[25b] B. M. Ciungu,[162] A. Clark,[52] P. J. Clark,[48] J. M. Clavijo Columbie,[44] S. E. Clawson,[98] C. Clement,[43a,43b] L. Clissa,[21b,21a] Y. Coadou,[99] M. Cobal,[64a,64c] A. Coccaro,[53b] J. Cochran,[76] R. F. Coelho Barrue,[135a] R. Coelho Lopes De Sa,[100] S. Coelli,[66a] H. Cohen,[157] A. E. C. Coimbra,[34] B. Cole,[37] J. Collot,[56] P. Conde Muiño,[135a,135h] S. H. Connell,[31c] I. A. Connelly,[55] E. I. Conroy,[130] F. Conventi,[67a,n] H. G. Cooke,[19] A. M. Cooper-Sarkar,[130] F. Cormier,[170] L. D. Corpe,[34] M. Corradi,[70a,70b] E. E. Corrigan,[94] F. Corriveau,[101,o] M. J. Costa,[169] F. Costanza,[4] D. Costanzo,[145] B. M. Cote,[123] G. Cowan,[91] J. W. Cowley,[30] J. Crane,[98] K. Cranmer,[121] R. A. Creager,[132] S. Crépé-Renaudin,[56] F. Crescioli,[131] M. Cristinziani,[147] M. Cristoforetti,[73a,73b,p] V. Croft,[165] G. Crosetti,[39b,39a] A. Cueto,[4] T. Cuhadar Donszelmann,[166] H. Cui,[13a,13d] A. R. Cukierman,[149] W. R. Cunningham,[55] S. Czekierda,[82] P. Czodrowski,[34] M. M. Czurylo,[59b] M. J. Da Cunha Sargedas De Sousa,[58a] J. V. Da Fonseca Pinto,[78b] C. Da Via,[98] W. Dabrowski,[81a] T. Dado,[45] S. Dahbi,[31f] T. Dai,[103] C. Dallapiccola,[100] M. Dam,[38] G. D'amen,[27] V. D'Amico,[72a,72b] J. Damp,[97] J. R. Dandoy,[132] M. F. Daneri,[28] M. Danninger,[148] V. Dao,[34] G. Darbo,[53b] S. Darmora,[5] A. Dattagupta,[127] S. D'Auria,[66a,66b] C. David,[163b] T. Davidek,[138] D. R. Davis,[47] B. Davis-Purcell,[32] I. Dawson,[90] K. De,[7] R. De Asmundis,[67a] M. De Beurs,[116] S. De Castro,[21b,21a] N. De Groot,[115] P. de Jong,[116] H. De la Torre,[104] A. De Maria,[13c] D. De Pedis,[70a] A. De Salvo,[70a] U. De Sanctis,[71a,71b] M. De Santis,[71a,71b] A. De Santo,[152] J. B. De Vivie De Regie,[56] D. V. Dedovich,[77] J. Degens,[116] A. M. Deiana,[40] J. Del Peso,[96] Y. Delabat Diaz,[44] F. Deliot,[140] C. M. Delitzsch,[6] M. Della Pietra,[67a,67b] D. Della Volpe,[52] A. Dell'Acqua,[34] L. Dell'Asta,[66a,66b] M. Delmastro,[4] P. A. Delsart,[56] S. Demers,[178] M. Demichev,[77] S. P. Denisov,[119] L. D'Eramo,[117] D. Derendarz,[82] J. E. Derkaoui,[33d] F. Derue,[131] P. Dervan,[88] K. Desch,[22] K. Dette,[162] C. Deutsch,[22] P. O. Deviveiros,[34] F. A. Di Bello,[70a,70b] A. Di Ciaccio,[71a,71b] L. Di Ciaccio,[4] C. Di Donato,[67a,67b] A. Di Girolamo,[34]

G. Di Gregorio,[69a,69b] A. Di Luca,[73a,73b] B. Di Micco,[72a,72b] R. Di Nardo,[72a,72b] C. Diaconu,[99] F. A. Dias,[116] T. Dias Do Vale,[135a] M. A. Diaz,[142a] F. G. Diaz Capriles,[22] J. Dickinson,[16] M. Didenko,[169] E. B. Diehl,[103] J. Dietrich,[17] S. Díez Cornell,[44] C. Diez Pardos,[147] A. Dimitrievska,[16] W. Ding,[13b] J. Dingfelder,[22] I-M. Dinu,[25b] S. J. Dittmeier,[59b] F. Dittus,[34] F. Djama,[99] T. Djobava,[155b] J. I. Djuvsland,[15] M. A. B. Do Vale,[143] D. Dodsworth,[24] C. Doglioni,[94] J. Dolejsi,[138] Z. Dolezal,[138] M. Donadelli,[78c] B. Dong,[58c] J. Donini,[36] A. D'onofrio,[13c] M. D'Onofrio,[88] J. Dopke,[139] A. Doria,[67a] M. T. Dova,[86] A. T. Doyle,[55] E. Drechsler,[148] E. Dreyer,[148] T. Dreyer,[51] A. S. Drobac,[165] D. Du,[58b] T. A. du Pree,[116] F. Dubinin,[108] M. Dubovsky,[26a] A. Dubreuil,[52] E. Duchovni,[175] G. Duckeck,[111] O. A. Ducu,[34,25b] D. Duda,[112] A. Dudarev,[34] M. D'uffizi,[98] L. Duflot,[62] M. Dührssen,[34] C. Dülsen,[177] A. E. Dumitriu,[25b] M. Dunford,[59a] S. Dungs,[45] A. Duperrin,[99] H. Duran Yildiz,[3a] M. Düren,[54] A. Durglishvili,[155b] B. Dutta,[44] D. Duvnjak,[1] B. L. Dwyer,[117] G. I. Dyckes,[132] M. Dyndal,[81a] S. Dysch,[98] B. S. Dziedzic,[82] B. Eckerova,[26a] M. G. Eggleston,[47] E. Egidio Purcino De Souza,[78b] L. F. Ehrke,[52] T. Eifert,[7] G. Eigen,[15] K. Einsweiler,[16] T. Ekelof,[167] Y. El Ghazali,[33b] H. El Jarrari,[33e] A. El Moussaouy,[33a] V. Ellajosyula,[167] M. Ellert,[167] F. Ellinghaus,[177] A. A. Elliot,[90] N. Ellis,[34] J. Elmsheuser,[27] M. Elsing,[34] D. Emeliyanov,[139] A. Emerman,[37] Y. Enari,[159] J. Erdmann,[45] A. Ereditato,[18] P. A. Erland,[82] M. Errenst,[177] M. Escalier,[62] C. Escobar,[169] O. Estrada Pastor,[169] E. Etzion,[157] G. Evans,[135a] H. Evans,[63] M. O. Evans,[152] A. Ezhilov,[133] F. Fabbri,[55] L. Fabbri,[21b,21a] V. Fabiani,[115] G. Facini,[173] V. Fadeyev,[141] R. M. Fakhrutdinov,[119] S. Falciano,[70a] P. J. Falke,[22] S. Falke,[34] J. Faltova,[138] Y. Fan,[13a] Y. Fang,[13a] Y. Fang,[13a] G. Fanourakis,[42] M. Fanti,[66a,66b] M. Faraj,[58c] A. Farbin,[7] A. Farilla,[72a] E. M. Farina,[68a,68b] T. Farooque,[104] S. M. Farrington,[48] P. Farthouat,[34] F. Fassi,[33e] D. Fassouliotis,[8] M. Faucci Giannelli,[71a,71b] W. J. Fawcett,[30] L. Fayard,[62] O. L. Fedin,[133,q] M. Feickert,[168] L. Feligioni,[99] A. Fell,[145] C. Feng,[58b] M. Feng,[13b] M. J. Fenton,[166] A. B. Fenyuk,[119] S. W. Ferguson,[41] J. Ferrando,[44] A. Ferrari,[167] P. Ferrari,[116] R. Ferrari,[68a] D. Ferrere,[52] C. Ferretti,[103] F. Fiedler,[97] A. Filipčič,[89] F. Filthaut,[115] M. C. N. Fiolhais,[135a,135c,r] L. Fiorini,[169] F. Fischer,[147] W. C. Fisher,[104] T. Fitschen,[19] I. Fleck,[147] P. Fleischmann,[103] T. Flick,[177] B. M. Flierl,[111] L. Flores,[132] L. R. Flores Castillo,[60a] F. M. Follega,[73a,73b] N. Fomin,[15] J. H. Foo,[162] G. T. Forcolin,[73a,73b] B. C. Forland,[63] A. Formica,[140] F. A. Förster,[12] A. C. Forti,[98] E. Fortin,[99] M. G. Foti,[130] D. Fournier,[62] H. Fox,[87] P. Francavilla,[69a,69b] S. Francescato,[70a,70b] M. Franchini,[21b,21a] S. Franchino,[59a] D. Francis,[34] L. Franco,[4] L. Franconi,[18] M. Franklin,[57] G. Frattari,[70a,70b] A. C. Freegard,[90] P. M. Freeman,[19] B. Freund,[107] W. S. Freund,[78b] E. M. Freundlich,[45] D. Froidevaux,[34] J. A. Frost,[130] Y. Fu,[58a] M. Fujimoto,[122] E. Fullana Torregrosa,[169] J. Fuster,[169] A. Gabrielli,[21b,21a] A. Gabrielli,[34] P. Gadow,[44] G. Gagliardi,[53b,53a] L. G. Gagnon,[16] G. E. Gallardo,[130] E. J. Gallas,[130] B. J. Gallop,[139] R. Gamboa Goni,[90] K. K. Gan,[123] S. Ganguly,[175] J. Gao,[58a] Y. Gao,[48] Y. S. Gao,[29,s] F. M. Garay Walls,[142a] C. García,[169] J. E. García Navarro,[169] J. A. García Pascual,[13a] M. Garcia-Sciveres,[16] R. W. Gardner,[35] D. Garg,[75] S. Gargiulo,[50] C. A. Garner,[162] V. Garonne,[129] S. J. Gasiorowski,[144] P. Gaspar,[78b] G. Gaudio,[68a] P. Gauzzi,[70a,70b] I. L. Gavrilenko,[108] A. Gavrilyuk,[120] C. Gay,[170] G. Gaycken,[44] E. N. Gazis,[9] A. A. Geanta,[25b] C. M. Gee,[141] C. N. P. Gee,[139] J. Geisen,[94] M. Geisen,[97] C. Gemme,[53b] M. H. Genest,[56] S. Gentile,[70a,70b] S. George,[91] T. Geralis,[42] L. O. Gerlach,[51] P. Gessinger-Befurt,[97] M. Ghasemi Bostanabad,[171] M. Ghneimat,[147] A. Ghosh,[166] A. Ghosh,[75] B. Giacobbe,[21b] S. Giagu,[70a,70b] N. Giangiacomi,[162] P. Giannetti,[69a] A. Giannini,[67a,67b] S. M. Gibson,[91] M. Gignac,[141] D. T. Gil,[81b] B. J. Gilbert,[37] D. Gillberg,[32] G. Gilles,[116] N. E. K. Gillwald,[44] D. M. Gingrich,[2,f] M. P. Giordani,[64a,64c] P. F. Giraud,[140] G. Giugliarelli,[64a,64c] D. Giugni,[66a] F. Giuli,[71a,71b] I. Gkialas,[8,t] E. L. Gkougkousis,[12] P. Gkountoumis,[9] L. K. Gladilin,[110] C. Glasman,[96] G. R. Gledhill,[127] M. Glisic,[127] I. Gnesi,[39b,u] M. Goblirsch-Kolb,[24] D. Godin,[107] S. Goldfarb,[102] T. Golling,[52] D. Golubkov,[119] J. P. Gombas,[104] A. Gomes,[135a,135b] R. Goncalves Gama,[51] R. Gonçalo,[135a,135c] G. Gonella,[127] L. Gonella,[19] A. Gongadze,[77] F. Gonnella,[19] J. L. Gonski,[37] S. González de la Hoz,[169] S. Gonzalez Fernandez,[12] R. Gonzalez Lopez,[88] C. Gonzalez Renteria,[16] R. Gonzalez Suarez,[167] S. Gonzalez-Sevilla,[52] G. R. Gonzalvo Rodriguez,[169] R. Y. González Andana,[142a] L. Goossens,[34] N. A. Gorasia,[19] P. A. Gorbounov,[120] H. A. Gordon,[27] B. Gorini,[34] E. Gorini,[65a,65b] A. Gorišek,[89] A. T. Goshaw,[47] M. I. Gostkin,[77] C. A. Gottardo,[115] M. Gouighri,[33b] V. Goumarre,[44] A. G. Goussiou,[144] N. Govender,[31c] C. Goy,[4] I. Grabowska-Bold,[81a] K. Graham,[32] E. Gramstad,[129] S. Grancagnolo,[17] M. Grandi,[152] V. Gratchev,[133] P. M. Gravila,[25f] F. G. Gravili,[65a,65b] H. M. Gray,[16] C. Grefe,[22] I. M. Gregor,[44] P. Grenier,[149] K. Grevtsov,[44] C. Grieco,[12] N. A. Grieser,[124] A. A. Grillo,[141] K. Grimm,[29,v] S. Grinstein,[12,w] J.-F. Grivaz,[62] S. Groh,[97] E. Gross,[175] J. Grosse-Knetter,[51] Z. J. Grout,[92] C. Grud,[103] A. Grummer,[114] J. C. Grundy,[130] L. Guan,[103] W. Guan,[176] C. Gubbels,[170] J. Guenther,[34] J. G. R. Guerrero Rojas,[169] F. Guescini,[112] D. Guest,[17] R. Gugel,[97] A. Guida,[44] T. Guillemin,[4] S. Guindon,[34] J. Guo,[58c] L. Guo,[62] Y. Guo,[103] R. Gupta,[44] S. Gurbuz,[22] G. Gustavino,[124] M. Guth,[50] P. Gutierrez,[124] L. F. Gutierrez Zagazeta,[132] C. Gutschow,[92] C. Guyot,[140] C. Gwenlan,[130] C. B. Gwilliam,[88] E. S. Haaland,[129] A. Haas,[121] M. Habedank,[17] C. Haber,[16] H. K. Hadavand,[7] A. Hadef,[97] M. Haleem,[172] J. Haley,[125] J. J. Hall,[145] G. Halladjian,[104]

G. D. Hallewell,[99] L. Halser,[18] K. Hamano,[171] H. Hamdaoui,[33e] M. Hamer,[22] G. N. Hamity,[48] K. Han,[58a] L. Han,[13c] L. Han,[58a] S. Han,[16] Y. F. Han,[162] K. Hanagaki,[79,x] M. Hance,[141] M. D. Hank,[35] R. Hankache,[98] E. Hansen,[94] J. B. Hansen,[38] J. D. Hansen,[38] M. C. Hansen,[22] P. H. Hansen,[38] K. Hara,[164] T. Harenberg,[177] S. Harkusha,[105] Y. T. Harris,[130] P. F. Harrison,[173] N. M. Hartman,[149] N. M. Hartmann,[111] Y. Hasegawa,[146] A. Hasib,[48] S. Hassani,[140] S. Haug,[18] R. Hauser,[104] M. Havranek,[137] C. M. Hawkes,[19] R. J. Hawkings,[34] S. Hayashida,[113] D. Hayden,[104] C. Hayes,[103] R. L. Hayes,[170] C. P. Hays,[130] J. M. Hays,[90] H. S. Hayward,[88] S. J. Haywood,[139] F. He,[58a] Y. He,[160] Y. He,[131] M. P. Heath,[48] V. Hedberg,[94] A. L. Heggelund,[129] N. D. Hehir,[90] C. Heidegger,[50] K. K. Heidegger,[50] W. D. Heidorn,[76] J. Heilman,[32] S. Heim,[44] T. Heim,[16] B. Heinemann,[44,y] J. G. Heinlein,[132] J. J. Heinrich,[127] L. Heinrich,[34] J. Hejbal,[136] L. Helary,[44] A. Held,[121] S. Hellesund,[129] C. M. Helling,[141] S. Hellman,[43a,43b] C. Helsens,[34] R. C. W. Henderson,[87] L. Henkelmann,[30] A. M. Henriques Correia,[34] H. Herde,[149] Y. Hernández Jiménez,[151] H. Herr,[97] M. G. Herrmann,[111] T. Herrmann,[46] G. Herten,[50] R. Hertenberger,[111] L. Hervas,[34] N. P. Hessey,[163a] H. Hibi,[80] S. Higashino,[79] E. Higón-Rodriguez,[169] K. K. Hill,[27] K. H. Hiller,[44] S. J. Hillier,[19] M. Hils,[46] I. Hinchliffe,[16] F. Hinterkeuser,[22] M. Hirose,[128] S. Hirose,[164] D. Hirschbuehl,[177] B. Hiti,[89] O. Hladik,[136] J. Hobbs,[151] R. Hobincu,[25e] N. Hod,[175] M. C. Hodgkinson,[145] B. H. Hodkinson,[30] A. Hoecker,[34] J. Hofer,[44] D. Hohn,[50] T. Holm,[22] T. R. Holmes,[35] M. Holzbock,[112] L. B. A. H. Hommels,[30] B. P. Honan,[98] J. Hong,[58c] T. M. Hong,[134] J. C. Honig,[50] A. Hönle,[112] B. H. Hooberman,[168] W. H. Hopkins,[5] Y. Horii,[113] P. Horn,[46] L. A. Horyn,[35] S. Hou,[154] J. Howarth,[55] J. Hoya,[86] M. Hrabovsky,[126] A. Hrynevich,[106] T. Hryn'ova,[4] P. J. Hsu,[61] S.-C. Hsu,[144] Q. Hu,[37] S. Hu,[58c] Y. F. Hu,[13a,13d,z] D. P. Huang,[92] X. Huang,[13c] Y. Huang,[58a] Y. Huang,[13a] Z. Hubacek,[137] F. Hubaut,[99] M. Huebner,[22] F. Huegging,[22] T. B. Huffman,[130] M. Huhtinen,[34] R. Hulsken,[56] N. Huseynov,[77,e] J. Huston,[104] J. Huth,[57] R. Hyneman,[149] S. Hyrych,[26a] G. Iacobucci,[52] G. Iakovidis,[27] I. Ibragimov,[147] L. Iconomidou-Fayard,[62] P. Iengo,[34] R. Ignazzi,[38] R. Iguchi,[159] T. Iizawa,[52] Y. Ikegami,[79] A. Ilg,[18] N. Ilic,[162] H. Imam,[33a] T. Ingebretsen Carlson,[43a,43b] G. Introzzi,[68a,68b] M. Iodice,[72a] V. Ippolito,[70a,70b] M. Ishino,[159] W. Islam,[125] C. Issever,[17,44] S. Istin,[11c,aa] J. M. Iturbe Ponce,[60a] R. Iuppa,[73a,73b] A. Ivina,[175] J. M. Izen,[41] V. Izzo,[67a] P. Jacka,[136] P. Jackson,[1] R. M. Jacobs,[44] B. P. Jaeger,[148] C. S. Jagfeld,[111] G. Jäkel,[177] K. B. Jakobi,[97] K. Jakobs,[50] T. Jakoubek,[175] J. Jamieson,[55] K. W. Janas,[81a] G. Jarlskog,[94] A. E. Jaspan,[88] N. Javadov,[77,e] T. Javůrek,[34] M. Javurkova,[100] F. Jeanneau,[140] L. Jeanty,[127] J. Jejelava,[155a,bb] P. Jenni,[50,cc] S. Jézéquel,[4] J. Jia,[151] Z. Jia,[13c] Y. Jiang,[58a] S. Jiggins,[50] J. Jimenez Pena,[112] S. Jin,[13c] A. Jinaru,[25b] O. Jinnouchi,[160] H. Jivan,[31f] P. Johansson,[145] K. A. Johns,[6] C. A. Johnson,[63] D. M. Jones,[30] E. Jones,[173] R. W. L. Jones,[87] T. J. Jones,[88] J. Jovicevic,[51] X. Ju,[16] J. J. Junggeburth,[34] A. Juste Rozas,[12,w] A. Kaczmarska,[82] M. Kado,[70a,70b] H. Kagan,[123] M. Kagan,[149] A. Kahn,[37] C. Kahra,[97] T. Kaji,[174] E. Kajomovitz,[156] C. W. Kalderon,[27] A. Kaluza,[97] A. Kamenshchikov,[119] M. Kaneda,[159] N. J. Kang,[141] S. Kang,[76] Y. Kano,[113] J. Kanzaki,[79] D. Kar,[31f] K. Karava,[130] M. J. Kareem,[163b] I. Karkanias,[158] S. N. Karpov,[77] Z. M. Karpova,[77] V. Kartvelishvili,[87] A. N. Karyukhin,[119] E. Kasimi,[158] C. Kato,[58d] J. Katzy,[44] K. Kawade,[146] K. Kawagoe,[85] T. Kawaguchi,[113] T. Kawamoto,[140] G. Kawamura,[51] E. F. Kay,[171] F. I. Kaya,[165] S. Kazakos,[12] V. F. Kazanin,[118b,118a] Y. Ke,[151] J. M. Keaveney,[31a] R. Keeler,[171] J. S. Keller,[32] D. Kelsey,[152] J. J. Kempster,[19] J. Kendrick,[19] K. E. Kennedy,[37] O. Kepka,[136] S. Kersten,[177] B. P. Kerševan,[89] S. Ketabchi Haghighat,[162] M. Khandoga,[131] A. Khanov,[125] A. G. Kharlamov,[118b,118a] T. Kharlamova,[118b,118a] E. E. Khoda,[170] T. J. Khoo,[17] G. Khoriauli,[172] E. Khramov,[77] J. Khubua,[155b] S. Kido,[80] M. Kiehn,[34] A. Kilgallon,[127] E. Kim,[160] Y. K. Kim,[35] N. Kimura,[92] A. Kirchhoff,[51] D. Kirchmeier,[46] J. Kirk,[139] A. E. Kiryunin,[112] T. Kishimoto,[159] D. P. Kisliuk,[162] V. Kitali,[44] C. Kitsaki,[9] O. Kivernyk,[22] T. Klapdor-Kleingrothaus,[50] M. Klassen,[59a] C. Klein,[32] L. Klein,[172] M. H. Klein,[103] M. Klein,[88] U. Klein,[88] P. Klimek,[34] A. Klimentov,[27] F. Klimpel,[34] T. Klingl,[22] T. Klioutchnikova,[34] F. F. Klitzner,[111] P. Kluit,[116] S. Kluth,[112] E. Kneringer,[74] T. M. Knight,[162] A. Knue,[50] D. Kobayashi,[85] M. Kobel,[46] M. Kocian,[149] T. Kodama,[159] P. Kodys,[138] D. M. Koeck,[152] P. T. Koenig,[22] T. Koffas,[32] N. M. Köhler,[34] M. Kolb,[140] I. Koletsou,[4] T. Komarek,[126] K. Köneke,[50] A. X. Y. Kong,[1] T. Kono,[122] V. Konstantinides,[92] N. Konstantinidis,[92] B. Konya,[94] R. Kopeliansky,[63] S. Koperny,[81a] K. Korcyl,[82] K. Kordas,[158] G. Koren,[157] A. Korn,[92] S. Korn,[51] I. Korolkov,[12] E. V. Korolkova,[145] N. Korotkova,[110] B. Kortman,[116] O. Kortner,[112] S. Kortner,[112] V. V. Kostyukhin,[145,161] A. Kotsokechagia,[62] A. Kotwal,[47] A. Koulouris,[34] A. Kourkoumeli-Charalampidi,[68a,68b] C. Kourkoumelis,[8] E. Kourlitis,[5] O. Kovanda,[152] R. Kowalewski,[171] W. Kozanecki,[140] A. S. Kozhin,[119] V. A. Kramarenko,[110] G. Kramberger,[89] D. Krasnopevtsev,[58a] M. W. Krasny,[131] A. Krasznahorkay,[34] J. A. Kremer,[97] J. Kretzschmar,[88] K. Kreul,[17] P. Krieger,[162] F. Krieter,[111] S. Krishnamurthy,[100] A. Krishnan,[59b] M. Krivos,[138] K. Krizka,[16] K. Kroeninger,[45] H. Kroha,[112] J. Kroll,[136] J. Kroll,[132] K. S. Krowpman,[104] U. Kruchonak,[77] H. Krüger,[22] N. Krumnack,[76] M. C. Kruse,[47] J. A. Krzysiak,[82] A. Kubota,[160] O. Kuchinskaia,[161] S. Kuday,[3b] D. Kuechler,[44] J. T. Kuechler,[44] S. Kuehn,[34] T. Kuhl,[44] V. Kukhtin,[77] Y. Kulchitsky,[105,dd] S. Kuleshov,[142b] M. Kumar,[31f] N. Kumari,[99] M. Kuna,[56] A. Kupco,[136] T. Kupfer,[45] O. Kuprash,[50] H. Kurashige,[80] L. L. Kurchaninov,[163a]

Y. A. Kurochkin,[105] A. Kurova,[109] M. G. Kurth,[13a,13d] E. S. Kuwertz,[34] M. Kuze,[160] A. K. Kvam,[144] J. Kvita,[126] T. Kwan,[101] C. Lacasta,[169] F. Lacava,[70a,70b] H. Lacker,[17] D. Lacour,[131] N. N. Lad,[92] E. Ladygin,[77] R. Lafaye,[4] B. Laforge,[131] T. Lagouri,[142c] S. Lai,[51] I. K. Lakomiec,[81a] N. Lalloue,[56] J. E. Lambert,[124] S. Lammers,[63] W. Lampl,[6] C. Lampoudis,[158] E. Lançon,[27] U. Landgraf,[50] M. P. J. Landon,[90] V. S. Lang,[50] J. C. Lange,[51] R. J. Langenberg,[100] A. J. Lankford,[166] F. Lanni,[27] K. Lantzsch,[22] A. Lanza,[68a] A. Lapertosa,[53b,53a] J. F. Laporte,[140] T. Lari,[66a] F. Lasagni Manghi,[21b] M. Lassnig,[34] V. Latonova,[136] T. S. Lau,[60a] A. Laudrain,[97] A. Laurier,[32] M. Lavorgna,[67a,67b] S. D. Lawlor,[91] M. Lazzaroni,[66a,66b] B. Le,[98] B. Leban,[89] A. Lebedev,[76] M. LeBlanc,[34] T. LeCompte,[5] F. Ledroit-Guillon,[56] A. C. A. Lee,[92] C. A. Lee,[27] G. R. Lee,[15] L. Lee,[57] S. C. Lee,[154] S. Lee,[76] L. L. Leeuw,[31c] B. Lefebvre,[163a] H. P. Lefebvre,[91] M. Lefebvre,[171] C. Leggett,[16] K. Lehmann,[148] N. Lehmann,[18] G. Lehmann Miotto,[34] W. A. Leight,[44] A. Leisos,[158,ee] M. A. L. Leite,[78c] C. E. Leitgeb,[44] R. Leitner,[138] K. J. C. Leney,[40] T. Lenz,[22] S. Leone,[69a] C. Leonidopoulos,[48] A. Leopold,[131] C. Leroy,[107] R. Les,[104] C. G. Lester,[30] M. Levchenko,[133] J. Levêque,[4] D. Levin,[103] L. J. Levinson,[175] D. J. Lewis,[19] A. Li,[131] B. Li,[13b] B. Li,[58b] C. Li,[58a] C-Q. Li,[58c,58d] H. Li,[58a] H. Li,[58b] J. Li,[58c] K. Li,[144] L. Li,[58c] M. Li,[13a,13d] Q. Y. Li,[58a] S. Li,[58d,58c,ff] X. Li,[44] Y. Li,[44] Z. Li,[58b] Z. Li,[130] Z. Li,[101] Z. Li,[88] Z. Liang,[13a] M. Liberatore,[44] B. Liberti,[71a] K. Lie,[60c] K. Lin,[104] R. A. Linck,[63] R. E. Lindley,[6] J. H. Lindon,[2] A. Linss,[44] A. L. Lionti,[52] E. Lipeles,[132] A. Lipniacka,[15] T. M. Liss,[168,gg] A. Lister,[170] J. D. Little,[7] B. Liu,[13a] B. X. Liu,[148] J. B. Liu,[58a] J. K. K. Liu,[35] K. Liu,[58d,58c] M. Liu,[58a] M. Y. Liu,[58a] P. Liu,[13a] X. Liu,[58a] Y. Liu,[44] Y. Liu,[13c,13d] Y. L. Liu,[103] Y. W. Liu,[58a] M. Livan,[68a,68b] A. Lleres,[56] J. Llorente Merino,[148] S. L. Lloyd,[90] E. M. Lobodzinska,[44] P. Loch,[6] S. Loffredo,[71a,71b] T. Lohse,[17] K. Lohwasser,[145] M. Lokajicek,[136] J. D. Long,[168] R. E. Long,[87] I. Longarini,[70a,70b] L. Longo,[34] R. Longo,[168] I. Lopez Paz,[12] A. Lopez Solis,[44] J. Lorenz,[111] N. Lorenzo Martinez,[4] A. M. Lory,[111] A. Lösle,[50] X. Lou,[43a,43b] X. Lou,[13a] A. Lounis,[62] J. Love,[5] P. A. Love,[87] J. J. Lozano Bahilo,[169] G. Lu,[13a,13d] M. Lu,[58a] S. Lu,[132] Y. J. Lu,[61] H. J. Lubatti,[144] C. Luci,[70a,70b] F. L. Lucio Alves,[13c] A. Lucotte,[56] F. Luehring,[63] I. Luise,[151] L. Luminari,[70a] B. Lund-Jensen,[150] N. A. Luongo,[127] M. S. Lutz,[157] D. Lynn,[27] H. Lyons,[88] R. Lysak,[136] E. Lytken,[94] F. Lyu,[13a] V. Lyubushkin,[77] T. Lyubushkina,[77] H. Ma,[27] L. L. Ma,[58b] Y. Ma,[92] D. M. Mac Donell,[171] G. Maccarrone,[49] C. M. Macdonald,[145] J. C. MacDonald,[145] R. Madar,[36] W. F. Mader,[46] M. Madugoda Ralalage Don,[125] N. Madysa,[46] J. Maeda,[80] T. Maeno,[27] M. Maerker,[46] V. Magerl,[50] J. Magro,[64a,64c] D. J. Mahon,[37] C. Maidantchik,[78b] A. Maio,[135a,135b,135d] K. Maj,[81a] O. Majersky,[26a] S. Majewski,[127] N. Makovec,[62] B. Malaescu,[131] Pa. Malecki,[82] V. P. Maleev,[133] F. Malek,[56] D. Malito,[39b,39a] U. Mallik,[75] C. Malone,[30] S. Maltezos,[9] S. Malyukov,[77] J. Mamuzic,[169] G. Mancini,[49] J. P. Mandalia,[90] I. Mandić,[89] L. Manhaes de Andrade Filho,[78a] I. M. Maniatis,[158] M. Manisha,[140] J. Manjarres Ramos,[46] K. H. Mankinen,[94] A. Mann,[111] A. Manousos,[74] B. Mansoulie,[140] I. Manthos,[158] S. Manzoni,[116] A. Marantis,[158,ee] L. Marchese,[130] G. Marchiori,[131] M. Marcisovsky,[136] L. Marcoccia,[71a,71b] C. Marcon,[94] M. Marjanovic,[124] Z. Marshall,[16] S. Marti-Garcia,[169] T. A. Martin,[173] V. J. Martin,[48] B. Martin dit Latour,[15] L. Martinelli,[70a,70b] M. Martinez,[12,w] P. Martinez Agullo,[169] V. I. Martinez Outschoorn,[100] S. Martin-Haugh,[139] V. S. Martoiu,[25b] A. C. Martyniuk,[92] A. Marzin,[34] S. R. Maschek,[112] L. Masetti,[97] T. Mashimo,[159] J. Masik,[98] A. L. Maslennikov,[118b,118a] L. Massa,[21b] P. Massarotti,[67a,67b] P. Mastrandrea,[69a,69b] A. Mastroberardino,[39b,39a] T. Masubuchi,[159] D. Matakias,[27] T. Mathisen,[167] A. Matic,[111] N. Matsuzawa,[159] J. Maurer,[25b] B. Maček,[89] D. A. Maximov,[118b,118a] R. Mazini,[154] I. Maznas,[158] S. M. Mazza,[141] C. Mc Ginn,[27] J. P. Mc Gowan,[101] S. P. Mc Kee,[103] T. G. McCarthy,[112] W. P. McCormack,[16] E. F. McDonald,[102] A. E. McDougall,[116] J. A. Mcfayden,[152] G. Mchedlidze,[155b] M. A. McKay,[40] K. D. McLean,[171] S. J. McMahon,[139] P. C. McNamara,[102] R. A. McPherson,[171,o] J. E. Mdhluli,[31f] Z. A. Meadows,[100] S. Meehan,[34] T. Megy,[36] S. Mehlhase,[111] A. Mehta,[88] B. Meirose,[41] D. Melini,[156] B. R. Mellado Garcia,[31f] F. Meloni,[44] A. Melzer,[22] E. D. Mendes Gouveia,[135a] A. M. Mendes Jacques Da Costa,[19] H. Y. Meng,[162] L. Meng,[34] S. Menke,[112] M. Mentink,[34] E. Meoni,[39b,39a] S. A. M. Merkt,[134] C. Merlassino,[130] P. Mermod,[52,a] L. Merola,[67a,67b] C. Meroni,[66a] G. Merz,[103] O. Meshkov,[110,108] J. K. R. Meshreki,[147] J. Metcalfe,[5] A. S. Mete,[5] C. Meyer,[63] J-P. Meyer,[140] M. Michetti,[17] R. P. Middleton,[139] L. Mijović,[48] G. Mikenberg,[175] M. Mikestikova,[136] M. Mikuž,[89] H. Mildner,[145] A. Milic,[162] C. D. Milke,[40] D. W. Miller,[35] L. S. Miller,[32] A. Milov,[175] D. A. Milstead,[43a,43b] A. A. Minaenko,[119] I. A. Minashvili,[155b] L. Mince,[55] A. I. Mincer,[121] B. Mindur,[81a] M. Mineev,[77] Y. Minegishi,[159] Y. Mino,[83] L. M. Mir,[12] M. Miralles Lopez,[169] M. Mironova,[130] T. Mitani,[174] V. A. Mitsou,[169] M. Mittal,[58c] O. Miu,[162] P. S. Miyagawa,[90] Y. Miyazaki,[85] A. Mizukami,[79] J. U. Mjörnmark,[94] T. Mkrtchyan,[59a] M. Mlynarikova,[117] T. Moa,[43a,43b] S. Mobius,[51] K. Mochizuki,[107] P. Moder,[44] P. Mogg,[111] A. F. Mohammed,[13a] S. Mohapatra,[37] G. Mokgatitswane,[31f] B. Mondal,[147] S. Mondal,[137] K. Mönig,[44] E. Monnier,[99] A. Montalbano,[148] J. Montejo Berlingen,[34] M. Montella,[123] F. Monticelli,[86] N. Morange,[62] A. L. Moreira De Carvalho,[135a] M. Moreno Llácer,[169] C. Moreno Martinez,[12] P. Morettini,[53b] M. Morgenstern,[156] S. Morgenstern,[173] D. Mori,[148] M. Morii,[57] M. Morinaga,[159] V. Morisbak,[129] A. K. Morley,[34]

A. P. Morris,[92] L. Morvaj,[34] P. Moschovakos,[34] B. Moser,[116] M. Mosidze,[155b] T. Moskalets,[50] P. Moskvitina,[115] J. Moss,[29,hh] E. J. W. Moyse,[100] S. Muanza,[99] J. Mueller,[134] R. Mueller,[18] D. Muenstermann,[87] G. A. Mullier,[94] J. J. Mullin,[132] D. P. Mungo,[66a,66b] J. L. Munoz Martinez,[12] F. J. Munoz Sanchez,[98] M. Murin,[98] P. Murin,[26b] W. J. Murray,[173,139] A. Murrone,[66a,66b] J. M. Muse,[124] M. Muškinja,[16] C. Mwewa,[27] A. G. Myagkov,[119,k] A. A. Myers,[134] G. Myers,[63] M. Myska,[137] B. P. Nachman,[16] O. Nackenhorst,[45] A. Nag Nag,[46] K. Nagai,[130] K. Nagano,[79] J. L. Nagle,[27] E. Nagy,[99] A. M. Nairz,[34] Y. Nakahama,[113] K. Nakamura,[79] H. Nanjo,[128] F. Napolitano,[59a] R. Narayan,[40] I. Naryshkin,[133] M. Naseri,[32] C. Nass,[22] T. Naumann,[44] G. Navarro,[20a] J. Navarro-Gonzalez,[169] P. Y. Nechaeva,[108] F. Nechansky,[44] T. J. Neep,[19] A. Negri,[68a,68b] M. Negrini,[21b] C. Nellist,[115] C. Nelson,[101] K. Nelson,[103] M. E. Nelson,[43a,43b] S. Nemecek,[136] M. Nessi,[34,ii] M. S. Neubauer,[168] F. Neuhaus,[97] J. Neundorf,[44] R. Newhouse,[170] P. R. Newman,[19] C. W. Ng,[134] Y. S. Ng,[17] Y. W. Y. Ng,[166] B. Ngair,[33e] H. D. N. Nguyen,[99] T. Nguyen Manh,[107] R. B. Nickerson,[130] R. Nicolaidou,[140] D. S. Nielsen,[38] J. Nielsen,[141] M. Niemeyer,[51] N. Nikiforou,[10] V. Nikolaenko,[119,k] I. Nikolic-Audit,[131] K. Nikolopoulos,[19] P. Nilsson,[27] H. R. Nindhito,[52] A. Nisati,[70a] N. Nishu,[2] R. Nisius,[112] T. Nitta,[174] T. Nobe,[159] D. L. Noel,[30] Y. Noguchi,[83] I. Nomidis,[131] M. A. Nomura,[27] M. B. Norfolk,[145] R. R. B. Norisam,[92] J. Novak,[89] T. Novak,[44] O. Novgorodova,[46] L. Novotny,[137] R. Novotny,[114] L. Nozka,[126] K. Ntekas,[166] E. Nurse,[92] F. G. Oakham,[32,f] J. Ocariz,[131] A. Ochi,[80] I. Ochoa,[135a] J. P. Ochoa-Ricoux,[142a] K. O'Connor,[24] S. Oda,[85] S. Odaka,[79] S. Oerdek,[167] A. Ogrodnik,[81a] A. Oh,[98] C. C. Ohm,[150] H. Oide,[160] R. Oishi,[159] M. L. Ojeda,[162] Y. Okazaki,[83] M. W. O'Keefe,[88] Y. Okumura,[159] A. Olariu,[25b] L. F. Oleiro Seabra,[135a] S. A. Olivares Pino,[142c] D. Oliveira Damazio,[27] D. Oliveira Goncalves,[78a] J. L. Oliver,[166] M. J. R. Olsson,[166] A. Olszewski,[82] J. Olszowska,[82] Ö. O. Öncel,[22] D. C. O'Neil,[148] A. P. O'neill,[130] A. Onofre,[135a,135e] P. U. E. Onyisi,[10] H. Oppen,[129] R. G. Oreamuno Madriz,[117] M. J. Oreglia,[35] G. E. Orellana,[86] D. Orestano,[72a,72b] N. Orlando,[12] R. S. Orr,[162] V. O'Shea,[55] R. Ospanov,[58a] G. Otero y Garzon,[28] H. Otono,[85] P. S. Ott,[59a] G. J. Ottino,[16] M. Ouchrif,[33d] J. Ouellette,[27] F. Ould-Saada,[129] A. Ouraou,[140,a] Q. Ouyang,[13a] M. Owen,[55] R. E. Owen,[139] V. E. Ozcan,[11c] N. Ozturk,[7] S. Ozturk,[11c] J. Pacalt,[126] H. A. Pacey,[30] K. Pachal,[47] A. Pacheco Pages,[12] C. Padilla Aranda,[12] S. Pagan Griso,[16] G. Palacino,[63] S. Palazzo,[48] S. Palestini,[34] M. Palka,[81b] P. Palni,[81a] D. K. Panchal,[10] C. E. Pandini,[52] J. G. Panduro Vazquez,[91] P. Pani,[44] G. Panizzo,[64a,64c] L. Paolozzi,[52] C. Papadatos,[107] S. Parajuli,[40] A. Paramonov,[5] C. Paraskevopoulos,[9] D. Paredes Hernandez,[60b] S. R. Paredes Saenz,[130] B. Parida,[175] T. H. Park,[162] A. J. Parker,[29] M. A. Parker,[30] F. Parodi,[53b,53a] E. W. Parrish,[117] J. A. Parsons,[37] U. Parzefall,[50] L. Pascual Dominguez,[157] V. R. Pascuzzi,[16] F. Pasquali,[116] E. Pasqualucci,[70a] S. Passaggio,[53b] F. Pastore,[91] P. Pasuwan,[43a,43b] J. R. Pater,[98] A. Pathak,[176] J. Patton,[88] T. Pauly,[34] J. Pearkes,[149] M. Pedersen,[129] L. Pedraza Diaz,[115] R. Pedro,[135a] T. Peiffer,[51] S. V. Peleganchuk,[118b,118a] O. Penc,[136] C. Peng,[60b] H. Peng,[58a] M. Penzin,[161] B. S. Peralva,[78a] M. M. Perego,[62] A. P. Pereira Peixoto,[135a] L. Pereira Sanchez,[43a,43b] D. V. Perepelitsa,[27] E. Perez Codina,[163a] M. Perganti,[9] L. Perini,[66a,66b] H. Pernegger,[34] S. Perrella,[34] A. Perrevoort,[116] K. Peters,[44] R. F. Y. Peters,[98] B. A. Petersen,[34] T. C. Petersen,[38] E. Petit,[99] V. Petousis,[137] C. Petridou,[158] P. Petroff,[62] F. Petrucci,[72a,72b] M. Pettee,[178] N. E. Pettersson,[34] K. Petukhova,[138] A. Peyaud,[140] R. Pezoa,[142d] L. Pezzotti,[68a,68b] G. Pezzullo,[178] T. Pham,[102] P. W. Phillips,[139] M. W. Phipps,[168] G. Piacquadio,[151] E. Pianori,[16] F. Piazza,[66a,66b] A. Picazio,[100] R. Piegaia,[28] D. Pietreanu,[25b] J. E. Pilcher,[35] A. D. Pilkington,[98] M. Pinamonti,[64a,64c] J. L. Pinfold,[2] C. Pitman Donaldson,[92] D. A. Pizzi,[32] L. Pizzimento,[71a,71b] A. Pizzini,[116] M.-A. Pleier,[27] V. Plesanovs,[50] V. Pleskot,[138] E. Plotnikova,[77] P. Podberezko,[118b,118a] R. Poettgen,[94] R. Poggi,[52] L. Poggioli,[131] I. Pogrebnyak,[104] D. Pohl,[22] I. Pokharel,[51] G. Polesello,[68a] A. Poley,[148,163a] A. Policicchio,[70a,70b] R. Polifka,[138] A. Polini,[21b] C. S. Pollard,[44] Z. B. Pollock,[123] V. Polychronakos,[27] D. Ponomarenko,[109] L. Pontecorvo,[34] S. Popa,[25a] G. A. Popeneciu,[25d] L. Portales,[4] D. M. Portillo Quintero,[56] S. Pospisil,[137] P. Postolache,[25c] K. Potamianos,[130] I. N. Potrap,[77] C. J. Potter,[30] H. Potti,[1] T. Poulsen,[44] J. Poveda,[169] T. D. Powell,[145] G. Pownall,[44] M. E. Pozo Astigarraga,[34] A. Prades Ibanez,[169] P. Pralavorio,[99] M. M. Prapa,[42] S. Prell,[76] D. Price,[98] M. Primavera,[65a] M. A. Principe Martin,[96] M. L. Proffitt,[144] N. Proklova,[109] K. Prokofiev,[60c] F. Prokoshin,[77] S. Protopopescu,[27] J. Proudfoot,[5] M. Przybycien,[81a] D. Pudzha,[133] P. Puzo,[62] D. Pyatiizbyantseva,[109] J. Qian,[103] Y. Qin,[98] A. Quadt,[51] M. Queitsch-Maitland,[34] G. Rabanal Bolanos,[57] F. Ragusa,[66a,66b] G. Rahal,[95] J. A. Raine,[52] S. Rajagopalan,[27] K. Ran,[13a,13d] D. F. Rassloff,[59a] D. M. Rauch,[44] S. Rave,[97] B. Ravina,[55] I. Ravinovich,[175] M. Raymond,[34] A. L. Read,[129] N. P. Readioff,[145] D. M. Rebuzzi,[68a,68b] G. Redlinger,[27] K. Reeves,[41] D. Reikher,[157] A. Reiss,[97] A. Rej,[147] C. Rembser,[34] A. Renardi,[44] M. Renda,[25b] M. B. Rendel,[112] A. G. Rennie,[55] S. Resconi,[66a] E. D. Resseguie,[16] S. Rettie,[92] B. Reynolds,[123] E. Reynolds,[19] M. Rezaei Estabragh,[177] O. L. Rezanova,[118b,118a] P. Reznicek,[138] E. Ricci,[73a,73b] R. Richter,[112] S. Richter,[44] E. Richter-Was,[81b] M. Ridel,[131] P. Rieck,[112] P. Riedler,[34] O. Rifki,[44] M. Rijssenbeek,[151] A. Rimoldi,[68a,68b] M. Rimoldi,[44] L. Rinaldi,[21b,21a] T. T. Rinn,[168] M. P. Rinnagel,[111] G. Ripellino,[150] I. Riu,[12] P. Rivadeneira,[44] J. C. Rivera Vergara,[171]

F. Rizatdinova,[125] E. Rizvi,[90] C. Rizzi,[52] B. A. Roberts,[173] S. H. Robertson,[101,o] M. Robin,[44] D. Robinson,[30] C. M. Robles Gajardo,[142d] M. Robles Manzano,[97] A. Robson,[55] A. Rocchi,[71a,71b] C. Roda,[69a,69b] S. Rodriguez Bosca,[59a] A. Rodriguez Rodriguez,[50] A. M. Rodríguez Vera,[163b] S. Roe,[34] J. Roggel,[177] O. Røhne,[129] R. A. Rojas,[142d] B. Roland,[50] C. P. A. Roland,[63] J. Roloff,[27] A. Romaniouk,[109] M. Romano,[21b] A. C. Romero Hernandez,[168] N. Rompotis,[88] M. Ronzani,[121] L. Roos,[131] S. Rosati,[70a] G. Rosin,[100] B. J. Rosser,[132] E. Rossi,[162] E. Rossi,[4] E. Rossi,[67a,67b] L. P. Rossi,[53b] L. Rossini,[44] R. Rosten,[123] M. Rotaru,[25b] B. Rottler,[50] D. Rousseau,[62] D. Rousso,[30] G. Rovelli,[68a,68b] A. Roy,[10] A. Rozanov,[99] Y. Rozen,[156] X. Ruan,[31f] A. J. Ruby,[88] T. A. Ruggeri,[1] F. Rühr,[50] A. Ruiz-Martinez,[169] A. Rummler,[34] Z. Rurikova,[50] N. A. Rusakovich,[77] H. L. Russell,[34] L. Rustige,[36] J. P. Rutherfoord,[6] E. M. Rüttinger,[145] M. Rybar,[138] E. B. Rye,[129] A. Ryzhov,[119] J. A. Sabater Iglesias,[44] P. Sabatini,[169] L. Sabetta,[70a,70b] H. F-W. Sadrozinski,[141] R. Sadykov,[77] F. Safai Tehrani,[70a] B. Safarzadeh Samani,[152] M. Safdari,[149] P. Saha,[117] S. Saha,[101] M. Sahinsoy,[112] A. Sahu,[177] M. Saimpert,[140] M. Saito,[159] T. Saito,[159] D. Salamani,[52] G. Salamanna,[72a,72b] A. Salnikov,[149] J. Salt,[169] A. Salvador Salas,[12] D. Salvatore,[39b,39a] F. Salvatore,[152] A. Salzburger,[34] D. Sammel,[50] D. Sampsonidis,[158] D. Sampsonidou,[58d,58c] J. Sánchez,[169] A. Sanchez Pineda,[4] V. Sanchez Sebastian,[169] H. Sandaker,[129] C. O. Sander,[44] I. G. Sanderswood,[87] J. A. Sandesara,[100] M. Sandhoff,[177] C. Sandoval,[20b] D. P. C. Sankey,[139] M. Sannino,[53b,53a] Y. Sano,[113] A. Sansoni,[49] C. Santoni,[36] H. Santos,[135a,135b] S. N. Santpur,[16] A. Santra,[175] K. A. Saoucha,[145] A. Sapronov,[77] J. G. Saraiva,[135a,135d] J. Sardain,[99] O. Sasaki,[79] K. Sato,[164] C. Sauer,[59b] F. Sauerburger,[50] E. Sauvan,[4] P. Savard,[162,f] R. Sawada,[159] C. Sawyer,[139] L. Sawyer,[93] I. Sayago Galvan,[169] C. Sbarra,[21b] A. Sbrizzi,[64a,64c] T. Scanlon,[92] J. Schaarschmidt,[144] P. Schacht,[112] D. Schaefer,[35] L. Schaefer,[132] U. Schäfer,[97] A. C. Schaffer,[62] D. Schaile,[111] R. D. Schamberger,[151] E. Schanet,[111] C. Scharf,[17] N. Scharmberg,[98] V. A. Schegelsky,[133] D. Scheirich,[138] F. Schenck,[17] M. Schernau,[166] C. Schiavi,[53b,53a] L. K. Schildgen,[22] Z. M. Schillaci,[24] E. J. Schioppa,[65a,65b] M. Schioppa,[39b,39a] B. Schlag,[97] K. E. Schleicher,[50] S. Schlenker,[34] K. Schmieden,[97] C. Schmitt,[97] S. Schmitt,[44] L. Schoeffel,[140] A. Schoening,[59b] P. G. Scholer,[50] E. Schopf,[130] M. Schott,[97] J. Schovancova,[34] S. Schramm,[52] F. Schroeder,[177] H-C. Schultz-Coulon,[59a] M. Schumacher,[50] B. A. Schumm,[141] Ph. Schune,[140] A. Schwartzman,[149] T. A. Schwarz,[103] Ph. Schwemling,[140] R. Schwienhorst,[104] A. Sciandra,[141] G. Sciolla,[24] F. Scuri,[69a] F. Scutti,[102] C. D. Sebastiani,[88] K. Sedlaczek,[45] P. Seema,[17] S. C. Seidel,[114] A. Seiden,[141] B. D. Seidlitz,[27] T. Seiss,[35] C. Seitz,[44] J. M. Seixas,[78b] G. Sekhniaidze,[67a] S. J. Sekula,[40] L. Selem,[4] N. Semprini-Cesari,[21b,21a] S. Sen,[47] C. Serfon,[27] L. Serin,[62] L. Serkin,[64a,64b] M. Sessa,[58a] H. Severini,[124] S. Sevova,[149] F. Sforza,[53b,53a] A. Sfyrla,[52] E. Shabalina,[51] R. Shaheen,[150] J. D. Shahinian,[132] N. W. Shaikh,[43a,43b] D. Shaked Renous,[175] L. Y. Shan,[13a] M. Shapiro,[16] A. Sharma,[34] A. S. Sharma,[1] S. Sharma,[44] P. B. Shatalov,[120] K. Shaw,[152] S. M. Shaw,[98] P. Sherwood,[92] L. Shi,[92] C. O. Shimmin,[178] Y. Shimogama,[174] J. D. Shinner,[91] I. P. J. Shipsey,[130] S. Shirabe,[52] M. Shiyakova,[77] J. Shlomi,[175] M. J. Shochet,[35] J. Shojaii,[102] D. R. Shope,[150] S. Shrestha,[123] E. M. Shrif,[31f] M. J. Shroff,[171] E. Shulga,[175] P. Sicho,[136] A. M. Sickles,[168] E. Sideras Haddad,[31f] O. Sidiropoulou,[34] A. Sidoti,[21b] F. Siegert,[46] Dj. Sijacki,[14] M. V. Silva Oliveira,[34] S. B. Silverstein,[43a] S. Simion,[62] R. Simoniello,[34] S. Simsek,[11b] P. Sinervo,[162] V. Sinetckii,[110] S. Singh,[148] S. Sinha,[44] S. Sinha,[31f] M. Sioli,[21b,21a] I. Siral,[127] S. Yu. Sivoklokov,[110] J. Sjölin,[43a,43b] A. Skaf,[51] E. Skorda,[94] P. Skubic,[124] M. Slawinska,[82] K. Sliwa,[165] V. Smakhtin,[175] B. H. Smart,[139] J. Smiesko,[138] S. Yu. Smirnov,[109] Y. Smirnov,[109] L. N. Smirnova,[110,jj] O. Smirnova,[94] E. A. Smith,[35] H. A. Smith,[130] M. Smizanska,[87] K. Smolek,[137] A. Smykiewicz,[82] A. A. Snesarev,[108] H. L. Snoek,[116] S. Snyder,[27] R. Sobie,[171,o] A. Soffer,[157] F. Sohns,[51] C. A. Solans Sanchez,[34] E. Yu. Soldatov,[109] U. Soldevila,[169] A. A. Solodkov,[119] S. Solomon,[50] A. Soloshenko,[77] O. V. Solovyanov,[119] V. Solovyev,[133] P. Sommer,[145] H. Son,[165] A. Sonay,[12] W. Y. Song,[163b] A. Sopczak,[137] A. L. Sopio,[92] F. Sopkova,[26b] S. Sottocornola,[68a,68b] R. Soualah,[64a,64c] A. M. Soukharev,[118b,118a] Z. Soumaimi,[33e] D. South,[44] S. Spagnolo,[65a,65b] M. Spalla,[112] M. Spangenberg,[173] F. Spanò,[91] D. Sperlich,[50] T. M. Spieker,[59a] G. Spigo,[34] M. Spina,[152] D. P. Spiteri,[55] M. Spousta,[138] A. Stabile,[66a,66b] R. Stamen,[59a] M. Stamenkovic,[116] A. Stampekis,[19] M. Standke,[22] E. Stanecka,[82] B. Stanislaus,[34] M. M. Stanitzki,[44] M. Stankaityte,[130] B. Stapf,[44] E. A. Starchenko,[119] G. H. Stark,[141] J. Stark,[99] D. M. Starko,[163b] P. Staroba,[136] P. Starovoitov,[59a] S. Stärz,[101] R. Staszewski,[82] G. Stavropoulos,[42] P. Steinberg,[27] A. L. Steinhebel,[127] B. Stelzer,[148,163a] H. J. Stelzer,[134] O. Stelzer-Chilton,[163a] H. Stenzel,[54] T. J. Stevenson,[152] G. A. Stewart,[34] M. C. Stockton,[34] G. Stoicea,[25b] M. Stolarski,[135a] S. Stonjek,[112] A. Straessner,[46] J. Strandberg,[150] S. Strandberg,[43a,43b] M. Strauss,[124] T. Strebler,[99] P. Strizenec,[26b] R. Ströhmer,[172] D. M. Strom,[127] L. R. Strom,[44] R. Stroynowski,[40] A. Strubig,[43a,43b] S. A. Stucci,[27] B. Stugu,[15] J. Stupak,[124] N. A. Styles,[44] D. Su,[149] S. Su,[58a] W. Su,[58d,144,58c] X. Su,[58a] N. B. Suarez,[134] K. Sugizaki,[159] V. V. Sulin,[108] M. J. Sullivan,[88] D. M. S. Sultan,[52] S. Sultansoy,[3c] T. Sumida,[83] S. Sun,[103] S. Sun,[176] X. Sun,[98] O. Sunneborn Gudnadottir,[167] C. J. E. Suster,[153] M. R. Sutton,[152] M. Svatos,[136] M. Swiatlowski,[163a] T. Swirski,[172] I. Sykora,[26a] M. Sykora,[138] T. Sykora,[138]

D. Ta,[97] K. Tackmann,[44,kk] A. Taffard,[166] R. Tafirout,[163a] E. Tagiev,[119] R. H. M. Taibah,[131] R. Takashima,[84] K. Takeda,[80] T. Takeshita,[146] E. P. Takeva,[48] Y. Takubo,[79] M. Talby,[99] A. A. Talyshev,[118b,118a] K. C. Tam,[60b] N. M. Tamir,[157] A. Tanaka,[159] J. Tanaka,[159] R. Tanaka,[62] Z. Tao,[170] S. Tapia Araya,[76] S. Tapprogge,[97] A. Tarek Abouelfadl Mohamed,[104] S. Tarem,[156] K. Tariq,[58b] G. Tarna,[25b,ll] G. F. Tartarelli,[66a] P. Tas,[138] M. Tasevsky,[136] E. Tassi,[39b,39a] G. Tateno,[159] Y. Tayalati,[33e] G. N. Taylor,[102] W. Taylor,[163b] H. Teagle,[88] A. S. Tee,[176] R. Teixeira De Lima,[149] P. Teixeira-Dias,[91] H. Ten Kate,[34] J. J. Teoh,[116] K. Terashi,[159] J. Terron,[96] S. Terzo,[12] M. Testa,[49] R. J. Teuscher,[162,o] N. Themistokleous,[48] T. Theveneaux-Pelzer,[17] O. Thielmann,[177] D. W. Thomas,[91] J. P. Thomas,[19] E. A. Thompson,[44] P. D. Thompson,[19] E. Thomson,[132] E. J. Thorpe,[90] Y. Tian,[51] V. Tikhomirov,[108,mm] Yu. A. Tikhonov,[118b,118a] S. Timoshenko,[109] P. Tipton,[178] S. Tisserant,[99] S. H. Tlou,[31f] A. Tnourji,[36] K. Todome,[21b,21a] S. Todorova-Nova,[138] S. Todt,[46] M. Togawa,[79] J. Tojo,[85] S. Tokár,[26a] K. Tokushuku,[79] E. Tolley,[123] R. Tombs,[30] M. Tomoto,[79,113] L. Tompkins,[149] P. Tornambe,[100] E. Torrence,[127] H. Torres,[46] E. Torró Pastor,[169] M. Toscani,[28] C. Tosciri,[35] J. Toth,[99,nn] D. R. Tovey,[145] A. Traeet,[15] C. J. Treado,[121] T. Trefzger,[172] A. Tricoli,[27] I. M. Trigger,[163a] S. Trincaz-Duvoid,[131] D. A. Trischuk,[170] W. Trischuk,[162] B. Trocmé,[56] A. Trofymov,[62] C. Troncon,[66a] F. Trovato,[152] L. Truong,[31c] M. Trzebinski,[82] A. Trzupek,[82] F. Tsai,[151] A. Tsiamis,[158] P. V. Tsiareshka,[105,dd] A. Tsirigotis,[158,ee] V. Tsiskaridze,[151] E. G. Tskhadadze,[155a] M. Tsopoulou,[158] I. I. Tsukerman,[120] V. Tsulaia,[16] S. Tsuno,[79] O. Tsur,[156] D. Tsybychev,[151] Y. Tu,[60b] A. Tudorache,[25b] V. Tudorache,[25b] A. N. Tuna,[34] S. Turchikhin,[77] D. Turgeman,[175] I. Turk Cakir,[3b,oo] R. J. Turner,[19] R. Turra,[66a] P. M. Tuts,[37] S. Tzamarias,[158] P. Tzanis,[9] E. Tzovara,[97] K. Uchida,[159] F. Ukegawa,[164] G. Unal,[34] M. Unal,[10] A. Undrus,[27] G. Unel,[166] F. C. Ungaro,[102] K. Uno,[159] J. Urban,[26b] P. Urquijo,[102] G. Usai,[7] R. Ushioda,[160] M. Usman,[107] Z. Uysal,[11d] V. Vacek,[137] B. Vachon,[101] K. O. H. Vadla,[129] T. Vafeiadis,[34] C. Valderanis,[111] E. Valdes Santurio,[43a,43b] M. Valente,[163a] S. Valentinetti,[21b,21a] A. Valero,[169] L. Valéry,[44] R. A. Vallance,[19] A. Vallier,[99] J. A. Valls Ferrer,[169] T. R. Van Daalen,[12] P. Van Gemmeren,[5] S. Van Stroud,[92] I. Van Vulpen,[116] M. Vanadia,[71a,71b] W. Vandelli,[34] M. Vandenbroucke,[140] E. R. Vandewall,[125] D. Vannicola,[70a,70b] L. Vannoli,[53b,53a] R. Vari,[70a] E. W. Varnes,[6] C. Varni,[53b,53a] T. Varol,[154] D. Varouchas,[62] K. E. Varvell,[153] M. E. Vasile,[25b] L. Vaslin,[36] G. A. Vasquez,[171] F. Vazeille,[36] D. Vazquez Furelos,[12] T. Vazquez Schroeder,[34] J. Veatch,[51] V. Vecchio,[98] M. J. Veen,[116] I. Veliscek,[130] L. M. Veloce,[162] F. Veloso,[135a,135c] S. Veneziano,[70a] A. Ventura,[65a,65b] A. Verbytskyi,[112] M. Verducci,[69a,69b] C. Vergis,[22] M. Verissimo De Araujo,[78b] W. Verkerke,[116] A. T. Vermeulen,[116] J. C. Vermeulen,[116] C. Vernieri,[149] P. J. Verschuuren,[91] M. L. Vesterbacka,[121] M. C. Vetterli,[148,f] N. Viaux Maira,[142d] T. Vickey,[145] O. E. Vickey Boeriu,[145] G. H. A. Viehhauser,[130] L. Vigani,[59b] M. Villa,[21b,21a] M. Villaplana Perez,[169] E. M. Villhauer,[48] E. Vilucchi,[49] M. G. Vincter,[32] G. S. Virdee,[19] A. Vishwakarma,[48] C. Vittori,[21b,21a] I. Vivarelli,[152] V. Vladimirov,[173] E. Voevodina,[112] M. Vogel,[177] P. Vokac,[137] J. Von Ahnen,[44] S. E. von Buddenbrock,[31f] E. Von Toerne,[22] V. Vorobel,[138] K. Vorobev,[109] M. Vos,[169] J. H. Vossebeld,[88] M. Vozak,[98] L. Vozdecky,[90] N. Vranjes,[14] M. Vranjes Milosavljevic,[14] V. Vrba,[137,a] M. Vreeswijk,[116] N. K. Vu,[99] R. Vuillermet,[34] I. Vukotic,[35] S. Wada,[164] C. Wagner,[100] P. Wagner,[22] W. Wagner,[177] S. Wahdan,[177] H. Wahlberg,[86] R. Wakasa,[164] M. Wakida,[113] V. M. Walbrecht,[112] J. Walder,[139] R. Walker,[111] S. D. Walker,[91] W. Walkowiak,[147] A. M. Wang,[57] A. Z. Wang,[176] C. Wang,[58a] C. Wang,[58c] H. Wang,[16] J. Wang,[60a] P. Wang,[40] R.-J. Wang,[97] R. Wang,[57] R. Wang,[117] S. M. Wang,[154] S. Wang,[58b] T. Wang,[58a] W. T. Wang,[58a] W. X. Wang,[58a] X. Wang,[13c] X. Wang,[168] Y. Wang,[58a] Z. Wang,[103] C. Wanotayaroj,[34] A. Warburton,[101] C. P. Ward,[30] R. J. Ward,[19] N. Warrack,[55] A. T. Watson,[19] M. F. Watson,[19] G. Watts,[144] B. M. Waugh,[92] A. F. Webb,[10] C. Weber,[27] M. S. Weber,[18] S. A. Weber,[32] S. M. Weber,[59a] C. Wei,[58a] Y. Wei,[130] A. R. Weidberg,[130] J. Weingarten,[45] M. Weirich,[97] C. Weiser,[50] T. Wenaus,[27] B. Wendland,[45] T. Wengler,[34] S. Wenig,[34] N. Wermes,[22] M. Wessels,[59a] K. Whalen,[127] A. M. Wharton,[87] A. S. White,[57] A. White,[7] M. J. White,[1] D. Whiteson,[166] W. Wiedenmann,[176] C. Wiel,[46] M. Wielers,[139] N. Wieseotte,[97] C. Wiglesworth,[38] L. A. M. Wiik-Fuchs,[50] D. J. Wilbern,[124] H. G. Wilkens,[34] L. J. Wilkins,[91] D. M. Williams,[37] H. H. Williams,[132] S. Williams,[30] S. Willocq,[100] P. J. Windischhofer,[130] I. Wingerter-Seez,[4] F. Winklmeier,[127] B. T. Winter,[50] M. Wittgen,[149] M. Wobisch,[93] A. Wolf,[97] R. Wölker,[130] J. Wollrath,[166] M. W. Wolter,[82] H. Wolters,[135a,135c] V. W. S. Wong,[170] A. F. Wongel,[44] S. D. Worm,[44] B. K. Wosiek,[82] K. W. Woźniak,[82] K. Wraight,[55] J. Wu,[13a,13d] S. L. Wu,[176] X. Wu,[52] Y. Wu,[58a] Z. Wu,[140,58a] J. Wuerzinger,[130] T. R. Wyatt,[98] B. M. Wynne,[48] S. Xella,[38] J. Xiang,[60c] X. Xiao,[103] X. Xie,[58a] I. Xiotidis,[152] D. Xu,[13a] H. Xu,[58a] H. Xu,[58a] L. Xu,[58a] R. Xu,[132] T. Xu,[58a] W. Xu,[103] Y. Xu,[13b] Z. Xu,[58b] Z. Xu,[149] B. Yabsley,[153] S. Yacoob,[31a] N. Yamaguchi,[85] Y. Yamaguchi,[160] M. Yamatani,[159] H. Yamauchi,[164] T. Yamazaki,[16] Y. Yamazaki,[80] J. Yan,[58c] S. Yan,[130] Z. Yan,[23] H. J. Yang,[58c,58d] H. T. Yang,[16] S. Yang,[58a] T. Yang,[60c] X. Yang,[58a] X. Yang,[13a] Y. Yang,[159] Z. Yang,[103,58a] W-M. Yao,[16] Y. C. Yap,[44] H. Ye,[13c] J. Ye,[40] S. Ye,[27] I. Yeletskikh,[77] M. R. Yexley,[87] P. Yin,[37] K. Yorita,[174] K. Yoshihara,[76] C. J. S. Young,[34] C. Young,[149] R. Yuan,[58b,pp] X. Yue,[59a] M. Zaazoua,[33e] B. Zabinski,[82] G. Zacharis,[9] E. Zaffaroni,[52]

A. M. Zaitsev,[119,k] T. Zakareishvili,[155b] N. Zakharchuk,[32] S. Zambito,[34] D. Zanzi,[50] S. V. Zeißner,[45] C. Zeitnitz,[177] G. Zemaityte,[130] J. C. Zeng,[168] O. Zenin,[119] T. Ženiš,[26a] S. Zenz,[90] S. Zerradi,[33a] D. Zerwas,[62] M. Zgubič,[130] B. Zhang,[13c] D. F. Zhang,[13b] G. Zhang,[13b] J. Zhang,[5] K. Zhang,[13a] L. Zhang,[13c] M. Zhang,[168] R. Zhang,[176] S. Zhang,[103] X. Zhang,[58c] X. Zhang,[58b] Z. Zhang,[62] P. Zhao,[47] Y. Zhao,[141] Z. Zhao,[58a] A. Zhemchugov,[77] Z. Zheng,[149] D. Zhong,[168] B. Zhou,[103] C. Zhou,[176] H. Zhou,[6] N. Zhou,[58c] Y. Zhou,[6] C. G. Zhu,[58b] C. Zhu,[13a,13d] H. L. Zhu,[58a] H. Zhu,[13a] J. Zhu,[103] Y. Zhu,[58a] X. Zhuang,[13a] K. Zhukov,[108] V. Zhulanov,[118b,118a] D. Zieminska,[63] N. I. Zimine,[77] S. Zimmermann,[50,a] M. Ziolkowski,[147] L. Živković,[14] A. Zoccoli,[21b,21a] K. Zoch,[52] T. G. Zorbas,[145] O. Zormpa,[42] W. Zou,[37] and L. Zwalinski[34]

(ATLAS Collaboration)

[1]*Department of Physics, University of Adelaide, Adelaide, Australia*
[2]*Department of Physics, University of Alberta, Edmonton, Alberta, Canada*
[3a]*Department of Physics, Ankara University, Ankara, Turkey*
[3b]*Istanbul Aydin University, Application and Research Center for Advanced Studies, Istanbul, Turkey*
[3c]*Division of Physics, TOBB University of Economics and Technology, Ankara, Turkey*
[4]*LAPP, Univ. Savoie Mont Blanc, CNRS/IN2P3, Annecy, France*
[5]*High Energy Physics Division, Argonne National Laboratory, Argonne, Illinois, USA*
[6]*Department of Physics, University of Arizona, Tucson, Arizona, USA*
[7]*Department of Physics, University of Texas at Arlington, Arlington, Texas, USA*
[8]*Physics Department, National and Kapodistrian University of Athens, Athens, Greece*
[9]*Physics Department, National Technical University of Athens, Zografou, Greece*
[10]*Department of Physics, University of Texas at Austin, Austin, Texas, USA*
[11a]*Bahcesehir University, Faculty of Engineering and Natural Sciences, Istanbul, Turkey*
[11b]*Istanbul Bilgi University, Faculty of Engineering and Natural Sciences, Istanbul, Turkey*
[11c]*Department of Physics, Bogazici University, Istanbul, Turkey*
[11d]*Department of Physics Engineering, Gaziantep University, Gaziantep, Turkey*
[12]*Institut de Física d'Altes Energies (IFAE), Barcelona Institute of Science and Technology, Barcelona, Spain*
[13a]*Institute of High Energy Physics, Chinese Academy of Sciences, Beijing, China*
[13b]*Physics Department, Tsinghua University, Beijing, China*
[13c]*Department of Physics, Nanjing University, Nanjing, China*
[13d]*University of Chinese Academy of Science (UCAS), Beijing, China*
[14]*Institute of Physics, University of Belgrade, Belgrade, Serbia*
[15]*Department for Physics and Technology, University of Bergen, Bergen, Norway*
[16]*Physics Division, Lawrence Berkeley National Laboratory and University of California, Berkeley, California, USA*
[17]*Institut für Physik, Humboldt Universität zu Berlin, Berlin, Germany*
[18]*Albert Einstein Center for Fundamental Physics and Laboratory for High Energy Physics, University of Bern, Bern, Switzerland*
[19]*School of Physics and Astronomy, University of Birmingham, Birmingham, United Kingdom*
[20a]*Facultad de Ciencias y Centro de Investigaciónes, Universidad Antonio Nariño, Bogotá, Colombia*
[20b]*Departamento de Física, Universidad Nacional de Colombia, Bogotá, Colombia*
[21a]*Dipartimento di Fisica e Astronomia A. Righi, Università di Bologna, Bologna, Italy*
[21b]*INFN Sezione di Bologna, Italy*
[22]*Physikalisches Institut, Universität Bonn, Bonn, Germany*
[23]*Department of Physics, Boston University, Boston, Massachusetts, USA*
[24]*Department of Physics, Brandeis University, Waltham, Massachusetts, USA*
[25a]*Transilvania University of Brasov, Brasov, Romania*
[25b]*Horia Hulubei National Institute of Physics and Nuclear Engineering, Bucharest, Romania*
[25c]*Department of Physics, Alexandru Ioan Cuza University of Iasi, Iasi, Romania*
[25d]*National Institute for Research and Development of Isotopic and Molecular Technologies, Physics Department, Cluj-Napoca, Romania*
[25e]*University Politehnica Bucharest, Bucharest, Romania*
[25f]*West University in Timisoara, Timisoara, Romania*
[26a]*Faculty of Mathematics, Physics and Informatics, Comenius University, Bratislava, Slovak Republic*
[26b]*Department of Subnuclear Physics, Institute of Experimental Physics of the Slovak Academy of Sciences, Kosice, Slovak Republic*
[27]*Physics Department, Brookhaven National Laboratory, Upton, New York, USA*

[28]*Universidad de Buenos Aires, Facultad de Ciencias Exactas y Naturales, Departamento de Física, y CONICET, Instituto de Física de Buenos Aires (IFIBA), Buenos Aires, Argentina*
[29]*California State University, California, USA*
[30]*Cavendish Laboratory, University of Cambridge, Cambridge, United Kingdom*
[31a]*Department of Physics, University of Cape Town, Cape Town, South Africa*
[31b]*iThemba Labs, Western Cape, South Africa*
[31c]*Department of Mechanical Engineering Science, University of Johannesburg, Johannesburg, South Africa*
[31d]*National Institute of Physics, University of the Philippines Diliman (Philippines), Philippines*
[31e]*University of South Africa, Department of Physics, Pretoria, South Africa*
[31f]*School of Physics, University of the Witwatersrand, Johannesburg, South Africa*
[32]*Department of Physics, Carleton University, Ottawa, Ontario, Canada*
[33a]*Faculté des Sciences Ain Chock, Réseau Universitaire de Physique des Hautes Energies—Université Hassan II, Casablanca, Morocco*
[33b]*Faculté des Sciences, Université Ibn-Tofail, Kénitra, Morocco*
[33c]*Faculté des Sciences Semlalia, Université Cadi Ayyad, LPHEA-Marrakech, Morocco*
[33d]*LPMR, Faculté des Sciences, Université Mohamed Premier, Oujda, Morocco*
[33e]*Faculté des sciences, Université Mohammed V, Rabat, Morocco*
[34]*CERN, Geneva, Switzerland*
[35]*Enrico Fermi Institute, University of Chicago, Chicago, Illinois, USA*
[36]*LPC, Université Clermont Auvergne, CNRS/IN2P3, Clermont-Ferrand, France*
[37]*Nevis Laboratory, Columbia University, Irvington, New York, USA*
[38]*Niels Bohr Institute, University of Copenhagen, Copenhagen, Denmark*
[39a]*Dipartimento di Fisica, Università della Calabria, Rende, Italy*
[39b]*INFN Gruppo Collegato di Cosenza, Laboratori Nazionali di Frascati, Italy*
[40]*Physics Department, Southern Methodist University, Dallas, Texas, USA*
[41]*Physics Department, University of Texas at Dallas, Richardson, Texas, USA*
[42]*National Centre for Scientific Research "Demokritos", Agia Paraskevi, Greece*
[43a]*Department of Physics, Stockholm University, Sweden*
[43b]*Oskar Klein Centre, Stockholm, Sweden*
[44]*Deutsches Elektronen-Synchrotron DESY, Hamburg and Zeuthen, Germany*
[45]*Fakultät Physik, Technische Universität Dortmund, Dortmund, Germany*
[46]*Institut für Kern- und Teilchenphysik, Technische Universität Dresden, Dresden, Germany*
[47]*Department of Physics, Duke University, Durham, North Carolina, USA*
[48]*SUPA—School of Physics and Astronomy, University of Edinburgh, Edinburgh, United Kingdom*
[49]*INFN e Laboratori Nazionali di Frascati, Frascati, Italy*
[50]*Physikalisches Institut, Albert-Ludwigs-Universität Freiburg, Freiburg, Germany*
[51]*II. Physikalisches Institut, Georg-August-Universität Göttingen, Göttingen, Germany*
[52]*Département de Physique Nucléaire et Corpusculaire, Université de Genève, Genève, Switzerland*
[53a]*Dipartimento di Fisica, Università di Genova, Genova, Italy*
[53b]*INFN Sezione di Genova, Italy*
[54]*II. Physikalisches Institut, Justus-Liebig-Universität Giessen, Giessen, Germany*
[55]*SUPA—School of Physics and Astronomy, University of Glasgow, Glasgow, United Kingdom*
[56]*LPSC, Université Grenoble Alpes, CNRS/IN2P3, Grenoble INP, Grenoble, France*
[57]*Laboratory for Particle Physics and Cosmology, Harvard University, Cambridge, Massachusetts, USA*
[58a]*Department of Modern Physics and State Key Laboratory of Particle Detection and Electronics, University of Science and Technology of China, Hefei, China*
[58b]*Institute of Frontier and Interdisciplinary Science and Key Laboratory of Particle Physics and Particle Irradiation (MOE), Shandong University, Qingdao, China*
[58c]*School of Physics and Astronomy, Shanghai Jiao Tong University, Key Laboratory for Particle Astrophysics and Cosmology (MOE), SKLPPC, Shanghai, China*
[58d]*Tsung-Dao Lee Institute, Shanghai, China*
[59a]*Kirchhoff-Institut für Physik, Ruprecht-Karls-Universität Heidelberg, Heidelberg, Germany*
[59b]*Physikalisches Institut, Ruprecht-Karls-Universität Heidelberg, Heidelberg, Germany*
[60a]*Department of Physics, Chinese University of Hong Kong, Shatin, N.T., Hong Kong, China*
[60b]*Department of Physics, University of Hong Kong, Hong Kong, China*
[60c]*Department of Physics and Institute for Advanced Study, Hong Kong University of Science and Technology, Clear Water Bay, Kowloon, Hong Kong, China*
[61]*Department of Physics, National Tsing Hua University, Hsinchu, Taiwan*
[62]*IJCLab, Université Paris-Saclay, CNRS/IN2P3, 91405, Orsay, France*

[63]*Department of Physics, Indiana University, Bloomington, Indiana, USA*
[64a]*INFN Gruppo Collegato di Udine, Sezione di Trieste, Udine, Italy*
[64b]*ICTP, Trieste, Italy*
[64c]*Dipartimento Politecnico di Ingegneria e Architettura, Università di Udine, Udine, Italy*
[65a]*INFN Sezione di Lecce, Italy*
[65b]*Dipartimento di Matematica e Fisica, Università del Salento, Lecce, Italy*
[66a]*INFN Sezione di Milano, Italy*
[66b]*Dipartimento di Fisica, Università di Milano, Milano, Italy*
[67a]*INFN Sezione di Napoli, Italy*
[67b]*Dipartimento di Fisica, Università di Napoli, Napoli, Italy*
[68a]*INFN Sezione di Pavia, Italy*
[68b]*Dipartimento di Fisica, Università di Pavia, Pavia, Italy*
[69a]*INFN Sezione di Pisa, Italy*
[69b]*Dipartimento di Fisica E. Fermi, Università di Pisa, Pisa, Italy*
[70a]*INFN Sezione di Roma, Italy*
[70b]*Dipartimento di Fisica, Sapienza Università di Roma, Roma, Italy*
[71a]*INFN Sezione di Roma Tor Vergata, Italy*
[71b]*Dipartimento di Fisica, Università di Roma Tor Vergata, Roma, Italy*
[72a]*INFN Sezione di Roma Tre, Italy*
[72b]*Dipartimento di Matematica e Fisica, Università Roma Tre, Roma, Italy*
[73a]*INFN-TIFPA, Italy*
[73b]*Università degli Studi di Trento, Trento, Italy*
[74]*Institut für Astro- und Teilchenphysik, Leopold-Franzens-Universität, Innsbruck, Austria*
[75]*University of Iowa, Iowa City, Iowa, USA*
[76]*Department of Physics and Astronomy, Iowa State University, Ames, Iowa, USA*
[77]*Joint Institute for Nuclear Research, Dubna, Russia*
[78a]*Departamento de Engenharia Elétrica, Universidade Federal de Juiz de Fora (UFJF), Juiz de Fora, Brazil*
[78b]*Universidade Federal do Rio De Janeiro COPPE/EE/IF, Rio de Janeiro, Brazil*
[78c]*Instituto de Física, Universidade de São Paulo, São Paulo, Brazil*
[79]*KEK, High Energy Accelerator Research Organization, Tsukuba, Japan*
[80]*Graduate School of Science, Kobe University, Kobe, Japan*
[81a]*AGH University of Science and Technology, Faculty of Physics and Applied Computer Science, Krakow, Poland*
[81b]*Marian Smoluchowski Institute of Physics, Jagiellonian University, Krakow, Poland*
[82]*Institute of Nuclear Physics Polish Academy of Sciences, Krakow, Poland*
[83]*Faculty of Science, Kyoto University, Kyoto, Japan*
[84]*Kyoto University of Education, Kyoto, Japan*
[85]*Research Center for Advanced Particle Physics and Department of Physics, Kyushu University, Fukuoka, Japan*
[86]*Instituto de Física La Plata, Universidad Nacional de La Plata and CONICET, La Plata, Argentina*
[87]*Physics Department, Lancaster University, Lancaster, United Kingdom*
[88]*Oliver Lodge Laboratory, University of Liverpool, Liverpool, United Kingdom*
[89]*Department of Experimental Particle Physics, Jožef Stefan Institute and Department of Physics, University of Ljubljana, Ljubljana, Slovenia*
[90]*School of Physics and Astronomy, Queen Mary University of London, London, United Kingdom*
[91]*Department of Physics, Royal Holloway University of London, Egham, United Kingdom*
[92]*Department of Physics and Astronomy, University College London, London, United Kingdom*
[93]*Louisiana Tech University, Ruston, Louisiana, USA*
[94]*Fysiska institutionen, Lunds universitet, Lund, Sweden*
[95]*Centre de Calcul de l'Institut National de Physique Nucléaire et de Physique des Particules (IN2P3), Villeurbanne, France*
[96]*Departamento de Física Teorica C-15 and CIAFF, Universidad Autónoma de Madrid, Madrid, Spain*
[97]*Institut für Physik, Universität Mainz, Mainz, Germany*
[98]*School of Physics and Astronomy, University of Manchester, Manchester, United Kingdom*
[99]*CPPM, Aix-Marseille Université, CNRS/IN2P3, Marseille, France*
[100]*Department of Physics, University of Massachusetts, Amherst, Massachusetts, USA*
[101]*Department of Physics, McGill University, Montreal, Québec, Canada*
[102]*School of Physics, University of Melbourne, Victoria, Australia*
[103]*Department of Physics, University of Michigan, Ann Arbor, Michigan, USA*

[104]Department of Physics and Astronomy, Michigan State University, East Lansing, Michigan, USA
[105]B.I. Stepanov Institute of Physics, National Academy of Sciences of Belarus, Minsk, Belarus
[106]Research Institute for Nuclear Problems of Byelorussian State University, Minsk, Belarus
[107]Group of Particle Physics, University of Montreal, Montreal, Québec, Canada
[108]P.N. Lebedev Physical Institute of the Russian Academy of Sciences, Moscow, Russia
[109]National Research Nuclear University MEPhI, Moscow, Russia
[110]D.V. Skobeltsyn Institute of Nuclear Physics, M.V. Lomonosov Moscow State University, Moscow, Russia
[111]Fakultät für Physik, Ludwig-Maximilians-Universität München, München, Germany
[112]Max-Planck-Institut für Physik (Werner-Heisenberg-Institut), München, Germany
[113]Graduate School of Science and Kobayashi-Maskawa Institute, Nagoya University, Nagoya, Japan
[114]Department of Physics and Astronomy, University of New Mexico, Albuquerque, New Mexico, USA
[115]Institute for Mathematics, Astrophysics and Particle Physics, Radboud University/Nikhef, Nijmegen, Netherlands
[116]Nikhef National Institute for Subatomic Physics and University of Amsterdam, Amsterdam, Netherlands
[117]Department of Physics, Northern Illinois University, DeKalb, Illinois, USA
[118a]Budker Institute of Nuclear Physics and NSU, SB RAS, Novosibirsk, Russia
[118b]Novosibirsk State University Novosibirsk, Russia
[119]Institute for High Energy Physics of the National Research Centre Kurchatov Institute, Protvino, Russia
[120]Institute for Theoretical and Experimental Physics named by A.I. Alikhanov of National Research Centre "Kurchatov Institute", Moscow, Russia
[121]Department of Physics, New York University, New York, New York, USA
[122]Ochanomizu University, Otsuka, Bunkyo-ku, Tokyo, Japan
[123]Ohio State University, Columbus, Ohio, USA
[124]Homer L. Dodge Department of Physics and Astronomy, University of Oklahoma, Norman, Oklahoma, USA
[125]Department of Physics, Oklahoma State University, Stillwater, Oklahoma, USA
[126]Palacký University, Joint Laboratory of Optics, Olomouc, Czech Republic
[127]Institute for Fundamental Science, University of Oregon, Eugene, Oregon, USA
[128]Graduate School of Science, Osaka University, Osaka, Japan
[129]Department of Physics, University of Oslo, Oslo, Norway
[130]Department of Physics, Oxford University, Oxford, United Kingdom
[131]LPNHE, Sorbonne Université, Université Paris Cité, CNRS/IN2P3, Paris, France
[132]Department of Physics, University of Pennsylvania, Philadelphia, Pennsylvania, USA
[133]Konstantinov Nuclear Physics Institute of National Research Centre "Kurchatov Institute", PNPI, St. Petersburg, Russia
[134]Department of Physics and Astronomy, University of Pittsburgh, Pittsburgh, Pennsylvania, USA
[135a]Laboratório de Instrumentação e Física Experimental de Partículas—LIP, Lisboa, Portugal
[135b]Departamento de Física, Faculdade de Ciências, Universidade de Lisboa, Lisboa, Portugal
[135c]Departamento de Física, Universidade de Coimbra, Coimbra, Portugal
[135d]Centro de Física Nuclear da Universidade de Lisboa, Lisboa, Portugal
[135e]Departamento de Física, Universidade do Minho, Braga, Portugal
[135f]Departamento de Física Teórica y del Cosmos, Universidad de Granada, Granada (Spain), Spain
[135g]Dep Física and CEFITEC of Faculdade de Ciências e Tecnologia, Universidade Nova de Lisboa, Caparica, Portugal
[135h]Instituto Superior Técnico, Universidade de Lisboa, Lisboa, Portugal
[136]Institute of Physics of the Czech Academy of Sciences, Prague, Czech Republic
[137]Czech Technical University in Prague, Prague, Czech Republic
[138]Charles University, Faculty of Mathematics and Physics, Prague, Czech Republic
[139]Particle Physics Department, Rutherford Appleton Laboratory, Didcot, United Kingdom
[140]IRFU, CEA, Université Paris-Saclay, Gif-sur-Yvette, France
[141]Santa Cruz Institute for Particle Physics, University of California Santa Cruz, Santa Cruz, California, USA
[142a]Departamento de Física, Pontificia Universidad Católica de Chile, Santiago, Chile
[142b]Universidad Andres Bello, Department of Physics, Santiago, Chile
[142c]Instituto de Alta Investigación, Universidad de Tarapacá, Arica, Chile
[142d]Departamento de Física, Universidad Técnica Federico Santa María, Valparaíso, Chile
[143]Universidade Federal de São João del Rei (UFSJ), São João del Rei, Brazil
[144]Department of Physics, University of Washington, Seattle, Washington, USA
[145]Department of Physics and Astronomy, University of Sheffield, Sheffield, United Kingdom

[146]*Department of Physics, Shinshu University, Nagano, Japan*
[147]*Department Physik, Universität Siegen, Siegen, Germany*
[148]*Department of Physics, Simon Fraser University, Burnaby, British Columbia, Canada*
[149]*SLAC National Accelerator Laboratory, Stanford, California, USA*
[150]*Department of Physics, Royal Institute of Technology, Stockholm, Sweden*
[151]*Departments of Physics and Astronomy, Stony Brook University, Stony Brook, New York, USA*
[152]*Department of Physics and Astronomy, University of Sussex, Brighton, United Kingdom*
[153]*School of Physics, University of Sydney, Sydney, Australia*
[154]*Institute of Physics, Academia Sinica, Taipei, Taiwan*
[155a]*E. Andronikashvili Institute of Physics, Iv. Javakhishvili Tbilisi State University, Tbilisi, Georgia*
[155b]*High Energy Physics Institute, Tbilisi State University, Tbilisi, Georgia*
[156]*Department of Physics, Technion, Israel Institute of Technology, Haifa, Israel*
[157]*Raymond and Beverly Sackler School of Physics and Astronomy, Tel Aviv University, Tel Aviv, Israel*
[158]*Department of Physics, Aristotle University of Thessaloniki, Thessaloniki, Greece*
[159]*International Center for Elementary Particle Physics and Department of Physics, University of Tokyo, Tokyo, Japan*
[160]*Department of Physics, Tokyo Institute of Technology, Tokyo, Japan*
[161]*Tomsk State University, Tomsk, Russia*
[162]*Department of Physics, University of Toronto, Toronto, Ontario, Canada*
[163a]*TRIUMF, Vancouver, British Columbia, Canada*
[163b]*Department of Physics and Astronomy, York University, Toronto, Ontario, Canada*
[164]*Division of Physics and Tomonaga Center for the History of the Universe, Faculty of Pure and Applied Sciences, University of Tsukuba, Tsukuba, Japan*
[165]*Department of Physics and Astronomy, Tufts University, Medford, Massachusetts, USA*
[166]*Department of Physics and Astronomy, University of California Irvine, Irvine, California, USA*
[167]*Department of Physics and Astronomy, University of Uppsala, Uppsala, Sweden*
[168]*Department of Physics, University of Illinois, Urbana, Illinois, USA*
[169]*Instituto de Física Corpuscular (IFIC), Centro Mixto Universidad de Valencia—CSIC, Valencia, Spain*
[170]*Department of Physics, University of British Columbia, Vancouver, British Columbia, Canada*
[171]*Department of Physics and Astronomy, University of Victoria, Victoria, British Columbia, Canada*
[172]*Fakultät für Physik und Astronomie, Julius-Maximilians-Universität Würzburg, Würzburg, Germany*
[173]*Department of Physics, University of Warwick, Coventry, United Kingdom*
[174]*Waseda University, Tokyo, Japan*
[175]*Department of Particle Physics and Astrophysics, Weizmann Institute of Science, Rehovot, Israel*
[176]*Department of Physics, University of Wisconsin, Madison, Wisconsin, USA*
[177]*Fakultät für Mathematik und Naturwissenschaften, Fachgruppe Physik, Bergische Universität Wuppertal, Wuppertal, Germany*
[178]*Department of Physics, Yale University, New Haven, Connecticut, USA*

[a]Deceased.
[b]Also at Department of Physics, King's College London, London, United Kingdom.
[c]Also at Istanbul University, Department of Physics, Istanbul, Turkey.
[d]Also at Instituto de Fisica Teorica, IFT-UAM/CSIC, Madrid, Spain.
[e]Also at Institute of Physics, Azerbaijan Academy of Sciences, Baku, Azerbaijan.
[f]Also at TRIUMF, Vancouver, British Columbia, Canada.
[g]Also at Physics Department, An-Najah National University, Nablus, Palestine.
[h]Also at Department of Physics, University of Fribourg, Fribourg, Switzerland.
[i]Also at Department of Physics and Astronomy, University of Louisville, Louisville, Kentucky, USA.
[j]Also at Departament de Fisica de la Universitat Autonoma de Barcelona, Barcelona, Spain.
[k]Also at Moscow Institute of Physics and Technology State University, Dolgoprudny, Russia.
[l]Also at Faculty of Physics, Sofia University, 'St. Kliment Ohridski', Sofia, Bulgaria.
[m]Also at Department of Physics, Ben Gurion University of the Negev, Beer Sheva, Israel.
[n]Also at Università di Napoli Parthenope, Napoli, Italy.
[o]Also at Institute of Particle Physics (IPP), Canada.
[p]Also at Bruno Kessler Foundation, Trento, Italy.
[q]Also at Department of Physics, St. Petersburg State Polytechnical University, St. Petersburg, Russia.
[r]Also at Borough of Manhattan Community College, City University of New York, New York, New York, USA.
[s]Also at Department of Physics, California State University, Fresno, USA.
[t]Also at Department of Financial and Management Engineering, University of the Aegean, Chios, Greece.
[u]Also at Centro Studi e Ricerche Enrico Fermi, Italy.

[v]Also at Department of Physics, California State University, East Bay, USA.
[w]Also at Institucio Catalana de Recerca i Estudis Avancats, ICREA, Barcelona, Spain.
[x]Also at Graduate School of Science, Osaka University, Osaka, Japan.
[y]Also at Physikalisches Institut, Albert-Ludwigs-Universität Freiburg, Freiburg, Germany.
[z]Also at University of Chinese Academy of Sciences (UCAS), Beijing, China.
[aa]Also at Yeditepe University, Physics Department, Istanbul, Turkey.
[bb]Also at Institute of Theoretical Physics, Ilia State University, Tbilisi, Georgia.
[cc]Also at CERN, Geneva, Switzerland.
[dd]Also at Joint Institute for Nuclear Research, Dubna, Russia.
[ee]Also at Hellenic Open University, Patras, Greece.
[ff]Also at Center for High Energy Physics, Peking University, China.
[gg]Also at The City College of New York, New York, New York, USA.
[hh]Also at Department of Physics, California State University, Sacramento, USA.
[ii]Also at Département de Physique Nucléaire et Corpusculaire, Université de Genève, Genève, Switzerland.
[jj]Also at Faculty of Physics, M.V. Lomonosov Moscow State University, Moscow, Russia.
[kk]Also at Institut für Experimentalphysik, Universität Hamburg, Hamburg, Germany.
[ll]Also at CPPM, Aix-Marseille Université, CNRS/IN2P3, Marseille, France.
[mm]Also at National Research Nuclear University MEPhI, Moscow, Russia.
[nn]Also at Institute for Particle and Nuclear Physics, Wigner Research Centre for Physics, Budapest, Hungary.
[oo]Also at Giresun University, Faculty of Engineering, Giresun, Turkey.
[pp]Also at Department of Physics and Astronomy, Michigan State University, East Lansing, Michigan, USA.

Paper IV

ATLAS PUB Note

ATL-PHYS-PUB-2022-019

18th March 2022

HEFT interpretations of Higgs boson pair searches in $b\bar{b}\gamma\gamma$ and $b\bar{b}\tau\tau$ final states and of their combination in ATLAS

The ATLAS Collaboration

This note presents interpretations of searches for Higgs boson pair (HH) production in the $b\bar{b}\gamma\gamma$ and $b\bar{b}\tau^+\tau^-$ final states, and of their combination, in the framework of Higgs Effective Field Theory (HEFT). The searches make use of 139 fb^{-1} of proton-proton collision data recorded with the ATLAS detector at a centre-of-mass energy of $\sqrt{s}$ = 13 TeV at the LHC. Upper limits on the HH production cross-section are set for seven HEFT benchmark models at 95% confidence level, with observed (expected) limits ranging from 50.4 (46.0) fb to 135.1 (135.1) fb. Exclusion limits are also set on two HEFT coupling parameters associated with the couplings of a Higgs boson pair with two gluons, c_{gghh}, and with a top-quark pair, c_{tthh}. Values of these parameters are excluded outside the observed (expected) ranges of $[-0.3, 0.4]$ ($[-0.3, 0.3]$) and $[-0.2, 0.6]$ ($[-0.2, 0.6]$), respectively, at 95% confidence level.

1 Introduction

The Higgs boson (H), a cornerstone of the Standard Model (SM), was discovered by the ATLAS and CMS collaborations in 2012 [1, 2]. Numerous measurements of its spin and couplings have been performed [3–5] since its discovery, showing consistency with SM predictions. The trilinear Higgs boson self-coupling, λ_{HHH}, provides direct access to the shape of the Higgs potential, and its measurement is a primary physics goal of the LHC and its forthcoming upgrade, the high-luminosity LHC. Modifications to the Higgs boson self-coupling can occur through physics phenomena beyond the SM (BSM), which can lead to an enhancement of the rate of Higgs boson pair production (HH) and modifications of the kinematic properties of the process.

Effective Field Theories (EFT) provide a generic approach to parametrise the effects of BSM physics at the high-energy scale in terms of effective couplings at the low-energy scale. Two different EFT formalisms are widely used: the SMEFT [6] and the Higgs EFT (HEFT) [7, 8]. This note focuses on the HEFT framework, where the Lagrangian is organised following the guidance of chiral perturbation theory [9] and where the low-energy dynamics of electroweak symmetry breaking are described using a non-linear realisation of $SU(2) \times U(1)$. In this formalism, anomalous Higgs boson couplings are expected to be the dominant source of new physics in the electroweak sector. Unlike in SMEFT, they are defined such to treat separately the couplings to the single Higgs boson and to a Higgs boson pair, making it more suitable for a simplified HH interpretation. Deviations from SM predictions can potentially be observed in HH production and can subsequently be interpreted in the HEFT framework.

In the SM, HH production via gluon-gluon fusion (ggF) is the dominant production process accounting for over 90% of the total production rate. At leading order (LO), it is described by the Feynman diagrams shown in Figure 1. The two diagrams interfere destructively, resulting in an HH production cross-section of $\sigma^{\text{SM}}_{\text{ggF}} = 31.05$ fb $\pm 3\%$ (PDF+α_s)$^{+6\%}_{-23\%}$ (Scale + m_{top}) [10–18], around three orders of magnitude smaller than the single Higgs boson production process.

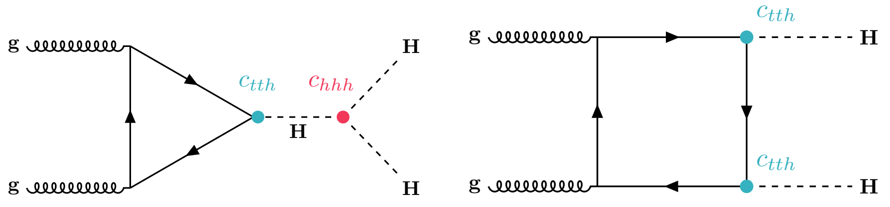

Figure 1: HEFT coupling parameters in SM-like leading-order Feynman diagrams for Higgs boson pair production through gluon-gluon fusion.

In the HEFT Lagrangian, ggF HH production is described at LO with 5 operators and their corresponding Wilson coefficients: $c_{hhh}, c_{tth}, c_{ggh}, c_{gghh}$ and c_{tthh}. The $c_{hhh} = \lambda_{HHH}/\lambda^{\text{SM}}_{HHH}$ and $c_{tth} = \lambda_{ttH}/\lambda^{\text{SM}}_{ttH}$ coefficients represent the coupling modifiers for the Higgs boson self-coupling and top-quark Yukawa coupling (λ_{ttH}). The remaining Wilson coefficients affect respectively the ggH, $ggHH$ and $ttHH$ vertex interactions and introduce the three BSM LO Feynman diagrams for ggF HH production shown in Figure 2. The HEFT Lagrangian reduces to the SM Lagrangian for $c_{hhh} = c_{tth} = 1$ and $c_{tthh} = c_{ggh} = c_{gghh} = 0$, when the Higgs boson self-coupling and top-quark Yukawa coupling have SM values and none of the BSM production modes are present. Higgs boson pair production is the most promising process to measure the Higgs boson self-coupling because it gives access to c_{hhh} at tree level. Furthermore, the HH process gives unique access to the two other Wilson coefficients, c_{gghh} and c_{tthh}. On the contrary, single Higgs boson processes have better sensitivity to the remaining two coefficients, c_{ggh} and c_{tth}. The HEFT formalism allows to interpret general searches in different BSM scenarios by simultaneously varying multiple Wilson coefficients.

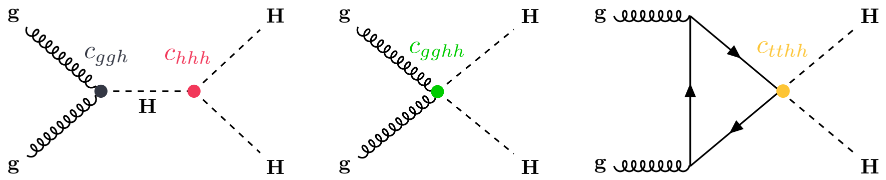

Figure 2: HEFT coupling parameters in BSM leading-order Feynman diagrams for Higgs boson pair production through gluon-gluon fusion.

Since several LO Feynman diagrams with different mass dependencies contribute to HH production, variations of the HEFT Wilson coefficients change their relative contributions and interference, thereby modifying the resulting invariant mass spectrum, m_{HH}.

Cluster analysis [19] is used to define groups of different HEFT models according to their impact on the shape of the m_{HH} distribution. At next-to-leading order (NLO), 7 HEFT benchmark (BM) models [20], defined in Table 1, describe representative shape features of the m_{HH} distribution, and can be used to explore multiple BSM scenarios. This largely reduces the number of signal points to probe while providing a wide variety of characteristic shapes of the m_{HH} distribution. Experimental constraints on the 5 HEFT couplings can rule out the existence of individual benchmark models defined by a given set of coupling values. However, many other combinations of the coupling values can give rise to similar m_{HH} shapes as in the benchmarks. Hence, the study of benchmark models still provides valuable new constraints on BSM physics.

Table 1: Values of the HEFT Wilson coefficients in the SM and in seven BSM benchmark models.

Benchmark model	c_{hhh}	c_{tth}	c_{ggh}	c_{gghh}	c_{tthh}
SM	1	1	0	0	0
BM 1	3.94	0.94	1/2	1/3	−1/3
BM 2	6.84	0.61	0.0	−1/3	1/3
BM 3	2.21	1.05	1/2	1/2	−1/3
BM 4	2.79	0.61	−1/2	1/6	1/3
BM 5	3.95	1.17	1/6	−1/2	−1/3
BM 6	5.68	0.83	−1/2	1/3	1/3
BM 7	−0.10	0.94	1/6	−1/6	1

The HH searches performed with the ATLAS Run 2 data in the $b\bar{b}\gamma\gamma$ [21] and $b\bar{b}\tau\tau$ [22] final states and their combination [23] produce constraints on the HH production cross-section and on c_{hhh}. The observed (expected) allowed range of c_{hhh} values at 95% confidence level (CL) from the combination of both channels is $-1.0 < c_{hhh} < 6.6$ ($-1.2 < c_{hhh} < 7.2$), assuming all other couplings have their SM values. In this note, a more general interpretation of these HH searches is performed, based on the HEFT framework. Upper limits on the ggF HH cross-sections are presented for the 7 benchmark models of m_{HH} shapes, and constraints on the c_{gghh} and c_{tthh} couplings are set one at a time, assuming SM values for all other couplings.

2 Data and simulation samples

The searches documented in this note use 139 fb^{-1} of pp collision data at $\sqrt{s} = 13$ TeV collected by the ATLAS experiment during the LHC Run 2 data-taking period from 2015 to 2018. The primary luminosity measurement is made by the LUCID-2 detector [24].

Both $b\bar{b}\gamma\gamma$ and $b\bar{b}\tau^+\tau^-$ search channels use a consistent set of signal Monte Carlo (MC) samples. SM non-resonant HH production via ggF is simulated at NLO precision and considering finite top-quark mass effects using the Powheg Box v2 generator [25–29] and the PDF4LHC15 parton distribution function (PDF) set [30]. Pythia 8.244 [31] is used for the parton shower and hadronisation simulation, utilising the NNPDF2.3lo [32] PDF set and the A14 tune [33]. It is prohibitively computationally expensive to simulate all of the possible variations of the Wilson coefficients described by EFTs. Instead, the m_{HH} distribution in different BSM scenarios described by HEFT can be obtained by a reweighting procedure based on the SM HH sample. As derived in Ref. [34], the NLO differential cross-section for the HH production via gluon-gluon fusion, $\mathrm{d}\sigma_{HH}/\mathrm{d}m_{HH}$, is parametrised in terms of coupling combinations as follows:

$$\begin{aligned}\frac{\mathrm{d}\sigma_{HH}}{\mathrm{d}m_{HH}} &= \mathrm{Poly}(\mathbf{A}, c_{hhh}, c_{tth}, c_{tthh}, c_{ggh}, c_{gghh}|m_{HH}) \\ &= A_1 c_{tth}^4 + A_2 c_{tthh}^2 + (A_3 c_{tth}^2 + A_4 c_{ggh}^2)\cdot c_{hhh}^2 + A_5 c_{gghh}^2 + (A_6 c_{tthh} + A_7 c_{tth} c_{hhh})\cdot c_{hhh}^2 \\ &+ (A_8 c_{tth} c_{hhh} + A_9 c_{ggh} c_{hhh})\cdot c_{tthh} + A_{10} c_{tthh} c_{gghh} + (A_{11} c_{ggh} c_{hhh} + A_{12} c_{gghh})\cdot c_{tth}^2 \\ &+ (A_{13} c_{hhh} c_{ggh} + A_{14} c_{gghh})\cdot c_{tth} c_{hhh} + A_{15} c_{ggh} c_{gghh} c_{hhh} + A_{16} c_{tth}^3 c_{ggh} \\ &+ A_{17} c_{tth} c_{tthh} c_{ggh} + A_{18} c_{tth} c_{ggh}^2 c_{hhh} + A_{19} c_{tth} c_{ggh} c_{gghh} + A_{20} c_{tth}^2 c_{ggh}^2 \\ &+ A_{21} c_{tthh} c_{ggh}^2 + A_{22} c_{ggh}^3 c_{hhh} + A_{23} c_{ggh}^2 c_{gghh},\end{aligned} \tag{1}$$

where the differential coefficients A_i are evaluated exclusively in the 240 GeV $< m_{HH} <$ 1040 GeV range in bins of 20 GeV. The binned m_{HH} distribution from simulated SM HH events can be reweighted to any point in the HEFT space using the event weights defined as:

$$w(m_{HH}) = \frac{\mathrm{d}\sigma_{HH}/\mathrm{d}m_{HH}}{\mathrm{d}\sigma_{HH}^{\mathrm{SM}}/\mathrm{d}m_{HH}} = \frac{\mathrm{Poly}(\mathbf{A}|m_{HH})}{\mathrm{Poly}^{\mathrm{SM}}(\mathbf{A}|m_{HH})}\,. \tag{2}$$

The reweighting procedure using $w(m_{HH})$ changes both the m_{HH} shape and the overall normalisation with respect to the simulated SM HH sample. To remove the normalisation effect, normalised weights

$w^{\text{norm}}(m_{HH})$ are defined as

$$w^{\text{norm}}(m_{HH}) = w(m_{HH}) \cdot \frac{\sigma_{HH}^{\text{SM}}}{\sigma_{HH}} = \frac{\text{Poly}(\mathbf{A}|m_{HH})}{\text{Poly}^{\text{SM}}(\mathbf{A}|m_{HH})} \cdot \frac{\text{Poly}^{\text{SM}}(\mathbf{A})}{\text{Poly}(\mathbf{A})}, \tag{3}$$

where inclusive A_i coefficients, derived from the full HH phase space, are used to cancel the cross-section contribution from $w(m_{HH})$.

In this note, the BSM processes are reweighted from simulated SM HH events using the event-per-event weight $w^{\text{norm}}(m_{HH})$. Events with $m_{HH} > 1040$ GeV are reweighted using the weight corresponding to the highest available m_{HH} bin with a central value of 1030 GeV. Systematic uncertainties stemming from reweighting are derived directly from events without detector response simulation (particle level) to account for possible discrepancies between the reweighted distributions and simulated distributions. The particle level m_{HH} distribution for the SM HH production and the modified m_{HH} distributions in different HEFT benchmark models are shown in Figure 3.

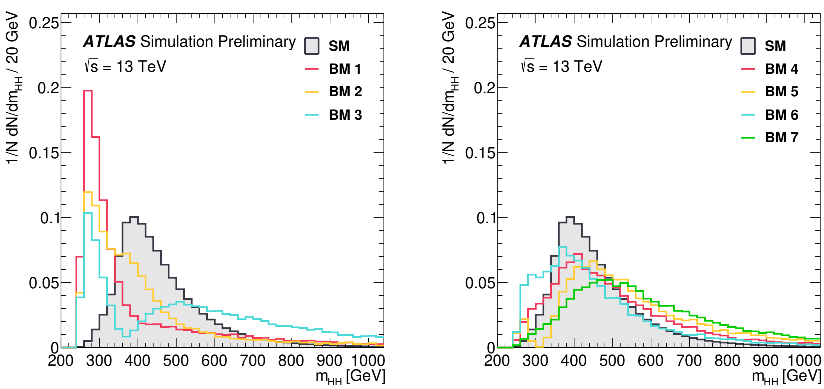

(a)

(b)

Figure 3: Particle level m_{HH} distributions for SM HH production and the HEFT benchmark models. All distributions are normalised to unity.

The SM vector-boson-fusion (VBF) HH process is simulated at LO with MadGraph5_aMC@NLO 2.60 [35] using the NNPDF3.0nlo PDF set interfaced with Pythia 8.244. In this note, the SM VBF HH process is treated as a background to all ggF HH signal configurations. Due to the small contribution of the VBF HH process to the total background, the c_{hhh} dependence of this process is neglected and c_{hhh} is therefore kept at its SM value of 1 in such simulated events and when evaluating the final results. The impact of varying the VBF process with c_{hhh} is found to change the expected limits in the combination by less than 2.4% for all benchmark models, while removing the VBF HH process altogether results in a change of less than 0.2%. The values of the 5 HEFT couplings in the simulation of the remaining SM backgrounds are also kept fixed at their SM value.

The single Higgs boson processes are simulated consistently for both the $b\bar{b}\gamma\gamma$ and $b\bar{b}\tau^+\tau^-$ channels using Powheg Box v2 with the NNPDF3.0nlo PDF set. Parton showering, hadronisation and underlying event for single Higgs boson ggF and VBF processes are simulated using Pythia 8.212 with the AZNLO tune [36] and the CTEQ6L1 PDF set [37], while for the $t\bar{t}H$ process, Pythia 8.230 with the A14 tune and the NNPDF2.3lo PDF set is used. In the $b\bar{b}\gamma\gamma$ channel, the tH and $b\bar{b}H$ production modes are also considered, as described in Ref. [38]. A combination of MC simulation and a data-driven method are used together to estimate the $\gamma\gamma$+jets background. The MC sample for the $\gamma\gamma$+jets process is generated using Sherpa 2.2.4 [39].

In the $b\bar{b}\tau^{+}\tau^{-}$ channel, the pair production of top quarks ($t\bar{t}$) and single top quark production in the t-, s- and Wt-channels are simulated using Powheg Box v2 and the NNPDF3.0nlo PDF set. The parton shower and hadronisation are performed using Pythia 8.230 with the NNPDF2.3lo PDF set using the A14 tune. The V+jets, diboson and $t\bar{t}Z$ processes are simulated using Sherpa 2.2.1, while the $t\bar{t}W$ process is simulated with Sherpa 2.2.8; the NNPDF3.0nnlo PDF set with dedicated process-specific parton shower tunes developed by the Sherpa authors is used for parton shower and hadronisation. The background contributions from quark- and gluon-initiated jets identified as hadronically decaying τ-leptons are estimated with a data-driven method.

3 Individual search channels

3.1 $HH \to b\bar{b}\gamma\gamma$

Despite the small branching fraction of the $HH \to b\bar{b}\gamma\gamma$ final state, the search benefits from an excellent di-photon mass resolution, clean di-photon triggers and relatively small backgrounds. The analysis described in Ref. [21] uses the full Run 2 dataset of 139 fb^{-1} and selects events with exactly two photons with $|\eta| < 2.37$, excluding the transition region of $1.37 < |\eta| < 1.52$ between the barrel and the endcap electromagnetic calorimeters. The invariant mass of the two leading photons, $m_{\gamma\gamma}$, must satisfy the requirement of 105 GeV $< m_{\gamma\gamma} <$ 160 GeV, and the transverse momenta of the leading and sub-leading photons must be greater than 0.35 and 0.25 times $m_{\gamma\gamma}$, respectively. Events are also required to contain two b-tagged jets, which are identified with the `DL1r` algorithm [40, 41], using the 77% efficiency working point. $t\bar{t}H$ processes with hadronic top-quark decays are rejected by requiring fewer than six central ($|\eta| < 2.5$) jets, while $t\bar{t}H$ processes with semi-leptonic top-quark decays are suppressed by rejecting events with electrons or muons. The events are classified in two, respectively low-mass and high-mass, regions according to the modified four-body mass of the di-photon plus b-tagged jets system, $m^{*}_{b\bar{b}\gamma\gamma}$, defined as $m^{*}_{b\bar{b}\gamma\gamma} = m_{b\bar{b}\gamma\gamma} - m_{b\bar{b}} - m_{\gamma\gamma} + 250$ GeV, where $m_{b\bar{b}\gamma\gamma}$ is the four-body mass and $m_{b\bar{b}}$ is the invariant mass of the two b-jets. A Boosted Decision Tree (BDT) algorithm is employed for further event classification to discriminate the SM HH signal in the high-mass region, and signals with $c_{hhh} > 1$ in the low-mass region, from the corresponding background processes. In each signal region, two classes of events are defined based on the BDT discriminant, resulting in four categories: High-Mass Tight, High-Mass Loose, Low-Mass Tight and Low-Mass Loose.

The final statistical results are then obtained from a simultaneous unbinned maximum likelihood fit to the observed $m_{\gamma\gamma}$ distribution across the four categories. The dominant continuum di-photon background, coming from $\gamma\gamma$, γ-jet and jet-jet event production, is modelled by an exponential function directly fitted to the data. The HH signal and single Higgs boson background components are modelled by a double-sided Crystal Ball function [42, 43]. No significant dependence of the $m_{\gamma\gamma}$ distribution on the HEFT parameters is found, and therefore the SM HH signal template is used for all HEFT signals. The signal reweighting is applied to model the dependence of the overall signal efficiency on the HEFT parameters in the four categories. Table 2 shows the signal efficiency of the individual HEFT benchmark models. The HH signal efficiency dependence on the c_{gghh} and c_{tthh} coupling parameters is shown in Figure 4.

Table 2: Efficiency of the HH signal selection for the SM and HEFT benchmark models within the $b\bar{b}\gamma\gamma$ signal regions, where LM and HM refer to the low- and high-mass regions, respectively, and Loose/Tight refer to the selection criteria on the BDT discriminant.

Acceptance × Efficiency [%]	HM Loose	LM Loose	HM Tight	LM Tight	Total
SM	3.2	0.6	7.7	0.4	11.9
BM 1	1.3	2.9	3.8	1.5	9.5
BM 2	1.8	2.2	4.5	1.2	9.7
BM 3	2.2	1.3	8.3	0.6	12.4
BM 4	2.9	0.7	8.6	0.4	12.6
BM 5	3.1	0.3	9.8	0.1	13.3
BM 6	2.6	1.2	7.0	0.7	11.5
BM 7	3.1	0.3	10.8	0.2	14.4

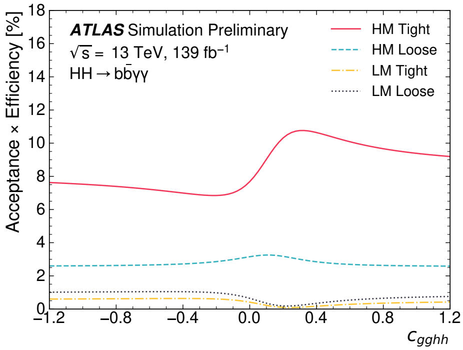

(a)

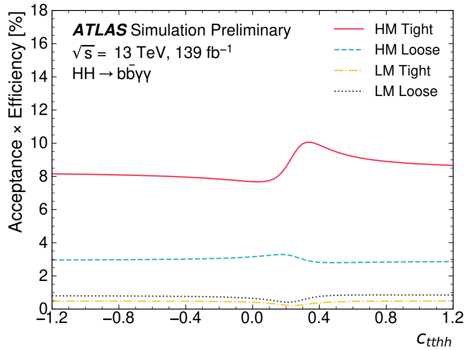

(b)

Figure 4: Efficiency of the HH signal selection for the c_{gghh} (a) and c_{tthh} (b) scans within the $b\bar{b}\gamma\gamma$ signal regions, where LM and HM refer to the low- and high-mass regions, respectively, and Loose/Tight refer to the selection criteria on the BDT discriminant.

3.2 $HH \to b\bar{b}\tau^+\tau^-$

The $b\bar{b}\tau^+\tau^-$ search channel benefits from a sizeable branching fraction and a moderate background. The analysis described in Ref. [22] uses the complete Run 2 dataset of 139 fb^{-1} and splits events into categories containing one lepton (electron or muon) and one hadronically decaying τ-lepton ($b\bar{b}\tau_{\text{lep}}\tau_{\text{had}}$), and events containing two hadronically decaying τ-leptons ($b\bar{b}\tau_{\text{had}}\tau_{\text{had}}$). The $b\bar{b}\tau_{\text{lep}}\tau_{\text{had}}$ category uses a combination of single-lepton triggers (SLT) and lepton + tau triggers (LTT), while the $b\bar{b}\tau_{\text{had}}\tau_{\text{had}}$ category utilises the single-tau and di-tau triggers. In both categories, priority is given to the single-lepton/tau triggers when the p_T of the corresponding offline object is above the p_T threshold of that trigger.

The $b\bar{b}\tau_{\text{lep}}\tau_{\text{had}}$ events are required to have exactly one lepton and exactly one hadronically decaying τ-lepton of opposite charge to the lepton. The $b\bar{b}\tau_{\text{had}}\tau_{\text{had}}$ events require exactly two hadronically decaying τ-leptons with opposite charge, and events with electrons or muons are vetoed. Both categories require two b-tagged jets (DL1r at the 77% efficiency working point) and the invariant mass of the $\tau\tau$ system (calculated using the Missing Mass Calculator [44]) to be greater than 60 GeV. Events passing these selection criteria form the $b\bar{b}\tau_{\text{lep}}\tau_{\text{had}}$ and $b\bar{b}\tau_{\text{had}}\tau_{\text{had}}$ signal regions. The $b\bar{b}\tau_{\text{lep}}\tau_{\text{had}}$ category is further split into SLT and LTT signal regions according to the trigger fired in the event.

The dominant SM backgrounds for the $b\bar{b}\tau^+\tau^-$ channel arise from top-quark, W/Z+jets, diboson, single Higgs boson and multi-jet production processes. The simulated estimates for the $t\bar{t}$ and Z+heavy-flavor jets processes are each normalised to data in a dedicated control region. For both the $b\bar{b}\tau_{\text{lep}}\tau_{\text{had}}$ and $b\bar{b}\tau_{\text{had}}\tau_{\text{had}}$ categories, fake factors for quark- and gluon-initiated jets misidentified as a hadronically decaying τ-lepton are estimated from data. For the $b\bar{b}\tau_{\text{lep}}\tau_{\text{had}}$ category, fake factors are derived for the $t\bar{t}$ and multi-jet processes, and then combined to give an overall estimation of the jet-to-τ_{had} misidentification rate.

A multivariate (MVA) classifier is trained to separate the SM HH signal from the backgrounds in each of the signal regions. For the $b\bar{b}\tau_{\text{lep}}\tau_{\text{had}}$ category, a deep neural network (NN) is trained in each of the signal regions using 11 (8) kinematic and angular input variables for SLT (LTT) events. A BDT classifier is trained for $b\bar{b}\tau_{\text{had}}\tau_{\text{had}}$ events using 5 kinematic and angular input variables. The final results are obtained through a fit to the multivariate classifier outputs in the signal regions, shown in Figures 5 and 6. The signal reweighting described in Section 2 is used to model the signal acceptance and the MVA output distributions for the different HEFT coupling configurations. Table 3 shows the signal efficiency obtained for the individual HEFT benchmark models. The signal efficiency for the c_{gghh} and c_{tthh} scans is shown in Figure 7.

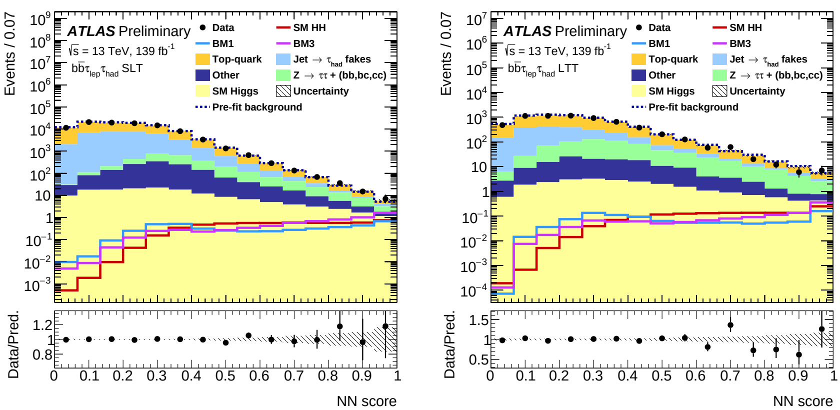

(a) (b)

Figure 5: Distributions of the $b\bar{b}\tau_{\text{lep}}\tau_{\text{had}}$ SLT (a), $b\bar{b}\tau_{\text{lep}}\tau_{\text{had}}$ LTT (b) MVA discriminant for the data, the SM backgrounds and a selection of reweighted HEFT benchmark signals.

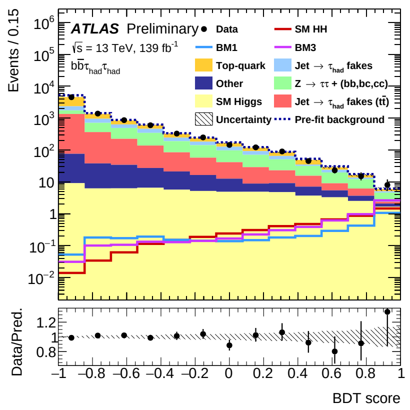

Figure 6: Distributions of the $b\bar{b}\tau_{\mathrm{had}}\tau_{\mathrm{had}}$ MVA discriminant for the data, the SM backgrounds and a selection of reweighted HEFT benchmark signals.

Table 3: Efficiency of the HH signal selection for the SM and HEFT benchmark models within the $b\bar{b}\tau^+\tau^-$ signal regions.

Acceptance × Efficiency [%]	$b\bar{b}\tau_{\mathrm{lep}}\tau_{\mathrm{had}}$ (SLT)	$b\bar{b}\tau_{\mathrm{lep}}\tau_{\mathrm{had}}$ (LTT)	$b\bar{b}\tau_{\mathrm{had}}\tau_{\mathrm{had}}$	Total
SM	4.1	1.0	4.1	9.2
BM 1	3.2	0.7	2.7	6.6
BM 2	3.3	0.8	2.9	7.0
BM 3	4.7	0.9	4.9	10.5
BM 4	4.6	1.0	4.7	10.3
BM 5	5.0	1.0	5.3	11.3
BM 6	4.0	0.9	4.0	8.9
BM 7	5.5	1.0	5.9	12.4

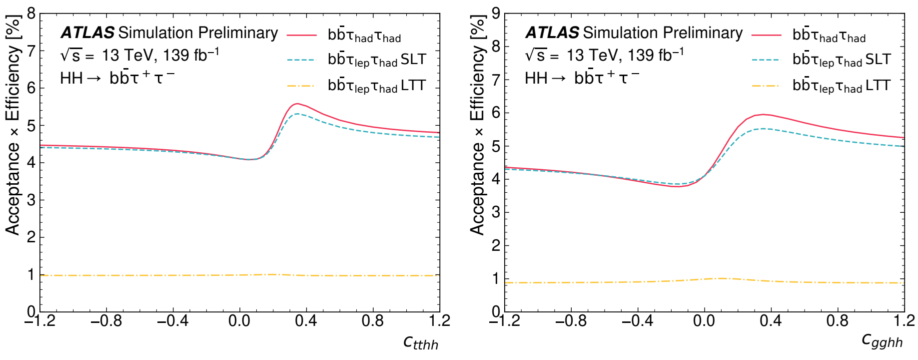

(a)

(b)

Figure 7: Efficiency of the HH signal selection for the c_{gghh} (a) and c_{tthh} (b) scans within the $b\bar{b}\tau^{+}\tau^{-}$ signal regions.

4 Systematic uncertainties

Uncertainties on the SM backgrounds are evaluated considering the data-taking conditions, the reconstruction and modelling of physics objects, and theoretical uncertainties of the simulation. These are described for the $HH \to b\bar{b}\gamma\gamma$ and $HH \to b\bar{b}\tau^+\tau^-$ searches in Ref. [21] and Ref. [22], respectively. In addition, for both search channels, uncertainties on the signal event yields from the reweighting procedure described in Section 2 must be considered. For this purpose, HH samples with 100 000 events are simulated for the 7 HEFT benchmark models and the SM HH process with the Powheg Box v2 generator [45] interfaced with Pythia 8.244 for parton showering and hadronisation. The reweighting uncertainty for each HEFT benchmark model is estimated as the difference in signal yields of the simulated benchmark sample and the reweighted sample. In all channels, the MVA is not applied when calculating the HEFT reweighting uncertainty due to the use of particle level samples for the evaluation of this uncertainty. The effect of the reweighting on the MVA shapes has been studied for each channel and signal region at reconstruction level for $c_{hhh} = 10$ and is found to be negligible. The uncertainties for each channel are summarised in Table 4. Furthermore, the acceptance uncertainties related to the choice of the strong coupling constant, α_S, the renormalisation and factorisation scales and the choice of PDF sets and parton shower model are evaluated for each HH signal configuration. Each signal acceptance uncertainty is taken as the envelope between the given signal hypothesis and the SM HH signal. In the case of the c_{gghh} and c_{tthh} couplings, the corresponding uncertainties are evaluated by comparing the simulated and reweighted samples with the coefficient values −0.5, 0.5 and 1.0, while all the other Wilson coefficients are fixed to their SM values. The envelope of the three sets of differences is defined as the uncertainty for the final fit of parameters. The uncertainties due to the choice of α_S, renormalisation and factorisation scales, the PDF sets are found to be below 5% in the $b\bar{b}\gamma\gamma$ channel and below 3% in the $b\bar{b}\tau^+\tau^-$ channel. The uncertainty due to the choice of the parton showering algorithm ranges from 2 to 15% in the $b\bar{b}\gamma\gamma$ channel while in the $b\bar{b}\tau^+\tau^-$ channel it ranges from 4 to 8%. The HEFT reweighting uncertainties are summarised in Table 5.

Table 4: Signal normalisation uncertainty due to the reweighting procedure, for each of the HEFT benchmarks. In the $b\bar{b}\gamma\gamma$ channel, the uncertainties presented are applied in both the Tight and Loose categories, separately for the low- and high-mass regions.

Channel	$b\bar{b}\gamma\gamma$		$b\bar{b}\tau^+\tau^-$		
Region	LM	HM	$b\bar{b}\tau_{\text{lep}}\tau_{\text{had}}$ (SLT)	$b\bar{b}\tau_{\text{lep}}\tau_{\text{had}}$ (LTT)	$b\bar{b}\tau_{\text{had}}\tau_{\text{had}}$
BM 1	4.9%	0.4%	14.6%	8.3%	3.8%
BM 2	2.4%	4.2%	12.6%	5.5%	3.7%
BM 3	6.1%	4.7%	9.9%	14.1%	14.8%
BM 4	5.3%	1.4%	2.1%	8.5%	2.5%
BM 5	10.8%	2.5%	8.4%	16.9%	10.0%
BM 6	2.8%	1.3%	3.3%	13.7%	2.8%
BM 7	0.3%	2.3%	1.0%	11.6%	5.9%

Following Ref. [23], in the statistical combination of the $HH \to b\bar{b}\gamma\gamma$ and $HH \to b\bar{b}\tau^+\tau^-$ searches, uncertainties related to the data-taking conditions, such as the uncertainties on the integrated luminosity and pile-up modelling, are treated as fully correlated across both channels. Systematic uncertainties related to the reconstruction and calibration of shared physics objects, such as jets and b-jets, are treated as correlated

Table 5: Normalisation uncertainties due to the reweighting procedure, for the c_{gghh} and c_{tthh} scans. In the $b\bar{b}\gamma\gamma$ channel, the uncertainties presented are applied in both the Tight and Loose categories, separately for the low- and high-mass regions.

Channel	$b\bar{b}\gamma\gamma$		$b\bar{b}\tau^+\tau^-$		
Region	LM	HM	$b\bar{b}\tau_{\text{lep}}\tau_{\text{had}}$ (SLT)	$b\bar{b}\tau_{\text{lep}}\tau_{\text{had}}$ (LTT)	$b\bar{b}\tau_{\text{had}}\tau_{\text{had}}$
c_{gghh}	9.8%	6.2%	10.5%	11.2%	21.6%
c_{tthh}	8.7%	1.6%	4.2%	10.1%	5.3%

where possible. Theoretical modelling uncertainties on both the signal and background processes, such as the QCD scale and the PDFs, are correlated where possible. Finally, HEFT reweighting uncertainties are also correlated between the two analyses. When setting exclusion limits, the dominant systematic uncertainties, which affect most the statistical combination of the $b\bar{b}\gamma\gamma$ and $b\bar{b}\tau^+\tau^-$ search channels, are found to be the modelling of top-quark backgrounds and the modelling of additional heavy-flavor jet radiation in single Higgs boson production processes.

5 Results

An interpretation of the HH searches in the $b\bar{b}\gamma\gamma$ and $b\bar{b}\tau\tau$ channels, and their combination, within the HEFT framework is performed, using a statistical framework based on the profile likelihood ratio [46]. Upper limits are set on the ggF HH production cross-section following the CL_s prescription [47], using the asymptotic approximation. The limits on $\sigma_{\text{ggF}}(HH)$ are presented for the 7 HEFT benchmark models, and constaints are set separately on the c_{gghh} and c_{tthh} couplings, assuming that all other couplings take their SM values. The contribution from SM VBF HH events is treated as a background in all limit computations.

5.1 $HH \to b\bar{b}\gamma\gamma$

The upper limits at 95% CL on the ggF HH cross-section for the different HEFT benchmarks derived in the $HH \to b\bar{b}\gamma\gamma$ channel are shown in Figure 8, and listed in Table 6. The most stringent observed (expected) upper limits are set for BM 7 at 88.9 fb (126.3 fb); the least stringent limits are set for BM 1 at 189.3 fb (293.0 fb). The expected limits are obtained assuming no ggF HH production. Figure 9 shows the upper limits at 95% CL on the ggF HH cross-section as a function of the c_{gghh} and c_{tthh} HEFT Wilson coefficients. The observed (expected) 95% CL intervals on c_{gghh} and c_{tthh} are $-0.4 < c_{gghh} < 0.5$ ($-0.5 < c_{gghh} < 0.7$), and $-0.3 < c_{tthh} < 0.8$ ($-0.4 < c_{tthh} < 0.9$), respectively.

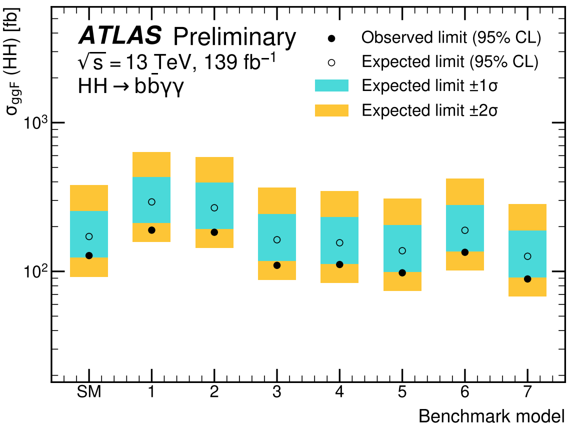

Figure 8: Observed and expected upper limits at 95% CL on $\sigma_{\text{ggF}}(HH)$ for the seven HEFT benchmarks and the SM, obtained from the $HH \to b\bar{b}\gamma\gamma$ analysis. The expected limits are obtained assuming no ggF HH production.

Table 6: Observed and expected upper limits at 95% CL on $\sigma_{\text{ggF}}(HH)$ for the seven HEFT benchmarks and the SM, obtained from the $HH \to b\bar{b}\gamma\gamma$ analysis. The expected cross-section limits assume no ggF HH production.

	Upper limits at 95% CL on the ggF HH cross-section [fb]					
Benchmark	Obs.	-2σ	-1σ	Exp.	$+1\sigma$	$+2\sigma$
SM	127.7	92.1	123.6	171.6	253.7	380.4
BM 1	189.3	157.3	211.2	293.0	429.2	632.5
BM 2	183.2	143.7	192.9	267.7	393.5	584.4
BM 3	109.8	87.6	117.6	163.2	242.2	366.4
BM 4	111.2	83.6	112.2	155.8	230.7	347.2
BM 5	97.8	73.9	99.2	137.7	204.2	308.3
BM 6	134.4	101.4	136.1	188.9	279.2	418.5
BM 7	88.9	67.8	91.0	126.3	187.4	283.1

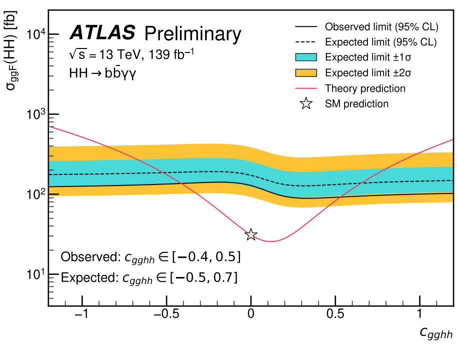

(a)

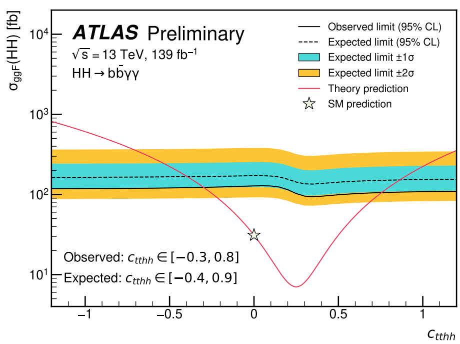

(b)

Figure 9: Upper limits at 95% CL on the ggF HH cross-section as a function of the c_{gghh} (a) and c_{tthh} (b) HEFT Wilson coefficients, obtained from the $HH \to b\bar{b}\gamma\gamma$ analysis. The expected limits are obtained assuming no ggF HH production. The theory prediction curve in red presents the scenario where all Wilson coefficients are set to their SM values except for the one under study.

5.2 $HH \to b\bar{b}\tau^+\tau^-$

The observed (expected) upper limits at 95% CL on the ggF HH cross-section for the different HEFT benchmarks derived in the $HH \to b\bar{b}\tau^+\tau^-$ channel are shown in Figure 10 and Table 7. The most stringent (expected) upper limits are set for BM 7 at 65.9 fb (51.2 fb). The least stringent limits are set for BM 2, at 203.0 fb (163.7 fb). The expected limits are obtained assuming no ggF HH production. Figure 11 shows the upper limits at 95% CL on the ggF HH cross-section as a function of the c_{gghh} and c_{tthh} HEFT Wilson coefficients. The observed (expected) 95% CL intervals on c_{gghh} and c_{tthh} are $-0.4 < c_{gghh} < 0.4$ ($-0.4 < c_{gghh} < 0.4$) and $-0.3 < c_{tthh} < 0.7$ ($-0.2 < c_{tthh} < 0.6$), respectively.

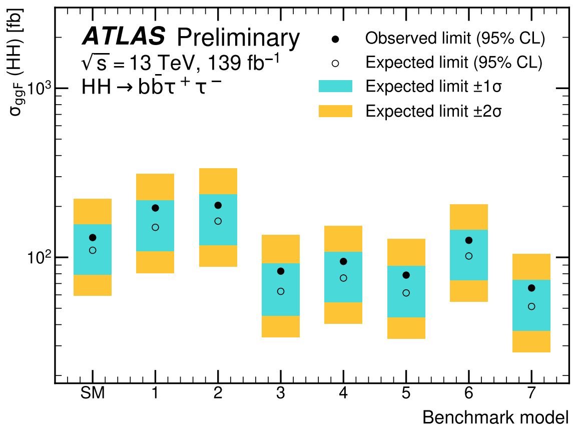

Figure 10: Observed and expected upper limits at 95% CL on $\sigma_{\text{ggF}}(HH)$ for the seven HEFT benchmarks and the SM, obtained from the $HH \to b\bar{b}\tau^+\tau^-$ analysis. The expected limits are obtained assuming no ggF HH production.

Table 7: Observed and expected upper limit at 95% CL on $\sigma_{\text{ggF}}(HH)$ for the seven HEFT benchmarks and the SM, obtained from the $HH \to b\bar{b}\tau^+\tau^-$ analysis. The expected cross-section limits assume no ggF HH production.

	Upper limits at 95% CL on the ggF HH cross-section [fb]					
Benchmark	Obs.	-2σ	-1σ	Exp.	$+1\sigma$	$+2\sigma$
SM	130.9	59.1	79.3	110.1	156.9	221.4
BM 1	195.8	80.8	108.4	150.5	216.9	312.0
BM 2	203.1	87.9	118.0	163.7	235.0	335.5
BM 3	82.8	33.8	45.3	62.9	92.1	136.3
BM 4	94.6	40.5	54.4	75.4	107.9	153.0
BM 5	78.5	33.1	44.4	61.6	89.1	129.1
BM 6	126.1	54.7	73.4	101.8	145.6	206.4
BM 7	65.9	27.5	36.9	51.2	73.5	104.8

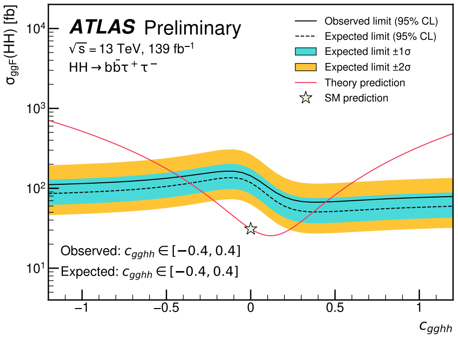

(a)

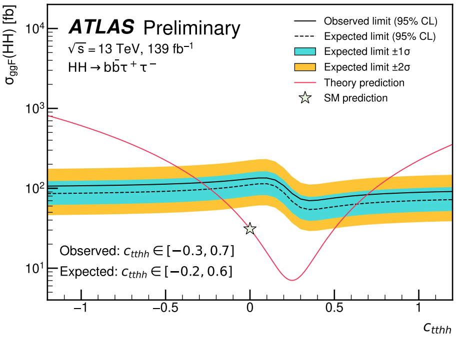

(b)

Figure 11: Upper limits at 95% CL on the ggF HH cross-section as a function of the c_{gghh} (a) and c_{tthh} (b) Wilson coefficients, obtained from the $HH \to b\bar{b}\tau^+\tau^-$ analysis. The expected limits are obtained assuming no ggF HH production. The theory prediction curve in red presents the situation where all Wilson coefficients are set to their SM values except for one under study.

5.3 Combination

The upper limits at 95% CL on the ggF HH cross-section for the combination of the $HH \to b\bar{b}\gamma\gamma$ and $HH \to b\bar{b}\tau^+\tau^-$ searches for the HEFT benchmarks are shown on Figure 12 and Table 8. The most stringent limits are set for BM 7 with an observed (expected) limit of 50.4 fb (46.0 fb) while the least stringent limits are set for BM 2 with an observed (expected) limit of 135.1 fb (135.1 fb). The expected limits are obtained assuming no ggF HH production. The combined upper limits at 95% CL on the ggF HH cross-section as a function of c_{gghh} and c_{tthh} are shown in Figure 13 and Table 9. The observed (expected) 95% CL intervals on c_{gghh} and c_{tthh} are $-0.3 < c_{gghh} < 0.4$ ($-0.3 < c_{gghh} < 0.3$) and $-0.2 < c_{tthh} < 0.6$ ($-0.2 < c_{tthh} < 0.6$), respectively.

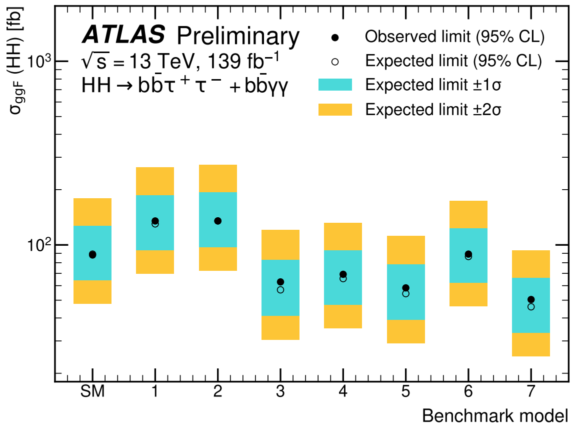

Figure 12: Observed and expected upper limits at 95% CL on $\sigma_{\text{ggF}}(HH)$ for the seven HEFT benchmarks and the SM, obtained from the combination of the $HH \to b\bar{b}\tau^+\tau^-$ and $HH \to b\bar{b}\gamma\gamma$ analyses. The expected limits are obtained assuming no ggF HH production.

Table 8: Observed and expected upper limits at 95% CL on $\sigma_{\text{ggF}}(HH)$ for the seven HEFT benchmarks and the SM, obtained from $HH \to b\bar{b}\gamma\gamma$, $HH \to b\bar{b}\tau^+\tau^-$, and their combination. The expected cross-section limits assume no ggF HH production.

Upper limits at 95% CL on the ggF HH cross-section [fb]										
	$b\bar{b}\gamma\gamma$		$b\bar{b}\tau^+\tau^-$		Combination					
Benchmark	Obs.	Exp.	Obs.	Exp.	Obs.	-2σ	-1σ	Exp.	$+1\sigma$	$+2\sigma$
SM	127.7	171.6	130.9	110.1	88.1	47.8	64.2	89.1	126.9	178.8
BM 1	189.3	293.0	195.8	150.5	135.0	69.9	93.8	130.2	186.3	264.7
BM 2	183.2	267.7	203.1	163.7	135.1	72.5	97.4	135.1	193.1	273.8
BM 3	109.8	163.2	82.8	62.9	62.9	30.6	41.0	56.9	82.7	120.8
BM 4	111.2	155.8	94.6	75.4	69.2	35.2	47.2	65.6	93.5	132.0
BM 5	97.8	137.7	78.5	61.6	58.4	29.1	39.1	54.3	78.1	111.9
BM 6	134.4	188.9	126.1	101.8	89.1	46.4	62.3	86.5	123.3	174.0
BM 7	88.9	126.3	65.9	51.2	50.4	24.7	33.2	46.0	65.8	93.3

Table 9: Allowed ranges at 95% CL for the c_{gghh} and c_{tthh} HEFT coupling coefficients, obtained from the $HH \to b\bar{b}\gamma\gamma$ and $HH \to b\bar{b}\tau^+\tau^-$ analyses, and their combination.

	$b\bar{b}\gamma\gamma$		$b\bar{b}\tau^+\tau^-$		Combination	
Wilson coefficient	Obs.	Exp.	Obs.	Exp.	Obs.	Exp.
c_{gghh}	$[-0.4, 0.5]$	$[-0.5, 0.7]$	$[-0.4, 0.4]$	$[-0.4, 0.4]$	$[-0.3, 0.4]$	$[-0.3, 0.3]$
c_{tthh}	$[-0.3, 0.8]$	$[-0.4, 0.9]$	$[-0.3, 0.7]$	$[-0.2, 0.6]$	$[-0.2, 0.6]$	$[-0.2, 0.6]$

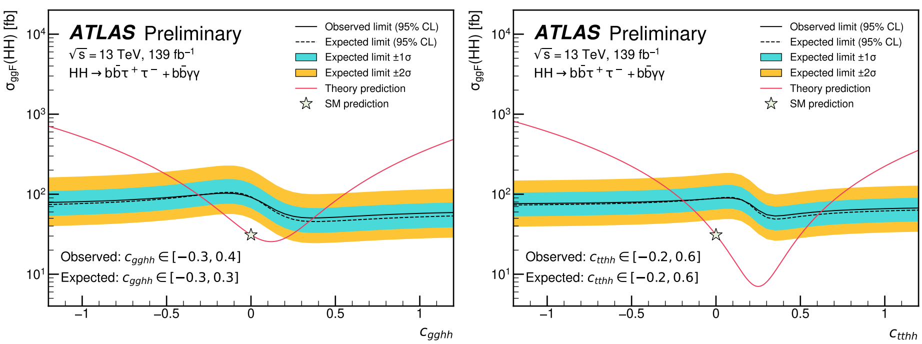

(a) (b)

Figure 13: Upper limits at 95% CL on the ggF HH cross-section as a function of the c_{gghh} (a) and c_{tthh} (b) HEFT Wilson coefficients, obtained from the combination of the $HH \to b\bar{b}\gamma\gamma$ and $HH \to b\bar{b}\tau^+\tau^-$ analyses. The expected limits are obtained assuming no ggF HH production. The theory prediction curve in red presents the situation where all Wilson coefficients are set to their SM values except for the one under study.

6 Conclusions

Exclusion limits on HEFT benchmark models with different m_{HH} shapes and on the individual HEFT coupling parameters c_{gghh} and c_{tthh} are presented, using searches for HH production in the $b\bar{b}\gamma\gamma$ and $b\bar{b}\tau^+\tau^-$ decay channels and their combination. These searches are performed with 139 fb^{-1} of pp collision Run 2 data recorded with the ATLAS detector at a centre-of-mass energy of $\sqrt{s}$ = 13 TeV at the LHC.

Using the statistical combination of the $HH \to b\bar{b}\gamma\gamma$ and $HH \to b\bar{b}\tau^+\tau^-$ search channels, upper limits at 95% CL are set on the HH production cross-section in the gluon-gluon fusion production mode for the seven HEFT benchmark models defined in Ref. [20]. The contribution from VBF HH events is treated as a background and is found to be neligible. The observed (expected) limits range from 50.4 (46.0) fb in benchmark model 7 to 135.1 (135.1) fb in benchmark model 2. Limits are also set on the HEFT Wilson coefficients c_{gghh} and c_{tthh}. Values outside the observed (expected) ranges of $[-0.3, 0.4]$ ($[-0.3, 0.3]$) and $[-0.2, 0.6]$ ($[-0.2, 0.6]$), respectively, are excluded at 95% CL for one coupling at a time, assuming that the other coefficients have their SM values.

References

[1] ATLAS Collaboration, *Observation of a new particle in the search for the Standard Model Higgs boson with the ATLAS detector at the LHC*, Phys. Lett. B **716** (2012) 1, arXiv: 1207.7214 [hep-ex] (cit. on p. 2).

[2] CMS Collaboration, *Observation of a new boson at a mass of 125 GeV with the CMS experiment at the LHC*, Phys. Lett. B **716** (2012) 30, arXiv: 1207.7235 [hep-ex] (cit. on p. 2).

[3] ATLAS Collaboration, *Study of the spin and parity of the Higgs boson in diboson decays with the ATLAS detector*, Eur. Phys. J. C **75** (2015) 476, arXiv: 1506.05669 [hep-ex], Erratum: Eur. Phys. J. C **76** (2016) 152 (cit. on p. 2).

[4] CMS Collaboration, *Constraints on the spin-parity and anomalous HVV couplings of the Higgs boson in proton collisions at* 7 *and* 8 *TeV*, Phys. Rev. D **92** (2015) 012004, arXiv: 1411.3441 [hep-ex] (cit. on p. 2).

[5] ATLAS Collaboration, *A combination of measurements of Higgs boson production and decay using up to* $139\,fb^{-1}$ *of proton–proton collision data at* $\sqrt{s} = 13$ *TeV collected with the ATLAS experiment*, ATLAS-CONF-2020-027, 2020, URL: https://cds.cern.ch/record/2725733 (cit. on p. 2).

[6] B. Grzadkowski, M. Iskrzynski, M. Misiak and J. Rosiek, *Dimension-Six Terms in the Standard Model Lagrangian*, JHEP **10** (2010) 085, arXiv: 1008.4884 [hep-ph] (cit. on p. 2).

[7] R. Alonso, M. Gavela, L. Merlo, S. Rigolin and J. Yepes, *The Effective Chiral Lagrangian for a Light Dynamical "Higgs Particle"*, Phys. Lett. B **722** (2012) 330, arXiv: 1212.3305 [hep-ph] (cit. on p. 2).

[8] G. Buchalla, O. Catà and C. Krause, *Complete Electroweak Chiral Lagrangian with a Light Higgs at NLO*, Nucl. Phys. B **880** (2014) 552, arXiv: 1307.5017 [hep-ph], Erratum: Nucl. Phys. B **913** (2016) 475 (cit. on p. 2).

[9] G. Buchalla, O. Catá and C. Krause, *On the Power Counting in Effective Field Theories*, Phys. Lett. B **731** (2014) 80, arXiv: 1312.5624 [hep-ph] (cit. on p. 2).

[10] S. Dawson, S. Dittmaier and M. Spira, *Neutral Higgs boson pair production at hadron colliders: QCD corrections*, Phys. Rev. D **58** (1998) 115012, arXiv: hep-ph/9805244 (cit. on p. 2).

[11] S. Borowka et al., *Higgs Boson Pair Production in Gluon Fusion at Next-to-Leading Order with Full Top-Quark Mass Dependence*, Phys. Rev. Lett. **117** (2016) 012001, arXiv: 1604.06447 [hep-ph], Erratum: Phys. Rev. Lett. **117** (2016) 079901 (cit. on p. 2).

[12] J. Baglio et al., *Gluon fusion into Higgs pairs at NLO QCD and the top mass scheme*, Eur. Phys. J. C **79** (2019) 459, arXiv: 1811.05692 [hep-ph] (cit. on p. 2).

[13] D. de Florian and J. Mazzitelli, *Higgs Boson Pair Production at Next-to-Next-to-Leading Order in QCD*, Phys. Rev. Lett. **111** (2013) 201801, arXiv: 1309.6594 [hep-ph] (cit. on p. 2).

[14] D. Y. Shao, C. S. Li, H. T. Li and J. Wang, *Threshold resummation effects in Higgs boson pair production at the LHC*, JHEP **07** (2013) 169, arXiv: 1301.1245 [hep-ph] (cit. on p. 2).

[15] D. de Florian and J. Mazzitelli, *Higgs pair production at next-to-next-to-leading logarithmic accuracy at the LHC*, 2015, arXiv: 1505.07122 [hep-ph] (cit. on p. 2).

[16] M. Grazzini et al., *Higgs boson pair production at NNLO with top quark mass effects*, JHEP **05** (2018) 059, arXiv: 1803.02463 [hep-ph] (cit. on p. 2).

[17] J. Baglio et al., *$gg \to HH$: Combined uncertainties*, Phys. Rev. D **103** (2021) 056002, arXiv: 2008.11626 [hep-ph] (cit. on p. 2).

[18] J. Alison et al., *Higgs boson potential at colliders: Status and perspectives*, Rev. Phys. **5** (2020) 100045, ed. by B. Di Micco, M. Gouzevitch, J. Mazzitelli and C. Vernieri, arXiv: 1910.00012 [hep-ph] (cit. on p. 2).

[19] A. Carvalho et al., *Higgs Pair Production: Choosing Benchmarks With Cluster Analysis*, JHEP **04** (2016) 126, arXiv: 1507.02245 [hep-ph] (cit. on p. 3).

[20] M. Capozi and G. Heinrich, *Exploring anomalous couplings in Higgs boson pair production through shape analysis*, JHEP **03** (2020) 091, arXiv: 1908.08923 [hep-ph] (cit. on pp. 3, 19).

[21] ATLAS Collaboration, *Search for Higgs boson pair production in the two bottom quarks plus two photons final state in pp collisions at $\sqrt{s} = 13$ TeV with the ATLAS detector*, (2021), arXiv: 2112.11876 [hep-ex] (cit. on pp. 3, 6, 11).

[22] ATLAS Collaboration, *Search for resonant and non-resonant Higgs boson pair production in the $b\bar{b}\tau^+\tau^-$ decay channel using 13 TeV pp collision data from the ATLAS detector*, ATLAS-CONF-2021-030, 2021, URL: https://cds.cern.ch/record/2777236 (cit. on pp. 3, 7, 11).

[23] ATLAS Collaboration, *Combination of searches for non-resonant and resonant Higgs boson pair production in the $b\bar{b}\gamma\gamma$, $b\bar{b}\tau^+\tau^-$ and $b\bar{b}b\bar{b}$ decay channels using pp collisions at $\sqrt{s} = 13$ TeV with the ATLAS detector*, ATLAS-CONF-2021-052, 2021, URL: https://cds.cern.ch/record/2786865 (cit. on pp. 3, 11).

[24] G. Avoni et al., *The new LUCID-2 detector for luminosity measurement and monitoring in ATLAS*, JINST **13** (2018) P07017 (cit. on p. 4).

[25] K. Hamilton, P. Nason, E. Re and G. Zanderighi, *NNLOPS simulation of Higgs boson production*, JHEP **10** (2013) 222, arXiv: 1309.0017 [hep-ph] (cit. on p. 4).

[26] K. Hamilton, P. Nason and G. Zanderighi, *Finite quark-mass effects in the NNLOPS POWHEG+MiNLO Higgs generator*, JHEP **05** (2015) 140, arXiv: 1501.04637 [hep-ph] (cit. on p. 4).

[27] S. Alioli, P. Nason, C. Oleari and E. Re, *A general framework for implementing NLO calculations in shower Monte Carlo programs: the POWHEG BOX*, JHEP **06** (2010) 043, arXiv: 1002.2581 [hep-ph] (cit. on p. 4).

[28] P. Nason, *A new method for combining NLO QCD with shower Monte Carlo algorithms*, JHEP **11** (2004) 040, arXiv: hep-ph/0409146 (cit. on p. 4).

[29] S. Frixione, P. Nason and C. Oleari,
Matching NLO QCD computations with parton shower simulations: the POWHEG method,
JHEP **11** (2007) 070, arXiv: 0709.2092 [hep-ph] (cit. on p. 4).

[30] J. Butterworth et al., *PDF4LHC recommendations for LHC Run II*, J. Phys. G **43** (2016) 023001,
arXiv: 1510.03865 [hep-ph] (cit. on p. 4).

[31] T. Sjöstrand, S. Mrenna and P. Skands, *A brief introduction to PYTHIA 8.1*,
Comput. Phys. Commun. **178** (2008) 852, arXiv: 0710.3820 [hep-ph] (cit. on p. 4).

[32] R. D. Ball et al., *Parton distributions with LHC data*, Nucl. Phys. B **867** (2013) 244,
arXiv: 1207.1303 [hep-ph] (cit. on p. 4).

[33] ATLAS Collaboration, *ATLAS Pythia 8 tunes to* 7 *TeV data*, ATL-PHYS-PUB-2014-021, 2014,
URL: https://cds.cern.ch/record/1966419 (cit. on p. 4).

[34] G. Buchalla, M. Capozi, A. Celis, G. Heinrich and L. Scyboz, *Higgs boson pair production in non-linear Effective Field Theory with full m_t-dependence at NLO QCD*, JHEP **09** (2018) 057,
arXiv: 1806.05162 [hep-ph] (cit. on p. 4).

[35] J. Alwall et al., *The automated computation of tree-level and next-to-leading order differential cross sections, and their matching to parton shower simulations*, JHEP **07** (2014) 079,
arXiv: 1405.0301 [hep-ph] (cit. on p. 5).

[36] ATLAS Collaboration, *Measurement of the Z/γ^* boson transverse momentum distribution in pp collisions at $\sqrt{s}$ = 7 TeV with the ATLAS detector*, JHEP **09** (2014) 145,
arXiv: 1406.3660 [hep-ex] (cit. on p. 6).

[37] J. Pumplin et al.,
New Generation of Parton Distributions with Uncertainties from Global QCD Analysis,
JHEP **07** (2002) 012, arXiv: hep-ph/0201195 (cit. on p. 6).

[38] ATLAS Collaboration, *Combined measurements of Higgs boson production and decay using up to* 80 *fb^{-1} of proton–proton collision data at $\sqrt{s}$ = 13 TeV collected with the ATLAS experiment*,
Phys. Rev. D **101** (2020) 012002, arXiv: 1909.02845 [hep-ex] (cit. on p. 6).

[39] E. Bothmann et al., *Event generation with Sherpa 2.2*, SciPost Phys. **7** (2019) 034,
arXiv: 1905.09127 [hep-ph] (cit. on p. 6).

[40] ATLAS Collaboration, *ATLAS b-jet identification performance and efficiency measurement with $t\bar{t}$ events in pp collisions at $\sqrt{s}$ = 13 TeV*, Eur. Phys. J. C **79** (2019) 970,
arXiv: 1907.05120 [hep-ex] (cit. on p. 6).

[41] ATLAS Collaboration,
Optimisation and performance studies of the ATLAS b-tagging algorithms for the 2017-18 LHC run,
ATL-PHYS-PUB-2017-013, 2017, URL: https://cds.cern.ch/record/2273281 (cit. on p. 6).

[42] M. Oreglia, *A Study of the Reactions $\psi' \to \gamma\gamma\psi$*, SLAC-R-236, PhD thesis, 1980,
URL: http://www.slac.stanford.edu/pubs/slacreports/slac-r-236.html
(cit. on p. 6).

[43] ATLAS Collaboration, *Search for scalar diphoton resonances in the mass range* 65-600 *GeV with the ATLAS detector in pp collision data at $\sqrt{s}$ = 8 TeV*, ATLAS-CONF-2014-031, 2014,
URL: https://cds.cern.ch/record/1706244 (cit. on p. 6).

[44] A. Elagin, P. Murat, A. Pranko and A. Safonov,
A new mass reconstruction technique for resonances decaying to $\tau\tau$,
Nucl. Instrum. Meth. A **654** (2011) 481, arXiv: 1012.4686 [hep-ex] (cit. on p. 8).

[45] G. Heinrich, S. P. Jones, M. Kerner and L. Scyboz,
A non-linear EFT description of $gg \to HH$ at NLO interfaced to POWHEG, JHEP **10** (2020) 021,
arXiv: 2006.16877 [hep-ph] (cit. on p. 11).

[46] G. Cowan, K. Cranmer, E. Gross and O. Vitells,
Asymptotic formulae for likelihood-based tests of new physics, Eur. Phys. J. C **71** (2011) 1554,
arXiv: 1007.1727 [physics.data-an] (cit. on p. 12), Erratum: Eur. Phys. J. C **73** (2013) 2501.

[47] A. L. Read, *Presentation of search results: the CL_S technique*, J. Phys. G **28** (2002) 2693
(cit. on p. 12).

This thesis describes different analyses of data from proton-proton collisions at a center-of-mass energy of 13 TeV recorded by the ATLAS detector during Run 2 of the Large Hadron Collider.

All the searches for beyond Standard Model physics presented in this thesis contain *beauty* quarks from the decay of Higgs bosons or top quarks. These particles are detected using the so-called b-tagging algorithms which are trained using simulated events and therefore need to be calibrated in data. A search for the supersymmetric partner of the top quark and two searches for beyond the Standard Model Higgs bosons are presented. The nature of these beyond the Standard Model particles is strongly influenced by the *breaking* of the supersymmetry or electroweak *symmetry*, respectively. Hence the title, *The Beauty in Broken Symmetries,* nicely encompasses the work that is presented in this thesis.

Laura Pereira Sánchez
was born in Barcelona, Spain. She studied a Bachelor in Physics and a Masters in Particle Physics, Astrophysics and Cosmology at the Universitat Autònoma de Barcelona. Between 2018-2023, Laura pursued a PhD at Stockholm University with the ATLAS Collaboration.

ISBN 978-91-8014-250-2

Department of Physics

Stockholm University